Habilitation à Diriger des Recherches

présentée devant

l'Institut Polytechnique de Grenoble

par

Michel GAY

Equipe Sigmaphy
Laboratoire Grenoble Image Parole Signal Automatique

Processing of optic and radar images

Application in satellite remote sensing of snow, ice and glaciers

Présentée le 25 septembre 2015 devant le jury constitué de :

Rapporteurs :

Madame Monique Bernier	Professeure, INRS, Canada
Monsieur Eric Pottier	Professeur, Université de Rennes
Monsieur Philippe Réfrégier	Professeur, Ecole centrale de Marseille

Examinateurs :

Monsieur Mark Simons	Professeur, California Institute of Technology, Pasadena
Monsieur Didier Massonnet	Ingénieur en Chef de l'Armement, Ingénieur CNES, Toulouse
Monsieur Jocelyn Chanussot	Professeur, Institut National Polytechnique de Grenoble

Table des matières

Chapitre 1

Synthèse des activités de recherche et d'encadrement

Ce document présente une synthèse de mes activités de recherche depuis la soutenance de ma thèse en 1999. L'activité rapportée ici est celle d'un ingénieur de recherche, et donc s'est déroulée en parallèle d'une activité "technique" comprenant des taches d'instrumentation en laboratoire, d'instrumentation de plateformes en montagne, de raids scientifiques sur les calottes polaires, d'élaboration de projets scientifiques, d'organisation d'équipes ou d'ordre administratif. Je suis Ingénieur de recherche CNRS depuis 2004 affecté au laboratoire Gipsa-lab, une unité mixte de recherche du CNRS, de Grenoble-INP, de l'université Joseph Fourier et de l'université Stendhal. Ce laboratoire (d'environ 400 personnes), conventionné avec l'INRIA, l'Observatoire de Grenoble et l'université Pierre Mendès France, est pluridisciplinaire et développe des recherches fondamentales et finalisées sur les signaux et les systèmes complexes.

Lors de la préparation de ma thèse (mi-temps 1995-99) au LGGE, je me suis intéressé au traitement des images de microstructures de la neige, du névé et de la glace. C'est assez naturellement que j'ai rejoint le laboratoire LIS devenu Gipsa-lab pour y développer des activités de traitement des images Radar à Synthèse d'Ouverture (RSO) appliqué aux milieux naturels neige, glace et glaciers. Etant le premier à générer un interférogramme différentiel des glaciers des Alpes, j'ai continué à travailler sur la phase interférométrique pour extraire des informations de déplacement et valider ces méthodes sur le glacier d'Argentière (massif du Mont-Blanc) qui présente l'énorme avantage de se déplacer de quelques centimètres par jour. Ces activités m'ont amené à développer, en collaboration avec les laboratoires LISTIC, LTCI et IETR, des méthodes plus générales pour extraire des informations dans les images RSO.

Ma formation initiale en électronique, puis de doctorat en physique m'ont amené à mettre à profit mes connaissances en traitement d'images et des signaux, en électromagnétisme, en calcul numérique, en informatique et en physique de la neige et de la glace pour étudier les problèmes de traitement des images RSO appliqués à la glace, aux glaciers et à la neige.

Bref Curriculum vitae

Nom patronyme : GAY
Prénom : Michel
Nationalité : Française.
Date/lieu de naissance : 12 juillet 1957 à Champigny sur Marne (94)
Situation familiale : Divorcé, un enfant, remarié.
Fonction actuelle : Ingénieur de recherche CNRS affecté au laboratoire Gipsa-lab.
11 rue des Mathématiques
38402 Saint Martin d'Hères
email : michel.gay@gipsa-lab.grenoble-inp.fr
Tél. : +33 476 826 260

Diplômes

1975 Baccalauréat d'électronique au lycée technique de Champigny sur Marne.

1977 DUT d'Electronique de l'Institut Universitaire de Technologie de Montpellier.

1983 Maîtrise E.E.A. à l'Université de Montpellier.

1987 Ingénieur en Micro-Electronique, de l'Université de Montpellier (ISIM).

1993 DEA de Sciences Physiques de l'Université Joseph Fourier de Grenoble.

1999 Docteur en Physique de l'Université Joseph Fourier de Grenoble.

Activités professionnelles

1979-80 Technicien en microscopie électronique à l'Institut de Botanique de Montpellier.

1983-85 Enseignant en Physique au lycée technique Le Clôt Banet de Perpignan.

1985-87 Formation professionnelle d'ingénieur à l'ISIM.

1987-88 Ingénieur à la société USSI de Pierrelatte, France.

1988-94 Ingénieur d'étude au CEMAGREF de Grenoble.

1994-03 Ingénieur au Laboratoire de Glaciologie et Géophysique de l'Environnement.

2004... Ingénieur de Recherche CNRS (LIS, puis GIPSA-lab). Les activités de recherche que je développe comprennent deux axes :

1. Le traitement des signaux et des images satellitaires Radar à Synthèse d'Ouverture (RSO) et la mise au point de nouveaux algorithmes permettant d'extraire des informations dans les images haute résolution spatiale.
2. La télédétection qualitative et quantitative qui a pour objectif de mettre au point des méthodes innovantes pour suivre l'évolution des glaciers ("blancs" et "rocheux") et de développer un procédé d'assimilation de données RSO, pour contraindre un modèle physique d'évolution de la neige.

1.1 Activités et collaborations nationales

1.1.1 Encadrements

Encadrement de thèses

2003-2007 Gabriel Vasile. *Imagerie radar à synthèse d'ouverture interférométrique et polarimétrique. Application au suivi des glaciers alpins.* Soutenue le 20 juillet 2007 à Annecy. Ecole doctorale : SISEO. Directeurs : Pr. P. Bolon (30%, LISTIC), Pr. V. Buzuloiu (30%, Univ. Bucarest), E. Trouvé (30%, LISTIC), **M. Gay (10%, LIS)**.

2005-2008 Lionel Bombrun. *Développement d'outils et de méthodes de télédétection spatiale optique et radar nécessaire à la haute résolution spatiale.* Soutenue le 18 novembre 2008 à Grenoble. Ecole doctorale : EEATS. Directeurs : Pr. J. Mars (10%, LIS), **M. Gay (90%, LIS)**.

2009-2012 Olivier Harant. *Méthodes statistiques en télédétection RSO polarimétrique haute résolution pour la modélisation et le suivi temporel des glaciers.* Soutenue le 20 juillet 2012 à 2012 à Grenoble. Ecole doctorale : MATISSE. Directeurs : Pr. L. Ferro-Famil (70%, IETR), **M. Gay (30%, GIPSA)**.

2010-2013 Fanny Ponton. *Correction des effets atmosphériques en interférométrie radar par fusion de données.* Soutenue le 22 Novembre 2013 à L'Université Joseph Fourier, Grenoble I. Ecole doctorale : TUE. Directeurs : Ph. A. Walpersdorf (35%, IsTerre), Pr. E. Trouvé (30%, LISTIC), **M. Gay (35%, GIPSA)**.

2010-2014 Xuan Vu Phan. *Télédétection RSO polarimétrique et interférométrique pour la caractérisation de la neige et de son évolution temporelle.* Soutenue le 21 mars 2014 à Grenoble. Ecole doctorale : MATISSE. Directeurs : Pr. L. Ferro-Famil (10%, IETR, Rennes), M. Dumont (10%, CEN Grenoble), **M. Gay (80%, GIPSA)**.

2010-2014 Thomas Echelard. *Détection et quantification des mouvements de surface du pergélisol par imagerie aérienne et sateliitaire.* Soutenue le 4 avril 2014 à Grenoble. Ecole doctorale : TUE. Directeurs : Pr. P. Schoneich (50%, IGA), **M. Gay (50%, GIPSA)**

Encadrement de Post-doc

2009-2010 Lionel Bombrun. *Processus stochastiques pour l'étude de la rétrodiffusion polarimétrique radar.* En collaboration avec G. Vasilé (GIPSA) et J.P. Ovarlez (SONDRA / ONERA).

2009-2010 Felix Totir. *Estimation paramétrique et segmentation optimale du fouillis radar non gaussien dans les images RSO multi-variées à haute résolution spatiale.* En collaboration avec G. Vasilé (GIPSA).

Encadrement de master

2002 Agnès Ferrié. *Potentiel de l'nterférométrie RSO pour l'établissement des champs de vitesse et de taux de déformation en surface des glaciers alpins.* DEA de l'Université Joseph Fourier-Grenoble I.

2003 Laurent Bousquet. *Etude de la dynamique des glaciers par télédétection spatiale.* DEA de l'Université Pierre et Marie Curie - Paris 6.

2005 Mathieu Desbazeille. *Représentations temps-fréquence appliquées à des signaux de bilan de masse de glaciers.* Master Recherche EEATS Grenoble I.

2005 Guillaume Gelabert . *Etude du mouvement des glaciers à l'aide d'une chaîne interférométrique RSO.* Master Signal, Télécommunication et Image ENST de Bretagne.

2005 Tarek Habib. *Segmentation of high resolution satellite images : Application to the Alpine lake detection.* Master Signal, Télécommunication et Image ENST de Bretagne.

2007 Loic Moreau. *Calculs de projections des vitesses 3D à partir d'images interférométriques RSO satellitaires.* Master Recherche EEATS-SIPT Grenoble I.

2008 Bertrand Coppa. *Remote sensing techniques for the retrieval of snow parameters.* Master Recherche EEATS-SIPT Grenoble I.

2008 Olivier Harant. *Méthodes polarimétriques et corrélation sur des images radar ENVISAT.* Master Recherche ETI-CPE Lyon I.

2009 Quentin Barthélemy. *Traitements des signaux RSO multidimensionnels pour l'estimation de l'équivalence en eau du manteau neigeux par télédétection radar.* Master Recherche EEATS-SIPT Grenoble I.

2010 Xuan-Vu Phan. *Change Detection in Polarimetric Synthetic Aperture Radar Imagery.* Master Recherche SIC-ENSEA Cergy Pontoise.

1.1.2 Rayonnement scientifique, prix et récompenses

1993 : Sapiteur pour une expertise d'une usine de « canon » à neige à Val Thorens.

2004 : Membre du comité d'expert du CNES dans le groupe GT4 Géologie pour le programme ORFEO Pléiade, Cosmo- Skymed.

2004 : Membre du GDR-ISIS, membre de la société IEEE.

2010 : Représentant au sein de l'OSUG (Observatoire des Sciences de l'Univers de Grenoble) pour l'équipe Sigmaphy.

2014 : Conférence aux journées "Les fondamentales du CNRS" organisées en partenariat avec "Le Monde".

Prix et récompenses :

1992 : 2^{nd} prix collaboration Laboratoire-Entreprise délivré par la Banque Populaire de la Région Dauphinoise.

2012 : Attribution du Cristal 2012 (INS2I) du CNRS.

1.1.3 Activités administratives et responsabilités collectives

2006-2010 Membre élu ITA au conseil de laboratoire du LIS.

2010, 2014 Membre du groupe national d'experts de la BAP E dans le cadre des campagnes d'avancement ITA/CNRS.

2011-2015 Membre élu (suppléant) ITA au Conseil De Laboratoire de GIPSA-lab.

1.1.4 Collaborations nationales

Organisation d'une conférence nationale

2010 Co-organisateur des "Journées ateliers Aussois" : échanges scientifiques sur les aspects méthodologiques et applicatifs du projet ANR EFIDIR : Extraction et Fusion d'Informations pour la mesure de Déplacement par Imagerie Radar (50 participants).

Depuis 1999, j'ai initié et/ou participé aux collaborations scientifiques suivantes :

PRANE : Ouvrages de Protection soumis à l'Action de la Neige.
Période : 2002-2004
Qualité : Scientifique CEMAGREF.

ACI : MEGATOR, Mesure de l'Evolution des Glaciers Alpins par Télédétection Optique et Radar.
Partenaires : LISTIC, LIS, LTCI, MAP-PAGE.
Période : 2004-2007
Qualité : Scientifique LIS.

Pôle Grenoblois sur les Risques Naturels : Développements méthodologiques pour la surveillance des glaciers par imagerie radar aéroportée et satellitaire et par GPR (Ground Penetrating Radar).
Partenaires : GIPSA, IsTerre.
Période : 2006-2007
Qualité : Scientifique GIPSA.

Fondation MAIF : Analyse des risques liés au permafrost.
Partenaires : GIPSA, IGA.
Période : 2007-2010
Qualité : Scientifique GIPSA.

ANR-MDCO : Extraction, Fusion of Information for ground displacement measurements with Radar Imagery.
Partenaires : LISTIC, LTCI, IETR, GIPSA, LGIT, LG-ENS Paris.
Période : 2008-2012
Qualité : Scientifique GIPSA.

Région Rhône-Alpes (CIBLE) : Développement de mesures combinées GPS-radar satellitaire pour la correction des artefacts atmosphériques dans des images satellitaires haute résolution.
Partenaires : LGIT, LISTIC, GIPSA.
Période : 2010-2013
Qualité : Scientifique GIPSA.

OSUG@2020 : Analyse de la déformation par Géodésie spatiale nouvelle génération.
Partenaires : IsTerre, GIPSA.
Période : 2012-2013
Qualité : Scientifique GIPSA.

OSUG@2020 : Localisation des chutes de séracs et des écoulements sous-glaciaires par ondes sismiques.
Partenaires : GIPSA, IsTerre.
Période : 2012-2013
Qualité : Scientifique GIPSA.

PEPS : Estimateurs Non Linéaires et Localisation de Sources en Aveugle : caractérisation d'un milieu dispersif (la glace) à partir de l'écoute passive du glacier d'Argentière.
Partenaires : GIPSA, IETR, University of Tromso, Dpt. Physics, Norway.
Période : 2013-2014
Qualité : Scientifique GIPSA.

TOSCA : Caractérisation et Evolution Spatio-Temporelle d'Environnements Neigeux et de Glaciers.
Partenaires : IETR, GIPSA, LISTIC, IPGS, University of Tromso, Dpt. Physics, Norway.
Période : 2013-2016
Qualité : Scientifique GIPSA.

1.2 Activités et collaborations internationales

1.2.1 Activités au sein de revues ou manifestations scientifiques

Je suis relecteur d'articles pour la revue Société Française de Photogrammétrie et de Télédétection et la revue IEEE-JSTARS.

Organisation d'une conférence internationale

2011 : Co-organisateur, avec E.Trouvé Professeur de l'Université de Savoie, et V. Pinel, chercheur IRD, de l'Ecole de Physique des Houches. Thème : "Extraction and Fusion of Information for Displacement measurement from RSO Imagery" (80 participants).

1.2.2 Collaborations scientifiques

INTERREG II : Amélioration des techniques paravalanches dans les régions alpines.
Partenaires : CEMAGREF, CEN, Suisse
Période : 1998-2000, Financement : 438 $kEuros$
Qualité : Scientifique CEMAGREF.

Glaciorisk : Surveillance et prévention des risques glaciologiques extrême dans les montagnes européennes.
http ://glaciorisk.grenoble.cemagref.fr/contacten.htm
Partenaires : CEMAGREF, ONF-RTM, LGGE-CNRS,, CNR-IRPI, University of OSLO, Norwegian Water Ressources and Energy Directorate, University of Iceland, University of Salzburg, VAW-ETHZ, SFP-Valais.
Période : 2001-2003, Financement : 900 $kEuros$
Qualité : Leader CEMAGREF.

INTERREG : PermaNET, Permafrost monitoring NETwork.
http ://www.permanet-alpinespace.eu
Partenaires : 13
Période : 2008-2011, Financement : 3.3 $MEuros$
Qualité : Scientifique GIPSA.

INTERREG : GlaRiskALp, Glacial Risks in the Alps.
http ://www.fondazionemontagnasicura.org/fr/archives-projets/le-projet-glariskalp
Partenaires : Fondation Montagne, CNR-IRPI, Université de Savoie (Laboratoire LISTIC) et CNRS France (Laboratoires LGGE, GIPSA, EDYTEM).
Période : 2010-2013, Financement : 1.8 $MEuros$
Qualité : Scientifique GIPSA.

1.3 Production scientifique depuis 1998

1.3.1 Synthèse

— 30 publications dans des revues internationales avec comité de lecture.
— 63 communications internationales avec actes et comité de lecture.
— 19 communications nationales sans actes.
— 21 rapports techniques.
— 6 interventions dans les médias.

1.3.2 Détails

Journaux à comité de lecture :

[30] X.V. Phan, L. Ferro-Famil, M. Gay, Y. Durand, S. Allain, and G. D'Urso, 1D-Var multilayer assimilation of X-band SAR data into a detailed snowpack model. *Cryopsphere, 8, p.1975-1987, 2014.*

[29] F. Ponton, E. Trouvé, M. Gay, A. Walpersdorf, R. Fallourd, J.M. Nicolas, F. Vernier, J.L. Mugnier, Observation of the Argentière Glacier Flow, Variability from 2009 to 2011 by TerraSAR-X and GPS Displacement Meausrements. *IEEE-JSTARS vo. 7, N° 8, 2014.*

[28] M. Gay, M. De Angelis, J.L. Lacoume, Dating a tropical ice core by time-frequency analysis of ion concentration depth profiles *Climate of the Past, 2014, n° 10, p.1-15.*

[27] T. Echelard, J.M. Krysiecki, M. Gay, P. Schoeneich, Rockglacier movements dy Differential Interferometric Synthetic Aperture Radar D-INSAR in French Alps using ERS archive data. *Géomophologie : relief, processus, environnement, 2013, n° 3, p. 231-242.* In review.

[26] E. Trouvé, J.M. Nicolas, L. Ferro-Famil, M. Gay, V. Pinel, M.P. Doin, N. Meger, C. Laserre, G. Mauris, F. Vernier, R. Fallourd, Y. Yan, O. Harant, R. Jolivet, Extraction et Fusion d'Informations pour la mesure de Déplacements par Imagerie Radar. *Traitement du Signal , 2011.N° 3-4, pp. 375-416.*

[25] R. Fallourd, O. Harant, E. Trouvé , J.-M. Nicolas, F. Tupin, M. Gay, G. Vasile, L. Bombrun, A. Walpersdorf, J. Serafini, N. Cotte, L. Moreau et P. Bolon, Monitoring Temperate Glaciers by Multi-Temporal TerraSAR-X Images and Continuous GPS Measurements. *IEEE Journal of Selected Topics in Signal Processing, Vol.4, N° 2 (2011) 372-386.*

[24] O. Harant, L. Bombrun, G. Vasile, L. Ferro-Famil et M. Gay, Displacement Estimation by Maximum Likelihood Texture Tracking. *IEEE Journal of Selected Topics in Signal Processing, Vol.5, N° 3 (2011) 398-407.*

[23] L. Bombrun, G. Vasile, M. Gay et F. Totir, Hierarchical Segmentation of Polarimetric SAR Images using Heterogeneous Clutter Models. *IEEE Transactions on Geoscience and Remote Sensing 49, 2 (2011) 726-737.*

[22] *IEEE Journal of Selected Topics in Applied Earth Observations and Remote Sensing, June 2011, VOL.4, N° 2, pp. 372-386.*G. Vasile, F. Pascal, J.-P. Ovarlez, P. Formont, M. Gay, Optimal Parameter Estimation in Heterogeneous Clutter for High Resolution Polarimetric SAR Data. *IEEE Geoscience and Remote Sensing Letters, 2011, Vol. 8, N0.6, November 2011, pp. 1046-1050.*

[21] Petillot, E. Trouvé, P. Bolon, A. Julea, Y. Yan, M. Gay, J.M. Vanpé, Radar-Coding and Geocoding Look Up Tables for the Fusion of GIS Data and SAR images in Mountain Areas. I. *IEEE Geoscience and Remote Sensing Letters, 7, 2, 2010, pp. 309-313.*

[20] F.C. Totir, G. Vasile, M. Gay, L. Anton, G. Ilie, Advanced ICA-Based Methods for PolSAR Processing. *MTA Review, Romanian Military Technical Academy Publishing House, Vol. 20, No. 3, 2010, pp. 151-162.*

[19] M. Koehl, L. Bombrun, M. Gay, E. Trouvé, P. Bolon, JM Nicolas, G. Vasile, I. Petillot, T. Landes, P. Grussenmeyer, Interférométrie radar satellitaire et mesures GPS à la surface du glacier d'Argentière : comparaisons et validations. *Traitement du Signal, 2009, Vol. 26, N° 2 pp. 109-126.*

[18] L. Bombrun, M. Gay, E. Trouvé, G. Vasile, J. Mars, DEM error retrieval by analyzing time series of differential interferograms. *IEEE Geoscience and Remote Sensing Letters 6, 4 (2009) 830-834.*

[17] G. Vasile, E. Trouvé, I. Petillot, P. Bolon, J.M. Nicolas, M. Gay, J. Chanussot, T. Landes, P. Grussenmeyer, V. Buzuloiu, I. Hajnsek, C. Andres, M. Keller and R. Horn, High resolution SAR interferometry : estimation of local frequencies in the context of Alpine glaciers. *IEEE Transactions on Geoscience and Remote Sensing 46, 4 (2008) 1079-1090.*

[16] E. Trouvé, G. Vasile, M. Gay, L. Bombrun, P. Grussenmeyer, T. Landes, J.M. Nicolas, P. Bolon, I. Petillot, A. Julea, L. Valet, J. Chanussot and M. Koehl, Combining airborne photographs ans spaceborne SAR data to monitor temperate glaciers. Potentials and limits. *IEEE Transactions on Geoscience and Remo te Sensing, Vol. 45, N° 4, April 2007.*

[15] J.M. Nicolas, M. Gay, E. Trouvé, F. Tupin, G. Vasile, Processing in the temporal domain : application to direct interferogram generation and mountain glacier monitoring. *Canadian Journal of Remote Sensing (2006) ASAR 2005, special collection.*

[14] M. Frezzotti, M. Pourchet, O. Flora, S. Gandolfi, M. Gay, S. Urbini, C. Vincent, S. Bacagli, R. Gragnani, M. Proposito, M. Severi, R. Traversi, R. Udisti, M. Fily, Spatial and temporal variability of snow accumulation in east Antarctica from traverse data. *Journal of Glaciology, Volume 51, Number 172, January 2005. pp. 113-124(12).*

[13] M. Frezzotti, M. Pourchet, O. Flora, S. Gandolfi, M. Gay, S. Urbini, C. Vincent, S. Bacagli, R. Gragnani, M. Proposito, M. Severi, R. Traversi, R. Udisti, M. Fily, New estimations of precipitation and surface sublimation in East Antarctica from snow accumulation measurements. *Climate Dynamics 23 (2004) 803-813.*

[12] J. Weiss, J. Vidot, M. Gay, L. Arnaud, P. Duval, and J.R. Petit J.R., Dome Concordia ice microstructure : impurities effect on grain growth. *Annals of Glaciology, 2002, N° 35, p.552-558.*

[11] Nicot F., Gay M., Modelling of interaction between a snow mantel and a flexible structure using discrete element method. *Natural Hazards and Earth System Science (2002) 2, 3-4 pp.163-167.*

[10] M. Gay, M. Fily, C. Genthon, M. Frezzotti, H. Oerter And Jan-Gunnar Winther, Snow grain size measurements in Antarctica. *Journal of Glaciology, 2002, Vol. 48 N° 16.*

[9] F. Nicot, M. Gay and J. M. Tacnet, Interaction between a snow mantel and a flexible structure : a new method to design avalanche nets. *Cold Regions Science and Technology. Volume 34, Issue 2, April 2002, Pages 67-84.*

[8] Nicot, F., Gay, M., Tacnet, J.M., 2001, Interaction entre un manteau neigeux et une structure souple : Une nouvelle méthode de dimensionnement des filets paravalanches. *Revue française de génie civil, Vol.5, No.5, 2001, pp.587-612.*

[7] L. Arnaud, J. Weiss, M. Gay and P. Duval, Shallow ice microstructure at Dome Concordia, Antarctica. *Annals of Glaciology, Vol. 30, p.8-12 2000*

[6] M. Gay and J. Weiss, Automatic reconstruction of polycrystalline ice microstructure from image analysis : application to the EPICA ice core at Dome Concordia Antarctica. *Journal of Glaciology, 1999, Vol. 45, N°151, p.547-554.*

[5] L. Arnaud, M. Gay, J.M. Barnola, and P. Duval, Imaging of firn and bubbly ice in coaxial reflected light : a new technique for the characterization of these porous media. *Journal of Glaciology, 1998, Vol. , N° 147, p.326-332.*

[4] J. Weiss, M. Gay, Fracturing of ice under compression creep as revealed by a multifractal analysis. *Journal of Geophysical Research, 1998,Vol. 103, N°B10, p. 24005-24016.*

[3] L. Arnaud, V. Lipenkov, J.M. Barnola, M. Gay, and P. Duval, Modelling of the densification of polar firn ; characterization of the snow-firn transition *Annals of Glaciology, 1998 N° 26, p.39-44.*

[2] I. Sherjal, M. Fily, O. Grosjean, J. Lemorton, B. Lesaffre, Y. Page, and M. Gay, Microwave Remote Sensing of Snow from a Cable Car Chamonix in the French Alps. *IEEE Transactions on Geoscience and Remote Sensing, 1998, Vol. 36, N°1, p.324-328.*

[1] D. Barbet, M. Gay, G. Oberlin, F. Valla, Preliminary hydrological results from Sarennes glacier basin, French Alps. *Acta Geological Hispanica. v.28 (1993), n°2-3, p.3-14.*

Conférences internationales et nationales (à comité de lecture) avec publications des actes :

[63] M. Gay, O. Harant, R. Fallourd, E. Trouve, J.M. Nicolas, A. Walpersdorf, F. Ponton, L. Ferro-Famil, L. Ott, Glacier-surface velocities in alpine area from Terra-SAR-X satellite imagery, Comparison with GPS measurements and quality assessment. *Earth observation and cryosphere science, ESA-ESRIN Italy 2012-11-13.*

[62] L. Ferro-Famil, C. Leconte, F. Boutet, X.V. Phan, M. Gay and Y. Durand, PoSAR : a VHR tomographic GB-SAR system Application to snow cover 3-D imaging at X and Ku band. *European Radar Conference, Netherland 2012-10-31.*

[61] X.V. Phan, L. Ferro-Famil, M. Gay, Y. Durand, M. Dumont, G. d'Urso, Multilayer snowpack backscattering model and assimilation of TerraSAR-X satellite data. *Proceedings of International Geoscience And Remote Sensing Symposium, IGARSS Germany 2012-07-22.*

[60] O. Harant, L. Ferro-Famil, M. Gay, R. Fallourd, E.Trouvé, Bootstrap method for maximum likehood displacement estimation of glacier surface. *Proceedings of International Geoscience And Remote Sensing Symposium, IGARSS Germany 2012-07-22.*

[59] J.-M. Nicolas, E. Trouvé, R. Fallourd, F. Vernier, F. Tupin, O. Harant, M. Gay and L. Moreau, A first comparison of Cosmo-Skymed and TerraSAR-X data over Chamonix Mont-Blanc test-site. *Proceedings of International Geoscience And Remote Sensing Symposium, IGARSS Germany 2012-07-22.*

[58] T. Echelard, JM Krysiecki, M. Gay, P. Schoeneich, Rockglaciers movements detection by D-InSAR in French Alps using ERS archive data. *Proceedings of Tenth International Conference On Permafrost Russia 2012-06-25.*

[57] F. Ponton, A. Walpersdorf, M. Gay, E. Trouve, J.L. Mugnier, R. Fallourd, N. Cotte, L.Ott, and J. Serafini, GPS and TerraSARX time series measure temperate glacier flow in the Mont Blanc massif (France) : the Argentière glacier test site. *Proceedings of European Geosciences Union Conference Austria 2012-04-22.*

[56] X.V. Phan , L. Ferro-Famil, M. Gay, Y. Durand , G. Guyomarch, G. d'Urso, Electromagnetic backscattering model for snowpack adapted to X-band and Ku-band SAR satellite data. *Proceedings of World Climate Research Programme Open Science Conference USA 2011-10-24.*

[55] M. Gay, M. De Angelis, J.L. Lacoume, Datation des carottes de glace Andine par analyse temps-fréquence. *Actes du colloque GRETSI, FR 2011-09-05.*

[54] O. Harant, L. Bombrun, M. Gay, L. Ferro-Famil, Suivi de texture par Maximum de Vraisemblance dans les images Radar Polarimétriques à Haute Résolution spatiale. *Actes du colloque GRETSI, FR 2011-09-05.*

[53] F. Ponton, A. Walpersdorf, M. Gay, E. Trouvé, J.L. Mugnier, N. Cotte, L. Ott and J. Serafini, Seasonal flow variability of a temperate glacier in the Mont Blanc massif observed by GPS. *Proceedings of the 3rd International Colloquium on Scientific and Fundamental Aspects of the Galileo Programme DK 2011-08-31.*

[52] A. Julea, F. Ledo, N. Meger, E.Trouvé, P. Bolon, C. Rigotti, R. Fallourd, J.M. Nicolas, G. Vasile, M. Gay, O. Harant, L. Ferro-Famil, F. Lodge, PolSAR Radarsat-2 Satellite Image Time Series Mining over the Chamonix Mont-Blanc test site. *Proceedings of the International Geoscience and Remote Sensing Symposium IGARSS, US 2011-07-26.*

[51] T. Echelard, J-M Krysiecki, C. Barboux, M. Gay, P. Schoeneich, Automatic movement detection by InSAR in permafrost areas. Application to the Queyras Natural Regional Park, Hautes-Alpes, France. *EGU'11, European Geosciences Union General Assembly AU 2011-03-08.*

[50] O. Harant, L. Bombrun, L. Ferro-Famil, M. Gay, G. Vasile, Maximum Likelihood Shift Estimation using High Resolution Polarimetric SAR Clutter Model. *ESA special publication SP-695 - 5th International Workshop on Science and Applications of SAR Polarimetry and Polarimetric Interferometry (POLinSAR 2011) IT 2011-01-24.*

[49] X. V. Phan, L. Bombrun, G. Vasile, and M. Gay , Heterogeneous Clutter Models for Change Detection in PolSAR Imagery. *ESA special publication SP-695 - 5th International Workshop on Science and Applications of SAR Polarimetry and Polarimetric Interferometry (POLinSAR 2011) IT 2011-01-24.*

[48] O. Harant, E. Le Meur, G. Vasile, L. Bombrun, L. Ferro-Famil, M. Gay, E. Trouvé , Using Quad-Pol and Single-Pol RADARSAT-2 data for monitoring Alpine and outlet Antarctic glaciers. *ESA special publication SP-695 - 5th International*

Workshop on Science and Applications of SAR Polarimetry and Polarimetric Interferometry (POLinSAR 2011) IT 2011-01-24.

[47] F. Totir, L. Bombrun, G. Vasile, M. Gay, POLSAR images characterization through blind sources separation techniques. *Proceedings of the International Geoscience and Remote Sensing Symposium IGARSS, US 2010-07-25.*

[46] G. Vasile, J.P. Ovarlez, Pascal F., S. Zozor, M. Gay, Optimal parameter estimation in heterogeneous clutter for high resolution polarimetric SAR data. *Proceedings of the International Geoscience and Remote Sensing Symposium IGARSS, US 2010-07-25.*

[45] O. Harant, L. Bombrun, G. Vasile, L. Ferro-Famil, M. Gay, Maximum likelihood texture tracking in highly heterogeneous POLSAR clutter. *Proceedings of the International Geoscience and Remote Sensing Symposium IGARSS, US 2010-07-25.*

[44] L. Bombrun, G. Vasile, M. Gay, J.P. Ovarlez, Pascal F., Roll invariant target detection based on POLSAR clutter models. *Proceedings of the International Geoscience and Remote Sensing Symposium IGARSS, US 2010-07-25.*

[43] P. Bolon, M. Chiarle, P. Deline, G. Fioraso, J.-P. Fosson, M. Gay, M. Gardent, U. Morra di Cella, G. Mortara, L. Ott, P. Pogliotti, A. Théodule, E. Trouvé, M. Vagliasindi, L. Valet, C. Vincent., A French-Italian project on glacial hazards in the western Alps in relation with the glacier retreat : GlaRiskAlp. *14 Alpine Glaciology Meeting th th. Milano, IT, 2010-03-25.*

[42] Julea A, Méger N, Trouvé E, Bolon P, Rigotti C, Fallourd R, Nicolas J, Vasile G, M. Gay, Harrant O, L. Ferro-Famil, Spatio-Temporal Mining of PolSAR Satellite Image Time Series. *ESA Living Planet Symposium Norvège (2010).*

[41] F. Totir, G. Vasile, M. Gay, ICA-based information extraction method for PolSAR images. *8th Communications International Conference, Bucharest, Romania, 2010.*

[40] G. Vasile, J.P. Ovarlez, F. Pascal, M. Gay, G. D'Urso, D. Boldo, Stable scatterers detection and tracking in heterogeneous clutter by repeat-pass SAR interferometry. *Asilomar Conference on Signals, Systems, and Computers, US, 2010-10.*

[39] F. Totir, L. Bombrun, G. Vasile, M. Gay, S. Toma, On Hierarchical Segmentation of High Resolution PolSAR Data. *Proceeding of the European Conference on Synthetic Aperture Radar EUSAR DR 2010-06-07.*

[38] R. Fallourd, O. Harant, E. Trouvé, J.M. Nicolas, F. Tupin, M. Gay, G. Vasile, L. Bombrun, A. Walpersdorf, N. Cotte, L. Moreau, Ph. Bolon, Alpine glacier 3D displacement derived from ascending and descending TerraSAR-X images on Mont-Blanc test site. *Proceeding of the European Conference on Synthetic Aperture Radar EUSAR DR 2010-06-07.*

[37] O. Harant, L. Bombrun, G. Vasile, M. Gay, L. Ferro-Famil, R. Fallourd, E. Trouvé, J.M. Nicolas, F. Tupin, Fisher PDF for Maximum Likelihood Texture Tracking with High Resolution PolSAR Data. *Proceeding of the European Conference on Synthetic Aperture Radar EUSAR DR 2010-06-07.*

[36] L. Bombrun, G. Vasile, M. Gay, J.P. Ovarlez, Pascal F., A combined TSVM model and GLRT detector for a roll invariant target detection. *Proceeding of the European Conference on Synthetic Aperture Radar EUSAR DR 2010-06-07.*

[35] L. Bombrun, G. Vasile, M. Gay, J.-P. Ovarlez et F. Pascal, KummerU Clutter Model for PolSAR Data : Application to Segmentation and Classification. *2nd workshop SONDRA, Cargèse 2010, France.*

[34] R. Fallourd, O Harant, E. Trouvé, J.M. Nicolas, F. Tupin, M. Gay, G. Vasile, L. Bombrun, A. Walpersdorf, J. Serafini, N. Cotte, L. Moreau and P. Bolon, Monitoring Temperate Glacier : Combined Use of Multi-date TerraSAR-X Images and Continuous GPS Measurement. *The Fifth International Workshop on the Analysis of Multi-temporal Remote Sensing Images, Groton, Connecticut, USA (2009).*

[33] O. Harant, R. Fallourd, L. Bombrun, M. Gay, E. Trouvé, G. Vasile, J.-M. Nicolas, Preliminary TerraSAR-X Observation for Temperate Glaciers on the Chamonix Mont Blanc test Site. *IEEE IGARSS'09 International Geoscience And Remote Sensing Symposium, july 2009, Cape Town, South Africa.*

[32] L. Bombrun, J.-M. Beaulieu , G. Vasile, J.P. Ovarlez, F. Pascal, M. Gay, Hierarchical Segmentation of Polarimetric SAR Images using Heterogeneous Clutter Models. *IEEE IGARSS'09 International Geoscience And Remote Sensing Symposium, july 2009, Cape Town, South Africa.*

[31] C. Barboux, M. Gay, Permafrost surface deformation and related hazards detection using InSAR technique in the Alpes de Haute Provence. *EGU'09, European Geosciences Union General Assembly, April 2009, Vienna, Austria.*

[30] G. Vasile, J.P Ovarlez, F. Pascal, M. Gay, Estimation of normalized coherency matrix through the sirv model. Application to high resolution POLSAR data. *POLinSAR'09, International Workshop on Science and Applications of SAR Polarimetry and Polarimetric Interferometry, january 2009, Frascati, Italy.*

[29] O. Harant, L. Bombrun, M. Gay, R. Fallourd, E. Trouvé, F. Tupin, Segmentation and Classification of Polarimetric SAR Data based on the KummerU Distribution. *POLinSAR'09, International Workshop on Science and Applications of SAR Polarimetry and Polarimetric Interferometry, january 2009, Frascati, Italy.*

[28] L. Bombrun, G. Vasile, M. Gay, Segmentation of Polarimetric SAR images based on the SIRV model and the PDF. *Actes du 22ème colloque GRETSI sur le Traitement du Signal et des Images, GRETSI 2009 - France (2009).*

[27] E. Trouvé, Ivan Pétillot, P. Bolon, M. Gay, L. Bombrun, J.M. Nicolas, Florence Tupin, Télécom Paris-Tech, A. Walpersdorf, Nathalie Cotte, Irena Hajnsek, Martin Kelle, Monitoring Alpine glacier activity by a combined use of TerraSAR-X images and continuous GPS measurements - the Argentière glacier experiment. *EUSAR'08, European Conference on Synthetic Aperture Radar, June 2008, Friedrichshafen, Germany.*

[26] G. Vasile, J.P. Ovarlez, Pascal F., Tison C., L. Bombrun, M. Gay, E. Trouvé, Normalized coherency matrix estimation under the SIRV model. alpine glacier polsar data analysis. *IEEE IGARSS'08 International Geoscience And Remote Sensing Symposium, July 2008, Boston, USA.*

[25] Landes T., M. Gay, E. Trouvé, J.M. Nicolas, L. Bombrun, G. Vasile, Hajnsek I., Monitoring temperate glaciers by high resolution Pol-InSAR data : first analysis of Argentière E-SAR acquisitions and in-situ measurements. *IEEE IGARSS'07 International Geoscience And Remote Sensing Symposium, july 2007, Barcelona, Spain.*

[24] G. Vasile, E. Trouvé, Valet L., J.M. Nicolas, L. Bombrun, M. Gay, I. Petillot, P. Bolon, Buzuloiu V., Coherent-stable scatterers detection in SAR multi-interferograms : feature fuzzy fusion in Alpine glacier geophysical context *IEEE IGARSS'07 International Geoscience And Remote Sensing Symposium, july 2007, Barcelona, Spain.*

[23] L. Bombrun, M. Gay, Landes T., Grussenmeyer P., J.M. Nicolas, E. Trouvé, G. Vasile, Three-dimensional surface velocities of Argentiere and Mer de Glace glaciers, France, derived from radar interferometry : Analysis and comparison with in-situ measurements. *EGU'07, European Geosciences Union General Assembly, April 2007, Vienna, Austria.*

[22] G. Vasile, E. Trouvé, Valet L., J.M. Nicolas, M. Gay, L. Bombrun, P. Bolon, Feature detection in POLinSAR images by an interactive fuzzy fusion approach. Application to glacier monitoring. *POLinSAR'07, International Workshop on Science and Applications of SAR Polarimetry and Polarimetric Interferometry, january 2007, Frascati, Italy.*

[21] Multi-date ERS tandem interferogram analysis : application to alpine glaciers L. Bombrun, I. Petillot, G. Vasile, M. Gay, E. Trouvé, P. Bolon, J.M. Nicolas, Landes T. *MULTITEMP'07, The Analysis of Multitemporal Remote Sensing Images, CD-ROM - , Belgique (2007).*

[20] P. Bolon, E. Trouvé, I. Petillot, G. Vasile, M. Gay, L. Bombrun, J.M. Nicolas, F. Tupin, Landes T., M. Koehl and al., Monitoring Alpine Glaciers with ALOS SAR and Optical data. *LSI, Japon (2007).*

[19] I. Petillot, G. Vasile, E.Trouvé, P. Bolon, M. Gay, M. Koehl, A. Julea, Radar rectification of georeferenced information for data analysis in high mountain areas. *ORASIS CD-ROM - Onzième congrès francophone des jeunes chercheurs en vision par ordinateur, France (2007).*

[18] G. Vasile, I. Petillot, A. Julea, E. Trouvé, P. Bolon, L. Bombrun, M. Gay, Landes T., Grussenmeyer P., J.M. Nicolas, High Resolution SAR Interferometry : influence of local topography in the context of glacier monitoring. *IEEE IGARSS'06, International Geoscience And Remote Sensing Symposium, july 2006, Denver, Colorado, USA.*

[17] A Julea, G. Vasile, I. Petillot, E. Trouvé, M. Gay, J.M. Nicolas, P. Bolon, Simulation of SAR Images and Radar Coding of Georeferenced Information for Temperate Glacier Monitoring. *10th International Conference on Optimization of Electrical and Electronic Equipments, OPTIM 06, Roumanie (2006).*

[16] A. Hérique, A. Roux, J.-P. Goutail, P. Grussenmeyer, L. Moreau, M. Dechambre, M. Gay, W. Kofman, J. Mouginot, P. Volcke., Tomography in transmission, a new technique for glaciers characterisation : Perspectives and preliminary results for the Glacier de l'Argentière. *EGU'06, European Geosciences Union General Assembly, April 2006, Vienna, Austria.*

[15] T. Habib, M. Gay, J. Chanussot, P. Bertolino, Segmentation of high resolution satellite images SPOT applied to lake detection *IEEE IGARSS'06, International Geoscience And Remote Sensing Symposium, july 2006, Denver, Colorado, USA.*

[14] M. Koehl, Trouve E., G. Vasile, M. Gay, P. Grussenmeyer, J.M. Nicolas, T. Landes, SIG pour la gestion cartographique des données du projet MEGATOR. *Conférence francophone ESRI, SIG 2006, France (2006).*

[13] M. Gay, T. Habib, Validated spectral angle mapper algorithm for glacial lake detection : comparative study between SPOT imagery and terrestrial measurements. *Conference Eurisy, 8-9 september 2005, Geneva, Switzerland.*

[12] E. Trouvé, G. Vasile, M. Gay, Grussenmeyer P., J.M. Nicolas, Landes T., M. Koehl, J. Chanussot, A. Julea, Combining Optical and SAR Data to Monitor Temperate Glaciers. *Proceedings of IGARSS, International Geoscience And Remote Sensing Symposium, République de Corée (2005).*

[11] G. Vasile, E. Trouvé, M. Gay, J.M. Nicolas, Amplitude-Driven-Adaptive-Neighbourhood Filtering of High-Resolution Pol-InSAR Information *PolInSAR'05, International Workshop on Science and Applications of SAR Polarimetry and Polarimetric Interferometry, Frascati, Italie (2005).*

[10] M. Gay, B. Legresy, G. Vasile, E. Trouvé, Velocities Field of Mountain Glacier Obtained by Synthetic Aperture Radar Interferometry. *IEEE IGARSS'04, International Geoscience and Remote Sensing Symposium, september 2004, Anchorage, Alaska.*

[9] B. Legresy, E. Berthier, M. Gay, C. Vincent, Y. Arnaud, F. Remy, Satellite imagery for investigation of small alpine glaciers dynamics. Physical and Mechanical Processes in relation to Glacier and Ice-Sheet Modelling. *IGS'02, International Glaciology Society, 26-30 August 2002, Chamonix, France.*

[8] Nicot, F., Gay, M., B. Boutillier, F. Darve, Modelling of interaction between a snow mantel and a flexible structure using a discrete element method. *NUMOG VIII, 2002, Pande, Pietruszczak eds, Balkema, pp.699-703.*

[7] F. Nicot and M. Gay, Modelling of interaction between snow mantel and structure by using a discrete element method. *EGU'01, European Geophysical Society. 2001 Nice, France.*

[6] M. Gay and F. Nicot, Interaction between a snowpack and a defensive net fences. *International seminar on snow and avalanches test sites FR 2001-11-, novembre 2001, Grenoble, France.*

[5] M. Frezzotti, M. Pourchet, O. Flora, M. Fily, G. Gandolfi, C. Genthon, S. Urbini, and M. Gay, New snow accumulation rate measurements in East Antarctica. Comparison with existing maps *ISMASS Workshop on Antarctic Ice Sheet Mass Balance, June 2001, USA.*

[4] J. Weiss, N. Hotellier and M. Gay, The coupling between viscoplastic deformation and damage in ice. *4th International IAHR Symposium on ice US 1998-07-27.*

[3] M. Gay, and M. Fily, Surface snow grain size measurements on the Antarctic ice sheet. *International symposium on snow and avalanches. Chamonix Mont-Blanc, May 1997, France.*

[2] J. Weiss, and M. Gay, Multifractal analysis of fracturation up to localization and failure during compression creep of ice samples. *Symposium on localization phenomena and dynamics of brittle and granular systems, (Scholz, C.H., Ed) US 1997-07-27.*

[1] M. Gay, Sound wave propagation measurements in snow flows. *Proceedings of the "Pierre Beghin" international workshop on rapid gravitational mass movements FR 1995-12-06.*

Conférences nationales sans publications :

[19] M. Gay, Modélisation et traitement des signaux et des images Radar à Synthèse d'Ouverture (RSO). Applications : mesure de déplacements, prévision des risques. *Comité Français de Géologie de l'Ingénieur, France 2012-10-04.*

[18] M. Gay, X.V. Phan., Traitement et analyse de données multi-temporelles TerraSAR-X appliqués la prévention des chutes de séracs. *Groupement de Recherche-Information Signal Image viSion FR 2012-06-07.*

[17] J. Chanussot, M. Dalla Mura, M. Gay, G. Vasile., Les activités en télédétection au sein de GIPSA-lab. *Journée nationale de photogrammétrie et télédétection FR 2012-05-10.*

[16] M. Gay, O. Michel, C. Gervaise, O. Harant, X.V. Phan, T. Echelard, Traitement de données radar et sonores haute résolution spatiale appliqués aux glaciers. *Surveillance, Etude et Reconnaissance de l'Environnement mariN par Acoustique DiscrètE FR 2012-04-04.*

[15] M. Gay, O. Harant, L Bombrun, XV Phan, L Ferro-Famil L Ott, R. Fallourd, E. Trouvé, Imagerie satellitaire radar Haute Résolution (HR) spatiale appliquée à la prévention des risques glaciaires. *Séminaire : Gestion des risques d'origine glaciaires et périglaciaires FR 2012-03-12.*

[14] F. Diotri, C. Lucianaz, E. Trouvé, R. Fallourd, P. Bolon, L. Valet, L. Ott, X.V. Phan, O. Harant, M. Gay (coordinateur)., Sites-pilotes- Métrologie et suivi de la dynamique des glaciers. *Restitution des projets axés sur les risques naturels FR 2012-01-27.*

[13] M. Gay, G. Vasile, S. Allain, Ph. Bolon, P. Briole, R. Fallourd, Faure-Vincent D., L. Ferro-Famil, O. Harant, A. Walsperdorf, Mesures in situ et polarimétrie : comprendre la rétrodiffusion et la dynamique des milieux neige/névé/glace. *Journée CNES CCT-TSI FR 2009-07-03*

[12] M. Gay, Landes T., E. Trouvé, J.M. Nicolas, Hajnsek I., L. Bombrun, G. Vasile, Moreau L., Suivi des glaciers tempérés à partir de données Pol-InSAR haute résolution spatiale : premières analyses d'acquisitions E-SAR couplées à des mesures in-situ sur le glacier d'Argentière. *Société Hydrotechnique de France, Section de Glaciologie-Nivologie SHF FR 2007.*

[11] M. Gay, J.M. Nicolas, Trouve E., P. Grusenmeyer, Imagerie optique et Radar à Synthèse d'Ouverture (RSO) appliquée au suivi des glaciers. *SHF'06, Société Hydrotechnique de France (SHF), Section de Glaciologie-Nivologie, Grenoble 2006, France.*

[10] C. Chambeyron, M. Gay, J. Chanussot, Détection et surveillance des lacs glaciaires de montagne à partir des images satellites SPOT. *SHF'05, Société Hydrotechnique de France section de Glaciologie-Nivologie, Grenoble 2005, France.*

[9] M. Gay, E. Thibert, C. Chauveau, Bilan de masse du glacier de Sarennes 55ième et 56ième saison 2003-2004-2005. *SHF'05, Société Hydrotechnique de France section de Glaciologie-Nivologie, Grenoble 2005, France.*

[8] J.P. Michel, M. Gay, F. Valla, Bilan de masse du glacier de Sarennes, 54ème saison. Analyse spectrale des 54 années de mesures. *SHF'03 Société Hydrotechnique de France section de Glaciologie-Nivologie, Grenoble 2003, France.*

[7] M. Gerbaux, C. Genthon, P. Etchevers, C. Vincent, et M. Gay., Impact d'un changements climatique sur les glaciers alpins. *Société Française de Physique FR 2003-07-07.*

[6] M. Gay, A. Ferrié, B. Legresy, Y. Arnaud, Suivi des glaciers des Alpes par télédétection spatiale. *Société Hydrotechnique de France section de Glaciologie-Nivologie SHF FR 2002.*

[5] M. Gay, B. Legresy, E. Berthier, Y. Arnaud, Potentiels de l'interférométrie radar satellitaire pour l'étude de la dynamique des glaciers. *10ième Carrefours de la Fondation Rhône-Alpes Futur FR 2002-10-21.*

[4] M. Gay et F. Nicot, Interaction entre un manteau neigeux et une structure souple. Une nouvelle méthode de dimensionnement des filets paravalanche. *Société Hydrotechnique de France SHF FR 2001-03-15.*

[3] M. Gay, and M. Fily, Application of image processing to determine structural properties of snow. *Euromech 350 Image Analysis, Porous Materials and Physical Properties, Carcans, 3-7 June - 1996, France.*

[2] F. Valla, and M. Gay, Mesure de débit de l'émissaire du glacier de Sarennes. *SHF'93, Société Hydrotechnique de France. Grenoble, 11 et 12 mars 1993.*

[1] M. Gay, P. Villemain and P. Journe, Un anémomètre ultrasonore corrélatif. *Colloque de la S.E.E., "les capteurs intelligents". Annecy 1991.*

Rapports techniques :

[21] M. Gay, F. Diotri, C. Lucianaz, E.Trouvé, P. Bolon, L. Valet, L. Ott, Xuan Vu Phan, O. Harant, Sites-pilotes- Métrologie de la dynamique des glaciers. *Projet simple n° 056 GlaRiskAlp -Risques glaciaires dans les Alpes occidentales, rapport final, 14/11/2012, 60 pages.*

[20] E. Trouvé, J.M. Nicolas, M. Gay, L. Ferro-Famil, M.P Doin, V. Pinel, Extraction et Fusion d'Informations pour la mesure des Déplacements en Imagerie Radar. *ANR-EFIDIR, Rapport final Part 8, 09/2012, 30 pages.*

[19] M. Gay, F. Diotri, C. Lucianaz, E.Trouvé, P. Bolon, L. Valet, L. Ott, Xuan Vu Phan, O. Harantl, Sites-pilotes- Métrologie de la dynamique des glaciers. *Projet simple n° 056 GlaRiskAlp -Risques glaciaires dans les Alpes occidentales, rapport N° 3, 20/07/2011, 6 pages.*

[18] E. Trouvé, J.M. Nicolas, M. Gay, L. Ferro-Famil, M.P Doin, V. Pinel, Extraction et Fusion d'Informations pour la mesure des Déplacements en Imagerie Radar. *ANR-EFIDIR, Rapport semestriel Part 7, 07/2011, 20 pages.*

[17] M. Gay, F. Diotri, C. Lucianaz, E.Trouvé, P. Bolon, L. Valet, L. Ott, Xuan Vu Phan, O. Harantl, Sites-pilotes- Métrologie de la dynamique des glaciers. *Projet simple n° 056 GlaRiskAlp -Risques glaciaires dans les Alpes occidentales, rapport N° 2, 28/01/2011, 5 pages.*

[16] E. Trouvé, J.M. Nicolas, M. Gay, L. Ferro-Famil, M.P Doin, V. Pinel, Extraction et Fusion d'Informations pour la mesure des Déplacements en Imagerie Radar. *ANR-EFIDIR, Rapport semestriel Part 6, 01/2011, 25 pages.*

[15] Ghera C., G. Vasile, M. Gay, G. D'Urso, Boldo D., Traitement des images RSO interférométriques à haute résolution spatiale pour la surveillance des barrages et des digues par télédétection radar : potentiel et limites. *Deliverable EDF, part-II, 2010, 80 pages.*

[14] Michel Gay, F. Diotri, Claudio Lucianaz, E.Trouvé, P. Bolon, L. Valet, L. Ott, Xuan Vu Phan, O. Harantl, Sites-pilotes- Métrologie de la dynamique des glaciers. *Projet simple n° 056 GlaRiskAlp -Risques glaciaires dans les Alpes occidentales, rapport N° 1, 08/10/2010, 7 pages*

[13] G. Vasile, P. Bolon, C. Deledalle, R. Fallourd, M. Gay, O. Harant, J.M. Nicolas, L. Ott, E. Trouvé, F. Tupin, New Cross-Correlation Shift Estimation Methods with High Resolution SAR Data. *Deliverable ANR-EFIDIR, France, 2010, 59 pages.*

[12] E. Trouvé, J.M. Nicolas, M. Gay, L. Ferro-Famil, M.P Doin, V. Pinel, Extraction et Fusion d'Informations pour la mesure des Déplacements en Imagerie Radar. *ANR-EFIDIR, Rapport semestriel Part 5, 07/2010, 58 pages.*

[11] L. Lorier, D. Fabre, M. Gay, P. Schoeneich, M. Vallon, Analyse des risques induits par la dégradation du permafrost. *Deliverable fundation MAIF, Final Report,Part 3, ADRGT, CNAM, GIPSA-lab, IGA, LGGE, RTM, 07/2010.*

[10] M. Gay, L.Ott, G. Vasile, G. d'Urso, Traitement des images RSO interférométriques à haute résolution spatiale pour la surveillance des barrages et digues par télédétection radar : potentiel et limites. *Deliverable EDF, part-I, 2009, 14 pages.*

[9] E. Trouvé, J.M. Nicolas, M. Gay, L. Ferro-Famil, M.P. Doin, V. Pinel, Extraction et Fusion d'Informations pour la mesure des Déplacements en Imagerie Radar. *ANR-EFIDIR, Rapport semestriel Part 4,12/2009, 56 pages.*

[8] L. Lorier, D. Fabre, M. Gay, P. Schoeneich, M. Vallon, Analyse des risques induits par la dégradation du permafrost. *Deliverable fundation MAIF Final report,Part 2, ADRGT, CNAM, GIPSA-lab, IGA, LGGE, RTM, 07/2009.*

[7] M. Gay, Q. Barthélemy, L. Bombrun, Doin M.P., R. Fallourd, L. Ferro-Famil, O. Harant, J.M. Nicolas, L. Ott, F. Tupin E. Trouvé, G. Vasile, Mesure de grands déplacements à partir de données Radar à Synthèse d'Ouverture (RSO) multivariées. *Deliverable ANR-EFIDIR, France, 2009, 66 pages.*

[6] E. Trouvé, J.M. Nicolas, M. Gay, L. Ferro-Famil, M.P Doin, V. Pinel, Extraction et Fusion d'Informations pour la mesure des Déplacements en Imagerie Radar. *ANR-EFIDIR, Rapport semestriel Part 3, 07/2009, 55 pages.* [5] E. Trouvé, J.M. Nicolas, M. Gay, L. Ferro-Famil, M.P Doin, V. Pinel, Extraction et Fusion d'Informations pour la mesure des Déplacements en Imagerie Radar. *ANR-EFIDIR, Rapport semestriel Part 2, 12/2008, 53 pages*

[4] L. Lorier, D. Fabre, M. Gay, P. Schoeneich, M. Vallon, Analyse des risques induits par la dégradation du permafrost *Deliverable fundation MAIF Final report, Part 1, ADRGT, CNAM, GIPSA-lab, IGA, LGGE, RTM, 12/2008.*

[3] E. Trouvé, J.M. Nicolas, M. Gay, L. Ferro-Famil, M.P Doin, V. Pinel, Extraction et Fusion d'Informations pour la mesure des Déplacements en Imagerie Radar. *ANR-EFIDIR, Rapport semestriel Part 1, 07/2008, 39 pages.*

[2] M. Gay, S. Garambois, Développements méthodologiques pour la surveillance des glaciers par imagerie radar aéroportée et satellitaire et par GPR (Ground Penetrating Radar). *Pôle Grenoblois d'Etudes et de Recherche pour la Prévention des Risques Naturels, Final Report, 06/2008, 34 pages.*

[1] E. Trouvé, M. Gay, J.M. Nicolas, P. Grussenmeyer, Mesure de l'Evolution des Glaciers Alpins par Télédétection Optique et Radar - des archives à ORFEO. *ACI-Masse de Données, Final report, 11/2007, 37 pages.*

Evénements médiatisés :

[6] Fête de la Science, Des satellites radar à l'observation des glaciers, Place aux sciences, Grenoble, France, 2008.

[5] Journal Télévisé, Envoyé spécial, France 2, 11 octobre 2007.

[4] Article, Des glaciers alpins en perte de vitesse , KAELE, journal Franco-Suisse, mars, 2007.

[3] Article, Des chercheurs surveillent les glaciers, journal de la région Rhône-Alpes, France, n°. 5, 2007.

[2] Article, La surveillance des glaciers se prépare à entrer dans l'ère satellitaire, journal Le Monde, France, 10 octobre 2006.

[1] Fête de la Science, Les RADARS imageurs, exposé à la cité scolaire de Chamonix, France, 2006.

Chapitre 2

Image processing of snow, firn and ice microstructures

The earth's surface plays a key role in the global radiation balance. Snow is extremely reflective, thus modification of both its optic properties and its spatial coverage modify the climate through direct feedback related to its reflection coefficient. [1]. Even slight modifications in the reflection of snow can either double or reduce by half the absorption of rays. On one hand, such modifictions are tied in with a rapid evolution of the snow's state. [2, 3]. On the other hand, one takes into account the importance of th ?se rapid changes, with regard to the global modelling of the climate (GMC). The errors associated with energy estimation, due to a wrongful représentation of radiation transf ?r (absorbed diffusion and resending), can affect the instance of snow melt and subsequently amplify a bias through the reflection coefficient feedback. [4]. Snow with its microstructure représentation (i.e. the size of its particles), along with its changing form (enlargement of its particles), has become a major topic of research, it being at the foundation of physical modelling and of specific key accomplishments. Michel Fily and I are studying the détermination of the size of snow particles, derived from a series of 2-D images of snow particle piles.

Another glaciology problem tied in with snowpack (the porous intermediate médium between snow and ice) and its densification is the interprétation of data gathered from the analysis of gas trapped in ice cores in the Arctic (Greenland) and in the Antarctic. The dating of gas contained inside air bubbles entrained in ice is carried out from the âge of the ice(dating from isotopic relations ($^{18}0/^{16}O$) and from the identity of the différence in âge between the gas and ice at the time of the closing of the pores. This research is fundamental in order to reconstituate the atmospheric composition of previous/past climates. In collaboration with L. Arnaud, we have developed treatment algorithms of snowpack, allowing to apply several physical models of densification, gas diffusion and closing of pores in snowpack. A final aspect tied in with glaciology surrounds the understanding of the laws of single crystals of ice. The analysis through treating images of thin blades allows for further analysis of the laws of snow particle enlargement and changes due to the climatic transition ? ? ?HOLOC¨CNE ? ? ?L'analyse par traitement d'images de lames minces permet l'analyse des lois de grossissement des grains et les changements dus à la transition climatique holocène, dernier maximum glaciaire (LGM Last Glacial Maximum), ...a research project carried out in collaboration with P. Duval et J. Weiss.

In this chapter, we will discuss methods of analysis concerning microstructures of snow, snow-

pack and ice taken from 2-D images and passed on to those of 3-D, along with the representativeness of each parameter (convex ray, SSA, optic diameter...) and laws of représentation in the development of snow, ice and snowpack. In the first section, we will continue study on the convex ray médium obtained from 2-D images of snow particles, begun during my doctor's thesis. This section displays a new technique to photograph and analyze images in order to caracterize snowpack. 2.2 The sections 2.3 and 2.4 présent the analysis of ice microstructures through treatment of images in polarized light. The section 2.5 underlines the analysis and the role of impurities in the growth of ice particles. The section 2.6 shows results from new estimates regarding precipitation and the surface sublimation in the Eastern Antarctic obtained from measurements of snow accumulation. In the section 2.7, we take into account the spatial and temporal variabilities of snow accumulation, which is a key parameter in the analysis of ice core and of mass assessment.

2.1 Snow optical image processing.

Here, the goal is to evaluate the size of snow particles via automatic treatment of images. One part of my doctorate research, defended in1999, corresponds to this very quantification which was published in [5] ' To give a synthetic overview, we can define the size of snow particles or of snowdrifts, realizing that numerous definitions exist . [6]. The size used by the Centre of Studies of Snow represents the average of convex rays of N grains ($N > 30$) [7]. The convex ray of a particle is the average of the convexities of the snow particle contour, and is calculated by approximation, from the 2-D images. This size is very sensitive to image resolution and can generate errors during the analysis of several particles having different sizes on the same image. The idea presented here was to calculate this convex ray, keeping in mind the integrality of the 2-D surface of particles (Fig. 2.1.1). Firstly, one calculates the median axis and the weighed particle and snowdrift skeletons [8].

FIGURE 2.1.1 – Grains de neige avec le squelette pondéré superposé (en violet).

The "average convex ray" R_{CM} of a particle (or a snowdrift) is thus, equal to the mean average of rays calculated for the n extremity points of terminal branches of the skeleton structures.

We worked out the median of convex N rays, calculated for N particles ($N > 30$). I showed that this calculation is robust whilst analyzing several particles of different sizes in the same image. This work leading to the analysis of sizes of particles R_{CM} , taken from 500 samples of 3000 images recorded at the surface of the East Antarctic allowed me to create a database on this zone. This data further allowed to explain the microwave signature of two sites, called M2 and MDP, situated at the midline between the coast and Dome C [9]. These two sites are caracterized by

some of the largest snow particles and by crusts of glaced formed by the wind, which explains the particular microwave signature observed [5]. This database serves as a reference point for the understanding of the metamorphosis of snow in the Antarctic, in relation with the climatic parameters.

The ideas formed in [5] were retaken by Pirazzini et al. [10] in recent studies, showing that one can simulate the albedo of snow from a size of particle calculated from the terminal points of the pondered skeleton (from 2-D images), to obtain a good agreement with mesured data.

Other research show that this study on the size of particles was followed-up : to quote specifically Leppanen [11], who established a relation between the size of particles measured visually and the specific surface (Snow Surface Specific : SSA) of snow, Essery [12], who demonstrated that the properties of snow are influenced by size of particles. Several models simulate the size of particles and demonstrate that this size can even be estimated visually or along with such instruments of measurement in-situ, as DUFISSS [13] or POSSUM [14].

We can also cite Dominé [15], who shows how the climatic conditions can affect a blanket of snow, represented by the variables SSA, albedo and thermal conductivity. Calculations of radiative transfer, using detailed methods in [16], show that the reductuction of the SSA of snow of 32.8 à 16.4 m^2kg^{-1} can diminish the reflectivity of the surface of 3%, producing a radiative forcing of 22 Wm^{-2} in the tropopause .

at noon (local time), $65°N$, during summer solstice.

One of my projects is to resume the above-mentioned study in order to extract 3-D parameters, starting from the tomography of snow [17] and to include these parameters in an interactive model of centimetric waves with the snow (see text further on).

2.2 Firn microstructures extraction algorithm.

The densification of snowpack is formed by plastic deformation of contact areas between its particles, under the force of a load of snow and snowpack columns located above the snowpack. The local forcing pressure at the level of the contact points rises with an average load, but diminishes with the rise in the number and the size of contact zones. Along with Laurent Arnaud, [18], we turned our interest to the development of a technique concerning the sublimation of snowpack samples [19], and of the elaboration of an algorithm of 2-D image treatment, allowing us to simultaneously visualize the pores (in black), the ice and the joints of ice particles (Fig. 2.2.1), as well as at various depths. The parameters automatically extracted, such as height and form of ice particles, or the size and form of porosities were integrated, due to the stereologic relations in three physical 3-D models of evolution of snowpack (densification, closing of pores, diffusion of gas[20]).

2.3 Ice microstructures reconstruction algorithm.

Thin slats of polycrystaline ice, illuminated by polarized light guided through two straight-lined polarized filters allow us to visualize the ice particles. Fig. 2.3.1. I developed an apparatus of acquisition, and elaborated an algorithm (via illumination of a series of thin slats) that captures 2-D images and automatically reconstituates the microstructures at various depths [21]. From analysis and

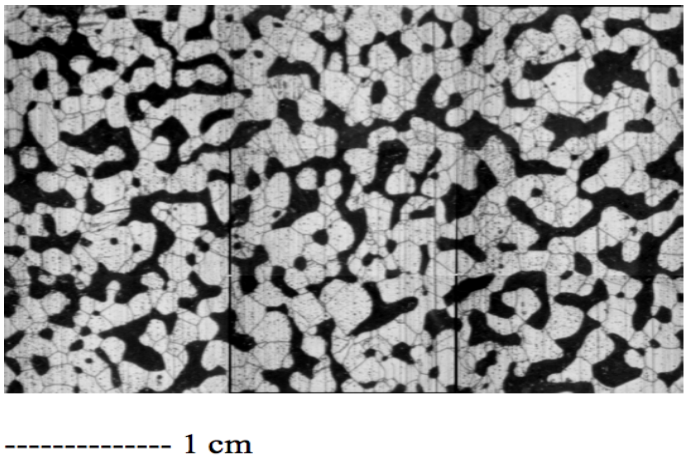

FIGURE 2.2.1 – Mosaique de 9 photographies contiguës reconstruites par traitement d'images

treatments (not detailed here) of these 2-D microstructure, derived from the ice core of EPICA (deep borehole in the Antarctic), in collaboration with J. Weiss, we demonstrated that the mean surface of crystals, averaged from all the crystals of the group, each calculated at depths of 100 to 330 meters, defines the size of particles having the best physical significance. Using the analysis of interception lengths of horizontal and vertical cuts of ice, we demonstrated that the flattening of particles enlarges with depth, and then remains constant up to 360 meters. The calculation of the relation of the surface divided by square perimeter (maximum for the sphere, equal to 0.08) of particles is stable (0.055) for the different depths. This result suggests that the morphology of particles (supposedly being extracted) is close to the average of an equilibrium minimizing the surface area in 3-D [22].

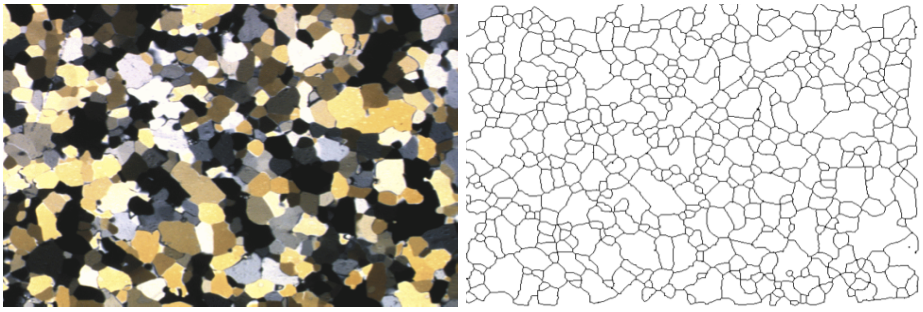

FIGURE 2.3.1 – Lame mince de glace éclairée en lumière polarisée et microstructure reconstituée par traitement d'images.

2.4 Physical ice microstructures.

The average surface of ice crystals from a transversal 2-D cut allowed us to deduct the kinetics of enlargement of particles in 3-D and to establish the law of growth of ice core particles, extracted from the borehole EPICA[23, Fig.1]. Taken from 100 m to 430 m, the results display a linear growth with depth, in accordance with the previous studies [24] :

$$A = A_0 + K(T)\ t \tag{2.4.1}$$

où $K(T)$ est un facteur dépendant de la température (loi d'Arrhenius), t le temps et A la superficie moyenne des grains.

For the deeper zones, the mean surface area of particles reduces (already previously shown [24]), starting from isotopic relations. This change is due to the climatic transition holocène last major ice age (20,000 years ago). With respect to previous analysis, we have shown that the transition is translated with time, and that this transition reveals the difference in accumulation rate of snow between the two sites. The accumulation could be less than 10% à Dome C (forage EPICA). Still, in this research with L. Arnaud, we showed that the distribution of particle size (normalized ray obtained by image treatment) at different depths are distributed log-normal. This is an indicator of a normal enlargement of particles [25, 26]. The analysis of the change of tendancies of the mean value and of the difference of the distribution during the climatic transition could even help to reveal the nature of the process of particle enlargement, and more specifically the role of impurities in the migration of particle joints.

2.5 Impurities and grain growth : analysis of microstructures.

In collaboration with Jerome Weiss, we concentrated this research [22] on the analysis of parameters of distribution of particle size at different depths. The main result of this study showed that the lessening of particle enlargement during the climatic transition Holocen/Last Glacial Maximum (LGM) primarily originates from a "pinning" of particle joints by the non soluble particles (the dust), present in the ice. These studies corroborated by [27] were followed-up, and showed that the mean size of particles is not a paleo-thermometer, but reflects a complex non-linear procedure, depending on the retention of dust durin the climatic transitions.

The two following sections are less tied in with microstructures. However, they provide an interest in the introduction of the last chapter concerning the assimilation of satellite data RSO, to constrain the physical model of the development of snow Crocus. We will see that the process of erosion, of sublimation and of snow transport by wind are intimately tied in to the metamorphosis of snow.

2.6 Estimation of precipitation and sublimation of the surface of Antarctica.

This work focuses on the distribution of the assessment of surface mass (or SMB : Surface Mass Balance) and of its spacial and temporal variability, being a parameter to note models of mass assessment. The variability of the rates of SMB and the process of redistribution of snow are equally fundamental for a better interpretation of the altimetric signal of changing surface elevation [28], and for improving climatological and meteorologicla models. [29].

During the austral summer of 1998-99, I participated in the first international scientific expedition : Terra Nova Bay-Dôme Concordia (International Antarctic Scientific Expedition ITASE), in order to collect necessary data for a deeper understanding of the phenomenons of accumulation, of snow mass assessment, and of redistribution of snow via the wind. In the course of this expedition, we excavated 39 boreholes in the ice, measured tags of ablation, executed GPS (Global Positioning System) and GPR (Ground Penetrating Radar measurements, as well as measurements of stratigra-

phic profiles of snow. All of this data, analyzed in the laboratory, allowed us to date ice cores with the level of Tritium markers $/\beta$ (1965-1966), and to provide information on surface accumulation (Surface Accumulation is abbreviated as SA). The depth of blankets of snow, measured by GPR, were converted into an assessment of mass (SMB), using the relationship of age-depth (obtained by the SA Tritium.

In collaboration with Massimo Frezzotti, we employed various methods in comparing and integrating different types of data (implantation of beacons, ice cores, radar, morphology of surface, teledetection) in eight sites (elaborated in [30], le long de la traverse scientifique de Terra Nova Bay (TNB) à Dôme C (DC), to establish a relationship on the assessment of surface mass. In a synthetic manner, I recapture the results that we had already obtained in s [30]. For further interesting reading, consult the integral publishing.

Mass balance of surface snow.

The deductions of certain authors [31, 32] suggest that the SMB is directly and globally correlated to temperature, altitude, pressure of saturated steam and the distance of the ocean, all of which have insufficiently documented. In [33] , Frezzotti et al. shows that the spatial variability of local meteorological conditions in this region (Eastern Antarctic) may not have any correlation with altitude and distance of the ocean. While suspecting that the interaction of catabatic winds, intrusion of storms and of temperature inversion during the winter all determine the local morphology and surface albedo, relying on the basis of our observations (Fig. 2.6.1), we have established an empirical relationship between mean annual temperature of snowpack (à -15 m) and the maximum of snow accumulation on the surface (SA_{max}) :

$$SA_{max} = 10.89\ T_c\ +\ 595 \tag{2.6.1}$$

où T_c est la température du névé à $-15\ m$ de profondeur.

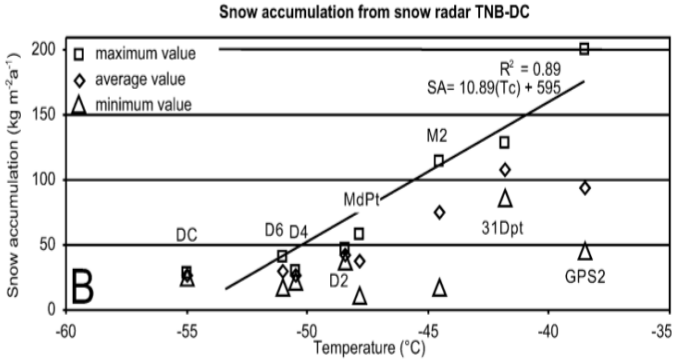

FIGURE 2.6.1 – Accumulation de neige le long de la traverse Terra Nova Bay-Dôme Concordia.

In considering the data of the two traverses $TerraNovaBay - Dumontd'Urville - DmeConcordia$ (Fig.2.6.2), we have recognized another relationship, being more global, between the mean annual temperature of snowpack (à -15 m) and the maximum accumulation of snow on the surface (SA_{max}).

$$SA_{max} = 15.91\ (T_c) + 858 \tag{2.6.2}$$

where T_c is the temperature of snowpack at a depth of $-15\ m$

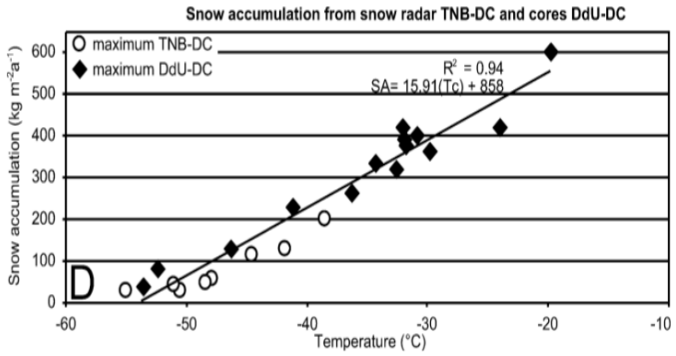

FIGURE 2.6.2 – Accumulation de neige le long de la traverse Terra Nova Bay-Dôme Concordia et Dumont d'Urville-Dôme Concordia.

Ablation and sublimation of the snow according to measurements of SMB.

The third relationship that we have established concerns the ablation of snow. The processes of local redistribution of snow have a strong impact on the variability of accumulation on a local metric scale. The large variability of mass assessment is tied in to the process of ablation, which is in turn determined by the processes of surface sublimation (decapitated by the wind, sublimation of blown snow...). Based on these observations, we suggest that the difference between the maximum and minimum values of SMB at each site represent the ablation of snow. The eight sites treated do not have neither the same topography, nor the same local meteorological conditions. The ablation values are a function of snowpack temperature (Fig. 2.6.3), showing that we can establish two relationships, function of slopes (P) determined by the Frequency (F) of dominant (D) wind (V) : PFVD. The ablation of sites GPS2, M2 and MdPt depass 80% of the maximum ablation ([30, Table 2]). Thus, we deduce the following relationship :

$$A_b = 3.0\ (T_c) + 162 \tag{2.6.3}$$

où T_c s the temperature of snowpack at $-15\ m$ depth.

Pour les autres sites, nous avons :

$$A_b = 10.87\ (T_c) + 575 \tag{2.6.4}$$

où T_c is the temperature of snowpack at $-15\ m$ depth. D'autres relations similaires (non détaillées ici) ont été obtenues le long de la traverse DdU-DC.

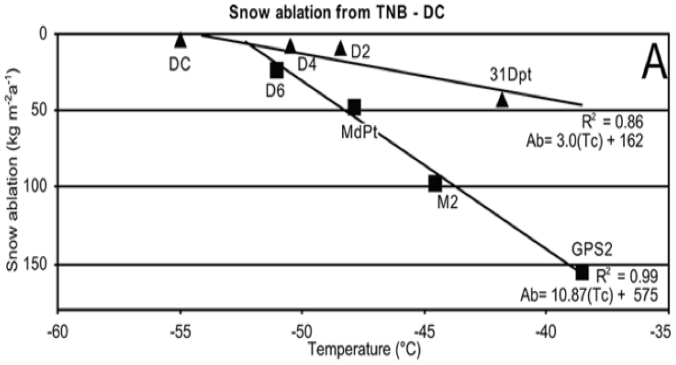

FIGURE 2.6.3 – Ablation de neige le long de la traverse Terra Nova Bay-Dôme Concordia.

During this crossing, we equally highlighted other phenomena. The variability of surface roughness shows the complexity of the processes tied in with the topography and local meteorology. The crusty surfaces of snow, created by the wind, have a weak coefficient of surface roughness, more weak than the sastrugis. This weak roughness generates an acceleration of the wind and the transportation of snow. We recall that captation begins at a windspeed value of less than 5 ms^{-1}. The weak roughness, the acceleration and changes in wind direction increase the turbulence that, by consequence, increases the coefficient of diffusion and modifies the humidity profile of the mixing with the air mass. This in turn increases the sublimation of blown snow. Our observations show that the threshold of snow erosion and transportation by the wind depends on the properties of snowpack, and changes in relation with the metamorphosis of snow. As a matter of fact, the form of freshly fallen snow crystals does not allow for good cohesiveness, compared with large particles : They have stronger mobility. These phenomena are actually taken into account in the models via the addition of a mobility coefficient. [29].

Comparison with existing mass balance.

We have confirmed that the values of SMB estimated in the previous studies [32], [34] overestimate the mass balance of the Eastern Antarctic. This difference is explained by the two following interpretations :

— The only values of accumulation between TNB-DC date from 1959-1960 [35]. These values were determined from radioactivity β. Koerner showed that this method is a bit weak in the case of little accumulation [36].

— The accumulation of snow was considered to be close to precipitation. Our research show that the processes of sublimation were either underestimated or not taken into account

.

The originality of these phenomenas and relationships that we have put into place has been recently taken up in LGGE, as part of the thesis of D. Verfaillie (2014), and published in [37].

2.7 Spatial and temporal variability of snow accumulation.

Here, we succinctly present the analysis of data selected during the crossing TNB-DC [38]. We have retaken the main conclusions of interest for the interpretation of the analysis of ice cores. The results of simple simulation (1-D model) showed that the spatial variability of snow accumulation on a kilometer scale is of an order of a larger size than the temporal decadale of ancient variability. Consequently, the reconstruction of a previous climate, using borehole data in the firn/ice in regions of strong spatial variability of snow accumulation, is complicating. In regions where one finds topography with "megadunes", the distortion of data is characterized by a temporal frequency of the accumulation of around a1500 year period. The length of the variation of this frequency tied to meso-relief (megadunes) depends on the speed of ice run-off and the accumulation of snow, and can consequently vary in time and space. The domes are the preferential site for boreholing ice cores, in order to study the temporal variability of the climate, since its interpretation is easier when snow is derived from the same surface point. Our measures and analysis equally confirmed a rise in accumulation of around 30% during the past two centuries, with regard to the average from the past 5000 years.

Chapitre 3

Algorithms of treatment of the satellite images Radar Synthesis of Opening (RSO)

The last paragraph of the preceding chapter introduced the spatialization of the treatment of information via satellite imagery. Thus, I focus my interests on the possibilities of treatment of RSO images on ice and glaciers. From at least a pragmatic point of view, one reason for this is that I could obtain the first interferogram on the alpine glaciers. I searched, therefore, for methods to execute fringes of interferences, from which a project collaboration was initiated with E. Trouvé, in the framework of project MEGATOR (work published in [39]). Interferometry is a technique which encompasses artifacts, necessary to evaluate, a project that we carried out with Lionel Bombrun in the framework of his thesis [40]. A synopsis of this work is provided in section 3.1. The section 3.2 succinctly revisitsthe works of Lionel Bombrun, regarding polarization. In the section 3.3, the concept of hierarchial segmentation is presented, taking into account the information of texture present in polarimetric images.

3.1 Interferometry differential SAR, applied to glaciers

Interferometry is a technique employed over a long time. We can quote the work of [41] for purposes of observation of the moon, and subsequently, obserations of Earth with the first interferograms in measuring the topography of San Francisco Bay [42]. This technique was then very much utilized to measure the deplacement of glaciers in the polar zones refGoldstein1993, [43, 44]. However, very few results were published, regarding the alpine glaciers [45], [46]. Because of this challenge, I contributed towards the first interferogram in the valley of Chamonix (in collaboration with Benoit Legresy) from two archived images of the ERS satellites dating from 1996. An original part of this work (achieved with Lionel Bombrun [40] was to show that these fringes of interference were very much representative of glacier movement.

The context of alpine glaciers is very particular :

— The topography having strong reliefs reduces the visibility of glaciers. They are rarely visible in ascending and descending passages of satellites. For this reason, we have only one single 3-D projection of displacement. It is necessary to make strong hypothesis on the flow, in order to obtain the speed 3 [43].

— The small size of glaciers (typically 10 km long, 1 km wide) reveals two consequences on the treatments : It reduces the dimension of filters of interferogram and enlarges the difficulties of progress of the phase.
— The temperature of the ice is near zero degrees, due to a rocky bed at its surface. This limits the penetration of electromagnetic waves and makes for trying measures of ice depth, and impedes the combined use of interferometry and the modelling of ice flow based on the principle of conservation of the mass. [44], [47].

Despite all of these limitations, we have attempted to interpret the fringes of of interferences obtained on the surface of the glaciers in the valley of Chamonix. This is the procedural idea : From the Chamonix valley, taken from an interferogram generated at alternating days, one obtains a variation of phase $\Delta\Phi$ in each point of the image. The information contained in this phase is derived from several contributions. [48] :

$$\Delta\Phi = \Phi^{orb} + \Phi^{topo} + \Phi^{depl} + \Phi^{atm} + \Phi^{bruit} \tag{3.1.1}$$

The topographic phase and the orbital phase are two determining components that one can extract from the interferogram. Taking into consideration the atmospheric phase and that which is due to negligible noise, the resulting interferometric phase only contains the displacement contribution Φ^{depl}. Consequently, in each point of the Argentiere glacier, for example, we acknowledge a projection of displacement according to the intended line of the satellite (Line of Sight, LOS), represented by Φ^{depl}.

While considerings the two following hypothesis :
— The flux of ice flows parallel to the surface (Surface Parallel Flow (SFP)), signalling absence of ice removal on the surface in winter, at an alternate day.
— The ice flows in the largest direction, the field of ice flow speed can be calculated.
A definite orthonomed marker follows :

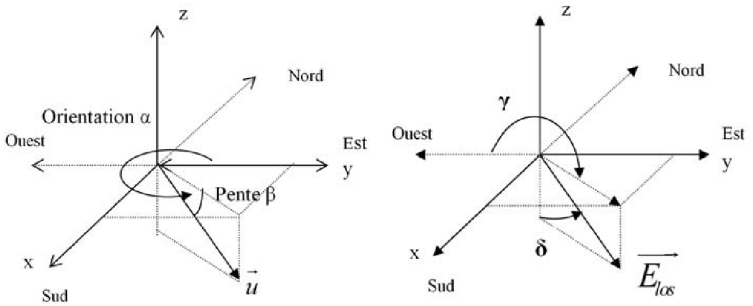

FIGURE 3.1.1 – orthonomic marker (x, y, z), with angles and directions of the vector flow $\overrightarrow{u}$ et du vecteur déplacement $\overrightarrow{E}_{LOS}$.

For each pixel of the numeric model of Terrain (MNT) belonging to the glacier, we calculate in an orthonormic marker (x, y, z), the unitarian vector of flow $\overrightarrow{u} in the direction of the largest slope$(3.1.1) :

$$\overrightarrow{u} = \begin{bmatrix} -\cos(\beta)\sin(\alpha) \\ -\cos(\beta)\cos(\alpha) \\ -\sin(\beta) \end{bmatrix} \tag{3.1.2}$$

α represents the angle between the geographic North and the projection of flow in the marker (x, y, z).

β represents the angle between the plan of the largest slope and the horizontal plan in the marker(x, y, z).

- For each pixel of the elapsed phase corresponding to the glacier, we calculate the unitarian vector $\overrightarrow{E}_{LOS}$ as follows :

$$\overrightarrow{E}_{LOS} = \begin{bmatrix} -\sin(\delta)\sin(\gamma) \\ -\sin(\delta)\cos(\gamma) \\ -\cos(\delta) \end{bmatrix} \tag{3.1.3}$$

δ represents the angle between the vertical and the aim of the satellite called "incidence".
γ represents the angle "azimutal" of the satellite in the marker (x, y, z).

The deplacement measured along the aimed line D_{los} is calculated, commencing from the value of the unwound phase Φ^{depl} , following the expression :

$$D_{los} = \lambda \frac{\Phi^{depl}}{4\pi} \tag{3.1.4}$$

In the case of ERS satellites : $\lambda = 5{,}66$ cm. Finally, the model of the surface speed of the glacier $\left|\overrightarrow{V}_s\right|$ in the direction of the line having the largest slope is obtained by :

$$\left|\overrightarrow{V}_s\right| = \frac{D_{los}}{\Delta t \cdot \langle \overrightarrow{E}_{los} \cdot \overrightarrow{u} \rangle} \tag{3.1.5}$$

The unwinding of the phase is achieved by a least-squares method [49]. Furthermore, it is necessary to know the offset to apply to the components azimut and distance of the interferometric phase. To accomplish this, we chose a stable zone of the Argenti ?re Glacier, determined from annual measurements of implanted tags in-situ, which provide a reference point. We can thus determine a field of speed of the surface, along with a longitudinal profile of speeds (Fig. 3.1.2). We take note (cf. Figure 3.1.2), that we have a good correspondence with the satellite measurements (yellow dash) and the in-situ measurements (black cross)

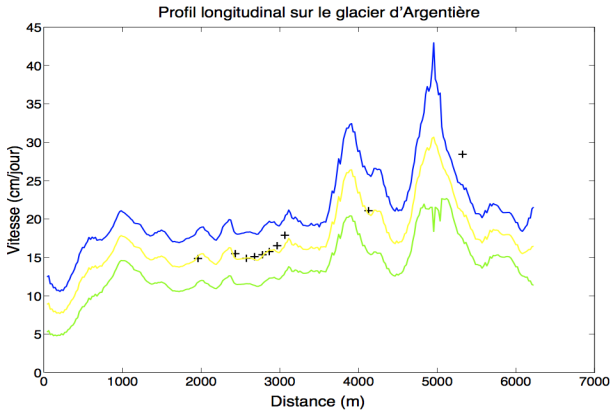

FIGURE 3.1.2 – Comparison between the interferometric measurements (yellow dash) and uncertainties (blue and green dash), and the ground measurements (black crosses) along a longitudinal profile on the Argenti ?re Glacier.

Incidentally, one can equally determine the offset from the rising passage and the descending passage of the satellite [50]. Another aspect that we have treated and published (Trouvé et al. [51]) is

the determination of the deplacement from a shining point (reflector corner) in the images. Stemming from a series of images ERS and from the combinasion of several interferograms, one can also analyse the residual fringes, in order to find their origins : fringes tied in with either atmospheric disruptions or the the topography, or even translating a spatial and temporal evolution of the glacier. These different results were shown at the IGARSS Congress (2009) and were published in the journal IEEE-GRSL [50].

3.2 Polarimetry radar

This section is purposely very succinct. It refers back to the main results obtained in the thesis of Lionel Bombrun [40].

From a synthetic standpoint, we focus our interests on theorems of polarimetric decomposition from an incoherent electromagnetic wave and, more precisely, of a decomposition method for correct values and vectors in the matrix of coherence **T**.

To be able to caracterize the radar backscattering, one must have a model to set up the exact vectors. We compared two existing models : α/β and the model proposed by R. Touzi Target Scattering Vector Model (TSVM) [52, 53]. We saw that in the case where the target is symmetric ($\tau_m = 0$), the two models drive at the same parameters. However, in the general case where the targets are asymmetrical ($\tau_m \neq 0$), the parameters of the two models are not equal. A complete description of the backscatter is provided by the conjoined study of three invariant via rotations of the TSVM : α_s, Φ_{α_s} et τ_m.

In a second attempt, departing from the decomposition in proper values and vectors of the matrix of coherence **T**, we have defined a coherence matrix associated with the mechanism of mean backscattering, being a matrix of placement 1. We have subsequently proposed a definition of the backscattering vector associated with the mechanism of mean backscattering, with the help of the linear combination of the proper vectors of the matrix of coherence **T**, where each proper vector is pondered by the square root of its associated proper value. These projects are developed in [40].

3.3 Algorithms of hierarchal segmenting of images SAR

The segmentation of images is directly related to the notions of difference and similarity of pixels, like the human visual system perceives. There is no single method of segmentation of an image. Two large families of segmentation seen to date are : the "frontier" approach and the "region" approach [54].

— The notion of frontier (or contour) is associated with a discontinuity between the properties of two related sets of points. We then define a region as being the interior of a closed line.

— The notion of region makes reference to the groups of pixels having common properties (intensity, texture,...). These methods directly lead to a partition of the image where each pixel belongs to a single image and unique region.

The original idea proposed here was an algorithm of hierarchal segmentation, taking into account the information of present texture in polarimetric images. [55]. We have demonstrated that the modelling of a texture by the Fisher distribution is adapted to the backscattering of radar

waves. The expressions of the vector statistics of backscattering (in 1- view) and of the covariance matrix (in L- views) in the case where the texture is distributed according to the Fisher law, were derived. With these established statistics, we have calculated the log-probability and expressed the value of the criteria used during the fusion of the segments in the algorithm of hierarchial segmentation.

This algorithm can be described as follows (Figure 3.3.1, dendrogramme) :

— or an initial partition of 12 segments.
— At each iteration, we fuse the two segments, closest 4-related in maximum probability, to obtain a final partition composed of a single segment.

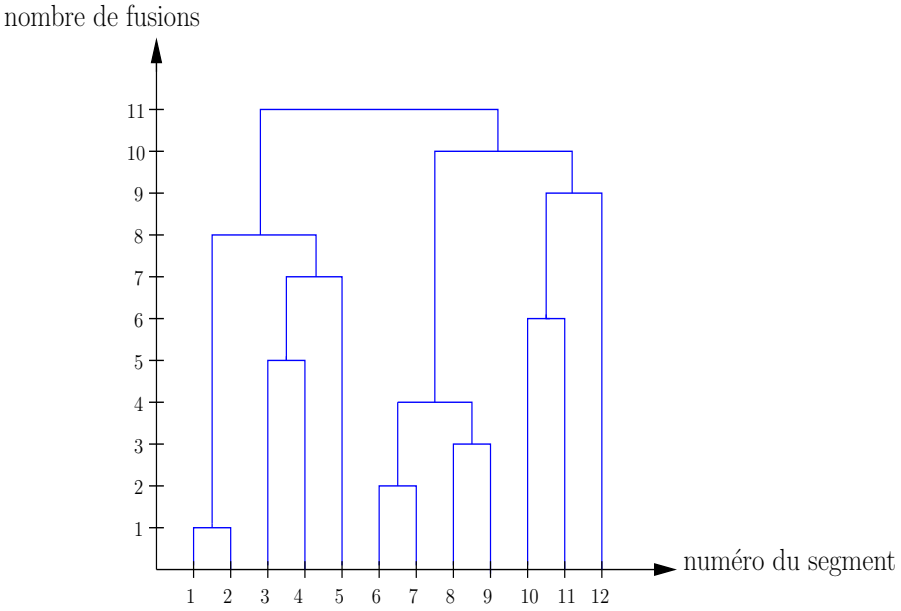

FIGURE 3.3.1 – example of dendrogram

Soit X collection des pixels x_i of the image I, $X = \{x_i,\ i \in I\}$ and a partition $P = \cup_{k\in 1}^{N_p} S_k^p$. Assuming $x_{i_k} \in S_k^P$ of parameter θ_k^p depending on the segment S_k^P (homogenous in a partition). Soit $\Theta_P = \left\{\theta_k^P,\ k = 1, .., N_p\right\}$ whole of possibilities associated with P, while making hypothesis that the $\mathbf{x}_i$ are independent - two by two, and of the same law, the probability to obtain $\mathbf{x}$ knowing Θ_P is equal at :

$$p\left(\mathbf{x}|P, \Theta_P\right) = \prod_{k=1}^{N_p} \prod_{i_k \in S_k^p} p\left(x_{ik}|\theta_k^P\right) \tag{3.3.1}$$

The approach in the sense of probability maximum looks for the division P as well as the ensemble Θ_P containing the parameters of the distribution of $\mathbf{x}$ for the partition P which maximize the function of probability.

From a given partition P, the parameters of the distribution of $\mathbf{x}$ for the segment S_k^p are estimated from statistics calculated on this segment. In general, these estimates $\widehat{\theta}_k^p$ are calculated by the method of moments or even from those compiling [56]. The log-probability, given the partition P and the estimates $\widehat{\theta}_k^p$, are espressed in function with the log-probability LLF(S_k^p) (Log Likelihood Function)

for each segment, precising :

$$\begin{aligned} \mathrm{LLF}\,(P) &= \sum_{k=1}^{N_p} \sum_{i_k \in S_k^p} \ln\left(p\left(x_{ik}|\widehat{\theta}_k^p\right)\right) \\ &= \sum_{k=1}^{N_p} \mathrm{MLL}\,(S_k^p) \end{aligned} \tag{3.3.2}$$

Furthermore, the log-probability for the partition P is equal to the sum of the maximum log probabilities, calculated in each segmentest S_k^p of the partition P (cf. [57]).

For a number of fixed segments k, the objective is to find the partition P_k that maximizes the probability (cf. eq. 3.3.2). If n designates the size of the image I, a large number of partition P_k à k segments exists. The research of the partition P_k that globally maximizes the log-probability takes too long to calculate.

To find a sub-optimal solution, but less time-costly (in calculating), we return to the properties of log-probability. Log-probability is a growing monotone function which rises with the number of segments in a partition. Log-probability is maximal, whereas the number of segments is equal to the number of pixels in the image. I. This is to say that each pixel corresponds to a segment. In opposition, log-probability is minimal when the partition is constituted of a single segment. The partition P_1 is equal to the total image I, and between these two extremes the log-probability diminishes as one merges segments.

As one uses an algorithm of hierarchal segmentation, the partition P_k à k segments is obtained by merging two segments 4-relevant of the partition P_{k+1}.

Note D_k, the decline of the log-probability during the fusion of two segments [57].

$$\mathrm{D}_k = \mathrm{LLF}\,(P_{k+1}) - \mathrm{LLF}\,(P_k) \tag{3.3.3}$$

One can rewrite the value of log-probability for a partition containing k segments as being equal to the log-probability for a partition of n segments in which one removes the log-probability lost at each iteration, to pass from n to k segments.

$$\mathrm{LLF}\,(P_k) = \mathrm{LLF}\,(P_n) - \sum_{q=k}^{n-1} \mathrm{D}_q \tag{3.3.4}$$

To find the partition P_k to k segments, return to maximize log-probability $\mathrm{LLF}\,(P_k)$.

If P_n refers to the initial partition, the maximization of $\mathrm{LLF}\,(P_k)$ is equal to the minimization of D_q. At each iteration, the algorithm of hierarchal segmentation merges the segments 4-incidental S_i et S_j which minimize the decrease D_q of the log-probability. The hierarchal segmentation thus gives a sub-optimal solution to the problem of maximization of probability.
From the equations (3.3.2) and (3.3.3), D_q is written [57] :

$$D_q = \mathrm{SC}_{i,j} = \mathrm{MLL}(S_i) + \mathrm{MLL}(S_j) - \mathrm{MLL}(S_i \cup S_j) \tag{3.3.5}$$

The criteria for fusion of segments of the hierarchal fragmentation being based on log-probability of segments brings forward an interest in the statistics of these segments and therefore, of polarimetric images. This work was devised in the thesis of Lionel Bombrun [40], and from collaboration with Jean-Marie Beaulieu [55]. The zones of images are textured or non-textured ; the choice of associated statistics in the multi-viewed case focus respectively on the distribution of Wishart, and on a Gamma or Fisher distribution. We will only focus on the textured zones (the case of field images of snow, for example).

Multiplying model of textured zones While the matrux of coherence Σ varies spatially in the image, the surface is textured. In the general case, the vector of backscattering observed $\mathbf{x}$ can decompose as does a matrix G diagonal, by a backscattering vector associated at an equivalent homogenic surface [58, 59].

$$\mathbf{x} = \mathrm{G}\mathbf{x}_h = \begin{bmatrix} \sqrt{\mu_1} & 0 & \cdots & 0 \\ 0 & \sqrt{\mu_2} & \ddots & \vdots \\ \vdots & \ddots & \ddots & 0 \\ 0 & \cdots & 0 & \sqrt{\mu_p} \end{bmatrix} \begin{bmatrix} \mathbf{x}_{h1} \\ \mathbf{x}_{h2} \\ \vdots \\ \mathbf{x}_{hp} \end{bmatrix} \tag{3.3.6}$$

The vector $\mathbf{x_h} = [\mathbf{S}_1, ..., \mathbf{S}_p]$ represents the components of the matrix $\mathbf{S}$ of backscattering of polarmetric data (p=3 dans le cas monostatique). The matrix G caracterizes the texture in each polarmetric canal. Assuming the hypothesis that the texture is independant of the canal of polarization and that the speckle is completely developed, the observed covariant matrix (Σ) is written as the product of a positive random scalar variable $\mu = \mu_1 = \cdots = \mu_p$ by a matrix of covariance associated with an homogenous zone.Σ_h.

$$\Sigma = \mu\Sigma_h \tag{3.3.7}$$

où Σ_h is distributed according to a law of Wishart.

If we consider the matrix of covariance $\mathbf{Z}$, the estimator in the sense of backscattering maximum of the texture is [60, 61] :

$$\hat{\mu}_{MV} \quad = \quad \mu \, \frac{1}{p} \operatorname{tr}\left({\Sigma_h}^{-1}\mathbf{Z}_h\right) \tag{3.3.8}$$

estimator non-biased because $E\left[\hat{\mu}_{MV}\right] = \mu$. The estimator in the sense of backscattering maximum of the matrix of homogenous covariance is written :

$$\hat{\Sigma}_h = \frac{1}{N}\sum_{n=1}^{N}\frac{1}{\mu_n}\mathbf{Z}_n \tag{3.3.9}$$

We have then established the expression for the distribution of the coherent matrix by using the multiplicative scalar model for the texture and a model of texture distributed according to a law of Fisher. We have shown that that density of probability of the covariant matrix for a distributed texture according to a law of Fisher is written [62, 63] :

$$p_{\mathbf{Z}}(\mathbf{Z}|\Sigma_h, \mathcal{L}, \mathcal{M}, m) = \frac{L^{Lp}|\mathbf{Z}|^{L-p}}{\pi^{\frac{p(p-1)}{2}}\Gamma(L)\cdots\Gamma(L-p+1)|\Sigma_h|^L}\frac{\Gamma(\mathcal{L}+\mathcal{M})}{\Gamma(\mathcal{L})\Gamma(\mathcal{M})}\left(\frac{\mathcal{L}}{\mathcal{M}m}\right)^{Lp}\Gamma\left(Lp+\mathcal{M}\right)U\left(a,b,z\right) \tag{3.3.10}$$

Consequently, for a distributed texture according to a law of Fisher, the covariant matrix follows a distribution of KummerU. It is now sufficient to recalculate the criteria of the maximum

of log-probability (MLL) for a distributed texture according to a law of Fisher. The maximum log-probability is deducted from the distributionKummerU from the covariant matrix (Eq. 3.3.10). In suppressing the terms that cancel themselves out during calculation of $\mathrm{SC}_{i,j}$, we obtain the following expression [62, 63] :

$$\begin{aligned}\mathrm{MLL}(S) &= -nL\ln|C_h| + n\ln\left\{\Gamma(\hat{\mathcal{L}}+\hat{\mathcal{M}})\right\} - n\ln\left\{\Gamma(\hat{\mathcal{L}})\right\} - n\ln\left\{\Gamma(\hat{\mathcal{M}})\right\} \\ &+ nLp\ln\left(\frac{\hat{\mathcal{L}}}{\hat{\mathcal{M}}\hat{m}}\right) + n\ln\left\{\Gamma(Lp+\hat{\mathcal{M}})\right\} \\ &+ \sum_{\mathbf{Z}_k\in S}\ln\left\{\mathrm{U}\left(Lp+\hat{\mathcal{M}};1+Lp-\hat{\mathcal{L}};\frac{L\ \mathrm{tr}\left({C_h}^{-1}\mathbf{Z}_k\right)\hat{\mathcal{L}}}{\hat{\mathcal{M}}\hat{m}}\right)\right\} \end{aligned} \tag{3.3.11}$$

where $\hat{\mathcal{L}}$, $\hat{\mathcal{M}}$, $\hat{m}$ are respectively the estimates of parameters $\mathcal{L}$, $\mathcal{M}$, m of the distribution of Fisher, by the method of log-cumulants [56, 64]. C_h being estimated in the sense of probability maximum of Σ_h for the segment S (Eq. 3.3.9).

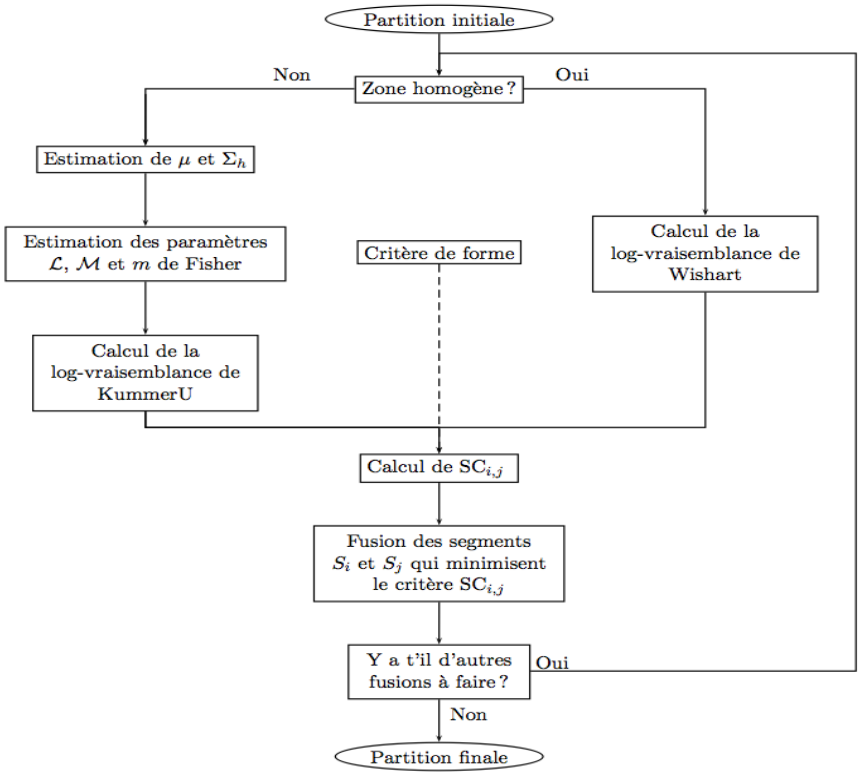

FIGURE 3.3.2 – Principal of the hierarchal fragmentation method.

The algorithm of hierarchal segmentation commences by an initial partition Fig.3.3.2. Then, for each pair of segments 4-relevant, one implements a test to determine if one is in presence of a certain texture :

- In the case where the zone is homogenous (no texture), the criteria of Wishart is calculated.
- In the opposing case, μ et Σ_h are estimated in the sense of probability maximum by the equations :3.3.8 and 3.3.9.
- Afterwards, commencing from the $n_i + n_j$ estimated from the texture, the parameters $\mathcal{L}$, $\mathcal{M}$

and m from the distribution of Fisher are estimated by the log-moments method.
— Then, we calculate the criteria of KummerU, based on log-probability (equation 3.3.11).
— We subsequently achieve $SC_{i,j}$ and search for the two segments S_i et S_j which minimize this criteria. We reiterate these steps until the number of segments in the final partition are achieved.

3.4 Conclusion

Following these publised projects in the jounal IEEE-TGRS [65], I count on applying this algorithm to the fragmentation of radar images acquired on snowpack. Starting from this fragmentation in homogeneus zones, it will be interesting to calculate the mean backscattering integrated from each zone, and to modify differently the parameters of the physical model of evolution of the snow Surfex/Crocus. This procedure is described in chapter 5 of this manuscript. Another aspect to examine is that of phase information. It has been recently shown, through in-situ multi-temporal measures, that it is possible to obtain the equivalent of dry snow through water (SWE, Snow Water Equivalent), from the evolution of the phase in bande X.

Chapitre 4

Estimators and statistics of RSO images for the measurement of deplacements

The emergence of spatial high resolution in imagery RSO leads us to attempt to model radar backscattering, according to different statistic laws of the gaussian laws. This concept is explored in the section4.1. The idea developed in the section 4.2 proceeds to further exploit the texture of several RSO images from the same zone, to attempt to follow the deplacement of geophysical objects. Finally, we apply this method regarding the glaciers in the section 4.3.

4.1 SIRV Model.

A jumble model PoISAR based on the use of Spherical Invariant Random Vectors (SIRV) - studied [66, 67]. The vector of complex polarmetric backscattering$\mathbf{k}$ can be defined as the product of the root of a random positive scalar variableτ with an independent gaussian vector $\boldsymbol{z}$:

$$\mathbf{k} = \sqrt{\tau}\ \boldsymbol{z}, \tag{4.1.1}$$

where τ represents the texture - that is to say, a process potentially non-homogenous. We attempt to separate the texture from the strength. The vector $\boldsymbol{z}$ that represents the speckle is complex, gaussian, of zero-mean and of a matrix of covariance.$\mathbf{M} = E\{\boldsymbol{z}\boldsymbol{z}^H\}$ (H is the operator of united complex transposition).

Estimated texture. τ

For a matrix of given covariance. [$\mathbf{M}$], estimated $\hat{\tau}_i$ in the sense of maximum probability, of parameter of texture τ for the pixel i is given by :

$$\hat{\tau}_i = \frac{\mathbf{k_i}^H [\mathbf{M}]^{-1} \mathbf{k_i}}{p}, \tag{4.1.2}$$

where p is the dimension of the backscattering vector $\mathbf{k}$ ($p = 3$ in the monostatic case, because the emission in horizontal polarization H and the reception in vertical polarization V is equivalent to VH (HV = VH)).

With the case of a determining texture, the estimator in the sense of maximum probability of the matrix of normalized covariance is the solution of the following recursive equation [68][69] :

$$[\hat{\mathbf{M}}]_{FP} = f([\hat{\mathbf{M}}]_{FP}) = \frac{p}{N}\sum_{i=1}^{N}\frac{\mathbf{k}_i\mathbf{k}_i^H}{\mathbf{k}_i^H[\hat{\mathbf{M}}]_{FP}^{-1}\mathbf{k}_i} = \frac{p}{N}\sum_{i=1}^{N}\frac{\boldsymbol{z}_i\boldsymbol{z}_i^H}{\boldsymbol{z}_i^H[\hat{\mathbf{M}}]_{FP}^{-1}\boldsymbol{z}_i}. \tag{4.1.3}$$

Concerning the case of a non-determining textur, the estimator (4.1.3) is only an approached version of the estimator of the matrix of covariance, in the sense of the maximum of probability. The estimator in the sense of maximum of probability of the matrix of normalized covariance depends, thus, on the distribution of τ. Its expression is :

$$[\hat{\mathbf{M}}_{ML}] = \frac{1}{N}\sum_{i=1}^{N}\frac{h_{p+1}\left(\mathbf{k}_i^H[\hat{\mathbf{M}}_{ML}]^{-1}\mathbf{k}_i\right)}{h_p\left(\mathbf{k}_i^H[\hat{\mathbf{M}}_{ML}]^{-1}\mathbf{k}_i\right)}\,\mathbf{k}_i\mathbf{k}_i^H \tag{4.1.4}$$

where the expression of the generating function of density $h_p(x)$ est donnée par [70] [71] :

$$h_p(x) = \int_0^{+\infty}\frac{1}{\tau^p}\exp\left(-\frac{x}{\tau}\right)f_\tau(\tau)\,d\tau \tag{4.1.5}$$

Pascal *et al.* established existence and uniqueness in a factor close to the matrix of normalized covariance of the Fixed Point $[\hat{M}]_{FP}$ as well as the convergence of the recursive algorithm which allows to estimate $\hat{\tau}$ and $[\hat{M}]_{FP}$ regardless of the initialization of $[\hat{M}]_{FP}$ [72, 73].

The recursive algorithm of estimation consists of calculating, in a first setting, an estimate of the matrix of covariance $\hat{\mathbf{M}}$ with (4.1.3) or (4.1.4) then, estimating the texture $\hat{\tau}$ with (4.1.2). In our case, the trace of the matrix of covariance is normalized by p. It is of importance that we insist upon the fact that absolutely no hypothesis had been made concerning the probability density of the texture in th definition of SIRV's. The SIRV's describe a whole class of stochastic processes. This class includes the conventional models of clutter, like the gaussian laws, $\mathcal{K}$, $\mathcal{G}^0$ et KummerU respectively corresponding to textures distributed according to the laws Dirac, Gamma, Inverse Gamma and Fisher [74, 75, 62].

In practice, the estimator (4.1.4) is only used in cases in which the distribution of τ is known, during which the analytical expression of h_p can be calculated. In other cases, this is the approached estimator (4.1.3) which is used.

Simulation of the texture.

The laws of Fisher are commonly used to simulate the data RSO in an urban context [56]. In our case, for natural ice and glacier fields, the law of Fisher more effectively simulates data than other laws, thus we have implemented it. The distribution of Fisher is a law of three parameters, defined by :

$$f_\tau(\tau) = \mathcal{F}[m,\mathcal{L},\mathcal{M}] = \frac{\Gamma(\mathcal{L}+\mathcal{M})}{\Gamma(\mathcal{L})\Gamma(\mathcal{M})}\frac{\mathcal{L}}{\mathcal{M}m}\frac{\left(\frac{\mathcal{L}\tau}{\mathcal{M}m}\right)^{\mathcal{L}-1}}{\left(1+\frac{\mathcal{L}\tau}{\mathcal{M}m}\right)^{\mathcal{L}+\mathcal{M}}} \tag{4.1.6}$$

où $m > 0$ is a scale parameter, $\mathcal{L} > 0$ and $\mathcal{M} > 0$ are two parameters of form

The particularity of this family of laws is its hybrid behavior, being "head-heavy" and "tail-heavy" at the same time. In this sense, it generalizes the laws Gamma and Gamma Inverse. The first three log-cumulatives of the law of Fisher are written :

$$\begin{aligned}
\tilde{\kappa}_{x(1)} &= \log(m) + \Psi(\mathcal{L}) - \log(\mathcal{L}) - (\Psi(\mathcal{M}) - \log(\mathcal{M})). \\
\tilde{\kappa}_{x(2)} &= \Psi(1, \mathcal{L}) + \Psi(1, \mathcal{M}). \\
\tilde{\kappa}_{x(3)} &= \Psi(2, \mathcal{L}) - \Psi(2, \mathcal{M}).
\end{aligned} \tag{4.1.7}$$

The plan formed by the log-cumulatives of order 2 and 3, $\tilde{\kappa}_2 - \tilde{\kappa}_3$, allow to represent the defined laws on $\mathbb{R}^+$. The plan $\tilde{\kappa}_2 - \tilde{\kappa}_3$ is represented in the figure 4.1.1 with the repartition of different families of laws, with which the Gamma and Gamma Inverse laws cut the plan in three. Here, we limit ourselves to the representation of the laws of monovaried random variable, however this type of representation could be expanded to a multivaried case [76].

FIGURE 4.1.1 – Representation of the laws derived from the Pearson system.

The illustration 4.1.2 shows an extract of image TerraSAR-X (28/01/2009) from the Argentiere Glacier. This illustrates the changes of distribution between intensity (here, from canal HH) and the texture τ extracted from a clear cut database TSX dula-pol, by the processes SIRV (previously presented). Although very similar, these two images cannot be modelled by the same fashion, as the associated histograms suggest.

If we use the plan $\tilde{\kappa}_2 - \tilde{\kappa}_3$ to represent these distributions, we notice that the cloud of points $(\kappa_3,\ \kappa_2)$ of the image of intensity traced in the illustration 4.1.3 corresponds more to the Gamma laws, whereas the cloud of the image of texture is more distributed in the region of the laws of Fisher (Figure 4.1.3).

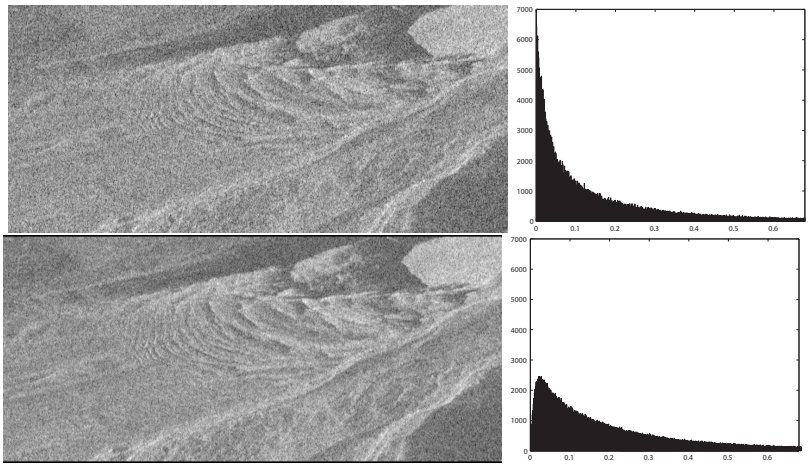

FIGURE 4.1.2 – Intensity HH (above), texture τ (below) and the 2 histograms associated with a zone of the Argentiere Glacier, extracted from polarimetric images (HH, HV) from satellite TerraSAR-X le 28-01-2009.

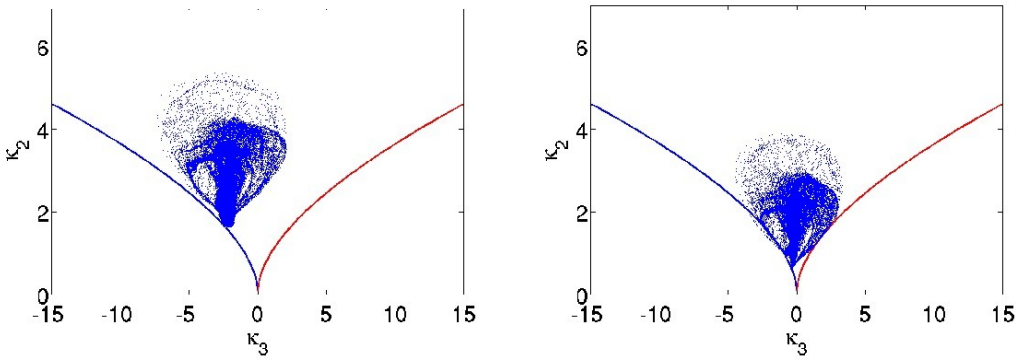

FIGURE 4.1.3 – Plan $\tilde{\kappa}_2 - \tilde{\kappa}_3$ of the intensity (left side) and of the texture τ (right side) calculated, commencing from the extract of image TerraSAR-X of Argentiere Glacier (width of pixel window is N=99). One notices that the whole of values of intensity gather together around the blue line which represents the class of gamma laws, while the values of texture are represented in the plan of Fisher.

4.2 Algorithm of textures follow-up by Maximum Likelihood (ML).

In collaboration with Olivier Harant, within the framework of his thesis [77], we have developed the concept of following texture by means of MV [78] while exploiting the local statiistics of an image. With Olivier Harant, we proposed [79] a new algorithm adapted to the characteristics of polarimetric HR RSO images. The illustration 4.2.1 represents the complete chain of this method. The three important steps are as follows :

1. The decomposition SIRV of dataset PolSAR.
2. The modelling of the texture τ.
3. Displacement estimate by MV.

Àlong with these three steps, two additional refining steps are added :

— A step of hierarchal fragmentation of data.

— The use of a constraint of flow in the case of measuring displacements.

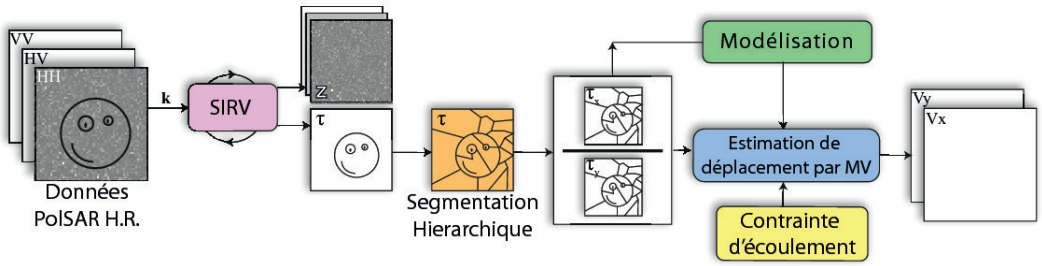

FIGURE 4.2.1 – General scheme of method to follow texture.

Formality of MV method

Soit $\mathbf{k}_x = [\mathbf{k}_{x_1}, \ldots, \mathbf{k}_{x_n}]$ et $\mathbf{k}_y^i = \left[\mathbf{k}_{y_1}^i, \ldots, \mathbf{k}_{y_n}^i\right]$ two zones of a couple of PolSAR data, respectively extracted from an image of reference and a secondary image. We assume that each zone contains n independent pixels, identically distributed (i.i.d.). The reference and secondary textures $\tau_x = [\tau_{x_1}, \ldots, \tau_{x_n}]$ and $\tau_y^i = \left[\tau_{y_1}^i, \ldots, \tau_{y_n}^i\right]$ are estimated, due to (4.1.2) and (4.1.3). These two zones are offset from a noted displacement i vector from which the components characterize the displacement in distance and azimuth. The method to measure displacement through Maximum Probability (Maximum-Likelihood, ML) consists of estimating the displacement vector $\mathbf{v}_{\mathrm{ML}}$ while maximizing the following Conditional Density Function (CDF) for each possible displacement i :

$$\mathbf{v}_{\mathrm{ML}} = \underset{i}{\mathrm{Argmax}} \; p\left(\tau_x | \tau_y^i, \mathbf{v}_i\right). \tag{4.2.1}$$

Calculation of laws of relation for two textures $\alpha = \frac{\tau_X}{\tau_Y}$.

In order to reduce the influence of multiplying noise (called speckle : characteristic of RSO images and according to [78]) we have decided to use the relation of images. Thus, we developed a formalism using the relation of the two images $\alpha = \frac{\tau_x}{\tau_y}$ which is a random variable defined in $\mathbb{R}_*^+$.

Relation of images

Being X and Y two random variables, and $Y = g(X)$ or g is strictly a monotone function. Being $F_X(x)$ and $F_Y(y)$ respectively the functions of class schemeC^1 from X and Y, on a :

$$F_Y(g(x)) = F_X(x) \tag{4.2.2}$$

Upon deriving this relation, with respect x, we obtain :

$$f_\alpha(\alpha)\frac{1}{\tau_Y} = f_{\tau_X}(\tau_x) \tag{4.2.3}$$

While using this new random variable α, the expression (4.2.1) becomes :

$$\mathbf{v}_{\mathrm{ML}} = \underset{i}{\mathrm{Argmax}} \prod_{k=1}^{N} f_{\tau_X}(\tau_{x_k} | \tau_y^i, \mathbf{v}_i) = \underset{i}{\mathrm{Argmax}} \prod_{k=1}^{N} \frac{1}{\tau_{y_k^i}} f_\alpha(\alpha_k | \tau_y^i, \mathbf{v}_i) \tag{4.2.4}$$

In the sequence, the proposed statistical methods use random variable α as one of study. This necessitates, above all, to characterize its law in function of distribution of images τ_X and τ_Y which make up the relation. Ǵiven the importance and the presence of the Gamma and Fisher laws in univariate RSO imagery (intensity, texture...), the law of relation α is calculated for these two ranges of law. The cases in which τ_X and τ_Y are uncorrelated and correlated are detailed.

Being τ_x as τ_y two correlated random variables, the distribution of ratio α of these two variables is provided by[80, Eq. 6.60] :

$$f_\alpha(\alpha) = \int_0^\infty f_{\tau_X,\tau_Y}(\alpha\tau,\tau)\tau d\tau. \tag{4.2.5}$$

We have generalized the proposed expressions in [78], have calculated the ratio distribution of random variables distributed according to Gamma and Fisher laws, and have given the expressions of displacement vectors in the example of correlated and non-correlated textures.

Variables example, non-correlated, Expression of displacement vector $\mathbf{v}_{\mathrm{ML}}$ s'écrit :

$$\mathbf{v}_{\mathrm{ML}} = \underset{i}{\mathrm{Argmax}} \frac{\Gamma(2\mathcal{L})^N}{\Gamma(\mathcal{L})^{2N}} \prod_{k=1}^{N} \frac{\tau_{x_k}^{\mathcal{L}-1}\tau_{y_k^i}^{\mathcal{L}}}{(\tau_{x_k}+\tau_{y_k^i})^{2\mathcal{L}}} \tag{4.2.6}$$

After being passed into log, the Probability of the images ratio to maximize is written :

$$\mathrm{VRG}(\tau_X,\tau_Y^i,\mathcal{L}) = -N\log\left(B(\mathcal{L},\mathcal{L})\right) + \sum_{k=1}^{N}(\mathcal{L}-1)\log\left(\tau_{x_k}\right) + \mathcal{L}\log\left(\tau_{y_k^i}\right) - 2\mathcal{L}\log\left(\tau_{x_k}+\tau_{y_k^i}\right) \tag{4.2.7}$$

where $B(\cdot,\cdot)$ is the function Beta of Euler.

Correlated variable cases

$$\begin{aligned}\mathrm{VRGB}(\tau_X,\tau_Y^i,\mathcal{L}) = &\sum_{k=1}^{N} \tau_{x_k} - \tau_{y_k^i} - 2\log\left(1+\exp(\tau_{x_k}-\tau_{y_k^i})\right) \\ &- \left(1+\frac{1}{2\mathcal{L}}\right)\log\left(1-\frac{4\rho_k\exp(\tau_{x_k}-\tau_{y_k^i})}{(1+\exp(\tau_{x_k}-\tau_{y_k^i}))^2}\right).\end{aligned} \tag{4.2.8}$$

Non-correlated variable cases with Laws of Fisher, Probability of ratio of images to maximize, to estimate displacement in the case of a decorrelated texture between images is :

$$\begin{aligned}\mathrm{VRF}(\tau_X,\tau_Y^i,\mathcal{L},\mathcal{M}) =& N\log\left(\frac{B(2\mathcal{L},2\mathcal{M})}{[B(\mathcal{L},\mathcal{M})]^2}\right) - (\mathcal{M}+1)\sum_{k=1}^{N}\log\tau_{x_k} + \mathcal{M}\sum_{k=1}^{N}\log\tau_{y_k}^i \\ &+ \sum_{k=1}^{N}\log\left({}_2F_1\left(\mathcal{L}+\mathcal{M},2\mathcal{M};2\left(\mathcal{L}+\mathcal{M}\right);1-\frac{\tau_{y_k}^i}{\tau_{x_k}}\right)\right).\end{aligned} \tag{4.2.9}$$

Correlated variable cases with Laws of Fisher, Probability of ratio of images to maximize, in order to estimate displacement with the case of correlated texture is provided by :

$$\mathrm{VRFB}(\tau_X,\tau_Y^i,\mathcal{L},\mathcal{M}) = K + \sum_{k=1}^{N}(\mathcal{L}_1-1)\log\tau_{x_k} + \mathcal{L}_2\log\tau_{y_k}^i - a\log\left(R_1\tau_{x_k}+R_2\tau_{y_k}^i\right) + \log\left({}_2F_1\left(a,b;c;z_k\right)\right), \tag{4.2.10}$$

avec $K = N\left(\log R_1^{\mathcal{L}_1} + \log R_2^{\mathcal{L}_2}\right) + N\log\left(\frac{B(\mathcal{L}_1+\mathcal{L}_2,\mathcal{M}_2)}{B(\mathcal{L}_1,\mathcal{M}_1)\ B(\mathcal{L}_2,\mathcal{L}_1+\mathcal{M}_2)}\right)$.

These different criteria were tested and evaluated. The method of following the texture, based on the probability of ratio of proposed images in [78] was generalized here, in the case of HR images, due to implementation of laws of Fisher.

Two large ranges of criteria in similarity were tested : criteria based on Gamma laws and those based on the laws of Fisher. We highlighted the sturdiness and the flexibility of statistic criteria, based on the laws of Fisher, and relative to Gamma laws. These criteria reach their limits in non-stationarity of underlying stochastic processes, such as temporal variations of surface state of glaciers in time.

The criteria defined by ratio probability/vraisemblance (VR) were tested by using the two models of possible laws (Gamma and Fisher) on simulated and on real data. In the situation of real data, we have shown interest in using all available polarimetric information. These series of tests underline the versatility and sturdiness of the laws of Fisher, on ratio probability. The VR give proof to more flexibility and allow to exploit non-crossed components (HH or VV) only (cf. thesis Olivier Harant, [77]).

4.3 Application at measurement of displacement of a glacier.

Data TerraSAR-X

We provide an example of results obtained on the Argentiere Glacier.

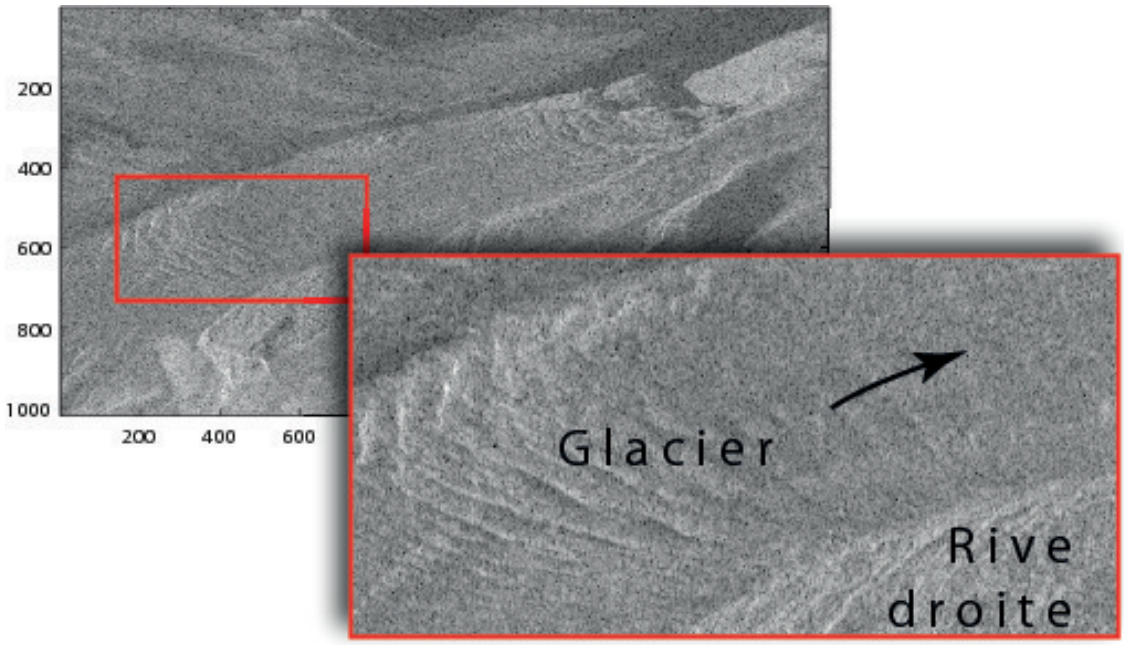

FIGURE 4.3.1 – $\log(\tau)$. Estimated reference texture, using models SIRV - TSX Dual-pol, 08/02/2009. Location of zone used for results of illustration 4.3.2.

The illustration 4.3.1 shows the texture estimated reference, while using the models SIRV - TSX Dual-pol, from 08/02/2009. The illustration 4.3.2 shows estimation results of displacement in the lower zone of Argentiere Glacier, taken from images TSX Dual-pol, from 08/02/2009. The first column in this illustration presents the results obtained with correlation criteria. The second column in the image presents stemming from criteria of Probability of the ratio of images based on the laws of Fisher (VRF) (**??**). The last column in the illustration represents the results obtained with criteria of Probability of Ratio of images based on Gamma laws (VRG). (4.2.7).

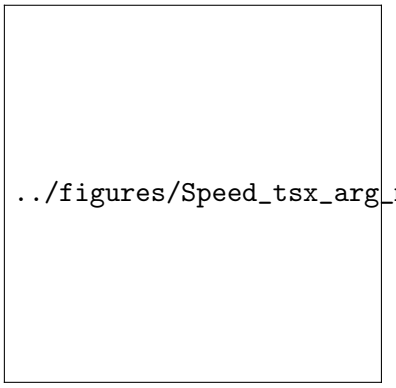

FIGURE 4.3.2 – Results of estimation of displacement on lower part of Argentiere Glacier, from extracted texture of images TSX dual-pol. Above left to right : model of displacement obtained with classic criteria of correlation, VRF, and VRG. Lower left to right : orientation of displacement obtained with classic criteria of correlation, VRF and VRG. Window of analysis : 64×64 pixels. Displacement zone : ± 10 pixels.

The model of criteria for intensity correlation presents a fenestration effect in the upper part of the image, corresponding to the crevassed zone. Orientation in this zone is opposite to sense of flow of glacier. The field of speed obtained with VRF criteria is much more homogenous, and one gets orientation matching with the glacier flow. The lower parts of the images are more problematic : Being very homogenous, the results are very noisy. This work was published in the congresses EUSAR and IGARSS [81, 82].

4.4 Conclusion

The results presented in the previous sections, and published in Harant et al. [79] underline the limits of literal application to theoretical methods introduced in section 4.2. As a matter of fact, the undertaken geophysical problematic shows constraints which exceed the simple statistic tracking of a surface. The nature of the terrain studied is deeply migrant in the weather conditions with which large variability of statistic properties are created in time. This element of non-stationarity reduces the efficiency of methods which implicitly make up the hypothsis of statistic stability. The choice of dates to couple the images is thus significant.

In order to compensate for this weakness, we used upstream hierarchal fragmentation of data, to attempt to optimize the form of windows of analysis, to make them more homogenous in distribution. The results encourage this algorithmic schema, because, other than a follow-up of texture made adaptive by this pre-treatment, giving considerable time conservation. Nevertheless, we must underline the fact that a segment in this study supposedly kept the same form in all the temporal series, of which turned out to be a very improbable hypothesis, but satisfactory in the first instance. An in-depth study of this aspect would necessitate the taking into account of the evolution of fragmentation in time.

In complementarity (or independent of) fragmentation, the addition of a flow constraint was proposed and implemented in the similarity criteria. The adopted formalism grafts this very constraint directly at the core of detection, and not as a weighting *a posteriori*. The resulting constraints are found to be greatly improved with weighting detection by matching with a flow model. The flow model used here is simple and can be improved, as well.

The calculated projection on the ground allowed us to give a sequence of measured displacements and to establish a brief comparative with available GPS data (not shown in this report, cf thèse Olivier Harant [77]). The comparatives confirm the coherence of size sequence of estimations.

Chapitre 5

Problem with assimilation of RSO satellite images for the modeling of snow.

Snow profiling is an important stake for management of water resources, for prediction of avalanche risks, and for simulating the evolution of climate. A better understanding of snow particle size will aid, for example, in modelling its albedo in climate simulation. As well, more effective constraint of densification procedures will allow to better predict the stability of snowpack. Snowpack is a dense, stratified, complex area which varies both spatially (at a scale of 10 meters, approximately) and temporally (at a rate of a few hours during several days). Improved knowledge of properties at each stratum (density, particle size, height, anisotropy, etc.) would allow for a more accurate estimation of water equivalence (Snow Water Equivalent, SWE) or of snowpack stability in case of emergency evacuation with risk of avalanche triggering. From another standpoint, the emergence of new RSO satellites, X (TSX, CSK,...) bands and C (Sentinel) bands, and possibly Ku (mission CorH2O), at high spatial and temporal resolution bring to light new information concerning the state of snow (to exploit in order to constraint a physical model of snow evolution).

This data incites us to improve the backscattering model of electromagnetic waves (EMO), initially achieved by [83], and to develop an algorithm of assimilation, for constraint of the physical SURFEX/Crocus model (developed by MeteoFrance at the Centre of Study of Snow) [84, 85]. Without re-initialization, this model simulates the evolution of snowpack with a timeframe of 15 minutes, from initial snowfall to springtime melt. Consequently, without exogenous information, the procedure can accumulate errors throughout the season. The motivation for this work was to develop an algorithm of assimilation of RSO satellite data, in order to constraint the SURFEX/Crocus model. The two proposed problems are thus :

1. How to adapt the electromagnetic model to frequencies X et Ku ?
2. How to develop the affiliate to this model as well as improve the evolution model of snow SURFEX/Crocus, while assimilating satellite radar RSO data ?

In the section 5.1, we present the modelling of the interaction of EMO with snow. The subsection 5.2 shows the algorithm of data assimilation. Finally, we present the results of the assimilation of data TerraSAR-X and RadarSat-2 in 5.3, applied to the model SURFEX/Crocus of snow evolution, and we conclude 5.4.

5.1 Electromagnetic diffusion from a dense area.

Snow is a dense, stratified, non-homogeneous, non-linear and non-isotropic medium. At initial perspective, we considered snowpack to be composed of layers of snow, where each stratum is modelled as a random continuous medium. The most commonly used method for simulating the EMO response from a diffusing volume constituted of n particles by volume unit is radiative transfer. This method is based on the conservation of energy flux through an elementary volume. In the work carried through with Xuan Vu Phan [86], and based on the model of Nicolas Longépé [83], we considered snow as a medium composed of n spherical particles, having a diffusion independent of and coherent with waves. It is important here to recall the hypothesized principles.

Dense medium :

In order to characterize the medium, we have chosen the approach of the Strong Fluctiation Theory (SFT), introduced by Stogrin [87]. This theory uses effective permittivity ε_{eff} of the medium, which allows to take into account multiple diffusions between ice particles at high frequency. This theory suggests that a non-homogenous layer of effective permittivity ε_{eff} would be modelled like a random continuous medium, defined by a function of correlation. Wang demonstrated this in the validity of Stogryn's model [87], which treats two components from an isotropic medium having the inhomogeneity distributed randomly in shape and size. The shape of the function of autocorrelation is exponential, and the length of correlation l_s is expressed by :

$$l_s = \frac{4f_v}{s}(1 - f_v) \tag{5.1.1}$$

with f_v Volumetric fraction. In the particular case of n particles of spheric snow distributed randomly, we have :

$$l_s = \frac{2D}{3}(1 - f_v) \tag{5.1.2}$$

with $f_v = \rho_s/\rho_{ip}$, ρ_s (snow) in (g/cm^3), $\rho_{ip}(T°C)(ip\ for\ ice\ pure) = 0.916 \times (1 - 1.53.10^{-4} \times T°C)$ and D the optic diameter of the grains (where Surface Specific Area (SSA) noted s). The coefficients of extinction and the function of diffusion phase are determined from this function of correlation.

Model of Strong Fluctuations of Strogryn : With the case of the theory of strong fluctuations, having spherically a function of symetric correlaton, quasi-static permittivity ε_g is determined by :

$$f_v.\frac{\varepsilon_i - \varepsilon_g}{\varepsilon_i + 2\varepsilon_g} + (1 - f_v).\frac{\varepsilon_b - \varepsilon_g}{\varepsilon_b + 2\varepsilon_g} = 0 \tag{5.1.3}$$

where ε_b is the permittivity of the medium, it is equal toε_0 in medium of air, ε_i is the permittivity of ice.
Note that δ is the variance of fluctuation, written as :

$$\delta = 9\frac{\varepsilon_g^2}{\varepsilon_0^2}\left[f_v.\left(\frac{\varepsilon_i - \varepsilon_g}{\varepsilon_i + 2\varepsilon_g}\right)^2 + (1 - f_v)\left(\frac{\varepsilon_0 - \varepsilon_g}{\varepsilon_0 + 2\varepsilon_g}\right)^2\right] \tag{5.1.4}$$

All calculations executed, by using the function of exponential correlation, one gets :

$$\varepsilon_{eff} = \varepsilon_g + j.\frac{2}{3}\delta.k_0^2 k_g \varepsilon_0 .l_s^3 \tag{5.1.5}$$

k_0 is the number of waves in the void $k_0 = \frac{2\pi f}{c}$ et $k_g = k_0\sqrt{\varepsilon_g}$.

Permittivity of ice

The research of Hufford [89] allows to determine the permittivity of ice in function of temperature T and of frequency f. Note that impurities which also influence permittivity are not taken into account in this model, being written :

$$\varepsilon_i(f,T) = \varepsilon' + j\varepsilon" \tag{5.1.6}$$

$\varepsilon' = 3.15$ et $\varepsilon" = [\alpha(\Theta) + \beta(\Theta)]/f$ with :

$$\alpha(\Theta) = (50.4 + 62\Theta) \times 10^{-4} \times e^{-22.1\Theta} \text{ en } GHz \tag{5.1.7}$$

$$\beta(\Theta) = \frac{0.502 - 0.131\Theta}{1+\Theta} \times 10^{-4} + 0.542 \times 10^{-6}(\frac{1+\Theta}{\Theta + 0.0073})^2 \text{ en } GHz^{-1} \tag{5.1.8}$$

and

$$\Theta(T) = \frac{300}{273.15 + T} - 1 \text{ with } T \text{ in } °C \tag{5.1.9}$$

The simplified formula of permittivity actually used in the model is of the following form :

$$\varepsilon_i(f) = 3.15 + 2.5j(6.10^5 f^{-1} + 65.10^{-6} f^{1.07}) \tag{5.1.10}$$

Equation of vectoral radiative transfer

Representation of diffusion of waves in the dense snow medium is based on the equation of radiative transfer 5.1.11. The intensity is described by the modified vector of Stokes $\tilde{\mathbf{I}}$. The absorption and diffusion, along with function of phase are matrix sizes respectively noted $\boldsymbol{\kappa}_a$, $\boldsymbol{\kappa}_s$ and $\mathbf{P}$. The written equation [90] :

$$d\tilde{\mathbf{I}}(\mathbf{r},\hat{s}) = -\boldsymbol{\kappa}_a\tilde{\mathbf{I}}(\mathbf{r},\hat{s})ds - \boldsymbol{\kappa}_s\tilde{\mathbf{I}}(\mathbf{r},\hat{s})ds + \int_{4\pi}\mathbf{P}(\mathbf{r},\hat{s}')\tilde{\mathbf{I}}(\mathbf{r},\hat{s}')d\Omega' \tag{5.1.11}$$

The integral term contains the matrix of phase $\mathbf{P}(\mathbf{r},\hat{s}')$ which gives an account of diffusion in the medium. In the case where diffusing particles of snow (considered spherical in radius r) are sufficiently small in front of the length of incident wave λ :

$$r << \frac{\lambda}{2\pi} \tag{5.1.12}$$

The medium is modelled from the means of estimate from Rayleigh [91]. In this case, for reasons of spherical symmetry of particles, the matrices of absorption $\boldsymbol{\kappa}_a$ and diffusion $\boldsymbol{\kappa}_s$ can be replaced by scalar coefficients, κ_a and κ_s [90] :

$$\kappa_a = \frac{4}{3}\pi\ f_v k_0 r^3 \varepsilon_{eff}\left|\frac{3}{\varepsilon_{eff}+2}\right|^2 \tag{5.1.13}$$

$$\kappa_s = \frac{8}{3}\pi\ f_v k_0^4 r^6\left|\frac{\varepsilon_{eff}-1}{\varepsilon_{eff}+2}\right|^2 \tag{5.1.14}$$

With the case of dry snow, according to Huin [92], κ_e can as well be calculated from the value of effective permittivity ε_{eff}, with a simplified manner :

$$\kappa_e = 2k_0 Im\left(\sqrt{\varepsilon_{eff}}\right) \tag{5.1.15}$$

Phase matrix

One of the hypotheses of radiative transfer is that in the case of a medium formed by randomly

distributed particles, waves diffused by the particles have random phases, thus enabling an incoherent addition of diffused waves [90]. With the case of spherical snow particles, where the angle of diffusion $\phi_s = \phi_i + \pi$, the phase matrix $\mathbf{P}$ [93] takes on the following form :

$$\mathbf{P} = \frac{3}{8\pi}\kappa_s \begin{bmatrix} 1 & 0 & 0 & 0 \\ 0 & 1 & 0 & 0 \\ 0 & 0 & -1 & 0 \\ 0 & 0 & 0 & -1 \end{bmatrix} \tag{5.1.16}$$

We are not examining the calculations of resolution of the equation for radiative transfer 5.1.11. However, we re-examine the reading of Audrey Martini's thesis [90]. With snowpack being a dense medium, we used the equation of radiative transfer, applied at dense mediums (DMRT) at each layer of snow (meaning that the energy is represented by the following phenomena :

— multiple diffusion of inconsistent intensities,
— conservation of energies
— diffusion via correlated particles,
— function of pair distribution for position of particles,
— effective propagation constant of a dense medium.

We must consider three physical phenomena in order to give an account of OEM diffusion of snow : Migitation, diffusion and refraction. In the situation of a dense medium, the theory of strong fluctuations (SFT) allows us to calculate effective permittivity and to deduce the coefficient of extinction of the medium. SFT equally allows us to calculate a new phase matrix and to introduce the concept of diffusion of OEM by way of permittivity fluctuations. For mechanisms of refraction, wave transmission at interfaces of air-snow and snow-snow are expressed at the middle of transmission matrices of Fresnel, from the medium 1, towards the medium 2 defined by Ulaby [94, 94] :

$$\mathbf{T}_{12} = \frac{\varepsilon_2}{\varepsilon_1} \begin{bmatrix} 1 - |r_v|^2 & 0 & 0 & 0 \\ 0 & |r_h|^2 & 0 & 0 \\ 0 & 0 & g & -h \\ 0 & 0 & h & g \end{bmatrix} \tag{5.1.17}$$

$$r_{hh} = \frac{n_1 \cos\theta_i - n_2 \cos\theta_t}{n_1 \cos\theta_i + n_2 \cos\theta_t} \tag{5.1.18}$$

$$r_{vv} = \frac{n_2 \cos\theta_i - n_1 \cos\theta_t}{n_2 \cos\theta_i + n_1 \cos\theta_t} \tag{5.1.19}$$

where the indices of refraction $n_k = \sqrt{\varepsilon_k}$.
The coefficients g and h are given by :

$$g = \frac{\cos\theta_t}{\cos\theta_i} \Re e \left|(1 + r_v)(1 + r_h^*)\right| \tag{5.1.20}$$

$$h = \frac{\cos\theta_t}{\cos\theta_i} \Im m \left|(1 + r_v)(1 + r_h^*)\right| \tag{5.1.21}$$

Considering a single-layered snowpack, in order to take it into account in the equation of radiative transfer of wave transmission at air-snow interface during round-trip journeys, it is necessary to multiply each term of the equation 5.1.11 on the right by T_{12} and on the left byT_{21}.

Integral equation model (IEM) for backscattering of air-snow and snow-ground interfaces.

The integral equation (Integral Equation Model - IEM), introduced by [95] allows to calculate

electromagnetic snowpack of a snow surface. This model represents surfaces of heavy roughness through approximation of Kirchhoff, and surfaces of weak roughness through the model of small perturbations. This model is written :

$$\sigma^0_{IEM} = \sigma^k + \sigma^{kc} + \sigma^c \tag{5.1.22}$$

in which σ^k represents the term of Kirchhoff, σ^{kc} the intersecting term and σ^c the complimentary term. For surfaces of medium roughness, a transitional function for IEM was introduced by Wu et. al. [96], to conserve the continuity of this model.

Backscattering coefficient is calculated from two parameters which characterize the roughness of the surface. These two parameters are the function of autocorrelation $\rho(r)$ and the standard deviation of heights σ_h. The reflectivity is thus written :

$$\sigma^0_{IEM,pp} = \frac{k_0^2}{4\pi} \exp(-2k_0^2\sigma_h^2 \cos^2\theta_0) \sum_{n=1}^{\infty} |I^n_{pp}|^2 \frac{w^n(2k_0 \sin\theta_0, 0)}{n!} \tag{5.1.23}$$

with p polarization equal to h or at$v$, in function to horizontal or vertical polarization, and $k_0 = \frac{2\pi f}{c}$ representing the number of waves in the vacuum.

The expression of the factor of reflexion/transmission $|I^n|$ and of the Fourier 2-D transform of the coefficient of surface correlation $w^{(n)}$ are detailed in [97].

The synthetic diagram of the model is shown in figure 5.1.1.

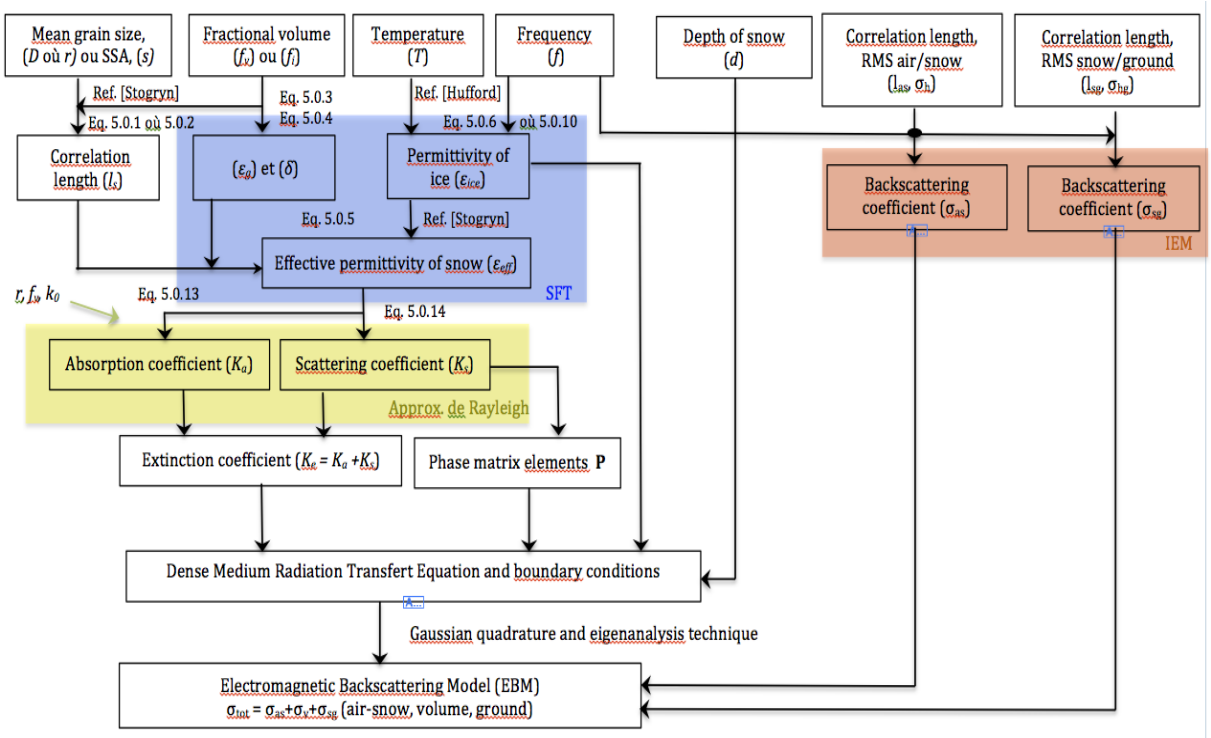

FIGURE 5.1.1 – Structure of model.

5.2 Data assimilation.

The method of variational assimilation consists of finding the most ressembling state, taken from available knowledge of laws of observation and draft error probability. This method consists of minimizing the distance in the sense of the least squares between the estimated state and the different sources of information, such as previous prediction and observations. The newly analyzed state is generally used as a starting point for the following prediction. Minimization is based on the cost function J :

$$J = (\mathbf{x} - \mathbf{x}_g)^t \mathbf{B}^{-1} (\mathbf{x} - \mathbf{x}_g) + (\mathbf{y} - H(\mathbf{x}))^t \mathbf{R}^{-1} (\mathbf{y} - H(\mathbf{x})) \tag{5.2.1}$$

Minimization of this function necessitates the calculation of its gradient :

$$\nabla J = 2\mathbf{B}^{-1}(\mathbf{x} - \mathbf{x}_g) - 2\nabla H^t \mathbf{R}^{-1}(\mathbf{y}_{obs} - H(\mathbf{x})) \tag{5.2.2}$$

where ∇H^t represents the associated operator of $H(\mathbf{x})$ in the neighbourhood of $\mathbf{x}$.
The calculation of ∇H^t requires the Jacobien definition ∇H :

$$\nabla H(i,j) = \frac{\partial H_i(\mathbf{x})}{\partial x_j} \tag{5.2.3}$$

In noting the backscattering model $H : \mathcal{B} \to \mathcal{R}$, with $\mathcal{B}$ and $\mathcal{R}$ the definition domains of $\mathbf{x}$ and$\mathbf{y}$, the associated operator ∇H^t is calculated as follows :

$$\forall \mathbf{x}, \mathbf{y}, \quad \langle \nabla H^t \mathbf{y}, \mathbf{x} \rangle_{\mathcal{B}} = \langle \mathbf{y}, \nabla H \mathbf{x} \rangle_{\mathcal{R}} \tag{5.2.4}$$

Once the association is developed, on can use the gradient fall to minimize the function J. Each iteration modifies the state vector $\mathbf{x}$, according to Newton's method :

$$\mathbf{x}_{n+1} = \mathbf{x}_n - \alpha(\nabla^2 J(\mathbf{x}_n))^{-1} \nabla J(\mathbf{x}_n) \tag{5.2.5}$$

where $\nabla^2 J(\mathbf{x}_n)$ is the second-order gradient (Hessian matrix) of J :

$$\nabla^2 J = 2\mathbf{B}^{-1} + 2\nabla H^t \mathbf{R}^{-1} \nabla H \tag{5.2.6}$$

We are not detailing the specific calculations with the case of our electromagnetic model EBM. Instead, we refer the reader to the thesis of X.-V. Phan [86]. We are simply presentling a synthetic scheme, 5.2.1 the illustration showing the architecture of our method.

5.3 Results.

The figure 5.3.1 shows an illustration of the results that can be achieved from physical simulation of the evolution of snow, and from a temporal series of radar data TerraSAR-X, acquired on the Argentiere Glacier. The dates of acquisition of satellite TSX are represented by black dashes in the figure 5.3.1 (right side). We can see the modifications from the grain size and from the density of each strata of snowpack, brought in by assimilation algorithm.

We can note that the changes in physical variables (optic diameter and density) are mainly in the the deepest layers of snow. This observation can be explained by the fact that the OEM in band X penetrate up to the snow-ice interface, and are more backscattered in inferior layers, due to large grains and a stronger density. This translates into a more heightened reduction than that which

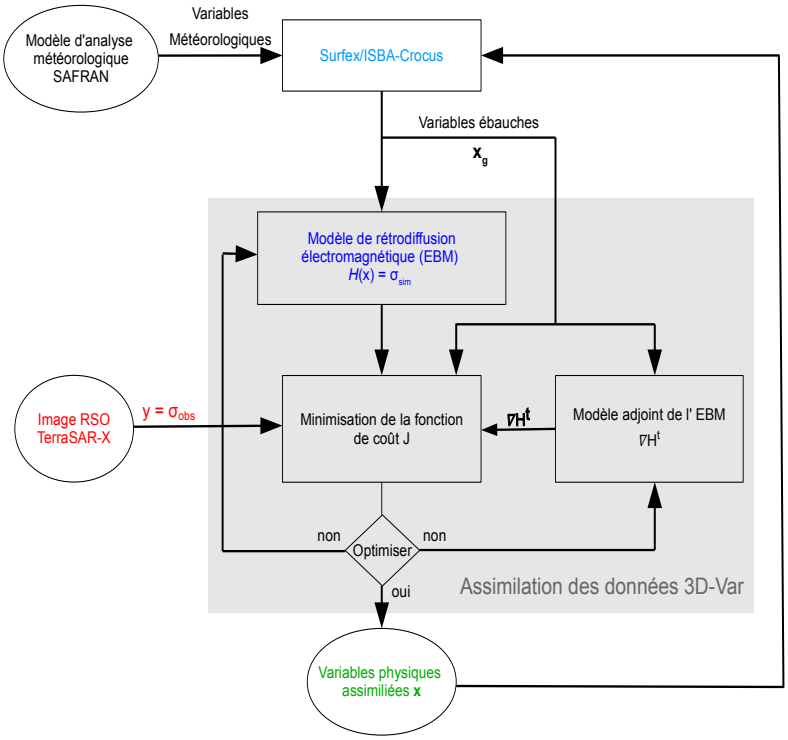

FIGURE 5.2.1 – Synthetic shcema of SAR data assimilation.

the assimilation algorithm propagates through modification of physical parameters of deep snow layers.

The sketch covariance matrix **B** is partially based on the correlation of error between the layers of snowpack. This correlation of error strongly depends on the distance between layers. A large space between two layers gives rise to a weak correlation value. Consequently, modifications of physical variables of distanced layers will be less affected.

5.4 Conclusion.

We adapted the electromagnetic model devised by [98] to frequencies X and Ku and formulated its adjunct. The total backscattering calculated by this exact model depends on the size of particles, on the volume fraction of ice, on temperature, on the frequency and height of snow at each stratum of snowpack, on the length of correlation and gap types of air-snow as well as ground-snow interface heights. The formulated adjunct model allows to modify the variables of the physicla Surfex/Crocus model arising from data of satellite observations. The results of this fieldwork were published at several congresses [99] and in the journal [100].

Il est maintenant nécessaire d'étudier l'étendue de la validité des paramétres du modèle, et de caractériser l'algorithme d'assimilation à partir de mesures in-situ. Ce problème est très difficile car il est sous déterminé (seule la rétro-diffusion intégrée est observable), mais on a une bonne idée de l'état moyen qui servira de condition initiale et des incertitudes associées qui permettront de définir la matrice de covariance des erreurs a priori. Pour ce faire un dispositif de radar sol est en cours

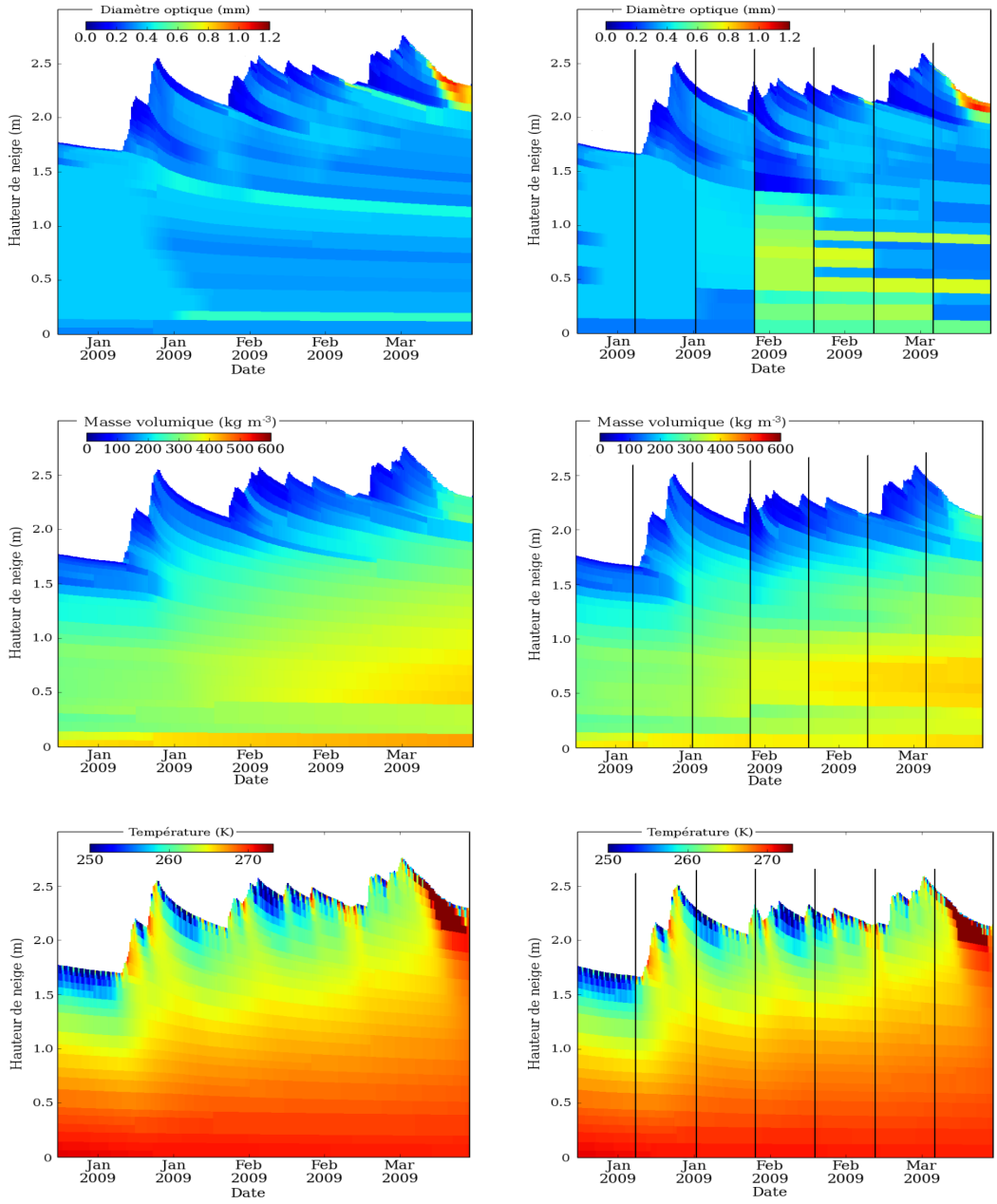

FIGURE 5.3.1 – Comparison between spatial and temporal evolutions of physical parameters (from top to bottom : optic diameter, density and temperature) of snowpack, modelled by SURFEX/Crocus - without assimilation (at left) and modelled with assimilation of TSX data (at right). Site : Argentiere Glacier, elevation - 2700 m).

d'élaboration. Ce radar va permettre de mesurer en continu, la rétro-diffusion électromagnétique du manteau neigeux de 2 à 18 GHz.

Chapitre 6

Displacement Evaluation of a Glacier, Taken From RSO Images

Challenges related to the tracking of temperate glaciers are numerous. A better understanding of parameters controlling the physical processes of glaciers allows us to constrain and, therefore improve dynamic models of glacial flux [101]. With glaciers being local indicators of the global climate state, tracking their evolution gives indications of climatic changes [102] and to anticipate economic impact of their evolution (access to water resources, for example) [103]. Climatic conditons, along with difficulty in reaching glacial regions, considerably limit the installation of material in-situ. Nowadays, very few glaciers are equipped with in-situ instrumentation [104], making it difficult to obtain a continuous database over the longterm.

Methods of satellite images are an alternative means. [105]. Optic satellite imagery is a source of information that enables us to identify the surface covered by a glacier, the position of the glacial front, the balance line of a temperate glacier, surface altitude changes, as well as the displacement field of the surface [106, 107, 108]. These parameters allow us to estimate the assessment of glacier mass [109, 107], and therefore its evolution. Several factors liit the use of optic imagery, like presence of cloud-cover or variations in solar illumination.

Radar imagery is complementary, and does not experience the same constraints. It is not affected by meteorological factors and in optimal conditions can achieve results from an inferior resolution at 1 m. To measure displacements, two methods exist : InSAR and amplitude correlation. We have previously discussed InSAR in chapter 3. It is interesting to look at the possibilities and the limitations of amplitude correlation, a project that we have carried out in the framework of Fanny Ponton's thesis. The images used for this project are extracted from TerraSAR-X satellite (TSX), possessing a temporal repeatability of 11 days. During this time interval, the change in the surface state of Argentiere Glacier is too great to conserve a high enough coherence for use of InSAR. The method of amplitude correlation is thus chosen for treatment of TSX images, as written in the paragraph **??**. I then presented the experimental site of Argentiere Glacier, where we accomplish our experiments to validate our methods 6.2. The results were then compared to results arising from treatment of GPS data at two present stations on the glacier **??**, resulting from work carried out in the thesis of Fanny Ponton [110].

6.1 Algorithm for measurement of displacements

The processing chain used was developed in the framework of the project EFIDIR. The different stages of application used to obtain 2-D and 3-D displacement fields is seen in figure 6.1.1.

1. The defined image, like slave image, is readjusted in the master image by using common fixed parts at the two images.
2. The shifts in the direction of the line of sight Δ^i_{LOS} and those in azimuthal direction Δ^i_{az} are obtained by using the method of maximum similarity. The similarity function used is the ZNCC function. A mask of visibility os applied to the images during application : It enables us to avoid side-effects due to interface glacier in fixed movement/borders. When fixed borders are taken into account during treatment, they cause an underestimate of glacier displacement [111].
3. The shifts obtained during stage (2) must be undergo a post-treatment, to represent displacements in 2 dimensions v^i_{LOS} and v^i_{az}. The first stage of post-treatment consists of removing displacement residue arising from the difference of geometric acquisition between the first and the second image. The satellite trajectories are not exactly the same between the different acquisitions. This causes a drift in recalibration of *near range* towards *far range*. The *near range*, being the closest part of the image to the nadir point of the satellite's flight trajectory and the *far range*, the most distanced part. The more significant the relief of the imaged zone is, the larger the drift becomes. The residual displacements are simulated with the help of satellite trajectories, along witha numeric model of terrain in the form of images. These images, representative of the pixel shift in azimuthal and LOS directions, are subtracted from offset images previously obtained.
4. The 2-D displacement fields are then converted into m/day, keeping in mind the size of pixels from TerraSAR-X images, as well as the time interval between images.
5. The 2-D displacement fields are filtered with the aid of a median filter on a 3×3 pixels window. This type of filter was chosen for its properties in preserving steps like the abrupt rise in displacement and suppression of impulsive sound (such as *outlayer*, due to matching errors).
6. The 2-D displacement fields and the similarity spike are then projected onto the ground - in latitude and longitude. The projection onto the ground is executed with the aid of the tables program of radar orthoectification : *Synthetic Aperture Radar Look Up Table (SARLUT) tool* [112]. The *Look Up Table (LUT)* are two images, allowing to establish correspondence between a pixel in SAR geometry and a pixel in ground geometry (in latitude and longitude, having WSG-84 ellipsoid as reference). The LUT are simulated, taking into account the satellite trajectories and the MNT [113, 111, 114]. At this stage, the 2-D displacement fields are always in accord to the 2 directions (LOS and azimutal) in radar geometry, but re-sampled on the ground.
7. This step consists of suppressing the aberrant displacement values. Previous studies showed that displacement estimates were conclusive if the associated value of the similarity peak was superior to 0.2 [115, 116]. All the zones where the peak of similarity is inferior to this threshold are, thus eliminated from the corresponding field of displacement.

Displacement 3-D

When a pair of ascending and a pair of descending images are acquired during the same period, the final step (step 8 of schema 6.1.1) consists of obtaining a 3-D displacement field.

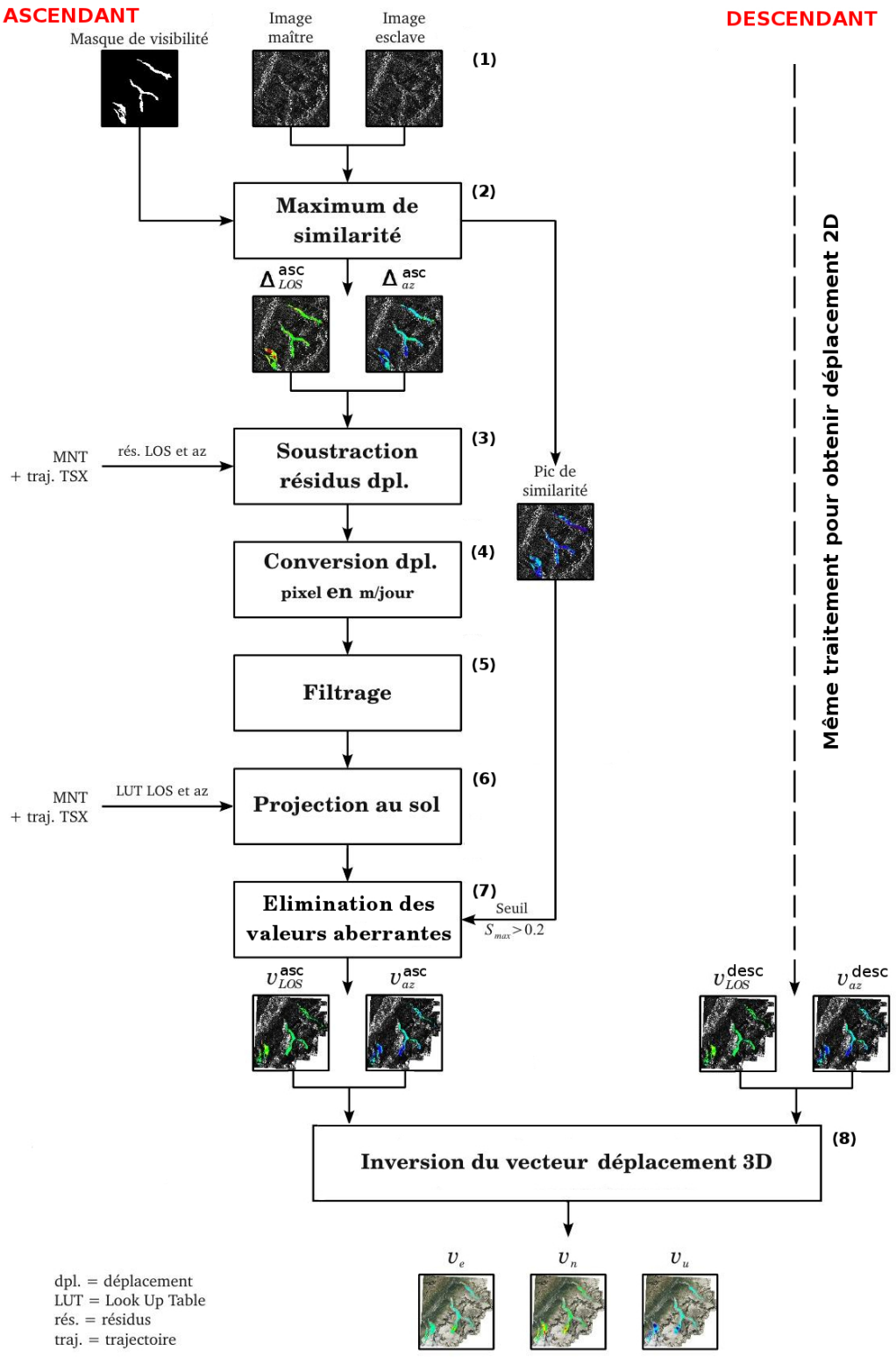

FIGURE 6.1.1 – Chain of application SAR.

The previous steps are applied to the two pairs of images. The measurements coming from the amplitude are the projections of the 3-D vector displacement at the Earth's surface, in LOS and azimutal directions. After application of the two image pairs, four projections of displacement fields from the same period are available, and can be regrouped in the matrix $V = [v_{LOS}^{des}, v_{AZ.}^{des}, v_{LOS}^{asc}, v_{AZ.}^{asc}]^t$. Only 3 projections are needed to find the 3-D displacement field, so it is possible to inverse the linear system :

$$V = P \times D \tag{6.1.1}$$

where D is the sought-after 3-D vector displacement. $D = [v_e, v_n, v_u]^t$ and P is the matrix of projection vector components in LOS and azimutal directions, according to ascending and descending trajectories :

$$P = \begin{bmatrix} -sin\theta_1 cos\alpha & sin\theta_1 sin\alpha & -cos\theta_1 \\ -sin\alpha & -cos\alpha & 0 \\ sin\theta_2 cos\alpha & sin\theta_2 si\alpha & -cos\theta_2 \\ -sin\alpha & cos\alpha & 0 \end{bmatrix} \tag{6.1.2}$$

Where $\theta_1 = 37°$ is the incident angle of radar in descending trajectory, $\theta_2 = 45°$ the incident angle of radar in ascending trajectory and $\alpha = 9°$ is the angle of satellite trajectory in relation to the North. The matrix is written so that α would always be equal to $+9°$. The solution to the problem represented in the equation 6.1.1 is calculated by the method of least squares :

$$D = (P^t \times P)^{-1} \times P^t \times V \tag{6.1.3}$$

The inversion of the 3-D displacement is carried out in zones of confidence, where the peak values of similarity are > 0.2, descending and ascending at the same time. These achieved steps, the North, East and vertical components of displacement, are available. The results of this work are presented in Fanny Ponton's thesis.

6.2 Results GPS in radar geometry

GPS data are those from stations anchored on the glacier, shown in figure6.2.1.

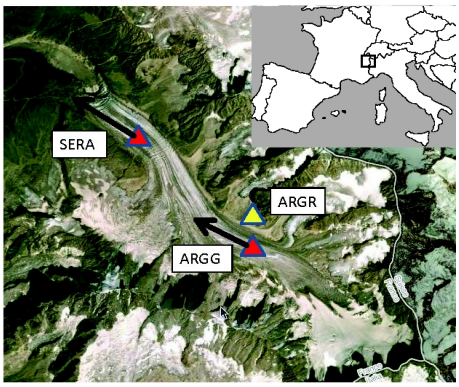

FIGURE 6.2.1 – reseau local de station GPS.

On the high part of the glacier, where the ARGG station is implanted, the glacier's

lack of surface texture impedes the correlation of ASR image amplitude, to carry-out displacement calculations. The validation of TSX results is thus accomplished at the SERA site, once the ascending and descending satellite data and GPS data are available at the same date, in 2009 and 2011.

GPS application is accomplished through 6-hour sessions. In order to be compared to SAR results, the displacements are calculated over 11 days. A mean position is calculated over the 4 sessions in a day, then another mean position 11 days later. The difference between the twe means is then standardized by 11 days, in order to get the cm/day.

To compare GPS results with SAR results in 2 dimensions, the GPS displacements are projected in 2-D radar geometries. The equations 6.2.1 and 6.2.2 represent the applicable projections, to obtain GPS displacements according to the 2 SAR directions, LOS (range) and azimutal, in ascending configuration. The equations 6.2.3 and 6.2.4 represent the same for the descending configuration.

$$V_{GPS\rightarrow SAR}^{Asc,LOS} = \sin(\theta_1)\cos(\alpha)V_e + \sin(\theta_1)\sin(\alpha)V_n - \cos(\theta_1)V_u \quad (6.2.1)$$

$$V_{GPS\rightarrow SAR}^{Asc,Az.} = -\sin(\alpha)V_e + \cos(\alpha)V_n \quad (6.2.2)$$

$$V_{GPS\rightarrow SAR}^{Des,LOS} = -\sin(\theta_2)\cos(\alpha)V_e + \sin(\theta_2)\sin(\alpha)V_n - \cos(\theta_2)V_u \quad (6.2.3)$$

$$V_{GPS\rightarrow SAR}^{Des,Az.} = -\sin(\alpha)V_e - \cos(\alpha)V_n \quad (6.2.4)$$

where θ_1 and θ_2 are incident angles of TSX satellite in ascending and descending cases, and are respectivly equal to 45° and 37°. V_n, V_e and V_u are the components of GPS measurement displacement.The equations are written in such a way as to use the azimutal angle : $\alpha = 9°$, in the ascending and descending case.

6.3 Mesures of 2-D displacement

The results of 2-D displacement measurement arising from analysis of TSX images are presented and compared with those of GPS analysis projected in 2-D SAR ascending and descending geometry.

Spatial resolution

The TSX images cover a large surface, allowing us to obtain results in large spatial resolution. The figures 6.1(a) and6.1(b) are zooms of amplitude images in ascending and descending geometry, extracted from complex SAR images on September 25 and on September 12, of 2011. Visually, we notice that the amplitude varies in function of the surface state of the glacier, being the reason for detecting the differences between smooth and textured zones. The crevices and the fall zones of seracs clearly appear in the lower part of the glacier. The Argentiere Glacier is more visible in figure 6.1(b), because its mean direction of outflow is nearly in the line of sight of the satellite as it passes in descension.

The success of method of amplitude correlation rests on two criteria, depending on the state of the glacier's surface :

1. the surface must be textured (i.e. to have structures, such as crevices, seracs or enough detrital cover so that amplitude is not constant).
2. If the surface is smooth, a stable object must serve to be a bright spot (rocky block, reflective

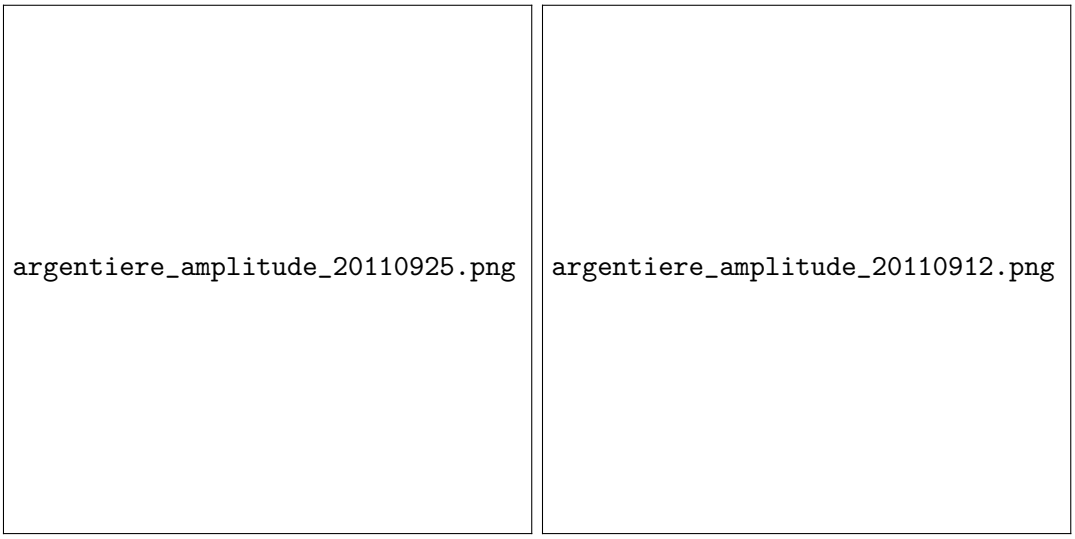

(a) Zoom of Argentiere Glacier, ascendingTSX image from 25/09/2011

(b) Zoom of Argentiere Glacier, descending TSX image from12/09/2011

FIGURE 6.3.1 – Zoom of amplitude images in ascending and descending geometry

corner).

Spatial variability

The higher part of the glacier does not allow us to provide good results at amplitude correlation, therefore we will concentrate on the lower part of Argentiere Glacier. The illustration 6.3.2 represents an enlargement of the concerned part. It presents the images in amplitude, 2-D fields of displacement, as well as their similarity peak for two pairs of images acquired in August of 2009. The illustrations 6.2(a), 6.2(c) and6.2(e) represent ascending configuration and show the results between the images of 16/08/2009 and 27/08/2009, while the illustrations 6.2(b), 6.2(d) and 6.2(f) show the results of images from 14/08/2009 and 25/08/2009, acquired in a descending pass. The displacements found lie between 0 and 1.50 m/jour. The large values are aberrants, associated with weak values of similarity peak.

In order to determine the spatial variability of the Argentiere Glacier, longitudinal profiles are extracted from 2-D fields of displacement. These profiles are represented in figures 6.2(a) and 6.2(b). They are achieved in zones where there is maximum confidence in the results, meaning that the similarity peak holds the greatest values (red zones in figures 6.2(e) and 6.2(f)).
From the profiles, spatial acceleration of the glacier can be observed, the high part presents weak displacements of around 10 cm/day, the movement accelerates as altitude lowers, reaching 30 cm/day in the lowest parts.

Temporal variability and comparison with GPSs

To identify temporal variability of glacial displacement and compare the results coming from SAR application, as well as the GPS results, the displacement values are extracted from each SAR displacement field near the station. With the results not always being available in pixels corrresponding to the position of the SERA station, the modal value of displacement of a small region around the GPS station is used. In 2-D, thes results are represented by the black circles in figure 6.3.3. The red crosses represent the GPS results, projected in ascending and descending radar geometry.

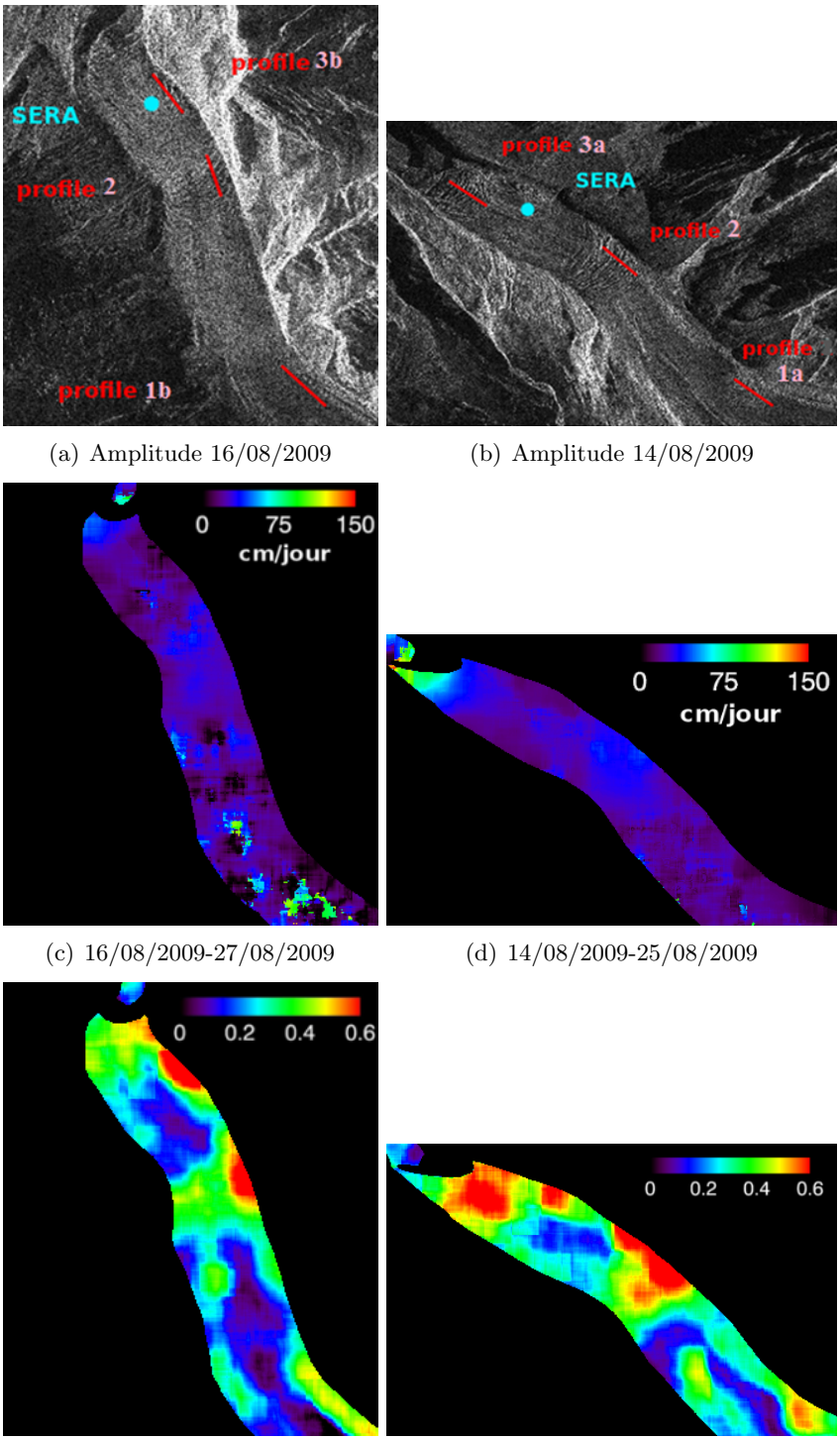

(a) Amplitude 16/08/2009 (b) Amplitude 14/08/2009

(c) 16/08/2009-27/08/2009 (d) 14/08/2009-25/08/2009

(e) Similarity peak (f) Similarity peak

FIGURE 6.3.2 – Amplitude image of Argentiere Glacier in ascending passes (figure 6.2(a)) and descending (figure 6.2(b)) ; 2-D displacement fields, arising from amplitude correlation (figures 6.2(c) and 6.2(d)) and their similarity peak (figures 6.2(e) and 6.2(f)).

At the level of temporal evolution, a seasonal variability was expected, with weak displacements in winter with cold temperatures and precipitation fall in the form of snow, and with accelerations in spring and summer when temperatures rise and ice melts. The SAR results follow more or less this interpretation. However, the GPS results show strong inter-seasonal variability, being able to reach

up to 15 cm/day amplitude (summer 2009) in less than one month, with the fastest displacement variations occuring in August. During the summer season, the mean temperature is positive, thus precipitation falls in the form of rain. These two factors strongly contribute to the melting of ice [117]. In order to explain these strong variations of displacement in short intervals, a possible hypothesis is as follows : During episodes of significant melting, due to a period of high heat or of heavy precipitation, a sufficiently large volume of water is created to be drained just at the ice/rocky bed interface. Under the lubricating effect of water at this interface, the basal slide rises, causing acceleration of surface displacement of the glacier.[118, 119, 117].
At the comparison level between the two datasets, we measured the gap by calculating the root of mean quadratic error (RMS) between the magnitude of GPS results and that of results coming from 2-D SAR displacement fields (équation 6.3.1) :

$$RMS_1 = \sqrt{\frac{1}{N}\sum_{i=1}^{N}(V_{GPS}^i - V_{SAR}^i)^2} \tag{6.3.1}$$

where n is the number of results to compare, V_{GPS}^i the module of GPS displacement and V_{SAR}^i being extracted from the SAR displacement field at the couple i. The obtained errors are from 6.7 cm/day for results in ascending geometry, 2.1 cm/day for results in descending geometry, and 5.8 cm/day on the total of the data.

A similar analysis was achieved in the work of Renaud Fallourd [111]. He compared the results of 2-D SAR displacement field value with 5 GPS results of the SERA in 2009. The obtained RMS was 7.2 cm/day for the ensemble of the data and 6 cm/day for the descending geometry. The 5 GPS results are from the period in which the station SERA was installed on a rockface. In the summer, the station became ustable when ice melted under the rock, thus recording a component due to movement of the rock along with the moving of the glacier. In our analysis, we took into account numerous more important data, as well as the periods where the station SERA was installed on a mast, to render it more stable. These differences are, no doubt, at the origin of improving our results.

These results are a brief overview of the main work accomplished in the thesis of Fanny Ponton [110], published in an article in the journal IEEE-JSTARS [120].

6.4 Conclusion

We can conclude that a favorable correlation is observed between the GPS and SAR data sets in 2 dimensions. The SAR fields of displacement allow us to obtain a good spatial resolution and to follow the evolution of surface displacement along the glacier. At a temporal level, global variations of displacement can be followed and are comparable to those of GPS. The disadvantage of radar is that the short-term variations are not visible. To bring to light the inter-seasonal variability, the GPS results are needed. They also allow us to validate the coherence of results of our treatment in radar imagery when the two data sources are available at the same time.

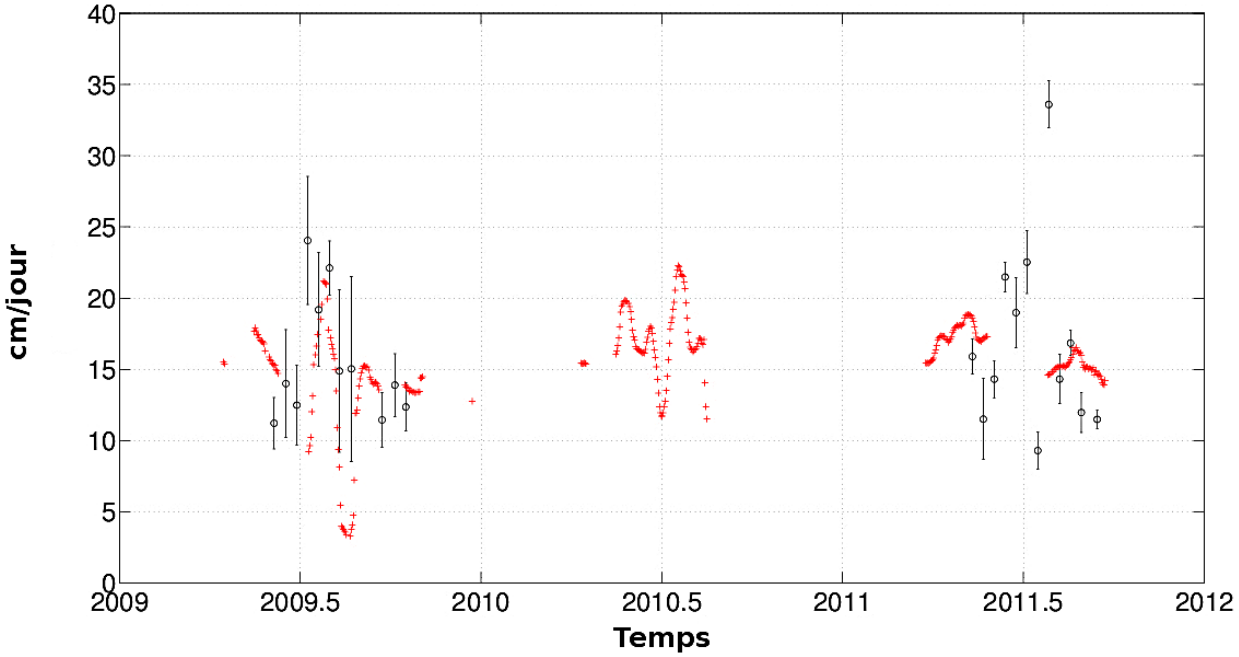

(a) Ascending geometry

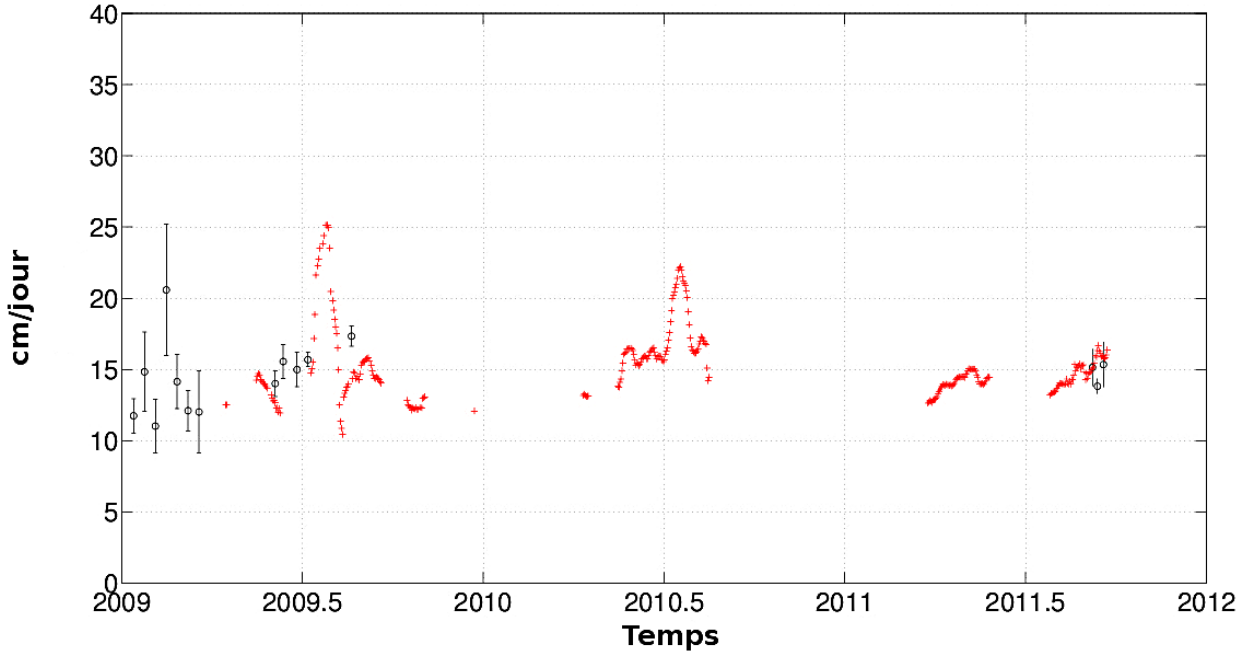

(b) Descending geometry

FIGURE 6.3.3 – Temporal series of 2-D displacement obtained by amplitude correlation of image pairs acquired at 11 day intervals, and bars of associated uncertainty (black circles) in ascending and descending case ; temporal series of GPS displacement projected in SAR 2-D geometries (red crosses).

Chapitre 7

Points forthcoming...

The presentation of this thesis is neither a means, nor an end to further research. It is considered, rather, a punctuation mark...
(*as the legend states : "One day, there was a huge research field. The majority of homosapiens, terrified, observed...The small man plunged into action, heading off to look for several formulas, to scratch onto a piece of paper. After a moment, the grand leader, bothered by this ridiculous restlessness, said to him : "Little man, are you crazy ? You cannot describe the expanse of possibilities with merely these 3 calculations !" Thus, the little man responded : "Yes, I know, but at least I'm doing my part". (extracted and modified from an Autochtone legend, told by Pierre Rabhi). Pierre Rabhi*).

In the previous pages, I showed to develop research from two focal points. The first corresponds to my interest in snow, ice and glaciers, in an attempt to represent, quantify, analyze and interperate essential data relative to the modelling and the understanding of the climate. The second focal point concerns the contribution of algorithms of treatment of satellite RSO images and of the spatialization of the information gathered with in-situ measures. Natural perspectives depart on the two axes.

As I commenced this thesis on the subject of snow, I will end it in full circle by firstly contemplating the perspectives in electromagnetic modelling of the interaction : wave-snow.

The complexity of the dense middle of snow gives rise to efforts to better characterize the interactions of centimetric waves with snowpack. This material is vey difficult to transport. One idea is to propose a study concerning various sites of interaction of waves-snow, from ground radar, in parallel with physical measures of the evolution of snow. This study was, in fact, carried out in collaboration with L. Ferro-Famil. With the aid of Fabien Ndagijimana, we contemplated on the development of a hyperfrequency anisotrophy measuring sensor of snow matter from 0 to 18 GHz. The measure of complex permittivity of the different strati of the medium should allow for an improved equation set-up in the modelling aspects. With regard to anisotrophy, it is not considered in the model that we are actually using : this allows to simplify the calculations. I deem the taking into account of this characteristic of matter to be important, while replacing the coefficients of extinction and phase by their matrices and tensur. This project could be launched with the collaboration of Pierre Comon.

Several models of radiative transfer exist. However, the comparison between models remains to be done. A study started with Ramata Magagi and his student, Francis Caron tackles this very problematic : we envisage simulations and validations taken from the same playing fields of data. If it

turns out that the models of radiative transfer are too incomplete or imprecise in order to represent the snowfield (which is neither linear, nor homogenous, nor isotropic), one must resolve to re-write a model of propagation of waves in a bi-continu milieu of air-ice.

Another prolongation of discreet geometric work that I tackled in chapter 2 of this manuscript is the 3-D measure of the anisotrophy of snow, taken from optic images of tomography. It is entirely feasible to tomograph snow samples of different structures, to carry out 3-D reconstruction and to then calculate the parameters on these structures. These projects were begun in collaboration with Dominique Attali and Isabelle Sivignon.

While pursuing this idea of retro-diffusion modelling, it would be interesting to observe what the implication of hierarchic segmentation (applied at multi-temporal, multi-frequency satellite images) of snowpack from a glacier would be. The statistics obtained, with which I wish to take an interest in (with the collaboration of Jean-Marie Beaulieu, and knowing that this is a textbook case), could eventually bring to light complimentary information on the spatial variability of this field of study. While still on the subject of this satellite aspect, the phase of complex signals was insufficiently exploited in the snow problematic. Recently, S. Leinss demonstrated (now, in the process of publishing) that one car directly obtain the SWE (Snow Water Equivalent) from a series of differential interferograms of data, from a ground band X radar. The possibility of retrieving similar results from spatial images needs to be further explored.

The algorithmic schema of assimilation of the RSO data, which we have implemented, is based on an interpolation 1D-VAR. In order to explore other methods, like the filtration of Kalman or Kalman-expanded (much better adapted for temporal series of RSO images), it is important to revisit this algorithm.

In the thesis of X.V.Phan, we very briefly approached an important point : the problem of the propagation of waves on interfaces air-snow, inter-stratum and snow-ground. An indepth study of the roughness of these interfaces, and of a better inclusion in the models, must be achieved.

In the different aspects of image RSO treatment, which we have presented, often give rise to the need of calculation of series of multi-temporal and multi-frequency data. I additionally envisage focusing more precisely and largely on the relevance between the series of multi-temporal, multi-frequency and multi-polarisation images, and on their contribution in the precision of modelling.

Finally, I formulated the structure of a process of radar data treatment for the modelling of snow (Figure 7.0.1). I count on implementing it, due to the platform "Ciment" méso-centre of calculations in the site Grenoblois (which actually has 6000 processors). This work was put into motion in collaboration with Jean-Bruno Bzeznik.

In the future, the spatial and temporal improvement of models of evolution of snow, thanks to the assimilation of satellite RSO data, coupled to the cartography of snowy zones of all the Earth's surface, will be of interest for a better knowledge of resources of water, of the evolution of the climate, of the dynamics of polar icecaps, of natural hazards, ...(*à laquelle je souhaite apporter ma petite part*).

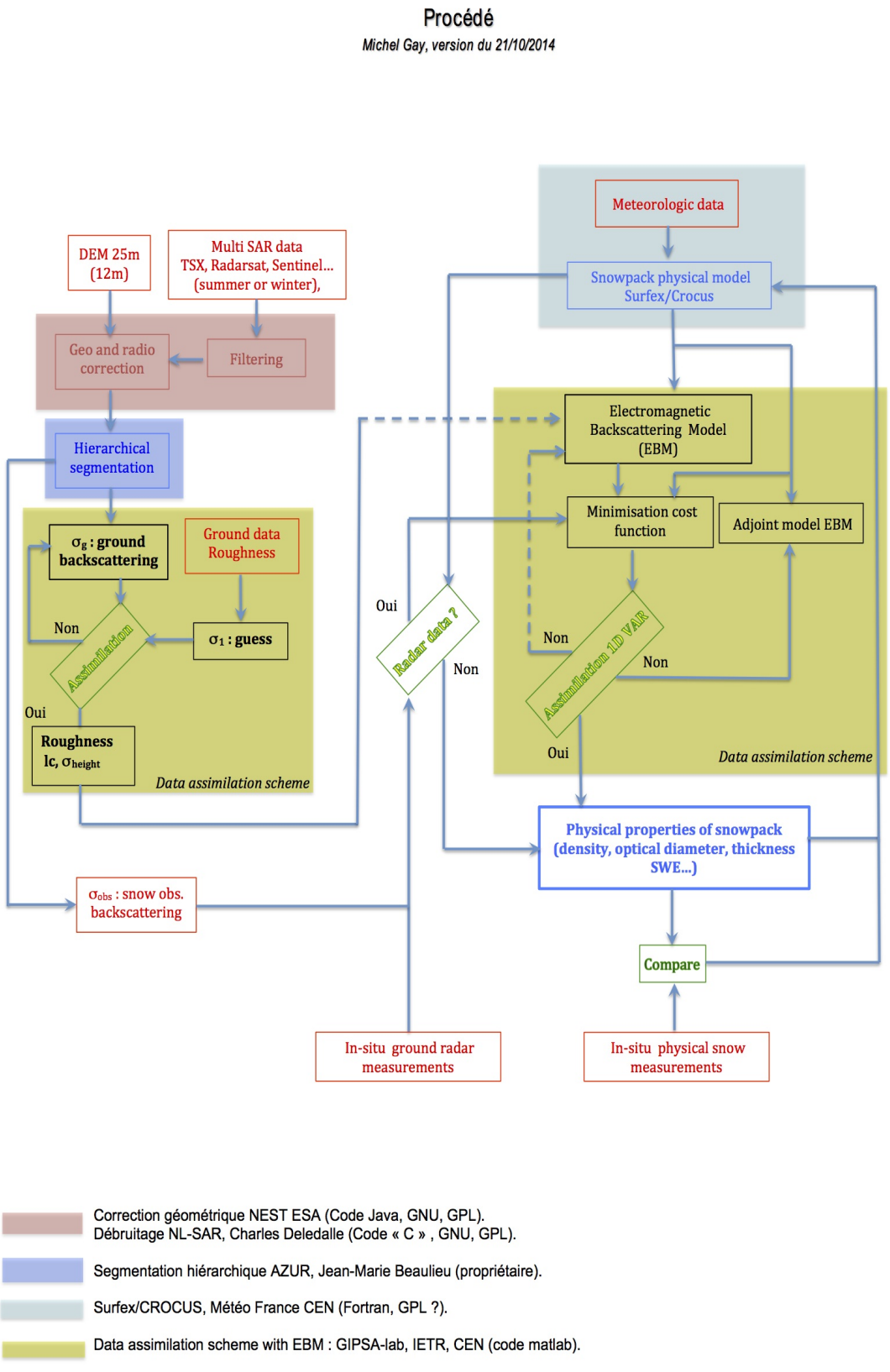

FIGURE 7.0.1 – Structure d'un procédé de traitement de données radar pour la modélisation de la neige.

Chapitre 8

Collection of publications

M. Gay, J. Weiss. "Automatic reconstruction of polycrystalline ice microstructure from image analysis : application to the EPICA ice core at Dome Concordia, Antarctica", *Journal of Glaciology*, *Vol.* 45, *N*° 151, 1999.

Automatic reconstruction of polycrystalline ice microstructure from image analysis: application to the EPICA ice core at Dome Concordia, Antarctica

Michel Gay, Jerome Weiss
Laboratoire de Glaciologie et Géophysique de l'Environnement du CNRS, BP 96, 38402 Saint-Martin-d'Hères Cedex, France

ABSTRACT. A digital image-processing approach is proposed which allows the extraction of two-dimensional polycrystalline ice microstructure (grain boundaries) from thin sections observed between cross-polarisers. It is based on image segmentation of colour images. The method is applied to the preliminary analysis of the shallow (Holocene) ice of the European Project for Ice Coring in Antarctica (EPICA) ice core at Dome Concordia. Structural parameters, such as the mean cross-sectional area, shape anisotropy and grain morphology, are obtained. The interest and limitations of this automatic procedure are discussed.

INTRODUCTION

As with many crystalline materials, ice microstructure, i.e. the size and morphology of grains, controls many physical and mechanical properties of the material. It is therefore very important to obtain as complete as possible a description of this microstructure. This includes not only mean grain-size measurements (we will come back later to the definition of the "size"), but also size distribution, shape anisotropy (elongation of grains along a preferential direction), grain morphology (through the volume/surface or surface/perimeter relations) and topological characteristics. Moreover, as stressed by Alley and others (1986) and Petit and others (1987), ice microstructure may record the age and past history of ice. Indeed, microstructure evolution depends on strain history, temperature and impurity content (Alley and others, 1986; Alley and Woods, 1996), parameters which vary with climate. This is of particular importance when studying polar ice from deep ice cores. For example, correlations have been observed between climatic record from $\delta^{18}O$ isotopic studies and mean grain-size evolution in polar ice (Duval and Lorius, 1980; Thorsteinsson and others, 1995). Correlations between grain-size and impurity content, though relatively noisy, have also been reported (Thorsteinsson and others, 1995; Alley and Woods, 1996).

Most of the analyses of ice microstructure presented so far were performed manually on two-dimensional thin sections. They were therefore laborious and time-consuming. For this reason, most of these analyses were restricted to the study of mean grain-size evolution. Several different methods were used to estimate this "size". Gow (1969), in polar firn, measured the length and breadth of the 50 largest crystals in each section with a "pocket comparator". These 50 crystals represented at least 25% of the total number of crystals, but this representativity depended on the number of crystals in the section and therefore on the mean grain-size itself. These crystals do not therefore represent the entire population of grains, especially if size distribution changes with time. Duval and Lorius (1980) estimated mean grain-size from crystal-counting on a given area, but did not take into account the smallest grains, sometimes of ambiguous existence. Once again, the entire population is not taken into account. Thorsteinsson and others (1995) and Alley and Woods (1996) used the linear intercept method. Alley and Woods (1996) reported some data about size distributions as well. Although probably less "subjective" than the others, this method can raise some problems of interpretation. The mean intercept length is related to the mean cross-sectional area through the average morphology of grains which can change with time. Moreover, Thorsteinsson and others (1995) performed linear intercept analysis along a unique (vertical) direction, which is not representative of real grain morphology if grains are not isotropic and if this shape anisotropy is changing (as observed during this work; see below). The definition of grain "size" is actually not trivial. As demonstrated in this work, different methods can lead to very different results (e.g. for grain-growth kinetics; see below), and can therefore be misleading. Another problem with manual methods is related to "human" bias. The acuity, concentration and measuring ability of a worker can vary greatly during a long, tiring day, especially in a cold environment. This will probably increase the discrepancy of results.

In order to obtain the most complete representation of ice microstructure on two-dimensional thin sections, all the grain boundaries have to be extracted. It is worth noting here that this complete description is necessary (though perhaps not sufficient) to reconstitute three-dimensional microstructure from two-dimensional analysis (Underwood, 1970). This cannot be reasonably achieved manually. Here, we present an automatic method, based on image analysis, which allows easy and rapid extraction of ice microstructure from thin sections examined between crossed polarisers. After a technical presentation of the method and the image-analysis procedure, we illustrate its interest with a preliminary study of ice microstructure in

the shallow part (Holocene ice) of the European Project for Ice Coring in Antarctica (EPICA) ice core at Dome C, discussing the definition of grain "size", shape anisotropy and grain morphology.

EXPERIMENTAL PROCEDURE

The method of extraction of grain boundaries from colour images of two-dimensional thin sections is based on image segmentation from variation of colour between neighbouring grains observed between crossed polarisers. Arnaud and others (1998) presented a different [illegible] and automatically characterise pores and grain boundaries in firn, based on sample sublimation, coaxial episcopy and image analysis. Using this technique, Arnaud (1997) determined distributions of grain cross-sectional areas at different depths in firn at Vostok station, Antarctica. Though worth using to study porous media (e.g. firn), optimal sublimation conditions are not easy to obtain, and hence sample preparation is difficult and time-consuming. The "standard" thin sections used in the present work are easily and rapidly obtained. Eicken (1993) proposed an automated image analysis of ice thin sections under crossed polarisers. Unlike the present work, this author used a universal (Rigsby) stage and grey-scale digitisation.

Preparation of thin sections and image recording

Ice thin sections are prepared by regular microtoming. Section thickness is an important parameter. The optimised thickness is a compromise between large enough colour differences between grains, and sharp enough colour transitions. Too thick sections have great colour differences, but grain boundaries appear too thick, with coloured interference fringes which can be misleading for image analysis. Too thin sections have well-defined spatial transitions but weak differences, most of the grains appearing within a grey range of colours. Experience shows that the optimised thickness corresponds to grain colours around a brown-yellow range. An example is given in Figure 1a. Note that in the case of examination of columnar ice, with column axis perpendicular to the section, this thickness problem would be less crucial, grain boundaries being almost perpendicular to the section.

For each thin section, three different pictures are taken while crossed polarizers are rotated together (at 0°, 30° and 60°), the thin section itself being fixed with respect to the camera. In this way, grains remaining dark for one rotation angle are illuminated for other angles, except if their c axes are perpendicular to the section. The image fields must coincide for the three different pictures. Note that a universal stage is not used in the present analysis. For the analysis of the EPICA ice core (see below), slides were taken with a regular camera, then digitalised using a charge coupled device colour camera. However, digital image recording can be performed directly with a digital camera. The format of the images was 640 × 480 pixels. The chosen image field resulted from a compromise between a good resolution and a reasonable statistical population of grains, i.e. at least 200. In the study of the shallow part of the EPICA ice core, with mean cross-sectional area of grains ranging between 1 and 2 mm^2, this corresponded to a resolution of 42.5 μm/pixel. The sampled population of grains varied from about 500 grains at 100 m depth to slightly less than 200 grains at 360 m.

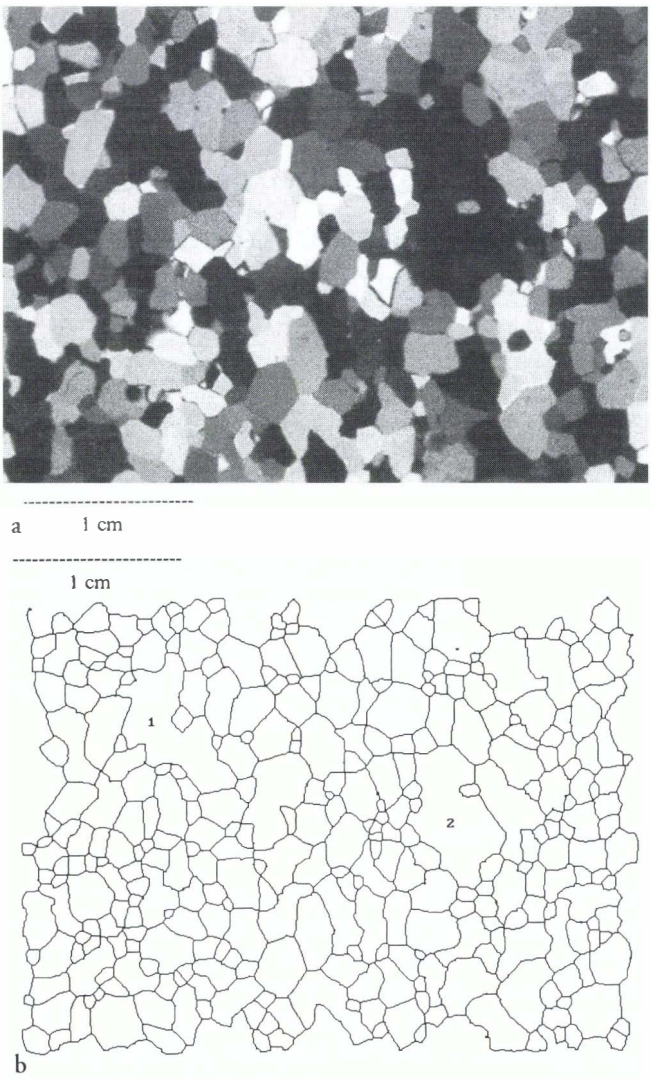

Fig. 1. (a) Thin section of polar ice examined between crossed polarisers, with an optimised thickness for image analysis, EPICA ice core, Dome C (depth 170 m). (b) The corresponding binary image of the microstructure (grain boundaries), after digital image processing. 1 and 2 are regions where the segmentation of grains was difficult, owing to c axes of grains perpendicular to the thin section.

Image analysis

Image segmentation aims to subdivide the image into regions of homogeneous colour characteristics (Gonzales and Woods, 1992). The discontinuities, i.e. grain boundaries in the present case, correspond to sharp spatial variations of these characteristics. They can be detected using derivative operators (or filters; Gonzales and Woods, 1992). However, pre-processing is generally required in order to remove sharp but small variations resulting from noise, while preserving large variations. Therefore, any image-segmentation processing should include a pre-processing step in order to remove noise and sharpen variations, followed by detection of the discontinuities using derivative filters. In the digital image processing developed for ice-microstructure extraction, summarised in Algorithm 1 and detailed below, steps 2.1 and 2.2 belong to the pre-processing, and steps 2.3 and 2.4 correspond to the detection of the discontinuities. Within this general framework, several different procedures can be considered at each step of the algorithm. The algorithm proposed results from such trials at each step. For example, at step 2.1, a "closing then opening" pro-

Algorithm 1

```
For colour image i = I–III
    begin
        The colour image i is decomposed into three grey-scale
            images, brightness, hue and saturation, called grey-scale
            images 1, 2 and 3, respectively.
        For grey-scale image j = 1–3
      begin
        Morphologic filter: opening then closing
        Median filter
        Sobel filter
        Thresholding
        Skeletonising ⇒ binary image j
      end
      Addition of the three binary images j ⇒ binary image i
    end
Addition of the three binary images i
Binary closing: dilation then erosion
Skeletonising
Trim
⇒ microstructure
```

cedure (instead of "opening then closing") was tested but found to be less efficient in reducing noise (see below). Although the proposed image-processing was found to be the most efficient, this does not exclude the possibility of another, completely different, efficient form of processing.

The proposed image segmentation processing is as follows:

1. The first colour image (see, e.g., Fig. 1a), denoted I, is decomposed into three grey-scale images, *brightness*, *hue* and *saturation* (Gonzales and Woods, 1992), denoted grey-scale images 1, 2 and 3, respectively. Other decompositions of colour images are possible, but this one is chosen because it is used by the human visual system to interpret and differentiate colours. To each pixel of a grey-scale image is assigned an intensity, or grey level, from 0 (black) to 255 (white) and denoted $I[x, y]$. x and y are the pixel coordinates. The saturation grey-scale image corresponding to Figure 1a is shown in Figure 2a, as well as the variation of intensity along a section.

2. For each grey-scale image 1–3, the following steps are performed:

   2.1. *Morphologic filter.* This filter consists of an opening operation, followed by a closing operation. An opening operation is an erosion followed by a dilation, whereas a closing operation is the reverse. Erosion of a grey-scale image consists in assigning to each pixel the minimum intensity of the set of pixels corresponding to this pixel and its neighbours (eight nearest neighbours in the present analysis). Similarly, dilation assigns the maximum intensity of the set to the pixel. More details are given in Gonzales and Woods (1992). This filter reduces high-frequency noise, and allows the removal of insignificant features such as microcracks and pits. The result for a typical image is shown in Figure 2b.

   2.2. *Median filter.* The median m of a set of values is such that half the values in the set are $< m$ and half are $> m$. In order to perform median filtering in the neighbourhood of a pixel, first the intensities I of the pixel and of its neighbours are sorted, then the median is determined and assigned to the pixel. In the present analysis, we limited the calculation to the eight nearest neighbours. This filter reduces noise while preserving the sharpness of the discontinuities. The result is shown in Figure 2c.

   2.3. *Sobel filter.* This filter is a derivative filter which detects discontinuities of intensity. The gradient of intensity (along directions x and y) is calculated. The maximum value of $\mathrm{d}I/\mathrm{d}x$ and $\mathrm{d}I/\mathrm{d}y$ is assigned to the pixel. This results in low values for homogeneous regions, and very high values along discontinuities (grain boundaries). Thresholding will therefore be easy to perform, in order to extract these discontinuities. More details about Sobel filtering are given in Gonzales and Woods (1992). The image obtained is shown in Figure 2d with its associated grey-level histogram.

   2.4. *Thresholding.* A threshold is defined on the histogram (Fig. 2d) by visual testing: the operator "moves" the threshold along the grey scale and selects the best result for the thresholding of boundaries. A grey level of 255 (white) is assigned to the pixels above the threshold, corresponding to discontinuities, and a grey level of 0 (black) is assigned to the pixels below the threshold. This results in a binary image. The three thresholds determined for the three grey-level images (*brightness*, *hue* and *saturation*) are memorised. They will be used for thresholding of the other two colour images, in order to accelerate the process.

   2.5. *Skeletonising.* This operation, also called thinning, determines the skeleton, one pixel wide, of the white regions of the binary image. This classical algorithm is detailed in Gonzales and Woods (1992). The skeleton is shown in Figure 2e.

3. The three binary images resulting from digital processing (steps 2.1–2.5) of the three grey-level images are summed.

4. Operations 1–3 are repeated for the other two colour images, II and III, using the previously memorised thresholds (see above).

5. The three binary images arising from each of the three colour images I–III are summed. The binary image obtained results from the addition of $3 \times 3 = 9$ binary images. The result is shown in Figure 2f.

6. Binary closing (dilation then erosion). After step 5, because the three colour images do not coincide perfectly, grain boundaries appear blurred. Binary closing allows blurred boundaries to be reassembled.

7. Skeletonising.

8. Final trimming to remove "dead-end" branches.

The microstructure obtained at the end of this algorithm is shown in Figure 1b, to be compared with one of the three starting colour images (Fig. 1a). Structural and topological parameters can now be computed on this final binary image. The digital image-processing proposed by Eicken (1993), though different, included some operations similar to that employed here, such as grey-scale image opening or Sobel filtering. The order specified in Algorithm 1 is important. If one step is omitted, the quality of image

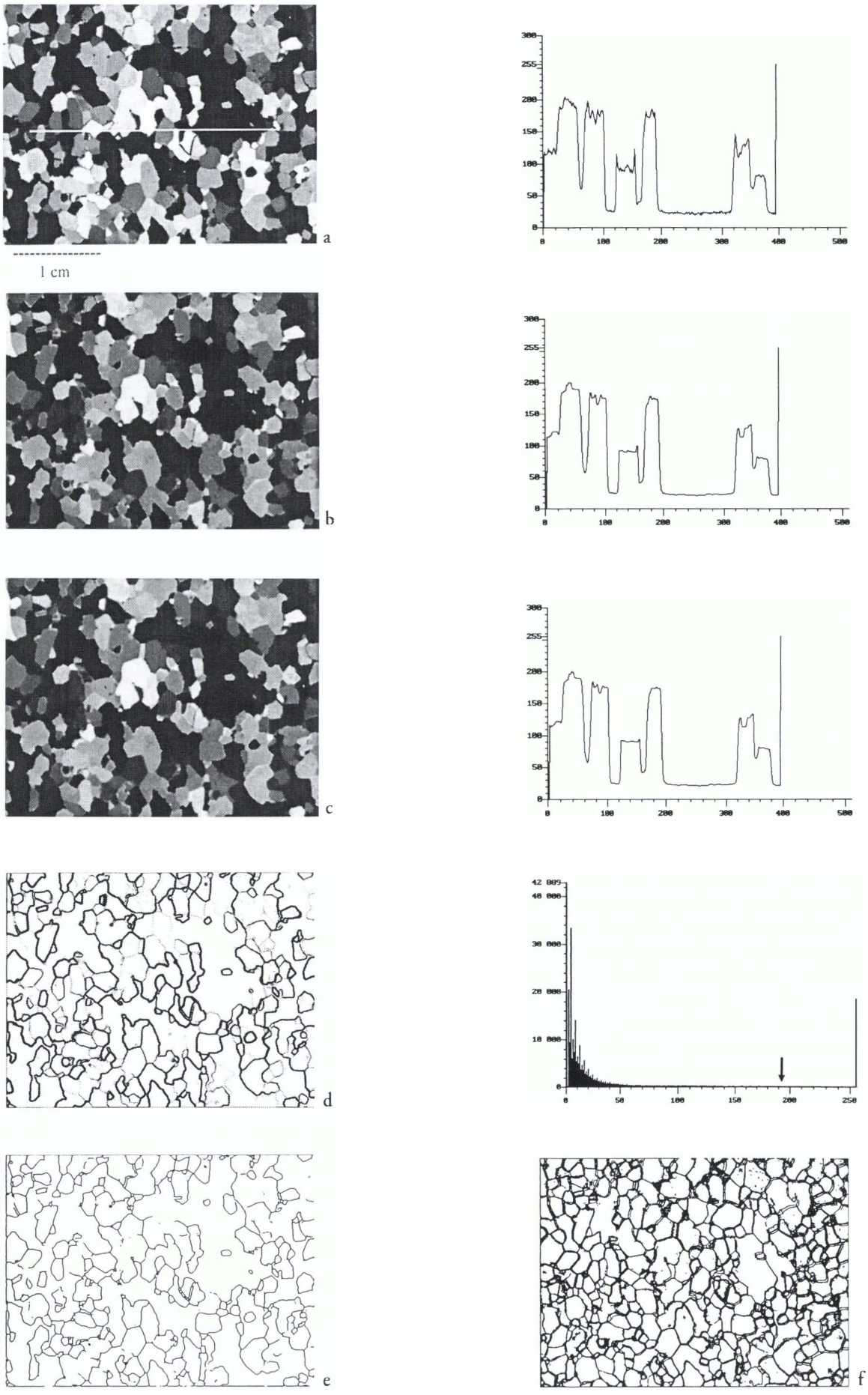

Fig. 2. Successive modifications of a digital image of grains. (a) Saturation grey-scale image of the colour image of Figure 1a. Left: morphologic filter. (c) Grey-scale image after median filter. (d) Grey-scale image after Sobel filter. Right: corresponding grey-level histogram. (e) Binary image after thresholding and skeletonising of the image in (d). (f) Binary image after summation of $3 \times 3 = 9$ binary images similar to that in (d) (see text for details).

segmentation decreases and we lose grain boundaries. The morphologic, median and Sobel filters are non-linear filters (Gonzales and Woods, 1992).
tempted, but it results in a broadening of the transitions (or discontinuities), thus making thresholding more difficult.

An intrinsic limitation of the proposed method is clearly illustrated in Figure 1b. When neighbouring grains have very similar *c*-axis orientations perpendicular to the section, they remain dark on the three colour images and are not easily segmented. This effect, which is particularly pronounced in Figure 1b, could be reduced with the help of a universal Rigsby stage. This limitation has little effect on the calculation of mean parameters (e.g. mean area, mean perimeter) but can have an effect on grain-size distribution towards the large sizes. The same limitations apply to manual estimation of grain-sizes. Note that a manual addition of the "obvious" missed boundaries can be performed easily on the computer. Another way to deal with this problem is to remove the most suspicious regions (e.g. regions 1 and 2 in Fig. 1b) from the subsequent statistical analyses.

APPLICATION TO THE EPICA ICE CORE (A PRELIMINARY STUDY)

The EPICA ice-coring started at Dome Concordia (75°06′ S, 123°24′ E; 3233 m a.s.l.) during the austral summer 1996–97, and reached 363 m depth at the end of the 1997–98 field season. During this season, thin sections of ice were produced along the core at 100–360 m depth, following the procedure described above, then digitalised and analyzed at the Laboratoire de Glaciologie at Géophysique de l'Environnment (LGGE). Most of them were vertical thin sections about 8 cm wide and (along the vertical direction) 11 cm long. Only a fraction of the section, representing a surface of about 27.2 mm × 20.4 mm, was digitalised. At three different depths (120, 218 and 357 m), three images were digitalised from the same section, but with different image fields, in order to estimate the experimental scatter on the structural parameters extracted. A few horizontal thin sections were also produced and digitalised at the same resolution.

From the microstructures obtained after image analysis, numerous structural and topological parameters can be extracted in order to characterise the material. To illustrate the potential of the procedure described above, we will now focus on three problems: the definition of grain "size", and its influence on grain-growth kinetics; shape anisotropy; and morphology of grains.

Mean grain-size and grain growth

Like many crystalline materials (see, e.g., Ralph, 1990) at elevated relative temperature (at least $T/T_F > 0.5$), polar ice experiences grain growth through time. The driving force for grain growth arises from a reduction of the total grain-boundary free energy within the system (Duval and Lorius, 1980; Ralph, 1990).
crease of the mean cross-sectional area, $\bar{A}$, with time t (Alley and Woods, 1996), has been reported for shallow ice of cold ice sheets (Gow and Williamson, 1976; Duval and Lorius, 1980).

$$\bar{A} = \bar{A}_0 + Kt, \qquad (1)$$

where $\bar{A}_0$ is the initial mean cross-sectional area and K is a constant showing an Arrhenius dependence on temperature. This was sometimes expressed as a parabolic growth law for the mean grain "size" $\bar{d}$:

$$\bar{d}^2 = \bar{d}_0^2 + Kt\,. \qquad (2)$$

It is not the purpose of the present work to discuss the validity, the physical or climatic significance of such a growth law (see Alley and others, 1986; Petit and others, 1987).
restrict our analysis to the relationship between grain "size", d, and grain cross-sectional area, A, and to the influence of the method of size estimation on subsequent growth law.

Figure 3 shows the evolution of the mean squared grain-size, $\bar{d}^2$, with depth for the EPICA ice core, $\bar{d}^2$ being estimated by a different method. The first method (squares) corresponds to the averaging of cross-sectional area of grains, $\bar{A}$, easily obtained from image analysis of an ice-microstructure map such as that shown in Figure 1b. Circles represent the mean cross-sectional area of the 50 largest grains in each section, $\bar{A}_{50}$, a way of estimating grain-size similar to that employed by Gow (1969). Triangles correspond to the square of the mean linear intercept length, $\bar{L}^2$. At the three depths where three different images were digitalised from the same sections, the corresponding different estimations of the mean cross-sectional area fall within a range of about 0.30 mm^2, whatever the method used ($\bar{A}$, $\bar{A}_{50}$ or $\bar{L}^2$). Estimation of $\bar{L}$ was performed automatically with lines along the vertical and horizontal directions and a line crossing the image each two pixels. This obviously represents a much larger line density than those used for manual measures, thus reducing scatter. These three differ-

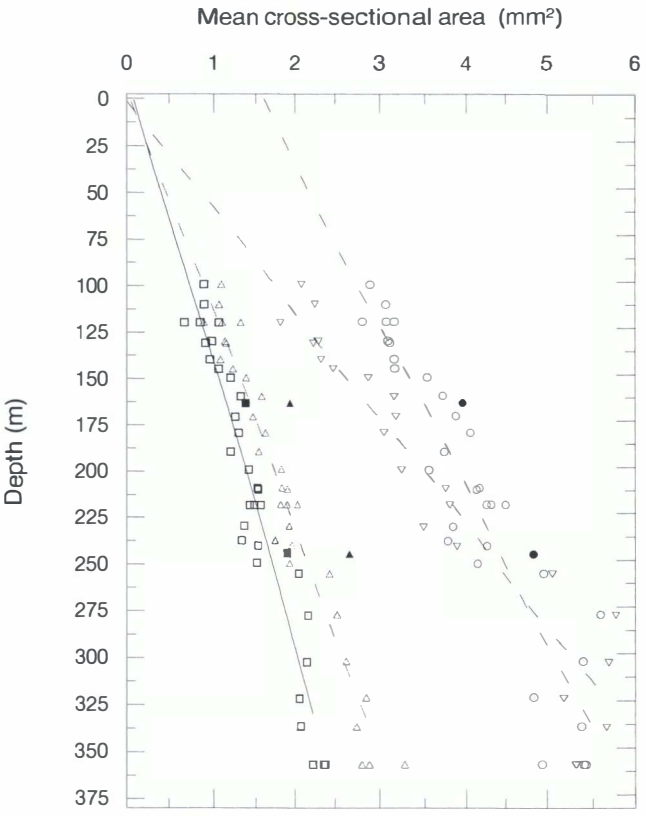

Fig. 3. Evolution of the mean cross-sectional area of grains with depth from the shallow part of the EPICA ice core. Squares: deduced directly from image analysis of ice microstructure.
Circles: mean cross-sectional area of the 50 largest grains. Inverted triangles: mean cross-sectional area of the largest 25% of grains.
bols: horizontal thin sections.

ent datasets are well described by linear fits, but with different slopes. For shallow ice of large ice sheets, a linear relationship between depth and age, t, is a very reasonable approximation. Therefore, the Figure 3 data seem to support Equation (1). However, the constant K varies with the method used to evaluate the mean squared grain-size up to a factor of about 2 (see Table 1). Moreover, if one extends the linear fit for $\bar{A}_{50}$ up to the surface (0 m), a much larger "initial" value is found compared to the $\bar{A}$ or $\bar{L}^2$ methods. This results from a bias introduced by a representativity evolving with mean grain-size (see above). The relationship between $\bar{A}$ and the mean cross-sectional area of the 50 largest grains, $\bar{A}_{50}$, is not trivial and obviously depends on size distribution, which could change over time and from site to site (because of temperature and climatic differences). During normal grain growth, the shape of the grain-size distribution is not supposed to change, and some authors have proposed log-normal distributions to describe experimental data or results of computer simulation (see, e.g., Atkinson, 1988; Anderson and others, 1989). Such a distribution, however, so far has no theoretical basis. Moreover, the peak value and the standard deviation of the distribution change over time. Therefore, an estimation of activation energy for grain growth by comparison of grain-growth kinetics, deduced from the $\bar{A}_{50}$ method, at different sites with different mean annual temperatures (see, e.g., Gow, 1969), has to be made with caution. As mentioned above, an additional problem of the $\bar{A}_{50}$ method comes from the increasing representativity of the 50 largest grains as the mean grain-size increases. In the present analysis, this representativity increased from about 10% at 100 m to 25% at 360 m, which is less than in the Gow (1969) analysis ($\geq$25%). To examine a possible effect of such increasing representativity, we computed the mean cross-sectional area of the largest 25% of grains in each section, $\bar{A}_{25\%}$ (see Fig. 3). With this method, the extrapolation of the linear fit up to 0 m is very close to that found with the $\bar{A}$ or $\bar{L}^2$ methods (see Table 1), and 75% of the available information is still lost.

In classical normal grain-growth analytical models (two-dimensional models; see, e.g., Hillert, 1965, adapted by Alley and others, 1986 for ice; Atkinson, 1988), the critical size parameter, d_{crit} or A_{crit}, such that grains larger than A_{crit} grow and smaller grains shrink, is equal to $\bar{A}$ (or $\bar{d}$). Any other value of A, including the mean cross-sectional area of the 50 largest grains, has much less physical significance with respect to theoretical models. However, three-dimensional parameters such as the mean grain volume would have even more physical meaning. From three-dimensional computer simulations of normal grain growth, Anderson and others (1989) showed that, if the morphology of grains is such that grain shapes are compact and exhibit close to minimal surface areas with respect to grain volume at all times, then the "true" grain-growth kinetics, based on the evolution of the mean grain volume, is very close to the kinetics derived from two-dimensional parameters (mean cross-sectional area, $\bar{A}$). In particular, the same constant K is found (Anderson and others, 1989). This similitude does not hold if morphology is changing over time. To the authors' knowledge, the only available dataset on the distribution of grain volumes and corresponding cross-sections and linear intercepts for a "realistic" microstructure is Anderson and other (1989). On this (limited) basis, we argue that the mean cross-sectional area method ($\bar{A}$) is the most "exact" for deriving true three-dimensional grain-growth kinetics from thin-section analyses. In Table 1, the constant K obtained with the 50 largest grains method is close to that obtained by Duval and Lorius (1980) from a former core drilled at the "old" Dome C site (74°39′ S, 124°10′ E, about 70 km from the current Dome Concordia drilling site), in agreement with the method used by these authors to estimate grain-sizes.

The linear intercept method gives results closer to $\bar{A}$ than the 50 largest grains method. However, for a given volume element (a "grain"), the relation between $\bar{A}$ and $\bar{L}$ depends on the element morphology (Underwood, 1970). The ratio $\bar{A}/\bar{L}^2$ is equal to $3\pi/8 \approx 1.18$ for a sphere. For a truncated octahedron, a volume element allowing space filling and sometimes used to model grains (Gibson and Ashby, 1988), this ratio is about 1.32. For a space-filling assembly of grains of different sizes, isotropic on average, $\bar{L}$ depends on both $\bar{A}$ and the mean perimeter of grains, $\bar{s}$ (Underwood, 1970):

$$\bar{L} = \pi \frac{\bar{A}}{\bar{s}} . \qquad (3)$$

For a grain assembly with shape anisotropy, the problem is even more complex. It is shown below that the average shape anisotropy of grains varies with depth (and so time) along the EPICA ice core. The linear intercept method is therefore unable to exactly reproduce the evolution of $\bar{A}$ and thus the evolution of the mean grain volume, as shown by Anderson and others (1989).

From the above discussion, it appears that in two dimensions the measure of the mean cross-sectional area, $\bar{A}$, is the size definition ($\bar{d} \sim \bar{A}^{1/2}$) with the best physical significance. This measure is difficult to determine manually, a fact which shows the relevance of the automatic procedure described here.

Finally, one can notice in Figure 3 that the mean crystal sizes observed on horizontal sections are systematically slightly larger than expected from the regression analysis, whatever the definition of the size. This results from the flattening of grains on the horizontal plane (see below).

Shape anisotropy

In order to show a possible anisotropy of grain shape, the ratio between the mean linear intercepts in the horizontal (X) and vertical (Z) directions, $\bar{L}_X/\bar{L}_Z$, has been cal-

Table 1. Grain-growth kinetics for the shallow part (Holocene ice) of the EPICA ice core, deduced from different grain-size definitions (see text for details).

	$\bar{A}$	$\bar{L}^2$	$\bar{A}_{50}$	$\bar{A}_{25\%}$	*Duval and Lorius (1980)*
K' (mm^2 m^{-1})	0.60×10^{-2}	0.80×10^{-2}	1.00×10^{-2}	1.68×10^{-2}	1.10×10^{-2}
R^2 (regression coeff.)	0.92	0.95	0.86	0.93	

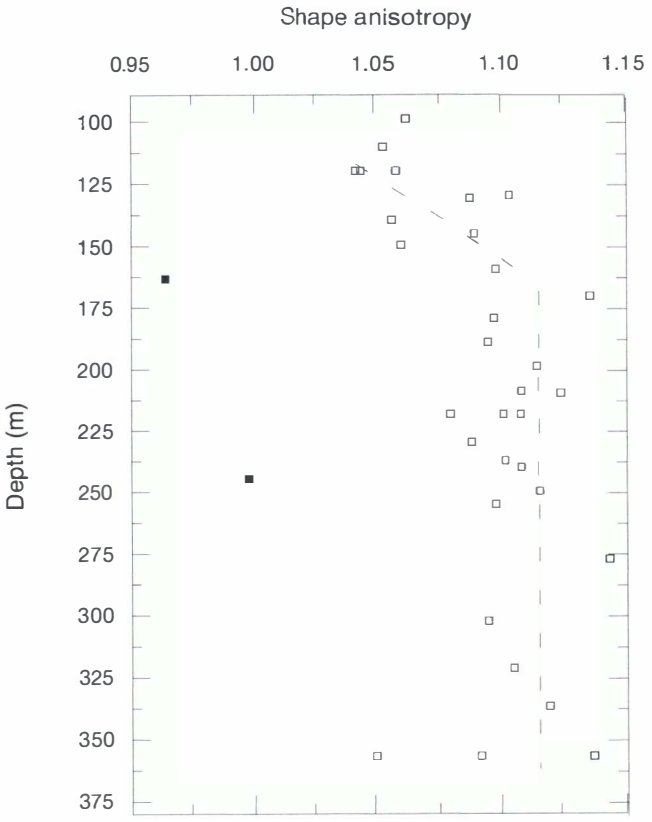

Fig. 4. Evolution of shape anisotropy with depth from the shallow part of the EPICA ice core. Triangles: vertical thin sections; anisotropy measured by $\bar{L}_X/\bar{L}_Z$ (Z: vertical direction, X: horizontal direction). Squares: horizontal thin sections; anisotropy measured by $\bar{L}_X/\bar{L}_Y$ (X and Y: horizontal directions).

culated on vertical thin sections (Fig. 4). This ratio is systematically larger than 1, which means that the grains are flattened along the horizontal plane. Flattening seems to increase with depth, from about 1.05 at 100 m to about 1.12 at 180–200 m, then remains roughly constant up to 360 m. At the three depths where three different images were digitalised from the same sections, the different estimations of $\bar{L}_X/\bar{L}_Z$ fall within a range of about 0.03–0.04, except for one image at 357 m which exhibits a surprisingly low flattening. On the other hand, grains are isotropic on horizontal thin sections, with a ratio $\bar{L}_X/\bar{L}_Y$, close to 1 (Y is a second horizontal direction). Such a shape anisotropy makes the link between $\bar{L}$ and $\bar{A}$ even more difficult to establish (see above).

Grain morphology

In Figure 5 is plotted the evolution of the ratio A/s^2 (cross-sectional area/perimeter^2) averaged over all the grains of the section, with depth. This adimensional mean form factor, which is maximum for spheres ($A/s^2 = 1/4\pi \approx 0.08$), is a measure of the average grain morphology. The latter is remarkably stable during grain growth, around a value of 0.055. This suggests that grain morphologies are close, on average, to an equilibrium-minimising surface area (in three dimensions) with respect to grain volume, while subject to topological constraints and flattening.

CONCLUSION AND PROSPECT

An automatic procedure, based on colour-image analysis of

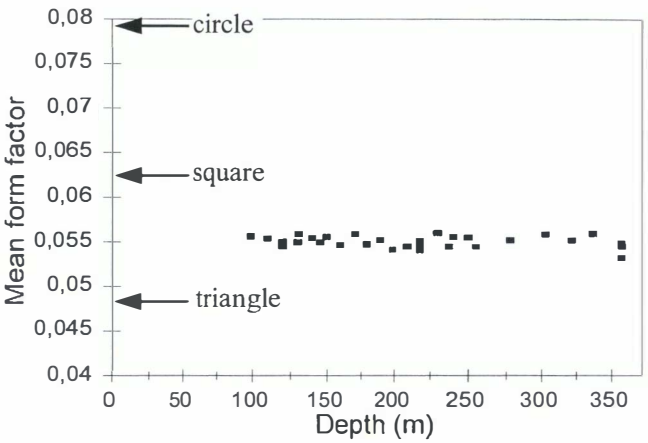

Fig. 5. Evolution of the average grain morphology, expressed by the form factor A/s^2 averaged over all the grains of the section, with depth, for the shallow part of the EPICA ice core. Arrows indicate, for comparison, the form factor of three simple two-dimensional shapes (circle, square and equilateral triangle).

thin sections observed between crossed polarisers, has been developed in order to extract two-dimensional (cross-sectional) ice microstructure. From these microstructures, numerous structural, morphological and topological parameters can be determined to characterise the material and its evolution. This has been illustrated with three examples on the shallow ice of the EPICA ice core, including mean cross-sectional area of grains, shape anisotropy and average grain morphology.

However, averaged values of parameters are not sufficient to follow in detail the evolution of the microstructure. For example, the evolution of grain-size distribution through time can be used to differentiate grain-growth regimes (normal vs abnormal; see, e.g., Hillert, 1965; Ralph, 1990). Statistical distributions of parameters can be extracted easily and automatically from microstructures such as that represented in Figure 1b. Arnaud (1997) obtained such distributions for Vostok firn, using a different technique to reveal the microstructure (see above).

Topological parameters (e.g. the number of sides per grain (in two dimensions)), are also important for characterising the physics of polycrystalline materials (Atkinson, 1988), including ice (Arnaud, 1997). Topological two-dimensional parameters are easily obtained from reconstructed ice microstructures.

The ultimate goal of the study of ice microstructure is to infer three-dimensional parameters, such as volumes of grains, from two-dimensional parameters obtained on cross-section. This is a difficult problem. As noted above, in the case of isotropic microstructures and compact grain shapes, mean grain volume could be correctly estimated from the mean cross-sectional area (Anderson and others, 1989). This is no longer true for anisotropic microstructures or changing morphologies. Thorvaldsen (1997) stressed that two polycrystals with identical mean linear intercepts on a two-dimensional section can have different mean grain volumes, depending on grain-volume distribution and grain shapes. The correspondence between cross-sectional area distributions and grain-volume distributions is even less straightforward (Anderson and others, 1989). A complete description of the two-dimensional microstructure, and especially statistical distributions of structural and topological parameters, is necessary, though perhaps not sufficient,

and simplifying stereological hypotheses on isotropy and morphology are required in order to infer three-dimensional parameters. Such an analysis would be impossible to perform from manual analysis of thin sections.

ACKNOWLEDGEMENTS

This work is a contribution to the "European Project for Ice Coring in Antarctica" (EPICA), a joint European Science Foundation/European Commission scientific programme, funded by the European Commission under Environment and Climate Programme (1994–98) contract ENV4-CT95-0074 and by national contributions from Belgium, Denmark, France, Germany, Italy, The Netherlands, Norway, Sweden, Switzerland and the U.K.

We would like to thank P. Duval and L. Arnaud for valuable discussions and comments, as well as two anonymous reviewers whose comments and suggestions helped to improve the clarity of the paper. LGGE is associated with Université Joseph Fourier, Grenoble I.

REFERENCES

Alley, R. B. and G. A. Woods. 1996. Impurity influence on normal grain growth in the GISP2 ice core, Greenland. *J. Glaciol.*, **42**(141), 255–260.

Alley, R. B., J. H. Perepezko and C. R. Bentley. 1986. Grain growth in polar ice: I. Theory. *J. Glaciol.*, **32**(112), 415–424.

Anderson, M. P., G. S. Grest and D. J. Srolovitz. 1989. Computer simulation of normal grain growth in three dimensions. *Philos. Mag. B*, **59**(3), 293–329.

Arnaud, L. 1997. Modélisation de la transformation de la neige en glace à la surface des calottes polaires: étude du transport des gaz dans ces milieux poreux. (Thèse de doctorat, Université Joseph Fourier, Grenoble I.)

Arnaud, L., M. Gay, J.-M. Barnola and P. Duval. 1998. Imaging of firn and bubbly ice in coaxial reflected light: a new technique for the characterization of these porous media. *J. Glaciol.*, **44**(147), 326–332.

Atkinson, H.V. 1988. Theories of normal grain growth in pure single phase systems. *Acta Metall.*, **36**(3), 469–491.

Duval, P. and C. Lorius. 1980. Crystal size and climatic record down to the last ice age from Antarctic ice. *Earth Planet. Sci. Lett.*, **48**(1), 59–64.

Eicken, H. 1993. Automated image analysis of ice thin sections — instrumentation, methods and extraction of stereological and textural parameters. *J. Glaciol.*, **39**(132), 341–352.

Gibson, L. J. and M. F. Ashby. 1987. *Cellular solids: structure and properties.* New York, Pergamon Press.

Gonzales, R. C. and R. E. Woods. 1992. *Digital image processing.* Reading, MA, Addison-Wesley Publishing Co.

Gow, A. J. 1969. On the rates of growth of grains and crystals in South Polar firn. *J. Glaciol.*, **8**(53), 241–252.

Gow, A. J. and T. Williamson. 1976. Rheological implications of the internal structure and crystal fabrics of the West Antarctic ice sheet as revealed by deep core drilling at Byrd Station. *Geol. Soc. Am. Bull.*, **87**(12), 1665–1677.

Hillert, M. 1965. On the theory of normal and abnormal grain growth. *Acta Metall.*, **13**, 227–238.

Petit, J. R., P. Duval and C. Lorius. 1987. Long-term climatic changes indicated by crystal growth in polar ice. *Nature*, **326**(6108), 62–64.

Ralph, B. 1990. Grain growth. *Mater. Sci. Tech.*, **6**, 1139–1144.

Thorsteinsson, Th., J. Kipfstuhl, H. Eicken, S. J. Johnsen and K. Fuhrer. 1995. Crystal size variations in Eemian-age ice from the GRIP ice core, central Greenland. *Earth Planet. Sci. Lett.*, **131**(3–4), 381–394.

Thorvaldsen, A. 1997. The intercept method — 2. Determination of spatial grain size. *Acta Materialia*, **45**(2), 595–600.

Underwood, E. E., *ed.* 1970. *Quantitative stereology.* Reading, MA, Addison-Wesley Publishing Co.

MS received 23 November 1998 and accepted in revised form 14 May 1999

L. Arnaud, J. Weiss, M. Gay, P. Duval. "Shallow-ice microstructure at Dome Concordia, Antarctica", *Annals of Glaciology*, *Vol.* 30, 2000.

Annals of Glaciology 30 2000
© International Glaciological Society

Shallow-ice microstructure at Dome Concordia, Antarctica

LAURENT ARNAUD, JÉRÔME WEISS, MICHEL GAY, PAUL DUVAL
Laboratoire de Glaciologie et Géophysique de l'Environnement, CNRS, B.P. 96, 38402 St Martin d'Hères Cedex, France

ABSTRACT. The shallow-ice microstructure at Dome Concordia, Antarctica, has been studied between 100 m and 580 m. An original digital-image-processing technique has been specially developed to extract ice microstructure (grain boundaries) from thin sections prepared during the two first scientific EPICA field seasons (1997/98 and 1998/99). Using this, not only the mean crystal size, but also crystal-size distributions and shape anisotropy, were determined. The mean crystal-size profile as well as crystal-size distributions reveal normal grain growth up to 430 m. Between 430 m and 500 m, a marked decrease of crystal size is observed and compared with a similar trend obtained in the "old" Dome C ice core formerly associated with the Holocene/Last Glacial transition (Duval and Lorius, 1980). This seems to indicate a slightly lower accumulation rate (by <10%) at Dome C. The shapes of the crystal-size distributions, though very similar, do evolve with depth and seem to be sensitive to climatic changes. An increasing flattening of crystal shape is observed with depth. This allowed estimation of the vertical strain rate in the shallow part of the ice sheet.

1. INTRODUCTION

The mean crystal size (see below for a definition of "size") has been recognized as an interesting parameter, independent of the isotopic composition of the ice, for revealing climatic changes from polar ice cores (Petit and others, 1987). This correlation between crystal size and climate is well illustrated by a strong decrease of the mean crystal size at a climatic transition, such as the Holocene/Last Glacial Maximum (LGM) transition (Duval and Lorius, 1980; Petit and others, 1987). Moreover, polar-ice microstructure (crystal size and crystal shape) is of interest because it controls different physical properties of the material and can give insight into the strain history and recrystallization processes of the ice, as for any crystalline material.

So far, most of the analyses of ice (or firn) microstructure from polar ice cores were performed manually on two-dimensional (2-D) thin sections, and therefore restricted to the study of the mean crystal-size profile (see, e.g., Gow, 1969; Duval and Lorius, 1980; Thorsteinsson and others, 1995). However, in order to fully characterize ice evolution, including grain growth, flattening of grains or recrystallization processes, not only the mean crystal size, but also size distribution, grain morphology and topological characteristics are needed. Alley and Woods (1996) reported some data about size distributions from the shallow ice of the Greenland Ice Sheet Project Two (GISP2) ice core. Such detailed analyses are difficult to perform manually and very time consuming. A digital-image processing based on the segmentation of colour images of 2-D thin sections of ice observed between cross-polarizers has been developed recently at the Laboratoire de Glaciologie et Géophysique de l'Environnement (LGGE), Grenoble (Gay and Weiss, in press). This allows the automatic extraction of all the grain boundaries on the section, from which morphological, statistical and topological parameters can be computed.

This paper presents a preliminary analysis of the ice microstructure from the European Project for Ice Coring in Antarctica (EPICA) ice core at Dome Concordia (Dome C), Antarctica (75°06′ S, 123°24′ E; 3233 m a.s.l.), to a depth of about 580 m, based on this automatic digital processing. After a short description of the experimental procedure employed, the mean crystal-size profile is given and discussed, especially the depth at which the Holocene/Last Glacial transition is observed. Then, crystal-size distributions are described and their evolution with depth discussed. This gives insight into the grain-growth process in shallow polar ice. Finally, preliminary results about the shape anisotropy of grains (flattening) are given.

2. EXPERIMENTAL PROCEDURE

The EPICA ice coring started at Dome Concordia during the austral summer 1996/97. It reached 787 m depth at the end of the 1998/99 field season. During the field seasons 1997/98 and 1998/99, thin sections of ice were produced along the core between 100 m and 581 m depth, then digitized and analyzed at LGGE. Because of the very brittle character of the ice below 581 m, deeper ice was left at the drilling site to relax and no thin sections have been prepared so far for the ice from 581–787 m.

The preparation of thin sections, the image recording and the digital-image processing used to extract the microstructures have been detailed in Gay and Weiss (in press) and will not be discussed here. Note simply that at each depth, three different pictures of the same thin section were taken while rotating crossed polarizers together (at 0°, 30° and 60°), the thin section itself being fixed with respect to the camera. The image analysis combined information from the three images to reveal grain boundaries. After digitizing, the image resolution was 48.1 mm/pixel whereas the image field covered 31 mm × 23 mm. The number of grains sampled in one image ranged from 200–500.

3. THE MEAN CRYSTAL-SIZE PROFILE

In previous analyses of mean crystal size in polar ice cores,

several different methods were used to estimate this "size". Gow (1969) measured the length and breadth of the 50 largest crystals in each section of polar firn with a pocket comparator. Duval and Lorius (1980) estimated mean grain-size from crystal counting over a given area, but did not take into account the smallest grains, sometimes of ambiguous existence, whereas Thorsteinsson and others (1995) and Alley and Woods (1996) used the linear-intercept method. The linear-intercept method expresses size in terms of *length*, whereas "size" is a mean crystal *area* with other analytical methods. More importantly, even after a re-scaling of all the measures to the same dimension (e.g. an area), these different size-estimation methods lead to very different results, for example for grain-growth kinetics, and can therefore be misleading (Arnaud, 1997; Gay and Weiss, in press). The size definition with the best physical significance would be a mean crystal volume. This three-dimensional (3-D) parameter cannot be directly determined from a single 2-D thin section. To the authors' knowledge, the only available data which allow a comparison of 3-D mean crystal volume with 2-D (or one-dimensional) parameters is the Anderson and others (1989) simulation of normal grain growth. On this (limited) basis, Gay and Weiss (in press) have shown that the mean cross-sectional crystal-area method, averaging over the entire crystal population of the section, is the most exact way to derive true 3-D grain-growth kinetics from thin-section analyses. This analysis, difficult to perform manually, can be computed easily from the 2-D microstructures extracted by image analysis (Gay and Weiss, in press). The crystal "sizes" reported below were estimated this way. From a limited analysis, Gay and Weiss (in press) estimate the dispersion of the mean cross-sectional area to less than 0.30 mm^2. A planned analysis of one meter continuous thin sections will furnish a better estimate of the dispersion and variability of the mean cross-sectional area.

Figure 1 shows the evolution of the mean cross-sectional crystal area vs depth. In the shallow part of the core (from 100–430 m), the results are in agreement with a linear increase of the mean crystal area with depth. According to previous glaciological studies (Gow, 1969; Duval and Lorius, 1980; Alley and others, 1986) normal grain growth in ice is characterized by a linear increase of the mean cross-sectional area, A, with time, t:

$$A = A_0 + K(T) \times t \qquad (1)$$

The growth rate $K(T)$ is an Arrhenius temperature-dependent factor. Therefore, the linear relation (Equation (1)) no longer holds with varying temperature, i.e. climatic changes. For shallow ice in a large ice sheet, a linear relationship between depth and age is a very reasonable approximation. Therefore, as previously described by Duval and Lorius (1980), the linear increase of the mean crystal area with depth characterizes a normal grain-growth process during Holocene.

For deeper ice (430–500 m), the mean crystal area was observed to decrease significantly in size (Figs 1 and 2a). The same feature (see Fig. 2b) was observed in the "old" Dome C ice core (74°39′ S, 124°10′ E; 3240 m a.s.l.) and associated by Duval and Lorius (1980) with isotopic variations due to the Holocene/LGM transition. If both decreases at Dome C (Fig. 2a) and at the "old" Dome C (Fig. 2b) are representative of the same climatic event, then a comparison of the two profiles enables us to compare the accumulation rate at these two different drilling sites, located about 70 km apart. The crystal-size decrease is observed over about the same thick-

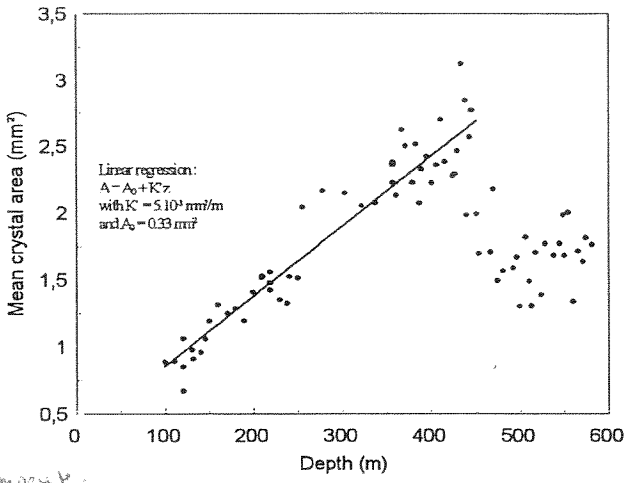

Fig. 1. Evolution of the mean cross-sectional area of crystals with depth, for the shallow part of the EPICA ice core. The straight line represents the linear regression of mean crystal-size data between 100 m and 430 m. The slope of this line gives the growth rate (K') in mm^2/m.

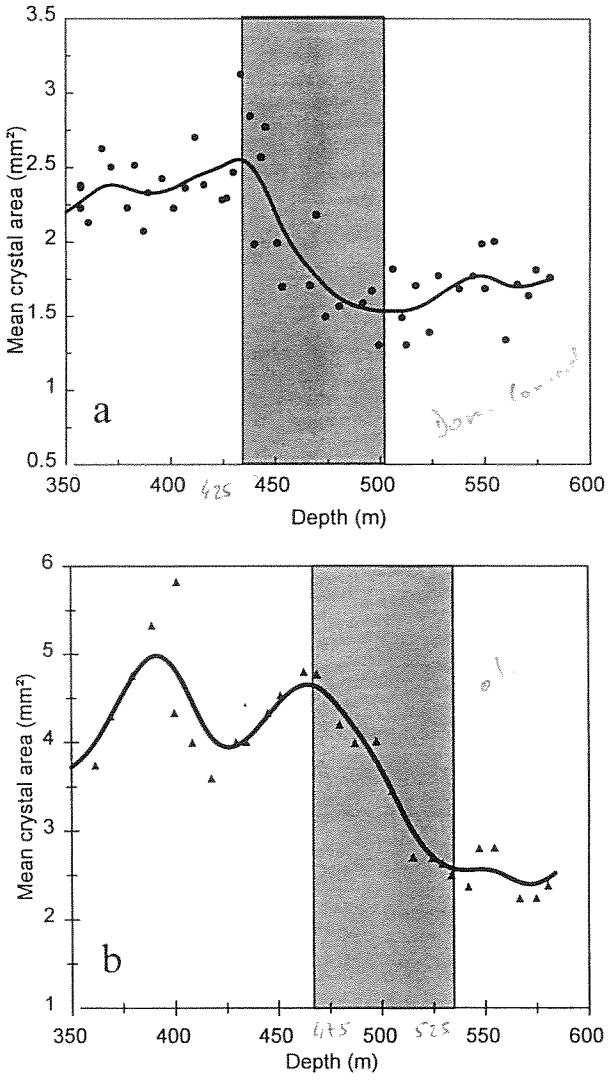

Fig. 2. Evolution of the mean cross-sectional area of crystals with depth from 350–580 m (a) at Dome C, EPICA and (b) at "old" Dome C (Duval and Lorius, 1980). The continuous lines represent the data splines smoothing and the shaded area indicates the zone of the crystal-size decrease.

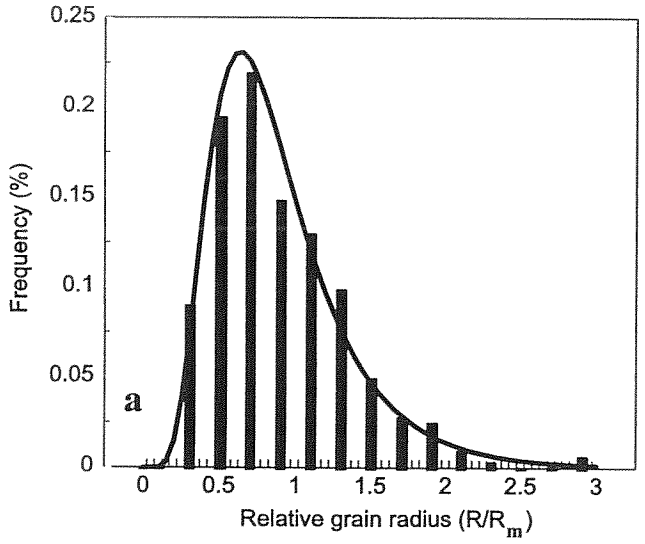

Fig. 3. Relative grain radius (R/R_m) determined from cross-sectional analysis: experimental data are shown as histograms and fitted with a log-normal distribution. (a) Dataset corresponding to 492 m depth (average value of $\ln R/R_m = -0.22$; std dev. = 0.49). (b) Dataset corresponding to all depths together (average value of $\ln R/R_m = -0.26$; std dev. = 0.53).

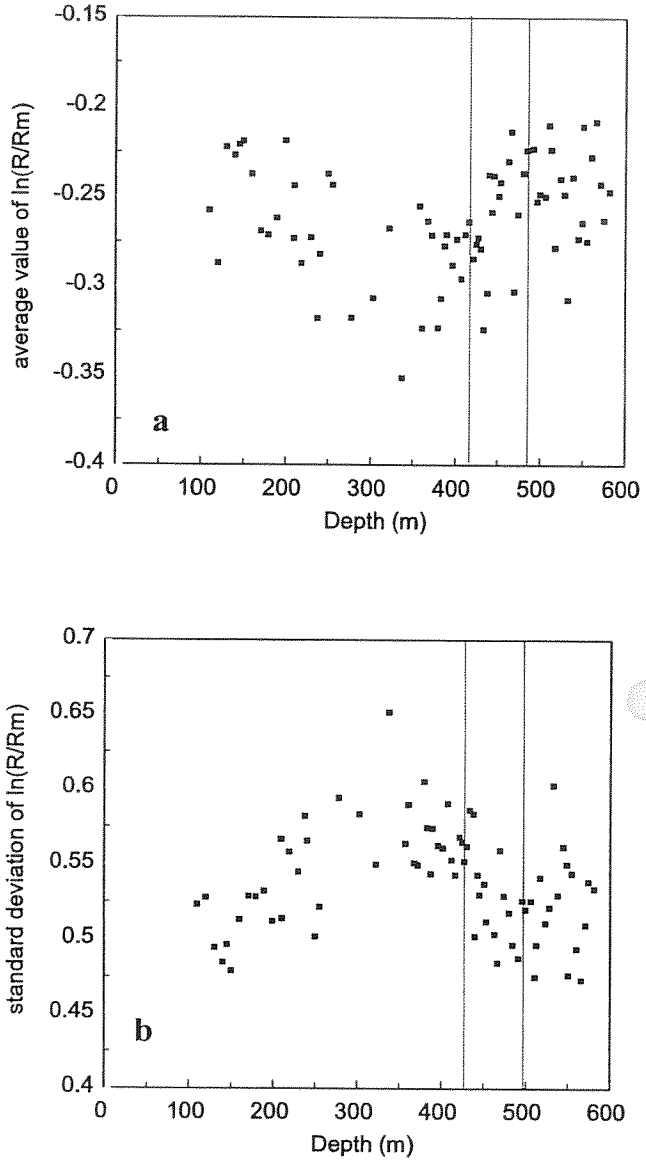

Fig. 4. Evolution of the two independent parameters characterizing the log-normal distributions fitting the experimental histogram ($\ln R/R_m$). Average value (a) and standard deviation (b) of $\ln R/R_m$ are plotted vs depth. The dashed lines indicate the limits of the grain-size transition defined in Figure 2.

ness of ice, i.e. ~70 m, but shifted slightly upwards at Dome C. This shift, <10%, gives an upper estimate for the difference between the accumulation rate at the two drilling sites.

After this marked decrease, the crystal size seems to increase again in the deepest part of the core, supposedly within the Last Glacial.

4. SIZE DISTRIBUTIONS

The shape of the grain-size distribution is another important parameter to characterize grain-growth or recrystallization processes in crystalline materials (see, e.g., Atkinson, 1988 or Ralph, 1990). It is customary to plot size distributions in terms of normalized grain "radius", R/R_m, where R can be calculated, for example, as the square root of a cross-sectional area, and R_m is the mean radius (see, e.g., Anderson and others, 1989). In material science, one classically divides the processes of grain growth into two types: normal and abnormal (Ralph, 1990). Normal grain growth is characterized by a grain-size distribution remaining the same shape (typically log-normal) with time (Atkinson, 1988; Ralph, 1990).

A typical crystal-size distribution is shown in Figure 3a. The experimental histogram fits a log-normal distribution well. Similar histograms were extracted from each thin section along the whole core between 100 m and 580 m. Log-normal distributions were systematically observed. In a first approximation, the shape of the normalized size distribution is independent of depth (see below); all grain-size data at all depths together (>20 000 grains) are log-normally distributed (Fig. 3b).

A log-normal distribution is fully characterized by two independent parameters: the average value and standard deviation of $\ln(R/R_m)$. The evolution of these two parameters with depth is plotted in Figure 4a and b, respectively. The range of variation is narrow in both cases (see above and Fig. 3b). This is illustrated in Figure 5 which shows the most different log-normal distributions observed are, indeed, very close. This strongly argues for a normal grain-

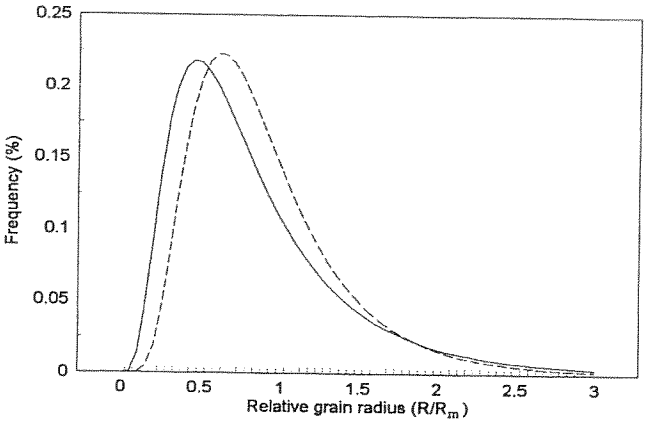

Fig. 5. Plots of the most different log-normal distributions fitting the experimental histograms of the relative grain radius. Continuous line is distribution corresponding to the beginning of the transition zone (average value of $\ln R/R_m = -0.35$*; std dev. = 0.65). Dashed line is distribution corresponding to the end of the transition zone (average value of* $\ln R/R_m = -0.22$*; std dev. = 0.51).*

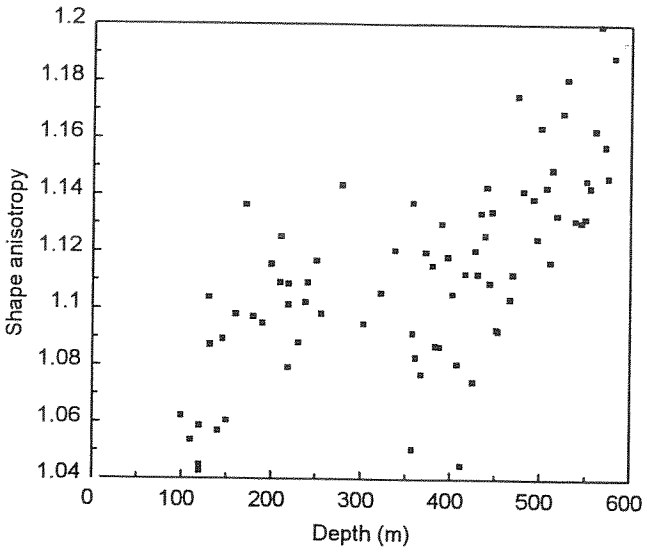

Fig. 6. Evolution of the vertical-shape anisotropy (ratio between the mean linear intercept along the horizontal direction and the mean linear intercept along the vertical) with depth.

growth process for shallow polar ice. An abnormal grain growth would have been characterized by a second maximum in the grain-size distribution at large grain-size (see, e.g., Ralph, 1990), never observed during this work.

However, within these narrow ranges of variation, significant trends can be detected, especially during the decrease of the mean grain-size previously associated with a climatic transition. The average value and standard deviation of $\ln(R/R_m)$ follow inverse trends throughout the entire depth. → Ongoing detailed analyses of the variations of crystal-size distributions will help reveal the very nature of the grain-growth process in polar ice and especially the role of impurities (bubbles, dust, dissolved impurities; Alley and others, 1986) on grain-boundary migration.

5. SHAPE ANISOTROPY

In order to show a possible anisotropy of grain shape, the ratio between the mean linear intercept along the horizontal (X) direction and the mean linear intercept along the vertical (Z) direction, $\bar{L}_X/\bar{L}_Z$, has been calculated on vertical thin sections (Fig. 6). Estimations of $\bar{L}_X$ and $\bar{L}_Z$ were performed automatically with a line crossing the image each two pixels, i.e. 96.2 μm. This ratio is systematically larger than 1, which means that the grains are flattened along the horizontal plane.

Flattening seems to increase with depth, from about 1.05 at 100 m to about 1.19 at 580 m. This corresponds to a flattening of roughly 13% over 480 m. Using the chronology given by Lorius and others (1979) for the "old" Dome C, corrected by a 10% decrease of the accumulation rate (see section 3), one can estimate from this flattening a vertical strain rate of 0.13/13 000 yr $= 1.00 \times 10^{-5}$ yr^{-1}. This is in good agreement with a simple estimate of this strain rate based on an equilibrium hypothesis for the ice sheet. At equilibrium, i.e. a constant thickness of the ice sheet, a 34 mm accumulation of ice (accumulation rate given by Lorius and others (1979)) for the "old" Dome C corrected by a 10% decrease (see section 3)) is spread each year over a 3200 m deep ice column leading to a strain rate of 3.4/3200 $= 1.04 \times 10^{-5}$ yr^{-1}. This agreement indirectly validates the hypothesis of homogeneity of the strain rate through the full ice thickness, used for the second estimate.

6. CONCLUSION

Experimental results on the ice microstructure (crystals size and shape) from the EPICA ice core at Dome Concordia have been obtained from image analysis of thin sections prepared during the first two field seasons (1997/98 and 1998/99). A novel digital-image processor developed at LGGE (Gay and Weiss, in press) allowed the extraction not only of the mean value of the crystal size, but also size distributions and shape anisotropy.

The mean crystal-size profile as well as crystal-size distributions reveal normal grain growth up to 430 m. Between 430 m and 500 m, a marked decrease of crystal size is observed and compared with similar trend obtained in the "old" Dome C ice core formerly associated with the Holocene/LGM transition (Duval and Lorius, 1980). This seems to indicate a slightly lower accumulation rate (by <10%) at Dome C. An increasing flattening of crystal shape is observed with depth. This enabled the vertical strain rate of the shallow part of the ice sheet to be estimated.

Completion of these preliminary experimental results will allow a better understanding of the physics of crystal growth and recrystallization processes in polar ice. Numerous different morphological and topological parameters will be extracted easily using our digital-image processing of the continuous thin section of the EPICA ice core. The effect on ice microstructure of parameters such as temperature, impurities content or stress–strain fields could be studied in order to use ice microstructure as a climatic record and to improve knowledge of the flow of ice sheets.

ACKNOWLEDGEMENTS

This work is a contribution to the "European Project for Ice Coring in Antarctica", a joint European Science Foundation ESF/European Commission (EC) scientific program, funded by the EC under the Environment and Climate Programme

(1994–98) contract ENV4-CT95-0074 and by national contributions from Belgium, Denmark, France, Germany, Italy, The Netherlands, Norway, Sweden, Switzerland and the United Kingdom.

We would like to thank A. Manouvrier for technical assistance.

REFERENCES

Alley, R. B. and G. A. Woods. 1996. Impurity influence on normal grain growth in the GISP2 ice core, Greenland. *J. Glaciol.*, **42**(141), 255–260.

Alley, R. B., J. H. Perepezko and C. R. Bentley. 1986. Grain growth in polar ice: I. Theory. *J. Glaciol.*, **32**(112), 415–424.

Anderson, M. P., G. S. Grest and D. J. Srolovitz. 1989. Computer simulation of normal grain growth in three dimensions. *Philos. Mag. B*, **59**(3), 293–329.

Arnaud, L. 1997. Modélisation de la transformation de la neige en glace à la surface des calottes polaires: étude du transport des gaz dans ces milieux poreux. (Thèse de doctorat, Université Joseph Fourier, Grenoble I.)

Atkinson, H. V. 1988. Theories of normal grain growth in pure single phase systems. *Acta Metall.*, **36**(3), 469–491.

Duval, P. and C. Lorius. 1980. Crystal size and climatic record down to the last ice age from Antarctic ice. *Earth Planet. Sci. Lett.*, **48**(1), 59–64.

Gay, M. and J. Weiss. In press. Automatic reconstruction of polycrystalline ice microstructure from image analysis: application to the EPICA ice core at Dome Concordia, Antarctica. *J. Glaciol.*

Gow, A. J. 1969. On the rates of growth of grains and crystals in South Polar firn. *J. Glaciol.*, **8**(53), 241–252.

Lorius, C., L. Merlivat, J. Jouzel and M. Pourchet. 1979. A 30,000-yr isotope climatic record from Antarctic ice. *Nature*, **280**(5724), 644–648.

Petit, J. R., P. Duval and C. Lorius. 1987. Long-term climatic changes indicated by crystal growth in polar ice. *Nature*, **326**(6108), 62–64.

Ralph, B. 1990. Grain growth. *Mater. Sci. Technol.*, **6**, 1139–1144.

Thorsteinsson, Th., J. Kipfstuhl, H. Eicken, S. J. Johnsen and K. Fuhrer. 1995. Crystal size variations in Eemian-age ice from the GRIP ice core, central Greenland. *Earth Planet. Sci. Lett.*, **131**(3–4), 381–394.

M. Gay, M. Fily, C. Genthon, M. Frezzotti, H. Oerter, J.G. Winther. "Snow grain-size measurements in Antartica" ***Journal of Glaciology*****, *Vol.* 48, *N*° 163, 2002.**

Snow grain-size measurements in Antarctica

Michel GAY,[1,2] Michel FILY,[1] Christophe GENTHON,[1] Massimo FREZZOTTI,[3] Hans OERTER,[4] Jan-Gunnar WINTHER[5]

[1]*Laboratoire de Glaciologie et Géophysique de l'Environnement du CNRS, 54 rue Molière, BP 96, 38402 Saint-Martin-d'Hères, France*
E-mail: michel.gay@cemagref.fr
[2]*Cemagref, Domaine universitaire, 2 rue de la Papeterie, BP 76, 38402 Saint-Martin-d'Hères Cedex, France*
[3]*ENEA, Centro Ricerche Casaccia, P.O. Box 2400, I-00100 Rome, Italy*
[4]*Alfred Wegener Institute for Polar and Marine Research, P.O. Box 120161, D-27515 Bremerhaven, Germany*
[5]*Norwegian Polar Institute, Polar Environmental Centre, N-9296 Tromsø, Norway*

ABSTRACT. Grain-size is an important but not well-known characteristic of snow at the surface of Antarctica. In the past, grain-size has been reported using various methods, the reliability, reproducibility and intercomparability of which is not warranted. In this paper, we present and recommend, depending on available logistical support, three techniques of snow-grain sampling and/or imaging in the field as well as an original digital image-processing method, which we have proved provides reproducible and intercomparable measures of a snow grain-size parameter, the mean convex radius. Results from more than 500 samples and 3000 images of snow grains are presented, which yield a still spatially limited yet unprecedentedly wide picture of near-surface snow grain-size distribution from fieldwork in Antarctica. In particular, except at sites affected by a very particular meteorology, surface grains in the interior of the ice sheet are uniformly small (0.1–0.2 mm). The climate-related increase of grain-size with depth through metamorphism is, as expected, not spatially uniform. Our Antarctic snow grain-size database will continue to grow as field investigations bring new samples, images and measures of snow grain.

INTRODUCTION

The knowledge of snow surface characteristics of ice sheets is important for many reasons. The snowpack is the interface between the atmosphere and the underlying ice, controlling the exchange of energy and mass (Brun and others, 1989, 1992). The albedo of snow depends on the snow effective grain-size and the surface characteristics (Grenfell and others, 1994; Marshall and Oglesby, 1994; Winther, 1994; Fily and others, 1998). The snow is the initial stage of the densification and trapping of air in the firn and the ice (Alley and Bentley, 1988; Arnaud and others, 1998), and finally the snow physical characteristics control the remote-sensing measurements (Alley, 1987; Bindschadler, 1998; Fily and others, 1998, 1999; Genthon and others, 2001).

Most physical properties of snow and ice cover are clearly defined and measurable except for the grain geometry which can be difficult to characterize (Colbeck and others, 1990; Colbeck 1991). A simple method suitable for field measurements of grain-size is to place a sample of snow grains on a ruled plate. The average size is then estimated by comparing the mean size of the grains with the marks on the plate. The definition of size is not unique for three-dimensional non-isotropic objects. One common definition of grain-size is the greatest extension of the grains (Colbeck and others, 1990) measured in millimeters or classified from "very fine" ($<$0.2 mm) to "very coarse" (2.0–5.0 mm). For the purpose of reflectance modelling, Grenfell and others (1994) used the same technique to measure the smallest, rather than the greatest, extension, which is generally closer to the diameter of an equivalent sphere with the same surface/volume ratio. An approximate distribution of grain-sizes may also be obtained by snow sieving or by automated image-processing techniques. Many other definitions of grain-size can be found (Alley, 1987) and this must be taken into account when comparing measurements reported by different authors.

Our goal in this paper is to propose an objective method to determine one well-defined snow grain-size parameter. Because the method is objective and reproducible, measurements made at different places and times by different operators are quantitatively comparable. The method is based on the analysis of digital images of snow grains. First, in a technical section, we describe the image-acquisition techniques and the numerical algorithm to determine grain-size from the images. Then, in a results section, data obtained from a large number of samples and images collected in different places in Antarctica are presented and discussed (Fig. 1). The samples were collected as part of national or international Antarctic scientific traverses (e.g. Winther and others, 1997). The spatial and depth coverage of the current archive is still very limited. It is expected to progressively develop into a comprehensive dataset of snow images and grain-sizes as new exploratory traverses (e.g. as part of International Trans-Antarctic Scientific Expeditions (ITASE); Mayewski and Goodwin, 1999) bring more high-quality data.

IMAGE-ACQUISITION TECHNIQUES

Slices of high-density firn can be cut, and thick sections have been produced with microtome before an image of the sur-

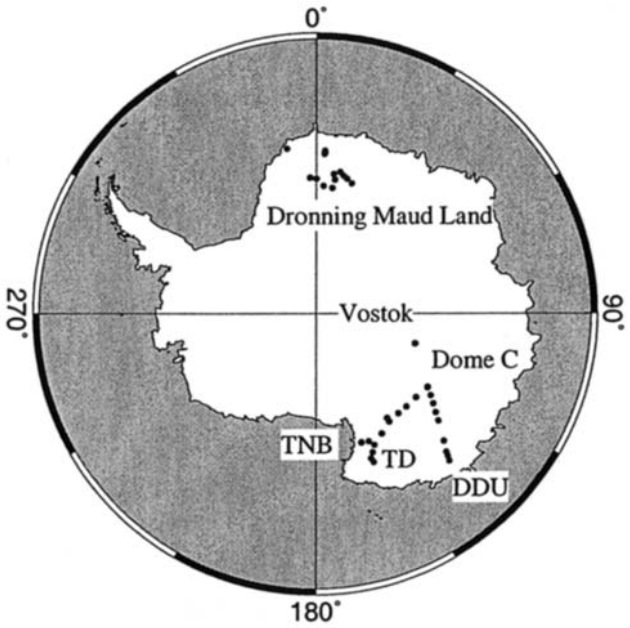

Fig. 1. Antarctic map showing location of sampling sites. TNB, Terra Nova Bay; DDU, Dumont d'Urville; TD, Talos Dome.

face is taken (Arnaud and others, 1998). The process cannot be applied to lower-density snow in the upper meters of the snowpack, unless cohesion is increased by impregnation before slicing (Alley, 1980; Good, 1989). This is technically too difficult and too labour-intensive to be implemented in situ on a regular basis. We have tested three lighter techniques to acquire digital images of snow grains.

Technique 1: Snow samples are collected in small flasks filled with isooctane (trimethyl 2-2-4-pentane) to prevent metamorphism after collection (Brun and Pahaut, 1991). The samples are then kept at temperatures well below freezing and transported to the Laboratoire de Glaciologie et Géophysique de l'Environnement (LGGE) where digital images are taken in a cold laboratory. For this, a binocular microscope is used with a mounted digital camera linked to a computer. After drying on filter paper, snow grains and clusters are separated (using a toothpick-like tool) on a glass window and illuminated from below (transmitted light). The magnifying factor depends on the mean grain-size. It is chosen to be between 2 and 3, so that three to four grains or clusters are captured on each image (Fig. 2a). Technique 1 (Lesaffre and others, 1998) was used at all sites for which results are presented in section 3. Additionally, other methods were tested at some of the sampling sites.

Technique 2: Classic (film) macrophotographies of snow grains are taken in the field and then digitized at LGGE (Fig. 2b). A 50 mm macro-lens and an additional ring set the magnifying factor to 2. In this case, the grains are dispersed on a dark plate and the illumination is diffuse from above (reflected light). As the film definition is very good, a second enlargement can be obtained when digitizing the slides. Technique 2 was used along a Terra Nova Bay–Dome Concordia (Dome C) traverse (Fig. 1).

Technique 3: Digital images were acquired in the field when adequate facilities were available. This was done at Dome C (Fig. 1) where a digital camera was available in a cold laboratory close to the sampling site. Because of the material resources needed, technique 3 may be used at a fixed point but generally not on traverses.

About 50 different grains (i.e. about 15 images, each showing 3–4 grains) of each snow sample were analyzed to obtain a statistically significant measure of the mean size. Dispersal and separation of grains for each image, a rather

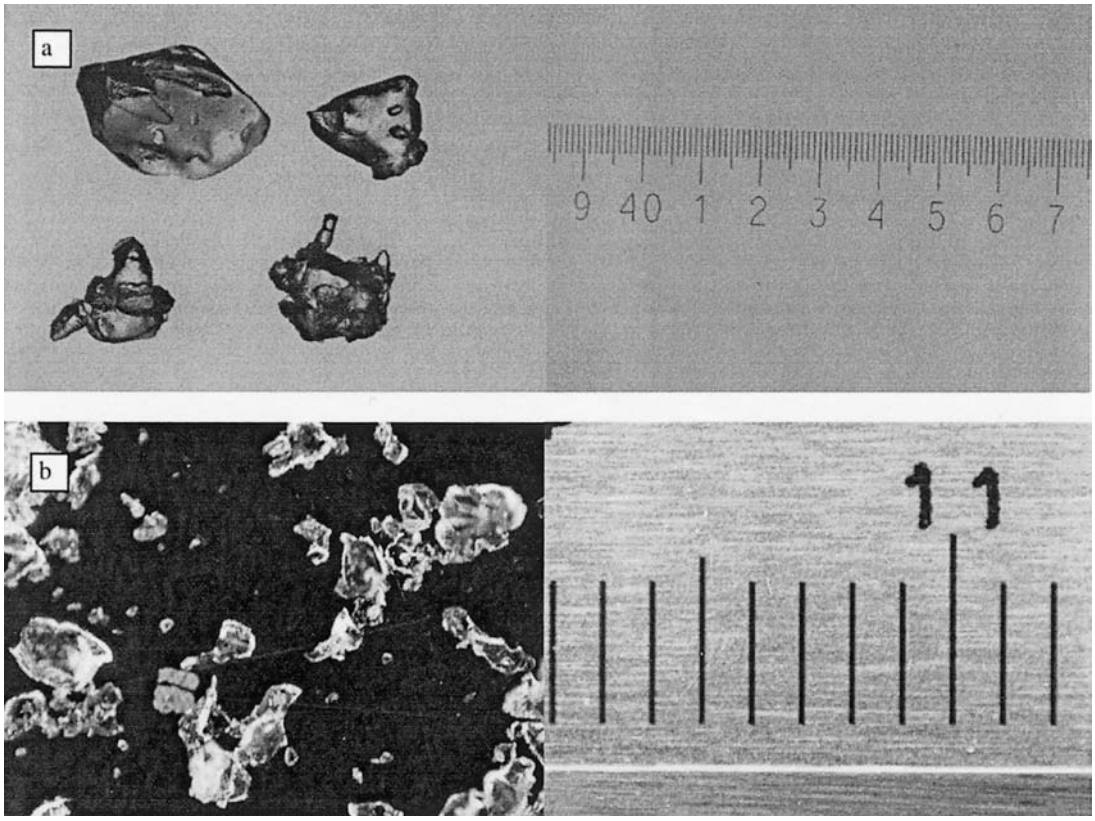

Fig. 2. (a) Digital image of snow grains collected in the field and transported in isooctane (technique 1) with scale in 1/10 mm. (b) Photograph of snow grains acquired in situ (technique 3) at the same site (itb8 at 1.5 m depth) along the Terra Nova Bay–Dome C traverse with scale in mm.

delicate and time-consuming operation, may be hard to accomplish in the field. On the other hand, taking photographs directly in the field (techniques 2 and 3) may be safer than sampling in isooctane flasks for imagery back in the laboratory (technique 1). Indeed, over the past few years, a number of snow samples have been lost due to insufficiently cold conditions during transport. Our results prove that all of the three above techniques yield good results and may be recommended, depending on the logistical and technical support available in the field and for the transport phase.

Digital image processing

Perfect separation of snow grains for imagery is generally difficult and barely fully realized. Clustering of snow grains is a major problem, which prevents the use of stereologic quantities based on the area or the lengths of the objects to determine grain-sizes. To avoid biases associated with grain clustering, a size parameter is defined only from the contour of the snow grains or clusters: it is the mean radius of all the convex parts of the ice/air boundaries, or the mean convex radius. This parameter was found to be representative of the grain-size for metamorphism (Lesaffre and others, 1998). For example, it is the size parameter, along with dendricity and sphericity, used in the snow-metamorphism model Crocus (Brun and others, 1992). The mean convex radius was also found to be the best grain-size parameter for modelling of snow reflectance in the near-wave infrared spectral domain (Fily and others, 1997, 1999; Sergent and others, 1998).

For mean convex radius measurement, the contour of the object needs to be digitally identified from an original grey-scale image. This is done by transforming the grey image into a binary (black and white) image, a process called image segmentation.

Image segmentation

For each pixel $P(x, y)$ of an image, the local gradient $G(x, y)$ is obtained from the surrounding pixels using a Sobel operator over a 3×3 region:

$$G(x, y) = (G_x^2 + G_y^2)^{0.5}$$

with

$$G_x = (z_3 + 2z_6 + z_9) - (z_1 + 2z_4 + z_7)$$
$$G_y = (z_7 + 2z_8 + z_9) - (z_1 + 2z_2 + z_3)\,,$$

where the z's are the grey levels of the pixels, z_5 corresponding to pixel $P(x, y)$ (Table 1).

Once the procedure is completed for all possible pixels, the result is a gradient image of the same size as the original image (Fig. 3a). The lines of highest gradients, above a minimum threshold (Fig. 3b), define discrete contours. Each object is then defined as the set of connected pixels whose gradient value is less than this minimum threshold. The image "background" is given the value 1, and all the objects (the grains) the value 0. The result is a binary image with each object being a grain or a cluster of grains (Fig. 3c).

Table 1. Grey-level indices used for the Sobel operator

z_1	z_2	z_3
z_4	z_5	z_6
z_7	z_8	z_9

Mean convex radius

The mean convex radius may simply be computed as the mean radius of curvature of the curves locally fitting the discrete contour where it is convex (Lesaffre and others, 1998). The accuracy of this method depends on the number N of contour pixels used to fit the discrete contour, and errors can be as high as 30%. In order to reduce the error, N must be optimized depending on the size of the grains on the digital image. Therefore, as N is kept constant, it is necessary to adapt the magnifying factor to the grain-size, which is not possible when there is a large range of grain-sizes on the same image. To overcome this problem, we use an alternate method based on the skeletization of each object (grain) on an image. This method is more robust and can provide various size parameters depending on the final application.

The weighted skeleton is a reduced but complete representation of an object. The construction of a skeleton (Sanniti di Baja and Thiel, 1996) requires determination of the distance between each object pixel and the object boundary. Consider a digital binary image, consisting of object and non-object pixels (Fig. 3c). We use a distance transformation which is an operation that converts this binary image to a grey-level image, where each object pixel has a value corresponding to the distance to the nearest contour pixel (Fig. 3d). The new image is called a distance map and can be interpreted as the result of a propagation process: a wave front originating from the object contour propagates at uniform speed towards the inside. This is described in detail in Sannitti di Baja and Thiel (1996). In particular, we use the chamfer distance transformation on a 5×5 pixel neighborhood (Borgefors, 1986; Thiel, 1994; Sanniti di Baja and Thiel, 1996) as a practical proxy for Euclidean distance. The difference with actual Euclidean distance is, in this case, then $< 2\%$.

From the distance map the skeleton is found. If we consider the distance map as a topographic map, with the highest pixels associated to the largest distances, the skeleton can be simply defined as the ridges of this topographic surface. For a two-dimensional digital image it is defined as the locus of centers of maximal disks contained in the object (Fig. 3e). A skeleton is composed of branches with nodal points at their intersections and end-points at their extremities.

A maximal disk, and therefore a radius, contained in the object can be associated to each pixel of the discrete skeleton (Chassery and Montanvert, 1991). In particular, one radius is associated to each end-point of the skeleton which is representative of the convexity of the contour close to it (Fig. 3e). The mean convex radius is the average of all these radii. The radii associated to nodal points of the skeleton are more representative of the volume of the grains, or clusters of grains. The weighted skeleton could also provide information on the shape of the grain (Chassery and Montanvert, 1991), but this is beyond the scope of this paper.

RESULTS

Comparison of sampling and image-analysis techniques

Images of more than 500 snow samples were collected for different locations and depths in Antarctica, thanks to the activity of French, German, Italian and Norwegian field parties in recent years (Table 2; Fig. 1). Sampling technique 1 (isooctane flasks) was systematically used at all sites and

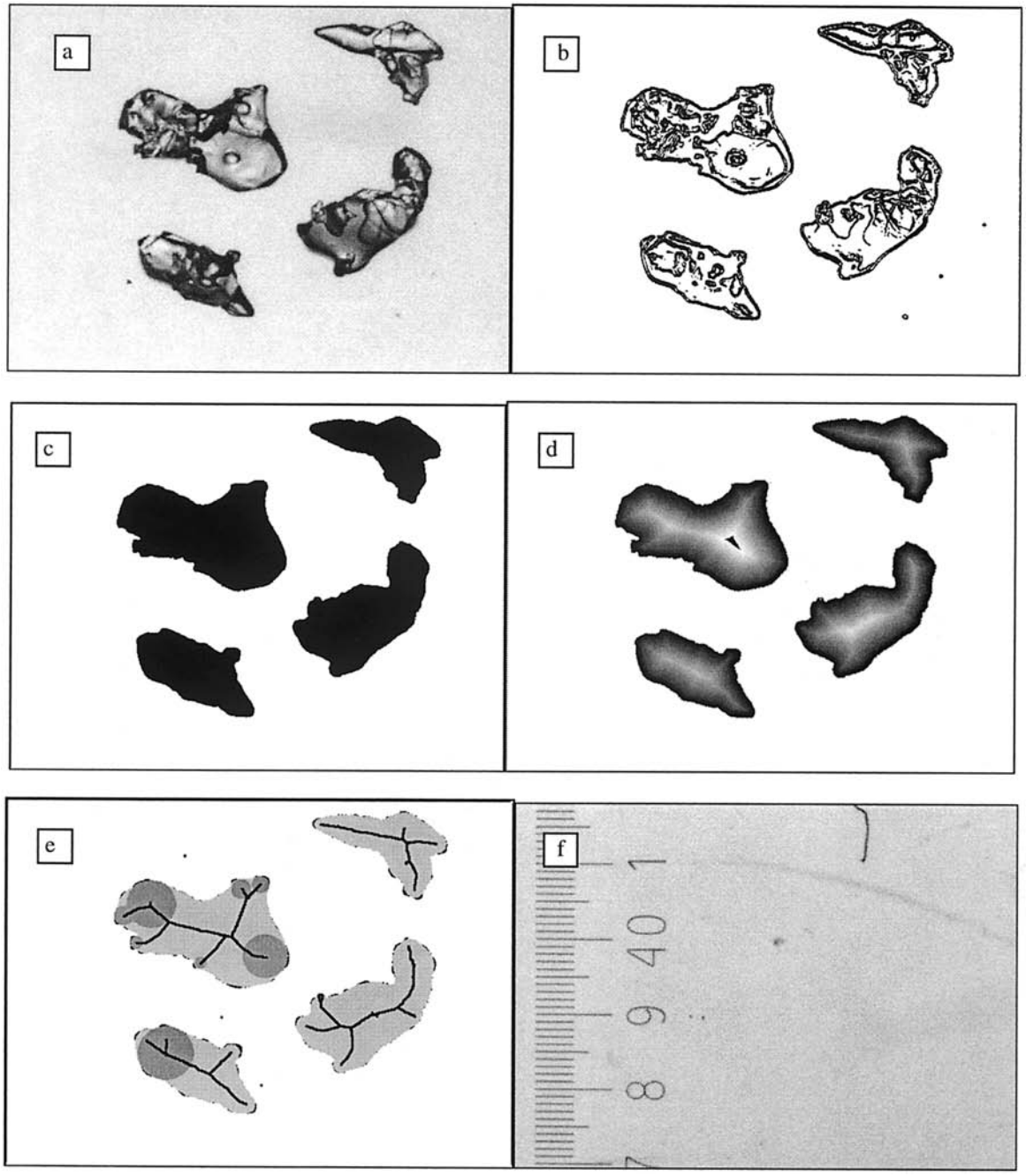

Fig. 3. (a) Original image of a few snow grains; (b) gradient image; (c) binary image; (d) distance map; (e) skeleton and examples of maximal disks contained in the snow grains; (f) scale in 1/10 mm.

along all traverses. Techniques 2 or 3 (imagery on the field) were also used at Dome C and along the Terra Nova Bay–Dome C traverse. All images (about 3000 altogether) were processed with the same image-analysis method for grain-size determination, as described above. The equivalence of the different sampling techniques can thus be assessed.

All the results are given in Figures 4–6. To allow a simple visual comparison of the grain-sizes, the same scale, but not the same range, is used for all the sites. The error bars represent the standard deviation of all the mean convex radii obtained for one sample.

At Dome C (Fig. 4) the sizes obtained from isooctane samples (technique 1) and from digital images (technique 3) acquired 2 years later are very similar. This demonstrates (1) that snow metamorphism in cold isooctane during transportation and storage in good conditions is negligible, and (2) that the same results are obtained when different techniques are applied by different operators at different times. This is further confirmed by Figure 5, which compares grain-sizes along a Terra Nova Bay–Dome C traverse as obtained from photographs taken in the field (technique 2) and from snow samples brought back to LGGE (technique 1). Photographs visibly showing massive clustering and insufficient separation of grains were discarded. In most cases, results from both techniques are very similar. Large differences may be found in some places because the samples were not taken in exactly the same layer and because the grains were too clustered.

From the same weighted skeleton, different size parameters can be computed. The radii computed from end-points and nodal points are compared for many sites (Fig. 6). Examples of digital images of snow grains are given for the two sites aw2 and aw6 in Figure 7. When the grains are well separated and easily identified (Fig. 7a; aw6 at 0.4 m) the two size parameters are similar (~0.15 mm). When the grains are clustered (Fig. 7b; aw2 at 0.2 m), the nodal radius (~0.5 mm) is larger than the end-point radius (0.1 mm) because it is more sensitive to the volume of the object than

Table 2. Sampling locations and dates

Sample	*Lat., long.*	*Altitude* m	*Date*	*Site*
aw1	71.45° S, 9.94° W	600	13 Feb. 1997	DML
aw2	74.86° S, 2.55° W	2830	13 Jan. 1997	DML
aw3	75.00° S, 0.01° E	2890	16 Jan. 1997	DML
aw4	75.75° S, 3.28° E	2970	22 Jan. 1997	DML
aw5	75.93° S, 7.21° E	3150	28 Jan. 1997	DML
aw6	74.40° S, 7.22° E	3180	24 Jan. 1997	DML
aw7	75.00° S, 8.01° E	3245	26 Jan. 1997	DML
ita1	74.82° S, 160.66° E	1270	8 Nov. 1996	TNB-Talos
ita2	74.64° S, 157.50° E	1780	9 Nov. 1996	GPS2
ita3	74.03° S, 155.96° E	2060	10 Nov. 1996	31DPT
ita4	73.37° S, 157.67° E	2205	11 Nov. 1996	PNI
ita5	72.80° S, 159.10° E	2305	23 Nov. 1996	Talos Dome
ita6	72.37° S, 158.75° E	2215	25 Nov. 1996	ST556
itb1	74.84° S, 160.82° E	1200	20 Nov. 1998	GPS 1
itb2	74.64° S, 157.50° E	1780	27 Nov. 1998	GPS2
itb3	74.03° S, 155.96° E	1925	1 Dec. 1998	31DPT
itb4	74.80° S, 151.27° E	2310	6 Dec. 1998	M2
itb5	75.55° S, 145.79° E	2460	11 Dec. 1998	MDP
itb6	75.53° S, 145.92° E	2450	14 Dec. 1998	MDPA
itb7	75.62° S, 140.63° E	2610	20 Dec. 1998	D2
itb8	75.60° S, 135.83° E	2790	26 Dec. 1998	D4
itb9	75.45° S, 129.81° E	3025	31 Dec. 1998	D6
np1	71.90° S, 3.08° E	1455	31 Dec. 1996	DML
np2	72.13° S, 3.18° E	2040	4 Jan. 1997	DML
np3	72.25° S, 2.88° E	2300	5 Feb. 1997	DML
np4	74.05° S, 9.50° E	3280	31 Jan. 1997	DML
np5	74.35° S, 9.05° E	3270	30 Jan. 1997	DML
np6	74.65° S, 12.78° E	3420	29 Jan. 1997	DML
np7	75.00° S, 15.00° E	3470	25–28 Jan. 1997	DML
ta1	68.06° S, 137.72° E	2045	22 Nov. 1995	DDU-DC
ta2	68.55° S, 137.07° E	2320	22 Nov. 1995	DDU-DC
ta3	68.97° S, 136.47° E	2360	23 Nov. 1995	DDU-DC
ta4	70.03° S, 134.82° E	2495	25 Nov. 1995	DDU-DC
ta5	71.99° S, 131.18° E	2990	27 Nov. 1995	DDU-DC
ta6	72.77° S, 129.46° E	3125	28 Nov. 1995	DDU-DC
ta7	73.59° S, 127.48° E	3140	29 Nov. 1995	DDU-DC
ta8	74.36° S, 125.46° E	3185	30 Nov. 1995	DDU-DC
ta9	75.10° S, 123.00° E	3230	Dec. 1995	20 km around DC
DC	75.16° S, 123.23° E	3230	1997 and 2000	Dome C: 5 m profile
Vost	78.47° S, 106.80° E	3480	Dec. 1997	Vostok: 2 m profile

Notes: aw: Alfred Wegener Institute, Germany. ita and itb: samples from ENEA, Italy. np: samples from Norwegian Polar Institute. ta, DC and Vost: samples from LGGE/IFRTP, France. Elevations are from the RADARSAT Antarctic Mapping Project digital elevation model 400 m ellipsoid WGS84 geoid OSU91 "Data provided by the EOS Distributed Active Archive Center (DAAC) at the National Snow and Ice Data Center, University of Colorado, Boulder, CO". DML: Dronning Maud Land. TNB: Terra Nova Bay. DDU-DC: Dumont d'Urville–Dome C.

to the shape of its contour. As clustering of snow grains is difficult to avoid, we prefer to use the mean convex radius as defined from the skeleton end-points. This also emphasizes the importance of the definition of the size parameter when different samples are compared.

Spatial and depth variations of Antarctic snow grain-size

The results obtained from the 42 sites in Antarctica tend to show that near the surface (0–0.5 m) the mean convex radius is surprisingly spatially homogeneous, of the order of 0.1–0.2 mm almost everywhere. They may be classified as very fine to fine grain (<0.2 to 0.5 mm) according to Colbeck and others (1990). Comparison with other in situ data reported in the literature is difficult because the size was determined visually and therefore it does not represent the same parameter.

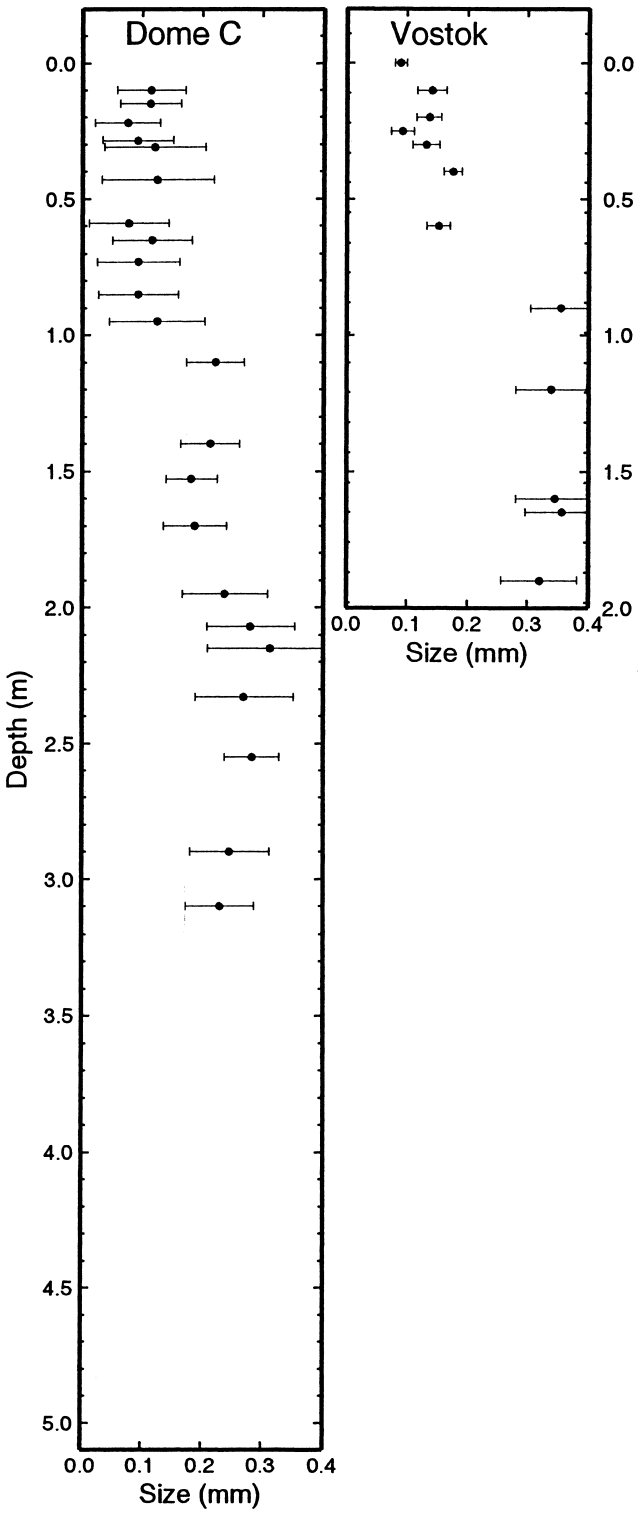

Fig. 4. Mean convex radius of snow grains vs depth at Dome C and Vostok. The error bars represent one standard deviation of all the measurements obtained for one sample. The dots (●) are from digital images of snow samples collected in the field in 1997 and transported to Grenoble in cold isooctane (technique 1). The squares (□) are from digital images acquired at Dome C in 2000 (technique 3).

The largest variability is found along the Terra Nova Bay–Dome C traverse (Figs 5 and 6). The sizes obtained from samples acquired at a 2 year interval are very similar for 31DPT (samples ita3 and itb3) and different for GPS2 (samples ita2 and itb2). GPS2 is a site with erosional forms up to 15 cm and seasonal wind crust, whereas 31DPT site presents depositional forms about 10 cm and has more homogeneous snow stratigraphy than GPS2. Larger grain-sizes are

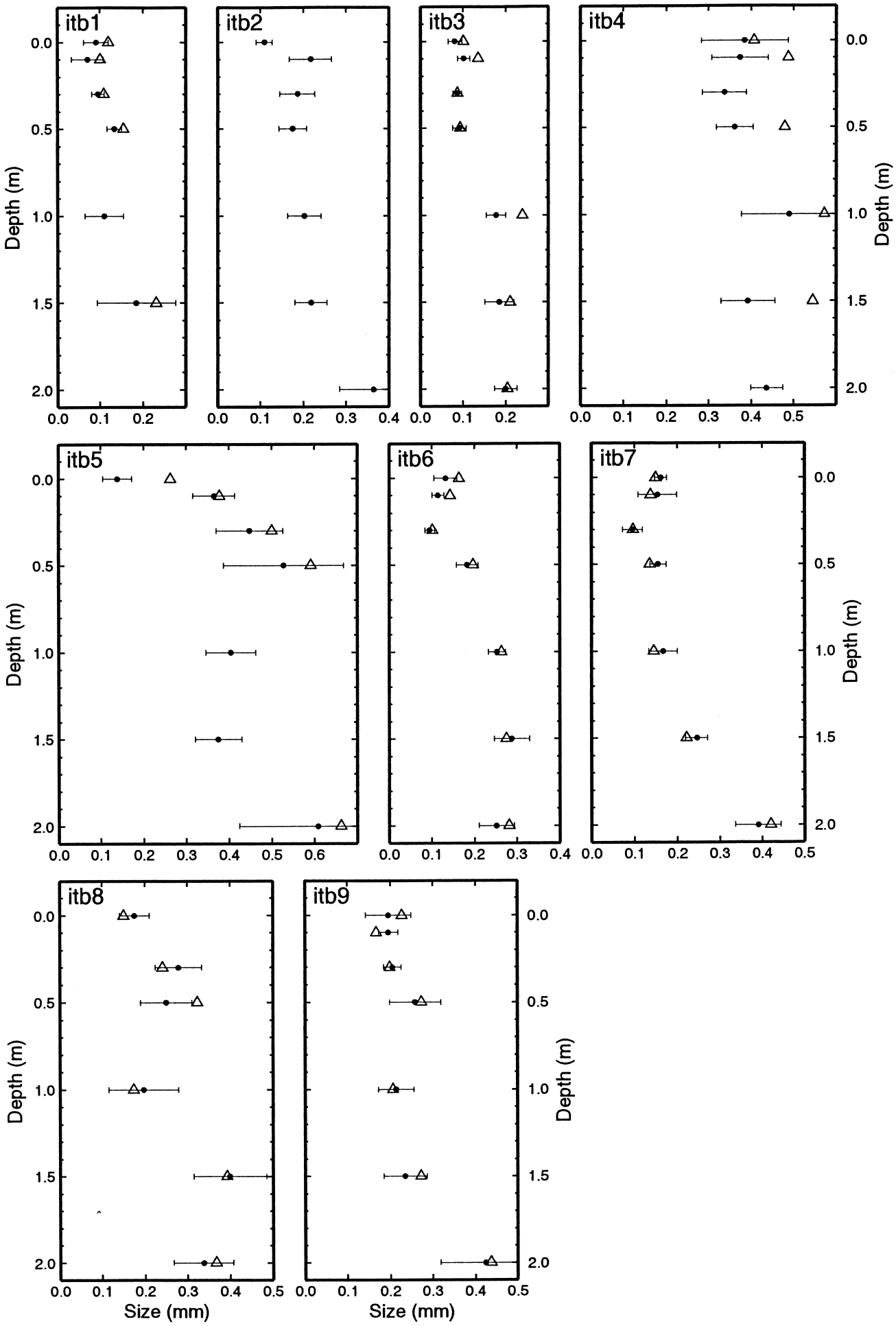

Fig. 5. Mean convex radius of snow grains vs depth along the Terra Nova Bay–Dome C traverse (Table 2; Fig. 1). The dots (●) are from digital images of snow samples collected in the field in 1997 and transported to Grenoble in cold isooctane (technique 1). The triangles (△) are from classical photos acquired in situ (technique 2).

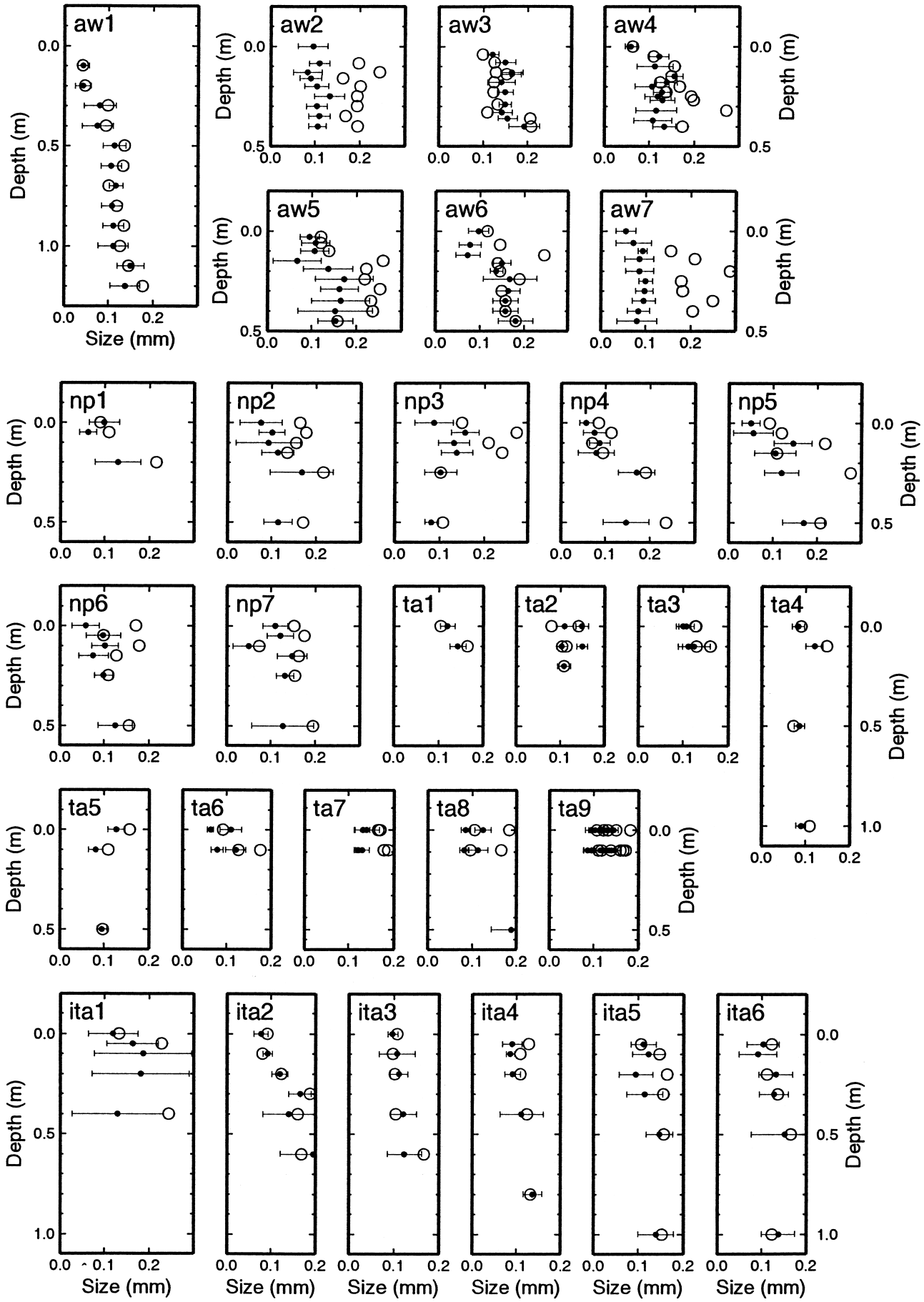

Fig. 6. Mean convex radius of snow grains vs depth along several traverses (Table 2; Fig. 1). Technique 1 is used for all the samples. The dots (●) are for radii corresponding to the end-points of the skeleton, and circles (○) are for nodal points.

found at M2 (itb4) and MDP (itb5) sites even at the surface. This is in agreement with older traverse data (Stuart and Heine, 1961) and could explain the peculiar microwave signature observed there (Surdyk and Fily, 1993). These sites are characterized by wind crust, consisting of a single snow-grain layer cemented by thin (0.1–2 mm) films of sublimated ice. Under strongly developed wind crust the depth-hoar layer clearly indicates prolonged sublimation due to a hiatus

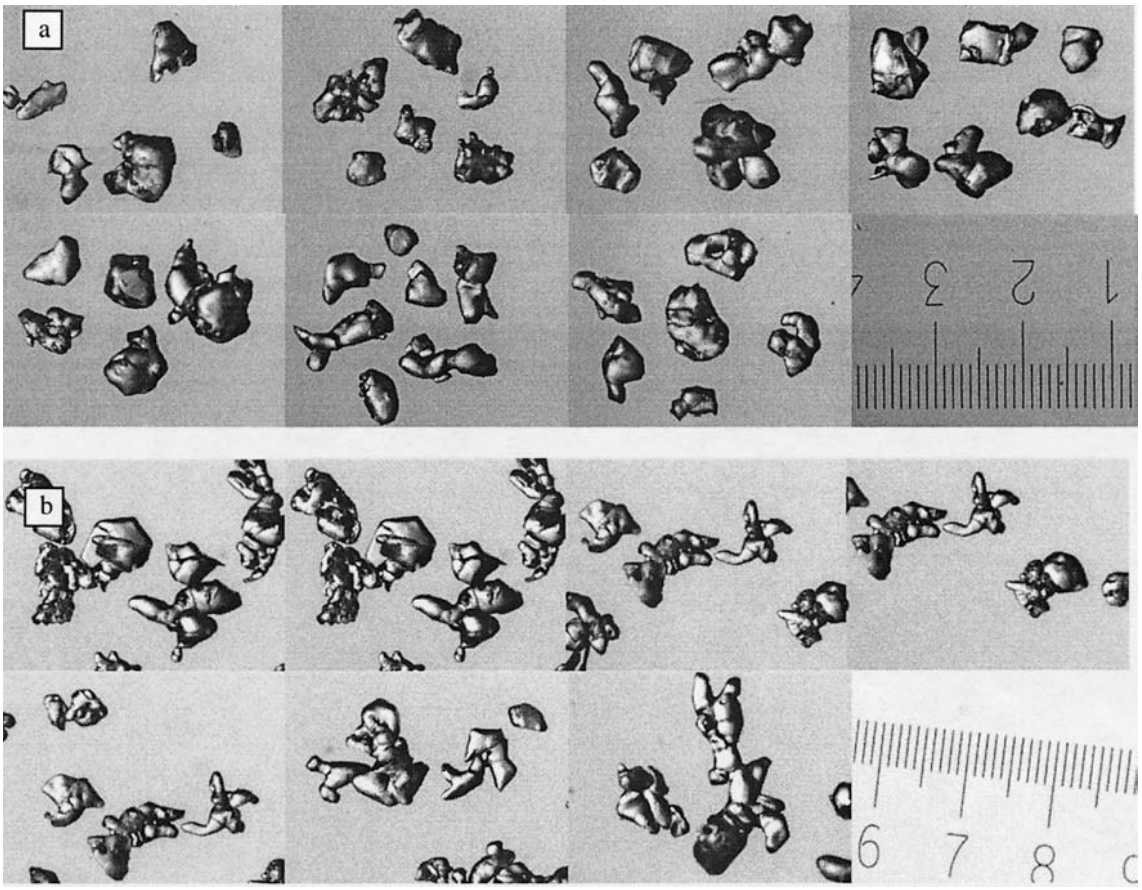

Fig. 7. Digital images (technique 1) of snow grains from the Dronning Maud Land area (Table 2; Fig. 1) with the corresponding scale in 1/10 mm: (a) site aw6 at 0.4 m depth; (b) site aw2 at 0.2 m depth.

in accumulation and therefore a long, multi-annual, steep temperature-gradient metamorphism (Gow, 1965). Either the large grain or the wind crust (Wiesmann and others, 2000) could explain the peculiar microwave signature observed (Surdyk and Fily, 1993). Sites MDP (itb5) and MDPA (itb6) are only at a distance of 5 km, and show quite different grain-size profiles, both for mean values and for variability. MDPA site shows sastrugi up to 20 cm high but no permanent wind crust. The large difference in grain-size between the two sites is due to the different snow-redistribution process at local scale. Frezzotti and others (2002) point out that along the Terra Nova–Dome C traverse, wind crusts are present in a wide area of the plateau, and are strictly correlated with snow-redistribution process due to downwind slope $> 0.25^{\circ}$ (0.4% or 4 m km^{-1}).

At Vostok and Dome C, more variations in grain-size occur below 1 m, and a significant difference is found between the two sites. At Vostok, there is a sharp increase in grain-size between 0.6 and 0.8 m depth. The evolution of size is smoother at Dome C. The size is almost identical between 2 and 5 m as observed in situ.

All sites where the variations of size with depth are significantly sampled show a broad increase with depth. This is expected, as metamorphism tends to favor the growth of the larger grains with time, at the expense of the smaller grains. The rate of increase with depth is not uniform. At Dome C and Vostok, grain-size remains fine in the upper few tens of cm (1 m at Dome C, 50 cm at Vostok), whereas grains are larger at or near the surface at itb4 and itb5. A simple age/depth relationship suggests that accumulation is lower at the latter sites. There is little increase in grain-size at itb4 and itb5 below 50 cm.

CONCLUSION

Size parameters automatically obtained from digital images of snow grains allowed comparisons between samples acquired by different people at different locations in Antarctica. Similar results were obtained with various acquisition techniques (classical photos or digital camera) that can be used during any scientific expedition with minimum equipment and facilities. One of the most difficult problems is the separation of snow grains, which is solved by choosing a size parameter based on the contour of the objects, the mean convex radius, and a robust image-analysis technique based on skeletization of the objects.

Data from 42 sites in Antarctica were analyzed. For radiative balance (albedo), only the surface grains must be considered, so no large variations due to grain-size are expected in those areas, except between Terra Nova Bay and Dome C. For metamorphism studies, the profiles obtained down to 2 m depth and even better down to 5 m at Dome C could be used with the available density profiles to validate and improve snow-metamorphism model results (Dang and others, 1997; Genthon and others, 2001).

The database which has been initiated will be increased in order to obtain a map of grain-size variations of the Antarctic ice sheet. This will improve understanding of the snow metamorphism in Antarctica in relation to climatic parameters.

ACKNOWLEDGEMENTS

This research was carried out within the framework of the European Community project Polar Snow (Contract ENV4-CT95-0076), the SPOT4/Vegetation Preparatory Pro-

gram (96/CNES/0394), a Project on Glaciology and Paleoclimatology of the Programma Nazionale di Ricerche in Antartide (PNRA), and was financially supported by Ente per le Nuove Tecnologie, l'Energia e l'Ambiente (ENEA) through a cooperation agreement with the Universit degli Studi di Milano. This work is a contribution of the Italian branch of the ITASE project. The authors wish to thank all members of the traverse teams, and the institutes which were in charge of the logistics: Institut Français de Recherche et Technologie Polaire (IFRTP), France; ENEA, Italy; Alfred Wegener Institute for Polar and Marine Research, Germany; Norwegian Polar Institute. A. Hubert (South Through the Pole Expedition) made a vital contribution to the design and tests of field photographic equipment.

REFERENCES

Alley, R. B. 1980. Densification and recrystallization of firn at Dome C, East Antarctica. *Ohio State Univ. Inst. Polar Stud. Rep.* 77.

Alley, R. B. 1987. Texture of polar firn for remote sensing. *Ann. Glaciol.*, **9**, 1–4.

Alley, R. B. and C. R. Bentley. 1988. Ice-core analysis on the Siple Coast of West Antarctica. *Ann. Glaciol.*, **11**, 1–7.

Arnaud, L., V. Lipenkov, J. M. Barnola, M. Gay and P. Duval. 1998. Modelling of the densification of polar firn: characterization of the snow–firn transition. *Ann. Glaciol.*, **26**, 39–44.

Bindschadler, R. 1998. Monitoring ice sheet behavior from space. *Rev. Geophys.*, **36**(1), 79–104.

Borgefors, G. 1986. Distance transformations in digital images. *Computer Vision, Graphics and Image Processing*, **34**(198), 344–371.

Brun, E. and E. Pahaut. 1991. An efficient method for a delayed and accurate characterization of snow grains from natural snowpacks. *J. Glaciol.*, **37**(127), 420–422.

Brun, E., E. Martin, V. Simon, C. Gendre and C. Coléou. 1989. An energy and mass model of snow cover suitable for operational avalanche forecasting. *J. Glaciol.*, **35**(121), 333–342.

Brun, E., P. David, M. Sudul and G. Brunot. 1992. A numerical model to simulate snow-cover stratigraphy for operational avalanche forecasting. *J. Glaciol.*, **38**(128), 13–22.

Chassery, J. M. and A. Montanvert. 1991. *Géométrie discrète en analyse d'images.* Paris, Edition Hermès.

Colbeck, S. C. 1991. The layered character of snow covers. *Rev. Geophys.*, **29**(1), 81–96.

Colbeck, S. C. *and 7 others*. 1990. *The international classification for seasonal snow on the ground.* Wallingford, Oxon, International Association of Scientific Hydrology. International Commission on Snow and Ice.

Dang, H., C. Genthon and E. Martin. 1997. Numerical modeling of snow cover over polar ice sheets. *Ann. Glaciol.*, **25**, 170–176.

Fily, M., B. Bourdelles, J.-P. Dedieu and C. Sergent. 1997. Comparison of in situ and Landsat thematic mapper derived snow grain characteristics in the Alps. *Remote Sensing Environ.*, **59**(3), 452–460.

Fily, M., C. Leroux, J. Lenoble and C. Sergent. 1998. Terrestrial snow studies from remote sensing in the Solar spectrum and the thermal infrared. *In* Schmitt, B., C. D. Bergh and M. Festou, *eds. Solar system ices.* Dordrecht, etc., Kluwer Academic Publishers, 421–441. (Astrophysics and Space Science Library 227.)

Fily, M., J. P. Dedieu and Y. Durand. 1999. Comparison between the results of a snow metamorphism model and remote sensing derived snow parameters in the Alps. *Remote Sensing Environ.*, **68**(3), 254–263.

Frezzotti, M., S. Gandolfi, F. La Marca and S. Urbini. 2002. Snow dunes and glazed surfaces in Antarctica: new field and remote-sensing data. *Ann. Glaciol.*, **34**, 81–88.

Genthon, C., M. Fily and E. Martin. 2001. Numerical simulations of Greenland snowpack and comparison with passive microwave spectral signatures. *Ann. Glaciol.*, **32**, 109–115.

Good, W. 1989. Laboratory techniques for the characterization of snow structure. *In* Hunt, J. and T. D. Guyenne, *eds. International Workshop on Physics and Mechanics of Cometary Materials, October 9–11, 1989, Münster, Westfalia, Germany. Proceedings*. Noordwijk, European Space Agency, 147–151. (ESA SP-302.)

Gow, A. J. 1965. On the accumulation and seasonal stratification of snow at the South Pole. *J. Glaciol.*, **5**(40), 467–477.

Grenfell, T. C., S. G. Warren and P. C. Mullen. 1994. Reflection of solar radiation by the Antarctic snow surface at ultraviolet, visible, and near-infrared wavelengths. *J. Geophys. Res.*, **99**(D9), 18,669–18,684.

Lesaffre, B., E. Pougatch and E. Martin. 1998. Objective determination of snow-grain characteristics from images. *Ann. Glaciol.*, **26**, 112–118.

Marshall, S. and R. J. Oglesby. 1994. An improved snow hydrology for GCMs. Part 1: Snow cover fraction, albedo, grain size, and age. *Climate Dyn.*, **10**(1–2), 21–37.

Mayewski, P. A. and I. Goodwin. 1999. Antarctic's role pursued in global climate change. *Eos*, **80**(35), 398–400.

Sanniti di Baja, G. and E. Thiel. 1996. Skeletization algorithm running on path-based distance maps. *Image Vision Comput.*, **14**, 47–57.

Sergent, C., C. Leroux, E. Pougatch and F. Guirado. 1998. Hemispherical–directional reflectance measurements of natural snows in the 0.9–1.45 μm spectral range: comparison with adding–doubling modelling. *Ann. Glaciol.*, **26**, 59–63.

Stuart, A. W. and A. J. Heine. 1961. *Glaciology, Victoria Land traverse, 1959–60.* Columbus, OH, Ohio State University. Research Foundation. Institute of Polar Studies. (Report 968-1.)

Surdyk, S. and M. Fily. 1993. Comparison of the passive microwave spectral signature of the Antarctic ice sheet with ground traverse data. *Ann. Glaciol.*, **17**, 161–166.

Thiel, E. 1994. Les distances de chanfrein en analyse d'images: fondements et applications. (Ph.D. thesis, Université Joseph Fourier, Grenoble I.)

Wiesmann, A., C. Fierz and C. Mätzler. 2000. Simulation of microwave emission from physically modeled snowpacks. *Ann. Glaciol.*, **31**, 397–405.

Winther, J.-G. 1994. Spectral bi-directional reflectance of snow and glacier ice measured in Dronning Maud Land, Antarctica. *Ann. Glaciol.*, **20**, 1–5.

Winther, J.-G. *and 9 others*. 1997. EPICA Dronning Maud Land pre-site survey 1996/97. *In* Winther, J.-G., *ed. Report of the Norwegian Antarctic Research Expedition (NARE) 1996/97.* Oslo, Norsk Polarinstitutt, 96–117. (Meddelelser 148.)

MS received 10 August 2001 and accepted in revised form 15 August 2002

J. Weiss, J. Vidot, M. Gay, L. Arnaud, P. Duval. "Dome Concordia, Antarctica ice microstructure : impurities effect on grain growth", *Annals of Glaciology*, *Vol.* 35, 2002.

Annals of Glaciology 35 2002
© International Glaciological Society

Dome Concordia ice microstructure: impurities effect on grain growth

JÉRÔME WEISS, JÉRÔME VIDOT, MICHEL GAY, LAURENT ARNAUD, PAUL DUVAL, JEAN ROBERT PETIT

Laboratoire de Glaciologie et Géophysique de l'Environnement du CNRS, 54 rue Molière, BP 96, 38402 Saint-Martin-d'Hères Cedex, France
E-mail: weiss@lgge.obs.ujf-grenoble.fr

ABSTRACT. We present a detailed analysis of the microstructure in the shallow part (100–580 m) of the European Project for Ice Coring in Antarctica (EPICA) ice core at Dome Concordia. In the Holocene ice, the average grain-size increases with depth. This is the normal grain-growth process driven by a reduction of the total grain-boundary energy. Deeper, associated with the Holocene–Last Glacial Maximum (LGM) climatic transition, a sharp decrease of the average grain-size is observed. To explain modifications to the microstructure with climatic change, we discuss the role of soluble and insoluble (microparticles) impurities in the grain-growth process of Antarctic ice, coupled with an analysis of the pinning of grain boundaries by microparticles. Our data indicate that high soluble impurity content does not necessarily imply a slowing-down of grain-growth kinetics, whereas the pinning of grain boundaries by dust particles located along the boundaries does explain modifications to the microstructure (small grain-sizes; change in grain-size distributions, etc.) observed in volcanic ash layers or dusty LGM ice. Moreover, classical mean-field models of grain-boundary pinning are in good quantitative agreement with the evolution of grain-size along the EPICA ice core. This suggests a major role for dust in the modification of shallow polar ice microstructure.

INTRODUCTION

Because it may record the past history of ice and climatic change and because it is sensitive to ice-sheet deformation history, the microstructure (grain-sizes and grain shapes) of polar ice is worth studying. During the last 30 years, the main focus has been on the evolution of the average grain-size with depth and thus age. This average grain-size was generally determined by manual counting on two-dimensional (2-D) thin sections of ice.

In the nearly isothermal upper part of cold ice sheets corresponding to the Holocene period, the average grain-size increases with depth (Gow, 1969; Alley and others, 1986b). This is the normal grain-growth process driven by a reduction in the total grain-boundary energy within the material (see, e.g., Ralph, 1990; Humphreys and Hatherly, 1996; and below). However, a sharp decrease in the average grain-size is generally associated with the Holocene–Last Glacial Maximum (LGM) climatic transition (Duval and Lorius, 1980). Several explanations have been proposed for this correlation between grain-size and climate, including soluble impurity drag on grain-boundary migration (Alley and Woods, 1996), pinning by (insoluble) microparticles (Fisher and Koerner, 1986; Li and others, 1998), or an effect of surface temperature conditions at the time of deposition (Petit and others, 1987). However, because many parameters, including isotopic record (δD), conductivity and concentrations of different soluble impurities or microparticles, exhibit abrupt changes together at climatic transitions, it is difficult to determine the correct mechanism solely on the basis of correlations between the average grain-size and these parameters.

Here we present a detailed analysis of the microstructure of the shallow part (100–580 m) of the European Project for Ice Coring in Antarctica (EPICA) ice core at Dome Concordia (75°06′ S, 123°24′ E; 3233 m a.s.l.). Using a recently developed image-analysis processing technique (Gay and Weiss, 1999), we were able to extract the complete microstructure (grain boundaries) in two dimensions from thin sections of ice. This allowed us to automatically determine not only the average grain-size but also other parameters such as grain-size distributions or grain-shape anisotropy (Arnaud and others, 2000). In what follows, we discuss the role of soluble and insoluble (microparticles) impurities in the grain-growth process of Antarctic ice, on the basis of this new dataset coupled with an analysis of grain-boundary pinning from classical mean-field models.

EXPERIMENTAL PROCEDURE

Vertical thin sections were prepared in the field from the EPICA ice core at 100–580 m depth. They were digitized and analyzed in France using an image-analysis processing technique described by Gay and Weiss (1999), to extract the microstructure in two dimensions. One section was digitized at approximately each 5 m through the core. In addition, thin sections were prepared and digitized at depths corresponding to "special events" revealed by the observation of a dust layer or a dielectric profiling (DEP) peak (Wolff and others, 1999). Each digitized section represented a surface of about 27.2×20.4 mm^2, i.e. about 200–400 grains depending on the average grain-size. The average grain-size (or grain radius) $\langle R \rangle$ was calculated over the entire population of grains within a section from the arithmetic average of grain areas,

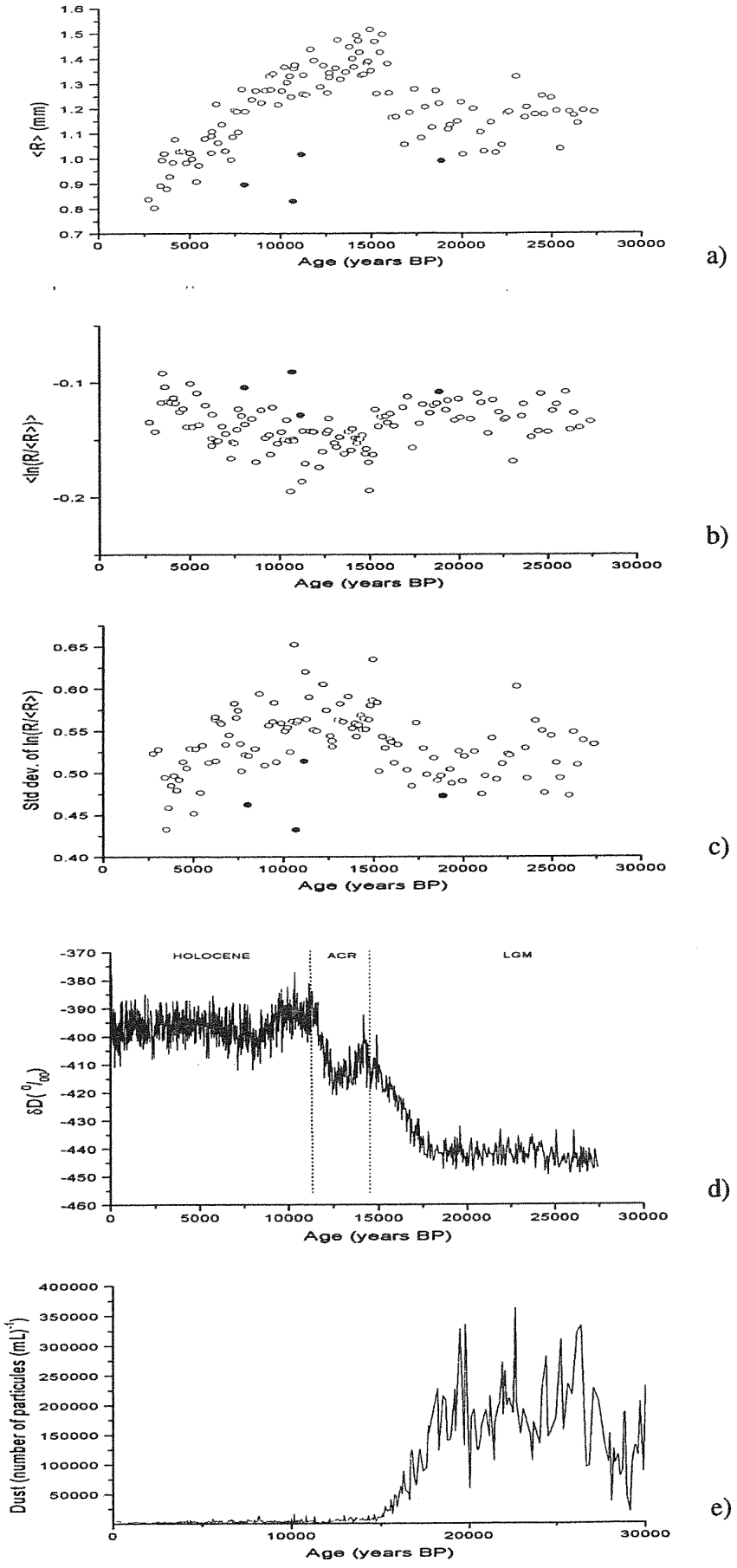

Fig. 1. (a) Average grain-size profile of the EPICA ice core. (b) Normalized grain-size distributions: evolution of $\langle \ln(R/\langle R \rangle) \rangle$. *(c) Normalized grain-size distributions: evolution of the standard deviation of* $\ln(R/\langle R \rangle)$. *(d) Deuterium profile (from Jouzel and others, 2001). (e) Dust number content (from Delmonte and others, 2002). Closed symbols in (a–c) are ash layers.*

$\langle\sqrt{A}\rangle$. As detailed by Gay and Weiss (1999), this method differs from those previously used to manually determine the average grain-size in thin sections of polar ice, such as the linear intercept method (Alley and Woods, 1996) or the average size of the 50 largest grains within the section (Gow, 1969). When estimating a "grain-size" within a three-dimensional (3-D) medium from a 2-D section, one should keep in mind stereographic difficulties. Ideally, grain radius should be determined from the cube root of the grain volume in three dimensions. This kind of analysis is difficult to perform experimentally. The scarce information available on the relationship between 3-D parameters and their estimation from 2-D sections comes from 3-D numerical simulations of grain growth (Anderson and others, 1989). The simulations of Anderson and others (1989) and Weygand and others (1998) show that the estimation of $\langle R\rangle$ from $\langle\sqrt{A}\rangle$ gives the best 2-D estimate of 3-D grain-growth kinetics, therefore validating the procedure followed in the present work. This discussion has been detailed in Gay and Weiss (1999).

THE GRAIN-SIZE PROFILE AND THE GRAIN-GROWTH PROCESS

Figure 1a shows the grain-size profile for the EPICA ice core at 100–580 m, i.e. between about 2500 and 28 000 BP. The depth–age correspondence comes from Schwander and others (2001). Grain growth is observed in the Holocene ice, whereas a marked decrease in $\langle R\rangle$ is associated with the Holocene–LGM climatic transition. Below the transition, the grain-size appears to remain constant, but the scatter, which is larger than in the Holocene ice, renders a definitive conclusion difficult.

To allow an interpretation of our grain-size profile in terms of physical processes, we first recall the classical models of grain-growth kinetics.

Growth kinetics

Ignoring the environment of a grain, i.e. the structural and topological constraints within an assembly of grains, and assuming the boundary is part of a sphere, Burke and Turnbull (1952) calculated the grain-boundary velocity v ($\mathrm{m\,s^{-1}}$) in the case where the reduction of grain-boundary energy is the unique driving force for normal grain growth:

$$v = \mu\frac{\gamma}{R}, \tag{1}$$

where μ is the mobility, γ is the grain-boundary free energy ($\mathrm{J\,m^{-2}}$) and R is the grain radius (m). In Equation (1), γ/R represents the driving force. Further assuming that $\mathrm{d}R/\mathrm{d}t$ is proportional to v, Burke and Turnbull (1952) deduced the parabolic grain-growth kinetics:

$$\langle R\rangle \sim Kt^{1/2}, \tag{2}$$

where K is a constant.

One of the shortcomings of the Burke and Turnbull analysis was ignorance of the topological space-filling requirements within an assembly of grains. One consequence of these requirements is that large grains grow to the detriment of small grains. The simplest way to model these requirements is by the mean-field approach, which considers an isolated grain embedded in an environment representing the average effect of the whole array of grains. Following the observed difference between grain-growth kinetics of small and large grains, Hillert (1965) proposed the following expression for the velocity of a grain of radius R:

$$v \sim \mu\gamma\left(\frac{1}{\langle R\rangle} - \frac{1}{R}\right). \tag{3}$$

This implies that if $R > \langle R\rangle$ the grain will grow, but it will shrink if $R < \langle R\rangle$. This mean-field approach predicts a unimodal grain-size distribution and parabolic grain-growth kinetics (Equation (2)). However, the exponent 1/2 in Equation (2) is an upper bound derived from mean-field approximations. A power law with exponent n of 0.2–0.5 better describes most of the experimental data for many different materials (Higgins, 1974; Anderson and others, 1989; Ralph, 1990):

$$\langle R\rangle = \langle R\rangle_0 + Kt^n, \tag{4}$$

where K is an Arrhenius temperature-dependent constant and $\langle R\rangle_0$ is the average grain-size at $t = t_0$. Departure from the upper bound $n = 0.5$ has been thought to result from solute drag, interactions with microparticles, the effect of texture, or a non-steady-state regime (Ralph, 1990).

Following these classical models of grain growth (Burke and Turnbull, 1952; Hillert, 1965), former investigations of grain-growth kinetics in the shallow part of ice sheets assumed parabolic kinetics (Equation (2)), in reasonable agreement with the measurements. However, shallow polar ice could also exhibit $n < 0.5$. A linear fit on a log–log scale of the data of Figure 1 corresponding to Holocene ice gives $n = 0.307 \pm 0.014$. A non-linear fit by Equation (4), using the Levenberg–Marquardt algorithm, gives the same exponent, $K = 7.5 \times 10^{-2}$ and $\langle R\rangle_0 = 0.01$ mm.

Grain-size distributions

In the regime of normal grain growth, the distribution of normalized grain-sizes $R/\langle R\rangle$ remains unchanged, unimodal and is generally well fitted by a lognormal distribution (Ralph, 1990; Humphreys and Hatherly, 1996). Note, however, that this lognormal fit has not so far received theoretical support. Moreover, if one starts from a distribution with a different shape (at $t = 0$), a transient regime is observed with an evolving distribution (Weygand, 1998). In the strictest sense, normal grain growth only refers to the "steady state".

For all the thin sections of ice analyzed along the EPICA ice core, the distributions of normalized grain-size are well fitted by lognormal distributions (Arnaud and others, 2000). However, the two independent parameters characterizing the lognormal distribution, i.e. the mean and the standard deviation of $\ln(R/\langle R\rangle)$, in part evolve through depth and thus time (Fig. 1b and c). Interestingly, both of them show a break at the Holocene/LGM transition, as does the average grain-size. Moreover, these parameters appear, within the large scatter, to continuously evolve during the Holocene. This could be interpreted as a transient regime (see above).

GRAIN GROWTH AND CLIMATIC CHANGES

As already observed by different authors, there is a marked decrease of $\langle R\rangle$ associated with the Holocene–LGM climatic transition (Fig. 1a and d). Several explanations have been proposed for this decrease of $\langle R\rangle$:

(i) The variation of K with temperature in Equation (4)

(ii) A memory effect of the surface temperature conditions at the time of deposition (Petit and others, 1988)

(iii) The drag of grain boundaries by soluble impurities

(iv) The pinning of grain boundaries by microparticles (dust).

We now review these possibilities in the light of a detailed analysis of ice microstructure, including grain-size distributions.

Note that recrystallization processes such as rotation recrystallization or migration recrystallization create new grains and thus may decrease the average grain-size (Alley and others, 1995; Duval and Castelnau, 1995). However, these mechanisms require significant strain rates and, for migration recrystallization, temperatures above −15°C, i.e. temperatures encountered near the base of ice sheets (Duval and Castelnau, 1995; De La Chapelle and others, 1998). At 600 m depth, the temperature of the ice measured at Dome Concordia is −50°C (personal communication from E. Lefebvre, 2001). Consequently, these mechanisms are unlikely to modify the microstructure in large, cold ice sheets at depths of >600 m (De La Chapelle and others 1998).

Variation of the grain-growth rate K with temperature

Because K is an Arrhenius temperature-dependent constant, a smaller growth rate and therefore smaller grains would be expected in colder ice. However, as noted by Duval and Lorius (1980), the difference in growth temperature needed to explain the difference in average grain-size between Holocene and LGM is far too large compared to the present temperature profile, which has, moreover, been smoothed by thermal conduction.

Memory effect of surface temperature conditions at the time of deposition

Petit and others (1987) proposed that the growth rate K could depend on the temperature of the snow at the time of deposition. They assumed that the grain-boundary mobility μ, and consequently K, were proportional to the concentration of interstitials (point defects), c, which in turn was supposed to follow an Arrhenius temperature dependence: $c \sim \exp(-E_f/RT_s)$, where E_f is an apparent formation energy of interstitials and T_s is the surface temperature at the time of deposition. With this mechanism, the average grain-size becomes a true palaeothermometer. The mechanism was proposed on the basis of a good correlation between the $\delta^{18}O$ record and the average grain-size for the former Dome C ice core (Duval and Lorius, 1980). Alley and others (1988) questioned this mechanism, arguing that the diffusion of the interstitials within ice would destroy the memory effect proposed by Petit and others (1987). (See also the reply (Petit and others, 1988).)

In terms of grain-boundary velocity (Equation (3)), the interstitials are assumed to affect the mobility μ, but not the driving force $\gamma(1/\langle R\rangle - 1/R)$. Besides the objection of Alley and others (1988), the scenario proposed by Petit and others (1987) appears to contradict the observations listed below.

(a) A reduced grain-boundary mobility, and therefore a reduced growth rate K, during the LGM would imply an increasing average grain-size during this period, although at a lower rate than during the Holocene, whereas a roughly constant grain-size is observed between 16 000 and 28 000 BP (within a large scatter).

(b) The Antarctic Cold Reversal (ACR), clearly identified in the δD record between 12 000 and 15 000 BP (Fig. 1d; Jouzel and others, 2001), is not marked by any grain-size decrease in the present profile (Fig. 1a), in contradiction with a direct effect of surface temperature. Note that we increased the sampling rate during this period to properly check this point.

(c) Within the context of "steady-state" normal grain growth with a stabilized normalized distribution, a modification of the grain-boundary mobility in Equation (1) or (3) cannot explain a modification of this distribution at the climatic transition. Indeed, a reduction of mobility induced by point defects would apply equally to all grain boundaries, unless one assumes an (improbable) segregation of interstitials depending on the grain-size. In this situation, although the global kinetics would be slowed down, the behaviour of one grain relative to each of the others would remain unchanged, and so too the normalized grain-size distribution.

On the other hand, the normalized grain-size distribution also appears, within a large scatter, to slowly evolve during the Holocene (Fig. 1b and c). This might indicate a transient rather than "steady-state" regime of grain growth. The values of $\langle R\rangle$, $\langle \ln(R/\langle R\rangle)$ and of the standard deviation of $\ln(R/\langle R\rangle)$ observed in the LGM are similar to those observed within the Holocene at about 7500 BP (see Fig. 1a–c). Therefore, a slowing-down of a "transient" growth process by point defects could be a plausible explanation of a simultaneous evolution of these three parameters at the climatic transition.

(d) We identified in the shallow ice of Dome Concordia a few layers with abnormally small grains (Fig. 1a). Some of these correspond to volcanic ash layers detectable by eye (e.g. at 339.5 m depth, i.e. 10 700 BP). These layers show exactly the same trend as the ice below the transition for the three independent grain-size parameters (Fig. 1a–c). Because there is no reason to expect a high concentration of interstitials associated with these volcanic dust layers in the Holocene, the scenario of Petit and others (1987) is unable to give a universal explanation for the modification of the ice microstructure.

The drag of soluble impurites by grain boundaries

Two kinds of impurities are found in polar ice: insolubles, which are second-phase particles of dust; and soluble impurities which dissolve as ions when the ice is melted. The exact location and form of these solutes within ice is still largely unknown and probably varies with the nature of the impurity. Sulfates may form hydrates, but it has recently been demonstrated that relatively large concentrations (up to 1 ppm) of Na and Cl can be distributed within the ice lattice as solute atoms (Montagnat and others, 2001). While the effect of dust particles of relatively large size (around 1 μm) is to pin the grain boundaries (see below), solutes are dragged by the moving boundary (Alley and others, 1986a; Humphreys and Hatherly, 1996). This drag of impurities reduces the grain-boundary mobility μ. Classical models of this effect are of the form (Lucke and Detert, 1957; Lucke and Stuwe, 1971; Humphreys and Hatherly, 1996):

$$\mu(c) = \frac{\mu_i}{1 + \mu_i \alpha c}, \qquad (5)$$

where c is the impurity concentration (non-dimensional), μ_i

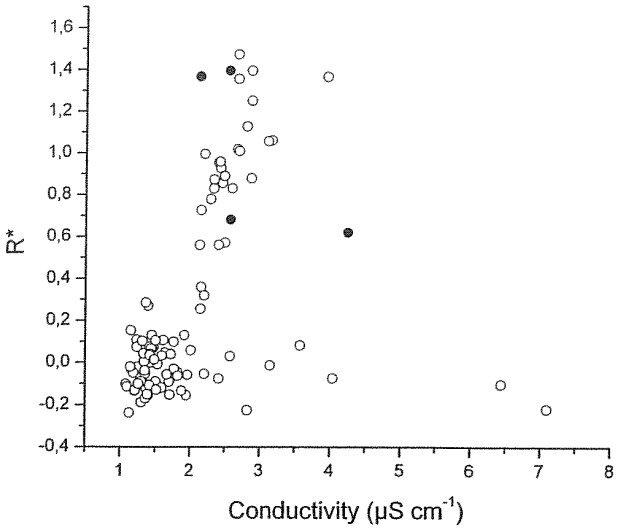

Fig. 2. Correlation between liquid conductivity (from Röthlisberger, 2000) and R (see text for details). Closed symbols are ash layers.*

is the intrinsic mobility of the boundary and α is a constant. More recently Gottstein and others (1998) argued that impurity drag modifies the activation enthalpy of mobility rather than the pre-exponential factor, and proposed a slightly different expression for $\mu(c)$.

In any case, soluble impurities, like interstitials in the scenario of Petit and others (1987) (see above), are found to modify the mobility and not the driving force. Therefore, the arguments (a) and (c) of the previous section hold. An impurity drag effect is also in contradiction with other observations. Figure 2 shows the relation between liquid conductivity, σ (Röthlisberger, 2000), and the non-dimensional parameter R^*:

$$R^* = \left(\frac{{R_{\mathrm{th}}}^2}{\langle R \rangle^2} - 1 \right). \qquad (6)$$

R^* aims to quantify the grain-size decrease compared with normal grain growth. $\langle R \rangle$ is the measured average grain-size and R_{th} is the theoretical grain-size calculated for the same depth from grain-growth Equation (4). From relations (1), (2) and (5) it is easily shown that R^* should be proportional to the impurity content c if soluble impurities play a major role in grain growth. R^* is close to 0 for standard Holocene ice, and above zero for LGM ice as well as for a few anomalous layers within the Holocene. Some authors consider that liquid conductivity measures the total soluble impurity content (Fisher and Koerner, 1986). Note, however, that this relation between liquid conductivity and soluble impurity content is complex, different species contributing differently to the total conductivity. The global correlation observed between σ and R^* (Fig. 2) is not really informative, as many parameters, including isotopic record, conductivity, concentrations of different soluble impurities or of microparticles, and grain-size, exhibit simultaneous changes at climatic transitions. The behaviour of some special layers is more instructive in this respect. These layers, selected on the field from the DEP profile (Wolff and others, 1999; personal communication from E.W. Wolff, 1999) show very large conductivities but normal grain-sizes ($R^* \approx 0$). This shows that large soluble impurity contents do not necessarily imply abnormally small grain-sizes, thus raising doubts about the effectiveness of solute drag in reducing the average grain-size. From continuous flow analysis (CFA) of chemistry of the EPICA ice core (Röthlisberger, 2000), one can analyze similar correlations between grain-size and different species (Na^+, Ca^{2+}, K^+, NO_3^-, SO_4^{2-}, ...). Whereas a global correlation is generally found between impurity concentration and R^*, in each case some depths lie away from the global correlation, either because a large impurity content is associated with normal grain-size or because small grain-sizes are not associated with large impurity contents.

Pinning of grain boundaries by microparticles

Insoluble second-phase particles can also modify the grain-growth process, but through a rather different mechanism. Large (relative to solute atoms) particles cannot be dragged by moving boundaries. Rather, they pin these boundaries (see, e.g., Ralph, 1990; Humphreys and Hatherly, 1996). The role of pinning in the grain-growth process depends on the location of particles (see below), as well as on the ratio between the average grain-size and the mean distance between particles. For small grain-sizes compared to large inter-particle distances, most of the boundaries do not "feel" the particles and so the global growth process is unchanged. For small inter-particle distances, most of the boundaries are pinned and the growth process is stopped. Transient behaviour is found in between (Humphreys and Hatherly, 1996; Weygand, 1998).

C. Zener (cited by Smith, 1948) was the first to model this pinning effect. The interaction between a boundary of free energy γ and a spherical particle of radius r leads to the following restraining force F_z:

$$F_z = \pi \gamma r. \qquad (7)$$

Averaging the effect of N particles per unit volume by a mean-field approximation gives an expression for the (average) pinning pressure P_z exerted by the particles per unit area of boundary (Humphreys and Hatherly, 1996). P_z depends on where the particles are distributed within the matter. P_z is larger when particles are concentrated along the boundaries or at grain vertices rather than distributed randomly within the volume (the boundaries feel a larger particle density). Corresponding expressions for P_z are given in Table 1. This pinning pressure works against the driving force for grain-boundary motion $P = \alpha\gamma/R$. α is a geometrical constant that depends on the model considered ($0.25 < \alpha \leq 1$) (Humphreys and Hatherly, 1996). In the limiting case $P = P_z$, the growth process is stopped, and Zener (Smith, 1948) deduced a corresponding limiting (maximum) grain-

Table 1. Pinning of grain boundaries by microparticles. P_z is pinning pressure and R_z is limiting grain size

	Particles distributed randomly	*Particles along grain boundaries*	*Particles at grain vertices*
P_z	$2\pi\gamma r^2 N$	$\pi\gamma r R N/3$	$\pi\gamma r R N$
R_z	$\alpha/2\pi r^2 N$	$(3\alpha/\pi r N)^{1/2}$	$(\alpha/\pi r N)^{1/2}$
Limiting grain radius (mm)			
Holocene	1.15×10^4 to 2.3×10^4	8.3–11.7	4.8–6.7
ACR	5.7×10^3 to 1.15×10^4	5.9–8.3	3.4–4.8
LGM	23.4–46.8	1.2–1.65	0.7–1.2

ize R_z whose expressions are given in Table 1. Zener originally set $\alpha = 1$, but more recent models and observations argue for lower values of 0.25–0.5 (Humphreys and Hatherly, 1996).

The number and size distribution of dust particles has been measured along the EPICA ice core using a Coulter counter (Delmonte and others, 2002). As observed previously in other ice cores (Steffensen, 1997; Petit and others, 1999), the dust content is strongly influenced by climate changes, with a much larger number of particles during the LGM than during the Holocene (Fig. 1e), while the average particle size shows only slight change. As listed below, different observations suggest a major role for grain-boundary pinning by dust particles in explaining the variations of average grain-size with climate.

(a) In the presence of pinning, Equation (3) can be modified as (Hillert, 1965):

$$v \sim \mu\gamma\left(\frac{1}{\langle R\rangle} - \frac{1}{R} \pm \frac{1}{R_z}\right). \quad (8)$$

Grains in the size range $[(1/\langle R\rangle) + (1/R_z)] < 1/R < [(1/\langle R\rangle) - (1/R_z)]$ neither shrink nor grow. Grains larger or smaller than this will, respectively, grow or shrink but at a reduced rate. Therefore, unlike the drag of solute, pinning does not reduce the mobility μ. Rather, it modifies the driving force for boundary migration non-uniformly. Grain-size distributions are consequently modified by pinning (Riege and others, 1998) as observed at the Holocene–LGM transition (Fig. 1b and c). Analytical models (Abbruzzese and Lucke, 1992), 2-D (Weygand, 1998) as well as 3-D (Song and others, 2000) numerical simulations of Zener pinning, and some experimental evidence (Tweed and others, 1982) support narrower normalized distributions (i.e. smaller standard deviation) for pinned microstructures, in agreement with the data of Figure 1c. Similarly, Riege and others (1998) reported a shift of the mean for a 2-D simulation, in agreement with data of Figure 1b.

(b) Several layers of abnormally small grain-sizes have been identified within the Holocene ice, sometimes associated with a visible (by eye) dust layer. This association is another indication of particle pinning. Moreover, these small grain-size layers exhibit exactly the same features as LGM ice: small grains, narrower and shifted (larger mean) normalized distributions (see Fig. 1a–c). This supports a unique mechanism explaining small grains both in LGM ice and in Holocene ice dust layers. Note that Zener pinning is independent of the origin and nature of the second-phase particles: mostly continental dust in LGM ice, and volcanic ashes in Holocene dust layers. This is also in agreement with the observation of small grain-sizes associated with ash layers in the Byrd ice core (Gow and Williamson, 1976).

(c) From the measured number and size distribution of dust particles, one can apply the mean-field models briefly described above to estimate the limiting grain-sizes R_z associated with Holocene, ACR and LGM (see Table 1). For these estimations, we have taken the following averaged values for the number N of particles mL^{-1}: 3500 for Holocene, 7000 for ACR and 170 000 for LGM (Delmonte and others, 2002). The average particle radius r is considered to be constant at $r = 1\,\mu\mathrm{m}$ (Delmonte and others, 2002); measured variations of r have a negligible effect on R_z. The R_z values given in Table 1 are calculated for α in the range 0.25–0.5 (see above). If the particles are assumed to be randomly distributed within the grains, R_z is extremely large compared to the measured grain-sizes $\langle R\rangle$ for Holocene and ACR ice, thus excluding any effect of dust on grain growth, and very large for LGM ice. On the other hand, if the particles are mostly located along the boundaries, as is more likely at the time of snow deposition in central Antarctica (and for which there is some experimental evidence (Barnes and others, 2002)), we find R_z values 5–10 times larger than $\langle R\rangle$ for Holocene and ACR ice, but very close to $\langle R\rangle$ for LGM ice.

These mean-field estimates are in striking agreement with the observed grain-size profile (Fig. 1a). In the Holocene and ACR ice, the dust particle density is too low to have a strong effect on grain growth. This explains why the ACR is not revealed by the grain-size profile. Note, however, that particle pinning might have a limited slowing effect on grain growth during these periods and could explain the departure of the growth exponent n in Equation (4) from the theoretical upper bound of 0.5, especially if the particles are preferentially located at grain vertices. The strong increase in dust density at the climatic transition and during the LGM explains the simultaneous decrease of $\langle R\rangle$ at the transition as well as the plateau observed below; $\langle R\rangle$ has reached the limiting, asymptotic grain-size R_z around 1–1.2 mm. With this scenario, $\langle R\rangle$ should remain constant around this value as long as the number of particles N remains around 170 000 mL^{-1}, and no other recrystallization mechanisms exist. This scenario is also in excellent agreement with Fisher and Koerner (1986) who argued that a negative correlation exists between grain-size and N for $N > 15\,000\ \mathrm{mL}^{-1}$, and no correlation below (as for Holocene and ACR here).

Finally, this mechanism explains the large scatter on $\langle R\rangle$ observed during the LGM (Fig. 1a). Large fluctuations of the crystal size might be linked to the large variations of dust concentration, whereas the smaller scatter observed during the Holocene is an intrinsic scatter of the measure.

The pinning of grain boundaries by microparticles appears to be the only scenario able to explain qualitatively and quantitatively all the reported observations in a simple way: the grain-size profile (Fig. 1a), the grain-size distributions (Fig. 1b and c), the microstructure of ash layers within Holocene ice, etc. It is also in agreement with the fact that layers containing a large amount of soluble impurities, but not necessarily a large amount of dust, may exhibit no significant microstructural changes (Fig. 2)

CONCLUSION

A detailed analysis of the microstructure of the shallow part (100–580 m) of the EPICA ice core at Dome Concordia has been performed using image-analysis processing. The average grain-size profile revealed power-law grain-growth kinetics with an exponent $n \approx 0.3$ in Holocene ice. At the Holocene–LGM transition, the average grain-size strongly decreases, then remains roughly constant down to 580 m depth. Several explanations have been proposed in the literature for this correlation between grain-size and climate. These include soluble impurity drag on grain-boundary migration, pinning by (insoluble) microparticles, and an effect of surface temperature conditions at the time of deposition. We discussed this on the basis of a detailed analysis of the ice microstructure

coupled with classical mean-field modeling of grain-growth kinetics, solute drag and particle pinning. It is shown that the pinning of grain boundaries by dust particles located along the boundaries explains qualitatively and quantitatively all the reported observations: the grain-size profile, the grain-size distributions and the microstructure of ash layers within the Holocene ice. This strongly supports a major role for this mechanism in explaining correlations between grain-size and climate in the shallow parts of large ice sheets, although this does not completely rule out a limited effect of some soluble impurities on grain growth. This conclusion is in agreement with Fisher and Koerner (1986) and Li and others (1998).

ACKNOWLEDGEMENTS

This work is a contribution to the European Project for Ice Coring in Antarctica (EPICA), a joint European Science Foundation (ESF)/European Commission (EC) scientific programme, funded by the EC under the Environment and Climate Programme and by national contributions from Belgium, Denmark, France, Germany, Italy, the Netherlands, Norway, Sweden, Switzerland and the United Kingdom. We would like to thank two anonymous reviewers for helpful comments.

REFERENCES

Abbruzzese, G. and K. Lucke. 1992. Theory of grain growth in the presence of second phase particles. *Mater. Sci. Forum*, **94–96**, 597–604.

Alley, R. B. and G. A. Woods. 1996. Impurity influence on normal grain growth in the GISP2 ice core, Greenland. *J. Glaciol.*, **42**(141), 255–260.

Alley, R. B., J. H. Perepezko and C. R. Bentley. 1986a. Grain growth in polar ice: I. Theory. *J. Glaciol.*, **32**(112), 415–424.

Alley, R. B., J. H. Perepezko and C. R. Bentley. 1986b. Grain growth in polar ice: II. Application. *J. Glaciol.*, **32**(112), 425–433.

Alley, R. B., J. H. Perepezko and C. R. Bentley. 1988. Long-term climate changes from crystal growth. *Nature*, **332**(6165), 592–593.

Alley, R. B., A. J. Gow and D. A. Meese. 1995. Mapping *c*-axis fabrics to study physical processes in ice. *J. Glaciol.*, **41**(137), 197–203.

Anderson, M. P., G. S. Grest and D. J. Srolovitz. 1989. Computer simulation of normal grain growth in three dimensions. *Philos. Mag. B*, **59**(3), 293–329.

Arnaud, L., J. Weiss, M. Gay and P. Duval. 2000. Shallow-ice microstructure at Dome Concordia, Antarctica. *Ann. Glaciol.*, **30**, 8–12.

Barnes, P. R. F., R. Mulvaney, K. Robinson and E. W. Wolff. 2002. Observations of polar ice from the Holocene and the glacial period using the scanning electron microscope. *Ann. Glaciol.*, **35** (see paper in this volume).

Burke, J. E. and D. Turnbull. 1952. Recrystallization and grain growth. *Prog. Metal Phys.*, **3**, 220–292.

De La Chapelle, S., O. Castelnau, V. Lipenkov and P. Duval. 1998. Dynamic recrystallization and texture development in ice as revealed by the study of deep ice cores in Antarctica and Greenland. *J. Geophys. Res.*, **103**(B3), 5091–5105.

Delmonte, B., J.-R. Petit and V. Maggi. 2002. Glacial to Holocene implications of the new 27,000 year dust record from the EPICA Dome C (East Antarctica) ice core. *Climate Dyn.*, **18**(8), 647–660.

Duval, P. and O. Castelnau. 1995. Dynamic recrystallization of ice in polar ice sheets. *J. Phys.* (Paris), **IV**(5), Colloq. C3, 197–205. (Supplément au 3.)

Duval, P. and C. Lorius. 1980. Crystal size and climatic record down to the last ice age from Antarctic ice. *Earth Planet. Sci. Lett.*, **48**(1), 59–64.

Fisher, D. A. and R. M. Koerner. 1986. On the special rheological properties of ancient microparticle-laden Northern Hemisphere ice as derived from bore-hole and core measurements. *J. Glaciol.*, **32**(112), 501–510.

Gay, M. and J. Weiss. 1999. Automatic reconstruction of polycrystalline ice microstructure from image analysis: application to the EPICA ice core at Dome Concordia, Antarctica. *J. Glaciol.*, **45**(151), 547–554.

Gottstein, G., D. A. Molodov and L. S. Shvindlerman. 1998. Grain boundary mobility in metals: the current status. *In* Weiland, H., B. L. Adams and A. D. Rollett, *eds. Grain growth in polycrystalline materials III.* Warrendale, PA, The Minerals, Metals and Materials Society, 373–386.

Gow, A. J. 1969. On the rates of growth of grains and crystals in South Polar firn. *J. Glaciol.*, **8**(53), 241–252.

Gow, A. J. and T. Williamson. 1976. Rheological implications of the internal structure and crystal fabrics of the West Antarctic ice sheet as revealed by deep core drilling at Byrd Station. *Geol. Soc. Am. Bull.*, **87**(12), 1665–1677.

Higgins, G. T. 1974. Grain boundary migration and grain growth. *Metal Sci.*, **8**, 143–150.

Hillert, M. 1965. On the theory of normal and abnormal grain growth. *Acta Metall.*, **13**, 227–238.

Humphreys, F. J. and M. Hatherly. 1996. *Recrystallization and related annealing phenomena.* Oxford, etc., Pergamon Press.

Jouzel, J. *and 12 others.* 2001. A new 27 kyr high resolution East Antarctic climate record. *Geophys. Res. Lett.*, **28**(16), 3199–3202.

Li Jun, T. H. Jacka and V. Morgan. 1998. Crystal-size and microparticle record in the ice core from Dome Summit South, Law Dome, East Antarctica. *Ann. Glaciol.*, **27**, 343–348.

Lucke, K. and K. Detert. 1957. A quantitative theory of grain-boundary motion and recrystallization in metals in the presence of impurities. *Acta Metall.*, **5**, 628–637.

Lucke, K. and H. P. Stuwe. 1971. On the theory of impurity controlled grain boundary motion. *Acta Metall.*, **19**, 1087–1099.

Montagnat, M. *and 6 others.* 2001. High crystalline quality of large single crystals of subglacial ice above Lake Vostok (Antarctica) revealed by hard X-ray diffraction. *C.R. Acad. Sci.* (Série IIa), **333**(8), 419–425.

Petit, J. R., P. Duval and C. Lorius. 1987. Long-term climatic changes indicated by crystal growth in polar ice. *Nature*, **326**(6108), 62–64.

Petit, J. R., P. Duval and C. Lorius. 1988. Reply to comment on "Long-term climate changes from crystal growth". *Nature*, **332**(6165), 593.

Petit, J.-R. *and 18 others.* 1999. Climate and atmospheric history of the past 420,000 years from the Vostok ice core, Antarctica. *Nature*, **399**(6735), 429–436.

Ralph, B. 1990. Grain growth. *Mater. Sci. Technol.*, **6**, 1139–1144.

Riege, S. P., C. V. Thompson and H. J. Frost. 1998. The effect of particle-pinning on grain size distributions in 2D simulations of grain growth. *In* Weiland, H., B. L. Adams and A. D. Rollett, *eds. Grain growth in polycrystalline materials III.* Warrendale, PA, The Minerals, Metals and Materials Society, 295–301.

Röthlisberger, R. 2000. Chemische Spuren in antarktischen Eis: Resultate des EPICA-Eisbohrkerns von Dom Concordia. (Ph.D. thesis, University of Bern.)

Schwander, J., J. Jouzel, C. U. Hammer, J. R. Petit, R. Udisti and E. Wolff. 2001. A tentative chronology for the EPICA Dome Concordia ice core. *Geophys. Res. Lett.*, **28**(22), 4243–4246.

Smith, C. S. 1948. Grains, phases, and interfaces: an interpretation of microstructure. *Trans. Metall. Soc. AIME* 175, 15–51.

Song, X., G. Liu and N. Gu. 2000. Simulation of the influence of the quantity of second-phase particles on grain growth. *Z. Metallkd.*, **91**(3), 227–231.

Steffensen, J. P. 1997. The size distribution of microparticles from selected segments of the GRIP ice core representing different climatic periods. *J. Geophys. Res.*, **102**(C12), 26,755–26,763.

Tweed, C. J., N. Nansen and B. Ralph. 1982. Grain growth in samples of aluminium containing alumina particles. *Metall. Trans., Ser. A*, **14**, 2235–2243.

Weygand, D. 1998. Simulation numérique de la croissance des grains. (Thèse de doctorat, Institut National Polytechnique de Grenoble.)

Weygand, D., Y. Bréchet, J. Lépinoux and W. Gust. 1998. Three dimensional grain growth: a vertex dynamics simulation. *Philos. Mag. B*, **79**(5), 703–716.

Wolff, E., I. Basile, J.-R. Petit and J. Schwander. 1999. Comparison of Holocene electrical records from Dome C and Vostok, Antarctica. *Ann. Glaciol.*, **29**, 89–93.

M. Frezzotti, M. Pourchet, O. Flora, S. Gandolfi, M. Gay, S. Urbini, C. Vincent, S. Becagli, R. Gragnani, M. Proposito, M. Severi, R. Traversi, R. Udisti, M. Fily. "New estimations of precipitation and surface sublimation in East Antarctica from snow accumulation measurements", *Climate Dynamics*, *Vol* 23, 2004.

Climate Dynamics (2004) 23: 803–813
DOI 10.1007/s00382-004-0462-5

**Massimo Frezzotti · Michel Pourchet · Onelio Flora
Stefano Gandolfi · Michel Gay · Stefano Urbini
Christian Vincent · Silvia Becagli · Roberto Gragnani
Marco Proposito · Mirko Severi · Rita Traversi
Roberto Udisti · Michel Fily**

New estimations of precipitation and surface sublimation in East Antarctica from snow accumulation measurements

Received: 27 November 2003 / Accepted: 22 May 2004 / Published online: 8 September 2004
© Springer-Verlag 2004

Abstract Surface mass balance (SMB) distribution and its temporal and spatial variability is an essential input parameter in mass balance studies. Different methods were used, compared and integrated (stake farms, ice cores, snow radar, surface morphology, remote sensing) at eight sites along a transect from Terra Nova Bay (TNB) to Dome C (DC) (East Antarctica), to provide detailed information on the SMB. Spatial variability measurements show that the measured maximum snow accumulation (SA) in a 15 km area is well correlated to firn temperature. Wind-driven sublimation processes, controlled by the surface slope in the wind direction, have a huge impact (up to 85% of snow precipitation) on SMB and are significant in terms of past, present and future SMB evaluations. The snow redistribution process is local and has a strong impact on the annual variability of accumulation. The spatial variability of SMB at the kilometre scale is one order of magnitude higher than its temporal variability (20–30%) at the centennial time scale. This high spatial variability is due to wind-driven sublimation. Compared with our SMB calculations, previous compilations generally over-estimate SMB, up to 65% in some areas.

M. Frezzotti (✉) · R. Gragnani · M. Proposito
Ente per le Nuove Tecnologie, l'Energia e l'Ambiente,
'Progetto Clima Globale', Rome, Italy
E-mail: frezzotti@casaccia.enea.it

M. Pourchet · M. Gay · C. Vincent · M. Fily
Laboratoire de Glaciologie et Géophysique de l'Environnement,
CNRS, Saint Martin d'Hères, France

O. Flora
Dipartimento di Scienze Geologiche, Ambientali e Marine,
University of Trieste, Trieste, Italy

S. Gandolfi
Dipartimento di Ingegneria delle Strutture, dei Trasporti,
delle Acque, del Rilevamento, del Territorio,
University of Bologna, Bologna, Italy

S. Urbini
Istituto Nazionale di Geofisica e Vulcanologia,
Rome, Italy

S. Becagli · M. Severi · R. Traversi · R. Udisti
Dipartimento di Chimica, University of Florence,
Florence, Italy

1 Introduction

Precipitation over Antarctica is recognised as an important climate variable. Snow accumulation (SA) rate or surface mass balance (SMB) on the Antarctic Plateau is the sum of precipitation, sublimation/deposition and wind-blown snow. Large gaps in observations mean that any estimate of the current mass input involves a large error factor (Genthon and Krinner 2001; Rignot and Thomas 2002). Spatial SMB is known to vary greatly (e.g. Richardson et al. 1997; van den Broeke et al. 1999; Frezzotti et al. 2002a; Frezzotti et al., in press). Representative observations of the SMB are important in estimating the characteristics of spatial and temporal variability at local scales (< 10 km^2) and at the scale of a drainage basin. Snow redistribution changes the topography, and the topography in turn alters the wind field in a feedback system between the cryosphere and atmosphere. On the local scale, there is continual interaction between processes such as wind, snow precipitation, sublimation and SMB variations; in particular, the surface-energy balance and katabatic wind patterns are closely inter-related.

Antarctica is the highest and flattest of the Earth's continents, but small changes in slope have a strong impact on wind direction and speed (Frezzotti et al. 2002a). It has long been known that slope and curvature can play an important role in the SMB; for example, concave depressions accumulate snow at the expense of convex rises (Black and Budd 1964; Whillans 1975; Pettré et al. 1986; van den Broeke et al. 1999; Liston et al. 2000; Frezzotti et al. 2002a). A large area of the plateau, where the slope along the wind direction is

higher than 4 m km^{-1}, has a nil or slightly negative SMB (Frezzotti et al. 2002b).

Surface mass balance studies based on numerical weather prediction models (e.g. Bromwich 1988; Genthon and Braun 1995; Turner et al. 1999) yield results which are comparable to those based on the interpolation of observations, but the horizontal resolution of the meteorological fields is not better than ~100 km and is affected by systematic biases (Gallée et al. 2001; Genthon and Krinner 2001). It is known that sublimation in Antarctica is not negligible (e.g. Stearns and Weidner 1993; Bintanja 1998; Gallée 1998; Gallée et al. 2001), and methods for describing spatial and temporal variability must be further developed (Cullather et al. 1998). The snowdrift process is not explicitly included in numerical weather prediction and general circulation models (Gallée et al. 2001; Genthon and Krinner 2001). One of the largest areas of uncertainty regarding SMB is the role of surface and wind-driven sublimation (e.g. Genthon and Krinner 2001; Turner et al. 2002). The fraction of precipitation on the grounded ice which is returned to the atmosphere through sublimation ranges from 6 to 25% in high-resolution models (van der Broeke 1997; Genthon and Krinner 2001). Van der Broeke (1997) pointed out four areas (east Dronning Maud Land, Lambert Glacier basin, Victoria Land and the southern part of Ross Ice Shelf) clearly stand out where sublimation on an annual basis removes more than 70% of the precipitation. Some authors even note that, due to small-scale spatial variability in net SMB, it is impossible to determine 'true' precipitation or SMB in large sectors of the Antarctic (Turner et al. 1999).

Alley (1988) found that a depth hoar layer lost 25% of its mass, probably by migrating upward to the atmosphere; even larger mass loss during sublimation is documented by Alley et al. (1990). In wind crust area, very light winds (< 2 m s^{-1}) could be sufficient to initiate snowdrifts on this smooth surface (Bintanja et al. 2001), particularly in the case of fresh snow falls. Wind scouring does not allow the SA (due to surface smoothness) during the winter period, while low albedo of some snow surfaces promotes sublimation during summer. Both factors have a positive feedback effect on the development of permanent wind crust.

At Vostok Station, accumulation stake network allowed determining a mean accumulation rate of 23 ± 4.4 kg m^{-2} a^{-1} and a precipitation rate of 26 ± 4.5 kg m^{-2} a^{-1} for the last 30 years. The total sublimation, for the period November–February, varies from 4.4 to 2 kg m^{-2} a^{-1} of total annual precipitation (Ekaykin et al., in press). King et al. (2001) have pointed out that, at Halley Station, surface and blowing sublimation make roughly equal contributions to ablation (about 82 kg m^{-2} a^{-1}). Bintanja (1999) shows that there is a clear positive correlation between sublimation and air temperature in blue ice areas. Stearns and Weidner (1993) estimated a net annual surface sublimation of 35 and 80 kg m^{-2} a^{-1}, respectively at the South Pole Station and Ross Ice Shelf, with a SMB of 80 and 100 kg m^{-2} a^{-1}, respectively. Kobayashi et al. (1985) and Takahashi et al. (1988) estimated that the precipitation rate at Mizuho Stations (East Antarctica) was between 140 and > 200 kg m^{-2} a^{-1}. The measured surface sublimation was 54 kg m^{-2} a^{-1}, with a SMB of 58 kg m^{-2} a^{-1} determined by strong sublimation in summer (Fujii and Kusunoki 1982). The deficit between precipitation and surface sublimation at Mizuho Stations can be explained by blowing sublimation (Takahashi et al. 1988). We define the blowing sublimation as the sublimation of the snow blown into the air.

Observation of the SMB rate variability and the study of redistribution processes not only provide input for the mass balance estimation but are also essential for better interpreting surface elevation change signals from satellite altimeters (Rémy et al. 2002) and for improving climate and meteorological models (e.g. Cullather et al. 1998; Genthon and Krinner 1998, 2001; Turner et al. 1999; Gallée et al. 2001). Interpretation and dating of palaeoenvironmental records extracted from Antarctic ice cores depend on the knowledge of past accumulation changes (e.g. Bromwich and Weaver 1983; Jouzel et al. 1983). Atmospheric/ocean warming in the coming century may lock up greater volumes of ocean water due to increased precipitation above the Antarctic ice sheet. The SMB trend on a century scale is required to evaluate Antarctica's present mass balance and how it may change over the coming decades and centuries.

As part of the International TransAntarctic Scientific Expedition (ITASE) project (Mayewski and Goodwin 1999) and in the framework of the Franco-Italian Concordia Station collaboration (between 1998 and 2000), a traverse between Terra Nova Bay (TNB) and Dome C (DC) and a research at DC were undertaken (Fig. 1). The study aimed to better understand latitudinal and longitudinal environmental gradients, while documenting climatic, atmospheric and surface conditions over the last 200–1,000 years in the eastern and north-eastern portions of the DC drainage area and in northern Victoria Land.

Frezzotti et al. (in press) combine geophysical surveys (GPR and GPS), field and remote sensing surface observations and firn core analyses to describe spatial and temporal variability of SA along the traverse and at DC. This paper uses these results to provide new information on the SMB process and carries implications for SMB distribution and variability.

2 Methodology

Different methods were used, compared and integrated (stake farms, ice cores, snow radar, surface morphology, remote sensing) at eight sites along a transect from TNB to DC (Fig. 1) to evaluate the SA variability. Three cores were drilled 5–7 km apart at each of the seven main sites along the traverse (23 total cores), while at DC 16 shallow firn cores were drilled within a 25-km radius from

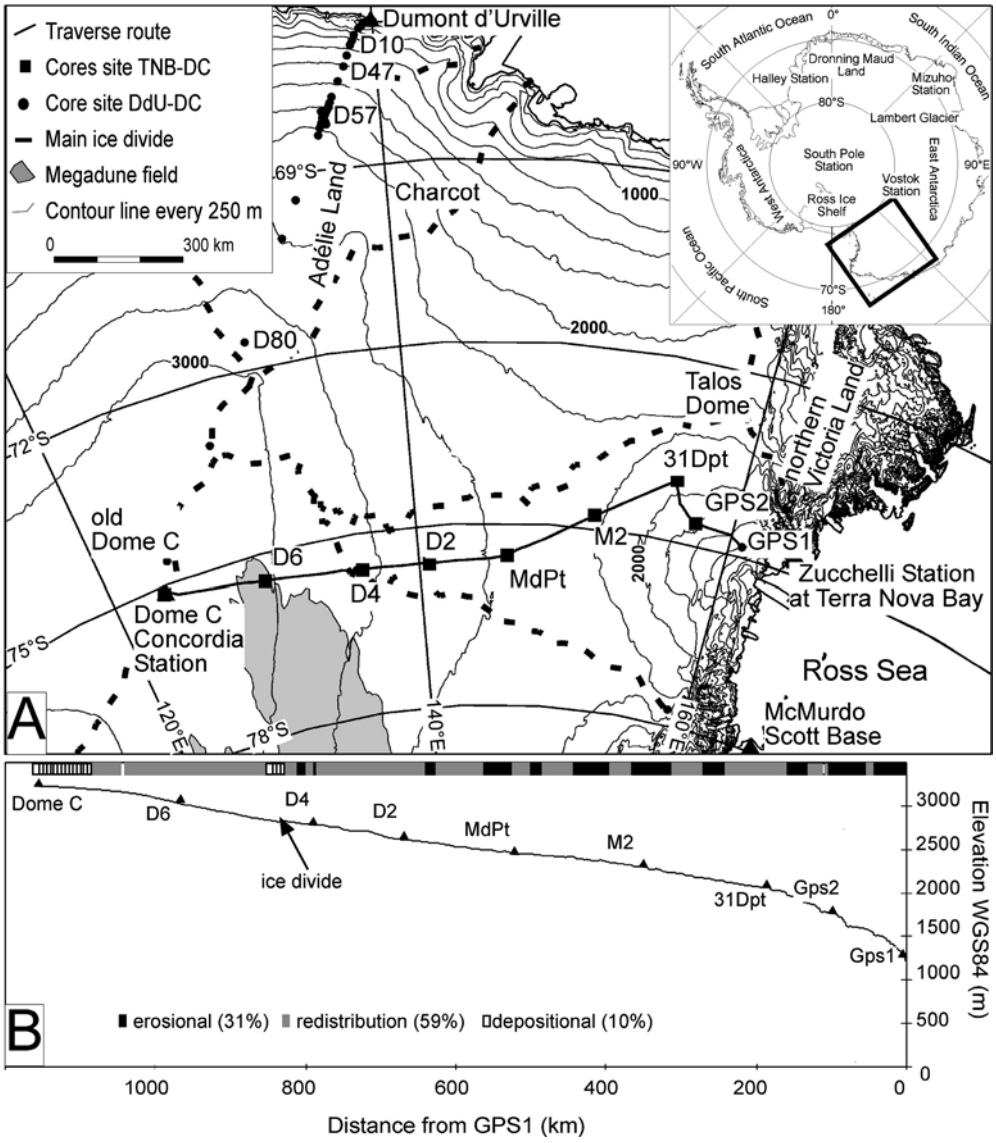

Fig. 1 Schematic map of traverse from TNB to DC and site location (**a**), surface elevation (*solid line*) and micro-relief distribution along TNB–DC traverse. Core sites are indicated with *triangles* (**b**)

Concordia Station. Cores were linked by snow radar and GPS surveys to provide detailed information on spatial variability in SMB. The 39 cores were dated by identifying Tritium/β marker levels (1965–1966) to provide information on SA at core site. The depth of the snow radar layer was converted into SMB (GPR_SA) using the depth/age ratio from the Tritium SA. The mean depth and the relative standard deviation (standard deviation/average of site) were computed for GPR_SA, and the minimum and maximum accumulations were recorded at each site. SA data derived from core records are in good agreement with data derived from GPR_SA (Table 1). The survey methods and analytical procedures for core and snow radar measurements are described in Frezzotti et al. (in press). We also use in this paper the SA data (41 cores) that were collected along the transect between Dumont d'Urville (DdU) and DC (Pourchet et al. 1997) using the β radioactive horizons in the cores.

The snow temperature measured at a depth of 10 or 15 m gives a fairly close approximation to the mean annual "surface temperature" in the dry snow, and is also close to the mean annual "screen air temperature" (Loewe 1970). This assumption is acceptable in areas where maximum temperature is below 0°C during summer time, as it is the case in the actual sampling sites. Snow temperature profiles were measured at core sites (Frezzotti and Flora 2002; Pourchet et al. 1997), and 15 m depth temperatures were used in this paper.

3 Results and discussion

3.1 Surface mass balance

In this chapter, we first analyse the spatial variability of the SA. Then we discuss the evaluation of the precipitation and ablation values from the SA ones and compare our results to existing accumulation maps.

Table 1 Location, morphological and climatological characteristic of drill sites

Site	Longitude E	Latitude S	Elevation (m WGS84)	T –15m (°C)	Slope direction	Wind direction	Katabatic wind speed (m s^{-1})	β1966–1998 β1955–1998^{+} Tritium 1966–1998* (kg m^{-2} a^{-1})	GPR_SA (kg m^{-2} a^{-1})
GPS1							>18		
Core A	160°39.60′	74°48.94′	1,192	−32.7				58 ± 2.9*	–
Core B	160°39.60′	74°48.94′	1,192	–				47 ± 4.7	–
GPS2							>18		
Core A	157°30.13′	74°38.69′	1,804	−38.5	132°	80°		54 ± 2.7*	54 (27%)
Core B	157°22.80′	74°36.81′	1,810	–	132°	80°		137 ± 13.7	200 (100%)
Core C	157°30.13′	74°38.69′	1,804	–	132°	80°		62 ± 6.2	54 (27%)
31Dpt							12–18		
Core A	155°57.6′	74°01.52′	2,069	−41.8	158°	72°		112 ± 5.6*	112 (77%)
Core B	156°0.64′	74°03.51′	2,040	–	158°	72°		137 ± 13.7*	145 (100%)
Core C	155°55.99′	74°03.80′	2,041	–	158°	72°		–	97 (67%)
M2							12–18		
Core A	151°16.17′	74°48.27′	2,278	−44.5	162°	62°		15 ± 7.5*	15 (14%)
Core D	151°09.13′	74°49.86′	2,265	–	111°	62°		82 ± 8.2	107 (100%)
Core C	151°05.91′	74°48.01′	2,272	–	247°	62°		44 ± 4.4	61 (57%)
MdPt							12–18		
Core A	145°51.43′	75°32.16′	2,454	−47.8	78°	32°		45 ± 2.7*	45 (60%)
Core B	145°47.31′	75°33.03′	2,460		78°	32°		11 ± 1.1	13 (18%)
Core C	145°55.35′	75°31.74′	2,452		78°	32°		60 ± 6.0	75 (100%)
D2							6–12		
Core A	140°37.84′	75°37.33′	2,479	−48.4	89°	37°		31 ± 1.6*	31 (94%)
Core B	140°28.61′	75°38.76′	2,482		89°	37°		40 ± 4.0^{+}	33 (100%)
Core C	140°28.54′	75°36.06′	2,483		89°	37°		38 ± 3.8	29 (87%)
D4							6–12		
Core A	135°49.89′	75°35.88′	2,793	−50.5	116°	42°		–	22 (79%)
Core B	135°40.43′	75°37.13′	2,795		116°	42°		29 ± 2.9	28 (100%)
Core C	135°40.74′	75°34.43′	2,798		116°	42°		20 ± 2.0	22 (72%)
D6							6–12		
Core A	129°48.53′	75°26.85′	3,027	−51.0	97°	46°		29 ± 1.4*	29 (85%)
Core B	129°42.41′	75°25.19′	3,035		97°	46°		38 ± 3.8	34 (100%)
Core C	129°38.04′	75°26.42′	3,038		97°	46°		22 ± 2.2	16 (46%)
Dome C						40°	<6		
EPICA-DC1	123°20.86′	75°06.06′	3,233						
FIRETRAC	123°20.86′	75°06.06′	3,233	−54.5					
DCN	123°18.72′	75°07.32′	3,233	−55.0				29 ± 1.5*	
DC-1 A17	123°36.26′	75°00.53′	3,233					26 ± 1.3*	
DC-2 E16	123°01.95′	75°02.86′	3,230					27 ± 1.4*	
DC-3 D10	123°11.13′	75°11.68′	3,233					26 ± 1.3*	
DC-4 C12	123°45.51′	75°09.29′	3,229					23 ± 1.2*	
DC-A18	123°49.85′	74°54.55′	3,226					32 ± 3.2	
DC-DORIS	123°05.92′	75°09.16′	3,232					33 ± 3.3	
DC-B11	124°15.97′	75°05.99′	3,225					29 ± 2.9	
DC-F10	123°11.30′	75°00.50′	3,230					29 ± 2.9	
DC-DAU	122°57.04′	75°17.72′	3,233					29 ± 2.9	
DC-E19	122°38.83′	74°59.31′	3,223					30 ± 3.0	
DC-A17	123°36.26′	75°00.53′	3,232					29 ± 2.9	
DC-D11	122°57.45′	75°17.71′	3,230					27 ± 2.7	
DC-A15	122°56.66′	75°17.71′	3,233					30 ± 3.0	
DC-C17	123°23.65′	75°12.52′	3,229					26 ± 2.6	
DC-C18	123°49.83′	75°17.51′	3,221					28 ± 2.8	

Snow accumulation from stake farms and core analyses, and comparison with snow radar depths (water equivalent) in percent. GPR_SA depth of the snow radar layer converted into SMB using the depth/age ratio from the 'core A' core Tritium snow accumulation. Katabatic wind speed from Parish and Bromwich (1991)

3.2 Snow precipitation vs. surface mass balance

The maximum value of SMB revealed by snow radar (along 15 km) and core data along the traverse presents an excellent correlation with firn temperature (Fig. 2a; $R^2 = 0.84$ core data; Fig. 2b: $R^2 = 0.89$ snow radar). The average core data value is not well correlated with firn temperature ($R^2 = 0.37$). Core and snow radar minimum values show no significant correlation with elevation or temperature ($R^2 = 0.31$ and 0.32), but values are linked with the change of Slope along the Prevalent Wind Direction (SPWD). Noone et al. (1999) found that precipitation reflects large (synoptic) scale phenomena connected to circulation on a global scale.

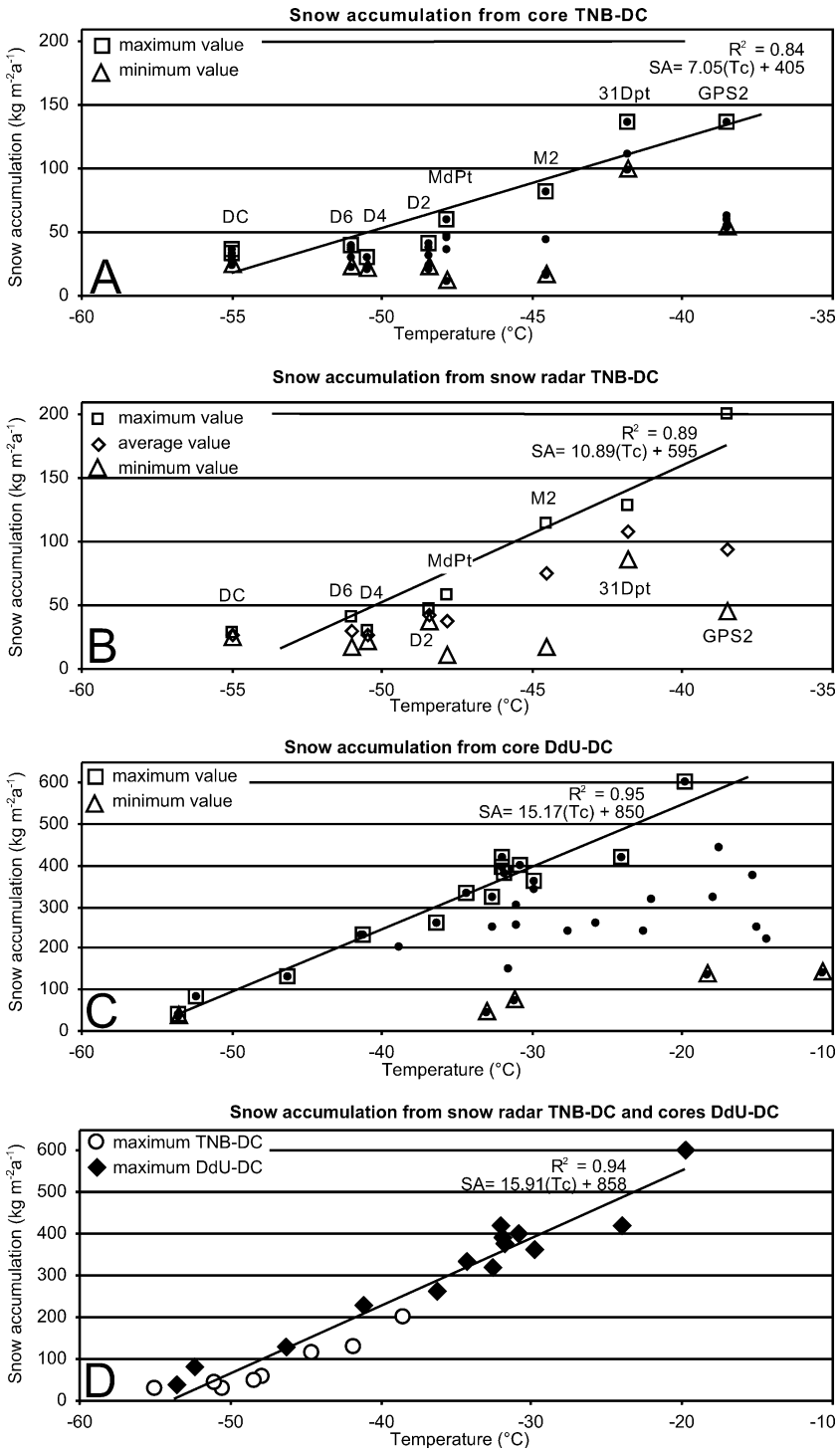

Fig. 2 Snow accumulation vs. temperature from core analysis (**a**) ($R^2 = 0.84$, significance level >95%) and from snow radar (**b**) ($R^2 = 0.89$, significance level >95%) along the TNB–DC traverse. SA vs. temperature from core analysis (**c**) ($R^2 = 0.95$, significance level >99%) along DdU–DC traverse (Pourchet et al. 1997) and maximum SA vs. temperature along TNB–DC and DdU–DC (**d**) ($R^2 = 0.94$, significance level >99%). Snow temperature was measured at 15 m depth

Several authors (e.g. Robin 1977; Muszynski and Birchfield 1985; Fortuin and Oerlemans 1990; Giovinetto et al. 1990) suggest that the SMB is directly correlated with temperature, elevation, saturation vapour pressure and distance from the open ocean (continentality). However, the firn temperature is the only ground field climatological datum available in most of Antarctica. Young et al. (1982) pointed out that for the Pionerskaya DC line the smooth accumulation trend followed temperature very closely. Frezzotti and Flora (2002) and Magand et al. (in press) show that the spatial variability in the local climate in this area may be unrelated to altitude and distance from the open ocean. No single process accounts entirely for the firn temperature patterns. However, we suspect that the interplay of katabatic winds, storm intrusions and the winter temperature inversion driven by the local and regional morphology (slope, convex or

concave surface) and surface albedo (wind crust, sastrugi, etc.) may be very important.

On the basis of our observations, we suggest that the maximum SA rate value at each site, which is well correlated with the mean annual temperature ($R^2 = 0.89$, $n = 8$), represents a value close to snow precipitation, according to the following function:

$$\mathrm{SA} = 10.89(\mathrm{Tc}) + 595 \quad (1)$$

where SA is the maximum SA (kg m^{-2} a^{-1}) and Tc is the firn temperature at 15 m (°C).

This hypothesis is confirmed by the fact that snow radar and satellite image analysis along the traverse reveal that only megadune and some occasional transversal dunes represent depositional features. Frezzotti et al. (2002a) pointed out that megadunes have a wave formed by a variable net accumulation, ranging from 25% (lee-ward slopes) to 120% (windward slopes) of the snow accumulated in adjacent non-megadune areas. All other sites show no clear accumulation morphology at the km scale, but a surface morphology prevalently determined by ablation processes (Frezzotti et al. 2002a, b). The analysis of δ^{18}O, performed every 5 km along the traverse (1 m core), shows a good correlation ($R^2 = 0.83$, $n = 227$) between δ^{18}O values and site temperatures with a slope of 0.99‰°C^{-1} (Proposito et al. 2002). It follows that the snow sampled every 5 km was not blown from far away, but fell close to the sample site.

Along the transect between DdU and DC, the SA vs. firn temperature plot shows a very scattered distribution of data points, but with a clear trend in maximum values (Fig. 2c). On the basis of observations along the TNB–DC transect, we suggest that, also for DdU–DC transect, the maximum accumulation value represents a value close to snow precipitation, which is in turn very well correlated ($R^2 = 0.95$, $n = 14$) with firn temperature at each site, according to the following function:

$$\mathrm{SA} = 15.17(\mathrm{Tc}) + 850 \quad (2)$$

this equation is very similar to the one calculated along the TNB–DC transect (Eq. 1).

Using the maximum data from both transects (TNB–DdU–DC), the accumulation is highly correlated ($R^2 = 0.94$, significance level $> 99\%$, $n = 22$) with firn temperature at each site, according to the following function (Fig. 2d):

$$\mathrm{SA} = 15.91(\mathrm{Tc}) + 858 \quad (3)$$

3.3 Snow ablation and sublimation vs. surface mass balance measurements

Snow redistribution is a local process and has a strong impact on the variability of accumulation at the annual/metre scale (i.e. noise in ice cores). The high variability of SMB is linked to the ablation process. Ablation is determined by the surface sublimation process (wind scouring and, subsequently, sublimation of blowing snow "blowing sublimation") on the plateau and by the snow blown into the sea in coastal areas. Based on these observations, we suggest that the difference between the maximum and minimum SMB value at each site represents the ablation value (Table 2, Fig. 3): GPS2, M2 and MdPt ablation exceeds about 80% of maximum SA, whereas D6 ablation represents 58%, 31Dpt, D2 and D4 range between 20 and 33% and DC represents 12% (the lowest value) of maximum SA. A clear decrease is observed from the coast to the plateau (GPS2-DC; Maximum-Minimum absolute value in Table 2).

The sites where wind action has less impact (site with a small SPWD) present a standard deviation of less than 10% (31Dpt, D2, D4 and DC, Table 2, Fig. 4a) and a good correlation ($R^2 = 0.86$, $n = 4$) between ablation (maximum–minimum accumulation value) and firn temperature according to the following linear equation:

$$\mathrm{Ab} = 3.0(\mathrm{Tc}) + 162 \quad (4)$$

where Ab is snow ablation (kg m^{-2} a^{-1}) and Tc is the firn temperature at 15 m (°C).

Equation 4 could be mainly related with a small amount of blowing sublimation in areas with no

Table 2 Spatial variability in SMB from snow radar calibrated using accumulation at main core

Site	Spatial variability of SMB from GPR[a]						SMB compilation	
	Average (kg m^{-2} a^{-1})	Standard deviation (%)	Minimum (kg m^{-2} a^{-1})	Maximum (kg m^{-2} a^{-1})	Maximum-Minimum (kg m^{-2} a^{-1})	Maximum-Minimum (%)	Vaughan et al. (1999) (kg m^{-2} a^{-1})	Giovinetto and Zwally (2000) (kg m^{-2} a^{-1})
GPS2	93	47	45	201	156	78	121	135
31Dpt	108	10	86	128	42	33	131	110
M2	76	34	17	115	98	85	97	64
MdPt	38	37	10	59	48	82	107	45
D2	43	5	37	46	9	20	67	39
D4	26	9	22	30	8	26	47	37
D6	29	24	17	41	24	58	41	34
Dome C[a]	26	3	25	28	3	12	49	38

[a]Spatial variability has been evaluated along 15 km in each site along the traverse and along 100 km at DC

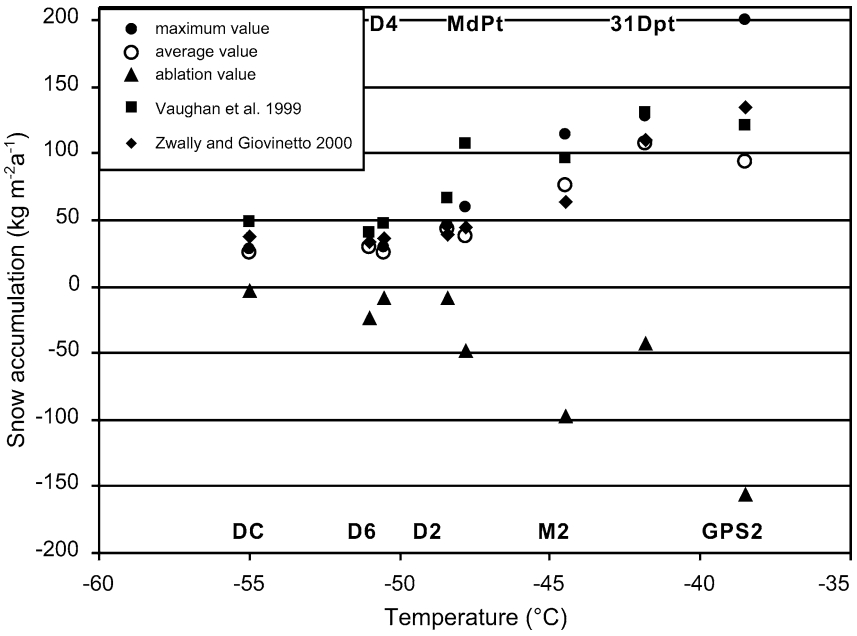

Fig. 3 Maximum and average SA value, ablation value and map compilation value along the TNB–DC transect

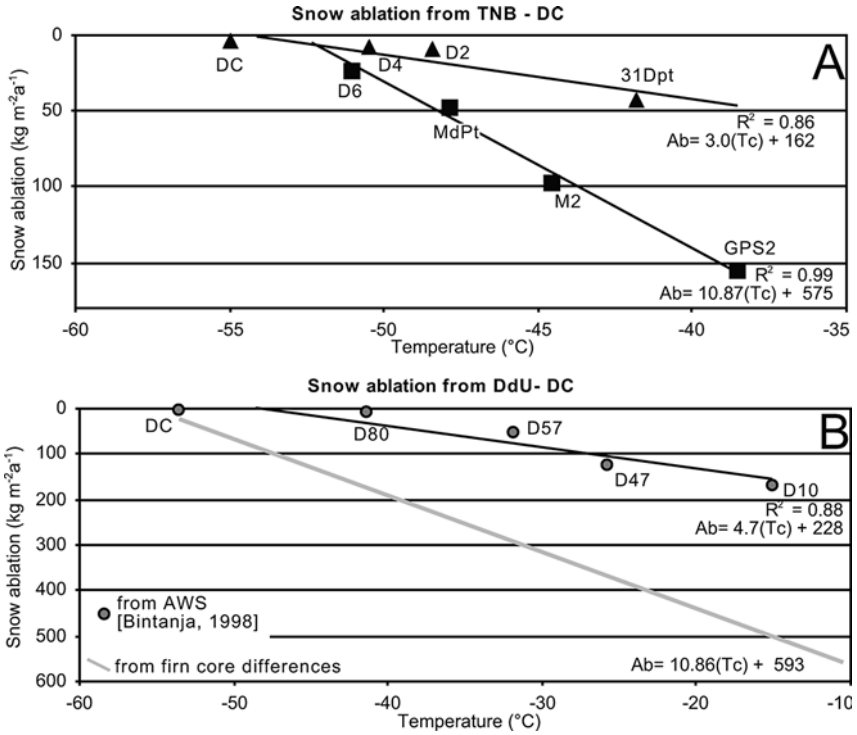

Fig. 4 Ablation vs. temperature along TNB–DC (**a**) and DdU–DC (**b**) traverses. Values along TNB–DC were calculated from maximum and minimum snow radar values; values along DdU–DC represent the difference between firn core maximum and minimum values, and the result of AWS calculations by Bintanja (1998). Confidence level is >95% for correlations

significant change in SPWD (DC, D4, D2 and 31Dpt). Blowing sublimation is negligible at DC, where the mean wind speed is 2.8 m s^{-1} and maximum wind speed is 17 m s^{-1}, but it is still an important factor in SMB at D4 (26%). From the values obtained by Bintanja (1998) along the transect DdU–DC using a model to calculate snow sublimation rates from year-round automatic weather stations data, a linear function is found which is very similar to Eq. 4:

$$\mathrm{Ab} = 4.7(\mathrm{Tc}) + 228 \quad (5)$$

The sites where the wind action has a greater impact (GPS2, M2, MdPt, D6) show ablation values (from 48 to 156 kg m^{-2} a^{-1}) ranging from 58 to 85% of SA (maximum SA value; Table 2). The standard deviation in SMB at these sites is higher than 10% (Table 2); they have a high variability of SPWD (GPS2, M2, MdPt and D6) and show a very good correlation ($R^2 = 0.99$, $n = 4$)

between ablation (maximum–minimum accumulation value) and firn temperature, according to the following function (Fig. 4a):

$$Ab = 10.87(Tc) + 575 \quad (6)$$

Using the maximum and minimum values for SA along the DdU–DC traverse (Fig. 4b), it is possible to calculate the analogous ablation function (Eq. 6) along this transect:

$$Ab = 10.86(Tc) + 593 \quad (7)$$

The ablation functions (Eqs. 6 and 7) along the two transects are very similar. For functions in Eqs. 4 and 5 the constant parameters range from 30 to 45% of functions in Eqs. 6 and 7 constant values, with higher values inland (reduction in wind speed and turbulence), making both surface and blowing sublimation negligible at DC; nevertheless, blowing sublimation is still an important factor in SMB at D6 (Figs. 3 and 4a).

Along the TNB–DC transect, the sites with high standard deviation and high ablation values are extensively covered by permanent wind crust with cracks in polygonal patterns (GPS2, M2, MdPt and D6). Depth hoar layer under well-developed wind crust with cracks clearly indicates prolonged sublimation due to an interruption in accumulation and therefore long, multi-annual, steep temperature-gradient metamorphism (Gow 1965; Watanabe 1978; Goodwin et al. 1994). Wind crusts and snow surfaces have distinctly different albedos, with wind crusts absorbing more solar energy (Frezzotti et al. 2002b; Cagnati et al. 2003). Solar radiation penetrates below the wind crust and warms the subsurface snow layer; this causes an upward transport of water vapour from the subsurface snow layer, condensation of vapour and the growth of loose depth hoar below the crust (Fujii and Kusunoki 1982).

The roughness parameter of wind crust is smaller than that of snow surfaces with sastrugi, dunes and barchans. The lower roughness promotes wind acceleration and divergence of drifting snow (Takahashi et al. 1988). Measurements at the Charcot camp show that snow transportation by saltation starts at wind speeds less than 5 m s^{-1} (Pettré et al. 1986). King and Turner (1997) used Ball's (1960) formula to calculate wind speed as a function of slope gradient and inter-layer potential temperature difference (20 K); wind speeds increase rapidly from 2 to 5 m s^{-1} for slopes between 1 and 2 m km^{-1}. Changes in slope and roughness in the wind direction increase turbulence, thereby increasing the diffusion coefficient and breaking the stable profile of absolute humidity through air mass mixing (Takahashi et al. 1988), which also promotes sublimation of blowing snow.

Eleven metre per second appears to be the threshold wind speed at which the sublimation of blowing snow starts to contribute substantially to katabatic flows in a feedback mechanism (Kodama et al. 1985; Wendler et al. 1993). An increase in drifting snow leads to an increase in air density due to cooling from drifting snow sublimation and to particle incorporation, thus increasing katabatic flow speeds by another 20–30% (Kodama et al. 1985). The threshold wind velocity which differentiates drifting snow (with snow particles moving at low levels) from blowing snow (with snow particles moving at high levels) is 13–14 m s^{-1}. Wind speeds less than 15 m s^{-1} produce transverse features such as ripples, waves and barchans (depositional features), whereas those greater than 15 m s^{-1} produce longitudinal features such as dunes and sastrugi (Kobayashi and Ishida 1979). The extensive presence of erosional (wind crust) and redistribution (sastrugi) features (up to 90%) along the TNB–DC traverse (Frezzotti et al. 2002b) indicates that the threshold wind velocity of 15 m s^{-1} is commonly exceeded over most of the traverse (Fig. 1b).

Surface and blowing sublimation increase with temperature, and blowing sublimation also increases greatly with wind speed. Additional parameters significantly influencing snowdrift sublimation are: turbulence, humidity and friction velocity (Bintanja 1998; Bintanja and Reijmer 2001; Pomeroy 1989). Moreover, high variability of slopes at local scales could drive higher wind turbulence due to changes in SPWD at the kilometre scale. The blowing snow particles are more continuously ventilated on their entire surface in turbulent conditions, and this leads to steeper temperature and humidity profiles, thereby causing higher wind-driven sublimation.

Observations show that the erosion and snowdrift threshold depends on the properties of the snow pack and that it changes as a function of snow metamorphism: the crystal shape of freshly fallen snow does not allow large grain cohesion in snow pack, and this is reflected in relatively high snow mobility values (Gallée et al. 2001). Satellite analysis at TNB (Zibordi and Frezzotti 1996) and field observations along the traverse reveal that the largest blowing snow and sublimation phenomena occur just after snow precipitation, before sintering begins. Very few strong wind events (wind speed higher than 15 m s^{-1}) can greatly increase sublimation through snowdrift, especially during summer.

The maximum value of SA at one site (15 km survey) is very highly correlated with firn temperature and represents the snow precipitation minus sublimation induced by solar radiation during summer.

3.4 Comparison with existing surface mass balance map compilations

The average values of SMB calculated (along 15 km GPR_SA) on the transects at the eight sites (Table 2) were compared with previous SMB map compilations, revealing a general over-estimation of SMB map compilations (Fig. 3). The difference between our data and previous compilations varies on average between 18% (Giovinetto and Zwally 2000) and 65% (Vaughan et al.

1999). The greatest differences are found at the sites from MdPt to DC with lower accumulation (Table 2). Differences between the two map compilations, with a concentration of positive residuals centred at 78°S–140°E, were already observed (Giovinetto and Zwally 2000; Genthon and Krinner 2001). The difference between the two compilations and data collected between DdU and DC is less marked (data are used in the compilations), with values close to survey maximum values (SA). However, values were over-estimated also in this case, with the greatest differences in the Vaughan et al. (1999) compilation. Magand et al. (in press) pointed out analogous overestimation (with an average of about 33%) for the transects along the Wilkes Land. The explanation for the large difference between our results and those reported in the SMB map compilations could be in relation to the following:

– The only accumulation values available in the TNB–DC area before our study were surveyed by the 1959–1960 US Traverse using snow-pit stratigraphy (Stuart and Heine 1961). Some authors (Koerner 1971; Picciotto et al. 1971) compared the accumulation determined by the variation of β-radioactivity with depth with the accumulation rate evaluated from firn stratigraphy in East Antarctica and concluded that the stratigraphic method was basically unreliable in regions of low accumulation and that it overestimated the snow accumulation rate.
– Snow accumulation is assumed close to snow precipitation in the interior of plateau, but our result shows that the sublimation process is underestimated or not even taken into account (e.g. Giovinetto et al. 1992; Genthon and Krinner 2001).

The SMB from European Centre for Medium-Range Weather Forecasts (ECMWF) re-analysis also shows relatively low accumulation rates (e.g. Cullather et al. 1998; Turner et al. 1999; van Lipzig et al. 2002) for this region.

4 Conclusions

This paper reports on a SMB study along the TNB–DC traverse, one of the most unknown areas of East Antarctica. The results provide a new quantification of the impact of surface and blowing sublimation processes on the SMB, its temporal and spatial variability. New data are compared with those of previous SMB studies. The main findings of the paper may be summarised as follows.

Snow precipitation is homogeneous at a large scale (hundreds of km^2), but the wind-driven sublimation phenomena controlled by SPWD have considerable impact on the spatial distribution of snow at short (tens of metre) and medium (kilometre) spatial scales. The maximum value of SA at one site (15 km survey) is very highly correlated with firn temperature and represents the snow precipitation minus ablation not induced by wind. The high variability of SMB is mainly due to ablation processes driven by katabatic winds (wind-driven sublimation); a few strong wind events can greatly decrease the mass through snowdrift sublimation, especially during summer.

Compilation and interpolation maps as done are essential contributions to evaluating the mass balance of the Antarctic ice sheet, however compared to our surface mass balance estimations, previous compilations generally over-estimate SMB, up to 65%. In these previous compilations there are large gaps in the SA observation coverage; this is due to the very sparse distribution and representativeness of in situ SMB measurements (1,860 accumulation data points for about 12 million km^2, i.e. one data point every 6,500 km^2 on average), particularly in East Antarctica. We have shown that single cores are not always representative of an area. An over-estimation of only 10% to entire Antarctica in the SMB is equivalent to 0.5 mm of annual sea level variation. Despite the fact that very large regions are without accumulation at times, the snow radar layers are traceable everywhere and could represent the tools to provide the spatial variability of the entire continent.

Wind-driven ablation greatly affects the SMB, and one of the largest areas of uncertainty regarding present and future SMB calculations is the role of wind-driven sublimation. An increase in snow precipitation coupled with an increase in temperature and/or wind could increase the SMB in the inner part of East Antarctica alone, whereas it could determine a decrease in SMB in the windy areas that represent 90% of the Antarctic surface.

Acknowledgements Research was carried out in the framework of the Project on Glaciology of the PNRA-MIUR and financially supported by PNRA through a co-operation agreement with ENEA Roma. This work is a contribution by the Italian-France branch of the ITASE project and is also supported by the French Polar Institute (IPEV). It is an associate program to the 'European Project for Ice Coring in Antarctica' (EPICA), a joint ESF (European Science Foundation)/UE scientific program. The authors wish to thank all members of the traverse team, the participants in PNRA 1998/99 who assisted at the Zucchelli Station at TNB and Concordia Station and everyone in Italy and France who helped to prepare the traverse. Thanks are due to M. Giovinetto and D. Vaughan, who provided SMB compilations, V. Masson-Delmotte, E. Isaksson and other anonymous reviewers whose comments and editing helped to improve the manuscript.

References

Alley RB (1988) Concerning the deposition and diagenesis of strata in polar firn. J Glaciol 34(118):283–290

Alley RB, Saltzman ES, Cuffey KM, Fitzpatrick (1990) Summertime formation of depth hoar in central Greenland. Geophys Res Lett 17(12):2,393–2,396

Ball FK (1960) Winds on the ice slopes of Antarctica. In: Antarctic meteorology. Pergamon Press, New York, pp 9–16

Bintanja R (1998) The contribution of snowdrift sublimation to the surface mass balance of Antarctica. Ann Glaciol 27:251–259

Bintanja R (1999) On the glaciological, meteorological, and climatological significance of Antarctic blue ice areas. Rev Geophys 37(3):337–359

Bintanja R, Lilienthal H, Tug H (2001) Observations of snowdrift over Antarctic snow and blue-ice surfaces. Ann Glaciol 32:168–174

Bintanja R, Reijmer CH (2001) A simple parameterization for snowdrift sublimation over Antarctic snow surface. J Geophys Res 106(D23):31,739–31,748

Black HP, Budd W (1964) Accumulation in the region of Wilkes, Wilkes Land, Antarctica. J Glaciol 5(37):3–15

Bromwich DH (1988) Snowfall in high southern latitudes. Rev Geophys 26(1):149–168

Bromwich DH, Weaver CJ (1983) Latitudinal displacement from main moisture source controls $\delta^{18}O$ of snow in coastal Antarctica. Nature 30:145–147

Cagnati A, Valt M, Casacchia R, Salvatori R (2003) Snowcover in Antarctica: physical and morphological features of surface layers. Terra Antartica Rep 8:5–10

Cullather RI, Bromwich DH, Van Woert ML (1998) Spatial and temporal variability of Antarctic precipitation from atmospheric methods. J Climate 11:334–367

Ekaykin AA, Lipenkov VYA, Kuzmina IN, Petit JR, Masson-Delmotte V, Johnsen SJ. The changes in isotope composition and accumulation of snow at Vostok Station over the past 200 years. Ann Glaciol 39 (in press)

Fortuin JPF, Oerlemans J (1990) The parameterization of the annual surface temperature and mass balance of Antarctica. Ann Glaciol 14:78–84

Frezzotti M, Flora O (2002) Ice dynamics and climatic surface parameters in East Antarctica from Terra Nova Bay to Talos Dome and Dome C: ITASE Italian Traverses. Terra Antartica 9(1):47–54

Frezzotti M, Gandolfi S, Urbini S (2002a) Snow megadune in Antarctica: sedimentary structure and genesis. J Geophys Res 107(D18):4,344. Doi: 10.1029/2001JD000673

Frezzotti M, Gandolfi S, La Marca F, Urbini S (2002b) Snow dune and glazed surface in Antarctica: new field and remote sensing data. Ann Glaciol 34:81–88

Frezzotti M, Pourchet M, Flora O, Gandolfi S, Gay M, Urbini S, Vincent C, Becagli S, Gragnani R, Proposito M, Severi M, Traversi R, Udisti R, Fily M Spatial and temporal variability of the surface mass balance in East Antarctica from traverse data. J Glaciol (in press)

Fujii Y, Kusunoki K (1982) The role of sublimation and condensation in the formation of ice sheet surface at Mizuho Station, Antarctica. J Geophys Res 87(C6):4,293–4,300

Gallée H (1998) Simulation of blowing snow over the Antarctic ice sheet. Ann Glaciol 26:203–206

Gallée H, Guyomarch G, Brun E (2001) Impact of snow drift on the Antarctic Ice Sheet surface mass balance: possible sensitivity to snow-surface properties. Boundary-Layer Meteorol 99:1–19

Genthon C, Braun A (1995) ECMWF analyses and predictions of surface climate of Greenland and Antarctica. J Climate 8(10):2,324–2,332

Genthon C, Krinner G (1998) Convergence and disposal of energy and moisture on the Antarctic polar cap from ECMWF reanalyses and forecasts. J Climate 11:1,703–1,716

Genthon C, Krinner G (2001) The Antarctic surface mass balance and systematic biases in GCMs. J Geophys Res 106:20,653–20,664

Giovinetto MB, Bromwich DH, Wendler G (1992) Atmospheric net transport of water vapor and latent heat across 70°S. J Geophys Res 97(D1):917–930

Giovinetto MB, Waters NM, Bentley CR (1990) Dependence of Antarctic surface mass balance on temperature, elevation, and distance to open ocean. J Geophys Res 95(D4):3,517–3,531

Giovinetto MB, Zwally HJ (2000) Spatial distribution of net surface accumulation on the Antarctic ice sheet. Ann Glaciol 3:171–178

Goodwin ID, Higham M, Allison I, Jaiwen R (1994) Accumulation variation in eastern Kemp Land, Antarctica. Ann Glaciol 20:202–206

Gow AJ (1965) On the accumulation and seasonal stratification of snow at the South Pole. J Glaciol 5:467–477

Jouzel J, Merlivat L, Petit JR, Lorius C (1983) Climatic information over the last century deduced from a detailed isotopic record in the South Pole snow. J Geophys Res 88(C4):2,693–2,703

King JC, Anderson PS, Mann GW (2001) The seasonal cycle of sublimation at Halley, Antarctica. J Glaciol 47(156):1–8

King JC, Turner J (1997) Antarctic meteorology and climatology. Cambridge University Press, Atmospheric and Space Science Series, Cambridge, p 408

Kobayashi S, Ishida T (1979) Interaction between wind and snow surface. Boundary Layer Meteorol 16:35–47

Kobayashi S, Ishikawa N, Ohata T (1985) Katabatic snow storms in stable atmospheric conditions at Mizuho Station, Antarctica. Ann Glaciol 6:229–231

Kodama Y, Wendler G, Gosink J (1985) The effect of blowing snow on katabatic winds in Antarctica. Ann Glaciol 6:59–62

Koerner RM (1971) A stratigraphic methods of determining the snow accumulation rate at Plateau Station, Antarctica, and application to South Pole—Queen Maud Land traverse 2, 1965–1966. In: Crary AP (ed) Antarctic snow and ice studies II. American Geophysical Union, Washington. Antarctic Res Ser 16:225–238

Liston GE, Winther JG, Bruland O, Elvehoy H, Sand K, Karlof L (2000) Snow and blue-ice distribution patterns on the coastal Antarctic ice sheet. Antarctic Sci 12(1):69–79

Loewe F (1970) Contributions to the glaciology of the Antarctic. J Glaciol 2(19):657–665

Magand O, Frezzotti M, Pourchet M, Stenni B, Genoni L, Fily M Climate variability along latitudinal and longitudinal transects in East Antarctica. Ann Glaciol 39 (in press)

Mayewski PA, Goodwin ID (1999) Antarctic's role pursued in global climate change. Eos Trans 80:398–400

Muszynski I, Birchfield GE (1985) The dependence of Antarctic accumulation rates on surface temperature and elevation. Tellus 37A:204–208

Noone D, Turner J, Mulvaney R (1999) Atmospheric signals and characteristics of accumulation in Dronning Maud Land, Antarctica. J Geophys Res 104(D16):19,191–19,211

Parish TR, Bromwich DH (1991) Continental scale of the Antarctic katabatic wind regime. J Climate 4(2):135–146

Pettré P, Pinglot JF, Pourchet M, Reynaud L (1986) Accumulation in Terre Adélie, Antarctica: effect of meteorological parameters. J Glaciol 32:486–500

Picciotto E, Crozaz G, De Breuk W (1971) Accumulation on the south Pole-Queen Maud Land Traverse, 1964–1968. In: Crary AP (ed) Antarctic snow and ice studies II. American Geophysical Union, Washington. Antarctic Res Series 16:257–291

Pomeroy JW (1989) A process-based model of snow drifting. Ann Glaciol 13:237–240

Pourchet M, Bartarya SK, Maignan M, Jouzel J, Pinglot JF, Aristarain A, Furdada G, Kotlyakov VM, Mosley-Thompson E, Preiss N, Young NW (1997) Distribution and fall out of ^{137}Cs and other radionuclides over Antarctica. J Glaciol 43(145):435–445

Proposito M, Becagli S, Castellano E, Flora O, Gragnani R, Stenni B, Traversi R, Udisti R, Frezzotti M (2002) Chemical and isotopic snow variability along the 1998 ITASE traverse from Terra Nova Bay to DC (East-Antarctica). Ann Glaciol 35:187–194

Rémy F, Testut L, Legrésy B (2002) Random fluctuations of snow accumulation over Antarctica and their relation to sea level change. Climate Dyn 19:267–276

Richardson C, Aarholt E, Hamran SE, Holmlund P, Isaksson E (1997) Spatial snow distribution mapped by radar. J Geophys Res 102(B9):20,343–20,353

Rignot E, Thomas RH (2002) Mass balance of polar ice sheets. Science 297:1,502–1,506

Robin G de Q (1977) Ice cores and climate change. Philos Trans R Soc Lond Ser B 280:143–168

Stearns CR, Weidner GA (1993) Sensible and latent heat flux estimates in Antarctica. In: Bromwich DH, Stearns CR (eds) Antarctic meteorology and climatology: studies based on

automatic weather stations. American Geophysical Union, Washington. Antarctic Res Ser 61:109–138
Stuart AW, Heine AJ (1961) Glaciological work of the 1959–1960 US Victoria Land Traverse. J Glaciol 997–1002
Takahashi S, Naruse R, Masayoshi N, Mae S (1988) A bare ice field in East Queen Maud Land, Antarctica, caused by horizontal divergence of snow. Ann Glaciol 11:150–160
Turner J, Connolley WM, Leonard S, Marshal GJ, Vaughan DG (1999) Spatial and temporal variability of net snow accumulation over the Antarctic from ECMWF re-analysis project data. Int J Climatol 19:697–724
Turner J, Lachlan-Cope TA, Marshall GJ, Morris EM, Mulvaney R, Winter W (2002) Spatial variability of Antarctic Peninsula net surface mass balance. J Geophys Res 107(D13):4,173. DOI 10.1029/2001JD000755
van der Broeke M (1997) Spatial and temporal variation of sublimation on Antarctica: result of a high-resolution general circulation model. J Geophys Res 102:29,765–29,777
van den Broeke MR, Winther JG, Isaksson E, Pinglot JF, Karlof L, Eiken T, Conrads L (1999) Climate variables along a traverse line in Dronning Maud Land, East Antarctica. J Glaciol 45(150):295–302
van Lipzig NPM, van Meijgaard E, Oerlemans J (2002) The spatial and temporal variability of the surface mass balance in Antarctica: result from a regional atmospheric climate model. Int J Climatol 22:1,197–1,217
Vaughan DG, Bamber JL, Giovinetto M, Russell J, Cooper PR (1999) Reassessment of net surface mass balance in Antarctica. J Climate 12:933–946
Watanabe O (1978) Distribution of surface features of snow cover in Mizuho Plateau. Mem Natl Inst Polar Res Spec Issue 7:154–181
Wendler G, André JC, Pettré P, Gosink J, Parish T (1993) Katabatic winds in Adélie Coast. In: Bromwich DH, Stearns CR (eds) Antarctic meteorology and climatology: studies based on automatic weather stations. American Geophysical Union, Washington. Antarctic Res Ser 61:23–46
Whillans IM (1975) Effect of inversion winds on topographic detail and mass balance on inland ice sheets. J Glaciol 14(70):85–90
Young NW, Pourchet M, Kotlyakov VM, Korolev PA and Dyugerov MB (1982) Accumulation distribution in the IAGP area, Antarctica: 90°E–150°E. Ann Glaciol 3:333–338
Zibordi G, Frezzotti M (1996) Orographic clouds in north Victoria Land from AVHRR images. Polar rec 32(183):317–324

M. Frezzotti, M. Pourchet, O. Flora, S. Gandolfi, M. Gay, S. Urbini, C. Vincent, S. Becagli, R. Gragnani, M. Proposito, M. Severi, R. Traversi, R. Udisti, M. Fily. "Spatial and temporal variability of snow accumulation in East Antarctica from traverse data", *Journal of Glaciology*, *Vol.* 51, *N*° 172, 2005.

Spatial and temporal variability of snow accumulation in East Antarctica from traverse data

Massimo FREZZOTTI,[1] Michel POURCHET,[2] Onelio FLORA,[3] Stefano GANDOLFI,[4] Michel GAY,[2] Stefano URBINI,[5] Christian VINCENT,[2] Silvia BECAGLI,[6] Roberto GRAGNANI,[1] Marco PROPOSITO,[1] Mirko SEVERI,[6] Rita TRAVERSI,[6] Roberto UDISTI,[6] Michel FILY[2]

[1]*ENEA, Centro Ricerche Casaccia, PO Box 2400, I-00100, Rome, Italy*
E-mail: frezzotti@casaccia.enea.it
[2]*Laboratoire de Glaciologie et Géophysique de l'Environnement, CNRS–UJF, 54 rue Mollère, BP 96, 38402 Saint-Martin-d'Hères Cedex, France*
[3]*Dipartimento di Scienze Geologiche, Ambientali e Marine, Università di Trieste, Via E. Weiss 6, Trieste, Italy*
[4]*DISTART, Università di Bologna, Viale Risorgimento 2, 1-40B6 Bologna, Italy*
[5]*Istituto Nazionale di Geofisica e Vulcanologia, Via de Vigna Murata 605, I-00143 Rome, Italy*
[6]*Dipartimento di Chimica, Università degli Studi di Firenze, Via della Lastruccia 3, I-50019 Sesto Fiorentino (Florence), Italy*

ABSTRACT. Recent snow accumulation rate is a key quantity for ice-core and mass-balance studies. Several accumulation measurement methods (stake farm, fin core, snow-radar profiling, surface morphology, remote sensing) were used, compared and integrated at eight sites along a transect from Terra Nova Bay to Dome C, East Antarctica, to provide information about the spatial and temporal variability of snow accumulation. Thirty-nine cores were dated by identifying tritium/β marker levels (1965–66) and non-sea-salt (nss) SO_4^{2-} spikes of the Tambora (Indonesia) volcanic event (1816) in order to provide information on temporal variability. Cores were linked by snow radar and global positioning system surveys to provide detailed information on spatial variability in snow accumulation. Stake-farm and ice-core accumulation rates are observed to differ significantly, but isochrones (snow radar) correlate well with ice-core derived accumulation. The accumulation/ablation pattern from stake measurements suggests that the annual local noise (metre scale) in snow accumulation can approach 2 years of ablation and more than four times the average annual accumulation, with no accumulation or ablation for a 5 year period in up to 40% of cases. The spatial variability of snow accumulation at the kilometre scale is one order of magnitude higher than temporal variability at the multi-decadal/secular scale. Stake measurements and firn cores at Dome C confirm an approximate 30% increase in accumulation over the last two centuries, with respect to the average over the last 5000 years.

INTRODUCTION

Antarctica is the highest and flattest of the Earth's continents, but small changes in slope have a strong impact on wind direction and speed (Frezzotti and others, 2002a). It is well known that slope and curvature play an important role in the accumulation of snow; for example, concave depressions accumulate snow relative to convex bumps (Black and Budd, 1964; Whillans, 1975; Pettré and others, 1986; Van den Broeke and others, 1999; Liston and others, 2000; Frezzotti and others, 2002a). A large area of the polar plateau, where the slope along the wind direction is larger than 4 m km^{-1}, has a nil or slightly negative snow accumulation (Frezzotti and others, 2002b).

The spatial scale of significance for a single ice-core record is a critical point in stratigraphic interpretation itself. Micro-relief introduces a high-frequency, quasi-stochastic variability into ice-core records of annual layer thickness (Fisher and others, 1985; Van der Veen and Bolzan, 1999).

The stratigraphic record of an ice core is affected by the flow of ice, so the material at depth is slowly moved away from the original deposition site. Richardson and Holmlund (1999) demonstrate the importance of determining the spatial significance of cores and recommend radar surveys prior to drilling. Snow radar is the most useful tool for detecting spatial snow accumulation variability, and firn-core time series have the best temporal resolution. Accumulation variability along the radar profile can be derived using both datasets.

Ablation processes on short (metre) and long (kilometre) spatial scales have a significant impact on post-depositional losses of chemical species by re-emission (Waddington and Cunningham, 1996; Wagnon and others, 1999) and on the interpretation of ice-core palaeoclimatic time series (Fisher and others, 1985). Interpretation and dating of palaeoenvironmental records extracted from Antarctic ice cores depends on the knowledge of past accumulation changes (e.g. Bromwich and Weaver, 1983; Jouzel and others, 1983).

As part of the ITASE (International Trans-Antarctic Scientific Expedition) project (Mayewski and Goodwin, 1999) and in the framework of the Franco-Italian Concordia Station collaboration, a traverse between Terra Nova Bay (TNB) and Dome C (DC), and research at DC were undertaken between 1998 and 2000. The study aimed to better understand latitudinal and longitudinal environmental gradients, while documenting climatic, atmospheric and surface conditions over the last 200–1000 years in the eastern and northeastern portions of the DC drainage area and in northern Victoria Land. The traverse (Frezzotti and Flora, 2002) started from GPS1 (74°50.04′ S 160°48.03′ E) on

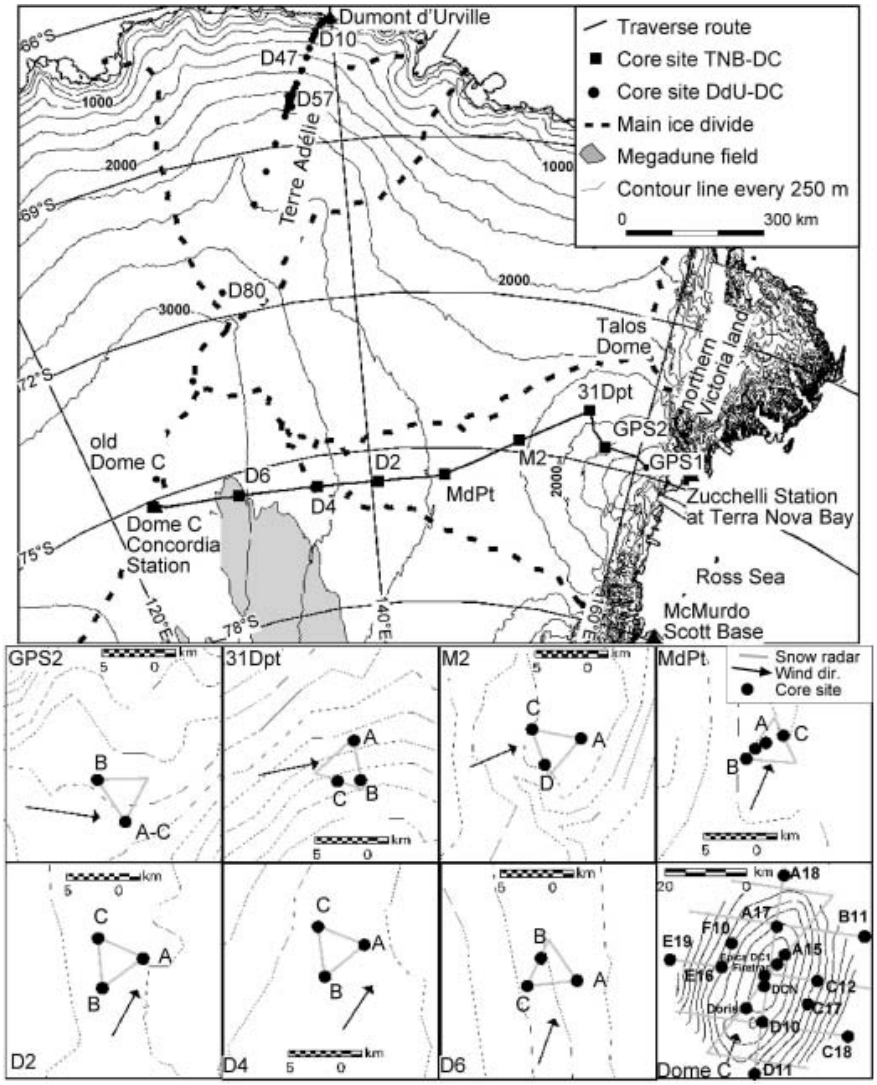

Fig. 1. Schematic map of the traverse from TNB to DC and site locations, and detailed maps of drill sites (contour every 10 m for GPS2, 31Dpt, M2, MdPt, D2, D4, D6, from Rémy and others, 1999); contour every 1 m for DC, from Capra and others (2000); prevalent wind direction from Frezzotti and others (2002b).

19 November 1998, reaching Concordia Station at DC (75°06′ S 123°23′ E, 3232 m) on 5 January 1999; a distance of 1300 km was covered (Fig. 1). The party performed several tasks (drilling, glaciological and geophysical exploration, etc.) during the traverse (Frezzotti and Flora, 2002; Gay and others, 2002; Proposito and others, 2002; Becagli and others, 2003; Traversi and others, 2004). GPR (ground penetrating radar or snow radar), GPS (global positioning system) and snow morphology surveys were carried out regularly along the traverse (Frezzotti and others, 2002a, b). In addition, shallow ice cores were drilled within a 25 km radius of Concordia Station between 15 and 25 December 1999 (Vincent and Pourchet, 2000). In 2000, GPR and GPS surveys, covering a total distance of about 500 km, were used to link all core sites to DC in order to provide detailed information on the spatial variability of snow accumulation.

This paper combines geophysical surveys (GPR and GPS), field and remote-sensing surface observations, and firn-core analyses to describe the snow accumulation variability at seven locations along the traverse and at DC. It also provides new information on the snow accumulation process and discusses implications for palaeoclimatic series from ice cores. Using these data, Frezzotti and others (2004) provide new information on the surface mass-balance process and implications for surface mass-balance distribution and variability.

METHODOLOGY

Twenty-three shallow snow–firn cores, up to 53 m deep, were drilled during the traverse at eight sites between TNB and DC (at intervals of 90–150 km); 16 more were drilled at DC using an electromechanical drilling system (Table 1). At seven sites a 43–53 m deep 'main core' was drilled at the site camp and two 7–15 m deep 'secondary cores' were drilled 5–7 km away. The location of the secondary sites was identified in the field after a detailed GPS–GPR profile along a 15 km triangular track (Fig. 1). Data processing in the field was used to identify variability in the internal layering of the snowpack. Snow temperature profiles, down to 30 m depth, were measured at main core sites after a 15–24 hour equilibration period (Frezzotti and Flora, 2002). Snow/firn density was determined immediately after retrieval by measuring and weighing core sections. Snow was poorly sintered in the uppermost layers; density was thus measured in a pit (close to main core and stake farm) where stratigraphic studies and snow sampling were also performed (Gay and others, 2002).

Table 1. Location, morphological and climatological characteristic of drill sites; snow accumulation from stake farms, core analyses, and comparison with GPR data (GPR_SA). GPR_SA value are reported as snow accumulation using the depth/age ratio from the 'main' core Tritium snow accumulation (Tambora for D4) and depth in % respect to the maximum depth of layering used for the statistical analysis. Katabatic wind speed from Parish and Bromwich (1991)

Site	Lat. S	Long. E	Elevation	Depth	T –15 m	Slope direction	Wind direction	Katabatic wind speed	Stake 1998–2002	β 1966–98 β 1955–98† Tritium 1965–98	$nssSO_4^{2-}$ Tambora 1816–1998	$nssSO_4^{2-}$ Tambora unknown 1810–16	GPR_SA unknown Tambora
			m WGS84	m	°C	°	°	$m\,s^{-1}$	$kg\,m^{-2}a^{-1}$	$kg\,m^{-2}a^{-1}$	$kg\,m^{-2}a^{-1}$	$kg\,m^{-2}a^{-1}$	$kg\,m^{-2}a^{-1}$ (%)
GPS1								>18					
Core A	74°48.94′	160°39.60′	1192	12.0	–32.7				–	58±2.9*	–	–	–
Core B	74°48.94′	160°39.60′	1192	8.0		–			–	47±4.7	–	–	–
GPS2								>18					
Core A	74°38.69′	157°30.13′	1804	43.6	–38.5	132	80		55 (1993–2000)	54±2.7*	60±3.0	161±16.1	54 (27%)
Core B	74°36.81′	157°22.80′	1810	11.4	–	132	80		–	137±13.7	–	–	200 (100%)
Core C	74°38.69′	157°30.13′	1804	8.0	–	132	80		–	62±6.2	–	–	54 (27%)
31Dpt								12–18					
Core A	74°01.52′	155°57.6′	2069	48.0	–41.8	158	72		98	112±5.6*	98±4.9	86±8.6	112 (77%)
Core B	74°03.51′	156° 0.64′	2040	16.2	–	158	72		–	137±13.7*	–	–	145 (100%)
Core C	74°03.80′	155°55.99′	2041	7.4	–	158	72		–	–	–	–	97 (67%)
M2								12–18					
Core A	74°48.27′	151°16.17′	2278	49.5	–44.5	162	62		8.5	15±7.5*	17±0.8	19±1.9	15 (14%)
Core D	74°49.86′	151°09.13′	2265	12.0	–	111	62		–	82±8.2	–	–	107 (100%)
Core C	74°48.01′	151°05.91′	2272	8.0	–	247	62		–	44±4.4	–	–	61 (57%)
MdPt								12–18					
Core A	75°32.16′	145°51.43′	2454	44.5	–47.8	78	32		47	45±2.7*	36±1.8	42±4.2	45 (60%)
Core B	75°33.03′	145°47.31′	2460	12.5	–	78	32		–	11±1.1	–	–	13 (18%)
Core C	75°31.74′	145°55.35′	2452	7.0	–	78	32		–	60±6.0	–	–	75 (100%)
D2								6–12					
Core A	75°37.33′	140°37.84′	2479	49.0	–48.4	89	37		30	31±1.6*	20±1.0	23±2.3	31 (94%)
Core B	75°38.76′	140°28.61′	2482	12.5	–	89	37		–	40±4.0†	24±1.4	–	33 (100%)
Core C	75°36.06′	140°28.54′	2483	8.5	–	89	37		–	38±3.8	–	–	29 (87%)
D4								6–12					
Core A	75°35.88′	135°49.89′	2793	43.0	–50.5	116	42		29	–	22±1.1	77±7.7	22 (79%)
Core B	75°37.13′	135°40.43′	2795	12.3	–	116	42		–	29±2.9	–	–	28 (100%)
Core C	75°34.43′	135°40.74′	2798	9.0	–	116	42		–	20±2.0	–	–	22 (72%)
D6								6–12					
Core A	75°26.85′	129°48.53′	3027	52.7	–51.0	97	46		39	29±1.4*	36±1.8	37±3.7	29 (85%)
Core B	75°25.19′	129°42.41′	3035	12.3	–	97	46		–	38±3.8	–	–	34 (100%)
Core C	75°26.42′	129°38.04′	3038	9.0	–	97	46		–	22±2.2	–	–	16 (46%)
Dome C							40	<6	39 (1969–99)				
EPICA-DC1	75°06.06′	123°20.86′	3233										
FIRETRAC	75°06.06′	123°20.86′	3233		–54.5				–		24±1.2	32±3.2	
DCN	75°07.32′	123°18.72′	3233	42.3	–55.0				–	29±1.5*	27±1.4	27±2.7	
DC-1 A17	75°00.53′	123°36.26′	3233	18.0	–				–	26±1.3*	25±1.3	30±3.0	
DC-2 E16	75°02.86′	123°01.95′	3230	18.0	–				–	27±1.4*	25±1.3	28±2.8	
DC-3 D10	75°11.68′	123°11.13′	3233	20.0	–				–	26±1.3*	26±1.3	32±3.2	
DC-4 C12	75°09.29′	123°45.51′	3229	18.0	–				–	23±1.2*	25±1.3	25±2.5	
DC-A18	74°54.55′	123°49.85′	3226	6.61	–				–	32±3.2	–	–	
DC-DORIS	75°09.16′	123°05.92′	3232	6.59	–				–	33±3.3	–	–	
DC-B11	75°05.99′	124°15.97′	3225	6.40	–				–	29±2.9	–	–	
DC-F10	75°00.50′	123°11.30′	3230	6.38	–				–	29±2.9	–	–	
DC-DAU	75°17.72′	122°57.04′	3233	5.85	–				–	29±2.9	–	–	
DC-E19	74°59.31′	122°38.83′	3223	6.60	–				–	30±3.0	–	–	
DC-A17	75°00.53′	123°36.26′	3232	6.44	–				–	29±2.9	–	–	
DC-D11	75°17.71′	122°57.45′	3230	6.56	–				–	27±2.7	–	–	
DC-A15	75°17.71′	122°56.66′	3233	6.62	–				–	30±3.0	–	–	
DC-C17	75°12.52′	123°23.65′	3229	6.60	–				–	26±2.6	–	–	
DC-C18	75°17.51′	123°49.83′	3221	6.59	–				–	28±2.8	–	–	

Two reference tritium peak levels resulting from 1965 and 1966 thermonuclear atmospheric bomb tests (Picciotto and others, 1971; Jouzel and others, 1979) and the volcanic sulphate signals of the Tambora (Indonesia) eruption (AD 1815) and of an unknown volcanic event (AD 1809) were used to determine the mean accumulation rate at the 'main' cores along the traverse and at DC (Table 1). Tritium depth profiles were transformed into time series by comparing them with the tritium content of precipitation at the Kaitoke (New Zealand) International Atomic Energy Agency station. In Antarctic ice cores the peaks in SO_4^{2-} signatures of Tambora and unknown are dated 1816 and 1810, and represent the most reliable volcanic markers for dating the last two centuries (e.g. Legrand and Delmas, 1987; Dai and others, 1991; Cole-Dai and others, 1997; Udisti and others, 2000; Stenni and others, 2002). The volcanic signal was obtained from sulphate profiles. No correction for sea-salt sulphate was made because its contribution is always <15% (Becagli and others, 2003). Analytical procedures for chemical and tritium measurements are described in detail elsewhere (Udisti and others, 1994; Gragnani and others, 1998; Stenni and others, 2002).

The β-radioactive reference horizons of January 1955 and January 1965 were used to determine the mean accumulation rate from 'secondary' cores along the traverse and from 6 m deep cores at DC (Table 1), using methods described in Pourchet and others (1983).

The experimental error ($\pm\sigma_e$) in the calculated snow accumulation rates for the different periods is estimated to be of the order of <10% for β radioactivity (1955/65–98), about 10% for the unknown–Tambora period (1810–16) and <5% for the tritium (1966–98) and Tambora–present (1816–1998) periods. These values take into account the different sources of error linked to density determination and the sampling resolution (20–40 cm for β, 3–5 cm for tritium, 2.5–4 cm for SO_4^{2-}).

At seven locations, farms consisting of 40 stakes, centred on the main core site, were geometrically positioned about

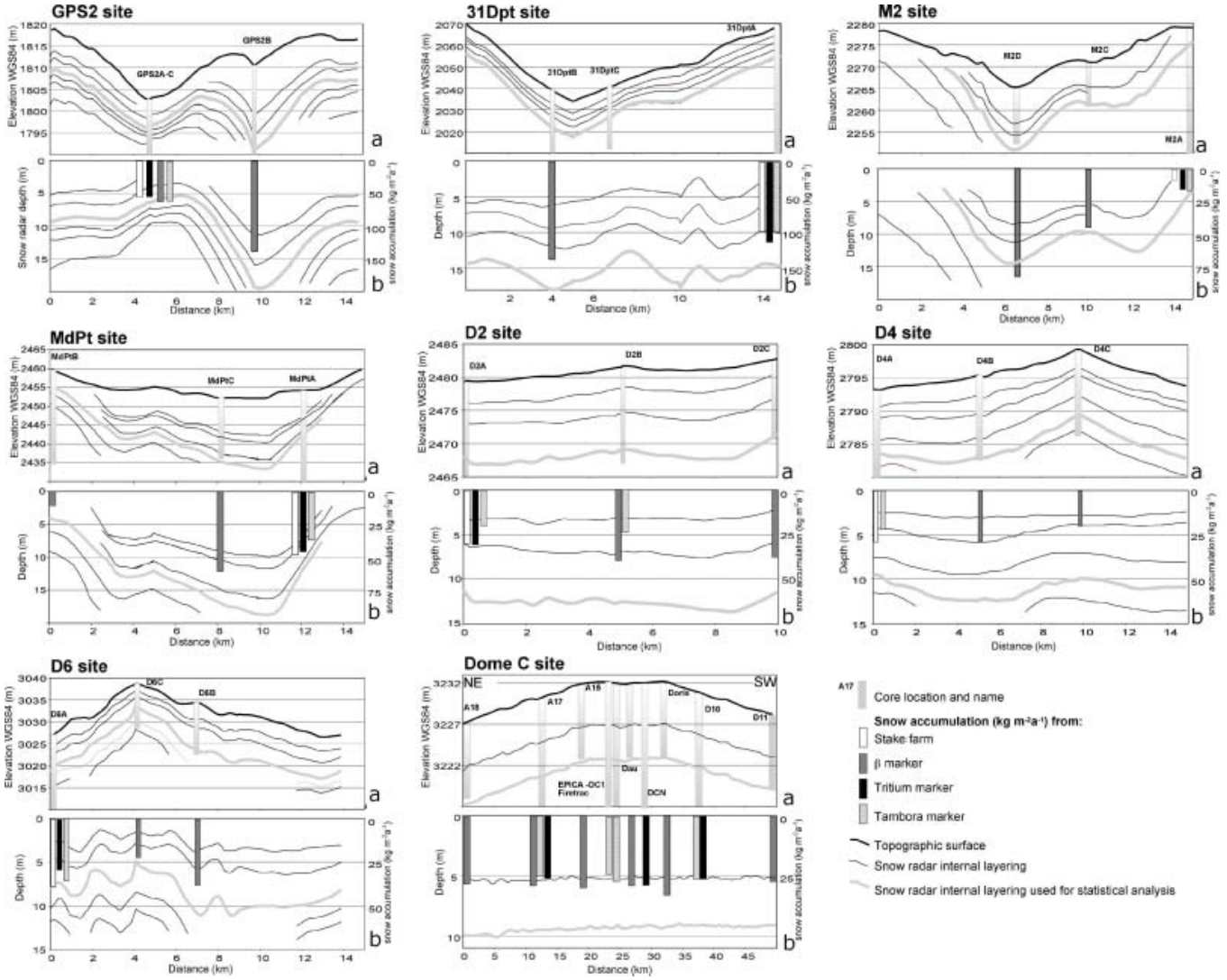

Fig. 2. (a) Core location and elevation of GPR selected horizons and surface profiles; (b) depth profile of GPR selected horizons and snow accumulation from firn cores using different methods.

Table 2. Stake farm results and surface morphology conditions at main core sites. The height of the stakes was measured at middle point (MdPt) in 1998, 1999, 2000, 2001 and 2002, at DC in 1996, 1999, at others sites (31Dpt, D2, D4, D6) in 1998, 2000 and 2002, at M2 in 1998 and 2002, and at GPS2 in 1993, 1996, 1998 and 2000

Site	Average snow accumulation, 1998–2000	Std. dev., 1998–2000	Number of stakes without accumulation or with ablation, 1998–2000	Average snow accumulation	Std. dev. 1998–2002	Number of stakes without accumulation or with ablation, 1998–2002	Surface morphology	Sastrugi average height	Sastrugi maximum height
	$kg\,m^{-2}\,a^{-1}$	%	%	$kg\,m^{-2}\,a^{-1}$	%	%		cm	cm
31Dpt	105.0	22	0	98.4	13	0	Sastrugi	5	10
M2	–	–	–	8.5	144	40	Wind-crust sastrugi	15	30
MdPt	47.4	65	11	46.7	40	3	Sastrugi	30	70
D2	31.8	99	19	30.4	67	14	Wind-crust sastrugi	10	70
D4	38.7	48	6	29.3	36	0	Deposition form	20	40
D6	38.0	72	9	39.3	78	9	Deposition form and sastrugi	30	150
Dome C 1996–99	–	–	–	39.0	36	0	Deposition form	10	30

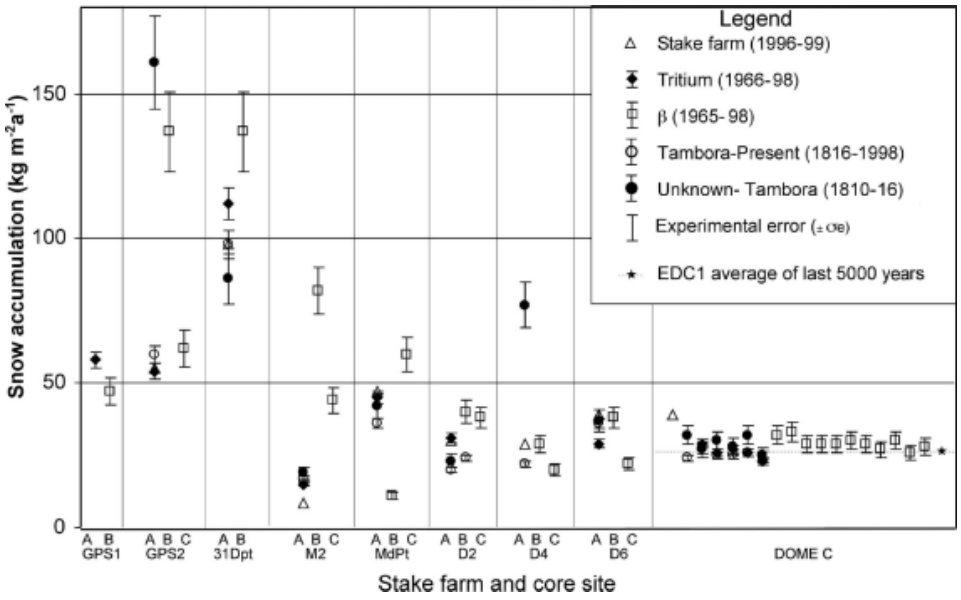

Fig. 3. Snow accumulation rates at core sites using stake farms and different stratigraphic markers.

100 m apart forming a cross with an area of 4 km^2 (Table 1). At DC, a total of 37 stakes were geometrically positioned at a radius of 3, 6, 12 and 25 km from the centre of DC. Stake heights were measured between 1996 and 2002 (Table 2). The snow accumulation at the stakes was multiplied by the snow density measured in a pit up to 2.5 m deep to obtain water equivalent values. At DC an average snow accumulation value of 340 mm of snow (39 kg m^{-2} a^{-1}), with a standard deviation of 125 mm (14 kg m^{-2} a^{-1}), was measured during the 1996–99 period at the stakes. The absolute elevations of the stakes (measured by GPS) change uniformly, with an average value of 0.9 cm and standard deviation of 0.9 cm during the 1996–99 period (Vittuari and others, 2004). The uniform decrease in elevation (0.9 ± 0.9 cm) with respect to the snow accumulation value (340 mm) indicates that the stakes are anchored to the stake bottom. Although snow compaction was not taken into account when calculating snow accumulation, it has often been found to be negligible for accumulation estimation at low-accumulation sites (Lorius, 1983). Snow accumulation variability at stake farms is investigated to determine how representative the results interpreted from a single core might be (Palais and others, 1982).

The integration of GPS and GPR data yields the ellipsoidal height of both the topographic surface and firn stratigraphy (Table 1; Fig. 2). GPS and GPR surveys and subsequent analyses are described elsewhere (Urbini and others, 2001; Frezzotti and others, 2002a). Data acquisition was performed with a Geophysical Survey Systems Inc. Sir10B unit equipped with one monostatic antenna with a central frequency of 400 MHz. Principal acquisition parameters were 150 ns for the vertical investigation range (15–20 m) and 1–5 scan s^{-1} for the acquisition rate, i.e. about one scan every 2–3 m (with the acquisition rate at 1 scan s^{-1}) and 0.4–0.7 m (with the acquisition rate at 5 scan s^{-1}). To determine travel times of electromagnetic waves, the depth–density/depth–speed relation for the snowpack was established using the density profile of three firn cores and one pit in each triangular area along the traverse, and using 17 firn cores and one pit at DC. Density data for each site were fitted with second-order polynomial functions, yielding a correlation coefficient of $R^2 > 0.9$. To facilitate comparison between firn cores and GPR records, the eight calculated polynomial functions were used to convert firn depths in the seven triangular areas and at DC into water equivalent depths. The depth of the GPR layer was then converted into snow accumulation (GPR_SA) using the depth/age ratio from the 'main' core tritium snow accumulation. Snow accumulation data derived from core records are in good agreement with data derived from GPR_SA (Table 1). In line with other authors (e.g. Richardson and others, 1997; Vaughan and others, 1999; Spikes and others, 2004), we assume that the layers producing strong radar reflections are isochronal.

Differences in snow accumulation between the main cores and the secondary cores (Figs 2 and 3) are equally reflected in tritium/β marker and GPR data (Table 1). The two methods yield different results because they sample different areas: the core diameter is 7–10 cm, while GPR works at the metre scale. Major differences between the results of the two methods (core and GPR) are found in regions of large spatial variability in accumulation (GPS2, M2 and MdPt sites). The maximum difference between core and GPR (20%), and the highest GPR relative standard deviation (47%) are found at site GPS2. GPS2A and GPS2C cores were drilled a few tens of metres apart and show a 13% difference in accumulation for the tritium/β marker horizons (Figs 1–3; Table 1). In contrast, the lowest standard deviation was obtained at DC (3%).

Topographic characterization of each site (elevation, slope, etc.) was performed using the European Remote-sensing Satellite-1 (ERS-1) radar altimeter digital terrain model, with a grid spacing of 1 km, provided by Rémy and others (1999). A 3 × 3 pixel window was used to calculate the slope of each grid using the digital terrain model.

RESULTS

Core sites morphological and climatological characteristics

Meteorological data and a continental-scale simulation of the surface wind field (Parish and Bromwich, 1991) show

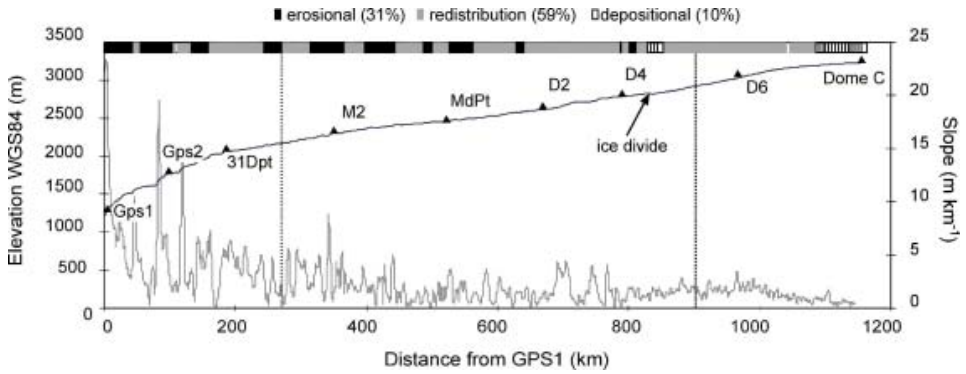

Fig. 4. Surface elevation (solid line), terrain slope (grey line) and micro-relief distribution along TNB–DC traverse. Core sites are indicated with triangles.

that the area between TNB and DC is characterized by a katabatic wind flow, with speeds ranging from <6 to >18 m s^{-1} (Table 1).

The topographic profile of the traverse indicates three sectors (Fig. 4): an area extending about 250 km from GPS1 (slope area), characterized by a large slope of up to 25 m km^{-1}, a second area (plateau area) up to about 900 km, with a slope of up to 4.5 m km^{-1}, and the dome area in the last 250 km, with a slope of <2 m km^{-1}. The slope profile shows very high variability in the first and second areas, and a nearly constant slope in the third area (Frezzotti and Flora, 2002). The surface morphology in the slope and plateau areas is very irregular and can be linked mainly to flow over undulations in the bedrock morphology and secondarily to environmental conditions (wind and accumulation). In the dome area, surface variability is derived mainly from environmental conditions and secondarily from the bedrock morphology. Only the megadunes in the dome area, close to D6 (Fig. 1), show a pattern of regular oscillation of the surface (Fahnestock and others, 2000). Megadune formation can be explained by a cyclic variation of the erosion and redistribution process of snow along a slope by an atmospheric wave, with the atmospheric wavelength the same order of magnitude as the megadune (Frezzotti and others, 2002a).

Analysis of the morphological conditions of the region shows that (Figs 1 and 2; Table 1):

GPS2, M2 and MdPt are characterized by relatively complex morphologies with 'abrupt' changes in slope and wind direction;

31Dpt area contains relatively 'steep' slopes (>4 m km^{-1}), but the wind direction is close to the direction of elevation contours, and the slope in the wind direction is therefore very low;

D2 and D4 present low slopes, with a 50–65° angle between the wind direction and the direction of the general surface slope; the D6 core site is located just a few kilometres leeward of the megadune field (Frezzotti and others, 2002a);

DC has the lowest slope, and the major axis of the dome is aligned in the direction of the prevailing wind.

Micro-relief along the TNB–DC traverse consists (Fig. 4) of 31% erosional features (wind crust), 59% redistribution features (sastrugi) and only 10% depositional features (Frezzotti and others, 2002b). The micro-relief characteristics of core sites (5 km apart), where topography is 'relatively complex' (GPS2, M2 and MdPt), are very different (Figs 1 and 2; Table 1). The D2 and 31Dpt areas are characterized by the alternation of sastrugi fields with sporadic longitudinal dunes (10–20 m long, a few metres wide and up to 1 m high), and by seasonal wind crust with sporadic sastrugi. Depositional micro-relief occurs extensively only in the D4 area, a point close to the David Glacier ice divide, and near DC (Frezzotti and others, 2002b). The GPS2A, M2A and MdPtC core sites are characterized by the extensive presence of wind crust, consisting of a single snow-grain layer cemented by thin (0.1–2 mm) films of ice, with cracks (up to 2 cm wide) and polygonal pattern. Wind crusts form on the surface due to the kinetic heating of saltating snow under constant katabatic wind flow (Goodwin, 1990) and the condensation–sublimation process on both sides of the crust (Fujii and Kusunoki, 1982). Larger grain-sizes are found at the GPS2A, M2A and MdPtC sites. At other sites smaller grains are found in sastrugi or depositional areas (31DptA, MdPtA, D2A, D4A, D6A and DC). Sites MdPtC and MdPtA are only 5 km apart (Fig. 1) but show quite different grain-size profiles, in terms of both mean values and variability (Gay and others, 2002). The MdPtA site contained sastrugi up to 20 cm high, but no permanent wind crust. The large difference in grain-size at the two sites is due to different local-scale snow accumulation processes.

Local spatial variability of snow accumulation

The accumulation/ablation pattern derived from the stake-farm measurements shows large standard deviations (Table 2), and largely reflects snow surface roughness (sastrugi) and/or an interruption in accumulation (wind crust) at the sites. This variability or 'noise' is important, and limits the degree to which a single annual snow accumulation value may be temporally representative (Fisher and others, 1985). Analysis of the MdPt stake-farm data surveyed each year from 1998 to 2002 reveals local-scale spatial variability, suggesting that the annual local noise (metre scale) in snow accumulation could be between ~2 and 4 times the mean snow accumulation, with accumulation $\leq$0 for 32% of annual-scale observations.

It appears that stake measurements and surface morphology are strongly related at all sites. The lowest standard deviation values are present when the slope along prevalent wind direction (SPWD) is low (31Dpt, D4

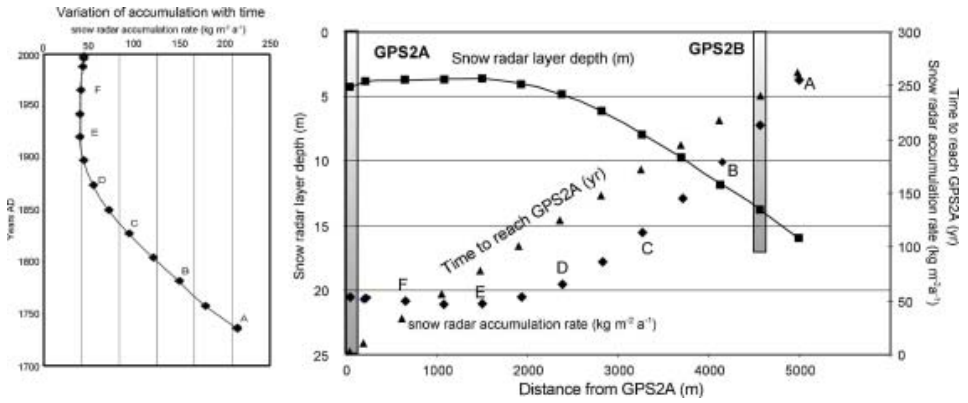

Fig. 5. 'Simulation' of snow accumulation rate at GPS2A core using snow-radar, ice velocity and core analyses.

and DC). In contrast, site M2, with a high SPWD variability, shows the lowest accumulation value and the highest standard deviation of 144%, with accumulation ≤ 0 for a 5 year period in 40% of cases. We generally obtained the same mean value for a 5 year period but a much lower variability between individual points, thus concurring with the observation at the old Dome C (Palais and others, 1982; Petit and others, 1982). Ekaykin and others (2004) pointed out that at Vostok the period of smoothing necessary to suppress the noise, due to micro-relief, was estimated to be 7 years both for snow accumulation and for δD time series. This is because the mean surface roughness tends to be conserved, implying a preferential deposition of snow at low-level points and erosion of sastrugi (Gow, 1965; Petit and others, 1982; Alley, 1988).

Temporal variability in snow accumulation and ice-core interpretations

The analysis of spatial variability in snow accumulation at different sites along the traverse also shows an extremely high variability of snow accumulation at the local (km) scale, particularly for sites with a standard deviation in snow accumulation greater than 10% of the mean value (GPS2, M2, MdPt, D6). Tables 1 and 3 show that snow accumulation variability reaches an order of magnitude in a single core (e.g. M2A and GPS2A). Table 1 and Figure 3 show that snow accumulation variability changes with depth (difference between stakes and Tambora accumulation) and reaches an order of magnitude in a single core. The very high spatial variability in snow accumulation may influence the interpretation of firn-/ice-core records. This is clear when looking at the GPS2A and GPS2B data. GPS2A and GPS2B cores are located along a flowline and the distance between the two core sites is about 5 km (Fig. 1). Snow deposited at GPS2B reaches GPS2A after about 250 years (ice velocity 19 m a^{-1}; Vittuari and others, 2004). GPR and core analyses reveal (Figs 2 and 3; Table 1) that snow accumulation at site GPS2B is three times higher (137 kg m^{-2} a^{-1}) than at site GPS2A (54 kg m^{-2} a^{-1}). A simple one dimensional (1-D) model can be used to calculate past accumulation rates at GPS2A using the snow accumulation rate derived from GPR, the depth–age function of firn cores and ice velocity. The 1-D model allows evaluation of the submergence velocity (or burial rate) of the surface and 'simulation' of the snow accumulation rate at core GPS2A (Fig. 5). We did not take into account layer thinning due to vertical strain, because the ratio of the investigated layer depth (20 m) to the entire ice thickness (>3000 m; Testut and others, 2000) is <1% and is therefore negligible. Other reasons to neglect strain thinning include the very small strain rates that are present in this part of the ice sheet, and the short duration (~250 years) of the records over which to accumulate this strain. The analysis of snow accumulation (stakes, tritium, Tambora, unknown) reveals an increase in accumulation with depth (1965–present: 54 kg m^{-2} a^{-1}; unknown–Tambora: 161 kg m^{-2} a^{-1}); 'simulation' and present snow accumulation values at GPS2B are very similar, showing that the core variability is due to a spatial variability and not a temporal variability.

Table 3. Spatial variability in surface mass balance from GPR calibrated using accumulation at the main core

Site	Average	Std. dev.	Spatial variability of surface mass balance from GPR* Std. dev.	Min	Max	Max – Min	Max – Min
	kg $m^{-2}a^{-1}$		%	kg $m^{-2}a^{-1}$	kg $m^{-2}a^{-1}$	kg $m^{-2}a^{-1}$	%
GPS2	93	44	47	45	201	156	78
31Dpt	108	11	10	86	128	42	33
M2	76	26	34	17	115	98	85
MdPt	38	14	37	10	59	48	82
D2	43	2	5	37	46	9	20
D4	26	2.5	9	22	30	8	26
D6	29	7	24	17	41	24	58
Dome C*	26	0.8	3	25	28	3	12

* Spatial variability has been evaluated along 15 km profile for each site along the traverse and along a 100 km profile at Dome C.

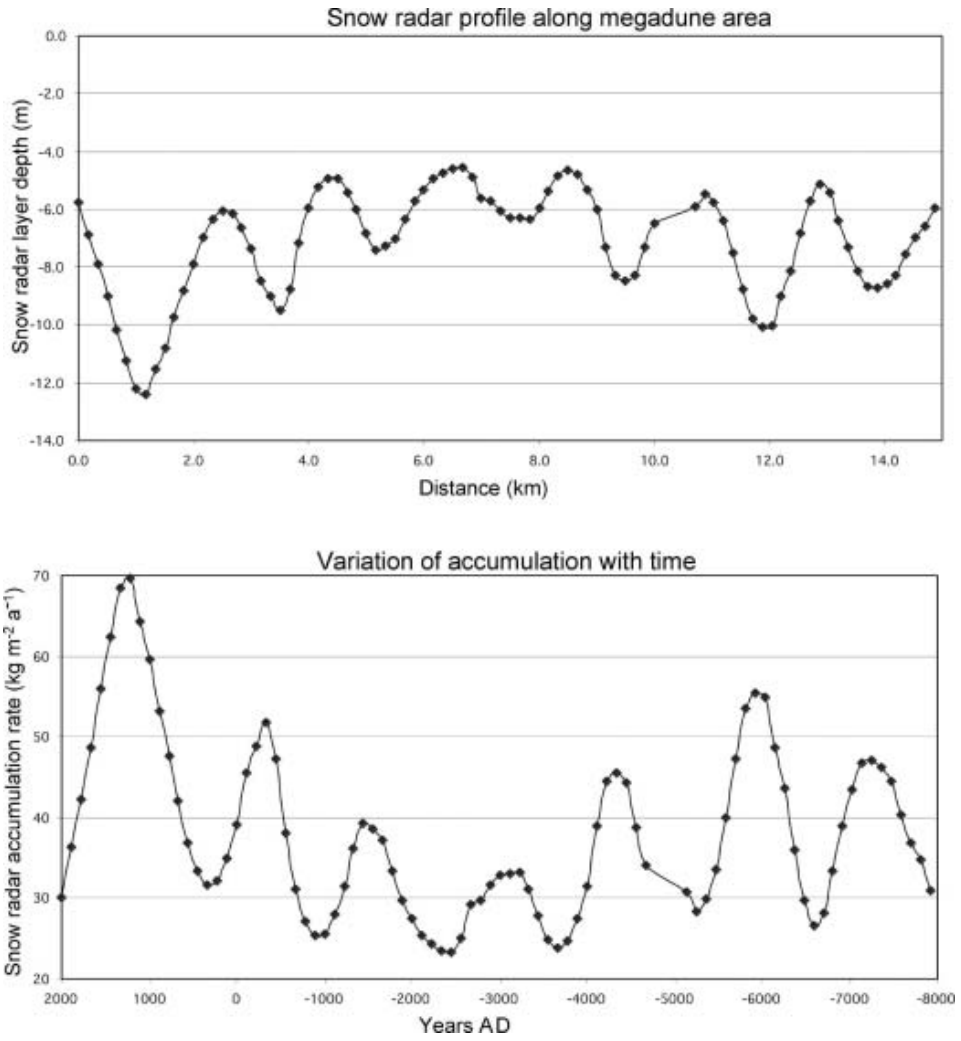

Fig. 6. 'Simulation' of snow accumulation rate at D6A core using snow-radar and core analyses.

Core site D6 is downstream of a field of megadunes with wavelengths of about 2–3 km and amplitudes of 2–4 m (Frezzotti and others, 2002a). Accumulation in this area is about 30 kg m^{-2} a^{-1}, which is too low to allow identification of seasonal signals in the isotope-chemistry stratigraphy of the firn core. A GPR profile 45 km west of D6 follows the ice-flow direction in the megadune area and reveals the presence of buried megadunes. As for GPS2, the 1-D model (GPR and ice velocity: 1.5 m a^{-1}; Vittuari and others, 2004) can be used to estimate the snow accumulation rate in the megadune area (Fig. 6). The 'simulated' accumulation rate shows a periodic variation of about 1500 years, with a standard deviation in the snow accumulation rate of about 28%.

The sites with <10% standard deviation (31Dpt, D2 and D4) show an increase in accumulation (14–55%) between Tambora–present (1816–1998) and tritium/β–present (1966–98; Table 1). Also DC shows a clear increase in accumulation from the Tambora marker (average 25.3 ± 1 kg m^{-2} a^{-1}) to tritium/β (average 28.3 ± 2.4 kg m^{-2} a^{-1}) to the stake farm (average 39 kg m^{-2} a^{-1} with a standard deviation of 14 kg m^{-2} a^{-1}). With respect to the Tambora marker, stake-farm values show a 30% increase in accumulation during the 1996–99 period. The tritium/β marker also records about a 10% increase. Based on the age–depth scale from the EPICA (European Project for Ice Coring in Antarctica) DC1 core, the accumulation average over the last 5000 years is 26.6 kg m^{-2} a^{-1}, with a standard deviation of 1.0 kg m^{-2} a^{-1} (Schwander and others, 2001).

DISCUSSION

The reconstruction of past climates based on ice-core data from areas with high accumulation spatial variability can be distorted. Processes induced by snow accumulation spatial variability that occur mainly in porous snow (depth hoar) under wind crust, such as:

mass exchange by diffusion (isotope),

gaseous re-emission (NO_3^-, nssCl^- and MSA),

densification, and metamorphic processes (highly re-crystallized firn, permeability, grain-size, snow porosity, close-off, total air content, etc.),

may be the source of ice record misinterpretation (e.g. Alley, 1988; Wolff, 1996; Mulvaney and others, 1998; Delmotte and others, 1999; Wagnon and others, 1999; Traversi and others, 2000; Proposito and others, 2002).

It is important to consider aeolian processes when selecting optimum sites for firn/ice coring because slope variations of even a few metres per kilometre have a significant impact on winds. As a consequence, a lack of information on local conditions (GPR) can lead to the incorrect definition of climatic conditions based on the interpretation of core stratigraphy alone. Based on our observations, the sites with high standard deviation of spatial variability in snow accumulation (GPS2, M2, MdPt and D6) are not useful in providing information on temporal

variations in snow accumulation, because interpretation is very difficult or impossible when the snow originates from different snow accumulation conditions.

At Vostok station, Antarctica, significant oscillations of snow accumulation and snow isotope composition up to 20 years and possibly $\sim 10^2$ years have been observed and are interpreted in terms of drift of snow accumulation waves of various scales on the surface of the ice sheet (Ekaykin and others, 2002). Those authors have observed similar periodicity in the δD profile of the Vostok ice core at different depths.

The Vostok core may contain sections of ice that were once megadunes, and accumulated snow may have also been affected by spatial variability. Based on present ice flow at the Vostok ice core (Bell and others, 2002), the slope change from the flat surface (due to the subglacial lake) to the slope coming from Ridge B occurred at the end of the Last Glacial Maximum (about 20 000 years ago). Variations in snow accumulation at that time could then be due to the change in slope and increase in wind-driven sublimation. Siegert (2003) pointed out that upstream of Vostok lake there is a significant difference between the accumulation rate during the glacial period and the more recent period. Udisti and others (2004) used stratigraphic correlation between the EPICA Dome C and Vostok ice cores to show the relative variations of snow accumulation over the past 45 kyr. The correlation shows higher variability between glacial and Holocene conditions at DC than at Vostok. They interpret the difference to be due to regional changes in atmospheric circulation with either a negative anomaly in DC or a positive accumulation anomaly in Vostok, or a combination of both.

The Dome C area was chosen for the EPICA deep-drilling project. Deep drilling recently (January 2003) recovered a 3201 m ice core that provides a climate record extending more than 750 kyr (EPICA community members, 2004). The drill site is about 1.4 km east of the present culmination. Our measurements show that the snow accumulation variability is smallest at DC and that over an area of 50 km in diameter (about 2000 km^2) the standard deviation in spatial variability (3%) and the difference between maximum and minimum values (12%) are very small.

An 11% increase in accumulation was observed at Talos Dome during the 20th century, while from 1966 to the present there has been a 7% increase with respect to the 800 year average (Stenni and others, 2002). The clear increase in accumulation at DC, as indicated by stakes and tritium/β compared to Tambora, is consistent with that observed at other sites in East Antarctica, suggesting a regional-scale phenomenon. Stenni and others (2002) found agreement between Talos Dome and DC isotopic profiles, which was attributed to similarly distributed storm tracks and sources of moisture. Recent increases in accumulation have been reported at other Antarctic locations. Pourchet and others (1983) observed a 30% increase in accumulation at 14 Antarctic sites (including Vostok, old Dome C, the South Pole and Ross Ice Shelf) in the period 1960–75 compared to the period 1955–60. This general trend was also observed some years later in the South Pole area, with a 32% increase between 1960 and 1990 (Mosley-Thompson and others, 1995, 1999). At Vostok station, the comparison between a stack of eight sites (six cores and three deep pits) for Tambora marker and nine sites for β marker suggests a slight increase of snow accumulation during the last two centuries (Ekaykin and others, 2004). Stacked records of δD and snow accumulation for the period 1774–1999 show a 50 year cycle. These variations seem to be in phase with the Pacific Decadal Oscillation index, which suggests a teleconnection between central Antarctica and the tropical Pacific (Ekaykin and others, 2004). In Wilkes Land, Morgan and others (1991) observed a decrease in the accumulation rate from 1955 to 1960, with an increase during the subsequent period. Stenni and others (1999) reported no significant accumulation change from a 200 year ice-core record in northern Victoria Land. In Dronning Maud Land (DML), Isaksson and others (1996) observed a decrease in accumulation from 1932 to 1991. Oerter and others (1999) reported a decrease in accumulation in DML during the 19th century followed by an increase during the 20th century, and these trends were linked to temperature variations derived from stable-isotope records. Mosley-Thompson and others (1999) suggest that South Pole's recent accumulation increase may be characteristic of the high East Antarctic plateau.

We observed that the increase in accumulation is mainly evident in the central part of the plateau or at dome sites, where the ablation processes have less impact on snow accumulation.

Mosley-Thompson and others (1995) pointed out that the observed increase is not well understood, but that there are several dominant processes that affect snow precipitation (e.g. variability in the sea-ice extent, changes in moisture source regions, frequency, duration and seasonality of cyclonic storms). Bromwich and others (2004), using atmospheric models (ECT/ERA-15, NCEP2 and DRM) to calculate precipitation over Antarctica from 1979 to 1999, found an upward trend of 1.3–1.7 $kg\,m^{-2}\,a^{-1}$, which is significant at 95% confidence level for all three datasets. They pointed out that the precipitation increase is consistent with the positive trend in sea-surface temperatures observed in the mid-latitudes of the Southern Ocean over the latter half of 20th century (Casey and Cornillon, 2001), this region encompassing the source region of Antarctic precipitation (Delaygue and others, 1999). In addition to these effects, wind-driven sublimation processes must be considered as factors affecting the snow accumulation. Wind-driven sublimation processes, controlled by the surface slope in the wind direction, have a huge impact (up to 85% of snow precipitation) on surface mass-balance and are significant in terms of past, present and future surface mass-balance evaluations (Frezzotti and others, 2004). The analysis of a 20 year (1980–2000) surface-temperature record shows a general cooling of the Antarctic continent, warming of the sea-ice zone, and moderate changes over the ocean (Doran and others, 2002; Kwok and Comiso, 2002; Torinesi and others, 2003). Wind speeds over sloping terrain increase with decreasing temperature; cold temperatures are associated with strong inversions and hence strong gravitational flows (Wendler and others, 1993). Cooler temperatures over East Antarctica and warming in sea-ice areas increase the temperature gradient, and the persistence of katabatic winds and associated wind-driven sublimation. The area with speeds less than 6 $m\,s^{-1}$ represents about 10% of the surface in the continental-scale simulation of the surface wind field (Parish and Bromwich, 1991). An increase in snow precipitation coupled with an increase in temperature and/or wind could increase the surface mass balance only in the inner part of East Antarctica where the wind speed is $<6\,m\,s^{-1}$, whereas it could lead to a decrease in surface

mass balance in the windy areas that represent 90% of the Antarctic surface (Frezzotti and others, 2004).

CONCLUSIONS

The accumulation/ablation pattern derived from stake-farm measurements, wind crust presence and sastrugi heights, suggests that the local annual noise (metre scale) in snow accumulation can be between ~2 and 4 times the average annual accumulation, with no accumulation or ablation for a 5 year period in up to 40% of cases. The lowest standard deviation value is present where the snow accumulation is the highest and/or where the slope along the prevalent wind direction is low. If we compare the stake-farm measurements to the series derived from stratigraphic core analysis, we observe that the number of gaps of one or more years increases with spatial variability and wind scouring.

At many sites stake-farm and ice-core accumulation rates are observed to differ significantly, but isochrones (GPR) correlate well with ice-core derived accumulation.

The spatial variability of snow accumulation at the kilometre scale is one order of magnitude higher than temporal variability (20–30%) at the multi-decade/secular scale. The reconstruction of past climates based on firn/ice cores drilled in areas with high snow accumulation spatial variability (>10%) will be complicated. In megadune areas the distortion of recordings is characterized by a snow accumulation periodicity of about 1500 years. A future intermediate ice core (about 500 m deep) downwind of the megadune area could provide information about the periodicity (about seven oscillations) induced by megadunes in deep ice cores. The length of periodic variations due to mesoscale relief and/or megadunes depends on ice velocity and snow accumulation, and can therefore vary in space and time. Nevertheless the length of these periodic variations should be consistent with the use of ice-core accumulation records to study temporal changes in snow accumulation (decade scale). Domes are the preferred sites for studying the temporal variability of climate using firn/ice cores, because interpretation is easier when all the snow originates from the same point on the surface. Ice/firn cores require surveys (snow radar, GPS, etc.) to characterize the site and its geographical/environmental representativeness.

Our results show that wind-driven sublimation has a strong impact on snow accumulation.

Stake measurements and firn cores at Dome C confirm an approximate 30% increase in accumulation over the last two centuries, with respect to the average over the last 5000 years. An increase in accumulation was also observed at other sites where the slope along the prevalent wind direction is small (31Dpt, D2 and D4). Ice-core records from relatively 'high'-slope (>2 m km^{-1}) areas should be avoided because wind processes are very likely to affect them; short-term changes in snow precipitation should thus be studied only in dome areas or at sites undisturbed by winds. Wind-driven ablation greatly affects snow accumulation, and one of the largest sources of uncertainty regarding present and future surface mass-balance calculations is the role of wind-driven sublimation. An increase in snow precipitation coupled with an increase in temperature and/or wind could increase the surface mass balance only in the inner part of East Antarctica where the wind speed is <6 m s^{-1}, whereas it could lead to a decrease in surface mass balance in the windy areas that represent 90% of the Antarctic surface.

ACKNOWLEDGEMENTS

Research was carried out in the framework of the Project on Glaciology of the Programma Nazionale di Ricerche in Antartide–Ministero Istruzione Universitá, Ricerca (PNRA–MIUR) and was financially supported by PNRA through a cooperation agreement with ENEA Roma. This work is a contribution by the Italian branch of the ITASE project and is also supported by the French Polar Institute (IPEV). It is an associate program to the 'European Project for Ice Coring in Antarctica' (EPICA), a joint European Science Foundation/European Commission scientific program. The authors wish to thank all members of the traverse team, the participants in PNRA 1998/99 who assisted at the Zucchelli station at Terra Nova Bay and Concordia Station and everyone who helped prepare the traverse. Thanks are due to V. Masson-Delmotte, E. Isaksson, M. Fahnestock and G. Hamilton whose comments and editing helped to improve the manuscript.

REFERENCES

Alley, R.B. 1988. Concerning the deposition and diagenesis of strata in polar firn. *J. Glaciol.,* **34**(118), 283–290.

Becagli, S. *and 6 others*. 2003. Variability of snow depositions along the 1998/99 ITASE traverse. *Terra Antartica Reports,* **8**, 43–48.

Bell, R.E., M. Studinger, A.A. Tikku, G.K.C. Clarke, M.M. Gutner and C. Meertens. 2002. Origin and fate of Lake Vostok water frozen to the base of the East Antarctic ice sheet. *Nature,* **416**(6878), 307–310.

Black, H.P. and W. Budd. 1964. Accumulation in the region of Wilkes, Wilkes Land, Antarctica. *J. Glaciol.,* **5**(37), 3–15.

Bromwich, D.H. and C.J. Weaver. 1983. Latitudinal displacement from main moisture source controls $\delta^{18}O$ of snow in coastal Antarctica. *Nature,* **301**(5896), 145–147.

Bromwich, D.H., Z. Guo, L. Bai and Q. Chen. 2004. Modelled Antarctic precipitation. Part I: spatial and temporal variability. *J. Climate,* **17**(3), 427–447.

Capra, A., R. Cefalo, S. Gandolfi, G. Manzoni, I.E. Tabacco and L. Vittuari. 2000. Surface topography of Dome Concordia (Antarctica) from kinematic interferential GPS and bedrock topography. *Ann. Glaciol.,* **30**, 42–46.

Casey, K.S. and P. Cornillon. 2001. Global and regional sea surface temperature trends. *J. Climate,* **14**(18), 3801–3818.

Cole-Dai, J., E. Mosley-Thompson and L.G. Thompson. 1997. Annually resolved Southern Hemisphere volcanic history from two Antarctic ice cores. *J. Geophys. Res.,* **102**(D14), 16,761–16,771.

Dai, J., E. Mosley-Thompson and L.G. Thompson. 1991. Ice core evidence for an explosive tropical volcanic eruption 6 years preceding Tambora. *J. Geophys. Res.,* **96**(D9), 17,361–17,366.

Delaygue, G., V. Masson and J. Jouzel. 1999. Climatic stability of the geographic origin of Antarctic precipitation simulated by an atmospheric general circulation model. *Ann. Glaciol.,* **29**, 45–48.

Delmotte, M., D. Raynaud, V. Morgan and J. Jouzel. 1999. Climatic and glaciological information inferred from air-content measurements of a Law Dome (East Antarctica) ice core. *J. Glaciol.,* **45**(150), 255–263.

Doran, P.T. *and 12 others*. 2002. Antarctic climate cooling and terrestrial ecosystem response. *Nature,* **415**(6871), 517–520. (doi:10.1038/nature710.)

Ekaykin, A.A., V.Ya. Lipenkov, N.I. Barkov, J.R. Petit and V. Masson-Delmotte. 2002. Spatial and temporal variability in isotope composition of recent snow in the vicinity of Vostok station, Antarctica: implications for ice-core record interpretation. *Ann. Glaciol.,* **35**, 181–186.

Ekaykin, A.A., V.Ya. Lipenkov, I.N. Kuz'mina, J.R. Petit, V. Masson-Delmotte and S.J. Johnsen. 2004. The changes in isotope composition and accumulation of snow at Vostok Station over the past 200 years. *Ann. Glaciol.,* **39**, 569–575.

EPICA community members. 2004. Eight glacial cycles from an Antarctic ice core. *Nature,* **429**(6992), 623–628. (doi:10.1038/nature02599.)

Fahnestock, M.A., T.A. Scambos, C.A. Shuman, R.J. Arthern, D.P. Winebrenner and R. Kwok. 2000. Snow megadune fields on the East Antarctic Plateau: extreme atmosphere–ice interaction. *Geophys. Res. Lett.,* **27**(22), 3719–3722.

Fisher, D.A., N. Reeh and H.B. Clausen. 1985. Stratigraphic noise in the time series derived from ice cores. *Ann. Glaciol.,* **7**, 76–83.

Frezzotti, M. and O. Flora. 2002. Ice dynamic features and climatic surface parameters in East Antarctica from Terra Nova Bay to Talos Dome and Dome C: ITASE Italian traverses. *Terra Antartica,* **9**(1), 47–54.

Frezzotti, M., S. Gandolfi, F. La Marca and S. Urbini. 2002a. Snow dunes and glazed surfaces in Antarctica: new field and remote-sensing data. *Ann. Glaciol.,* **34**, 81–88.

Frezzotti, M., S. Gandolfi and S. Urbini. 2002b. Snow megadunes in Antarctica: sedimentary structure and genesis. *J. Geophys. Res.,* **107**(D18), 4344. (doi: 10.1029/2001JD000673.)

Frezzotti, M. *and 12 others*. 2004. New estimations of precipitation and surface sublimation in East Antarctica from snow accumulation measurements. *Climate Dyn.* (doi: 10.1007/s00382-004-0462-5.)

Fujii, Y. and K. Kusunoki. 1982. The role of sublimation and condensation in the formation of ice sheet surface at Mizuho Station, Antarctica. *J. Geophys. Res.,* **87**(C6), 4293–4300.

Gay, M., M. Fily, C. Genthon, M. Frezzotti, H. Oerter and J.-G. Winther. 2002. Snow grain-size measurements in Antarctica. *J. Glaciol.,* **48**(163), 527–535.

Goodwin, I.D. 1990. Snow accumulation and surface topography in the katabatic zone of eastern Wilkes Land, Antarctica. *Antarct. Sci.,* **2**(3), 235–242.

Gow, A.J. 1965. On the accumulation and seasonal stratification of snow at the South Pole. *J. Glaciol.,* **5**(40), 467–477.

Gragnani, R., C. Smiraglia, B. Stenni and S. Torcini. 1998. Chemical and isotopic profiles from snow pits and shallow firn cores on Campbell Glacier, northern Victoria Land, Antarctica. *Ann. Glaciol.,* **27**, 679–684.

Isaksson, E., W. Karlén, N. Gundestrup, P. Mayewski, S. Whitlow and M. Twickler. 1996. A century of accumulation and temperature changes in Dronning Maud Land, Antarctica. *J. Geophys. Res.,* **101**(D3), 7085–7094.

Jouzel, J., L. Merlivat, M. Pourchet and C. Lorius. 1979. A continuous record of artificial tritium fallout at the South Pole (1954–1978). *Earth Planet. Sci. Lett.,* **45**(1), 188–200.

Jouzel, J., L. Merlivat, J.R. Petit and C. Lorius. 1983. Climatic information over the last century deduced from a detailed isotopic record in the South Pole snow. *J. Geophys. Res.,* **88**(C4), 2693–2703.

Kwok, R. and J.C. Comiso. 2002. Spatial patterns of variability in Antarctic surface temperature: connections to the Southern Hemisphere annual mode and the Southern Oscillation. *Geophys. Res. Lett.,* **29**(14). (doi: 10.1029/2002GL015415.)

Legrand, M.R. and R.J. Delmas. 1987. A 220-year continuous record of volcanic H_2SO_4 in the Antarctic ice sheet. *Nature,* **327**(6124), 671–676.

Liston, G.E., J.-G. Winther, O. Bruland, H. Elvehøy, K. Sand and L. Karlöf. 2000. Snow and blue-ice distribution patterns on the coastal Antarctic ice sheet. *Antarct. Sci.,* **12**(1), 69–79.

Lorius, C. 1983. Accumulation rate measurements on cold polar glaciers. *In* Robin, G.de Q., *ed. The climatic record in polar ice sheets*. Cambridge, Cambridge University Press, 65–70.

Mayewski, P.A. and I. Goodwin. 1999. Antarctic's role pursued in global climate change. *Eos,* **80**(35), 398–400.

Morgan, V.I., I.D. Goodwin, D.M. Etheridge and C.W. Wookey. 1991. Evidence from Antarctic ice cores for recent increases in snow accumulation. *Nature,* **354**(6348), 58–60.

Mosley-Thompson, E. *and 6 others*. 1995. Recent increase in South Pole snow accumulation. *Ann. Glaciol.,* **21**, 131–138.

Mosley-Thompson, E., J.F. Paskievitch, A.J. Gow and L.G. Thompson. 1999. Late 20th century increase in South Pole snow accumulation. *J. Geophys. Res.,* **104**(D4), 3877–3886.

Mulvaney, R., D. Wagenbach and E. Wolff. 1998. Postdepositional change in snowpack nitrate from observation of year-round near-surface snow in coastal Antarctica. *J. Geophys. Res.,* **103**(D9), 11,021–11,031.

Oerter, H., W. Graf, F. Wilhelms, A. Minikin and H. Miller. 1999. Accumulation studies on Amundsenisen, Dronning Maud Land, by means of tritium, dielectric profiling and stable-isotope measurements: first results from the 1995–96 and 1996–97 field seasons. *Ann. Glaciol.,* **29**, 1–9.

Palais, J.M., I.M. Whillans and C. Bull. 1982. Snow stratigraphic studies at Dome C, East Antarctica: an investigation of depositional and diagenetic processes. *Ann. Glaciol.,* **3**, 239–242.

Parish, T.R. and D.H. Bromwich. 1991. Continental-scale simulation of the Antarctic katabatic wind regime. *J. Climate,* **4**(2), 135–146.

Petit, J.R., J. Jouzel, M. Pourchet and L. Merlivat. 1982. A detailed study of snow accumulation and stable isotope content in Dome C (Antarctica). *J. Geophys. Res.,* **87**(C6), 4301–4308.

Pettré, P., J.F. Pinglot, M. Pourchet and L. Reynaud. 1986. Accumulation distribution in Terre Adélie, Antarctica: effect of meteorological parameters. *J. Glaciol.,* **32**(112), 486–500.

Picciotto, E., G. Crozaz and W. de Breuck. 1971. Accumulation on the South Pole–Queen Maud Land traverse, 1964–1968. *In* Crary, A.P., *ed. Antarctic snow and ice studies II*. Washington, DC, American Geophysical Union, 257–315. (Antarctic Research Series 16.)

Pourchet, M., J.F. Pinglot and C. Lorius. 1983. Some meteorological applications of radioactive fallout measurements in Antarctic snows. *J. Geophys. Res.,* **88**(C10), 6013–6020.

Proposito, M. *and 9 others*. 2002. Chemical and isotopic snow variability along the 1998 ITASE traverse from Terra Nova Bay to Dome C, East Antarctica. *Ann. Glaciol.,* **35**, 187–194.

Rémy, F., P. Shaeffer and B. Legrésy. 1999. Ice flow physical processes derived from ERS-1 high-resolution map of Antarctica and Greenland ice sheet. *Geophys. J. Int.,* **139**(3), 645–656.

Richardson, C. and P. Holmlund. 1999. Spatial variability at shallow snow-layer depths in central Dronning Maud Land, East Antarctica. *Ann. Glaciol.,* **29**, 10–16.

Richardson, C., E. Aarholt, S.E. Hamran, P. Holmlund and E. Isaksson. 1997. Spatial snow distribution mapped by radar. *J. Geophys. Res.,* **102**(B9), 20,343–20,353.

Schwander, J., J. Jouzel, C.U. Hammer, J.R. Petit, R. Udisti and E. Wolff. 2001. A tentative chronology for the EPICA Dome Concordia ice core. *Geophys. Res. Lett.,* **28**(22), 4243–4246.

Siegert, M.J. 2003. Glacial–interglacial variations in central East Antarctic ice accumulation rates. *Quat. Sci. Rev.,* **22**(5–7), 741–750.

Spikes, V.B., G.S. Hamilton, S.A. Arcone, S. Kaspari and P. Mayewski. 2004. Variability in accumulation rates from GPR profiling on the West Antarctic plateau. *Ann. Glaciol.,* **39**, 238–244.

Stenni, B. *and 8 others*. 1999. 200 years of isotope and chemical records in a firn core from Hercules Névé, northern Victoria Land, Antarctica. *Ann. Glaciol.,* **29**, 106–112.

Stenni, B. *and 6 others*. 2002. Eight centuries of volcanic signal and climate change at Talos Dome (East Antarctica). *J. Geophys. Res.,* **107**(D9), 4076. (doi: 10.1029/2000JD000317.)

Testut, L., I.E. Tabacco, C. Bianchi and F. Rémy. 2000. Influence of geometrical boundary conditions on the estimation of rheological parameters. *Ann. Glaciol.,* **30**, 102–106.

Torinesi, O., M. Fily and C. Genthon. 2003. Variability and trends of summer melt period of Antarctic ice margins since 1980 from microwave sensors. *J. Climate,* **16**(7), 1047–1060.

Traversi, R., S. Becagli, E. Castellano, O. Largiuni and R. Udisti. 2000. Stability of chemical species in firn layers from Antarctica. *In* Colacino, M. and G. Giovannelli, *eds. 8th Workshop, Italian Research on the Antarctic Atmosphere. Proceedings. Vol. 69.* Bologna, Società Italiana di Fisica, 421–443.

Traversi, R. *and 7 others*. 2004. Spatial and temporal distribution of environmental markers from coastal to plateau areas in Antarctica by firn core chemical analysis. *Int. J. Environ. Anal. Chem.,* **84**(6–7), 457–470. (doi: 10.1080/03067310310001640393.)

Udisti, R., S. Bellandi and G. Piccardi. 1994. Analysis of snow from Antarctica: a critical approach to ion-chromatographic methods. *Fresenius' J. Anal. Chem.,* **349**(4), 289–293.

Udisti, R. *and 6 others*. 2000. Holocene electrical and chemical measurements from the EPICA–Dome C ice core. *Ann. Glaciol.,* **30**, 20–26.

Udisti, R. *and 8 others*. 2004. Stratigraphic correlations between the European Project for Ice Coring in Antarctica (EPICA) Dome C and Vostok ice cores showing the relative variations of snow accumulation over the past 45 kyr. *J. Geophys. Res.,* **109**(D8), D08101. (doi: 10.1029/2003JD004180.)

Urbini, S., S. Gandolfi and L. Vittuari. 2001. GPR and GPS data integration: examples of application in Antarctica. *Ann. Geofis.,* **44**(4), 687–702.

Van den Broeke, M.R. *and 6 others*. 1999. Climate variables along a traverse line in Dronning Maud Land, East Antarctica. *J. Glaciol.,* **45**(150), 295–302.

Van der Veen, C.J. and J.F. Bolzan. 1999. Interannual variability in net accumulation on the Greenland ice sheet: observations and implications for mass balance measurements. *J. Geophys. Res.,* **104**(D2), 2009–2014.

Vaughan, D.G., H.F.J. Corr, C.S.M. Doake and E.D. Waddington. 1999. Distortion of isochronous layers in ice revealed by ground-penetrating radar. *Nature,* **398**(6725), 323–326.

Vincent, C. and M. Pourchet. 2000. *Geodetic measurements and accumulation rate at Dome Concordia, December 1999 and January 2000.* Grenoble, Laboratoire de Glaciologie et Géophysique de l'Environnement. Institut Français pour la Recherche et la Technologie Polaire and Ente per le Nuove Tecnologie, l'Energia e l'Ambiente. (Technical report.)

Vittuari, L. *and 6 others*. 2004. Space geodesy as a tool for measuring ice surface velocity in the Dome C region and along the ITASE traverse [030626.]. *Ann. Glaciol.,* **39**, 402–408.

Waddington, E.D., J. Cunningham and S.L. Harder. 1996. The effects of snow ventilation on chemical concentrations. *In* Wolff, E.W. and R.C. Bales, *eds. Chemical exchange between the atmosphere and polar snow.* Berlin, etc., Springer-Verlag, 403–451.

Wagnon, P., R.J. Delmas and M. Legrand. 1999. Loss of volatile acid species from upper firn layers at Vostok, Antarctica. *J. Geophys. Res.,* **104**(D3), 3423–3431.

Wendler, G., J.C. André, P. Pettré, J. Gosink and T. Parish. 1993. Katabatic winds in Adélie coast. *In* Bromwich, D.H. and C.R. Stearns, *eds. Antarctic meteorology and climatology: studies based on automatic weather stations.* Washington, DC, American Geophysical Union, 23–46. (Antarctic Research Series 61.)

Whillans, I.M. 1975. Effect of inversion winds on topographic detail and mass balance on inland ice sheets. *J. Glaciol.,* **14**(70), 85–90.

Wolff, E.W. 1996. Location, movement and reactions of impurities in solid ice. *In* Wolff, E.W. and R.C. Bales, *eds. Chemical exchange between the atmosphere and polar snow.* Berlin, etc., Springer-Verlag, 541–560.

MS received 2 March 2004 and accepted in revised form 14 November 2004

E. Trouve, G. Vasile, M. Gay, L. Bombrun, P. Grussenmeyer, T. Landes, JM Nicolas, P. Bolon, I. Petillot, A. Julea, L. Vallet, J. Chanussot, M. Koehl. "Combining airborne photographs and spaceborne SAR data to monitor temperate glaciers : Potentials and limits", *IEEE Transactions on Geoscience and Remote Sensing*, *Vol.* 45, *N*° 4, 2007.

Combining Airborne Photographs and Spaceborne SAR Data to Monitor Temperate Glaciers: Potentials and Limits

Emmanuel Trouvé, *Member, IEEE*, Gabriel Vasile, *Member, IEEE*, Michel Gay, Lionel Bombrun, *Student Member, IEEE*, Pierre Grussenmeyer, Tania Landes, Jean-Marie Nicolas, Philippe Bolon, *Member, IEEE*, Ivan Petillot, Andreea Julea, Lionel Valet, Jocelyn Chanussot, *Senior Member, IEEE*, and Mathieu Koehl

***Abstract*—Monitoring temperate glacier activity has become more and more necessary for economical and security reasons and as an indicator of the local effects of global climate change. Remote sensing data provide useful information on such complex geophysical objects, but they require specific processing techniques to cope with the difficult context of moving and changing features in high-relief areas. This paper presents the first results of a project involving four laboratories developing and combining specific methods to extract information from optical and synthetic aperture radar (SAR) data. Two different information sources are processed, namely: 1) airborne photography and 2) spaceborne C-band SAR interferometry. The difficulties and limitations of their processing in the context of Alpine glaciers are discussed and illustrated on two glaciers located in the Mont-Blanc area. The results obtained by aerial triangulation techniques provide digital terrain models with an accuracy that is better than 30 cm, which is compatible with the computation of volume balance and useful for precise georeferencing and slope measurement updating. The results obtained by SAR differential interferometry using European Remote Sensing Satellite images show that it is possible to measure temperate glacier surface velocity fields from October to April in one-day interferograms with approximately 20-m ground sampling. This allows to derive ice surface strain rate fields required to model the glacier flow. These different measurements are complementary to results obtained during the summer from satellite optical data and ground measurements that are available only in few accessible points.**

***Index Terms*—Airborne photogrammetry, digital terrain model (DTM), synthetic aperture radar (InSAR) interferometry, temperate glacier, velocity field.**

Manuscript received July 5, 2006; revised November 15, 2006. This work was supported by the French Research Agency under the MEGATOR Project.

E. Trouvé and G. Vasile are with the Laboratoire d'Informatique, Systèmes, Traitement de l'Information et de la Connaissance, Université de Savoie, Polytech'Savoie, F.74944 Annecy-le-Vieux Cedex, France, and also with the Grenoble Image Parole Signal et Automatique Laboratory, Institut National Polytechnique de Grenoble, Centre National de la Recherche Scientifique, 38402 Saint-Martin-d'Hères, France (e-mail: emmanuel.trouve@univ-savoie.fr; gabriel.vasile@univ-savoie.fr).

M. Gay, L. Bombrun, and J. Chanussot are with the Grenoble Image Parole Signal et Automatique Laboratory, Institut National Polytechnique de Grenoble, Centre National de la Recherche Scientifique, 38402 Saint-Martin-d'Hères, France (e-mail: michel.gay@lis.inpg.fr; lionel.bombrun@lis.inpg.fr; jocelyn.chanussot@lis.inpg.fr).

P. Grussenmeyer, T. Landes, and M. Koehl are with the Equipe Photogrammétrie et Géomatique, Modèles et Simulations Pour l'Architecture, l'Urbanisme et le Paysage-Photogrammetrie Architechturale et Geomatique UMR 694, Institut National des Sciences Appliquees de Strasbourg, 67084 Strasbourg, France (e-mail: pierre.grussenmeyer@insa-strasbourg.fr; tania.landes@insa-strasbourg.fr; mathieu.koehl@insa-strasbourg.fr).

J.-M. Nicolas is with the Département Traitement du Signal et des Images GET-Télécom Paris, Ecole Nationale Supérieure des Télécommunications, 75013 Paris, France (e-mail: nicolas@tsi.enst.fr).

P. Bolon, I. Petillot, and L. Valet are with the Laboratoire d'Informatique, Systèmes, Traitement de l'Information et de la Connaissance, Université de Savoie, Polytech'Savoie, F.74944 Annecy-le-Vieux Cedex, France (e-mail: philippe.bolon@univ-savoie.fr; ivan.petillot@univ-savoie.fr; lionel.valet@univ-savoie.fr).

A. Julea is with the Laboratoire d'Informatique, Systèmes, Traitement de l'Information et de la Connaissance, Université de Savoie, Polytech'Savoie, 74016 Annecy, France, and also with Space Sciences Institute, 76900 Bucharest, Romania (e-mail: andreea.julea@univ-savoie.fr).

Color versions of one or more of the figures in this paper are available online at http://ieeexplore.ieee.org.

Digital Object Identifier 10.1109/TGRS.2006.890554

I. Introduction

In recent decades, a spectacular retreat has been observed on most of the monitored Alpine glaciers [1], [2]. If this evolution is confirmed in the coming years, it will have some important consequences in terms of water resources, economical development, and risk management in the surrounding areas [3], [4]. Up to now, only 1% of the existing world temperate glaciers have been monitored [5], mostly by ground measurements, which often provide information only once or twice a year at a few points. Because of the difficulty of reaching high-altitude glaciers in risky mountainous areas, acquisition and processing of remotely sensed data should provide more information to improve glacier monitoring [4], [6]. Satellite-based glacier monitoring programs such as Global Land Ice Measurements from Space (http://www.glims.org) have started to build a database of glaciers around the world [7]. In the Alps, in high mountain areas where the glacier activity has to be monitored, a large series of airborne photographs and spaceborne synthetic aperture radar (SAR) images is often available through local environmental agencies [8] and space agencies. However, gathering multisource data sets for a given area and extracting the desired measurements (surface velocity fields, surface and bottom topography, etc.) remain difficult tasks.

This paper presents the first results of a project that involves four laboratories specializing in optical and SAR image processing, and data fusion techniques. A global strategy illustrated in Fig. 1 is proposed to extract from the large number of remotely sensed images information that is useful in monitoring

0196-2892/$25.00 © 2007 IEEE

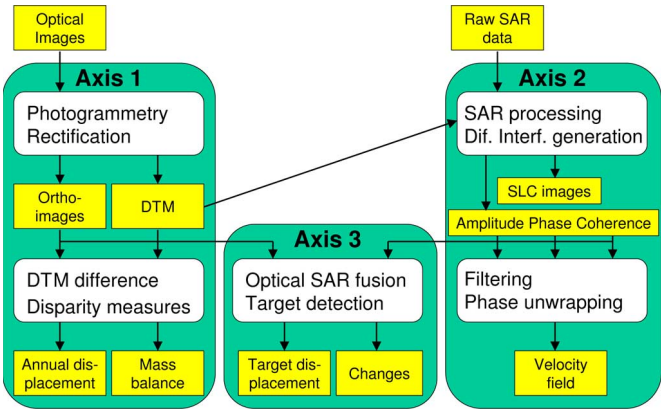

Fig. 1. Flowchart of the three main research axes proposed to extract information from optical and SAR data to monitor glacier activity; the main processing steps are in white, while the data are in yellow (light gray).

glacier evolution and evaluating the risk in the surrounding areas. The three main research axes are given as follows:

1) construction of digital terrain models (DTMs) and orthoimages from high-resolution optical images, and computation of differences after one or several years to detect changes such as volume variations, glacier retreat, lakes appearing/disappearing, etc.;
2) computation of differential C-band SAR interferograms by subtracting the topography provided by the previous results to obtain displacement fields over only a few days;
3) fusion of the feature detections and displacement measurements provided by the first two axes, in order to improve the confidence in the displacement/evolution measurements and to obtain higher level information such as change detection and risk maps.

In this paper, we focus on the first steps of the optical and SAR axes, which are given as follows:

- computation of DTMs by photogrammetry from airborne photographs;
- computation of velocity fields by SAR differential interferometry (D-InSAR) from satellite SAR images.

The principles of these two techniques are well established, but conventional processing is often difficult to apply in the context of Alpine glaciers.

In the field of photogrammetry, DTMs have been generated in similar studies dealing with monitoring high mountain terrain deformation. In [9], digital photogrammetry is applied to analyze changes in elevation and horizontal surface velocities. The goal of this paper was to determine surface topography and surface kinematics via high-altitude aerial photographs of two different years. Previously, Fox and Nuttall showed that photogrammetry can be used as a research tool by glaciologists [10]. Indeed, they produced photogrammetric compilations of two of the glaciers under study using 1990 aerial photographs. They examined the results and difficulties encountered in assessing the accuracy of the photogrammetric data. Photogrammetry was regarded primarily as a source of DTMs rather than as a cartographic tool. The derived digital model proved its efficiency for glaciological analysis [9], [11].

In the field of SAR interferometry, different approaches have been applied for studying glacier dynamics. The repeat-pass SAR acquisitions of the European Remote Sensing (ERS)-1/2 tandem mission provided a large database for glacier monitoring. One of the approaches used to study small movements over large areas is D-InSAR, which consists in differencing either two SAR interferograms or one interferogram and a topographical interferogram simulated by using a DTM over the same target area [12], [13]. In [14], nine ERS-1/2 tandem interferograms with useful scene coherence have been reported for measuring the surface flow of the Saskatchewan alpine glacier in the Canadian Rocky Mountains. With a mean velocity of about 15 cm/day, the obtained results agreed with the mean from surveying techniques. In addition, by using one interferogram formed by two acquisitions of the ERS-1 satellite at three-day intervals, the motion of the Black Rapids Glacier (AK) was assessed in [15]. The obtained accuracy was in the range of 5%–10% with a mean annual velocity of about 13 cm/day. Other geophysical properties can be extracted directly from the InSAR wrapped phase. In [16], the longitudinal strain rates of the Recovery Glacier (east Antarctica) have been estimated from RADARSAT-1 interferograms. Comparisons with the available ground data revealed a strain rate error of 17%, corresponding to a tensile strength error of 5.3%.

Although the D-InSAR processing chain is built from standard well-established InSAR algorithms as coregistration of interferograms, phase subtraction, and phase unwrapping, this procedure is often error prone because of complex glacier topography, phase noise at glacier boundaries, or atmospheric heterogeneities [17]. As the phase-unwrapping algorithm is the most sophisticated procedure in interferometric signal processing, a gradient approach (GINSAR) has been proposed by Sharov *et al.* [18] for differential processing of repeat-pass SAR interferograms in the context of glacier change detection and motion estimation. It has been validated on several tidewater glaciers from the Arctic regions. In order to separate ground displacement from atmospheric perturbations, a different approach based on the concept of permanent scatterers (PS) has been proposed [19] and successfully applied in urban areas. In the glacier areas where exposed rocks are visible, various backscatterers with a constant signature can be considered as potential PS, but results using this approach have not been reported. Beside the use of interferometric phase, a different approach based on intensity images has been proposed to measure displacement [20], [21]. In [22], the surface displacements are measured by correlating and tracking the image speckle pattern between two repeat-pass SAR acquisitions (speckle tracking). The advantages of the speckle tracking approach are less sensitivity to decorrelation and lack of need for the phase-unwrapping procedure [23]. However, the local amplitude variations (texture) should be high enough and the two speckle realizations should be quite dependent within the interferometric SAR image pair to ensure high correlation values.

Most of the published results are based on conventional SAR interferometry and obtained on glaciers located near polar regions [24], [25]. Fewer InSAR results have been published on temperate glaciers [14], [26], and up to now, only communications have reported results over Alpine glaciers [27], [28].

The context of temperate glaciers, especially with the climate in the Alps, is rather different from the context of polar and high-latitude glaciers.

- High-relief topography reduces the visibility of valley glaciers. They are rarely visible in both ascending and descending passes. When only one projection of the displacement on the SAR line of sight (LOS) is available, deriving 3-D velocity fields requires a stronger hypothesis (the flow direction) than when two projections are available [24]. Moreover, even when two projections are available, the high latitude increases the angle between ascending and descending tracks. Angles close to 90° are more suitable than the approximately 20° angle at the Alps' latitude.
- The small size of Alpine glaciers (typically about 10 km long and often just 1 or 2 km wide) has two main consequences for the processing: It reduces the size of possible filtering of the interferograms and the DTM, and increases the phase-unwrapping difficulty when glaciers are separated in several disconnected parts.
- The ice temperature of the low-altitude glaciers is very close to zero from the bedrock up to the surface. This strongly reduces the penetration length of electromagnetic waves [29]. The measurement of the ice-thickness distribution by low-frequency ground-penetrating radar or airborne ice-sounding radar is more difficult. This distribution is required to use the principle of mass conservation to convert InSAR velocity measurements to 3-D velocities as successfully performed over the Storströmmen glacier in northeast Greenland [30], [31].

Such differences have an impact on D-InSAR measurement feasibility, complementary data availability, and the processing chain: Different steps and hypotheses are strongly context dependent.

In order to apply photogrammetry and SAR interferometry in the context of Alpine glaciers, their potential and limitations have to be carefully investigated. The objective of this paper is to perform such investigations for airborne optical images and SAR D-InSAR using ERS C-band images. Airborne photography allows the computation of high-resolution DTMs on the glacier surface and the surrounding moraines, whereas spaceborne SAR interferometry provides the projection of the surface velocity field in the SAR LOS. The DTM information is necessary for the D-InSAR processing to remove topographic fringes, resample the results in ground geometry, and reconstruct the three components of the displacement vectors. Since the studied glaciers are visible only in descending passes, the three components are obtained using the surface-parallel flow (SPF) assumption and the maximum slope direction [15]. The result should be considered as "quasi-3-D" velocity vectors since pure velocity and ablation/accumulation effects are merged. The different steps of the processing chains and seasonal limitations are carefully analyzed with a series of ERS tandem interferograms over Alpine glaciers located in the Mont-Blanc area.

The remainder of this paper is organized as follows. The test site and the data set collected over the Mer de Glace and Argentière glaciers are presented in Section II. The processing of optical airborne images and high-resolution DTM obtained over Mer de Glace glacier are described in Section III. The different steps of the D-InSAR processing chain are presented and analyzed in Section IV. Section V presents the displacement field derived from the previous results and the comparisons with ground measurements.

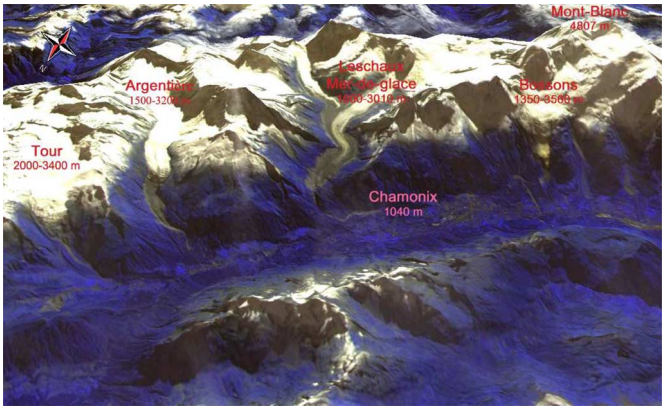

Fig. 2. Chamonix–Mont-Blanc test site. Main glaciers and geographical features. Shown is the 3-D model draped with a SPOT-2 multispectral image during the summer of 2000.

II. Test Area and Data Sets

The project test site is located in the Alps, near the borders between France, Italy, and Switzerland. It goes from the glacier of Le Grand Plateau (45° 50′ N, 6° 51′ E) about 4000 m above sea level (ASL) up to the Trient glacier (46° 59′ N, 7° 01′ E) about 2000 m ASL. It includes the Mont-Blanc (4810 m), the Chamonix valley (1000 m), and two well-known and instrumented glaciers, i.e., Mer de Glace and Argentière (Fig. 2).

This test site is suitable for investigating the potential of remotely sensed data to monitor glacier activity for several reasons, such as the following:

- *geophysical diversity of glaciers:* a large range of altitudes (1000–4800 m) and glacial velocities (0–30 cm/day over Mer de Glace and Argentière glaciers, and up to 3 m/day in the Géant icefall [32]), complex surface cover (mixture of snow, ice, and rocks), and the presence of water-collecting tunnels (Argentière), which enable subglacial point velocity measurements [33];
- *data availability:* the existence of various data sets from spaceborne or airborne sensors, which are acquired with different time intervals in different seasons, and ground measurements, which help in the data processing, information fusion, and validation of the final results [34].

A. Optical Data

For several decades, airborne photography has been an important source of information over a large number of glaciers in the Alps [8], [35]. In the French part, the main glaciers of three different regions have been covered by airborne photography every three years between 1975 and 1995 (Table I). More recent campaigns (1998, 2000, and 2004) have been performed over the whole "Haute-Savoie" (4598 km^2), where the studied glaciers are located [8]. The advantage of such data is the high

TABLE I
AIRBORNE PHOTOGRAPHY CAMPAIGNS OVER THREE DIFFERENT GLACIER REGIONS IN THE FRENCH ALPS ("X" DENOTES EXISTENCE OF A CAMPAIGN THAT YEAR). THE MONT-BLANC REGION HAS ALSO BEEN COVERED IN 1998, 2000, AND 2004 BY CAMPAIGNS PERFORMED OVER THE WHOLE "HAUTE SAVOIE"

	1975	1976	1978	1979	1981	1982	1983	1984
Mont-Blanc		×		×		×		
Savoie	×		×		×		×	
Oisans	×		×		×			×
	1985	1986	1988	1989	1990	1991	1992	1995
Mont-Blanc	×				×			×
Savoie		×		×			×	
Oisans			×			×		

resolution of digitized photos or digital image acquisitions. They allow the computation of high-resolution DTMs and orthoimages with accurate positioning obtained by using a few GPS control points (see Section III). Another advantage is the ability to reconstruct past glacier configurations. Indeed, data from 1990 and 1995 are available and will be of particular interest for interpretations over the last decades. However, the main disadvantage is the high cost of each campaign, which usually covers only a few glaciers, making such data rarely available for the scientific community.

Spaceborne optical images with their increasing resolution are a potential alternative. A detailed map of the summer ice velocity field for our study area has been obtained previously by cross-correlating SPOT5 optical images [36]. One of the advantages of such data is that a single image can cover the whole group of glaciers of a mountain area. Moreover, along-track stereo-pair acquisition capability and multispectral sensors allow satellites such as the Advanced Spaceborne Thermal Emission and Reflection Radiometer (ASTER) to contribute to ice measurements by providing both elevation models and surface classification based on spectral signature [7]. This information can be used to identify specific features (e.g., emerging lakes, ice cracks, glacier tongues) for change detection and risk assessment. Hybrid DTMs produced by the merging of optical and SAR DTMs also seem to be promising [4], [6].

Nevertheless, the spatial resolution of these images compared to that of aerial photography remains a disadvantage. The achievable accuracy for elevation changes and horizontal displacements approximates the spatial resolution, i.e., 15 m for ASTER against less than 0.30 m for aerial photography [9]. In [9], a photogrammetrically derived DTM was compared with an ASTER DTM. The latter one provided an accuracy between ± 18 m rms (in moderately mountainous terrain) and ± 60 m rms (in rough high mountain topography). Thus, ASTER and SPOT image pairs provide DTMs but with a DTM accuracy not comparable to that reached by photogrammetric techniques. Satellite DTM can be used to derive elevation changes if the time separation is a few years [37]. The aerial DTM high accuracy should allow to compute annual elevation changes that are useful in deriving annual mass balance. Moreover, because of the weather conditions on mountainous areas and orbital constraints, existing data with a meter-scale resolution are still rare, and programmed acquisition of stereoscopic pairs remains uncertain.

B. SAR Data

Satellite SAR images are more and more used to observe glaciers particularly because of two great advantages: 1) The active SAR sensor acquires images regardless of weather conditions. 2) It measures both the amplitude and phase of the backscattered signal. With the resolution of the data that have been available up to now (about 20 m with ERS images), the amplitude is often difficult to use in extracting precise information on specific features. The next generation of SAR satellites should provide meter-resolution images and fully polarimetric data, which will be useful to detect different features and backscattering mechanisms [38]. With interferometric data, the geometric deterministic component of the phase offers the opportunity to measure the glacier displacement between the two acquisitions with a precision of a fraction of the wavelength (5.6 cm in C-band). The two main limitations of this technique are the temporal decorrelation of the signal over glaciers (see Section IV-B2) and the need to separate the topographical fringes from the displacement fringes. Among the different techniques that can be used [18], the safest one consists in using a DTM and the radar geometry to simulate the phase signal due to the topography and to compute the difference with the real interferogram.

In this paper, 16 raw SAR images from ERS 1 and ERS 2 have been selected to study the feasibility of SAR interferometry in order to extract the surface velocity fields of the studied glaciers. The data set presented in Table II includes different time intervals (one day with tandem couples, three days, and six days), different seasons, and ascending and descending passes.

C. Large-Scale DTM

A large-scale DTM is required for InSAR processing in order to remove the topographic fringes and to georeference the information obtained in radar geometry (unwrapped phase and complementary information such as amplitude and coherence). For topographic fringe removal, the DTM accuracy requirement increases with the baseline between the two SAR acquisitions, which makes interferograms more and more sensitive to the topography, especially in the high-relief areas of Alpine glaciers. In the georefencing step, the impact of low-resolution DTM or low planimetric accuracy can be important since in the last step, the displacement measured on the radar LOS is converted into velocity fields using the hypothesis of surface-parallel motion in the direction of maximum slope, as described in Section V. This last step requires only a low-resolution slope estimate, but registration of the SAR measurements and the topography is error prone, especially on the margins of the narrow Alpine glaciers.

Since the 1995 aerial photographs cover only the most important glaciers and a high-resolution DTM has been produced until now only on the Mer de Glace and the lower part of the Leschaux glacier, a large-scale DTM has been used for the SAR processing. Normally, the Shuttle Radar Topography Mission (SRTM) DTM would be sufficient, even though only the Digital Terrain Elevation Data-1 resolution (about 90 m) is available in Europe. However, in the studied mountainous area, the SRTM DTM is not complete due to the forshortening and shadow

TABLE II
ERS SAR RAW DATA ACQUIRED OVER THE MONT-BLANC AREA [B: BASELINES (PARALLEL AND PERPENDICULAR TO THE RADAR LOS), e_a: ALTITUDE OF AMBIGUITY]

Dates	Δt	Satellite(s)	Orbites	Frame	Pass	$B_{\parallel}$ (m)	$B_{\perp}$ (m)	e_a (m)
91.08.17 / 91.08.20	3 days	ERS-1/1	00449 / 00492	2682	Des.	-44	-7	1202
91.08.29 / 91.09.04	6 days	ERS-1/1	00621 / 00707	2682	Des.	36	291	29
95.07.09 / 95.07.10	1 day	ERS-1/2	20830 / 01157	0909	Asc.	17	52	162
95.08.13 / 95.08.14	1 day	ERS-1/2	21331 / 01658	0909	Asc.	-37	-98	86
95.10.22 / 95.10.23	1 day	ERS-1/2	22326 / 02653	2673	Des.	-44	-107	87
95.12.31 / 96.01.01	1 day	ERS-1/2	23328 / 03655	2673	Des.	79	208	45
96.03.10 / 96.03.11	1 day	ERS-1/2	24330 / 04657	2673	Des.	26	9	935
96.04.14 / 96.04.15	1 day	ERS-1/2	24831 / 05158	2673	Des.	39	93	100

effects. For this paper, it has been completed using an 80-m-resolution DTM provided by the French National Geographic Institute (IGN), which was built from 1980 photos by photogrammetric restitution at 1/60 000 scale and from digitalized contour maps at 1/25 000 scale. With large altitude of ambiguity as in the March 1996 ERS pair (about 900 m), the impact of the resulting DTM uncertainty is still negligible in the fringe pattern. This DTM has been used for the georeferencing of the whole SAR image. In the last InSAR processing step, it was updated by the DTM computed by aerial triangulation (AT) from the 1995 photos (Section III).

III. HIGH-RESOLUTION DTM COMPUTATION

Several series of photos were selected over the Leschaux/Mer de Glace glacier. The 9 × 9 in (approximately 23 × 23 cm) negatives were scanned at a resolution of 15 μm, providing 15 360 × 15 360 pixels per image. They cover each glacier with about 80% overlap. On the 1995 acquisition over the Mer de Glace glacier (Fig. 3), the pixel size in the original photos corresponds to 36 cm at the bottom of the glacier (1000 m ASL) and 18 cm at its top (2800 m ASL). The plane was flying at an altitude of 4650 m ASL.

In the first step of the processing, the digital images are oriented using the bundle-block AT technique, which enables global restitution of a block of photos and reduction of ground control points (GCPs). This creates the possibility of working over terrain with poor geodetic point density. Bundle-block adjustment is an iterative method based on the use of photo coordinates as observations. Then, the application of the central projection method [39] enables the conversion of these observations into terrain coordinates in one step. This requires a block of photos with at least 60% overlap and 20% side-lap (often more). Moreover, a set of eight points located on both sides of the glacier and measured by GPS with an accuracy of 10 cm in X, Y, and Z is needed for the orientation process. Fig. 3 shows the location of the GCPs used in the AT process. It is obvious that the distribution and number of GCPs are not optimal, especially in the inaccessible parts of the glacier. Only a few targets fixed in the past on rocks along the glacier were visible on the 1995 images. Some additional points close to huts have been measured by GPS.

The input to AT calculations consists of picking both GCPs and tie points (used to join photos together along and between strips), and their quality affects the reliability of the overall model. Point measurement uncertainty is estimated from rms errors. Finally, the main advantage of processing by the bundle-block adjustment is to produce a global and homogeneous result over the whole area.

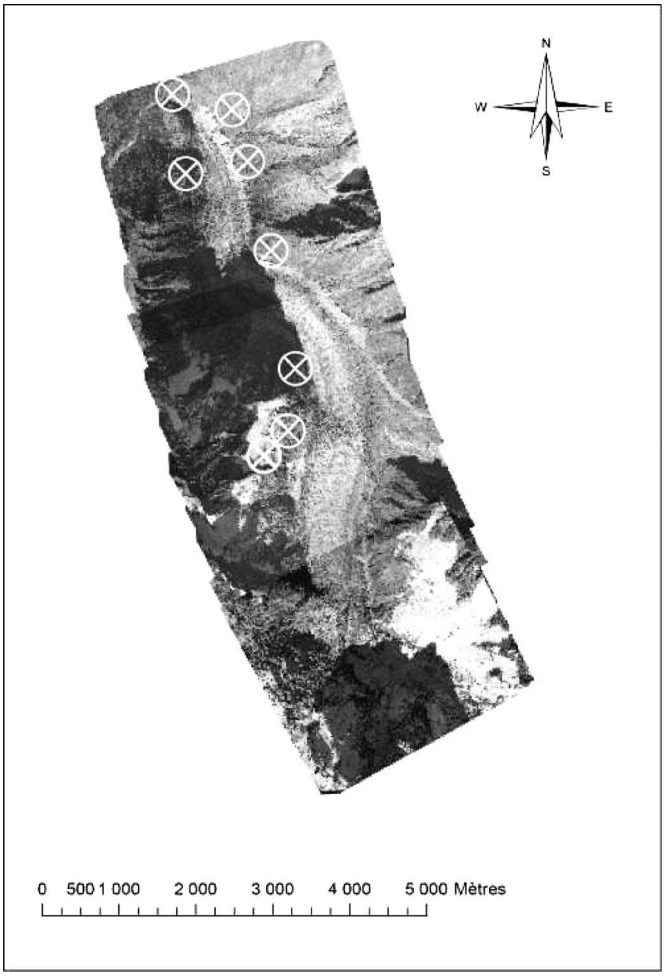

Fig. 3. Layout of the set of 13 photos that were taken over the Mer de Glace in 1995 and are entering in the AT processing. Circles represent the points measured by GPS.

On the Mer de Glace, approximately 3700 AT points were computed, including 2000 three-ray points (the same point measured in three overlapping images), 500 four-ray points, and about 200 five-ray points due to the high degree of overlap. Each correlated point is processed from at least three images, and this redundancy leads to high accuracy. The rms errors of the computed AT points are $\sigma_{X,Y} = \pm 20$ cm and $\sigma_Z = \pm 30$ cm.

These images are then used to compute about 5 million complementary points on a regular grid by photogrammetric matching techniques (using the KLT software package) based on the correlation of image patches in two or more successive images. Break lines and structure lines are defined by manual stereoscopic measurements. Break lines and structure lines are specific edges of topographic significance on the terrain. They define physical discontinuities in slope and are materialized by linear features. The aerial photos were acquired during the summer, so only a few areas were covered by snow in the upper part of the glacier. Matching was problematic when saturation of the optical images occurred, leading to failure of automatic correlation. Thus, manual stereoscopic measurement was necessary to supplement the terrain model. Specific problems also arise in matching ice cracks. Manual points have to be taken at the top and bottom of crevasses. The result is controlled by stereo-viewing (superimposing previously matched points and selected stereo pairs). The global result is obtained with 80% automatic or semiautomatic measurements, where semiautomatic processing entails guidance from the operator, who increases the density in weak areas by stereoscopic measurements. About 20% are completed manually in areas where steep slopes or poor contrast prevents reliable matching.

At this stage of the processing, a DTM can be computed with a resulting horizontal resolution ranging from 2 to 5 m depending on the slopes. Generally, a 5-m grid is used, except in very steep areas, where one point for every 2 m was necessary in order to guarantee the required altimetric accuracy. The accuracy of the final DTM, despite manual intervention, is assessed to lie in the accuracy interval announced previously ($\sigma_{X,Y} = \pm 20$ cm, $\sigma_Z = \pm 30$ cm) since an experienced operator reaches at least that measurement precision.

The resulting final DTM over Mer de Glace is shown in Fig. 4. By superimposing the orthoimages processed with the 1995 photos on the produced DTM, a 3-D model of the Mer de Glace is obtained (Fig. 5).

Fig. 4. Mer de Glace DTM processed by photogrammetric techniques.

IV. D-InSAR Processing

Despite many applications already using differential SAR interferometry, the processing of such data and the extraction of the sought-after information are still a difficult task. This is even more difficult in the context of the proposed test site with high-relief topography, large and irregular displacements, and snow and ice backscattering mechanisms, which are still under investigation [40]. In this section, results obtained by different processing chains are presented to evaluate the feasibility and the limitation of D-InSAR glacier monitoring with ERS data.

A. SAR Processors

In this paper, two standard D-InSAR processors have been used: Differential Interferometric Automated Process Applied to Survey Of Nature (DIAPASON) and Repeated Orbit Interferometry Package (ROI-PAC) software packages. The first results obtained with an original InSAR time-domain processor called the SYnthèse TEmporelle Radar (SYTER) are also presented.

1) Standard Processors: The standard DIAPASON processor provides a complete D-InSAR processing chain that allows scientists from different application fields (e.g., volcanology, seismology) to obtain meaningful results from the use of SAR interferometry to measure displacements [13]. This processing chain was developed at the Centre National d'Etudes Spatiales [41] in the beginning of the 1990s and provides better results when the processing starts with raw data instead of single-look complex (SLC) images. The focusing is performed in the frequency domain to reduce the computation load, which was a critical issue at that time. DIAPASON can be used without a DTM (using a flat earth with a constant elevation), which leads to reasonable measurements in the case of very large altitude of ambiguity. When DTMs are introduced at the interferogram generation stage, the registration step is improved, and the intensity, coherence, and phase images can be computed directly in the DTM geometry. However, generating interferograms in the radar geometry is more appropriate for further processing such as filtering or phase unwrapping.

Another D-InSAR processor that is widely used in the academic and research community is the ROI-PAC. From the initial experiments in spaceborne radar interferometry [42], ROI-PAC has been developed through the collaboration of many researchers at the Jet Propulsion Laboratory and Caltech [43]. It uses raw radar data, telemetry information, and DTMs for generating displacement maps [44]. In this processing chain, DTMs become necessary only after the interferogram

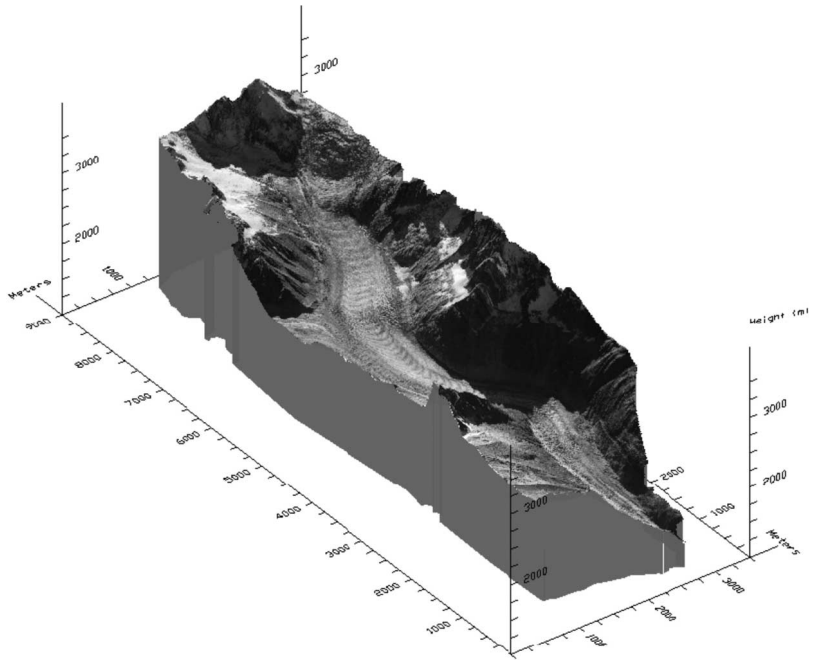

Fig. 5. Mer de Glace glacier 3-D model (orthophotos from 1995 that were draped on the computed DTM).

generation stage to enable topographic fringe removal and precise orbital phase corrections. It also allows resampling of the results in ground geometry.

It is important to notice that in both cases, the SAR focusing is performed with a mean altitude hypothesis, which is valid with ERS data and slow height variations. This hypothesis tends to introduce focusing errors in areas with strong topographic relief: Indeed, there is, for example, almost a 4000-m-height difference between Chamonix valley and the Mont-Blanc summit, corresponding to a foreshortening that can be compared to the ERS field of view (several kilometers). For high-resolution data, this effect is more severe, and a DTM is usually required for SAR synthesis.

2) Temporal-Domain Processor: To overcome the previous difficulty in specific areas, such as the studied glaciers, and to benefit from accurate DTM information earlier in the processing, an original approach is currently being developed at Télécom Paris [45]. It is based on the processing of raw data in the temporal domain. The main ideas of the proposed SAR processing consist of the following.

- Using local circular approximation of the satellite orbit and the Earth rotation to take into account the relative displacement of the imaged points. This allows us to search for the closest point approach (CPA), which is the time of the shortest distance between the Earth target point and the sensor. The CPA corresponds to a zero Doppler Centroïd value. All the relative positions of the Earth target point can be tabulated around this CPA. Actually, in this approach, nonzero Doppler Centroïd data correspond to a slight squint angle in the acquisitions.
- Performing in the time domain a coherent summation of the delayed complex raw data. Delays required for this beamforming are deduced from previous tabulated relative positions. Subaperture images can be obtained by selecting a reduced set of raw data.
- Choosing a ground range geometry for reconstructed pixels. In this way, the computation of interferograms does not require any coregistration as, by introducing the baseline in the SAR processing, the two SAR images are directly obtained in the same ground geometry. Moreover, in order to obtain two images with the same Doppler Centroïd, data are processed with squint angles corresponding to the same subaperture. This allows us to reduce the noise in the resulting interferogram.

Fig. 6 presents the results obtained with the three SAR processors previously described. The fringe pattern visible along the diagonal (from upper left-hand side to bottom right-hand side) corresponds to the Mer de Glace and Leschaux glaciers' displacement. The three fringe patterns on the bottom left-hand side also correspond to three small glaciers moving West toward the Chamonix valley. Global fringe patterns obtained by the different processors are similar. Differences in shape and orientation are due to different sampling geometries: The ROI-PAC and DIAPASON results are in radar geometry, whereas the temporal processor result is in the ground geometry. The reduced noise and apparently smoothed result of the temporal approach are due to the common band filtering resulting from the selection of the same subaperture.

At this stage, the SYTER experimental processor takes only a constant baseline and the distance to the geoid into account. The next development will introduce the precise orbits and the elevation provided by the DTM in the sensor-target distance computation. The results obtained by the ROI-PAC processor with the precise obits from Delft University, Delft, The Netherlands, are used in the following steps.

B. Interferogram Generation

1) Glacier Visibility: In order to assess the glacier visibility in ERS ascending and descending passes, several simulations

Fig. 6. ERS-1/2 March 1996 tandem interferometric phase after orbital fringe correction. (a) and (b) DIAPASON and ROI-PAC results in slant range geometry. (c) Temporal-domain processing result in ground range geometry.

have been performed with the DTM of Fig. 7(a). A SPOT 2 multispectral orthoimage where the main glaciers are clearly visible [Fig. 7(b)] is used to illustrate the results. The masks, which correspond to the nonvisible regions (layover, shadow), are shown in red over the SPOT optical image. The nonvisible areas for ERS ascending and descending acquisitions are presented in Fig. 7(c) and (d), respectively. Due to the orientation of the Argentière and Mer de Glace glaciers, the results show that approximately 85% of their surface is visible from ERS descending orbits. On the contrary, less than 20% of the two studied glacier surfaces can be investigated from ascending orbits. Accordingly, only the descending ERS-1/2 images may provide useful information for velocity assessment by means of D-InSAR processing.

2) Coherence Analysis: The descending ERS-1 three-day interval pair acquired during the summer of 1991 has been processed by the processors presented in Section IV-A to ensure that the results and the associated conclusions are not influenced by processing artifacts. The obtained interferograms have good overall quality, showing a high level of coherence on the nearby mountains and in the Chamonix valley. However, the coherence is low on the studied glaciers [Fig. 8(b)]. Despite the lack of glacier visibility, the same result can be observed with the ascending pairs during the summer of 1995 [Fig. 8(d)]. The loss of interferometric coherence can be explained by either a large change of the glacier surface state or a strong glacier displacement that would affect the global coregistration algorithm.

In order to investigate which assumption holds, controlled displacements were introduced in artificial interferograms computed by using twice the same acquisition (ROI-PAC SLC image from ERS1 1991-08-17). The displaced images were obtained by SLC resampling (four-point cubic convolution [46]) and then by shifting in the glacier flow direction by multiples of 0.25 pixels. Several interferograms were constructed between the original SLC image and the displaced SLC images. Fig. 9 shows the coherence mean and standard deviation computed on these artificial interferograms within a mask including only the Mer de Glace and Leschaux glaciers. The resulting plot shows that a satisfactory coherence level can be obtained even for displacements that are much larger than those expected for the studied glaciers within intervals of a few days: in the absence of any other decorrelation factor, the coherence level is above 0.6 for displacement up to 15 m.

With the real ERS August 1991 three-day interferogram, the displacement of the Mer de Glace and Leschaux glaciers is approximately only 1 m, whereas the coherence mean is equal to 0.2 [see Fig. 8(b)]. This loss of coherence in summer pairs can be interpreted only by glacier surface changes probably due to ice melting and variation in the number and position of elementary backscatters in the resolution cell. An empirical model derived from observed ablation confirms this interpretation: Each positive degree yields 6.6 mm of ablation per day [34]. With the summer positive temperature often encountered at daytime in the studied glaciers, the ablation is too important compared to the C-band 5.6-cm wavelength to preserve interferometric coherence. This conclusion is also consistent with the results reported by Fischer *et al.* [47] over Iceland glacier

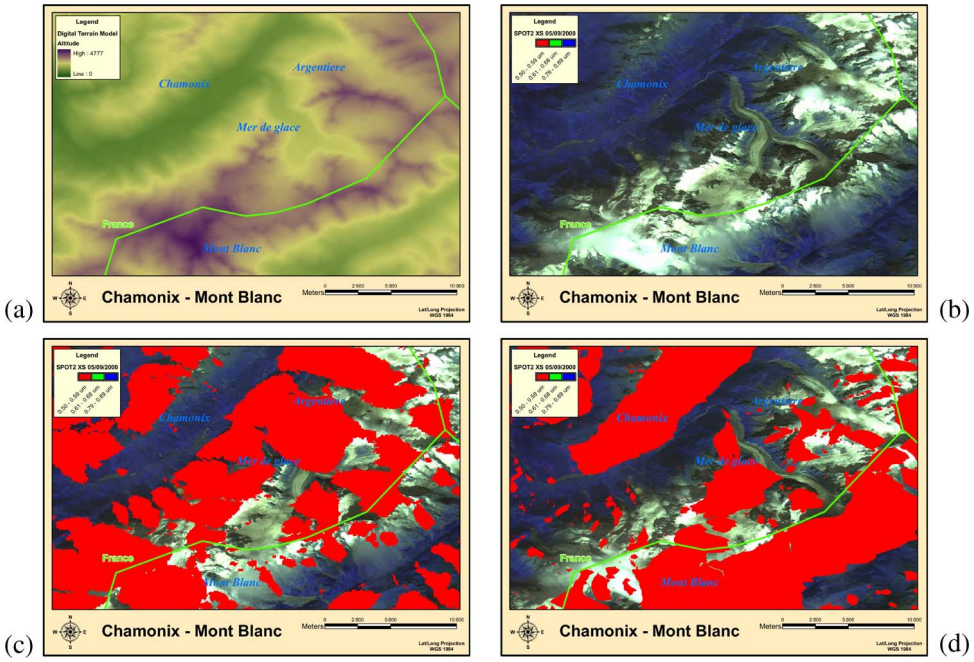

Fig. 7. ERS satellite visibility assessment. (a) Large-scale DTM. (b) Orthorectified SPOT-2 multispectral image. (c) Ascending ERS visibility (nonvisible parts masked in red). (d) Descending ERS visibility.

surges: they succeeded in measuring displacement that is often greater than 1 m/day (up to 7 m/day) mostly in ERS tandem winter interferograms, whereas changes of glacier surface due to precipitation, melt, and wind cause fast decorrelation of the phase signal.

So, the most likely explanation of the summer results is that on the Mer de Glace and Argentière glaciers that are below 3200 m, the interferometric coherence at three-day intervals is completely lost because they are below the 0 °C isotherm (snow line), which is often above 4000 m during the summer according to the Chamonix weather station and an assumed lapse rate of 6°/km. Note also that the coherence map seems to be a good parameter to automatically delimitate glaciarized areas: the surroundings have either an intermediate coherence level in forested areas or a good coherence level at higher altitudes, where rock and low vegetation do not create volume decorrelation.

To investigate the potential of ERS tandem SAR interferometry during the rest of the year, four descending InSAR pairs from October 1995 to April 1996 have been processed (cf. Table II). After the ROI-PAC orbital and topographic fringe removal, an adaptive neighborhood filter [48] has been applied to reestimate the phase and the coherence. Such filtering is required, especially for large baselines, to obtain a sufficient number of samples to reduce the phase noise and the coherence bias and noise. This approach prevents smoothing of edges such as glacier margins and strong backscatterers, which might be useful for further analysis [38].

Among the four interferograms illustrated in Fig. 10, the highest coherence can be observed in the March pair, which has the smallest perpendicular baseline and is still acquired in the cold season. The "new-year" pair has the lowest coherence due to the volume decorrelation caused by the large baseline. Over the Mer de Glace, Leschaux, and Argentière glaciers, the results show good preservation of coherence in the winter interferograms (December and March), whereas in the October and April interferograms, the coherence is well preserved only in the upper parts of the glaciers (south east).

Accordingly, we can conclude that in three-day intervals during the summer season, the variations of the glacier surface state in temperate alpine glaciers such as those of the Chamonix valley are stronger than C-band SAR interferometric tolerances for ERS data. By contrast, coherence is preserved in tandem pairs acquired in the winter season and allows the measurement of glacier displacement at this time of the year. The limitation in using InSAR in intermediate seasons depends on the meteorological conditions and the glacier's altitude. In the following, the most correlated interferogram (March 1996) will be used to illustrate the processing steps applied to obtain velocity fields over the studied glaciers.

3) Phase Analysis: Generally, the interferometric phase between two SAR images is assumed to contain independent contributions from orbit geometry, surface topography, surface motion, and atmospheric changes between the two acquisitions [17].

Due to the fact that the glacier surface is very small compared to a full satellite frame, only local (not regional) atmospheric changes can affect InSAR measurements over the studied glaciers. As radiowave velocity mainly depends on local water vapor pressure and temperature (Smith and Weintraub formula) [49] and as saturation water vapor pressure is rather small near 273 K (i.e., the surface glacier temperature), one-day variations should be minimal in winter.

This can be verified by comparing several different pairs collected during the same season. The similarity of the glacier fringe pattern from the four tandem interferograms presented in Fig. 10 can be visually observed in the high and medium coherence areas. This is confirmed by the wrapped phase

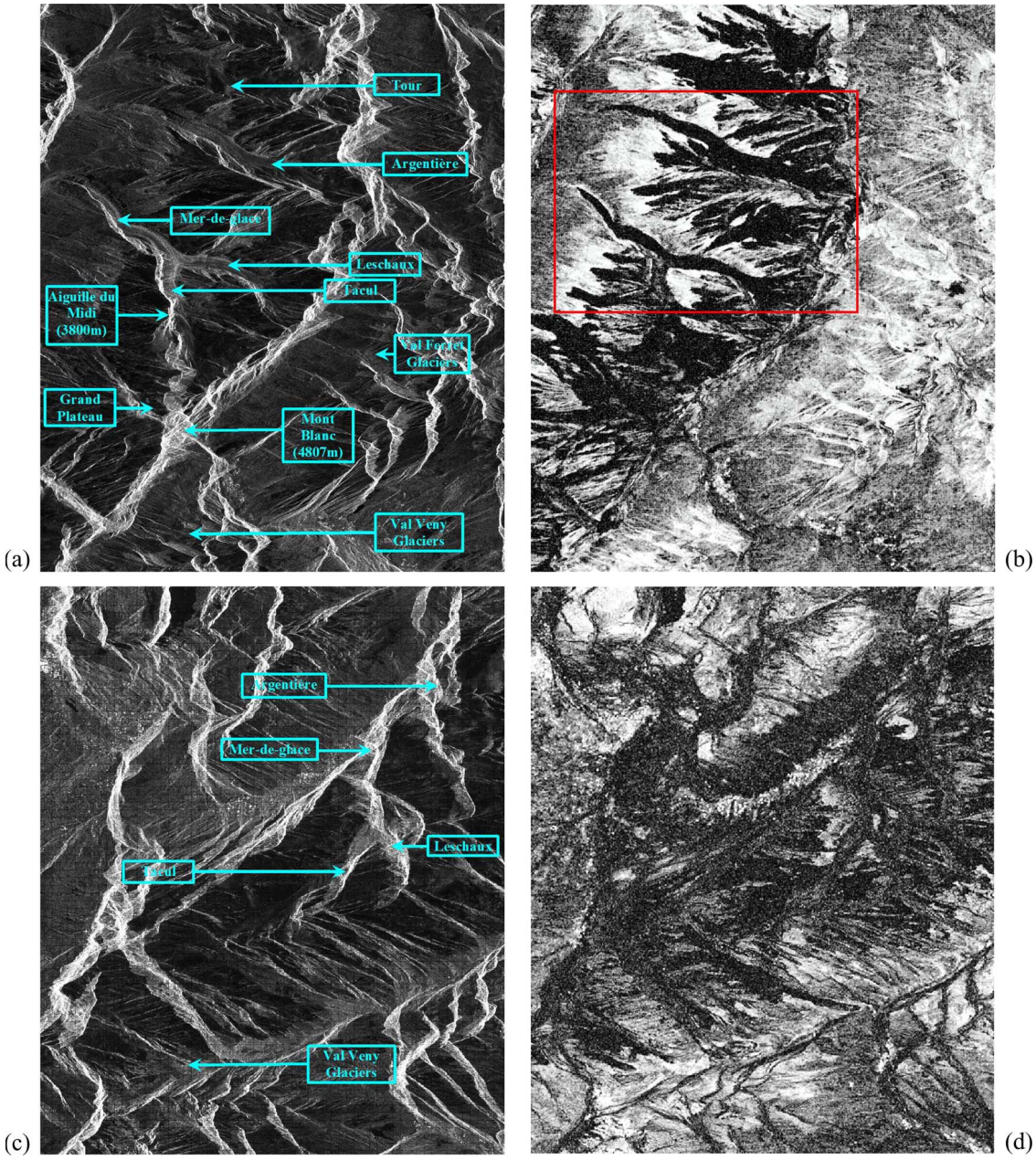

Fig. 8. (a) and (b) ERS1 three-day descending pass interferogram for the summer of 1991, annotated amplitude and coherence map of 1251 × 1531 pixels. The rectangle marked in red will be used in the sequel for further illustration. (c) and (d) ERS-1/2 one-day ascending pass interferogram for the summer of 1995, annotated amplitude and coherence map of 837 × 1024 pixels. These images are in radar geometry (slant range, azimuth) and obtained from SLC data by 1 × 5 multilooking.

differences between interferograms presented in Fig. 11. The difference is almost zero with two consecutive interferograms [March and April pairs, Fig. 11(a)] and slightly increases in some parts of the glaciers when more distanced periods are compared: the March/December pairs [Fig. 11(b)] and the March/October pairs [Fig. 11(c)]. The observed differences are also in quite good agreement with the *in situ* measurements presented in [50]. According to these results, at the scale of the glaciers located in the Alps, the atmospheric perturbations can be considered negligible in winter.

The removal of orbital and topographic fringes can be performed by using the large-scale DTM from Fig. 7(a) and precise orbit information from Delft University [44]. The visual analysis of the four interferograms presented in Fig. 10 shows the accuracy of the processing: out of the glaciers, the phase is almost constant along track and less than half a fringe appears in range direction, even with different perpendicular baselines and 3000-m height variations between the Chamonix valley and the mountain summits.

According to these results, the remaining fringe patterns can be considered to correspond only to the glacier one-day displacement, projected on the SAR LOS, and wrapped in the $[0, 2\pi]$ interval.

C. Phase Unwrapping and Orthorectification

To extract quantitative velocity information from the interferometric fringes shown in Fig. 10, the phase must be unwrapped.

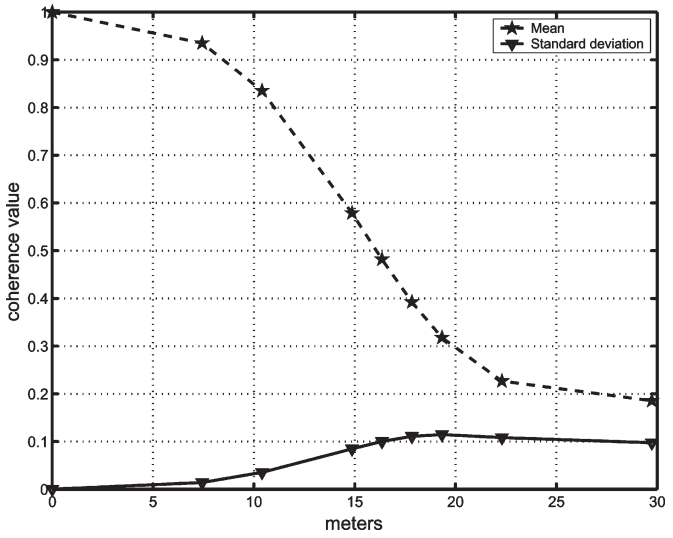

Fig. 9. Coherence values function of the artificially induced displacement created by using twice the same acquisition (ERS-1, August 17, 1991). Coherence mean and standard deviation are measured after 5 × 1 complex averaging on the Mer de Glace and Leschaux glaciers.

Several obstacles make fully automatic phase unwrapping difficult in the case of glacier displacement fringes. First, at the glacier margins, the motion phase signal is discontinuous with the rest of the interferogram, which should be a constant when all geometrical effects are perfectly corrected (orbital and topographic fringe removal). Depending on the studied glaciers, some parts such as the top of the accumulation area might move very slowly and allow the assumption that the velocity is close to zero in these areas. Accordingly, it is possible to assume that there is no displacement within one day for ERS tandem interferograms in such areas and to use them as a zero reference for the phase unwrapping. In the case of the Argentière glacier, the accumulation area is visible in SAR descending passes, but the surface topography is quite steep, which does not allow such an assumption. In the case of the Mer de Glace and Leschaux glaciers, motionless parts can be found in the Mallet glacier at the top of the Leschaux, but with the ERS 23° incidence angle, this part of the glacier is not visible. When there is no zero-speed area connected to the glacier in the interferogram, the observed fringe pattern can be unwrapped, but the result is obtained with an unknown offset. This offset can be found as soon as the motion of one point is known (by ground measurement for instance). This difficulty is increased when the glacier surface is separated in several disconnected parts because of the SAR geometry (shadow/layover) and the lack of coherence or aliasing, which occurs when the glacier accelerates, in ice fall areas for instance: the Nyquist criterion is not satisfied due to the image low sampling compared to the narrow fringe pattern. In this case, for the lowest part of the Argentière glacier for instance, a multiple of 2π is unknown between the different unwrapped parts of the glacier. This problem can be solved by complementary approaches such as speckle tracking [23] or measurement of the displacement of a coherent target to find the right multiple of 2π.

The two main approaches conventionally used to perform phase unwrapping are either local methods based on branch-cut algorithms, which unwrap the phase by propagation along paths as safe as possible [51], or global methods based on least square minimization of the distance between the wrapped phase gradient and the resulting unwrapped phase gradient [52]. With the first approach, the misplacement of branch cuts yields to the propagation of errors, which are multiples of 2π. The second approach has the advantage of allowing the detection and visual assessment of phase-unwrapping errors by computing the wrapped difference between the interferogram and the result.

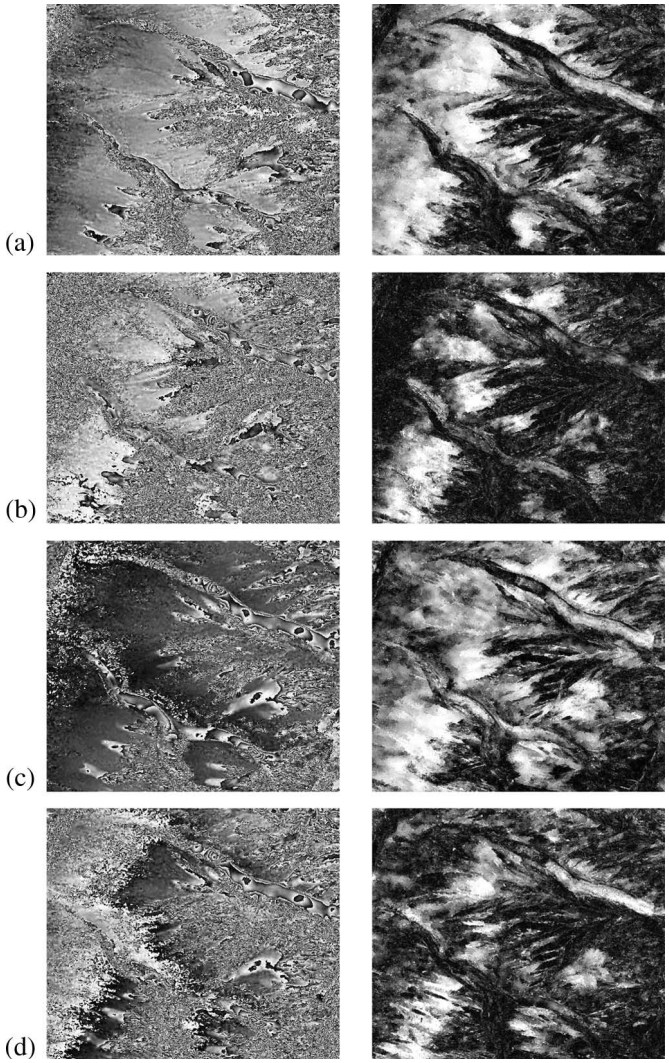

Fig. 10. ERS-1/2 tandem interferograms over the Mer de Glace/Leschaux and Argentière glaciers area (600 × 700 pixels). Differential phase and coherence filtered by amplitude-driven adaptive neighborhood. (a) October 22–23, 1995. (b) December 31, 1995–January 1, 1996. (c) March 10–11, 1996. (d) April 14–15, 1996.

To reduce the phase noise and to obtain a coherence level that reveals unreliable phase areas, the ROI-PAC initial 5 × 1 interferogram is filtered using local frequency estimation [53] and adaptive neighborhoods [48]. The filtered wrapped phase and associated coherence are illustrated in Fig. 10(c). Then, the weighted least squares phase-unwrapping approach has been applied to unwrap the phase over the Mer de Glace/Leschaux and Argentière glaciers. In order to avoid the influence of surrounding discontinuous fringes and corrupted areas, binary weights have been computed from the manual selection of the

Fig. 11. Wrapped phase differences between interferograms presented in Fig. 10. (a) April 14–15, 1996 and March 10–11, 1996. (b) December 31, 1995–January 1, 1996 and March 10–11, 1996. (c) October 22–23, 1995 and March 10–11, 1996.

glacier SAR visible parts. The displacement field resulting from this unwrapping has an unknown offset on each glacier since they are disconnected.

Finally, the whole image is orthorectified, enabling easier computation of the final velocity field and comparison with ground measurements. This step is performed using the ROI-PAC software and the combined DTM described in Section II-C. It is based on the simulation of noise-free intensity images in SAR geometry using the distance to the satellite orbit and the local slope orientation provided by the DTM. Once the simulated image is registered on the real satellite image, the geometrical transformation is coded as a "lookup table," which provides the position in the SAR data of each DTM pixel illuminated by the radar. This allows to resample on the DTM grid any parameter initially computed in SAR geometry using, for instance, a bilinear interpolation.

Once the unwrapped phase is georeferenced, the unknown offsets can be set according to the knowledge of zero displacement areas or by using *in situ* measurements. One ground measurement point is necessary for each separated glacier, with a conversion into SAR LOS one-day displacement. Fig. 12 presents the georeferenced amplitude and coherence, which can be used to assess the confidence in the unwrapped phase. The unwrapped georeferenced differential phase is overlapped over a high-resolution airborne orthophoto to illustrate the portion of the glaciers that has been unwrapped and the geocoding accuracy of the database formed by SAR and optical orthoimages.

V. Motion Estimation

This section discusses the last stage of the processing: the use of the DTM to convert the one-day displacement field measured on the SAR LOS into a glacier velocity field. It presents the final results, comparisons with ground measurements, and uncertainty assessment.

A. From SAR LOS Displacement to Glacier Velocity

Due to the visibility of the studied glaciers with ERS data (Section IV-B1), the velocity field can be measured only through its projection on the LOS of descending acquisitions. The missing information is obtained by using an accurate DTM of the glacier surface and hypothesis often used when there is no reliable complementary information source. The hypotheses are given as follows:

- SPF assumption, which does not take the submergence/emergence velocity into account [30];
- direction of the maximum averaged downhill slope, which does not take a possible sliding component into account [15].

According to these hypotheses, the following steps are performed.

- In each pixel of the DTM, the two components of the elevation gradient are computed to derive the slope Sl and orientation Or angles of the glacier surface according to the angle conventions illustrated in Fig. 13. Then, the three-component unit vector $\overrightarrow{E}_m$ provides the main slope direction

$$\overrightarrow{E}_m = \begin{bmatrix} \cos(Sl) \cdot \cos(Or - \pi) \\ \cos(Sl) \cdot \sin(Or - \pi) \\ -\sin(Sl) \end{bmatrix}. \quad (1)$$

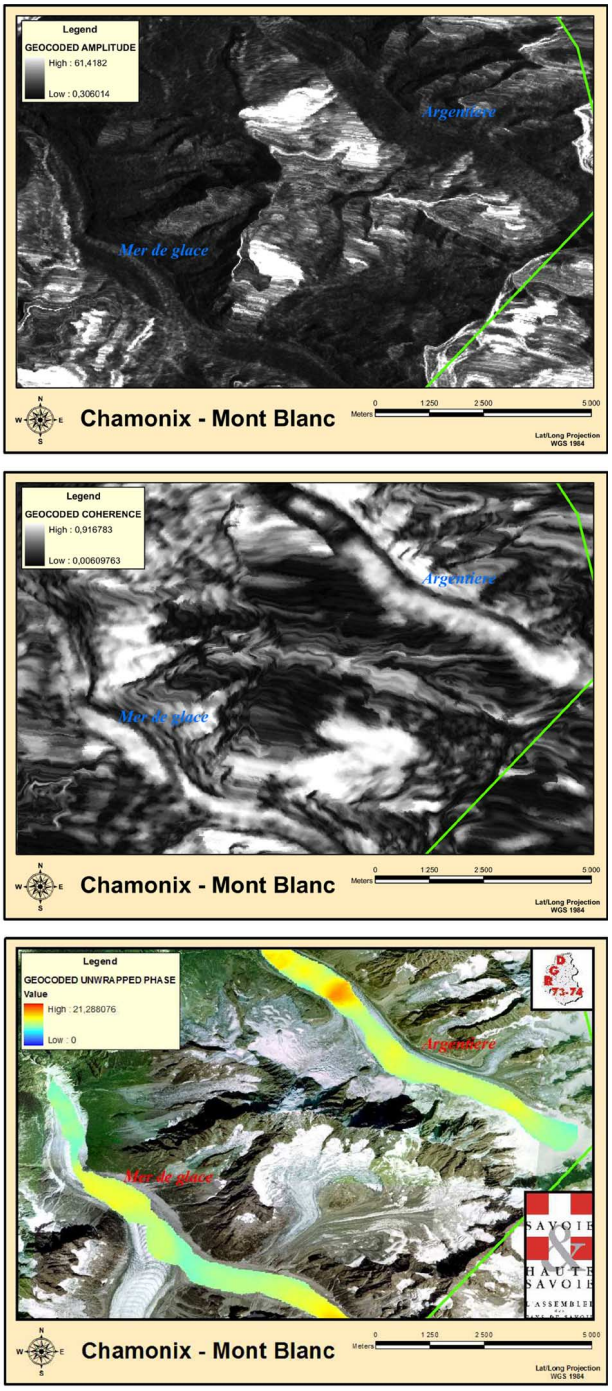

Fig. 12. ERS-1/2 tandem March 1996 interferogram. (a) and (b) Georeferenced amplitude and coherence. (c) Georeferenced unwrapped differential phase of the Mer de Glace and Argentière glaciers overlapped on an airborne orthophoto provided by the RGD-73/74; the color scalebar corresponds to the one-day LOS displacement in centimeters.

- In each pixel of the unwrapped phase image, the orientation of the LOS and the displacement along the movement direction are computed. First, the direction of the satellite must be determined with precision. Two angles are needed as parameters in the model, i.e., vertical and horizontal incidences. Vertical incidence inc_v is the conventional wave incidence angle, while horizontal incidence inc_h is the angle between the horizontal projection of the LOS and the local parallel of latitude

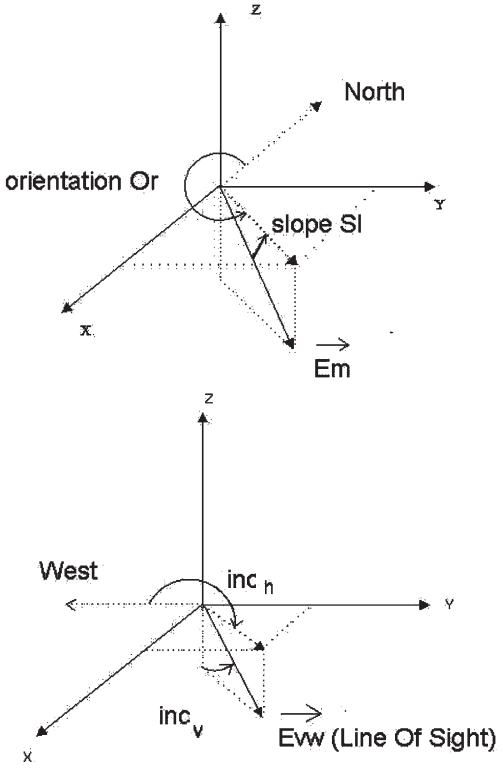

Fig. 13. Glacier surface and SAR LOS orientation angles.

at the current point. The vector representing the satellite LOS is

$$\overrightarrow{E}_{\mathrm{vw}} = \begin{bmatrix} -\sin(inc_v)\cdot\sin(inc_h) \\ -\sin(inc_v)\cdot\cos(inc_h) \\ -\cos(inc_v) \end{bmatrix}. \tag{2}$$

Then, the displacement measured along the LOS D_{vw} is computed from the value of the unwrapped phase Φ_u, i.e.,

$$D_{\mathrm{vw}} = \alpha\frac{\Phi_u}{2\pi} \tag{3}$$

where α is a coefficient containing the geometrical constraints (in the case of ERS satellites $\alpha = 28$ mm). The absolute value of the displacement along the movement direction of the glacier D_m is

$$D_m = \frac{D_{\mathrm{vw}}}{\overrightarrow{E}_{\mathrm{vw}}\cdot\overrightarrow{E}_m}. \tag{4}$$

Finally, the vector of the velocity field on the glacier surface is

$$\overrightarrow{V}_m = \frac{D_m}{\Delta t}\overrightarrow{E}_m \tag{5}$$

where Δt is the time interval of the InSAR pair.

The displacement field obtained between the two interferometric SAR acquisitions in the March 1996 descending pass has been converted into quasi-3-D velocity field according to this processing, using either the aerial optical 1995 DTM where it was available or the large-scale DTM. In both cases, the surface gradient has been computed after 200×200 m^2 smoothing

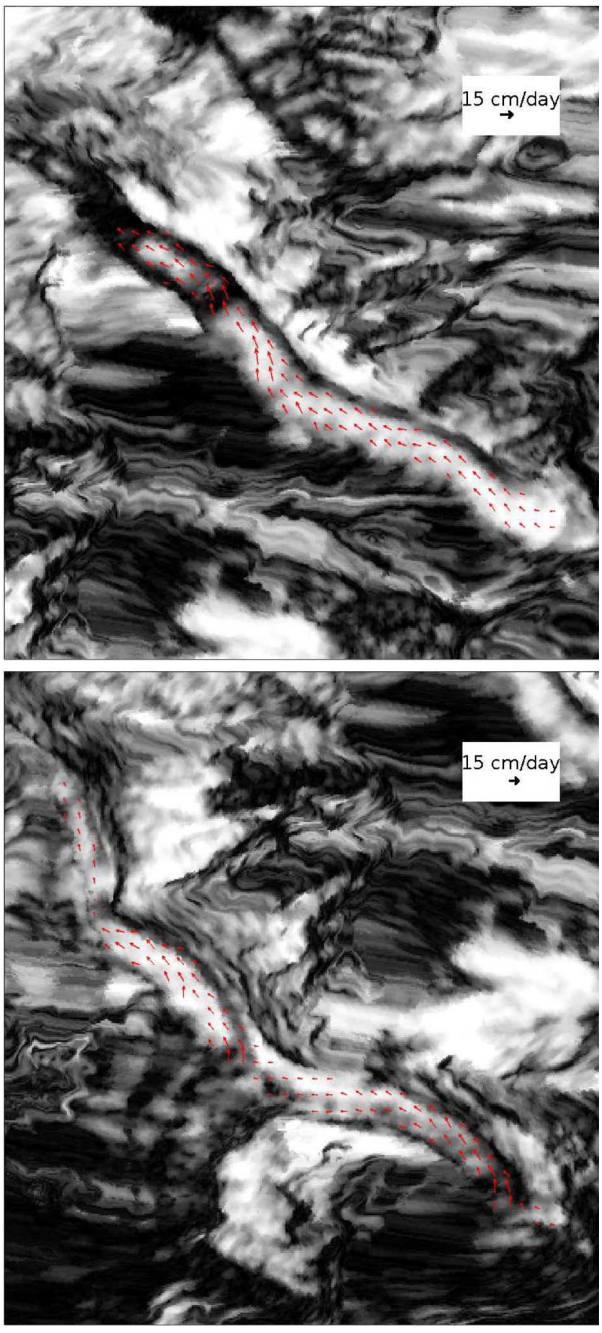

(a)

(b)

Fig. 14. Velocity field derived from the ERS-1/2 March 1996 tandem interferogram over the (a) Argentière and (b) Mer de Glace glaciers, which are overlayed on the orthorectified coherence.

in order to avoid taking microrelief into account. The result presented in Fig. 14 illustrates the flow of the Mer de Glace and Argentière glaciers. Vectors are overlayed on the orthorectified coherence, which can be interpreted as a measure of confidence.

B. Comparison With Ground Measurements

In the following, interferometric and *in situ* velocity measurements are compared. Three velocity profiles are extracted from the quasi-3-D velocity field described in the previous section from the ERS-1/2 March 1996 tandem interferogram. They are compared to the annual mean velocity derived from the annual displacement of ablation stakes between 1995 and 1996 over the Argentière and Mer de Glace/Leschaux glaciers. Fig. 15 illustrates the three profiles and associated uncertainty computed, as described in Section V-C. Along the Argentière longitudinal profile [Fig. 15(b)], the InSAR result reveals the velocity evolution: an increasing speed in the accumulation area up to the first crevasse field. The first point of ground measurements (the highest one) has been used to set the phase-unwrapping unknown offset. The InSAR profile keeps close to the following points.

On the Mer de Glace/Leschaux glacier [Fig. 15(b)], the velocity starts with low values in the upper part close to the Mallet glacier, increases quite fast in the Leschaux where the slopes are very steep, and decreases before the junction point with the Mer de Glace. The low velocity observed in this area is probably due to the weak slope and the fluxes, which are too small upstream to sustain a high velocity. Below the confluence, the speed observed on the Mer de Glace is higher than that of the lower part of the Leschaux glacier. Then, it decreases again on the Mer de Glace glacier tongue. The global profile corresponds to the known behavior of these glaciers and to the published results [36], [54].

On the Mer de Glace longitudinal profile, a strong artifact can be observed at the same location as strong slope changes (about 9000 m from the beginning of the profile). This artifact is due to the conversion of the LOS velocity into 3-D velocity. When the flow direction vector becomes almost perpendicular to the LOS direction, the denominator in (4) becomes close to zero. In this case, the LOS velocity should also be close to zero, but the conversion into 3-D velocity is numerically unstable. This configuration occurs for instance if the slope is oriented toward the radar (this corresponds to the foldover constraint and can be avoided by the use of visibility masks) or when the flow direction is parallel to the azimuth direction (the sensor displacement). In the lower part of the Mer de Glace, the tongue is narrow, and the main slope direction becomes closer to the azimuth direction, which makes the 3-D conversion more sensitive to such artifacts.

C. Uncertainty Assessment

A complete performance assessment of the InSAR velocity measurements is rather difficult because of the complex processing chain and the lack of ground truth (only the one-year displacement of a few ablation stakes between the summers of 1995 and 1996 is available). The effect of the different sources of uncertainty is strongly dependent on the available data, the processing strategy, and the characteristics of the glacier [31]. For the results obtained on the studied glacier, two different sources should be distinguished.

1) Uncertainty linked to the data and their processing. In this experiment, the three information sources are the interferometric pair, the DTM, and the *in situ* measurements used to set the phase-unwrapping offset.
2) Uncertainty linked to the hypotheses used to replace the missing information: in this case, the SPF and the maximum downhill slope assumptions.

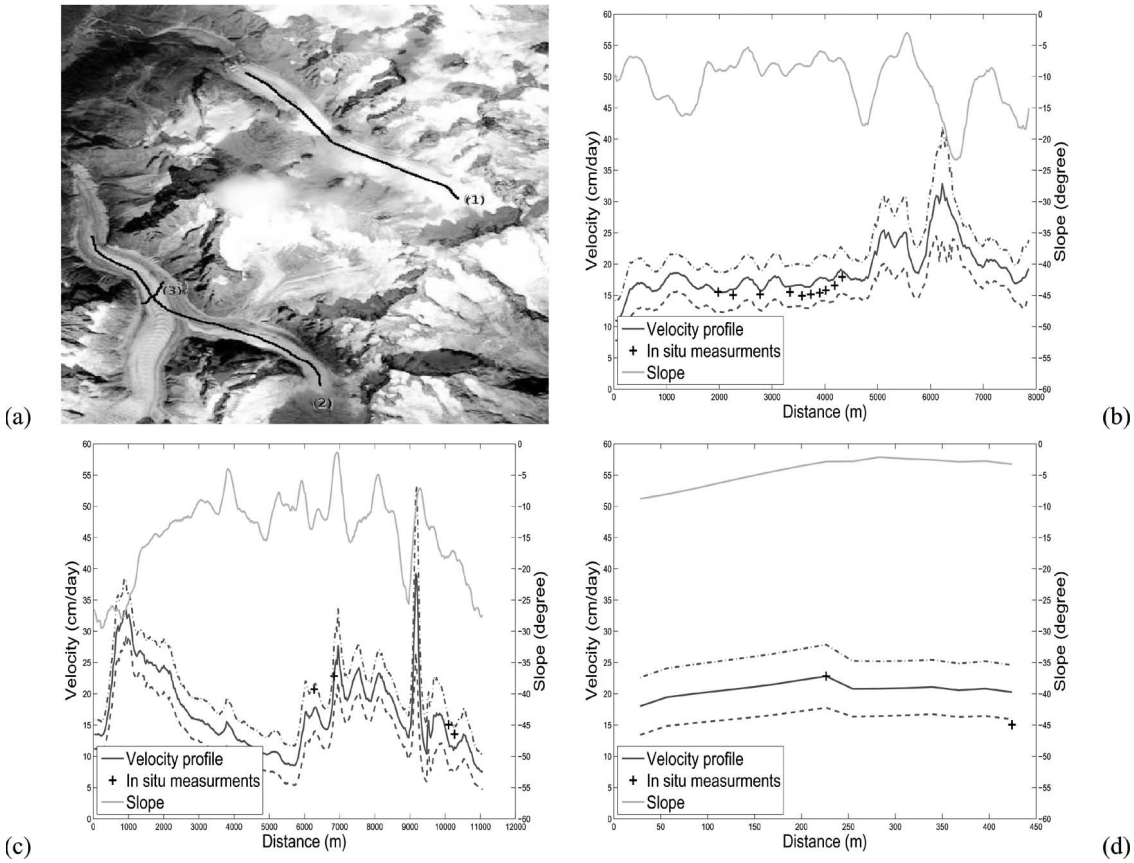

Fig. 15. ERS-1/2 March 10–11, 1996 velocity profiles. (a) SPOT image and profile location. (b) Longitudinal velocity profile on the Argentière glacier [curve 1 in (a)]. (c) Longitudinal velocity profile on the Leschaux/Mer de Glace glacier [curve 2 in (a)]. (d) Transversal velocity profile on the Mer de Glace glacier [curve 3 in (a)].

1) Data and Processing Uncertainty: The D-InSAR phase measure is affected by three different kinds of uncertainty.

1) The first one comes from the speckle noise, which affects the interferograms, especially in low-coherence areas, and requires appropriate filtering to preserve the small size features of Alpine glaciers. This kind of uncertainty affects each point with random values described by a standard deviation, which can be approximated by the Cramer–Rao lower bound [55], i.e.,

$$\sigma_\phi = \sqrt{\left\langle \left(\hat{\phi} - \langle\hat{\phi}\rangle\right)^2 \right\rangle} = \frac{1}{\sqrt{2M}} \frac{\sqrt{1-\gamma^2}}{\gamma}$$

where γ is the coherence level and M is the number of independent looks averaged to obtain the phase estimate $\hat{\phi}$.

2) The second kind of uncertainty is the presence of fringes due to atmospheric perturbations, remaining orbital or topographic fringes, or hazardous phenomena, which are sometimes encountered in ERS interferograms [24]. Regarding atmospheric perturbations, the small scale of Alpine glaciers and the low winter temperatures should prevent large effect as confirmed by the comparison of different pairs from the same season. Regarding orbital and topographical fringes, this experiment has shown that the use of an accurate DTM and the available precise orbits is sufficient to obtain results that are free of the remaining fringes at the scale of the studied glaciers, even with large baselines. The strong surrounding topography of the Alpine glaciers and the availability of accurate DTMs from airborne photographs help to obtain accurate DTM-SAR registration and fringe removal.

3) The last kind of uncertainty comes from the phase-unwrapping step. Least squares unwrapping errors can be estimated by visual assessment of the remaining fringes. The unknown offset can be obtained by using a single-point *in situ* measurement for a whole connex part of a glacier. The precision depends on how this point is measured (by means of differential GPS, etc.) and how it is temporally related to the SAR measurement (same day/month/year, etc.). The resulting error is the same constant on the whole LOS velocity field.

For the results obtained with the March 10–11, 1996, ERS interferogram, the phase correction and unwrapping error is less than π (half a fringe), and the number of looks is approximately $M \simeq 25$ after filtering. Accordingly, the uncertainty that affects the final results can be obtained through the following:

1) computing the LOS uncertainty by adding $\pm\pi/2$ and $\pm\sigma_\phi$ according to the coherence level;
2) applying to this LOS uncertainty the same slope-dependent correction as applied to the LOS velocity (4), which brings the final uncertainty to infinity when the main slope direction is perpendicular to the LOS.

The resulting uncertainty is illustrated on the velocity profiles (Fig. 15) and with the corresponding error bar in Fig. 16, which

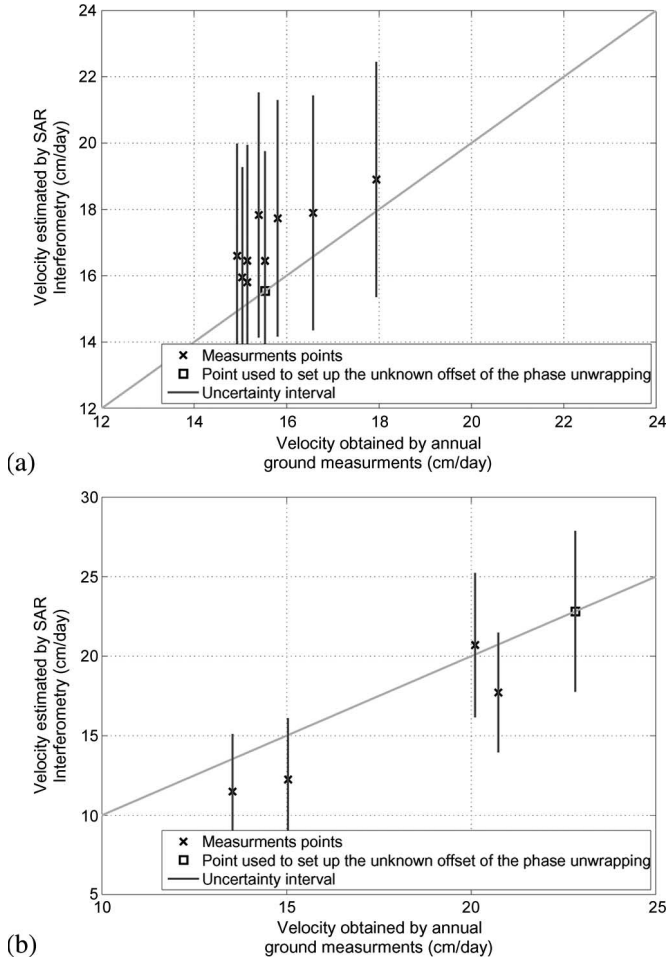

Fig. 16. Comparison between the velocity obtained by SAR interferometry during March 10–11, 1996 and the corresponding annual (August 1995–August 1996) *in situ* measurement on the (a) Argentière and (b) Mer de Glace glaciers. The rectangle points are those used to set up the phase-unwrapping unknown offsets. The vertical error bars show the D-InSAR velocity uncertainty due to the phase noise, phase corrections, and unwrapping errors, with backprojection in the main slope direction.

presents the InSAR measurement versus the *in situ* one-year measurement. This comparison does not take the offset error into account. This would yield a translation of the whole set of points. The distance to the diagonal illustrates the agreement of the dense D-InSAR velocity field with the set of *in situ* measurements.

2) Hypothesis Uncertainty: The hypotheses used to convert InSAR LOS displacement into 3-D velocities is a different source of error, which mainly depends on the studied glaciers and the available complementary information. In this experiment, since only descending measurements are available, the assumptions of SPF and maximum slope direction are used. Uncertainty comes from the slope estimation and the deviation from the hypotheses. Regarding the DTM slope information, a large smoothing (low-pass filter) has to be applied to obtain the main slope direction. This smoothing is large enough to consider that the DTM noise does not affect the slope estimate. The misregistration effect is difficult to assess since it is strongly dependent on the software used for the orthorectification (ROI-PAC from JPL in our case) and the topography itself since it creates the features that are necessary for the registration

TABLE III
IN SITU ONE-YEAR DISPLACEMENT AND LOCAL ABLATION OF TWO TRANSVERSE PROFILES. COMPARISON OF *IN SITU* AND DTM DERIVED FLOW DIRECTIONS

Glacier	Altitude	No. stakes	Horizontal disp.	Vertical disp.	Ablation	Flow direction error	
						Mean	RMS
Argentière	2700 m	11	56.6 m	-5.0 m	-0.9 m	8.9°	17.0°
Mer de Glace	1900 m	4	82.4 m	-8.9 m	-6.7 m	8.4°	30.7°

in the simulated intensity image. From this experiment, it seems that misregistration does not go over 100 m. Since a larger smoothing (200×200 m^2 averaging) has been applied to obtain the main slope and a mask has been used to avoid introducing a glacier border in the smoothing, misregistration should not strongly affect the slope estimate.

The uncertainty due to the SPF assumption is usually small for the fast moving glaciers with strong topography. It mostly affects the vertical component of the velocity, whereas the estimates of the horizontal component should remain relatively unaffected by deviations from the SPF [24]. Errors depend on the submergence/emergence velocity compared to the vertical component of the velocity due to the SPF. For the studied glaciers, it is possible to compare the local mass balance with the one-year displacement of ablation stakes on transverse profiles (cf. Table III). On the Argentière and Mer de Glace glaciers, the ablation represents 20% up to 75% of the vertical displacement, depending on the local altitude. Accordingly, the error due to the SPF assumption is not negligible on the vertical component of the velocity. However, in this experiment, the SPF vertical error should be smaller since the InSAR measurements are performed in winter.

A sliding component of the velocity might also affect the assumption that the velocity is in the direction of maximum downward slopes. However, the studied glaciers are quite narrow and long. Even without knowing the basal topography, one can assume that if there is a sliding component (probably small in winter), it will be in the main direction of the valley, which is given by the surrounding mountains and is not very different from the main slope orientation. This assumption has been confirmed by comparing the horizontal direction derived from the DTM with the displacement of ablation stakes. Results reported in Table III show quite good agreement between the DTM directions and *in situ* measurements on the two glaciers.

VI. CONCLUSION AND PERSPECTIVE

In this paper, the results presented on the Mont-Blanc temperate glaciers show the benefits of using both optical and SAR remote sensing data to obtain geophysical measurements on the glacier surfaces. A DTM has been computed using photogrammetric techniques. This high-resolution DTM has been semiautomatically generated, allowing complex and detailed surfaces to be accurately modeled and to generate orthophotos and 3-D representations. SAR interferograms have been computed from the ERS tandem and three-day pairs. SAR processing issues and difficulties due to the geophysical context have been investigated. Displacement fringes have been obtained over several Alpine glaciers in four winter one-day interferograms. The displacement field measured on the radar LOS has been converted into a quasi-3-D velocity field using the DTM under the assumption of surface-parallel motion in the

direction of the maximum downward slope. A mean velocity provided by *in situ* measurement at one point has been used to set the unknown offset of the field due to the lack of visibility of the motionless part of the glacier. In this case, the InSAR measurement allows to extend ground-point measurements and provides dense velocity fields, which are consistent with the rest of the available *in situ* measurements.

These results show the feasibility of using SAR D-InSAR in winter over temperate glaciers and combining this technique with photogrammetry for modeling and monitoring the glacier activity. The spatial resolution of glacier surface velocity fields is increased compared to the sparse terrestrial measurements. Depending on the satellite repeat-pass periodicity, SAR interferometry allows measurements of this field along the cold season. A new SAR observation potential should be investigated with the future TerraSAR-X satellite with a 11-day repeat cycle.

Furthermore, with the higher resolution of recently launched or future SAR satellites (RADARSAT-2, TerraSAR-X, ALOS, and Cosmo-SkyMed), high-quality DTMs become fundamental for D-InSAR applications at different stages in the processing chain: SLC image synthesis, data georeferencing, and computation of the displacement local direction and orientation when a single LOS is available. The next steps in the project described in this paper will focus on the fusion of the obtained measurements and extracted features (lakes, crevasses, ice falls, etc.) to derive higher level information such as hazard factors and risk maps.

ACKNOWLEDGMENT

The authors would like to thank the ESA for the ERS images provided through Cathegory 1 Projects 1088 and 3525, B. Legresy for the SPOT images, Régie de Gestion des Pays de Savoie (RGD-73/74) for the access to the RIS 73-74 database, and the Laboratory of Glaciology and Geophysics of Environment/Observatoire des Sciences de l'Univers de Grenoble for the *in situ* measurements. They would also like to thank the anonymous reviewers for providing very precise comments and useful advice on this paper.

REFERENCES

[1] IPCC, *Climate change 2001: The scientific basis*, 2001. [Online]. Available: http://www.grida.no/climate/ipcc_tar/wg1

[2] M. B. Dyurgerov, "Mountain and subpolar glaciers show an increase in sensitivity to climate warming and intensification of the water cycle," *J. Hydrol.*, vol. 282, no. 1–4, pp. 164–176, 2003.

[3] S. Richardson and J. Reynolds, "An overview of glacial hazards in the Hymalayas," *Quat. Int.*, vol. 65/66, pp. 31–47, Apr. 2000.

[4] A. Kääb, C. Huggel, L. Fischer, S. Guex, F. Paul, I. Roer, N. Salzmann, S. Schlaefli, K. Schmutz, D. Schneider, T. Strozzi, and Y. Weidmann, "Remote sensing of glacier- and permafrost-related hazards in high mountains: An overview," *Nat. Hazards Earth Syst. Sci.*, vol. 5, no. 4, pp. 527–554, Jul. 2005.

[5] R. J. Braithwaite, "Glacier mass balance: The first 50 years of international monitoring," *Prog. Phys. Geogr.*, vol. 26, no. 1, pp. 76–95, Mar. 2002.

[6] A. Kääb, "Combination of SRTM3 and repeat ASTER data for deriving alpine glacier flow velocities in the Bhutan Himalayas," *Remote Sens. Environ.*, vol. 94, no. 4, pp. 463–474, Feb. 2005.

[7] J. Kargel, M. Abrams, M. Bishop, A. Bush, G. Hamilton, H. Jiskoot, A. Kääb, H. Kieffer, E. Lee, F. Paul, F. Rau, B. Raup, J. Shroder, D. Soltesz, D. Stainforth, L. Stearns, and R. Wessels, "Multispectral imaging contributions to global land ice measurements from space," *Remote Sens. Environ.*, vol. 99, no. 1/2, pp. 187–219, Nov. 2005.

[8] Régie de gestion des données des pays de savoie. [Online]. Available: http://www.rgd73-74.fr

[9] A. Kääb, "Monitoring high mountain terrain deformation from repeated air- and spaceborne optical data: Examples using digital aerial imagery and ASTER data," *ISPRS J. Photogramm. Remote Sens.*, vol. 57, no. 1/2, pp. 39–52, Nov. 2002.

[10] J. Fox and A. M. Nuttall, "Photogrammetry as a research tool for glaciology," *Photogramm. Rec.*, vol. 15, no. 89, pp. 725–737, 1997.

[11] L. M. Andreassen, H. Elvehoy, and B. Kjollmoen, "Using aerial photography to study glacier changes in Norway," *Ann. Glaciol.*, vol. 34, no. 1, pp. 343–348, Jan. 2002.

[12] A. K. Gabriel, R. M. Goldstein, and H. A. Zebker, "Mapping small elevation changes over large areas: Differential radar interferometry," *J. Geophys. Res.*, vol. 94, no. B7, pp. 9183–9191, 1989.

[13] D. Massonnet and T. Rabaute, "Radar interferometry, limits and potential," *IEEE Trans. Geosci. Remote Sens.*, vol. 31, no. 2, pp. 455–464, Mar. 1993.

[14] K. E. Mattar, P. W. Vachon, D. Geudtner, A. L. Gray, I. G. Cumming, and M. Brugman, "Validation of alpine glacier velocity measurements using ERS tandem-mission SAR data," *IEEE Trans. Geosci. Remote Sens.*, vol. 36, no. 3, pp. 974–984, May 1998.

[15] B. T. Rabus and D. R. Fatland, "Comparison of SAR-interferometric and surveyed velocities on a mountain glacier: Black rapids glacier," *J. Glaciol.*, vol. 152, no. 46, pp. 119–128, 2000.

[16] R. R. Forster, K. C. Jezek, L. Koenig, and E. Deeb, "Measurement of glacier geophysical properties from InSAR wrapped phase," *IEEE Trans. Geosci. Remote Sens.*, vol. 41, no. 11, pp. 2595–2604, Nov. 2003.

[17] D. Massonnet and K. Feigl, "Radar interferometry and its application to changes in the Earth's surface," *Rev. Geophys.*, vol. 36, no. 4, pp. 441–500, Nov. 1998.

[18] A. I. Sharov, K. Gutjahr, F. Meyer, and M. Schardt, "Methodical alternatives to the glacier motion measurement from differential SAR interferometry," in *Proc. Photogramm. Comput. Vis., ISPRS Tech. Commission III Symp.*, Graz, Austria, 2002, vol. 34, pt. 3A/B, pp. A-324–A-329.

[19] A. Ferretti, C. Prati, and F. Rocca, "Permanent scatterers in SAR interferometry," *IEEE Trans. Geosci. Remote Sens.*, vol. 39, no. 1, pp. 8–20, Jan. 2001.

[20] R. Michel, J. P. Avouac, and J. Taboury, "Measuring ground displacements from SAR amplitude images: Application to the Landers earthquake," *Geophys. Res. Lett.*, vol. 26, no. 7, pp. 875–878, Apr. 1999.

[21] R. Michel and E. Rignot, "Flow of glaciar Moreno, Argentina, from repeat-pass shuttle imaging radar images: A comparison of the phase correlation method with radar interferometry," *J. Glaciol.*, vol. 45, no. 149, pp. 93–100, 1999.

[22] A. L. Gray, N. Short, K. E. Matter, and K. C. Jezek, "Velocities and ice flux of the Filchner ice shelf and its tributaries determined from speckle tracking interferometry," *Can. J. Remote Sens.*, vol. 27, no. 3, pp. 193–206, 2001.

[23] T. Strozzi, A. Luckman, T. Murray, U. Wegmuller, and C. L. Werner, "Glacier motion estimation using SAR offset-tracking procedures," *IEEE Trans. Geosci. Remote Sens.*, vol. 40, no. 11, pp. 2384–2391, Nov. 2002.

[24] I. Joughin, R. Kwok, and M. A. Fahnestock, "Interferometric estimation of three-dimensional ice-flow using ascending and descending passes," *IEEE Trans. Geosci. Remote Sens.*, vol. 36, no. 1, pp. 25–37, Jan. 1998.

[25] N. Reeh, J. J. Mohr, S. N. Madsen, H. Oerter, and N. S. Gundestrup, "Three-dimensional surface velocities of Storstrommen glacier, Greenland, derived from radar interferometry and ice-sounding radar measurements," *J. Glaciol.*, vol. 49, no. 165, pp. 201–209, 2003.

[26] E. Rignot, R. Forster, and B. Isacks, "Radar interferometric observations of Glacier San Rafael, Chile," *J. Glaciol.*, vol. 42, no. 141, pp. 279–291, 1996.

[27] T. Strozzi, G. H. Gudmundsson, and U. Wegmüller, "Estimation of the surface displacement of Swiss alpine glaciers using satellite radar interferometry," in *Proc. 3rd Workshop Remote Sens. Land, Ice and Snow*, Bern, Switzerland, Mar. 11–13, 2002.

[28] P. Sterzai, F. Mancini, C. Corazzato, C. D. Agata, and G. Diolaiuti, "Contribution of SAR interferometry (InSAR) to the study of alpine glaciers. The example of Forni glacier (central Alps, Italy): Preliminary results," in *Proc. EGS—AGU—EUG Joint Assembly*, Nice, France, Apr. 6–11, 2003.

[29] C. Mätzler and U. Wegmüller, "Dielectric properties of fresh-water ice at microwave frequencies," *J. Phys. D, Appl. Phys.*, vol. 20, no. 12, pp. 1623–1630, Dec. 1987.

[30] N. Reeh, S. N. Madsen, and J. J. Mohr, "Combining SAR interferometry and the equation of continuity to estimate the three-dimensional

glacier surface-velocity vector," *J. Glaciol.*, vol. 45, no. 151, pp. 533–538, 1999.
[31] J. J. Mohr, N. Reeh, and S. N. Madsen, "Accuracy of three-dimensional glacier surface velocities derived from radar interferometry and ice-sounding radar measurements," *J. Glaciol.*, vol. 49, no. 165, pp. 210–222, 2003.
[32] L. Reynaud, "Etude de la dynamique des séracs du Géant (Massif du Mont Blanc)," Ph.D. dissertation, Univ. Sci. Méd. Grenoble, Grenoble, France, 1973.
[33] G. Bocquet and J. C. Ricq, "Measurement of ice movement in subglacial cavities: A new cavitometer beneath the Glacier d'Argentière (Mt-Blanc, France)," *J. Glaciol.*, vol. 18, no. 78, pp. 137–142, 1977.
[34] C. Vincent, "Influence of climate change over the 20th century on four French glacier mass balances," *J. Geophys. Res.*, vol. 107, no. D19, pp. 43–75, Oct. 2002.
[35] R. Burnet and R. Mura, "Surveillance des glaciers par photographie aérienne," *B.T.I.*, pp. 243–248, 1985. 399/401(B2-Geog.-25).
[36] E. Berthier, H. Vadon, D. Baratoux, Y. Arnaud, C. Vincent, K.L. Feigl, F. Rémy, and B. Legrésy, "Mountain glacier surface motion derived from satellite optical imagery," *Remote Sens. Environ.*, vol. 95, no. 1, pp. 14–28, 2005.
[37] E. Berthier, Y. Arnaud, D. Baratoux, C. Vincent, and F. Rémy, "Recent rapid thinning of the 'Mer de Glace' glacier derived from satellite optical images," *Geophys. Res. Lett.*, vol. 31, no. 17, L17401, 2004.
[38] G. Vasile, E. Trouvé, J.-S. Lee, and V. Buzuloiu, "Intensity-driven-adaptive-neighborhood technique for polarimetric and interferometric sar parameters estimation," *IEEE Trans. Geosci. Remote Sens.*, vol. 44, no. 6, pp. 1609–1621, Jun. 2006.
[39] K. Kraus, *Photogrammetrie*, 7. Auflage ed, vol. Band 1. Berlin, Germany: Walter de Gruyter Verlag, 2004.
[40] K. Papathanassiou, I. Hajnsek, H. Rott, and T. Nagler, "Polarimetric sar interferometry for snow cover parameter estimation," in *Proc. POLinSAR Workshop*, 2005, CD-ROM.
[41] D. Massonnet, "Producing ground deformation maps automatically: The DIAPASON concept," in *Proc. IGARSS*, Singapore, 1997, vol. 3, pp. 1338–1340.
[42] H. A. Zebker and R. M. Goldstein, "Topographic mapping from interferometric SAR observations," *J. Geophys. Res.*, vol. 91, no. B5, pp. 4993–4999, Apr. 1986.
[43] P. A. Rosen, S. Hensley, I. R. Joughin, F. K. Li, S. N. Madsen, E. Rodriguez, and R. M. Goldstein, "Synthetic aperture radar interferometry," *Proc. IEEE*, vol. 88, no. 3, pp. 333–382, Mar. 2000.
[44] P. A. Rosen, S. Hensley, G. Peltzer, and M. Simons, "Updated repeat orbit interferometry package released," *Earth Observation Syst. Trans., Amer. Geophys. Union*, vol. 85, no. 5, p. 47, 2004. Electronic Supplement. [Online]. Available: http://www.agu.org
[45] J.-M. Nicolas, F. Tupin, G. Vasile, and E. Trouvé, "SAR processing in the temporal domain. Application to direct interferogram generation and mountain glacier monitoring," in *Proc. Adv. SAR Workshop, Can. Space Agency*, St. Hubert, QC, Canada, Nov. 15–17, 2005, CD-ROM.
[46] R. Hanssen and R. Bamler, "Evaluation of interpolation kernels for SAR interferometry," *IEEE Trans. Geosci. Remote Sens.*, vol. 37, no. 1, pp. 318–321, Jan. 1999.
[47] A. Fischer, H. Rott, and H. Björnsson, "Observation of recent surges of Vatnajkull, Iceland, by means of ERS SAR interferometry," *Ann. Glaciol.*, vol. 37, no. 1, pp. 69–76, Jun. 2003.
[48] G. Vasile, E. Trouvé, M. Ciuc, and V. Buzuloiu, "General adaptive neighborhood technique for improving SAR interferometric coherence estimation," *J. Opt. Soc. Amer. A, Opt. Image Sci.*, vol. 21, no. 8, pp. 1455–1464, Aug. 2004.
[49] H. Tarayre and D. Massonnet, "Atmospheric propagation heterogeneities revealed by ERS-1 interferometry," *Geophys. Res. Lett.*, vol. 23, no. 9, pp. 989–992, 1996.
[50] D. Hantz, "Dynamique et hydrologie du glacier d'Argère," Ph.D. dissertation, CNRS, Lab. Glaciol. Géophys. l'Environ., Saint Martin d'He`res, France, Apr. 1981.
[51] R. M. Goldstein, H. A. Zebker, and C. L. Werner, "Satellite radar interferometry: Two-dimensional phase unwrapping," *Radio Sci.*, vol. 23, no. 4, pp. 713–720, Jul. 1988.
[52] D. C. Ghiglia and L. A. Romero, "Robust two-dimensional weighted and unweighted phase unwrapping that uses fast transforms and iterative methods," *J. Opt. Soc. Amer. A, Opt. Image Sci.*, vol. 11, no. 1, pp. 107–117, Jan. 1994.
[53] E. Trouvé, J. M. Nicolas, and H. Maître, "Improving phase unwrapping techniques by the use of local frequency," *IEEE Trans. Geosci. Remote Sens.*, vol. 36, no. 6, pp. 1963–1972, Nov. 1998.
[54] L. Lliboutry and L. Reynaud, "'Global dynamics' of a temperate valley glacier, Mer de Glace, and past velocities deduced from Forbes'bands," *J. Glaciol.*, vol. 27, no. 96, pp. 207–226, 1981.
[55] E. Rodriguez and J. M. Martin, "Theory and design of interferometric synthetic aperture radars," *Proc. Inst. Electr. Eng.—F*, vol. 139, no. 2, pp. 147–159, Apr. 1992.

Emmanuel Trouvé (M'99) received the Engineer degree in electrical engineering from the Ecole Nationale Supérieure de Techniques Avancées, Paris, France, in 1990 and the Ph.D. degree in signal and image processing from the Ecole Nationale Supérieure des Télécommunications, Paris, in 1996.

From 1996 to 1998, he was with Thomson Marconi Sonar in underwater acoustic and signal processing. Since September 1998, he has been an Associate Professor of signal processing and computer vision with the Université de Savoie, Polytech'Savoie, Annecy, France, and has been working at the Laboratoire d'Informatique, Systèmes, Traitement de l'Information et de la Connaissance. He is also currently with the Laboratoire des Images et des Signaux, Institut National Polytechnique de Grenoble, Centre National de la Recherche Scientifique, Saint-Martin-d'Hères, France. He coordinates the French multilaboratory MEGATOR project (Monitoring the Evolution of Alpine Glaciers by Optical and Radar Remote Sensing). His research interests include SAR image processing and data fusion in remote sensing.

Dr. Trouvé is a member of the IEEE Geoscience and Remote Sensing Society Data Fusion Technical Committee.

Gabriel Vasile (S'04–M'04) received the Engineer degree in electrical engineering and computer science and the M.S. degree in image, shapes, and artificial intelligence from the University Politehnica of Bucharest, Bucharest, Romania, in 2003 and 2004, respectively. He is currently working toward the Ph.D. degree at the University Politehnica of Bucharest and the University of Savoie, Polytech'Savoie, Annecy, France. Since 2004, he has been working on his Ph.D. dissertation on SAR multivariate signal processing with joint supervision from both the University Politehnica of Bucharest and the University of Savoie, Polytech'Savoie, in the framework of the French multilaboratory MEGATOR Project.

From 2001 to 2003, he was an Engineering Assistant with the Center of Microsystems and Microstructures for Environmental Monitoring and Biomedical Applications, National Institute for Research and Development in Micro and Nanotechnologies, Romania. He is currently with the Laboratoire d'Informatique, Systèmes, Traitement de l'Information et de la Connaissance, Université de Savoie and also with the Laboratoire des Images et des Signaux, Institut National Polytechnique de Grenoble, Centre National de la Recherche Scientifique, Saint-Martin-d'Hères, France. His research interests are signal and image processing, polarimetric and interferometric SAR applications, and glacier monitoring.

Michel Gay received the Engineer degree in electrical engineering from the Institut des Sciences de l'Ingénieur de Montpellier, Montpellier, France, in 1987 and the Ph.D. degree in physics from the University Joseph Fourier, Grenoble, France, in 1999.

From 1988 to 2003, he was with Cemagref Grenoble, Grenoble, where he worked on electrical engineering for environmental applications. Since 2003, he has been a Research Engineer with the Laboratoire des Images et des Signaux, Institut National Polytechnique de Grenoble, Centre National de la Recherche Scientifique, Saint-Martin-d'Hères, France. His research interests include remote sensing, image processing, and survey of Alpine glaciers.

Lionel Bombrun (S'06) received the Engineer degree in electrical engineering and the M.S. degree in signal, image, speech, and telecommunications from the Grenoble National Polytechnic Institute (INPG), Grenoble, France, in 2005. He is currently working toward the Ph.D. degree at the Grenoble Image Parole Signal et Automatique Laboratory, INPG, Centre National de la Recherche Scientifique, Saint-Martin-d'Hères, France. Since 2005, he has been working on his Ph.D. dissertation on the development of SAR signal processing at the Laboratoire des Images et des Signaux, INPG, Centre National de la Recherche Scientifique, in the framework of the French multilaboratory MEGATOR Project.

His research interests include SAR polarimetry and interferometry, and glacier monitoring.

Pierre Grussenmeyer received the Engineer degree in geodetic surveying and topography from Ecole Nationale Supérieure des Arts et Industries de Strasbourg (ENSAIS) [currently Institut National des Sciences Appliquees (INSA) de Strasbourg (a Graduate School of Science and Technology)], Strasbourg, France, in 1984 and the Ph.D. degree in photogrammetry from the University of Strasbourg I (in relationship with the Institut Geographique National, Paris, France), Strasbourg, in 1994.

From 1988 to 2004, he was an Associate Professor with ENSAIS. Since 2004, he has been a Professor with INSA Strasbourg and the Head of the Equipe Photogrammétrie et Géomatique, Modèles et Simulations pour l'Architecture, l'Urbanisme et le Paysage-Photogrammetrie Architechturale et Geomatique UMR 694. His current research interests include close-range photogrammetry, architectural photogrammetry and lasergrammetry, visual and virtual models, and cultural heritage documentation.

Prof. Grussenmeyer has been a member of the International Society for Photogrammetry and Remote Sensing since 1996 and the Treasurer and a Member of the board of the International Committee for Architectural Photogrammetry since 1999. He is also a Vice President of the Association Française de Topographie.

Tania Landes received the Engineer degree in geodetic surveying and topography in 1995 from ENSAIS [currently Institut National des Sciences Appliquees (INSA) de Strasbourg (Graduate School of Science and Technology)], Strasbourg, France, and the Ph.D. degree in radar remote sensing from the University of Karlsruhe, Karlsruhe, Germany, in 2000.

Since 2006, she has been an Associate Professor with ENSAIS. She is currently with the Equipe Photogrammétrie et Géomatique, Modèles et Simulations pour l'Architecture, l'Urbanisme et le Paysage-Photogrammetrie Architechturale et Geomatique UMR 694, INSA. Her current research interests include remote sensing and lasergrammetry.

Jean-Marie Nicolas received the M.S. degree from the Ecole Normale Superieure de Saint Cloud, Lyon, France, in 1979 and the Ph.D. degree in physics from the University of Paris XI, Paris, France, in 1982.

He was a Research Scientist with the Laboratoire d'Electronique Philips in medical imaging and was then with Thomson CSF, working in signal and image processing. He is currently with the Département TSI, Ecole Nationale Superieure des Telecommunications, Paris, as a Professor. His research interests include radar imaging.

Philippe Bolon (M'94) was born in 1956. He received the Engineer degree in electrical engineering and the Ph.D. degree in signal processing from the National Polytechnic Institute of Grenoble (INPG), Grenoble, France, in 1978 and 1981, respectively.

From 1984 to 1994, he was an Associate Professor with the Université de Savoie, Polytech'Savoie, Annecy, France. He has been Professor with the Université de Savoie, Polytech'Savoie since September 1994 and the Head of the Laboratoire d'Informatique, Systèmes, Traitement de l'Information et de la Connaissance since 2002. Since 1996, he has been a Member of the steering committee of the French national research group in Signal and Image Processing (GdR ISIS). His current research interests include information fusion, nonlinear image processing, image segmentation, and image analysis.

Dr. Bolon is a member of the European Association for Signal Processing. He was the Chairman or a Cochairman of the Scientific Committee of the International Conference on Quality Control by Artificial Vision (QCAV) in 1997, 1998, 1999, 2001, and 2003.

Ivan Petillot received the Engineer degree in electrical engineering and computer sciences and the M.S. degree in image, information, and hypermedia from the Institut de Recherche en Informatique de Toulouse, Toulouse, France, in 2005. He is currently working toward the Ph.D. degree at the Laboratoire d'Informatique, Systèmes, Traitement de l'Information et de la Connaissance, Université de Savoie, Polytech'Savoie, Annecy, France. Since 2005, he has been working on his Ph.D. dissertation on the information fusion systems for remote sensing at the University of Savoie, in the framework of the MEGATOR Project.

His research interests include information fusion, risk assessment, and glacier monitoring.

Andreea Julea received the Engineer degree in electrical engineering and computer science and the M.S. degree in image processing and artificial intelligence from the University Politehnica of Bucharest, Bucharest, Romania, in 2005 and 2006, respectively. She is currently working toward the Ph.D. degree at the Laboratoire d'Informatique, Systèmes, Traitement de l'Information et de la Connaissance, Université de Savoie, Polytech'Savoie, Annecy, France. Since 2006, she has been working on her Ph.D. dissertation on data mining in remote sensing applications with joint supervision from the University Politehnica of Bucharest and University of Savoie.

Since 2006, she has been with the Space Sciences Institute, Bucharest. Her research interests are data mining, image processing, and remote sensing.

Lionel Valet received the M.S. degree from the Ecole Superieur d'Ingenieur d'Annecy, University of Savoie, Annecy, France, in 1998 and the Ph.D. degree in signal and image processing from the University of Savoie, in 2001.

He is currently an Associate Professor in computer science with the Laboratoire d'Informatique, Systèmes, Traitement de l'Information et de la Connaissance, Université de Savoie, Polytech'Savoie. His research interests include information fusion system conception with applications to image analysis.

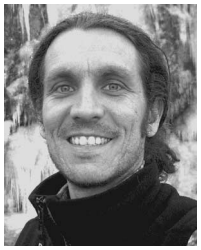

Jocelyn Chanussot (M'04–SM'04) received the Engineer degree in electrical engineering from the Institut National Polytechnique de Grenoble (INPG), Grenoble, France, in 1995 and the Ph.D. degree from Savoie University, Annecy, France, in 1998.

In 1999, he was with the Geography Imagery Perception Laboratory for the Delegation Generale de l'Armement (French National Defence Department). Since 1999, he has been an Associate Professor of signal and image processing with INPG, Centre National de la Recherche Scientifique, Saint-Martin-d'Hères, France, and has been working at the Laboratoire des Images et des Signaux. His research interests include statistical modeling, multicomponent image processing, nonlinear filtering, remote sensing, and data fusion. He is an Associate Editor for *Pattern Recognition* (2006–2008).

Dr. Chanussot is an Associate Editor of the IEEE GEOSCIENCE AND REMOTE SENSING LETTERS (since 2005). He is a Cochair of the IEEE Geoscience and Remote Sensing Society Data Fusion Technical Committee (2005–2007) and a member of the Machine Learning for Signal Processing Technical Committee of the IEEE Signal Processing Society (2006–2008). He serves as a regular reviewer for various conferences (e.g., IEEE ICASSP, IEEE ICIP, ACIVS).

Mathieu Koehl received the Engineer degree in geodetic surveying and topography from ENSAIS [currently Institut National des Sciences Appliquees (INSA) de Strasbourg (a Graduate School of Science and Technology)], Strasbourg , France, in 1990 and the Ph.D. degree in geomatics from the University of Strasbourg I, Strasbourg (in relationship with the Technische Universitat Vienna, Vienna, Austria), in 1999.

Since 1994, he has been an Associate Professor with the Equipe Photogrammétrie et Géomatique, Modèles et Simulations pour l'Architecture, l'Urbanisme et le Paysage-Photogrammetrie Architechturale et Geomatique UMR 694, INSA de Strasbourg. His current research interests include 3-D modeling, 3-D GIS, and WebGIS.

L. Bombrun, M. Gay, E. Trouve, G. Vasile, J. Mars. "DEM Error Retrieval by Analyzing Time Series of Differential Interferograms", *IEEE-GRSL*, 2009.

DEM Error Retrieval by Analyzing Time Series of Differential Interferograms

Lionel Bombrun, *Member, IEEE*, Michel Gay, Emmanuel Trouvé, *Member, IEEE*, Gabriel Vasile, *Member, IEEE*, and Jérôme Mars, *Member, IEEE*

***Abstract*—Two-pass differential synthetic aperture radar interferometry processing have been successfully used by the scientific community to derive velocity fields. Nevertheless, a precise digital elevation model (DEM) is necessary to remove the topographic component from the interferograms. This letter presents a novel method to detect and retrieve DEM errors by analyzing time series of differential interferograms. The principle of the method is based on the comparison of fringe patterns with the perpendicular baseline. First, a mathematical description of the algorithm is exposed. Then, the algorithm is applied on a series of four one-day European Remote Sensing 1 and 2 satellite (ERS-1/2) interferograms.**

***Index Terms*—Digital elevation model (DEM), interferogram time series, synthetic aperture radar (SAR) interferometry (InSAR).**

I. Introduction

SYNTHETIC aperture radar (SAR) interferometry (InSAR) is widely used to create high-resolution and high-accuracy topographic maps [1], [2] and to derive velocity fields [3]–[6]. The interferometric phase is sensitive to different contributions, such as the topography, the atmospheric perturbations, and the ground displacement between the two acquisitions. The latter can be estimated by InSAR techniques if and only if nondisplacement terms can be compensated or neglected.

In two-pass differential SAR interferometry (D-InSAR), a digital elevation model (DEM) is introduced in the processing to remove the topographic component from the interferograms. When the DEM is not precise enough, residual topographic fringe patterns appear and can be misinterpreted or confused with the sought-after displacement fields. This may happen for instance when studying Alpine glacier displacement, since DEMs derived from optical data need correction in snow covered areas and Shuttle Radar Topography Mission DEM is interpolated in shadow areas. When no DEM is available to compensate the topographic phase, an alternative consists in using only SAR interferometric data with three or four acquisitions. In the so-called "four-pass method," two independent interferograms are computed and combined according to their baselines to remove the topographic fringes.

In this letter, a different strategy based on the same principle is proposed to detect and retrieve DEM errors by analyzing time series of differential interferograms. The proposed method is dedicated to the analysis of time series of differential interferograms computed with the available DEM. It consists in computing the phase differences between differential interferograms and comparing the resulting fringe patterns with the perpendicular baseline differences. A test is applied in order to discriminate residual topographic fringes due to DEM errors from fringes due to the evolution of the displacement field between the interferograms or other error sources. If residual fringes vary with the perpendicular baselines, they are identified as topographic error fringes. In this case, an estimation of the DEM errors can be performed followed by DEM corrections. Otherwise, if the other error sources can be neglected (mainly tropospheric effects), the residual fringes reveal a variation of the displacement field which provides useful information on the studied area.

In the following sections, some definitions and a description of the proposed method are first provided. Then, the experimental results are presented on a series of European Remote Sensing 1 and 2 (ERS-1/2) satellite interferograms acquired in the Alps to study glacier displacement fields in Chamonix Mont-Blanc area.

II. Methodology

A. Mathematical Considerations

Let us denote by Φ^i a tandem interferogram acquired at date $(i, i+1)$. Φ^i_{topo} represents the interferometric component at date i corresponding to topographic fringes, i.e., fringes due to the true height variation Δz over the studied area. To take DEM errors into account, Δz is expressed as the sum of the height given by the DEM (Δz^{DEM}) and the DEM error (Δz^{err})

$$\Delta z = \Delta z^{\text{DEM}} + \Delta z^{\text{err}}. \tag{1}$$

Φ^i_{topo} can be expressed as a function of the perpendicular baseline at date i $(B^i_\perp)$ by the following equation as:

$$\Phi^i_{\text{topo}} = \frac{4\pi}{\lambda}\frac{B^i_\perp}{R_1 \sin\theta}\Delta z = \frac{2\pi}{e^i_a}\Delta z \tag{2}$$

Manuscript received February 14, 2008; revised June 13, 2008, November 7, 2008, February 27, 2009, and June 8, 2009. First published August 28, 2009; current version published October 14, 2009. This work was supported by the MEGATOR and EFIDIR projects (ACI-MD-04 and ANR-2007-MDCO-04).

L. Bombrun, M. Gay, G. Vasile, and J. Mars are with the GIPSA Laboratory, Grenoble Institute of Technology, 38031 Grenoble, France (e-mail: lionel.bombrun@gipsa-lab.grenoble-inp.fr; michel.gay@gipsa-lab.grenoble-inp.fr; gabriel.vasile@gipsa-lab.grenoble-inp.fr; jerome.mars@gipsa-lab.grenoble-inp.fr).

E. Trouvé is with the Laboratoire d'Informatique, Systèmes, Traitement de l'Information et de la Connaissance, 74016 Annecy, France (e-mail: emmanuel.trouve@univ-savoie.fr).

Color versions of one or more of the figures in this paper are available online at http://ieeexplore.ieee.org.

Digital Object Identifier 10.1109/LGRS.2009.2026434

1545-598X/$26.00 © 2009 IEEE

Authorized licensed use limited to: Bombrun Lionel. Downloaded on December 16, 2009 at 09:45 from IEEE Xplore. Restrictions apply.

with the height of ambiguity defined as

$$e_a^i = \frac{\lambda}{2}\frac{R_1 \sin\theta}{B_\perp^i}. \tag{3}$$

By combining (1) and (2), the topographic component can be expressed as the sum of two terms by

$$\Phi_{\text{topo}}^i = \frac{4\pi}{\lambda}\frac{B_\perp^i}{R_1 \sin\theta}\Delta z^{\text{DEM}} + \frac{4\pi}{\lambda}\frac{B_\perp^i}{R_1 \sin\theta}\Delta z^{\text{err}} \tag{4}$$

$$= \Phi_{\text{topo}}^{i,\text{DEM}} + \Phi_{\text{topo}}^{i,\text{err}} \tag{5}$$

where $\Phi_{\text{topo}}^{i,\text{DEM}}$ represents the topographic component compensated by the DEM and $\Phi_{\text{topo}}^{i,\text{err}}$ is defined as residual topographic fringes, i.e., topographic fringes which are not removed from the interferogram by using the DEM.

The differential interferometric phase (named Φ_{d}^i) is defined as the tandem interferogram acquired at date $(i, i+1)$ minus the topographic component compensated by the DEM. Φ_{d}^i can be expressed as follows:

$$\Phi_{\text{d}}^i = \Phi^i - \Phi_{\text{topo}}^{i,\text{DEM}}. \tag{6}$$

Let ρ_{d}^i and ρ_{d}^j be two differential interferograms acquired at date $(i, i+1)$ and $(j, j+1)$. The interferogram difference (noted ρ^{ij}) is defined as the Hermitian product between the two differential interferograms by

$$\rho^{ij} = \rho_{\text{d}}^i {\rho_{\text{d}}^j}^\dagger = c^i c^j e^{i\left(\Phi_{\text{d}}^i - \Phi_{\text{d}}^j\right)} \tag{7}$$

$$= c^{ij} e^{i\Delta\Phi^{i-j}} \tag{8}$$

where c^{ij} is defined as the equivalent coherence.

The phase difference between differential interferograms $\Delta\Phi^{i-j}$ is defined in (9) as the difference between tandem differential interferograms phases acquired at dates $(i, i+1)$ and $(j, j+1)$

$$\Delta\Phi^{i-j} = Arg(\rho^{ij}) = \left[\Phi_{\text{d}}^i - \Phi_{\text{d}}^j\right] \text{ modulo } 2\pi. \tag{9}$$

The phase difference between differential interferograms can be expressed as the sum of four terms as

$$\Delta\Phi^{I-j} = \Delta\Phi_{\text{topo}}^{ij} + \Delta\Phi_{\text{atm}}^{ij} + \Delta\Phi_{\text{displ}}^{ij} + \Delta\Phi_{\text{noise}}^{ij} \tag{10}$$

where $\Delta\Phi_{\text{topo}}^{ij}$ characterizes the residual topographic fringes, $\Delta\Phi_{\text{atm}}^{ij}$ is the residual phase due to atmospheric artifacts, $\Delta\Phi_{\text{displ}}^{ij}$ is the component due to variations of the displacement field between the two interferograms, and $\Delta\Phi_{\text{noise}}^{ij}$ is a term of residual noise, due, for example, to temporal decorrelation.

In this letter, $\Delta\Phi_{\text{topo}}^{ij}$ is considered as the "signal part." All other terms can be viewed as the "noise part." Let us now focus on the topographic term.

1) Characterization of the "Signal Part": The residual topographic fringes $\Delta\Phi_{\text{topo}}^{ij}$ in the phase difference between interferograms at dates i and j can be expressed as a function of the DEM error Δz^{err} by

$$\Delta\Phi_{\text{topo}}^{ij} = \left(\Phi_{\text{topo}}^i - \Phi_{\text{topo}}^{i,\text{DEM}}\right) - \left(\Phi_{\text{topo}}^j - \Phi_{\text{topo}}^{j,\text{DEM}}\right)$$

$$= \frac{4\pi}{\lambda}\frac{\left(B_\perp^i - B_\perp^j\right)}{R_1 \sin\theta}\Delta z^{\text{err}}$$

$$= \frac{4\pi}{\lambda}\frac{\Delta B_\perp^{ij}}{R_1 \sin\theta}\Delta z^{\text{err}} \tag{11}$$

$$= \frac{2\pi}{\Delta e_a^{ij}}\Delta z^{\text{err}} \tag{12}$$

where the equivalent perpendicular baseline $\Delta B_\perp^{ij}$ can be defined as the difference of the two perpendicular baseline at dates i and j. Similarly, the equivalent height of ambiguity Δe_a^{ij} can be defined by (14)

$$\Delta B_\perp^{ij} = B_\perp^i - B_\perp^j \tag{13}$$

$$\Delta e_a^{ij} = \frac{\lambda}{2}\frac{R_1 \sin\theta}{B_\perp^i - B_\perp^j} = \frac{1}{\frac{1}{e_a^i} - \frac{1}{e_a^j}}. \tag{14}$$

Let $\Delta N_{\text{topo}}^{ij}(X, Y)$ be the number of fringes observed on $\Delta\Phi_{\text{topo}}^{ij}$ between two points X and Y, and $\Delta z^{\text{err}}(X, Y)$ the elevation error between X and Y points. It yields

$$\Delta\Phi_{\text{topo}}^{ij}(X, Y) = 2\pi\Delta N_{\text{topo}}^{ij}(X, Y) \tag{15}$$

and by combining (12) and (15) to

$$\Delta z^{\text{err}}(X, Y) = \Delta N_{\text{topo}}^{ij}(X, Y)\Delta e_a^{ij}. \tag{16}$$

In (16), it is interesting to note that for residual topographic fringes, the product $\Delta N_{\text{topo}}^{ij}(X, Y)\,\Delta e_a^{ij}$ is constant over the different interferogram pairs (i, j). The principle of the proposed method is to test the equality from (16) over all the differential interferogram pairs of the stack in order to detect DEM errors.

2) Hypothesis Test: For real data, let $\Delta N^{ij}(X, Y)$ be the number of fringes observed on $\Delta\Phi^{i-j}$ between X and Y points. $\Delta N^{ij}(X, Y)$ can be expressed as the sum of two terms, one due to the topography $\Delta N_{\text{topo}}^{ij}(X, Y)$ ("signal part") and one due to other contributions (displacement fringes, atmospheric perturbations, ...) $\Delta N_{\text{other}}^{ij}(X, Y)$ ("noise part")

$$\Delta N^{ij}(X, Y) = \Delta N_{\text{topo}}^{ij}(X, Y) + \Delta N_{\text{other}}^{ij}(X, Y). \tag{17}$$

As $\Delta N_{\text{other}}^{ij}(X, Y)$ is not inversely proportional to the equivalent height of ambiguity Δe_a^{ij}, one can test if the product $\Delta N^{ij}(X, Y)\Delta e_a^{ij}$ is constant over the different interferograms pairs (i, j). This leads to the following hypothesis test:

$$\begin{cases} H_0 : \forall(ij) & \Delta N_{ij}(X, Y)\Delta e_a^{ij} = K(X, Y) \\ H_1 : \exists(ij) & \Delta N_{ij}(X, Y)\Delta e_a^{ij} \neq K(X, Y). \end{cases} \tag{18}$$

1) If the first hypothesis H_0 is decided, $K(X, Y)$ is considered as a constant over all the interferograms pairs (i, j). Equation (16) implies that the DEM used to remove topographic phase contribution has error. In that case, (12) allows one to estimate the DEM error $(\text{DEM}_{\text{error}}^i)$ for the

Authorized licensed use limited to: Bombrun Lionel. Downloaded on December 16, 2009 at 09:45 from IEEE Xplore. Restrictions apply.

interferogram difference at date i and j. This estimation is performed for all the interferograms differences. The DEM error map is the average value of the DEM error found for all the interferograms differences

$$\mathrm{DEM}_{\mathrm{error}} = \frac{1}{N}\sum_{i=1}^{N}\mathrm{DEM}^{i}_{\mathrm{error}}.$$

The new DEM is equal to the old DEM plus the $\mathrm{DEM}_{\mathrm{error}}$.

2) If H_0 is rejected, $K(X,Y)$ cannot be considered as a constant over all the interferograms pairs (i,j). Residual fringes are not only due to DEM error.

B. Comparison With the Four-Pass InSAR Method

The conventional four-pass D-InSAR method [7] uses four independent SAR acquisitions to derive displacement measures. This method does not require *a priori* DEM knowledge. The first two interferometric SAR acquisitions are used to compute the topographic phase component in each pixels of the interferograms. Then, this information is used to remove topography from the second interferogram which is generated from the last two acquisitions.

In the two-pass D-InSAR method, a DEM is introduced to remove the topographic phase. This processing can be repeated to each couple of interferometric SAR acquisitions to derive a stack of two-pass differential interferograms. The proposed approach presents a novel method to *a posteriori* evaluate the DEM accuracy over the interferogram stack. Based on the four-pass D-InSAR principles, the height error is expressed in terms of the equivalent height of ambiguity for each interferogram. Then, the DEM anomalies are detected by the basic hypothesis testing from (18).

One can notice that the phase measured in (7) corresponds to a double interferogram differentiation. This stage is similar to the double differential proposed by the four-pass InSAR method to remove topography. However, both the data set and the context are different between the two techniques.

1) The four-pass InSAR method uses two interferograms (therefore four independent SAR acquisitions) to isolate the topographic phase [8]. This method is applied when no DEM are available to compensate the topographic phase for displacement measures.
2) In the proposed method, a series of differential interferograms is analyzed. This stack is obtained with the same DEM. If N independent differential interferograms are generated, $N-1$ independent phase difference between differential interferograms are obtained. To test the hypothesis H_0, at least two independent phase difference between differential interferograms $(\Delta\Phi^{i-j})$ are necessary. It means that the proposed method requires at least three independent differential interferograms.

The proposed method can be viewed as an extension of the four-pass InSAR method to retrieve DEM error in a series of differential interferograms.

TABLE I
PERPENDICULAR BASELINE AND HEIGHT OF AMBIGUITY

interferogram date	$B_\perp$ (m)	e_a (m)
95.10.22/95.10.23	-107	80
95.12.31/96.01.01	208	41
96.03.10/96.03.11	9	960
96.04.14/96.04.15	93	93

TABLE II
EQUIVALENT PERPENDICULAR BASELINE AND EQUIVALENT HEIGHT OF AMBIGUITY

date	Dec. Oct.	Mar. Dec.	Mar. Oct.	Apr. Mar.	Apr. Dec.	Apr. Oct.
$\Delta B_\perp$ (m)	315	-199	116	84	-115	200
Δe_a (m)	27	-43	74	103	-75	43

III. APPLICATION ON ERS-1/2 INTERFEROGRAMS

In this section, experimental results are presented using four descending one-day ERS-1/2 tandem interferometric data acquired in the Alps over the Chamonix Mont-Blanc area from October 1995 to April 1996 (Table I). This time series has been used to estimate displacement fields over glaciers [6] and to analyze fringe patterns and coherence levels [9]. In this letter, those interferograms are analyzed to determine if topographic fringes are correctly removed from the interferograms. The proposed method described in Section II is applied over the nine studied glaciers.

First of all, the four one-day ERS-1/2 tandem interferometric pairs from October 1995 to April 1996 are processed with the Repeat Orbit Interferometry Package (ROI-PAC) software from the Jet Propulsion Laboratory. This processor takes into account the precise orbits from the Delft University, The Netherlands, to remove the orbital fringes [10]. Moreover, a DEM is used by ROI-PAC software to estimate the topographic component and remove it from the interferogram. The DEM used by the SAR processor is computed by photogrammetry from airborne photographs of 1980.

Once the four differential interferograms pairs are created, the three wrapped phase difference between differential interferograms ($\Delta\Phi_{\mathrm{April-March}}$, $\Delta\Phi_{\mathrm{April-December}}$, and $\Delta\Phi_{\mathrm{April-October}}$) and the three equivalent coherence are computed according to (8) and (9). Next, over each glacier, the three wrapped phase difference between differential interferograms are unwrapped [11].

The following algorithm is applied to determine if topographic fringes are correctly removed from the differential interferograms by means of the equivalent height of ambiguity (Table II): First, for each glacier, pixels with sufficient equivalent coherence for the three couples are selected. Then, for all the selected pixels X and Y, $K^{ij}(X,Y)$ is computed for the three unwrapped phase difference between differential interferograms.

1) If $K^{ij}(X,Y)$ is a constant for all the couples, the hypothesis H_0 is decided. It means that the residual fringes are topographic ones, and the studied pixel is affected to the "topographic class."
2) If $K^{ij}(X,Y)$ varies with the interferometric couple, the hypothesis H_0 is rejected. Therefore, the pixel is affected to the "nontopographic class."

Authorized licensed use limited to: Bombrun Lionel. Downloaded on December 16, 2009 at 09:45 from IEEE Xplore. Restrictions apply.

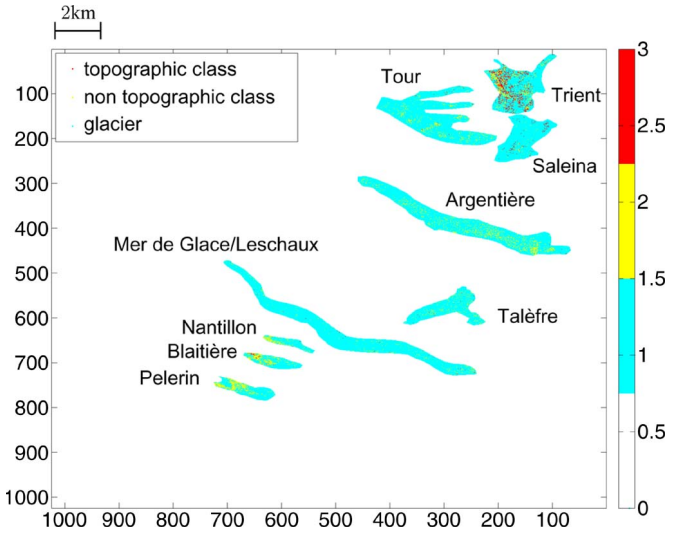

Fig. 1. Classification map into "topographic" and "nontopographic" class.

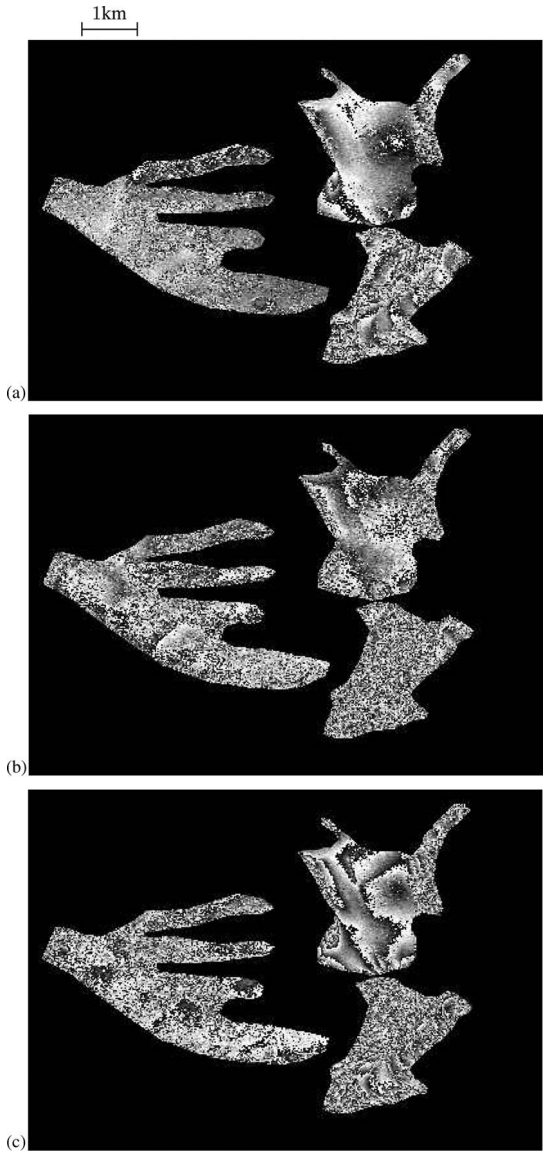

Fig. 2. Wrapped phase difference between interferograms on the Tour, Trient, and Saleina glaciers. (a) $\Delta\Phi_{\mathrm{April-March}}$. (b) $\Delta\Phi_{\mathrm{April-December}}$. (c) $\Delta\Phi_{\mathrm{April-October}}$.

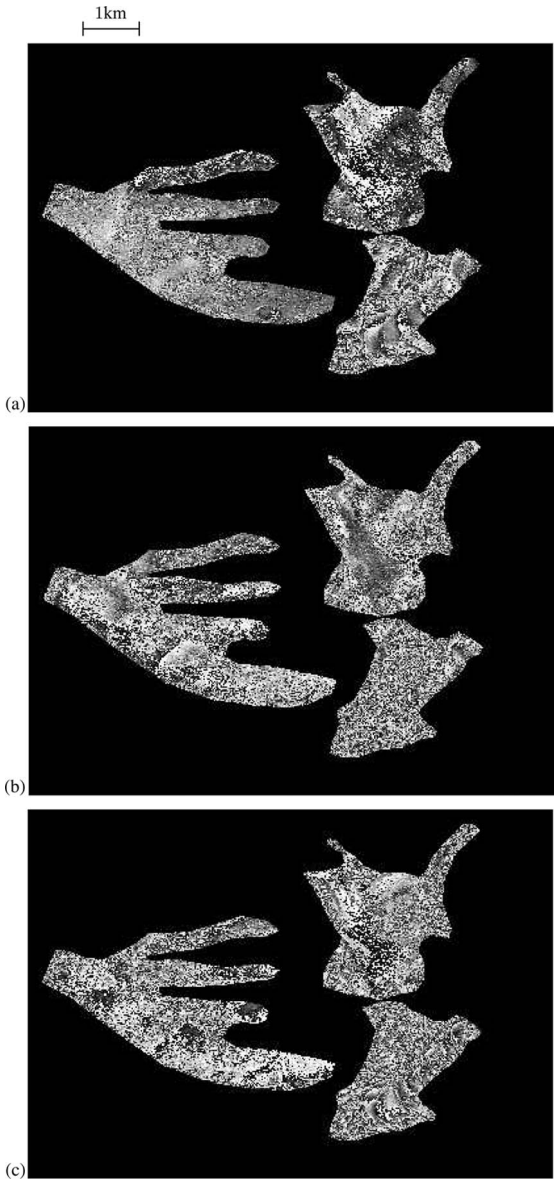

Fig. 3. Wrapped phase difference between interferograms on the Tour, Trient, and Saleina glaciers with the new DEM. (a) $\Delta\Phi_{\mathrm{April-March}}$. (b) $\Delta\Phi_{\mathrm{April-December}}$. (c) $\Delta\Phi_{\mathrm{April-October}}$.

The variation coefficient γ of the variable K^{ij} is the criterion chosen to achieve this assignment. Let $\overrightarrow{K}(X,Y)$ be the vector which contains the values of $K^{ij}(X,Y)$ for all the couples i and j at points X and Y. If $|\gamma(X,Y)|$ is lower than a given threshold, $K^{ij}(X,Y)$ can be said independent of the couples. The hypothesis that residual fringes are topographic ones is therefore assumed. If $|\gamma(X,Y)|$ is greater than a given threshold, the pixel is affected to the "nontopographic class."

Fig. 1 shows the result of the classification of the pixels into topographic and nontopographic class. The white color indicates nonglaciers area. Pixels in cyan are those which have not got a sufficient equivalent coherence for each couple. The proposed algorithm has not been applied on those pixels. There is not enough confidence on the interferometric phase. Pixels affected with the label "topographic class" are in red and those with the label "nontopographic class" are in yellow.

Authorized licensed use limited to: Bombrun Lionel. Downloaded on December 16, 2009 at 09:45 from IEEE Xplore. Restrictions apply.

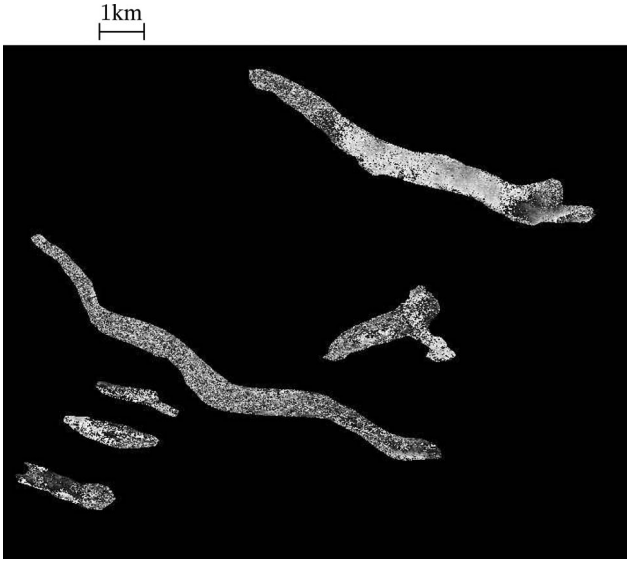

Fig. 4. Wrapped phase difference between interferograms on the Argentière glacier. $\Delta\Phi_{\mathrm{April-October}}$.

First, it can be noticed that on most of the studied glaciers, pixels are affected to the "nontopographic class." Topographic fringes seems to be correctly removed from the interferograms and displacement profiles along those glaciers are validated.

Nevertheless, one can see on the Trient glacier located on the northeast of the image that most of the pixels are affected to the "topographic class." We can conclude that topographic fringes are not well removed on the Trient glacier probably because of the insufficient precision of the DEM on the Trient glacier which is located in Switzerland. Fig. 2 shows the wrapped phase difference between interferograms on the Tour, Trient, and Saleina glaciers. Residual fringes can be observed on the Trient glacier situated on the northeast of the image. The proposed method allows characterizing those fringes as residual topographic fringes.

To remove topographic fringes on the Trient glacier, DEM errors are first estimated according to (12). Then, topographic fringes are calculated with the corrected DEM and removed from the interferograms. Fig. 3 shows the wrapped phase difference between interferograms on the Tour, Trient, and Saleina glaciers computed with the new DEM. Now, residual fringes do not vary with the equivalent height of ambiguity. It confirms that fringes observed previously on the Trient glaciers were topographic ones.

Fig. 4 shows the wrapped phase difference between differential interferograms $(\Delta\Phi_{\mathrm{April-October}})$. On the Argentière glacier, located on the north of the image, residual fringes are observed. The proposed algorithm does not detect those fringes as topographic ones. Residual fringes can be due to atmospheric artifacts or to an evolution of the velocity field. The authors have shown that one-day atmospheric changes are minimal in winter [6]. Residual fringes observed on the upper part of the Argentière glacier can be interpreted as an evolution of the displacement field. Those fringes show an acceleration of the upper part of the glacier in October 1995 compared to April 1996.

IV. Conclusion

In this letter, a novel method based on the analysis of a series of phase difference between differential interferograms was exposed to detect fringes due to DEM errors and separate them from fringes due to motion variation or atmospheric artifacts. Relations between DEM error, differential interferogram phase difference and the equivalent height of ambiguity were established. Then, an algorithm has been proposed to determine if topographic fringes are correctly removed from the interferograms. If not, DEM errors are retrieved from the differential interferogram differences. Then, interferograms are generated with the new DEM and fringes detected as topographic ones are removed. Nevertheless, it is quite difficult to quantify the DEM accuracy. Indeed, the detection of residual topographic fringes depends on the threshold value imposed during the hypothesis test, and on the possible presence of other fringe sources. If the new DEM is valid, tropospheric effects can be neglected or compensated with external data, and displacement fields variations can be studied as done on the upper part of the Argentière glacier.

Acknowledgment

The authors would like to thank the anonymous reviewers for providing useful comments and advice on this letter and the European Space Agency for providing ERS SAR data through the Category 1 proposals No. 1088 and 3525.

References

[1] H. Zebker, C. Werner, P. Rosen, and S. Hensley, "Accuracy of topographics map derived from ERS-1 interferometric radar," *IEEE Trans. Geosci. Remote Sens.*, vol. 32, no. 4, pp. 823–836, Jul. 1994.

[2] G. Rufino, A. Moccia, and S. Esposito, "DEM generation by means of ERS tandem data," *IEEE Trans. Geosci. Remote Sens.*, vol. 36, no. 6, pp. 1905–1912, Nov. 1998.

[3] D. Massonnet and T. Rabaute, "Radar interferometry, limits and potential," *IEEE Trans. Geosci. Remote Sens.*, vol. 31, no. 2, pp. 455–464, Mar. 1993.

[4] I. Joughin, R. Kwok, and M. Fahnestock, "Interferometric estimation of three-dimensional ice-flow using ascending and descending passes," *IEEE Trans. Geosci. Remote Sens.*, vol. 36, no. 1, pp. 25–37, Jan. 1998.

[5] K. Mattar, P. Vachon, D. Geudtner, A. Gray, I. Cumming, and M. Brugman, "Validation of alpine glacier velocity measurements using ERS tandem-mission SAR data," *IEEE Trans. Geosci. Remote Sens.*, vol. 36, no. 3, pp. 974–984, May 1998.

[6] E. Trouvé, G. Vasile, M. Gay, L. Bombrun, P. Grussenmeyer, T. Landes, J. Nicolas, P. Bolon, I. Petillot, A. Julea, L. Valet, J. Chanussot, and M. Koehl, "Combining airborne photographs and spaceborne SAR data to monitor temperate glaciers: Potentials and limits," *IEEE Trans. Geosci. Remote Sens.*, vol. 45, no. 4, pp. 905–924, Apr. 2007.

[7] Z. Li, X. Li, X. Ren, and Q. Dong, "Frozen group deformation monitoring using SAR interferometry," in *Proc. IGARSS*, 2003, vol. 4, pp. 2933–2935.

[8] J.-F. Zhang and Q. Qin, "The research of difference interferometric SAR technique," in *Proc. IGARSS*, Toulouse, France, 2003, vol. 6, pp. 3827–3829.

[9] L. Bombrun, I. Pétillot, G. Vasile, M. Gay, E. Trouvé, P. Bolon, J.-M. Nicolas, and T. Landes, "Multi-date ERS tandem interferogram analysis: Application to alpine glaciers," in *Proc. MULTITEMP*, Leuven, Belgium, 2007.

[10] R. Scharroo and P. Visser, "Precise orbit determination and gravity field improvement for the ERS satellites," *J. Geophys. Res.*, vol. 103, no. C4, pp. 8113–8127, Apr. 1998.

[11] E. Trouvé, J. M. Nicolas, and H. Maître, "Improving phase unwrapping techniques by the use of local frequency," *IEEE Trans. Geosci. Remote Sens.*, vol. 36, no. 6, pp. 1963–1972, Nov. 1998.

Authorized licensed use limited to: Bombrun Lionel. Downloaded on December 16, 2009 at 09:45 from IEEE Xplore. Restrictions apply.

L. Bombrun, G. Vasile, M. Gay, F. Totir, "Hierarchical Segmentation of Polarimetric SAR Images Using Heterogeneous Clutter Models", *IEEE Transactions on Geoscience and Remote Sensing*, *Vol.* 49, *N*° 2, 2011.

Hierarchical Segmentation of Polarimetric SAR Images Using Heterogeneous Clutter Models

Lionel Bombrun, *Member, IEEE*, Gabriel Vasile, *Member, IEEE*, Michel Gay, *Member, IEEE*, and Felix Totir

***Abstract*—In this paper, heterogeneous clutter models are used to describe polarimetric synthetic aperture radar (PolSAR) data. The KummerU distribution is introduced to model the PolSAR clutter. Then, a detailed analysis is carried out to evaluate the potential of this new multivariate distribution. It is implemented in a hierarchical maximum likelihood segmentation algorithm. The segmentation results are shown on both synthetic and high-resolution PolSAR data at the X- and L-bands. Finally, some methods are examined to determine automatically the "optimal" number of segments in the final partition.**

***Index Terms*—Fisher probability density function (PDF), KummerU PDF, polarimetric synthetic aperture radar (PolSAR) data, segmentation, spherically invariant random vectors (SIRV).**

I. Introduction

BECAUSE of its all-weather and all-day monitoring capabilities, synthetic aperture radar (SAR) imagery has been widely used for global Earth monitoring. Such systems offer a number of advantages for Earth-surface and feature observation compared to optical sensors. With the new generation of high-resolution SAR sensors, the high-quality images of the Earth's surface are acquired. They offer the opportunity to observe thinner spatial features from space. Nevertheless, with such sensors, only a small number of scatterers are present in each resolution cell. The xlassical statistical models can therefore be reconsidered. Many works have been recently dedicated to this problem. For example, Delignon *et al.* [1] have proposed to use the Pearson system KUBW for the statistical modeling of ocean SAR images. Other works have proposed to model agricultural fields and urban areas in high-resolution SAR images by means of the Fisher probability density functions (PDFs) [2], [3].

Polarimetric SAR (PolSAR) data describe the interactions between the electromagnetic wave and the scatterers present in each resolution cell. By means of the Sinclair matrix, the polarimetric diversity has been widely studied to retrieve the physical properties of the media [4]–[6]. For low-resolution images, the classical Wishart distribution has been used in the classification and segmentation of PolSAR data [7], [8]. With the new PolSAR sensors, the number of scatterers present in each resolution cell decreases considerably. The homogeneous hypothesis of the PolSAR clutter can be reconsidered. To overcome this difficulty, Anfinsen *et al.* [9] have introduced the relaxed Wishart distribution, which has shown promising results in modeling the forested scenes. Other heterogeneous clutter models have been proposed in the literature by means of the scalar product model. In this model, the spatial nonhomogeneity is incorporated by modeling the clutter as the product between the square root of a scalar random variable (texture) and an independent zero-mean complex circular Gaussian random vector (speckle). If the texture random variable is Gamma distributed, the target scattering vector follows the well-known $\mathcal{K}$ distribution [10]–[12]. Another class of multivariate distribution has been introduced : the $\mathcal{G}^0$ polarimetric distribution [13]. It assumes an inverse Gamma distributed texture. This model is able to fit an extremely heterogeneous clutter compared to the $\mathcal{K}$ distribution. Recently, some works have proposed to generalize those two classes with the multivariate KummerU distribution which implies a Fisher distributed texture [14], [15].

This paper is organized as follows. In Section II, the multivariate KummerU distribution is introduced. Some benefits of this model are discussed. Then, in Section III, the KummerU is implemented in a hierarchical maximum-likelihood (ML) segmentation algorithm. The segmentation results are next analyzed in both synthetic and high-resolution PolSAR images. Section IV presents some results to determine automatically the number of segments in the final partition. Finally, some conclusion and perspectives of this paper are discussed in Section V.

II. KummerU Heterogeneous Clutter

With the new generation of airborne and spaceborne SAR sensors, the number of scatterers present in each resolution cell decreases considerably. In certain applications such as segmentation or detection, the central limit theorem cannot be directly used to support the Gaussianity hypothesis of the backscattered clutter. The homogeneous hypothesis of the PolSAR clutter must then be reconsidered. Heterogeneous clutter models have therefore recently been studied. The generalizations of the Gaussian distribution are appealing since they allow to retrieve the basic Gaussian model under particular assumptions. Spherically invariant random processes (SIRPs) or vectors (SIRVs) are such a generalization. The SIRV has first been introduced by Yao [16] for the estimation/detection in the information theory. In the PolSAR, the target vector $\mathbf{k}$ is a complex vector of

Manuscript received November 20, 2009; revised April 29, 2010; accepted July 8, 2010. Date of publication September 13, 2010; date of current version January 21, 2011.

L. Bombrun is with the Grenoble Image sPeech Signal Automatics Laboratory (GIPSA-Lab), Grenoble Institute of Technology, 38402 Grenoble, France, and also with the Supelec, ONERA, NUS, DSTA Research Alliance (SONDRA), 91192 Gif-sur-Yvette, France (e-mail: lionel.bombrun@gipsa-lab.grenoble-inp.fr).

G. Vasile, M. Gay, and F. Totir are with the GIPSA-Lab, Grenoble Institute of Technology, 38402 Grenoble, France (e-mail: gabriel.vasile@gipsa-lab.grenoble-inp.fr; michel.gay@gipsa-lab.grenoble-inp.fr; felix.totir@gipsa-lab.grenoble-inp.fr).

Color versions of one or more of the figures in this paper are available online at http://ieeexplore.ieee.org.

Digital Object Identifier 10.1109/TGRS.2010.2060730

0196-2892/$26.00 © 2010 IEEE

TABLE I
KUMMERU PDF AND PARTICULAR CASES

Texture PDF		SIRV PDF	
Name	$p_\tau(\tau)$	Name	$p_{\mathbf{k}}(\mathbf{k})$
Dirac	$\delta(\tau-1)$	Gaussian	$\frac{1}{\pi^p\lvert[M]\rvert}\exp\left(-\mathbf{k}^H[M]^{-1}\mathbf{k}\right)$
Gamma	$\frac{1}{\Gamma(\mathcal{L})}\frac{\mathcal{L}}{m}\left(\frac{\mathcal{L}\tau}{m}\right)^{\mathcal{L}-1}e^{-\frac{\mathcal{L}\tau}{m}}$	$\mathcal{K}$	$\frac{2}{\pi^p\Gamma(\mathcal{L})\lvert[M]\rvert}\left(\frac{\mathcal{L}}{m}\right)^{\left(\frac{\mathcal{L}+p}{2}\right)}\left[\mathbf{k}^H[M]^{-1}\mathbf{k}\right]^{\left(\frac{\mathcal{L}-p}{2}\right)}\text{BesselK}_{p-\mathcal{L}}\left(2\sqrt{\frac{\mathcal{L}\,\mathbf{k}^H[M]^{-1}\mathbf{k}}{m}}\right)$
Inverse Gamma	$\frac{1}{\Gamma(\mathcal{M})}\frac{1}{\mathcal{M}m}\left(\frac{\mathcal{M}m}{\tau}\right)^{\mathcal{M}+1}e^{-\frac{\mathcal{M}m}{\tau}}$	$\mathcal{G}^0$	$\frac{1}{\pi^p\lvert[M]\rvert}\frac{(m\mathcal{M})^{\mathcal{M}}}{\Gamma(\mathcal{M})}\Gamma(p+\mathcal{M})\left(\mathbf{k}^H[M]^{-1}\mathbf{k}+m\mathcal{M}\right)^{-(\mathcal{M}+p)}$
Fisher	$\frac{\Gamma(\mathcal{L}+\mathcal{M})}{\Gamma(\mathcal{L})\Gamma(\mathcal{M})}\frac{\mathcal{L}}{\mathcal{M}m}\frac{\left(\frac{\mathcal{L}\tau}{\mathcal{M}m}\right)^{\mathcal{L}-1}}{\left(1+\frac{\mathcal{L}\tau}{\mathcal{M}m}\right)^{\mathcal{L}+\mathcal{M}}}$	KummerU	$\frac{1}{\pi^p\lvert[M]\rvert}\frac{\Gamma(\mathcal{L}+\mathcal{M})}{\Gamma(\mathcal{L})\Gamma(\mathcal{M})}\left(\frac{\mathcal{L}}{\mathcal{M}m}\right)^p\Gamma(p+\mathcal{M})\;U\left(p+\mathcal{M};1+p-\mathcal{L};\frac{\mathcal{L}}{\mathcal{M}m}\mathbf{k}^H[M]^{-1}\mathbf{k}\right)$

length three or four and could be written under the SIRV model hypothesis [17]. It is defined as the product of a square root of a positive random variable τ (representing the texture) with an independent circular complex Gaussian vector $\mathbf{z}$ with zero mean and covariance matrix $[M]=E\{\mathbf{z}\mathbf{z}^H\}$ (representing the speckle)

$$\mathbf{k}=\sqrt{\tau}\,\mathbf{z} \tag{1}$$

where the superscript H denotes the complex conjugate transposition and $E\{\cdot\}$ denotes the mathematical expectation.

The SIRV representation is not unique, so a normalization condition is necessary. Indeed, if $[M_1]$ and $[M_2]$ are two covariance matrices such that $[M_1]=\alpha[M_2]$ with $\alpha\in\mathbb{R}^{+*}$, then $\{\tau_1,[M_1]\}$ and $\{\tau_2=\tau_1/\alpha,[M_2]\}$ describe the same SIRV. In this paper, the trace of the covariance matrix is normalized to p, the dimension of the target scattering vector ($p=3$ for the reciprocal case) [17], [18].

For a given covariance matrix $[M]$, the ML estimator of the texture for the pixel i (τ_i) is given by

$$\hat{\tau}_i=\frac{\mathbf{k}_i^H[M]^{-1}\mathbf{k}_i}{p}. \tag{2}$$

The ML estimator of the normalized covariance matrix under the deterministic texture case is the solution of the following recursive equation

$$[\hat{M}]_{FP}=f\left([\hat{M}]_{FP}\right)=\frac{p}{N}\sum_{i=1}^{N}\frac{\mathbf{k}_i\mathbf{k}_i^H}{\mathbf{k}_i^H[\hat{M}]_{FP}^{-1}\mathbf{k}_i},\quad \text{with } Tr\left([\hat{M}]_{FP}\right)=p. \tag{3}$$

Pascal *et al.* have established the existence and the uniqueness, up to a scalar factor, of the fixed point estimator of the normalized covariance matrix, as well as the convergence of the recursive algorithm, whatever the initialization [18], [19].

When the texture is assumed to be deterministic, the ML estimator of the normalized covariance matrix is given by $\hat{M}_{FP}$ in (3). However, when the texture is a random variable, $\hat{M}_{FP}$ is not the ML estimator, it is an "approximate" ML estimator. The ML estimator of the normalized covariance matrix depends on the texture PDF $p_\tau(\tau)$, and its expression is linked with the density generator function $h_p(x)$ by

$$[\hat{M}_{ML}]=\frac{1}{N}\sum_{i=1}^{N}\frac{h_{p+1}\left(\mathbf{k}_i^H[\hat{M}_{ML}]^{-1}\mathbf{k}_i\right)}{h_p\left(\mathbf{k}_i^H[\hat{M}_{ML}]^{-1}\mathbf{k}_i\right)}\mathbf{k}_i\mathbf{k}_i^H \tag{4}$$

where the expression of the density generator function is given by [20], [21]

$$h_p(x)=\int_0^{+\infty}\frac{1}{\tau^p}\exp\left(-\frac{x}{\tau}\right)p_\tau(\tau)\,d\tau. \tag{5}$$

Chitour and Pascal have proven that (4) admits a unique solution and that its corresponding iterative algorithm converges to the fixed point solution for every admissible initial condition [22].

When the texture is a random variable with a given PDF, the expression of the density generator function $h_p(\cdot)$ given by (5) can be computed. If $h_p(\cdot)$ has an analytical expression, the ML estimator can be computed according to (4). When the texture is a random variable with an unknown PDF, the density generator function cannot be computed numerically. The ML estimator $\hat{M}_{ML}$ cannot be found, and the approximate ML estimator $\hat{M}_{FP}$ should be used instead.

It is important to notice that, in the SIRV definition, the PDF of the texture random variable is not explicitly specified. As a consequence, the SIRVs describe a whole class of stochastic processes. This class includes the conventional clutter models having Gaussian, $\mathcal{K}$-distributed, Rayleigh, or Weibull PDFs. Some of those distributions are shown in Table I.

According to the SIRV estimation scheme, the scalar texture parameter can be extracted from a PolSAR data set [17]. In the next sections, the analysis of this parameter is carried out, and a statistical model is proposed. Then, a new target scattering PDF is derived, and some properties are exposed.

A. Scalar Texture Modeling

1) Fisher PDF: Fisher PDFs are known as the type VI solution of the Pearson system. They are introduced as the Mellin convolution (denoted as $\hat{\star}$) of a Gamma PDF by an inverse Gamma PDF. Their PDF is defined by three parameters as [23]

$$\begin{aligned}\mathcal{F}[\tau|m,\mathcal{L},\mathcal{M}]&=\mathcal{G}[m,\mathcal{L}]\,\hat{\star}\,\mathcal{GI}[1,\mathcal{M}]\\&=\frac{\Gamma(\mathcal{L}+\mathcal{M})}{\Gamma(\mathcal{L})\Gamma(\mathcal{M})}\frac{\mathcal{L}}{\mathcal{M}m}\frac{\left(\frac{\mathcal{L}\tau}{\mathcal{M}m}\right)^{\mathcal{L}-1}}{\left(1+\frac{\mathcal{L}\tau}{\mathcal{M}m}\right)^{\mathcal{L}+\mathcal{M}}}\end{aligned} \tag{6}$$

with $\mathcal{L}>0$ and $\mathcal{M}>0$. m is a shape parameter. $\mathcal{L}$ and $\mathcal{M}$ are two shape parameters which control the behavior of the Fisher PDF between the heavy head and heavy tail distributions. The low values of the shape parameters lead to a significant texture.

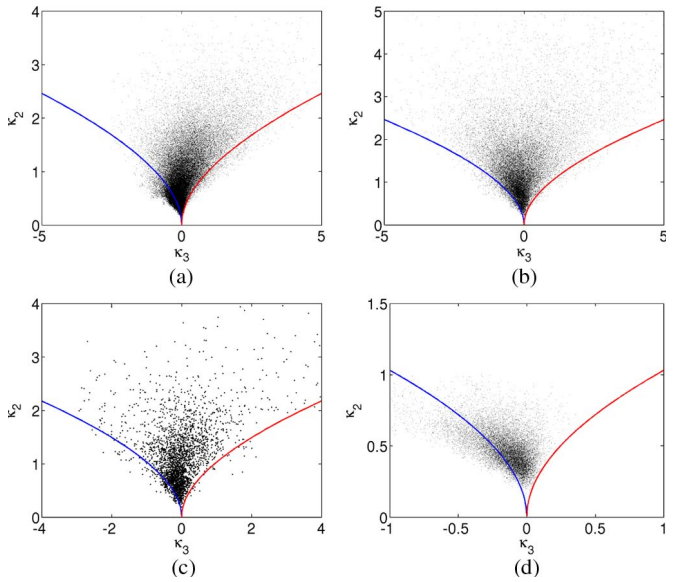

Fig. 1. κ_2/κ_3 plan for different bands and test sites. (a) X-band, Radar Aéroporté Multi-Spectral d'Etude des Signatures (RAMSES), Brétigny, France. (b) C-band, Convair, Ottawa, Canada. (c) L-band, Experimental SAR (ESAR), Oberpfaffenhofen, Germany. (d) P-band, RAMSES, Nezer, France.

2) Fisher PDF Parameter Estimation: Recent works have proposed to estimate the parameters of the Fisher PDF with the log-cumulants method, defined in the special framework of second kind statistics (where statistics—such as the second kind characteristic function—are defined using the Mellin transform instead of the Fourier transform) [23]. Nevertheless, these estimators are not ML estimators. The latter benefits from very desirable mathematical properties (asymptotic efficiency) and will be used through this paper. A description of the ML Fisher parameter estimation can be found in Appendix B.

3) Benefit of Fisher PDF: To evaluate the potential and limits of the Fisher PDFs to model the texture of PolSAR images, four data sets at the X-, C-, L-, and P-bands are analyzed. From those data sets, the covariance matrix $[M]_{FP}$ and texture parameter τ are estimated on a sliding 7×7 window according to (2) and (3). Then, the second (κ_2) and third (κ_3) log-cumulants of the texture parameter are computed. Next, the κ_2/κ_3 plan is plotted. In this plan, the Gamma and inverse Gamma PDFs are represented by the blue and red lines, respectively. The Fisher PDFs cover all the space between the blue and red lines [2], [24]. Fig. 1 shows the κ_2/κ_3 plan for the different bands and test sites (fields, forest, urban area, etc.). It shows that the Fisher PDFs can be suitable to model the scalar texture parameter of PolSAR data.

Table II shows the percentage of points $p_{\text{not Fisher}}$ which are outside the Fisher PDF domain definition. This percentage can be divided into two categories: the points which belong to the Beta model, denoted by p_{Beta}, (i.e., the points located under the blue Gamma line) and those which satisfy the inverse Beta PDF, denoted by $p_{\text{Inverse Beta}}$, (i.e., the points located under the red inverse Gamma line). It yields that, for the four studied data sets, at least 75% of the data belong to the Fisher κ_2/κ_3 domain. The other amount of points which does not satisfy the Fisher model is due to both the estimation errors (log-cumulants κ_2 and κ_3 are computed on a sliding 7×7 square window) and real data properties. For the RAMSES P-band data set over the Nezer Forest [see Fig. 1(d)], a trend in the κ_2/κ_3 plan can be observed around the blue line (Gamma model).

TABLE II
PERCENTAGE OF POINTS OUTSIDE THE FISHER PDFS DOMAIN DEFINITION

data set	RAMSES Brétigny X-band	CONVAIR Ottawa C-band	ESAR Oberpfaffenhofen L-band	RAMSES Nezer P-band
p_{Beta}	16.72%	3.61%	6.31%	24.35%
$p_{\text{Inverse Beta}}$	1.35%	0.63%	1.23%	0.06%
$p_{\text{not Fisher}}$	18.07%	4.24%	7.54%	24.41%

B. Target Scattering PDF

For a given texture PDF $p_\tau(\tau)$, the expression of the target scattering vector PDF is given by

$$p_{\mathbf{k}}(\mathbf{k}) = \frac{1}{\pi^p\,|[M]|}\int_0^{+\infty}\frac{1}{\tau^p}\exp\left(-\frac{\mathbf{k}^H[M]^{-1}\mathbf{k}}{\tau}\right)p_\tau(\tau)\,d\tau$$
$$= \frac{1}{\pi^p\,|[M]|}h_p\left(\mathbf{k}^H[M]^{-1}\mathbf{k}\right). \quad (7)$$

1) KummerU PDF: For a Fisher distributed texture, the target scattering vector PDF has been mathematically established [14], [15]

$$p_{\mathbf{k}}(\mathbf{k}|[M],m,\mathcal{L},\mathcal{M}) = \frac{1}{\pi^p\,|[M]|}\frac{\Gamma(\mathcal{L}+\mathcal{M})}{\Gamma(\mathcal{L})\Gamma(\mathcal{M})}\left(\frac{\mathcal{L}}{\mathcal{M}m}\right)^p \times \Gamma(p+\mathcal{M})\,U\,(a;b;z) \quad (8)$$

with $a = p+\mathcal{M}$, $b = 1+p-\mathcal{L}$, and $z = (\mathcal{L}/\mathcal{M}m)\mathbf{k}^H[M]^{-1}\mathbf{k}$. $|\cdot|$ and $U(\cdot;\cdot;\cdot)$ denote the determinant operator and the confluent hypergeometric function of the second kind (KummerU), respectively. Hereinafter, this multivariate distribution is named the KummerU PDF.

Consequently, the expression of the density generator function is given by

$$h_p\left(\mathbf{k}^H[M]^{-1}\mathbf{k}\right) = \frac{\Gamma(\mathcal{L}+\mathcal{M})}{\Gamma(\mathcal{L})\Gamma(\mathcal{M})}\left(\frac{\mathcal{L}}{\mathcal{M}m}\right)^p\Gamma(p+\mathcal{M})U\,(a;b;z)\,. \quad (9)$$

2) Asymptotic Cases: As Fisher distributions are a generalization of the Gamma and inverse Gamma PDFs, the asymptotic cases of the KummerU PDF can be studied.

1) For large $\mathcal{M}$, the Fisher PDFs have the same behavior as the Gamma PDFs. In Appendix A, a proof of the convergence of the KummerU PDF toward the well-known $\mathcal{K}$ PDF is achieved.
2) A similar approach can be done if $\mathcal{L}$ tends toward infinity. The Fisher PDFs have, therefore, the same behavior as the inverse Gamma PDFs. It yields that the KummerU PDF tends toward the multivariate Student distribution, also known as the $\mathcal{G}^0$ PDF [9], [13].
3) For the high values of $\mathcal{L}$ and $\mathcal{M}$, the texture parameter becomes less and less significant. Consequently, for the high values of the shape parameters, the KummerU PDF tends toward the Gaussian distribution.

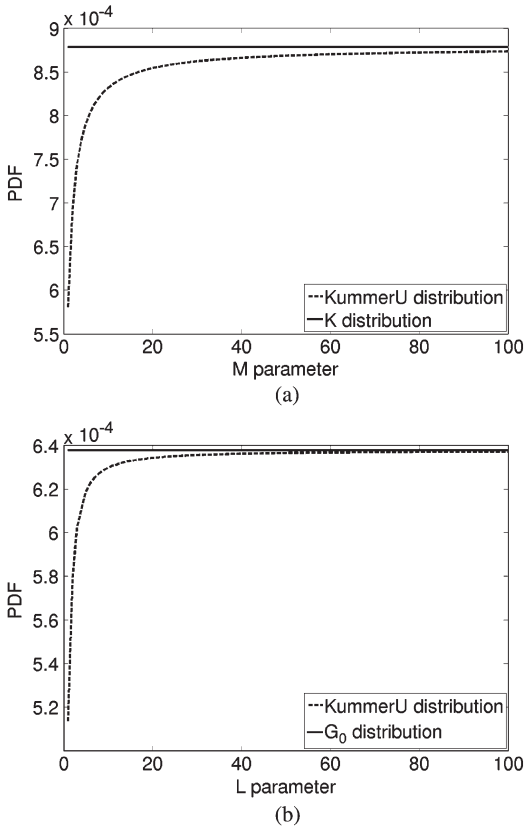

Fig. 2. Convergence of the KummerU PDF toward (a) the $\mathcal{K}$ distribution and (b) the $\mathcal{G}^0$ distribution as a function of the shape parameters $\mathcal{M}$ and $\mathcal{L}$.

Fig. 2 shows the convergence of the KummerU distribution toward the $\mathcal{K}$ and $\mathcal{G}^0$ distributions as a function of the shape parameters $\mathcal{M}$ and $\mathcal{L}$. The KummerU PDFs can be viewed as an extension of the classical multivariate $\mathcal{K}$ and $\mathcal{G}^0$ PolSAR models (see Table I for the analytical expressions).

C. ML Parameter Estimation

For a KummerU distributed clutter, one can replace in (4) the density generator function by its expression given in (9) to derive the expression of the ML estimator of the covariance matrix. It yields [15]

$$[\hat{M}_{ML}] = \frac{p+\mathcal{M}}{N}\left(\frac{\mathcal{L}}{\mathcal{M}m}\right) \times \sum_{i=1}^{N} \frac{U\left(p+1+\mathcal{M}2+p-\mathcal{L}\frac{\mathcal{L}}{\mathcal{M}m}\mathbf{k}_i^H[\hat{M}_{ML}]^{-1}\mathbf{k}_i\right)}{U\left(p+\mathcal{M}1+p-\mathcal{L}\frac{\mathcal{L}}{\mathcal{M}m}\mathbf{k}_i^H[\hat{M}_{ML}]^{-1}\mathbf{k}_i\right)} \times \mathbf{k}_i\mathbf{k}_i^H. \quad (10)$$

III. Hierarchical Segmentation

In this section, a segmentation application of the new multivariate KummerU PolSAR model is proposed. The hierarchical segmentation algorithm proposed by Beaulieu and Touzi [12] is adapted to the KummerU distributed target scattering vector. The segmentation algorithm is a classical iterative merge algorithm. At each iteration, the two four-connex segments (regions) which minimize the stepwise criterion (SC) are merged.

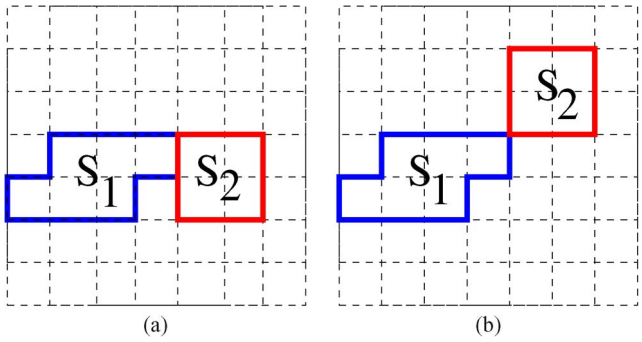

Fig. 3. (a) Four-connex segment pair. (b) Non-four-connex segment pair.

A four-connex segment pair is a group of two segments where at least one pixel of the first segment is in the neighborhood of one pixel of the second segment with the four-connexity sense. For illustrative purpose, a four-connex segment pair is shown in Fig. 3(a), and a non-four-connex segment pair is shown in Fig. 3(b).

The basic principle of the hierarchical segmentation algorithm can be divided into three steps.

1) Definition of an initial partition.
2) For each four-connex segment (regions) pair, the SC is computed. Then, the two segments which minimize the criterion are found and merged.
3) Stop if the maximum number of merges is reached; otherwise, go to Step 2.

A. Similarity Measure

At each iteration, merging two segments yields a decrease in the log-likelihood function. The SC is based on this consideration. The hierarchical segmentation algorithm merges the two adjacent segments S_i and S_j which minimizes the loss of likelihood of the partition (which is defined as the sum of likelihoods of the partition's segments). The SC ($\mathrm{SC}_{i,j}$) can be expressed as [12]

$$\mathrm{SC}_{i,j} = \mathrm{MLL}(S_i) + \mathrm{MLL}(S_j) - \mathrm{MLL}(S_i \cup S_j) \quad (11)$$

where $\mathrm{MLL}(\cdot)$ denotes the segment Maximum Log-Likelihood function (MLL). It is the log-likelihood of the segment (pixels in the segment are considered independent realizations) with respect to the assumed PDF (for example, the KummerU distribution) whose parameters are estimated in the ML (hence, the name) sense. Its expression is given by

$$\mathrm{MLL}(S) = \sum_{i \in S} \ln\left(p_{\mathbf{k}}(\mathbf{k}_i|\theta_S)\right) \quad (12)$$

where θ_S represents the set of distribution parameters.

1) GMLL: In general, the covariance matrix and the texture parameters are unknown. One solution consists in replacing the SIRV parameters by their estimates. After replacing the covariance matrix $[M]$ and texture parameters (m, $\mathcal{L}$, and $\mathcal{M}$ for the Fisher PDF) by their respective ML estimators, the SC becomes

$$\mathrm{SC}_{i,j} = \mathrm{GMLL}(S_i) + \mathrm{GMLL}(S_j) - \mathrm{GMLL}(S_i \cup S_j) \quad (13)$$

where $\mathrm{GMLL}(S)$ is the generalized maximum log-likelihood (GMLL) function for segment S.

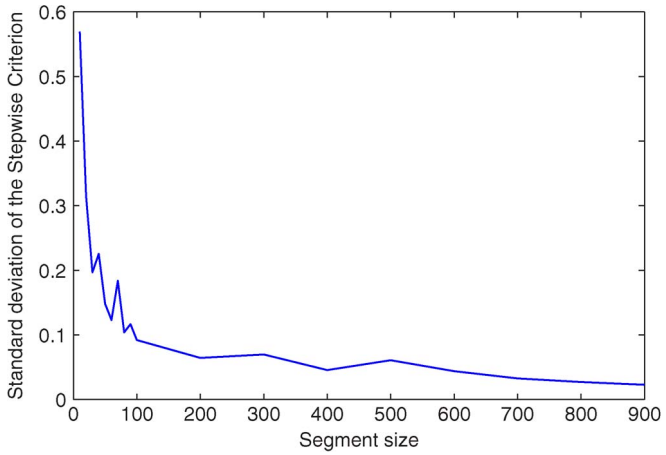

Fig. 4. Standard deviation of the normalized KummerU SC as a function of the window size N.

2) For the KummerU PDF: The GMLL function for segment S is derived from (9). It can be rewritten as

$$\begin{aligned}&\mathrm{GMLL}(S)\\&\quad=-pN\ln(\pi)-N\ln\left\{\left|[\hat{M}_{ML}]\right|\right\}\\&\qquad+N\ln\left\{\frac{\Gamma(\hat{\mathcal{L}}+\hat{\mathcal{M}})\Gamma(p+\hat{\mathcal{M}})}{\Gamma(\hat{\mathcal{L}})\Gamma(\hat{\mathcal{M}})}\right\}+pN\ln\left\{\frac{\hat{\mathcal{L}}}{\hat{\mathcal{M}}\hat{m}}\right\}\\&\qquad+\sum_{i\in S}\ln\left\{\mathrm{U}\left(p+\hat{\mathcal{M}};1+p-\hat{\mathcal{L}};\frac{\hat{\mathcal{L}}}{\hat{\mathcal{M}}\hat{m}}\mathbf{k}_i^H[\hat{M}_{ML}]^{-1}\mathbf{k}_i\right)\right\}\end{aligned}\tag{14}$$

where $\hat{\mathcal{L}}$, $\hat{\mathcal{M}}$, and $\hat{m}$ are the ML estimators of the Fisher parameters $\mathcal{L}$, $\mathcal{M}$, and m, respectively. $[\hat{M}_{ML}]$ is the ML estimator of $[M_{ML}]$ for segment S [see (4)].

It can be noticed that the second term of (14) corresponds to the Wishart criterion [12]. All other terms can be viewed as correction terms introduced by the texture modeling of the PolSAR data.

B. Segmentation Results

To evaluate the potential and limits of the method, the hierarchical segmentation algorithm proposed by Beaulieu and Touzi [12] has been implemented. Fig. 4 shows the standard deviation for the normalized KummerU criterion (SC/N) as a function of the window size N. This curve has been plotted for the two regions containing KummerU realizations with two different sets of parameters. As observed in Fig. 4, the standard deviation is stable for a sufficiently large region. For the segments containing less than 50 pixels, the standard deviation increases, probably due to a poor parameter estimation. It yields that a reasonable "minimum window" for the KummerU criterion should contain at least 50 pixels. In the following sections, the Gaussian and KummerU segmentation are tested with both synthetic and high-resolution single-look-complex images.

1) On a Synthetic Image: The synthetic data set consists of an image of 140 $\times$ 140 pixels. It is composed of six areas. Five of them contain the independent realizations of the multivariate KummerU distribution [see (9)]. The parameters of the KummerU PDF are different for each of the areas and are given in Tables III and IV. The outer area (class 1) is a special case since its texture is deterministic and constant (equals 1). It follows that the pixels in this area are drawn from a multivariate Gaussian PDF. It can also be viewed as a KummerU PDF with infinite shape parameters $\mathcal{L}$ and $\mathcal{M}$.

TABLE III
COVARIANCE MATRICES OF THE SPECKLE (PER AREA)

Area	$[M]_{11}$	$[M]_{22}$	$[M]_{33}$	$[M]_{12}$	$[M]_{13}$	$[M]_{23}$
1	2.677	0.171	0.152	$-0.018+0.064i$	$0.131-0.051i$	$0.008+0.032i$
2	2.500	0.300	0.200	$-0.018+0.064i$	$0.131-0.051i$	$0.008+0.032i$
3	2.677	0.171	0.152	$-0.018+0.064i$	$0.131-0.051i$	$0.008+0.032i$
4	2.677	0.171	0.152	$-0.018+0.064i$	$0.131-0.051i$	$0.008+0.032i$
5	2.677	0.171	0.152	$-0.018+0.064i$	$0.131-0.051i$	$0.008+0.032i$
6	2.677	0.171	0.152	$-0.018+0.064i$	$0.131-0.051i$	$0.008+0.032i$

TABLE IV
TEXTURE PDF (PER AREA)

Area	PDF	$\mathcal{L}$	$\mathcal{M}$	μ
1	dirac	∞	∞	1
2	Fisher	2	3	1
3	Fisher	2	3	2
4	Fisher	1	3	2
5	Fisher	2	5	2
6	Fisher	2	3	1

Note that the covariance matrices of the speckle satisfy the normalization condition $Tr([M]) = 3$. In order to test the segmentation algorithm thoroughly, only a limited set of parameters changes values between two neighboring regions. Thus, the successful segmentations show the ability of the underlying method to distinguish between similar areas.

The Gaussian distribution can be viewed as a particular case of the KummerU distribution (for large shape parameters $\mathcal{L}$ and $\mathcal{M}$). It is expected that, asymptotically (for a large number of samples N), the KummerU segmentation gives at least the same performances as the Gaussian criterion.

The hierarchical segmentation algorithm is initialized with a partition where each segment is a bloc of 10 $\times$ 10 pixels. The initial partition is composed of 196 segments. The segmentation results based on the Gaussian and KummerU criteria are respectively shown in Fig. 5(c) and (d) with the partitions containing six segments. This example clearly shows that the segmentation based on the KummerU criterion gives the best segmentation results. This is quite logical because the six segments can be viewed as six different KummerU clutter models.

Nevertheless, for purely Gaussian distributed regions, some problems with the KummerU criterion can occur. A synthetic data set composed by three Gaussian distributed regions (S_1, S_2, and S_3) has been generated. S_1 and S_2 follow a Gaussian distribution with covariance matrix $[M_1]$ $(\mathcal{N}(0,[M_1]))$, whereas S_3 has a covariance matrix $[M_2]$ $(\mathcal{N}(0,[M_2]))$. Note that the Gaussian regions are very similar as observed on the Frobenius norm between $[M_1]$ and $[M_2]$ (0.0012). Table V shows the SC for the Gaussian and KummerU criteria between S_1 and S_2 $(d(S_1,S_2))$ and between S_1 and S_3 $(d(S_1,S_3))$. It can be seen that, for a finite number of samples N, the KummerU segmentation may fail due to the higher dimensionality of the parameter space.

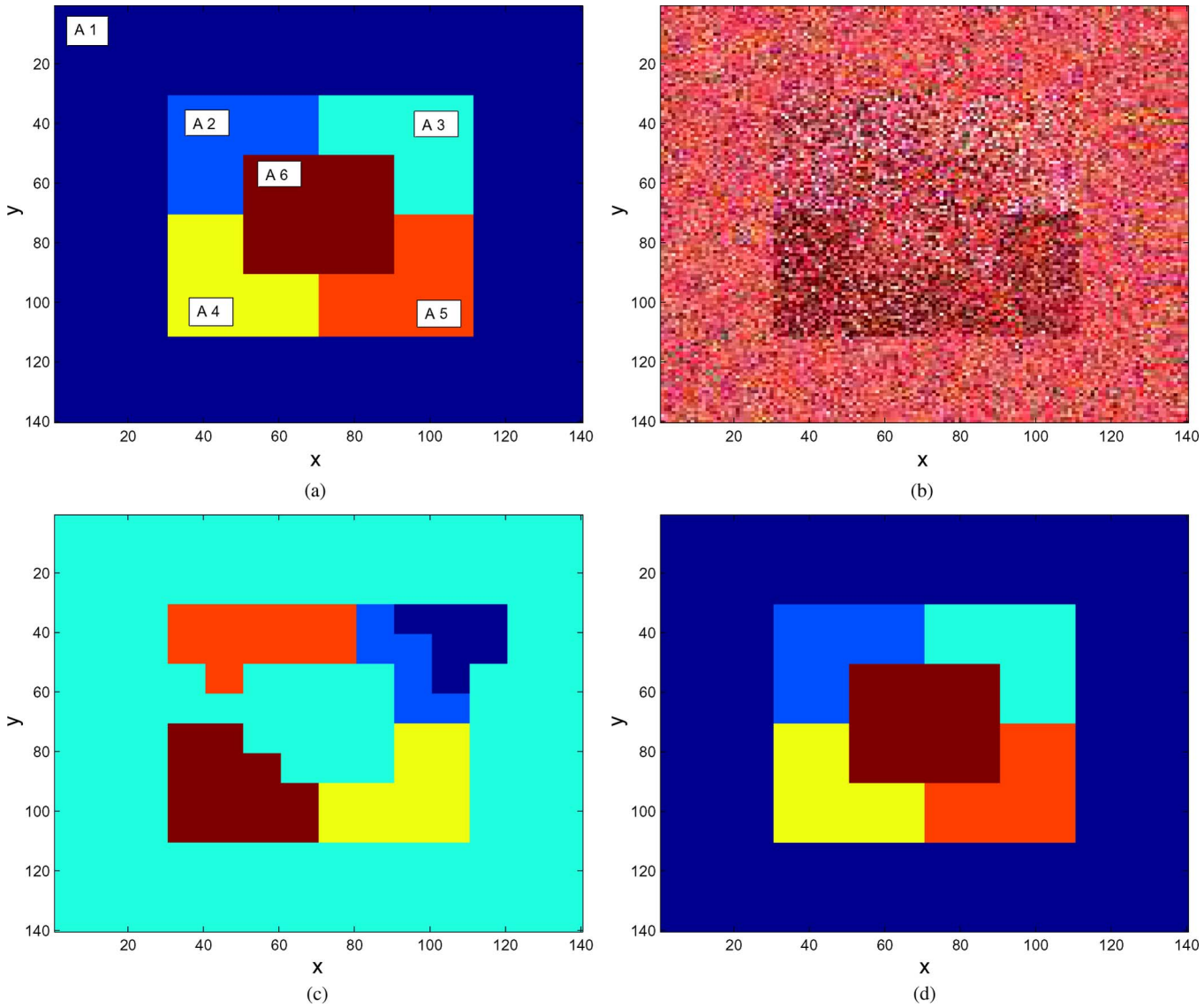

Fig. 5. Segmentation results of a simulated data set (140 × 140 pixels). (a) Areas of the matrix. (b) Colored composition of the target vector in the Pauli basis $[k]_1 - [k]_3 - [k]_2$. Partitions containing six segments: (c) Gaussian criterion and (d) KummerU criterion.

TABLE V
SC FOR GAUSSIAN REGIONS

SC	$d(S_1, S_2)$	$d(S_1, S_3)$
Gaussian	2.443	2.975
KummerU	5.322	2.702

2) On High-Resolution L-Band Data: In this part, a forested area (500 × 400 pixels) over the Oberpfaffenhofen test site (ESAR, L-band) has been segmented. The initial partition is composed of 2000 segments where each segment is a bloc of 10 × 10 pixels. The segmentation results with the Gaussian and KummerU criteria are shown in Fig. 6(a) and (b), respectively.

For the Gaussian criterion, only the determinant of the sample covariance matrix is taken into account. Both the structure of the covariance matrix and the power (texture) of the clutter are ignored. Consequently, the Gaussian criterion cannot distinguish between two regions having different texture values and/or covariance matrices whose determinants are equal but which have different structures. The KummerU criterion uses information about the texture and full information about the covariance matrix and is able to give a better segmentation of heterogeneous scenes, such as forested areas, as observed in Fig. 6(b).

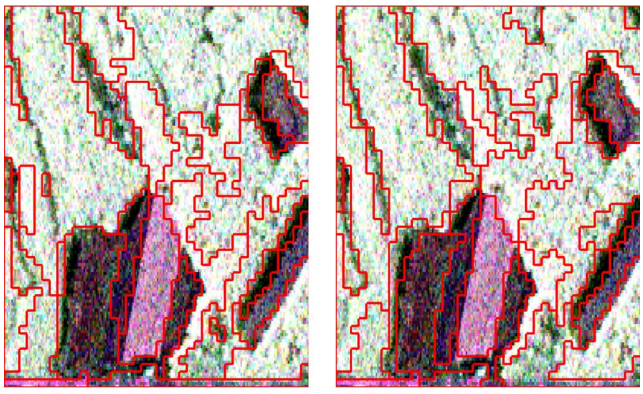

Fig. 6. Segmentation results for the L-band ESAR data over the Oberpfaffenhofen test site (500 × 400 pixels). Partitions containing 30 segments over a colored composition of the target vector in the Pauli basis $[k]_1 - [k]_3 - [k]_2$: (a) Gaussian criterion and (b) KummerU criterion.

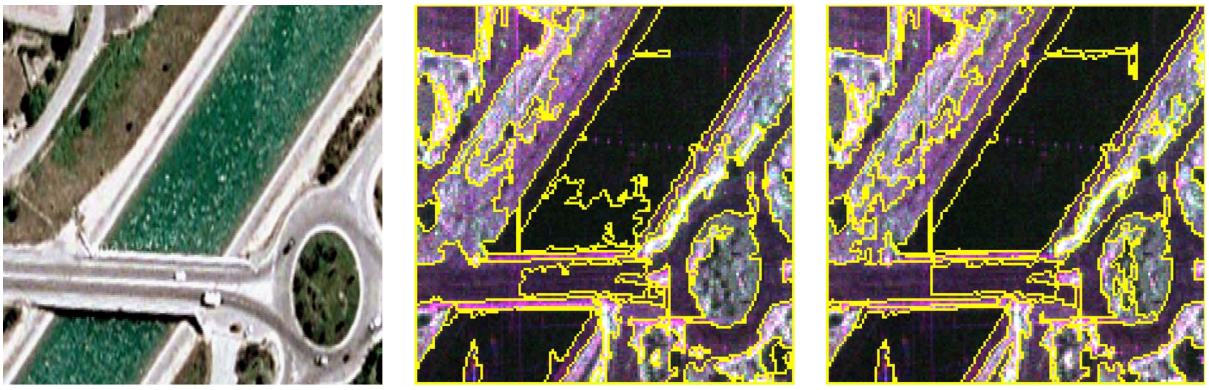

(a) (b) (c)

Fig. 7. Segmentation results for the X-band RAMSES data over the Salon de Provence test site (1050 × 1050 pixels). Partitions containing 55 segments over a colored composition of the target vector in the Pauli basis $[k]_1 - [k]_3 - [k]_2$: (a) Optical image Centre National d'Etudes Spatiales/spot image, (b) Gaussian criterion, and (c) KummerU criterion.

3) On Very High Resolution X-Band Data: In this section, a very high resolution data set acquired by the X-band RAMSES sensor over the Salon de Provence test site with a resolution of 10 cm is analyzed. Fig. 7(a) shows an optical image of the test site. The segmentation results with the Gaussian and KummerU criteria are shown in Fig. 7(b) and (c), respectively. The segmentation algorithm is initialized with a partition where each segment is a bloc of 7 × 7 pixels.

From this data set, it can be noticed that more features are segmented in the traffic circle with the KummerU criterion than with the Gaussian criterion. Moreover, the artifact in the water (on the northeast of the image) is better retrieved with the KummerU segmentation. Concerning the water itself, the Gaussian criterion leads to an oversegmented partition, particularly near the bridge.

IV. Determining the Number of Clusters Automatically

A. General Context

Based on the initial partition, the hierarchical segmentation iteratively merges the segments that are both statistically similar (MLL criterion) and spatially close (neighboring condition). The procedure may continue until a partition with a single segment, comprising the whole image, is obtained.

Note that the hierarchical segmentation algorithm is generally suboptimal since neither the initial partition nor the iterative merging of the segments is guaranteed to be optimal in the general sense (i.e., with respect to maximizing the sum of the segments' log-likelihood), although the iterative merging is still the optimal processing for the imposed initial partitioning and a segment neighboring condition.

Summarily, it is useful to describe the hierarchical segmentation method as an iterative transition from the oversegmented partitioning to an undersegmented one. Each iteration results in an intermediate partition, and thus, a sequence of partitions is created. It would be valuable to determine the most appropriate partition in this sequence, with respect to some optimality criterion.

It is, however, difficult to decide between over- and undersegmentation, except for the carefully chosen images [25], [26]. As stated in [27], the ideal segmentation maximizes the homogeneity of the retained data clusters while ensuring that they are as dissimilar as possible. Such a perfect tradeoff is, however, difficult to obtain since, during the region merging (as what happens in the hierarchical segmentation algorithms), both the homogeneity of the clusters and the dissimilarity between them become weaker.

This problem is encountered in most of the data clustering and image segmentation algorithms, and a number of techniques have been applied (a comprehensive review is found in [28]). However, some of the techniques are not applicable for many SAR images. For example, the solution retained in [27] is to incorporate the boundary curvature ratio, region homogeneity, and boundary smoothness into a single merging criterion, which is also used to estimate and to threshold the intervariance of the obtained data clusters. This is not appropriate for the SAR images for two reasons: First, many regions of interest in the SAR images have irregular shapes (forests, lakes, buildings, etc.), and second, the textured characteristic of the SAR images makes both the boundary smoothness and the region homogeneity unreliable information. The latter remark is in line with preferring stochastic approaches over contour approaches in the SAR image segmentation.

B. Between-Cluster Entropy

The use of the information theory framework, closely related to the retained statistical description of the SAR images, has been attempted first. The cluster evaluation function, defined in [29], is used in [30] as a measure for the between-cluster entropy (intervariance). Formally, for all pairs of pixels (vectors) $\mathbf{x_i}$ and $\mathbf{x_j}$ in a partitioned image, a membership function $M(\mathbf{x_i}, \mathbf{x_j})$ is defined, which equals one if $\mathbf{x_i}$ and $\mathbf{x_j}$ belong to different clusters (referred as segments under the terminology used in this paper) and zero if they belong to the same cluster. Thus, the between-cluster entropy is defined as

$$H = -\log(V)$$

$$V = \frac{1}{2\prod_{k=1}^{K} N_k} \sum_{i=1}^{N} \sum_{j=1}^{N} M(\mathbf{x_i}, \mathbf{x_j}) G(\mathbf{x_i} - \mathbf{x_j}, 2\sigma^2 \mathbf{I}). \quad (15)$$

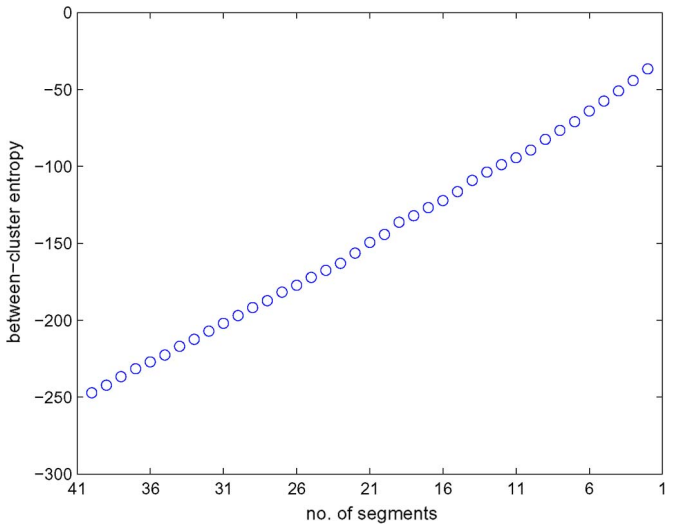

Fig. 8. Between-cluster entropy for the iterative hierarchical KummerU segmentation.

In the aforementioned equations, σ is a positive parameter, namely, the width of the centered Gaussian kernel $G(\cdot)$ used in computing the nonparametric Parzen estimate of the PDF and, consequently, the estimate of Renyi's quadratic (obtained for $\alpha = 2$) entropy. The between-cluster entropy is defined, by analogy, on the basis of this estimate.

Note that the between-cluster entropy equals $+\infty$ for the ending one-segment partition (indeed, the membership function $M(\mathbf{x_i}, \mathbf{x_j})$ is always zero in that case and so is V). On the other hand, if many segments tend to be very close such that the (norm of the) difference $\mathbf{x_i} - \mathbf{x_j}$ is rather small (consequently, the value of $G(\mathbf{x_i} - \mathbf{x_j}, 2\sigma^2\mathbf{I})$ is large) while $M(\mathbf{x_i}, \mathbf{x_j})$ equals one, the value of the between-cluster entropy is small. The latter occurs in oversegmented images, for example, in the initial partition of the considered hierarchical segmentation method. Consequently, it is expected for the between-cluster entropy to start with small values and, as the segments are hierarchically merged, to progressively increase.

Jenssen *et al.* use the variation of the between-cluster entropy quantity (during an iterative clustering process) to automatically find the true number of clusters [30]. Specifically, a sudden increase is observed in the between-cluster entropy when the number of clusters is reduced to a value less than the true number of the clusters (i.e., the partitioning goes into undersegmentation). A similar behavior was expected for the PolSAR hierarchical segmentation problem.

To this end, the between-cluster entropy has been computed for each partitioning issued during the iterative hierarchical segmentation proposed in this paper. A value of 0.1 has been considered for σ. The obtained values for the hierarchical segmentation of the considered synthetic PolSAR image [see Fig. 5(a)] are presented in Fig. 8.

While the between-cluster entropy is constantly increasing, as expected, unfortunately, no sudden change seems to occur in the vicinity of the desired number of segments (namely, six).

Several justifications may be advanced for this behavior. First, unlike the data clusters considered in [30], which are well separated geometrically (belonging to disjoint geometrical regions), the data in the six areas of the considered synthetic PolSAR image are not. Specifically, while the vectors are drawn from different PDFs for each area, their ranges superpose.

C. L-Method

Another approach has been then considered, namely, the use of the L-method [28]. This method uses the very error (quality) function that is used to perform the cluster merging during the hierarchical segmentation algorithm, specifically the Log-Likelihood Function (LLF) of the partition (i.e., the sum of the MLL values for all the segments of the partition). As this is readily computed during the proposed method, no further computational effort is required. The *knee* of this error function is identified, and the optimal number of clusters is chosen at that point. The knee of a curve is somewhat similar to the point of the maximum curvature.

The interest for the particular knee point comes from the fact that it separates the two linearlike parts of the error function graph. For example, the proposed hierarchical segmentation algorithm starts by merging the relatively similar clusters and the trend; thus, the error (quality) function slowly increases. This remains almost unchanged during the oversegmentation. Anyway, after the correct number of segments is reached and the undersegmentation begins, the dissimilar segments begin to be merged. As such, the homogeneity of the newly obtained segments drops fast, and the quality function of the partition degrades rapidly. Obviously, the optimal tradeoff lies somewhere between the over- and undersegmented partitions.

The L-method divides the graph of the error (quality) function into two parts and approximates each part with a straight line. The pair of lines that most closely fit the error function curve is retained, and their junction point is the looked-for knee. The best pair of lines is that which minimizes the weighted sum of approximation errors for the two parts of the error function graph.

For many images, the hierarchical segmentation algorithms spend many iterations in the oversegmentation since it usually starts from an overrefined, sometimes even pixel level, partition of the image. As this tends to unbalance the error contributions of the over- and undersegmented parts in determining the knee of the error curve, it is reasonable to do both of the following: 1) Drop some of the initial iterations of the hierarchical segmentation algorithms, and 2) use an iterative procedure in searching for the knee. The first step relocates the searching of the knee toward the final steps of the algorithm (toward the undersegmented region) while the second step refines the found knee by considering a converging procedure toward a stable procedure. Specifically, after a knee is found, the search is performed again, the focus region being adjusted so that the previously found knee is in the middle. The procedure is described in [28].

1) On Synthetic Image: First, we present the results obtained with the L-method for the synthetic six-area image. The quality functions during the hierarchical segmentation algorithm are shown in Fig. 9.

While the number of the optimal number of segments [see (6)] for the considered image is not accurately retrieved by the L-method, the estimate is quite close [see (5)]. This

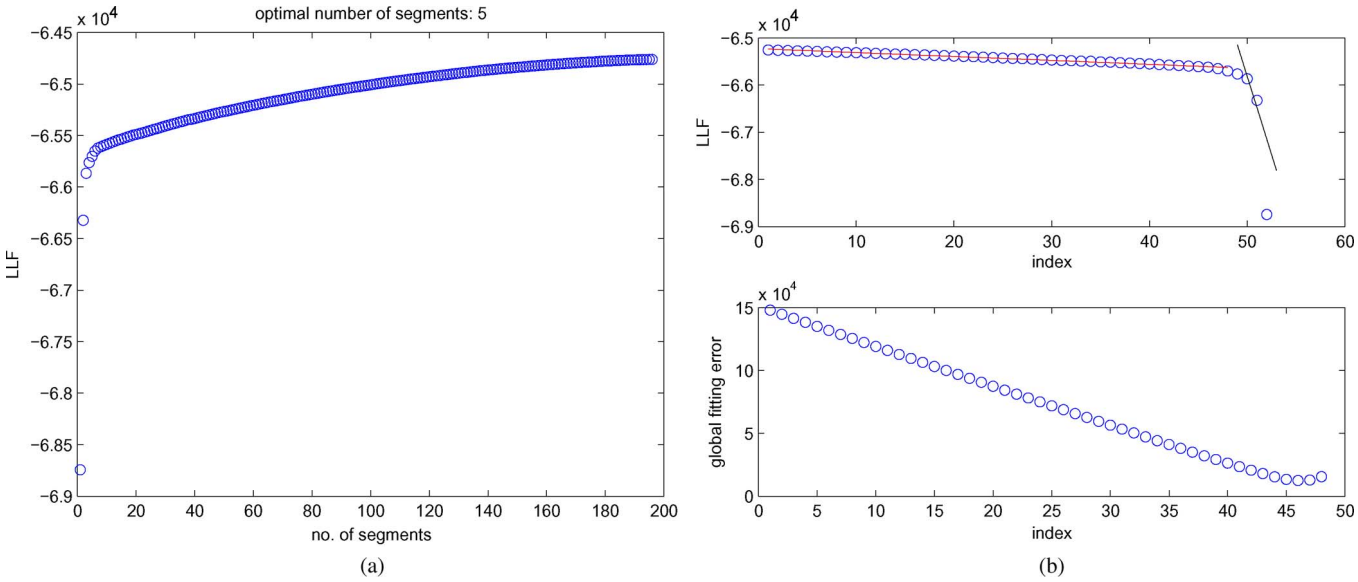

Fig. 9. Determination of the final partition for the KummerU segmentation on the synthetic image. (a) LLF. (b) LLF and global fitting error for the last 50 iterations.

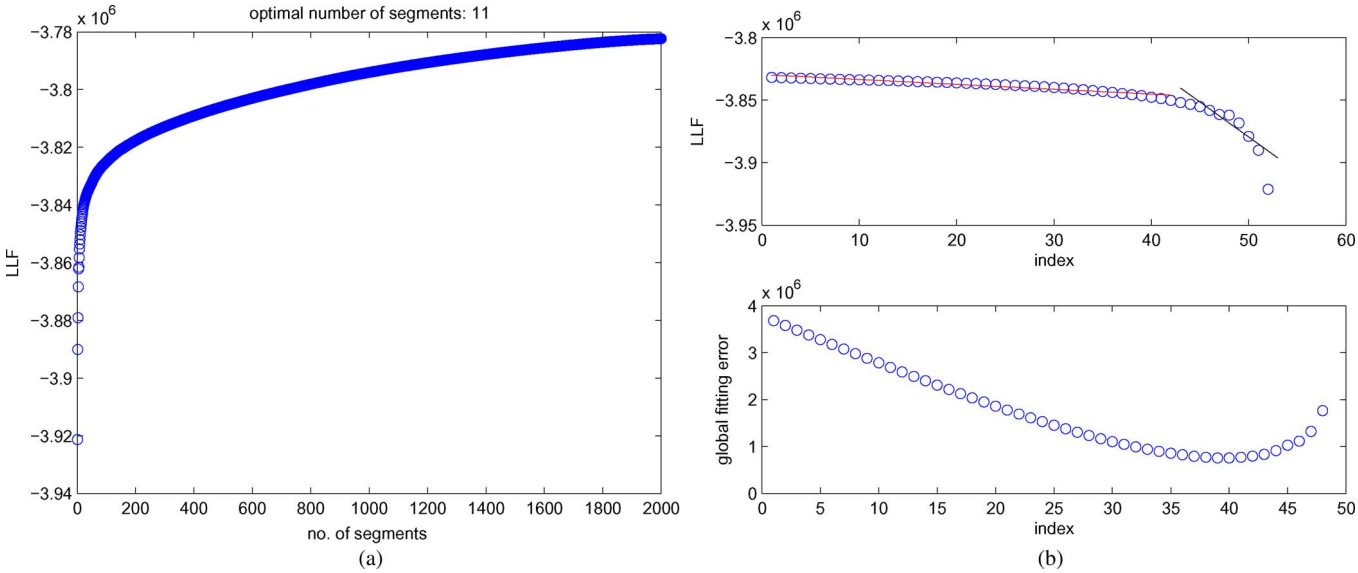

Fig. 10. Determination of the final partition for the KummerU segmentation over the Oberpfaffenhofen test site. (a) LLF. (b) LLF and global fitting error for the last 50 iterations.

number has been determined using the noniterative version of the L-method, applied to a focus region containing the last 50 iterations of the hierarchical segmentation algorithm [meaning, the leftmost 50 points of the graphs in Fig. 9(a)].

The application of the L-method under these conditions is illustrated in Fig. 9(b). The upper graphs show the dual-line approximation of the quality function in the optimal position while the lower graphs present the variation of the global (weighted) fitting error.

2) On High-Resolution L-Band Data: Using the L-method for automatically determining the optimal number of segments for the real images has been also assessed. The results are presented for the Oberpfaffenhofen image, as shown in Fig. 10. Note that the identified optimal number of segments is around ten. The noniterative L-method has been applied to a focus region containing the last 50 iterations of the hierarchical segmentation algorithm [meaning, the leftmost 50 points of the graphs in Fig. 10(a)]. The application of the L-method under these conditions is illustrated in Fig. 10(b).

Finally, the iterative version of the L-method has been applied on the same data set (the Oberpfaffenhofen image) in order to test the convergence properties of this procedure. We found a relatively fast convergence. Indeed, for the KummerU segmentation, the optimal number of segments was found to be through the series $[508 \rightarrow 191 \rightarrow 65 \rightarrow 22 \rightarrow 9]$. The final value is quite close to that obtained in the previous case, when the noniterative L-method has been applied.

Note, however, that the optimal segmentation is still a very subjective notion and that the L-method is not completely objective since the notion of the knee is quite loose and, more, is not necessarily the most appropriate from the user point of view (the same concerns the hierarchical segmentation algorithm).

Fig. 11. Segmentation results with the KummerU criterion for the L-band ESAR data over the Oberpfaffenhofen test site (500 × 400 pixels). Partition containing ten segments over a colored composition of the target vector $[k]_1 - [k]_3 - [k]_2$.

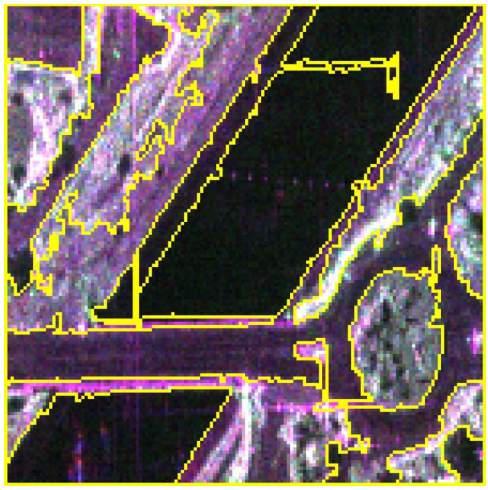

Fig. 12. Segmentation results with the KummerU criterion for the X-band RAMSES data over the Salon de Provence test site (1050 × 1050 pixels). Partition containing 19 segments over a colored composition of the target vector $[k]_1 - [k]_3 - [k]_2$.

For illustrative purposes, the partition of the Oberpfaffenhofen image with ten segments (in the range of those obtained using the L-method) is presented in Fig. 11.

3) On Very High Resolution X-Band Data: In this part, the iterative version of the L-method has been applied on the X-band RAMSES data set over the Salon de Provence test site. For the KummerU segmentation, the optimal number of segments was found to be through the series $[7298 \rightarrow 3889 \rightarrow 1472 \rightarrow 457 \rightarrow 147 \rightarrow 52 \rightarrow 21]$. The partition containing the optimal estimated number of segments is shown in Fig. 12.

It has been shown that the L-method provides an objective and pertinent criterion for automatically identifying the optimal number of segments in the hierarchical segmentation procedure. A more in-depth analysis is given in [28].

V. Conclusion

In this paper, the authors have proposed to apply the SIRV estimation scheme to derive the covariance matrix and the texture parameter. By rewriting the texture variable as the product of a mean backscattered power μ with a normalized texture component ξ, the Beta prime PDF has been introduced to characterize the ξ variable. In this case, the texture parameter τ is Fisher distributed, and the target scattering vector follows a KummerU PDF. The asymptotic cases of this multivariate distribution have been studied. It generalizes the well-known $\mathcal{K}$ and $\mathcal{G}^0$ distributions. Some experiments at the X-, C-, L-, and P-bands have shown that this new statistical model is well adapted to fit a wide range of PolSAR clutters.

Based on those considerations, the multivariate KummerU distribution has been implemented in an ML hierarchical segmentation algorithm. The segmentation results on the synthetic and real PolSAR data have shown that the SIRV estimation scheme combined with the KummerU PDF provides the best performances compared to the classical Gaussian criterion. Next, a method based on the knee of the LLF has been implemented to determine automatically the "optimal" number of segments in the final partition.

Further works will deal with the use of texture and polarimetric informations for the ML texture tracking with high-resolution PolSAR data.

Appendix A
Convergence of the KummerU PDF Toward the $\mathcal{K}$ PDF

For large $\mathcal{M}$, the Fisher PDF tends toward the Gamma PDF. This appendix shows a proof of the convergence of the KummerU PDF toward the $\mathcal{K}$ PDF as $\mathcal{M}$ tends toward infinity. Abramowitz and Stegun have shown the following relation [see 31, Eq. 13.3.3] which links an asymptotic case of the KummerU function with the modified Bessel function of the second kind (denoted by BesselK).

$$\lim_{a\to\infty} \{\Gamma(1+a-b)U(a,b,z/a)\} = 2\, z^{\frac{1}{2}-\frac{b}{2}}\, \text{BesselK}_{b-1}\left(2\sqrt{z}\right) \tag{16}$$

Let $a = p + \mathcal{M}$, $b = 1 + p - \mathcal{L}$, and $z = (p + \mathcal{M}/\mathcal{M}m)\mathcal{L}\mathbf{k}^H[M]^{-1}\mathbf{k}$. By injecting the expression of a, b, and z in (16) and taking the limit when $\mathcal{M}$ tends toward infinity, it yields

$$\lim_{\mathcal{M}\to\infty} \left\{\Gamma(\mathcal{L}+\mathcal{M})\, U\left(p+\mathcal{M}, 1+p-\mathcal{L}, \frac{\mathbf{k}^H[M]^{-1}\mathbf{k}\mathcal{L}}{\mathcal{M}m}\right)\right\}$$
$$= 2\left[\frac{\mathcal{L}\,\mathbf{k}^H[M]^{-1}\mathbf{k}}{m}\right]^{\frac{1}{2}-\frac{(1+p-\mathcal{L})}{2}}$$
$$\times\, \text{BesselK}_{p-\mathcal{L}}\left(2\sqrt{\frac{L\mathbf{k}^H[M]^{-1}\mathbf{k}}{m}}\right). \tag{17}$$

Moreover, one can easily prove that

$$\lim_{\mathcal{M}\to\infty} \frac{\Gamma(p+\mathcal{M})}{\Gamma(\mathcal{M})\mathcal{M}^p} = 1. \tag{18}$$

By combining (17) and (18) in (9), we retrieve the expression of the $\mathcal{K}$ distribution

$$p_{\mathbf{k}}(\mathbf{k}|[M],\mathcal{L},m)=\frac{2}{\pi^p\Gamma(\mathcal{L})\,|[M]|}\left(\frac{\mathcal{L}}{m}\right)^{\left(\frac{\mathcal{L}+p}{2}\right)} \times\left[\mathbf{k}^H[M]^{-1}\mathbf{k}\right]^{\left(\frac{\mathcal{L}-p}{2}\right)} \times\text{BesselK}_{p-\mathcal{L}}\left(2\sqrt{\frac{\mathcal{L}\,\mathbf{k}^H[M]^{-1}\mathbf{k}}{m}}\right). \quad (19)$$

APPENDIX B
ML FISHER PARAMETER ESTIMATION

The scalar texture parameter τ is the random power of the clutter; it characterizes the randomness induced by the variations in the radar backscattering over different realizations (pixels). This scalar texture parameter is assumed to be independent from the polarization channel. For pixel i, it can be rewritten as the product of a normalized texture parameter ξ_i with the mean backscattered power μ by

$$\tau_i=\mu\,\xi_i \quad (20)$$

where μ is assumed as a deterministic quantity (parameter). Note that the current sample i is excluded from the computation of μ. Its expression is given by

$$\mu=\frac{1}{N-1}\sum_{\substack{j=1\\ j\neq i}}^{N}\tau_j. \quad (21)$$

By inserting (2) and (21) in (20), one can express ξ_i as the following ratio:

$$\xi_i=\frac{\tau_i}{\mu}=\frac{\tau_i}{\frac{1}{N-1}\sum\limits_{\substack{j=1\\ j\neq i}}^{N}\tau_j}=\frac{\mathbf{k}_i^H[M]^{-1}\mathbf{k}_i}{\frac{1}{N-1}\sum\limits_{\substack{j=1\\ j\neq i}}^{N}\mathbf{k}_j^H[M]^{-1}\mathbf{k}_j}. \quad (22)$$

If τ follows a Fisher PDF, denoted by $\mathcal{F}[\cdot]$, one can prove that

$$\mathcal{F}\left[\tau\,\middle|\,m=\frac{\mu\mathcal{L}}{\mathcal{M}},\mathcal{L},\mathcal{M}\right]=\mu\,\mathcal{BP}[\xi|\mathcal{L},\mathcal{M}]. \quad (23)$$

It yields that ξ follows a Beta prime PDF, denoted by $\mathcal{BP}[\cdot]$. The ML estimators of the Beta prime PDF parameters do not have an analytical expression. They are the solution of the following two equations, which contain the digamma function $\Psi(\cdot)$ by

$$\Psi(\hat{\mathcal{L}})-\Psi(\hat{\mathcal{L}}+\hat{\mathcal{M}})=\frac{1}{N}\sum_{i=1}^{N}\ln\left(\frac{\xi_i}{1+\xi_i}\right) \quad (24)$$

$$\Psi(\hat{\mathcal{M}})-\Psi(\hat{\mathcal{L}}+\hat{\mathcal{M}})=\frac{1}{N}\sum_{i=1}^{N}\ln\left(\frac{1}{1+\xi_i}\right). \quad (25)$$

Next, the transformation $A=\xi/(1+\xi)$ is applied on the data. Indeed, if $\xi\sim\mathcal{BP}(\mathcal{L},\mathcal{M})$, then $A\sim\mathcal{B}(\mathcal{L},\mathcal{M})$ where $\mathcal{B}(\cdot)$ is the Beta PDF. The Beta shape parameters ($\mathcal{L}$ and $\mathcal{M}$) are then numerically estimated by solving the ML equations [32]. Finally, the scale parameter m is estimated by the relation $m=\mu\mathcal{L}/\mathcal{M}$.

ACKNOWLEDGMENT

The authors would like to thank Prof. J. M. Beaulieu (Laval University, Canada) for the very fruitful discussions and advices. The authors would also like to thank the German Aerospace Center (DLR) and the French Aerospace Lab (ONERA) for providing the high and very high resolution PolSAR images. The authors would also like to thank the anonymous reviewers for their helpful comments and suggestions.

REFERENCES

[1] Y. Delignon, R. Garello, and A. Hillion, "Statistical modelling of ocean SAR images," *Proc. Inst. Elect. Eng.—Radar, Sonar Navig.*, vol. 144, no. 6, pp. 348–354, Dec. 1997.
[2] C. Tison, J.-M. Nicolas, F. Tupin, and H. Maître, "A new statistical model for Markovian classification of urban areas in high-resolution SAR images," *IEEE Trans. Geosci. Remote Sens.*, vol. 42, no. 10, pp. 2046–2057, Oct. 2004.
[3] F. Galland, J.-M. Nicolas, H. Sportouche, M. Roche, F. Tupin, and P. Réfrégier, "Unsupervised synthetic aperture radar image segmentation using Fisher distributions," *IEEE Trans. Geosci. Remote Sens.*, vol. 47, no. 8, pp. 2966–2972, Aug. 2009.
[4] S. Cloude and E. Pottier, "An entropy based classification scheme for land applications of polarimetric SAR," *IEEE Trans. Geosci. Remote Sens.*, vol. 35, no. 1, pp. 68–78, Jan. 1997.
[5] A. Freeman and S. Durden, "A three-component scattering model for polarimetric SAR data," *IEEE Trans. Geosci. Remote Sens.*, vol. 36, no. 3, pp. 963–973, May 1998.
[6] R. Touzi, "Target scattering decomposition in terms of roll-invariant target parameters," *IEEE Trans. Geosci. Remote Sens.*, vol. 45, no. 1, pp. 73–84, Jan. 2007.
[7] J. Lee, M. Grunes, T. Ainsworth, L. Du, D. Schuler, and S. Cloude, "Unsupervised classification using polarimetric decomposition and the complex Wishart classifier," *IEEE Trans. Geosci. Remote Sens.*, vol. 37, no. 5, pp. 2249–2258, Sep. 1999.
[8] H. Skriver, J. Schou, A. Nielsen, and K. Conradsen, "Polarimetric segmentation using the comple Wishart test statistic," in *Proc. IGARSS*, Toronto, ON, Canada, 2002, vol. 2, pp. 1011–1013.
[9] S. Anfinsen, T. Eltoft, and A. Doulgeris, "A relaxed Wishart model for polarimetric SAR data," in *Proc. PolInSAR*, Frascati, Italy, 2009.
[10] S. Quegan and I. Rhodes, "Statistical models for polarimetric SAR data," in *Proc. IEE Semin. Texture Anal. Radar Sonar*, 1993, pp. 8/1–8/8.
[11] J. Lee, D. Schuler, R. Lang, and K. Ranson, "K-distribution for multi-look processed polarimetric SAR imagery," in *Proc. IGARSS*, Pasadena, CA, 1994, pp. 2179–2181.
[12] J.-M. Beaulieu and R. Touzi, "Segmentation of textured polarimetric SAR scenes by likelihood approximation," *IEEE Trans. Geosci. Remote Sens.*, vol. 42, no. 10, pp. 2063–2072, Oct. 2004.
[13] C. Freitas, A. Frery, and A. Correia, "The polarimetric G distribution for SAR data analysis," *Environmetrics*, vol. 16, no. 1, pp. 13–31, 2005.
[14] L. Bombrun and J.-M. Beaulieu, "Fisher distribution for texture modeling of polarimetric SAR data," *IEEE Geosci. Remote Sens. Lett.*, vol. 5, no. 3, pp. 512–516, Jul. 2008.
[15] L. Bombrun, J.-M. Beaulieu, G. Vasile, J.-P. Ovarlez, F. Pascal, and M. Gay, "Hierarchical segmentation of polarimetric SAR images using heterogeneous clutter models," in *Proc. IGARSS*, Cape Town, South Africa, 2009, vol. 3, pp. 5–8.
[16] K. Yao, "A representation theorem and its applications to spherically-invariant random processes," *IEEE Trans. Inf. Theory*, vol. IT-19, no. 5, pp. 600–608, Sep. 1973.
[17] G. Vasile, J.-P. Ovarlez, F. Pascal, and C. Tison, "Coherency matrix estimation of heterogeneous clutter in high resolution polarimetric SAR images," *IEEE Trans. Geosci. Remote Sens.*, vol. 48, no. 4, pp. 1809–1826, Apr. 2010.
[18] F. Pascal, Y. Chitour, J. P. Ovarlez, P. Forster, and P. Larzabal, "Covariance structure maximum-likelihood estimates in compound Gaussian noise: Existence and algorithm analysis," *IEEE Trans. Signal Process.*, vol. 56, no. 1, pp. 34–48, Jan. 2008.
[19] F. Pascal, P. Forster, J. P. Ovarlez, and P. Larzabal, "Performance analysis of covariance matrix estimates in impulsive noise," *IEEE Trans. Signal Process.*, vol. 56, no. 6, pp. 2206–2217, Jun. 2008.
[20] K. Fang, S. Kotz, and K. Ng, *Symmetric Multivariate and Related Distributions*. London, U.K.: Chapman & Hall, 1990.

[21] S. Zozor and C. Vignat, "Some results on the denoising problem in the elliptically distributed context," *IEEE Trans. Signal Process.*, vol. 58, no. 1, pp. 134–150, Jan. 2010.
[22] Y. Chitour and F. Pascal, "Exact maximum likelihood estimates for SIRV covariance matrix: Existence and algorithm analysis," *IEEE Trans. Signal Process.*, vol. 56, no. 10, pp. 4563–4573, Oct. 2008.
[23] J.-M. Nicolas, "Introduction aux Statistiques de deuxième espèce: Applications des Logs-moments et des Logs-cumulants à l'analyse des lois d'images radar," *Traitement du Signal*, vol. 19, no. 3, pp. 139–167, 2002.
[24] J.-M. Nicolas, "Application de la transformée de Mellin: Étude des lois statistiques de l'imagerie cohérente," TELECOM ParisTech, Paris, France, Rapport de Recherche, 2006D010, 2006.
[25] J. Lee, M. Grunes, E. Pottier, and L. Ferro-Famil, "Segmentation of polarimetric SAR images," in *Proc. IGARSS*, Sydney, Australia, 2001, pp. 414–416.
[26] J. Morio, F. Goudail, X. Dupuis, P. Dubois-Fernandez, and P. Réfrégier, "Polarimetric and interferometric SAR image partition into statistically homogeneous regions based on the minimization of the stochastic complexity," *IEEE Trans. Geosci. Remote Sens.*, vol. 45, no. 11, pp. 3599–3609, Nov. 2007.
[27] X. He, N. H. C. Yung, K. P. Chow, F. Y. L. Chin, R. H. Y. Chung, K.-Y. K. Wong, and K. S. H. Tsang, "Watershed segmentation with boundary curvature ratio based merging criterion," in *Proc. 9th IASTED Int. Conf. SIP*, Honolulu, HI, 2007, pp. 7–12.
[28] S. Salvador and P. Chan, "Determining the number of clusters/segments in hierarchical clustering/segmentation algorithms," in *Proc. 16th IEEE ICTAI*, 2004, pp. 576–584.
[29] E. Gokcay and J. Principe, "Information theoretic clustering," *IEEE Trans. Pattern Anal. Mach. Intell.*, vol. 24, no. 2, pp. 158–171, Feb. 2002.
[30] R. Jenssen, K. Hild, J. Principe, and T. Eltoft, "Clustering using Renyi's entropy," in *Proc. Int. Joint Conf. Neural Netw.*, 2003, vol. 1, pp. 523–528.
[31] M. Abramowitz and I. Stegun, *Handbook of Mathematical Functions With Formulas, Graphs, and Mathematical Tables*. Washington, DC: NBS, 1964.
[32] G. Hahn and S. Shapiro, *Statistical Models in Engineering*. Hoboken, NJ: Wiley, 1994.

Lionel Bombrun (S'06–M'09) was born in Tournon, France, in 1982. He received the M.S. and Ph.D. degrees in signal, image, speech, and telecommunications from the Grenoble National Polytechnic Institute (INPG), Grenoble, France, in 2005 and 2008, respectively.

In 2008, he was a Teaching Assistant at Phelma, Grenoble. Since October 2009, he has been a Postdoctoral Fellow with the French National Council for Scientific Research (CNRS) between the Grenoble Image sPeech Signal Automatics Laboratory (GIPSA-lab), Grenoble, and the Supelec, ONERA, NUS, DSTA Research Alliance (SONDRA), Gif-sur-Yvette, France. His research interests include signal and image processing, synthetic aperture radar remote sensing, polarimetry, and interferometry.

Gabriel Vasile (S'06–M'07) received the M.Eng. degree in electrical engineering and computer science and the M.S. degree in image, shapes, and artificial intelligence from the POLITEHNICA University, Bucharest, Romania, in 2003 and 2004, respectively. He received the Ph.D. degree in signal and image processing from Savoie University, Annecy, France, in 2007.

From 2007 to 2008, he was a Postdoctoral Fellow with the French Space Agency (CNES) and was with the French Aerospace Lab (ONERA), Palaiseau, France. Since 2008, he has been with the French National Council for Scientific Research (CNRS), where he is currently a Research Scientist and a member of the Grenoble Image sPeech Signal Automatics Laboratory (GIPSA-lab), Grenoble, France. His research interests include signal and image processing, synthetic aperture radar remote sensing, polarimetry, and interferometry.

Michel Gay (M'10) received the B.Eng. degree in electrical engineering from the Institut des Sciences de l'Ingénieur de Montpellier, Montpellier, France, in 1987, and the Ph.D. degree in physics from the University Joseph Fourier, Grenoble, France, in 1999.

From 1988 to 2003, he was with Cemagref Grenoble, Grenoble, where he worked on electrical engineering for environmental applications. Since 2003, he has been a Research Engineer with the Grenoble Image sPeech Signal Automatics Laboratory (GIPSA-lab), Grenoble Institute of Technology, French National Council for Scientific Research (CNRS), Grenoble, France. His research interests include remote sensing, image processing, and the survey of Alpine glaciers.

Felix Totir received the B.S. degree in radar and guidance systems from the Military Technical Academy of Bucharest, Bucharest, Romania, in 2002. He received the M.S. degree in telecommunications and the Ph.D. degree in signal processing from the University of Brest, Brest, France, in 2003 and 2006, respectively.

He is currently with the Grenoble Image sPeech Signal Automatics Laboratory (GIPSA-lab), Grenoble, France. His research interests include radar signal processing, automatic object recognition, time-frequency analysis, dynamical systems, and cellular automata.

O. Harant, L. Bombrun, G. Vasile, L. Ferro-Famil, M. Gay, "Displacement Estimation by Maximum-Likelihood Texture Tracking", *IEEE Journal of Selected Topics in signal processing*, *Vol.* 5, *N*° 3, 2011.

Displacement Estimation by Maximum-Likelihood Texture Tracking

Olivier Harant, Lionel Bombrun, *Member, IEEE*, Gabriel Vasile, *Member, IEEE*, Laurent Ferro-Famil, *Member, IEEE*, and Michel Gay, *Member, IEEE*

***Abstract*—This paper presents a novel method to estimate displacement by maximum-likelihood (ML) texture tracking. The observed polarimetric synthetic aperture radar (PolSAR) data-set is composed by two terms: the scalar texture parameter and the speckle component. Based on the Spherically Invariant Random Vectors (SIRV) theory, the ML estimator of the texture is computed. A generalization of the ML texture tracking based on the Fisher probability density function (pdf) modeling is introduced. For random variables with Fisher distributions, the ratio distribution is established. The proposed method is tested with both simulated PolSAR data and spaceborne PolSAR images provided by the TerraSAR-X (TSX) and the RADARSAT-2 (RS-2) sensors.**

***Index Terms*—Maximum-likelihood (ML), offset tracking, polarimetric synthetic aperture radar (SAR), spherically invariant random vectors, texture.**

I. Introduction

GLACIER monitoring is a widely common problem which is investigated for years. The progressive awareness to climate changes makes these investigations more and more required as the glaciers are good indicators for local climate variation.

Different approaches using both optical and SAR sensors have been proposed to derive displacement fields. In the optical domain, optical flow methods have been successfully validated [1], but those methods are strongly dependent by weather phenomenon (snow fall, etc.) which will change the scene illumination. In addition, optical flow methods required cloudless images. Because of its all weather and all-day monitoring capabilities, SAR imagery offers a number of advantages for Earth-surface and feature observation. Different approaches have been proposed to derive displacement fields with SAR imagery: Differential Interferometric SAR (D-InSAR) and offset tracking techniques.

Although the potential of D-InSAR methods [2] have been successfully validated on different geophysical objects such as volcanoes, landslides [3], glaciers [4]–[7], its application is limited to coherence preservation. For the generation of new high resolution sensors (RADARSAT-2, TSX), the repeat time observation intervals becomes larger. It varies from 11 days for TSX to 24 days for RADARSAT-2 compared to 1 day during the ERS-1/2 tandem mission. For TSX data, coherence is not preserved at 11 days in winter on Alpine glaciers [8]. Another limitation of D-InSAR techniques concerns the fact that the displacement estimated is only a projection in the line-of-sight (LOS) direction. Different hypothesis have been proposed to retrieve the three components. A common assumption is to consider a flow parallel to the glacier surface and in the direction of maximum averaged downhill slope [7]. Another approach is to combine both ascending and descending passes [9].

Nevertheless, the new generation of recently launched SAR sensors are now able to produce high quality images of the Earth's surface with meter resolution. The decrease of the resolution cell offers the opportunity to observe much thinner spatial features. Offset tracking methods in the SAR domain are now more and more studied. It exists different techniques:

- The **speckle tracking** technique correlates small blocks to determine the relative displacement in the range and azimuth (along-track) directions [10] [11]. This technique does not depend on image feature tracking but rather on the fact that there is coherence between the blocks. As coherence is not preserved with TSX for temperate Alpine glaciers, the speckle tracking method is not well suited.
- Recently, a novel tracking method based on **Isolated Point Scatterer** (IPS) has been proposed [12]. It corresponds to the matched filter between the signal backscattered by an IPS and the ideal response: a double cardinal sinus. This method is valid only for particular objects such as corner reflector.
- The classical **intensity tracking** technique based on the normalized cross-correlation (NCC) criterion [13] [14].
- The **Maximum-Likelihood (ML) texture tracking** algorithm which takes into account the statistics of the backscattered signal [15].

In this paper, authors propose an algorithm closed to the ML texture tracking algorithm introduced by Erten *et al.* [15]. It takes into accounts the statistics of the texture parameter extracted from the PolSAR data. Fig. 1 shows the global scheme of this method.

Manuscript received April 20, 2010; revised November 17, 2010; accepted November 28, 2010. Date of publication December 17, 2010; date of current version May 18, 2011. This work was supported by the French Research Agency (ANR) through the EFIDIR Project (ANR-2007-MCDC0-04, The associate editor coordinating the review of this manuscript and approving it for publication was Prof. Jocelyn Chanussot.

O. Harant is with the GIPSA-Lab, CNRS INPG-961, 46-38402 Saint-Martin-d'Hères, France, and also with the IETR Laboratory, SAPHIR Team, University of Rennes 1, 35042 Rennes, France (e-mail: olivier.harant@gipsa-lab.grenoble-inp.fr).

L. Bombrun, G. Vasile, and M. Gay are with the GIPSA-Lab, CNRS INPG-961, 46-38402 Saint-Martin-d'Hères, France (e-mail: lionel.bombrun@gipsa-lab.grenoble-inp.fr; gabriel.vasile@gipsa-lab.grenoble-inp.fr; michel.gay@gipsa-lab.grenoble-inp.fr).

L. Ferro-Famil is with the IETR Laboratory, SAPHIR Team, University of Rennes 1, 35042 Rennes, France (e-mail: laurent.ferro-famil@univ-rennes1.fr).

Color versions of one or more of the figures in this paper are available online at http://ieeexplore.ieee.org.

Digital Object Identifier 10.1109/JSTSP.2010.2100365

1932-4553/$26.00 © 2010 IEEE

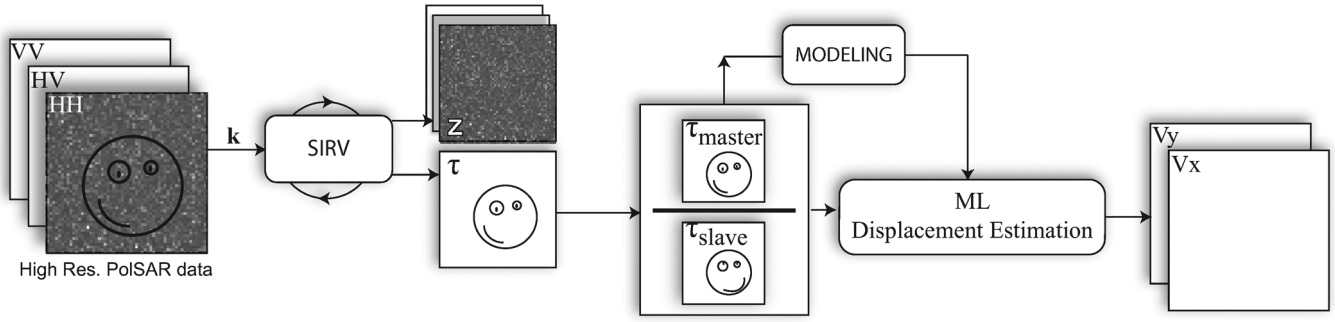

Fig. 1. Global scheme of the generalized ML texture tracking method.

This paper is organized as follows. In Section II, the Spherically Invariant Random Vectors (SIRV) model is introduced to extract the texture component from PolSAR data. Next, we focus on the texture modeling. Then, in Section III, the ML texture tracking algorithm is presented and adapted to the proposed texture model with both uncorrelated and correlated texture between images. Section IV presents results on simulated data, on dual-pol TSX and quad-pol RADARSAT-2 data over the Argentière glacier. Finally, some conclusion and perspectives of this work are discussed.

II. SIRV Model

A. Principle

With the new generation of airborne and spaceborne SAR sensors, the number of scatterers present in each resolution cell decreases considerably, homogeneous hypothesis of the PolSAR clutter can be reconsidered. Heterogeneous clutter models have therefore recently been studied with POLSAR data with the SIRV processes [16].

From a PolSAR point of view, the target vector $\mathbf{k}$ can be defined as the product of a square root of a positive random variable τ (representing the texture) with an independent complex Gaussian vector $\mathbf{z}$ with zero mean and covariance matrix $[M] = E\{\mathbf{z}\mathbf{z}^H\}$ (representing the speckle):

$$\mathbf{k} = \sqrt{\tau}\,\mathbf{z} \tag{1}$$

where the superscript H denotes the complex conjugate transposition and $E\{\cdot\}$ the mathematical expectation.

B. SIRV Estimation Scheme

For a given covariance matrix $[M]$, the ML estimator of the texture parameter τ for the pixel i ($\hat{\tau}_i$) is given by

$$\hat{\tau}_i = \frac{\mathbf{k}_i^H [M]^{-1} \mathbf{k}_i}{p} \tag{2}$$

where p is the dimension of the target scattering vector $\mathbf{k}$ ($p = 3$ for the reciprocal case).

The ML estimator of the normalized covariance matrix under the deterministic texture case is the solution of the following recursive equation:

$$[\hat{M}]_{FP} = f\left([\hat{M}]_{FP}\right) = \frac{p}{N}\sum_{i=1}^{N} \frac{\mathbf{k}_i \mathbf{k}_i^H}{\mathbf{k}_i^H [\hat{M}]_{FP}^{-1} \mathbf{k}_i} = \frac{p}{N}\sum_{i=1}^{N} \frac{\mathbf{z}_i \mathbf{z}_i^H}{\mathbf{z}_i^H [\hat{M}]_{FP}^{-1} \mathbf{z}_i}. \tag{3}$$

In the random texture τ case, the ML estimator of the normalized covariance matrix depends on the texture pdf $p_\tau(\tau)$ and is given by [17]

$$[\hat{M}_{ML}] = \frac{1}{N}\sum_{i=1}^{N} \frac{h_{p+1}\left(\mathbf{k}_i^H [\hat{M}_{ML}]^{-1} \mathbf{k}_i\right)}{h_p\left(\mathbf{k}_i^H [\hat{M}_{ML}]^{-1} \mathbf{k}_i\right)} \mathbf{k}_i \mathbf{k}_i^H \tag{4}$$

where $h_p(x)$ is the density generator function defined by [18] [19]

$$h_p(x) = \int_0^{+\infty} \frac{1}{\tau^p} \exp\left(-\frac{x}{\tau}\right) p_\tau(\tau)\, d\tau. \tag{5}$$

For sake of simplicity and computational efficiency, this study is limited to the "approximate" ML estimator (3). Pascal *et al.* have established the existence and the uniqueness, up to a scalar factor, of the Fixed Point estimator of the normalized covariance matrix, as well as the convergence of the recursive algorithm whatever the initialization [20] [21]. In this paper, the trace of the covariance matrix is normalized to p the dimension of target scattering vector. In practice, the normalized covariance matrix is first computed because it does not depend on the texture component. Then, the ML estimator of the texture parameter is estimated according to (2).

It is important to notice that in the SIRV definition, the probability density function (pdf) of the texture random variable is not explicitly specified. As a consequence, SIRVs describe a whole class of stochastic processes. This class includes the conventional clutter models having Gaussian, $\mathcal{K}$, $\mathcal{G}^0$, KummerU pdfs which correspond respectively to Dirac, Gamma, Inverse Gamma, and Fisher distributed texture [22]–[24].

C. Texture Modeling

1) Fisher pdf: The Fisher pdf is the Pearson type VI distribution, it is defined by three parameters as [25]–[27]

$$p_\tau(\tau) = \mathcal{F}[m, \mathcal{L}, \mathcal{M}] = \frac{\Gamma(\mathcal{L}+\mathcal{M})}{\Gamma(\mathcal{L})\Gamma(\mathcal{M})} \frac{\mathcal{L}}{\mathcal{M}m} \frac{\left(\frac{\mathcal{L}\tau}{\mathcal{M}m}\right)^{\mathcal{L}-1}}{\left(1+\frac{\mathcal{L}\tau}{\mathcal{M}m}\right)^{\mathcal{L}+\mathcal{M}}} \tag{6}$$

with $\mathcal{L} > 0$ and $\mathcal{M} > 0$.

As Fisher pdfs can be viewed as the Mellin convolution of a Gamma pdf by an Inverse Gamma pdf [26], they can fit distributions with either heavy heads or heavy tails.

2) Benefit of Fisher PDF: A glacier area (80 × 35 pixels) from the X-band TSX data over the Chamonix Mont-Blanc test-

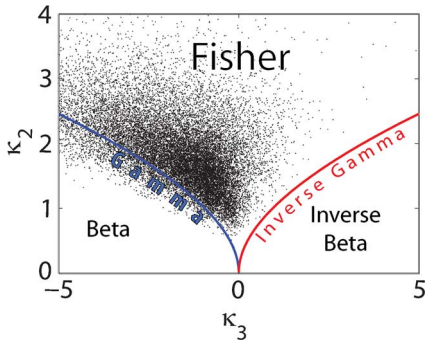

Fig. 2. κ_2/κ_3 plan for a glacier area over the Chamonix Mont-Blanc test-site (TSX, X-band).

site has been extracted. Then, the covariance matrix $[M]_{FP}$ and the texture parameter τ are estimated according to (2) and (3). To see the benefit of Fisher pdfs to model the texture of PolSAR data, the κ_2/κ_3 plan has been plotted in Fig. 2. It shows the evolution of the second log-cumulant κ_2 versus the third log-cumulant κ_3. In this plan, Gamma and Inverse Gamma pdf are respectively represented by the blue and red lines. The first three log-cumulants estimates are

$$\begin{aligned}\hat{\kappa}_1 &= \frac{1}{N}\sum_{i=1}^{N}\ln\tau_i \\ \hat{\kappa}_2 &= \frac{1}{N}\sum_{i=1}^{N}(\ln\tau_i-\hat{\kappa}_1)^2 \\ \hat{\kappa}_3 &= \frac{1}{N}\sum_{i=1}^{N}(\ln\tau_i-\hat{\kappa}_1)^3\end{aligned} \tag{7}$$

where N is the number of pixels in the sliding window. In the case of Fig. 2, a 7×7 pixels sliding window has been used to compute the log-cumulants. Fisher pdfs cover all the space between the blue and red line [25].

In this example, 15.53% of the pixels are Beta distributed (under the blue line), 0.004% are Inverse Beta distributed (under the red line) and 84.47% are Fisher distributed. It shows that Fisher pdfs are well adapted to model PolSAR clutter [24]. In the following, the texture parameter will be considered to be Fisher distributed.

After having shown the benefit of Fisher pdfs to model the texture of high-resolution PolSAR data, we propose to implement this distribution in the ML texture tracking algorithm. As Fisher pdfs are a generalization of Gamma pdfs, the proposed algorithm can be seen as an extension of the algorithm proposed by Erten *et al.* [15].

III. Texture Tracking

A. Principle

Classical algorithms estimate the shift between images by maximizing the normalized cross-correlation coefficient. This criterion is the ML solution for optical data corrupted by additive noise [28] or for complex SAR data having circular Gaussian statistics [29]. With increasing the resolution of PolSAR data, the number of scatterers in each resolution decreases. The central limit theorem may not be respected and the Gaussian hypothesis may be reconsidered. Consequently, the NCC criterion may not be optimal for high-resolution PolSAR data. In this section, the texture tracking algorithm is improved based on the SIRV model and the Fisher distribution for texture modeling.

Let $\mathbf{k}_y^i = [\mathbf{k}_{y_1}^i, \ldots, \mathbf{k}_{y_k}^i]$ and $\mathbf{k}_x = [\mathbf{k}_{x_1}, \ldots, \mathbf{k}_{x_k}]$ be two blocks of the PolSAR data-set containing k pixels. They represent respectively the slave and master images. According to (2) and (3), the texture blocks $\tau_y^i = [\tau_{y_1}^i, \ldots, \tau_{y_k}^i]$ and $\tau_x = [\tau_{x_1}, \ldots, \tau_{x_k}]$ are estimated. The slave block i is shifted from the master one with a displacement $\mathbf{v}_i$. In this study, the vector $\mathbf{v}_i$ is limited to a translation and has only two components $[v_i{}^d, v_i^{az}]$ in range and azimuth. The ML texture tracking algorithm estimates the shift vector $\mathbf{v}_{\mathrm{ML}}$ by maximizing for each slave block i the conditional density function (cdf) [15]. It yields

$$\mathbf{v}_{\mathrm{ML}} = \underset{i}{\mathrm{Argmax}}\; p\left(\tau_x|\tau_y^i, \mathbf{v}_i\right). \tag{8}$$

By following the same procedure as described in [15], the pdf of the texture ratio $\alpha = \tau_x/\tau_y$ must be established to estimate the shift vector. This study has to be done when the texture between images is uncorrelated and correlated.

B. Texture Model With Uncorrelated Texture Between Images

If τ_x and τ_y are two independent and identically distributed (i.i.d.) random variables, the pdf of the texture ratio α is given by [30, Eq. 6.56]

$$p_\alpha(\alpha) = \int_0^\infty p_{\tau_x}(\alpha\tau)p_{\tau_y}(\tau)\tau d\tau. \tag{9}$$

For Fisher distributed texture, the pdf of the ratio of two uncorrelated texture has been established (see Appendix A), its expression is given by

$$\begin{aligned}p_\alpha(\alpha) = &\frac{B(2\mathcal{L},2\mathcal{M})}{[B(\mathcal{L},\mathcal{M})]^2}\frac{1}{\alpha^{\mathcal{M}+1}} \\ &\times {}_2F_1\left(\mathcal{L}+\mathcal{M}, 2\mathcal{M}; 2(\mathcal{L}+\mathcal{M}); \frac{\alpha-1}{\alpha}\right)\end{aligned} \tag{10}$$

where ${}_2F_1(\cdot,\cdot;\cdot;\cdot)$ and $B(\cdot,\cdot)$ are respectively the Gauss hypergeometric function and the Euler Beta function ($B(z,w) = \Gamma(z)\Gamma(w)/\Gamma(z+w), \Re\mathrm{e}(z) \geq 0, \Re\mathrm{e}(w) \geq 0$). $\mathcal{L}$ and $\mathcal{M}$ are the two shape parameters of the Fisher pdf. The scale parameter m simplifies because the texture ratio variable is studied.

According to [15], (8) is equivalent to

$$\mathbf{v}_{\mathrm{ML}} = \underset{i}{\mathrm{Argmax}} \prod_{j=1}^{k} \frac{1}{\tau_{y_j}^i}\, p_\alpha\left(\frac{\tau_{x_j}}{\tau_{y_j}^i}\right). \tag{11}$$

It yields

$$\begin{aligned}\mathbf{v}_{\mathrm{ML}} = \underset{i}{\mathrm{Argmax}} &\prod_{j=1}^{k} \frac{B(2\mathcal{L},2\mathcal{M})}{[B(\mathcal{L},\mathcal{M})]^2}\frac{1}{\tau_{y_j}^i}\left(\frac{\tau_{x_j}}{\tau_{y_j}^i}\right)^{-1-\mathcal{M}} \\ &\times {}_2F_1\left(\mathcal{L}+\mathcal{M}, 2\mathcal{M}; 2(\mathcal{L}+\mathcal{M}); 1-\frac{\tau_{y_j}^i}{\tau_{x_j}}\right).\end{aligned} \tag{12}$$

By taking the natural logarithm of (12), one can prove that the criterion to maximize to estimate the shift vector for uncorrelated texture between images is

$$\mathrm{L}(\mathbf{v}_i) = k \ln \left(\frac{B(2\mathcal{L}, 2\mathcal{M})}{[B(\mathcal{L}, \mathcal{M})]^2} \right) + \mathcal{M} \sum_{j=1}^{k} \ln \frac{\tau_{y_j}^i}{\tau_{x_j}} - \sum_{j=1}^{k} \ln \tau_{x_j}^i + \sum_{j=1}^{k} \ln \left({}_2F_1 \left(\mathcal{L} + \mathcal{M}, 2\mathcal{M}; 2(\mathcal{L} + \mathcal{M}); 1 - \frac{\tau_{y_j}^i}{\tau_{x_j}} \right) \right). \quad (13)$$

C. Texture Model With Correlated Texture Between Images

In the case of correlated texture between two images, the bivariate Fisher distribution with marginal Fisher pdf should be used. Its pdf is defined by six parameters as [31]

$$\begin{aligned} p_{X_1,X_2}(x_1, x_2) &= \frac{R_1^{\mathcal{L}_1} R_2^{\mathcal{L}_2}}{B(\mathcal{L}_1, \mathcal{M}_1) B(\mathcal{L}_2, \mathcal{L}_1 + \mathcal{M}_2)} \\ &\quad \times x_1^{\mathcal{L}_1 - 1} x_2^{\mathcal{L}_2 - 1} (1 + R_1 x_1 + R_2 x_2)^{-(\mathcal{L}_1 + \mathcal{L}_2 + \mathcal{M}_2)} \\ &\quad \times {}_2F_1(\mathcal{L}_1 + \mathcal{L}_2 + \mathcal{M}_2, \mathcal{M}_2 - \mathcal{M}_1; \mathcal{L}_1 + \mathcal{M}_2; w) \end{aligned} \quad (14)$$

with $R_1 = \mathcal{L}_1/\mathcal{M}_1 m_1$, $R_2 = \mathcal{L}_2/\mathcal{M}_2 m_2$ and $w = R_1 x_1/1 + R_1 x_1 + R_2 x_2$.

For Fisher distributed texture, the pdf of the ratio of two correlated texture has been established (see Appendix B), its expression is given by

$$p_\alpha(\alpha) = \frac{R_1^{\mathcal{L}_1} R_2^{\mathcal{L}_2} B(\mathcal{L}_1 + \mathcal{L}_2, \mathcal{M}_2)}{B(\mathcal{L}_1, \mathcal{M}_1) B(\mathcal{L}_2, \mathcal{L}_1 + \mathcal{M}_2)} \frac{\alpha^{\mathcal{L}_1 - 1}}{(R_1 \alpha + R_2)^{\mathcal{L}_1 + \mathcal{L}_2}} \times {}_2F_1(\mathcal{L}_1 + \mathcal{L}_2, \mathcal{M}_2 - \mathcal{M}_1; \mathcal{L}_1 + \mathcal{M}_2; z) \quad (15)$$

with $z = 1/1 + (R_2/R_1)(1/\alpha)$.

By following the same procedure as described in Section III-B, the criterion to maximize to estimate the shift vector for correlated texture between images is given by

$$\begin{aligned} \mathrm{L}(\mathbf{v}_i) = K &+ (\mathcal{L}_1 - 1) \sum_{j=1}^{k} \ln \tau_{x_j} + (\mathcal{L}_2 + 1) \sum_{j=1}^{k} \ln \tau_{y_j}^i \\ &- (\mathcal{L}_1 + \mathcal{L}_2) \sum_{j=1}^{k} \ln \left(R_1 \tau_{x_j} + R_2 \tau_{y_j}^i \right) \\ &+ \sum_{j=1}^{k} \ln \left({}_2F_1(\mathcal{L}_1 + \mathcal{L}_2, \mathcal{M}_2 - \mathcal{M}_1; \mathcal{L}_1 + \mathcal{M}_2; z) \right) \end{aligned} \quad (16)$$

with $K = k(\ln R_1^{\mathcal{L}_1} + \ln R_2^{\mathcal{L}_2}) + k \ln(B(\mathcal{L}_1 + \mathcal{L}_2, \mathcal{M}_2)/B(\mathcal{L}_1, \mathcal{M}_1) B(\mathcal{L}_2, \mathcal{L}_1 + \mathcal{M}_2))$.

In (16), the term $R_1 \tau_{x_j} + R_2 \tau_{y_j}^i$ depends on the samples order. It plays a role similar as the cross-correlation coefficient which takes into account the spatial arrangement of pixels.

IV. Results

A. On Simulated Data

Simulations have been performed to test the reliability of the ML shift estimators. One Master/Slave image pair is sampled from the same Fisher pdf for each region. The master and slave images are shaped according to a 2-D rectangular function. The border is sampled from $\mathcal{F}[1, 2, 0.5]$. The center is sampled from $\mathcal{F}[5, 6, 0.8]$ and corresponds to the size of the estimation neighborhood. The simulated dataset has been corrupted with independent multiplicative noise sampled from a Gamma pdf $\mathcal{G}[1, 1]$. Fig. 3(a) shows an example of one simulation.

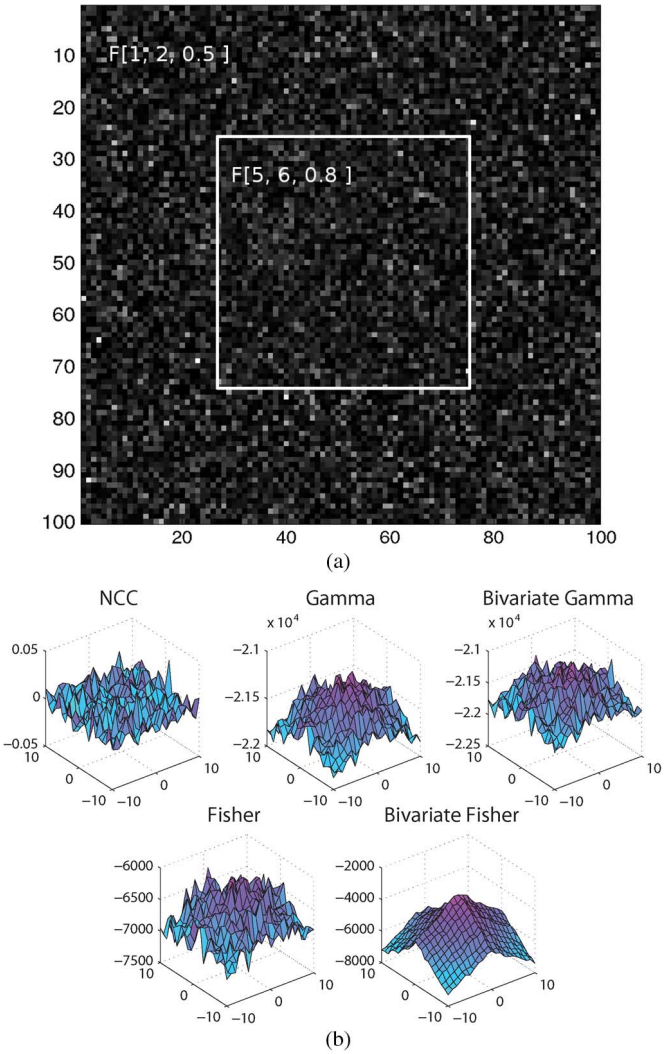

Fig. 3. NCC, uncorrelated and correlated Gamma ML, uncorrelated and correlated Fisher ML criteria computed on simulations. (a) Simulated texture data. (b) Detection surfaces for the multiplicative noised dataset: NCC, uncorrelated and correlated Gamma ML, uncorrelated and correlated Fisher ML.

Five shift estimators are then computed: NCC, uncorrelated and correlated Gamma ML, uncorrelated and correlated Fisher ML. Since there is no motion between the two texture images, the detection surface should be flat except in the center, where a peak is expected.

Fig. 3(b) illustrates the results obtained where 1000 Monte Carlo simulations have been performed for the shift estimators (NCC and MLs). The NCC, both uncorrelated and correlated Gamma ML and the uncorrelated Fisher ML estimators fail to detect the no-motion: the criteria are very noisy without any peak. However, the correlated Fisher ML gives a smoother detection surface with a more pronounced detection peak. This recommends the correlated Fisher ML texture tracking with multiplicative noise.

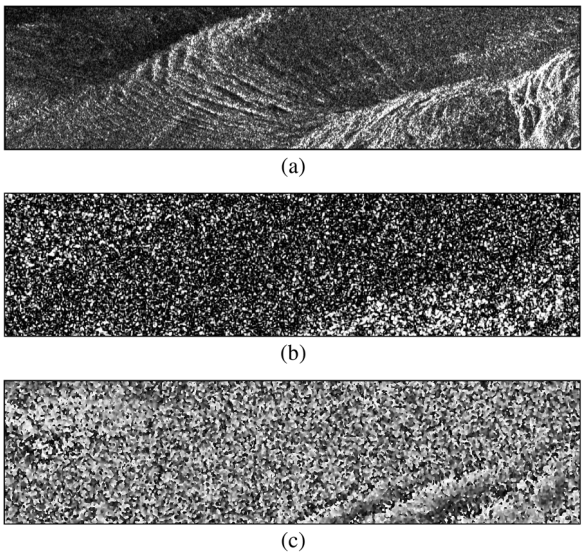

Fig. 4. D-InSAR results from 2009-01-06/2009-01-17 couple. (a) Amplitude. (b) Coherence. (c) Phase images.

B. On Real Data

1) Argentière Glacier Test-Site: This work introduces some preliminary TSX and RADARSAT-2 observations of the Argentière glacier in order to estimate its displacement. It is located in the Mont-Blanc massif, its head (catchment area) starts near 3000 m. Its slope is quite regular and not steep except at the bottom where the seracs fall breaks the slope and disconnects the terminal part from the rest of the glacier. 14 TSX and 4 RADARSAT-2 images have been acquired on the Argentière glacier during the winter and spring 2008–2009.

2) D-InSAR Potential: As the surface of the temperate glacier changes from one day to another, in the TSX case and more generally at X-band, the interferometry on the surface of temperate glaciers is difficult and its potential is quite limited [8]. Fig. 4 shows amplitude, coherence and phase of an 11-day interferogram acquired in winter (2009-01-06/2009-01-17). For this interferometric couple, coherence is not preserved on the Argentière glacier. The interferometric phase cannot be used to derive displacement fields.

3) Texture Tracking: As the new sensors provide higher resolution and according to the limitation of the interferometric methods on the temperate glaciers, incoherent methods seems promising. From October 2007 to June 2009, 14 TSX complex dual-pol images in stripmap mode and 4 RADARSAT-2 complex fine quad-pol images have been acquired over the Chamonix Mont-Blanc test-site. Table I summaries the main details of the two images pairs on which we have worked. Only a coarse coregistration has been processed in each images pair to avoid any distortion which could affect the polarimetric and statistical properties. The subpixel coregistration values should be subtracted to the texture tracking results.

a) On TSX data: Fig. 5 shows the displacement field derived over one crevasses area of the Argentière glacier. The texture image pair is extracted using the SIRV estimation scheme [16]. A 64 × 256 pixels sliding window has been used to derive the displacement map. As expected, the displacement on the border of the glacier is closed to zero. Note that the mean displacement over the crevasse field is about two times higher than over the homogeneous area of the glacier. This corresponds to the annual displacement estimation provided by glaciologists.[1] Further studies need to quantitatively assess the derived shift estimates.

TABLE I
DETAILS OF TSX AND RADARSAT-2 PRODUCTS

Prod.	Date	Pixel Spacing Rng × Az	Polarizations	Inc. angle
TSX	2009-01-06 2009-02-08	1.4m × 2.5m	HH / HV	37.8°
RS-2	2009-01-29 2009-02-22	4.7m × 5.1m	HH / HV / VV	31.5°

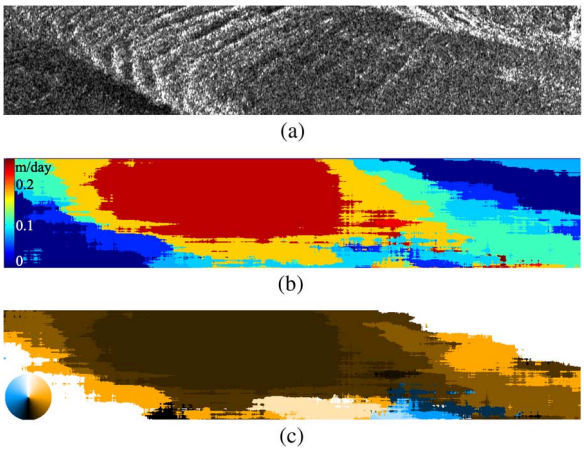

Fig. 5. Displacement estimation over a crevasse field of the Argentière glacier, dual-pol TSX data, 2009-01-06/2009-02-08. (a) Master texture estimated using SIRV model. (b) Displacement field in LOS. (c) Orientation map.

Note also that orientation of the motion field is consistent with the conventional temperate glacier flow model: from the upper left to the bottom right of the image.

Contrary to the NCC criterion, the confidence interval for the ML similarity measure is hard to qualify. Further investigations should be necessary to derive the false alarm probability for Fisher distributed texture. In [15], Erten *et al.* have introduced the following $\mathcal{Q}_{ML}$ index defined by

$$\mathcal{Q}_{ML} = \frac{\max(ML) - \text{mean}(ML)}{\text{mean}(ML) - \min(ML)}. \tag{17}$$

$\mathcal{Q}_{ML}$ is a measure of confidence. The higher is $\mathcal{Q}_{ML}$, the more accurate is the displacement estimation.

Table II shows the mean and variance of two samples extracted respectively from a crevasses area and an homogeneous area of the glacier. The mean of $\mathcal{Q}_{ML}$ is higher on crevasses area and its variance is lower. It highlights the sensitivity of the ML criterion to the texture heterogeneity. Reliable displacement results are obtained on the crevasses areas.

b) Regularisation: For the study of geophysical objects, *a priori* flow model can be added to similarity measure to estimate

[1]LGGE. Glacioclim.

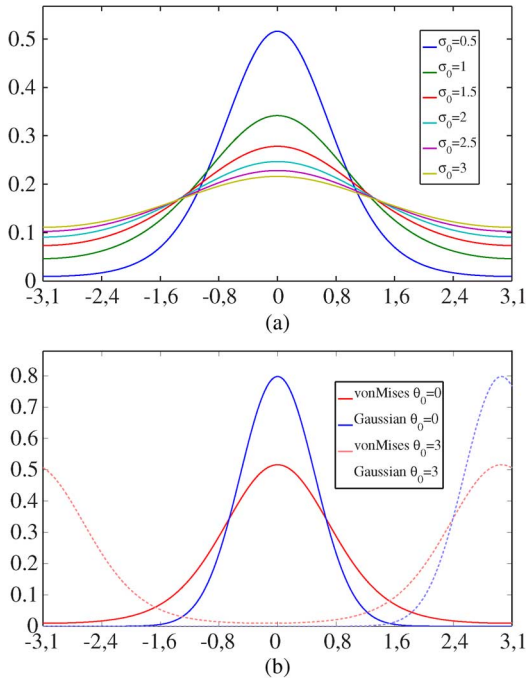

Fig. 6. von Mises pdf is the circular analogue of the normal distribution. (a) von Mises pdf. $\theta_i^0 = 0$. (b) Normal and von Mises pdfs. $\sigma_i^0 = 0.5$. $\theta_i^0 \neq 0$: circularity of the von Mises pdf on $-\pi, +\pi$.

TABLE II
$\mathcal{Q}_{ML}$ MEAN AND VARIANCE OVER TWO AREAS ON THE ARGENTIÈRE GLACIER COMPUTED FROM TSX DATA

$\mathcal{Q}_{ML}$	Crevasses area	Homogeneous area
Mean	1.2858	0.9224
Variance	0.2470	0.0728

the displacement field. According to Bayes' rule, the problem formulation becomes

$$p\left(\tau_y^i, \mathbf{v}_i | \tau_x^i\right) = \frac{p\left(\tau_x^i | \tau_y^i, \mathbf{v}_i\right) p\left(\tau_y^i | \mathbf{v}_i\right) p(\mathbf{v}_i)}{p\left(\tau_x^i\right)}. \quad (18)$$

Let v_i^d and v_i^{az} be, respectively, the two components of the displacement vector $\mathbf{v}_i$ along the distance and azimuth direction. In (18), the prior term $p(\mathbf{v}_i)$ can be rewritten as

$$p(\mathbf{v}_i) = p_\rho(\rho_i)\, p_\theta(\theta_i) \quad (19)$$

where ρ_i and θ_i are the polar coordinates of the displacement vector $\mathbf{v}_i$. They are linked with the distance and azimuth component by $\rho_i = \sqrt{v_i^{d\,2} + v_i^{az\,2}}$ and $\theta_i = \operatorname{atan}(v_i^{az}/v_i^d)$.

For the Argentière glacier, the assumptions of a flow parallel to the glacier surface and in the direction of the maximum downhill slope have been successfully validated with *in situ* measurements [7]. Those information can be included in the prior model. Consequently, the orientation angle θ_i is assumed to be normally distributed and having circular values between $-\pi$ and $+\pi$. This parameter follows the *von Mises* distribution (also known as the circular normal distribution) which is the circular analog of the normal distribution [32] (Fig. 6)

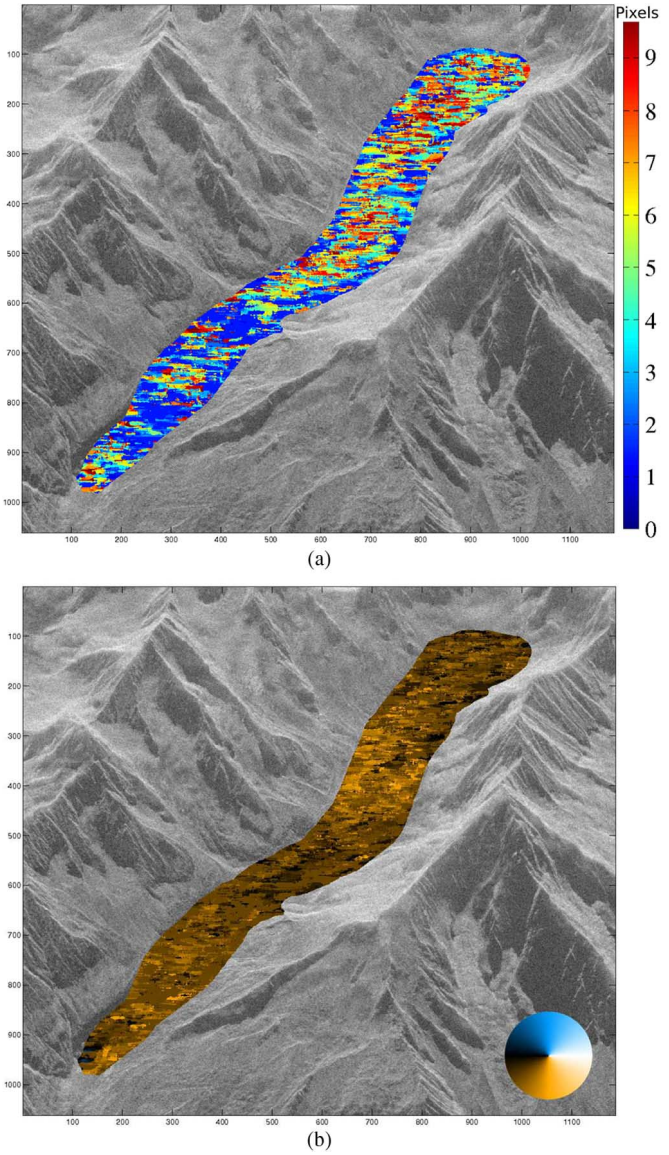

Fig. 7. Displacement estimation over the Argentière glacier with regularisation according to Bayes' rule, quad-pol RADARSART-2 data, 2009-01-29/2009-02-22. (a) Displacement field in LOS. (b) Orientation map.

$$p_\theta(\theta_i) = \frac{1}{2\pi I_0\left(\frac{1}{\sigma_i^0}\right)} \exp\left(\frac{1}{\sigma_i^0} \cos\left(\theta_i - \theta_i^0\right)\right) \quad (20)$$

with θ_i^0 mean and σ_i^0 standard deviation. θ_i^0 is the direction in the maximum downhill slope issued from a digital elevation model. σ_i^0 is fixed here to π. $I_0(.)$ is the modified Bessel function of order 0. Concerning the absolute value of the displacement ρ_i, no constraint is imposed. ρ_i is therefore assumed to be uniformly distributed in the search neighborhood.

c) On RADARSAT-2 data: Fig. 7 illustrates a displacement estimation using quad-pol RADARSAT-2 data. On this example, a regularization process has been applied according to a Bayes' rule formulation. The orientation map has been extracted from a DEM of the Mont-Blanc massif with a resolution

of 10 m and projected in SAR geometry. As expected, the orientation map [Fig. 7(b)] is consistent with the glacier flow model.

V. Discussion

In this paper, the study has been focused on the generalization of the ML texture tracking using the Fisher pdfs which have the ability to fit a wide range of texture scenes. For glacier texture tracking, we recommend to use low-frequency bands as the C-band or less to penetrate under the dry snow. This will permit to observe structures (dust, eratic blocks, relief, etc.) present on the ice surface which is more heterogeneous and more stable in time than the snow.

In this paper, the ML texture tracking algorithm has been applied on Alpine glaciers. They present the advantage to have large displacement. Nevertheless, their surface is quite homogeneous and does not highlight the benefit of Fisher pdfs for texture modeling. This kind of method can be relevant for the monitoring of other geophysical objects such as volcanoes, earthquakes, etc., which have rough surfaces. The more heterogeneous the ground is and/or the higher the resolution is, the more relevant the texture information is for displacement estimation, segmentation and denoising.

Many recent works have been dedicated to the statistical modeling of the backscattering signal. For this purpose, Mellin transform and second kind statistics define a well-suited formalism [27]. In this context, many distributions have been introduced as a generalization of the well-known Gamma pdf. Here, the 3-parameter Fisher pdf has been used but other statistics such as the KWBU pdfs system may be considered [33]. Those 4-parameter distributions should permit a better texture modeling. Further investigations still remains necessary to quantify the benefit of models with more freedom degrees.

VI. Conclusion

With the new generation of launched PolSAR sensors, the Earth's surface is imaged with meter resolution. Small spatial features can then be observed from the space. Recently, more and more studies are dedicated to texture extraction and modeling. Based on this consideration, this paper has presented a new texture tracking method to derive displacement fields from PolSAR data. According to the SIRV estimation scheme, the texture parameter can be estimated and isolated from the speckle component. The proposed algorithm estimates a shift vector through maximizing the cdf of two matched texture blocks.

Due to their capability to fit distributions with either heavy heads or heavy tails, Fisher pdfs are well adapted to model the texture variable. This observation has been illustrated on real PolSAR data. Next, based on the assumption of Fisher distributed texture, the pdfs of the ratio of two texture variables have been established for both uncorrelated and correlated texture between images. Then, a ML criterion has been established to measure the similarity between two blocks: one for the master and one for the slave texture images. This similarity measure is computed in a neighborhood of the slave image. The shift vector which leads to the largest log-likelihood value yields to the estimated displacement.

Then, the ML texture tracking algorithm has been applied on simulated and real PolSAR data. The proposed algorithm has been compared to the NCC criterion and the ML tracking algorithm based on Gamma assumption for the texture component.

Contrary to the NCC criterion, the confidence interval for the ML similarity measure is hard to qualify. Further investigations should be necessary to derive the false alarm probability for Fisher distributed texture.

As discussed before, the ML texture tracking confidence interval is hard to be qualify. Erten *et al.* have introduced the $\mathcal{Q}_{ML}$ factor which provides some information on the behavior of the ML distribution. Nevertheless, some works are necessary to define the PFA for the ML criteria. This will permit to threshold the similarity image and conclude or not on the relevance of the results.

Further works will deal with the addition of the covariance matrix information to estimate displacement. Indeed, only the texture variable is used in the ML tracking algorithm. The polarimetric diversity contains very useful information concerning the scattering mechanisms. This type of information has been widely used in classification of PolSAR data. It should probably improve tracking performances.

Appendix A

This appendix gives the mathematical details of the pdf of α for uncorrelated Fisher distributed texture. In such case, the pdf of α is obtained by replacing the expression of the Fisher pdf (6) in (9), it yields

$$\begin{aligned} p_\alpha(\alpha) &= \int_0^\infty \frac{\Gamma(\mathcal{L}+\mathcal{M})}{\Gamma(\mathcal{L})\Gamma(\mathcal{M})}\frac{\mathcal{L}}{\mathcal{M}m}\frac{\left(\frac{\mathcal{L}\alpha\tau}{\mathcal{M}m}\right)^{\mathcal{L}-1}}{\left(1+\frac{\mathcal{L}\alpha\tau}{\mathcal{M}m}\right)^{\mathcal{L}+\mathcal{M}}} \\ &\quad\times \frac{\Gamma(\mathcal{L}+\mathcal{M})}{\Gamma(\mathcal{L})\Gamma(\mathcal{M})}\frac{\mathcal{L}}{\mathcal{M}m}\frac{\left(\frac{\mathcal{L}\tau}{\mathcal{M}m}\right)^{\mathcal{L}-1}}{\left(1+\frac{\mathcal{L}\tau}{\mathcal{M}m}\right)^{\mathcal{L}+\mathcal{M}}}\tau\, d\tau \\ &= \left[\frac{\Gamma(\mathcal{L}+\mathcal{M})}{\Gamma(\mathcal{L})\Gamma(\mathcal{M})}\frac{\mathcal{L}}{\mathcal{M}m}\left(\frac{\mathcal{L}\alpha}{\mathcal{M}m}\right)^{\mathcal{L}-1}\right]^2 \\ &\quad\times \alpha^{1-\mathcal{L}}\, I(\alpha,m,\mathcal{L},\mathcal{M}). \end{aligned} \tag{21}$$

Next, by using the substitution $u = (\mathcal{L}/\mathcal{M}m)\tau$ in (21), it yields

$$\begin{aligned} I(\alpha,m,\mathcal{L},\mathcal{M}) &= \left(\frac{\mathcal{M}m}{\mathcal{L}}\right)^{2\mathcal{L}} \alpha^{-(\mathcal{L}+\mathcal{M})} \\ &\quad\times \int_0^\infty u^{2\mathcal{L}-1}\left(\frac{1}{\alpha}+u\right)^{-(\mathcal{L}+\mathcal{M})}(1+u)^{-(\mathcal{L}+\mathcal{M})}du. \end{aligned} \tag{22}$$

It has been shown the following relation which links an integral to the Gauss hypergeometric function [32]

$$\begin{aligned} {}_2F_1(a,b;c;z) &= \frac{\Gamma(c)}{\Gamma(b)\Gamma(c-b)} \\ &\quad\times \int_0^\infty t^{-b+c-1}(t+1)^{a-c}(t-z+1)^{-a}dt \end{aligned} \tag{23}$$

with $\Re\mathrm{e}(c) > \Re\mathrm{e}(b) > 0$ and $|\arg(1-z)| < \pi$.

Let $a = \mathcal{L}+\mathcal{M}$, $b = 2\mathcal{M}$, $c = 2a = 2(\mathcal{L}+\mathcal{M})$, $z = 1-(1/\alpha) = (\alpha-1/\alpha)$. By identification between (22) and

(23), one can express I with the Gauss hypergeometric function by

$$I(\alpha,m,\mathcal{L},\mathcal{M}) = \left(\frac{\mathcal{M}m}{\mathcal{L}}\right)^{2\mathcal{L}} \frac{1}{\alpha^{(\mathcal{L}+\mathcal{M})}} \frac{\Gamma(2\mathcal{M})\Gamma(2\mathcal{L})}{\Gamma(2\mathcal{L}+2\mathcal{M})} \times {}_2F_1\left(\mathcal{L}+\mathcal{M}, 2\mathcal{M}; 2(\mathcal{L}+\mathcal{M}); \frac{\alpha-1}{\alpha}\right). \quad (24)$$

By combining (21) and (24), one can obtain the analytical pdf of α by

$$p_\alpha(\alpha) = \left[\frac{\Gamma(\mathcal{L}+\mathcal{M})}{\Gamma(\mathcal{L})\Gamma(\mathcal{M})}\right]^2 \frac{\Gamma(2\mathcal{M})\Gamma(2\mathcal{L})}{\Gamma(2\mathcal{L}+2\mathcal{M})} \frac{1}{\alpha^{\mathcal{M}+1}} \times {}_2F_1\left(\mathcal{L}+\mathcal{M}, 2\mathcal{M}; 2(\mathcal{L}+\mathcal{M}); \frac{\alpha-1}{\alpha}\right). \quad (25)$$

One can rewrite (25) with the Euler Beta function it yields to (10).

Appendix B

If τ_x and τ_y are two correlated random variables, the pdf of the texture ratio α is given by [30, Eq. 6.60]:

$$p_\alpha(\alpha) = \int_0^\infty \tau\, p_{\tau_x\tau_y}(\alpha\tau, \tau)\, d\tau. \quad (26)$$

For correlated Fisher distributed texture, the bivariate Fisher pdf (14) should be used to derive the pdf of α. By replacing its expression in (26), it leads

$$\begin{aligned} p_\alpha(\alpha) = & \frac{\left(\frac{\mathcal{L}_1}{\mathcal{M}_1 m_1}\right)^{\mathcal{L}_1}\left(\frac{\mathcal{L}_2}{\mathcal{M}_2 m_2}\right)^{\mathcal{L}_2}}{B(\mathcal{L}_1,\mathcal{M}_1)\,B(\mathcal{L}_2,\mathcal{L}_1+\mathcal{M}_2)} \\ & \times \int_0^\infty \tau(\alpha\tau)^{\mathcal{L}_1-1}(\tau)^{\mathcal{L}_2-1} \\ & \times \left(1+\frac{\mathcal{L}_1}{\mathcal{M}_1 m_1}\alpha\tau + \frac{\mathcal{L}_2}{\mathcal{M}_2 m_2}\tau\right)^{-(\mathcal{L}_1+\mathcal{L}_2+\mathcal{M}_2)} \\ & \times {}_2F_1(\mathcal{L}_1+\mathcal{L}_2+\mathcal{M}_2, \mathcal{M}_2-\mathcal{M}_1; \\ & \qquad \mathcal{L}_1+\mathcal{M}_2; w) d\tau \end{aligned} \quad (27)$$

with
$w = (\mathcal{L}_1/\mathcal{M}_1 m_1)\alpha\tau/1 + (\mathcal{L}_1\mathcal{M}_1 m_1)\alpha\tau + (\mathcal{L}_2/\mathcal{M}_2 m_2)\tau$.

By replacing in (27) the Gauss hypergeometric function by its expression defined with the Pochhammer symbols ($(a)_n = \Gamma(a+n)/\Gamma(a)$) by

$$\begin{aligned} {}_2F_1(\alpha,\beta;\gamma;t) &= \sum_{n=0}^\infty \frac{\Gamma(n+\alpha)}{\Gamma(\alpha)} \frac{\Gamma(n+\beta)}{\Gamma(\beta)} \frac{\Gamma(\gamma)}{\Gamma(n+\gamma)} \frac{t^n}{n!} \\ &= \sum_{n=0}^\infty \frac{(\alpha)_n(\beta)_n}{(\gamma)_n} \frac{t^n}{n!} \end{aligned} \quad (28)$$

and if we swap the sum and the integral, it yields

$$\begin{aligned} p_\alpha(\alpha) = & \frac{\left(\frac{\mathcal{L}_1}{\mathcal{M}_1 m_1}\right)^{\mathcal{L}_1}\left(\frac{\mathcal{L}_2}{\mathcal{M}_2 m_2}\right)^{\mathcal{L}_2}\alpha^{\mathcal{L}_1-1}}{B(\mathcal{L}_1,\mathcal{M}_1)\,B(\mathcal{L}_2,\mathcal{L}_1+\mathcal{M}_2)} \\ & \times \sum_{k=0}^\infty \frac{\Gamma(\mathcal{L}_1+\mathcal{L}_2+\mathcal{M}_2+k)}{\Gamma(\mathcal{L}_1+\mathcal{L}_2+\mathcal{M}_2)} \frac{\Gamma(\mathcal{M}_2-\mathcal{M}_1+k)}{\Gamma(\mathcal{M}_2-\mathcal{M}_1)} \\ & \times \frac{\Gamma(\mathcal{L}_1+\mathcal{M}_2)}{\Gamma(\mathcal{L}_1+\mathcal{M}_2+k)} \frac{1}{k!}\, J(k). \end{aligned} \quad (29)$$

where $J(k) =$

$$\begin{aligned} & \left(\frac{\mathcal{L}_1\alpha}{\mathcal{M}_1 m_1}\right)^k \int_0^\infty \frac{(\tau)^{\mathcal{L}_1+\mathcal{L}_2+k-1}}{\left(1+\left(\frac{\mathcal{L}_1}{\mathcal{M}_1 m_1}\alpha+\frac{\mathcal{L}_2}{\mathcal{M}_2 m_2}\right)\tau\right)^{\mathcal{L}_1+\mathcal{L}_2+k+\mathcal{M}_2}} d\tau \\ & \qquad = \left(\frac{\mathcal{L}_1\alpha}{\mathcal{M}_1 m_1}\right)^k K(k). \end{aligned} \quad (30)$$

The integral $K(k)$ looks like an integral of a Fisher pdf defined by parameters $m = \mathcal{L}\mathcal{M}((\mathcal{L}_1\mathcal{M}_1 m_1)\alpha + (\mathcal{L}_2\mathcal{M}_2 m_2))$, $\mathcal{L} = \mathcal{L}_1+\mathcal{L}_2+k$ and $\mathcal{M} = \mathcal{M}_2$, it yields

$$\begin{aligned} K(k) &= \int_0^\infty \frac{(\tau)^{\mathcal{L}-1}}{\left(1+\frac{\mathcal{L}\tau}{\mathcal{M}m}\right)^{\mathcal{L}+\mathcal{M}}} d\tau = \frac{\Gamma(\mathcal{L})\Gamma(\mathcal{M})}{\Gamma(\mathcal{L}+\mathcal{M})}\left(\frac{\mathcal{M}m}{\mathcal{L}}\right)^{\mathcal{L}} \\ &= \frac{\Gamma(\mathcal{L}_1+\mathcal{L}_2+k)\Gamma(\mathcal{M}_2)}{\Gamma(\mathcal{L}_1+\mathcal{L}_2+k+\mathcal{M}_2)} \\ &\quad \times \frac{1}{\left(\frac{\mathcal{L}_1}{\mathcal{M}_1 m_1}\alpha+\frac{\mathcal{L}_2}{\mathcal{M}_2 m_2}\right)^{\mathcal{L}_1+\mathcal{L}_2+k}}. \end{aligned} \quad (31)$$

By combining (29), (30), and (31), one can prove that

$$\begin{aligned} p_\alpha(\alpha) = & \frac{R_1^{\mathcal{L}_1}\, R_2^{\mathcal{L}_2}\alpha^{\mathcal{L}_1-1}}{B(\mathcal{L}_1,\mathcal{M}_1)\,B(\mathcal{L}_2,\mathcal{L}_1+\mathcal{M}_2)} \\ & \times \frac{\Gamma(\mathcal{L}_1+\mathcal{L}_2)\Gamma(\mathcal{M}_2)}{\Gamma(\mathcal{L}_1+\mathcal{L}_2+\mathcal{M}_2)(R_1\alpha+R_2)^{\mathcal{L}_1+\mathcal{L}_2}} \\ & \times \sum_{k=0}^\infty \frac{(\mathcal{M}_2-\mathcal{M}_1)_k(\mathcal{L}_1+\mathcal{L}_2)_k}{(\mathcal{L}_1+\mathcal{M}_2)_k} \\ & \times \left[\frac{\left(\frac{\mathcal{L}_1\alpha}{\mathcal{M}_1 m_1}\right)}{(R_1\alpha+R_2)}\right]^k \frac{1}{k!} \\ = & \frac{R_1^{\mathcal{L}_1}\, R_2^{\mathcal{L}_2}\alpha^{\mathcal{L}_1-1}}{B(\mathcal{L}_1,\mathcal{M}_1)\,B(\mathcal{L}_2,\mathcal{L}_1+\mathcal{M}_2)} \frac{B(\mathcal{L}_1+\mathcal{L}_2,\mathcal{M}_2)}{(R_1\alpha+R_2)^{\mathcal{L}_1+\mathcal{L}_2}} \\ & \times {}_2F_1\left(\mathcal{L}_1+\mathcal{L}_2, \mathcal{M}_2-\mathcal{M}_1; \right. \\ & \qquad \left. \mathcal{L}_1+\mathcal{M}_2; \frac{\left(\frac{\mathcal{L}_1\alpha}{\mathcal{M}_1 m_1}\right)}{(R_1\alpha+R_2)}\right) \end{aligned} \quad (32)$$

with $R_1 = (\mathcal{L}_1/\mathcal{M}_1 m_1)$ and $R_2 = (\mathcal{L}_2/\mathcal{M}_2 m_2)$. It yields to the pdf of the ratio of two correlated Fisher distributed texture shown in (15).

REFERENCES

[1] E. Berthier, H. Vadon, D. Baratoux, Y. Arnaud, C. Vincent, K. L. Feigl, F. Rémy, and B. Legrésy, "Mountain glacier surface motion derived from satellite optical imagery," *Remote Sens. Environ.*, vol. 95, no. 1, pp. 14–28, 2005.

[2] D. Massonnet and T. Rabaute, "Radar interferometry, limits and potential," *IEEE Trans. Geosci. Remote Sens.*, vol. 31, no. 2, pp. 455–464, Mar. 1993.

[3] D. Massonnet and K. Feigl, "RADAR interferometry and its application to changes in the Earth's surface," *Rev. Geophys.*, vol. 36, no. 4, pp. 441–500, 1998.

[4] K. E. Mattar, P. W. Vachon, D. Geudtner, A. L. Gray, I. G. Cumming, and M. Brugman, "Validation of alpine glacier velocity measurements using ERS tandem-mission SAR data," *IEEE Trans. Geosci. Remote Sens.*, vol. 36, no. 3, pp. 974–984, May 1998.

[5] B. T. Rabus and D. R. Fatland, "Comparison of SAR-interferometric and surveyed velocities on a mountain glacier: Black rapids glacier," *J. Glaciol.*, vol. 152, no. 46, pp. 119–128, 2000.

[6] N. Reeh, J. J. Mohr, S. N. Madsen, H. Oerter, and N. S. Gunderstrup, "Three-Dimensional surface velocities of Storstømmen Glacier, Greenland, derived from radar interferometry and ice-sounding radar measurements," *J. Glaciol.*, vol. 49, no. 165, pp. 201–209, 2009.

[7] E. Trouvé, G. Vasile, M. Gay, L. Bombrun, P. Grussenmeyer, T. Landes, J. M. Nicolas, Ph. Bolon, I. Petillot, A. Julea, L. Valet, J. Chanussot, and M. Koehl, "Combining airborne photographs and spaceborne SAR data to monitor temperate glaciers. potentials and limits," *IEEE Trans. Geosci. Remote Sens.*, vol. 45, no. 4, pp. 905–924, Apr. 2007.

[8] R. Fallourd, O. Harant, E. Trouvé, J.-M. Nicolas, F. Tupin, M. Gay, G. Vasile, L. Bombrun, A. Walpersdorf, J. Serafini, N. Cotte, L. Moreau, and P. Bolon, "Monitoring temperate glacier: Combined use of multidate terra SAR-X images and continuous GPS measurements," in *Proc. MultiTemp'09*, Groton, CT, 2009.

[9] I. R. Joughin, R. Kwok, and M. A. Fahnestock, "Interferometric estimation of three-dimensional ice-flow using ascending and descending passes," *IEEE Trans. Geosci. Remote Sens.*, vol. 36, no. 1, pp. 25–37, Jan. 1998.

[10] A. L. Gray, N. Short, K. E. Matter, and K. C. Jezek, "Velocities and ice flux of the filchner ice shelf and its tributaries determined from speckle tracking interferometry," *Can. J. Remote Sens.*, vol. 27, no. 3, pp. 193–206, 2001.

[11] N. H. Short and A. L. Gray, "Potential for RADARSAT-2 interfermerometry: Glacier monitoring using speckle tracking," *Can. J. Remote Sens.*, vol. 30, no. 3, pp. 504–509, 2004.

[12] F. Serafino, "SAR image coregistration based on isolated point scatterers," *IEEE Geosci. Remote Sens. Lett.*, vol. 3, no. 3, pp. 354–358, Jul. 2006.

[13] R. Michel, J. P. Avouac, and J. Taboury, "Measuring ground displacements from SAR amplitude images: Application to the landers earthquake," *Geophys. Res. Lett.*, vol. 26, no. 7, pp. 875–878, 1999.

[14] T. Strozzi, A. Luckman, T. Murray, U. Wegmuller, and C. L. Werner, "Glacier motion estimation using SAR offset-tracking procedures," *IEEE Trans. Geosci. Remote Sens.*, vol. 40, no. 11, pp. 2384–2391, Nov. 2002.

[15] E. Erten, A. Reigber, O. Hellwich, and P. Prats, "Glacier velocity monitoring by maximum likelihood texture tracking," *IEEE Trans. Geosci. Remote Sens.*, vol. 47, no. 2, pp. 394–405, Feb. 2009.

[16] G. Vasile, J.-P. Ovarlez, F. Pascal, and C. Tison, "Coherency matrix estimation of heterogeneous clutter in high resolution polarimetric SAR images," *IEEE Trans. Geosci. Remote Sens.*, vol. 48, no. 4, pp. 1809–1826, Apr. 2010.

[17] L. Bombrun, G. Vasile, M. Gay, and F. Totir, "Hierarchical segmentation of polarimetric SAR images using heterogeneous clutter models," *IEEE Trans. Geosci. Remote Sens.*, vol. 49, no. 2, pp. 726–737, Feb. 2011.

[18] K. T. Fang, S. Kotz, and K. W. Ng, *Symmetric Multivariate and Related Distributions*. London, U.K.: Chapman & Hall, 1990.

[19] S. Zozor and C. Vignat, "Some results on the denoising problem in the elliptically distributed context," *IEEE Trans. Signal Process.*, vol. 58, no. 1, pp. 134–150, Jan. 2010.

[20] F. Pascal, Y. Chitour, J. P. Ovarlez, P. Forster, and P. Larzabal, "Covariance structure maximum-likelihood estimates in compound gaussian noise: Existence and algorithm analysis," *IEEE Trans. Signal Process.*, vol. 56, no. 1, pp. 34–48, Jan. 2008.

[21] F. Pascal, P. Forster, J. P. Ovarlez, and P. Larzabal, "Performance analysis of covariance matrix estimates in impulsive noise," *IEEE Trans. Signal Process.*, vol. 56, no. 6, pp. 2206–2216, Jun. 2008.

[22] J. S. Lee, D. L. Schuler, R. H. Lang, and K. J. Ranson, "K-distribution for multi-look processed polarimetric SAR imagery," in *Proc. Geosci. Remote Sens., IGARSS'94*, Pasadena, CA, 1994, pp. 2179–2181.

[23] C. C. Freitas, A. C. Frery, and A. H. Correia, "The polarimetric G distribution for SAR data analysis," *Environmetrics*, vol. 16, pp. 13–31, 2005.

[24] L. Bombrun and J.-M. Beaulieu, "Fisher distribution for texture modeling of polarimetric SAR data," *IEEE Geosci. Remote Sens. Lett.*, vol. 5, no. 3, pp. 512–516, Jul. 2008.

[25] C. Tison, J.-M. Nicolas, F. Tupin, and H. Maître, "A new statistical model for markovian classification of urban areas in high-resolution SAR images," *IEEE Trans. Geosci. Remote Sens.*, vol. 42, no. 10, pp. 2046–2057, Oct. 2004.

[26] J.-M. Nicolas, "Introduction aux Statistiques de Deuxième Espèce: Applications des Logs-moments et des Logs-cumulants á l'Analyse des lois d'Images Radar," *Traitement du Signal*, vol. 19, no. 3, pp. 139–167, 2002.

[27] J.-M. Nicolas, Application de la Transformée de Mellin: étude des Lois Statistiques de l' Imagerie Cohérente Rapport de recherche, 2006D010, 2006.

[28] M. G. Strintzis and I. Kokkinidis, "Maximum likelihood motion estimation in ultrasound image sequences," *IEEE Signal Process. Lett.*, vol. 4, no. 6, pp. 156–157, Jun. 1997.

[29] R. Bamler, "Interferometric stereo radargrammetry: Absolute height determination from ERS-ENVISAT interferograms," in *Proc. Geosci. Remote Sens., IGARSS'00*, 2000, vol. 2, pp. 742–745.

[30] A. Papoulis, *Probability, Random Variables, and Stochastic Processes*, 4th ed. New York: McGraw-Hill, 2002.

[31] A. H. El-Bassiouny and M. Jones, "A bivariate F distribution with marginals on arbitrary numerator and denominator degrees of freedom, and related bivariate beta and t distributions," *Statist. Methods Applicat.* , pp. 465–481, 2008.

[32] M. Abramowitz and I. A. Stegun, *Handbook of Mathematical Functions With Formulas, Graphs, and Mathematical Tables*. New York: Dover, 1964.

[33] Y. Delignon, "Etude statistique d'images radar de la surface de la mer," These de Doctorat, Univ. de Rennes I, Paris, France, 1993.

Olivier Harant was born in 1982. He received the Engineer degree in electrical engineering from the Ecole Suprieure de Chimie Physique et Electronique, Lyon, France, in 2008. He is currently working toward the Ph.D. degree in the SAR Polarimetry, Holography, Interferometry, and Radargrammetry (SAPHIR) Team, Institut of Electronic and Telecommunication, Rennes, in collaboration with the Grenoble Image sPeech and Automatic laboratory (GIPSA-Lab).

His research interests include information modeling in polarimetric SAR images and glaciers monitoring.

Lionel Bombrun (S'06–M'09) was born in Tournon, France, in 1982. He received the M.S. and Ph.D. degrees in signal, image, speech, and telecommunications from the Grenoble National Polytechnic Institute (INPG), Grenoble, France, in 2005 and 2008, respectively.

In 2008, he was a Teaching Assistant at Phelma, Grenoble. From 2009 to 2010, he was a Postdoctoral Fellow from the French National Council for Scientific Research (CNRS) between the Grenoble Image Speech Signal Automatics Laboratory and SONDRA, Gif-sur-Yvette, France. Since October 2010, he has been a Postdoctoral Fellow at the IMS Laboratory. His research interests include signal and image processing, texture analysis, synthetic aperture radar remote sensing, polarimetry, and interferometry.

Gabriel Vasile (S'06–M'07) received the M.Eng. degree in electrical engineering and computer science and the M.S. degree in image, shapes, and artificial intelligence from the POLITEHNICA University, Bucharest, Romania, in 2003 and 2004, respectively, and the Ph.D. degree in signal and image processing from Savoie University, Annecy, France, in 2007.

From 2007 to 2008, he was a Postdoctoral Fellow with the French Space Agency (CNES) and was with the French Aerospace Laboratory (ONERA), Palaiseau, France. In 2008, he joined the French National Council for Scientific Research (CNRS), where he is currently a Research Scientist and a member of the Grenoble Image Speech Signal Automatics Laboratory, Grenoble, France. His research interests include signal and image processing, synthetic aperture radar remote sensing, polarimetry, and interferometry.

Laurent Ferro-Famil (M'00) received the laurea degree in electronics systems and computer engineering, the M.S. degree in electronics, and the Ph.D. degree, all from the University of Nantes, Nantes, France, in 1996, 1996, and 2000, respectively.

Since 2001, he has been an Assistant Professor at the University of Rennes I, Rennes, France. He is a member of the Radar Polarimetry Remote Sensing Group, Institute of Electronics and Telecommunications of Rennes (IETR). His current activities in education concern analog electronics, digital communications microwave theory, and polarimetric radar imaging. He is especially interested in SAR signal processing, radar polarimetry theory, and natural media remote sensing from polarimetric interferometric SAR data, with application to segmentation, classification, electromagnetic scattering modeling, physical parameter inversion, and time–frequency analysis.

Michel Gay (M'10) received the Engineer degree in electrical engineering from the Institut des Sciences de l'Ingéieur de Montpellier, Montpellier, France, in 1987 and the Ph.D. degree in physics from the University Joseph Fourier, Grenoble, France, in 1999.

From 1979 to 1985, he worked with the Botanic Institute and with the local education authority of Montpellier. From 1988 to 2003, he was with Cemagref Grenoble, where he worked on electrical engineering for environmental applications. Since 2004, he has been a Research Engineer with the Grenoble Image Speech Signal Automatic Laboratory, Institut National Polytechnique de Grenoble, Centre National de la Recherche Scientifique, Saint-Martin-d'Hères, France. His current research interests include remote sensing, synthetic aperture radar (SAR) image processing, and survey of Alpine glaciers. He has been Co-Manager of four National Scientific projects and of three international projects and Leader Project of one international project.

Dr. Gay is a member of the IEEE Geoscience Remote Sensing Society.

X. V. Phan, L. Ferro-Famil, M. Gay, Y. Durand, M. Dumont, S. Morin, S. Allain, G. D ?Urso, and A. Girard. "1D-Var multilayer assimilation of X-band SAR data into a detailed snowpack model", *The Crypsohere* , *Vol.* 5, *N*° 8, 2014.

The Cryosphere, 8, 1975–1987, 2014
www.the-cryosphere.net/8/1975/2014/
doi:10.5194/tc-8-1975-2014
© Author(s) 2014. CC Attribution 3.0 License.

The Cryosphere
Open Access

1D-Var multilayer assimilation of X-band SAR data into a detailed snowpack model

X. V. Phan[1], L. Ferro-Famil[2], M. Gay[1], Y. Durand[3], M. Dumont[3], S. Morin[3], S. Allain[2], G. D'Urso[4], and A. Girard[4]

[1]Grenoble Image Parole Signal et Automatique lab, Grenoble, France
[2]Institut d'Electronique et de Télécommunications de Rennes, University of Rennes, Rennes, France
[3]Météo-France – CNRS, CNRM-GAME – UMR3589, Centre d'Etudes de la Neige, Grenoble, France
[4]Electricité de France, Paris, France

Correspondence to: X. V. Phan (xuan-vu.phan@gipsa-lab.grenoble-inp.fr)

Received: 27 August 2013 – Published in The Cryosphere Discuss.: 2 October 2013
Revised: 3 June 2014 – Accepted: 18 September 2014 – Published: 27 October 2014

Abstract. The structure and physical properties of a snowpack and their temporal evolution may be simulated using meteorological data and a snow metamorphism model. Such an approach may meet limitations related to potential divergences and accumulated errors, to a limited spatial resolution, to wind or topography-induced local modulations of the physical properties of a snow cover, etc. Exogenous data are then required in order to constrain the simulator and improve its performance over time. Synthetic-aperture radars (SARs) and, in particular, recent sensors provide reflectivity maps of snow-covered environments with high temporal and spatial resolutions. The radiometric properties of a snowpack measured at sufficiently high carrier frequencies are known to be tightly related to some of its main physical parameters, like its depth, snow grain size and density. SAR acquisitions may then be used, together with an electromagnetic backscattering model (EBM) able to simulate the reflectivity of a snowpack from a set of physical descriptors, in order to constrain a physical snowpack model. In this study, we introduce a variational data assimilation scheme coupling TerraSAR-X radiometric data into the snowpack evolution model Crocus. The physical properties of a snowpack, such as snow density and optical diameter of each layer, are simulated by Crocus, fed by the local reanalysis of meteorological data (SAFRAN) at a French Alpine location. These snowpack properties are used as inputs of an EBM based on dense media radiative transfer (DMRT) theory, which simulates the total backscattering coefficient of a dry snow medium at X and higher frequency bands. After evaluating the sensitivity of the EBM to snowpack parameters, a 1D-Var data assimilation scheme is implemented in order to minimize the discrepancies between EBM simulations and observations obtained from TerraSAR-X acquisitions by modifying the physical parameters of the Crocus-simulated snowpack. The algorithm then re-initializes Crocus with the modified snowpack physical parameters, allowing it to continue the simulation of snowpack evolution, with adjustments based on remote sensing information. This method is evaluated using multi-temporal TerraSAR-X images acquired over the specific site of the Argentière glacier (Mont-Blanc massif, French Alps) to constrain the evolution of Crocus. Results indicate that X-band SAR data can be taken into account to modify the evolution of snowpack simulated by Crocus.

1 Introduction

Accurate knowledge of snowpack internal structure is critical for better understanding the snowpack evolution over time, and is essential for snow forecasting, water resource monitoring and prediction of natural hazards, such as avalanches. For this purpose, snow metamorphism models, such as Crocus (Brun et al., 1992; Vionnet et al., 2012), are developed in order to simulate the evolution of snowpack based on meteorological variables. These models are currently limited due to the lack of in situ snow stratigraphic measurements. For example, in the French Alps, the network of snow and meteorological observations contains about 150–180 stations, which is not enough to adjust a snow model to predict the state and the spatial variability of snowpack at small scale

(20 m). This limitation results in potential divergences, accumulated errors and limited spatial resolution of the model. Therefore, exogenous data are crucial in order to constrain the simulator and improve its performance over time.

On the other hand, the radiometric properties of a snowpack measured at high frequencies depend strongly on its main physical parameters, like its depth, snow grain size and density. The electromagnetic backscattering model (EBM), initially developed by Longepe et al. (2009) based on dense media radiative transfer (DMRT) theory, allows for simulation of the backscattering coefficient σ^0 of dry snow from C band (5 GHz) to Ku band (14 GHz). The air–snow, σ_{as}, and snow–ground, σ_{sg} (or snow–ice, σ_{si}), interfaces backscattering components are calculated using the integral equation model (IEM) developed by Fung and Chen (2004). The snow permittivity is calculated using the strong fluctuation theory (SFT) (Stogryn, 1984). The SFT has been tested and verified in the literature (Wang et al., 2000; Tsang et al., 2007). It is also used in the DMRT model of multilayer snowpack developed by Longepe et al. (2009). This model is capable of simulating the interaction of electromagnetic waves with a layer of snow based on the physical parameters (thickness, optical diameter, snow density). The advantage of this model is the simple implementation and its moderate computation time, which is crucial in order to run the data assimilation process, where the electromagnetic model is repeatedly executed multiple times. With this model, we can calculate the total backscattering coefficient σ^0_{pq} for different polarization channels ($p, q =$ H or V) from the physical features of each snow layer, the roughness of air–snow and snow–ice interfaces, and specific radar illumination (frequency, incidence angle).

The new generation of synthetic-aperture radar (SAR) satellite data provides images with metric resolution and short revisit time. The TerraSAR-X satellite, with 1.477 m × 2.44 m resolution and revisit time of 11 days, gives dense information both spatially and temporally on snowpack evolution. In this study, we propose a new process which uses these multi-temporal images of TerraSAR-X to constrain the Crocus model through data assimilation.

Data assimilation has been widely used in meteorological studies (Courtier et al., 1998; Uppala et al., 2005) and land surface modeling (Slater and Clark, 2006; De Lannoy et al., 2010; Toure et al., 2011). Data assimilation using physically based multilayer models has been initiated in recent studies, using passive microwave radiance (Toure et al., 2011) or albedo observations (Dumont et al., 2012). The advantages of the assimilation using SAR images are the quasi-independence with respect to atmospheric conditions, the high resolution of analysis, and the sensitivity of SAR responses to the presence and structure of volumetric mediums. The use of data assimilation on SAR data and meteorological models to predict certain physical properties of snowpack has been developed in the literature (Nagler et al., 2008; Takala et al., 2011). This study attempts to implement

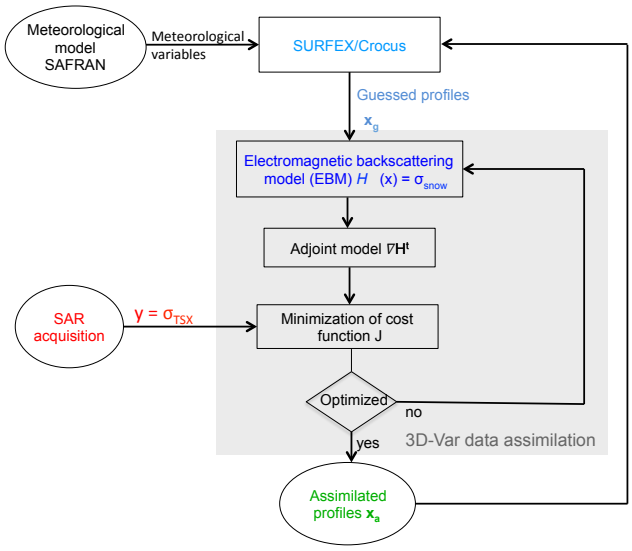

Figure 1. Global schematic of the data analysis used in this study. The inputs of the process are the SAR reflectivities, σ^0 (observation) and the snowpack stratigraphic profile calculated by Crocus (guess). The output is the analyzed snowpack profile $\boldsymbol{x}$ that minimizes the cost function.

a data assimilation system which is capable of constraining a detailed snow metamorphism model at a layer scale (modification of the physical properties of each layer) using X-band SAR data. The assimilation techniques have proven effective in combining observations and a priori information to more realistically simulate snowpack conditions (i.e., an a posteriori state). The a priori information is often referred to as "guess parameters", whereas the a posteriori state is called "the analysis". The guess parameters in this study are the physical properties of each snowpack layer simulated using a snow evolution model. The analysis is obtained by modifying the guess information based on the backscattering coefficient obtained from SAR acquisitions, according to the error statistics of both model and observations. The simulation of snowpack evolution is then continued with the analysis result. The intermittent assimilation algorithm is carried out each time a new SAR acquisition is available; therefore the assimilation is propagated over time, which allows us to constrain the snowpack simulation using remote sensing observations. The adjustment made to the snowpack physical properties is based on error statistics of modeling (Crocus) and observation (SAR).

This study reports, for the first time, on a new process based on the DMRT model and on the one-dimensional variational analysis (1D-Var) to assimilate TerraSAR-X data into the snow model Crocus. A global schematic of this process is presented in Fig. 1. Section 2 introduces the Crocus snowpack evolution model. Section 3 describes the DMRT electromagnetic backscattering model. The 1D-Var data assimilation method is presented in Sect. 4. Section 5 contains

the study of simulations and sensitivity of snowpack at X band. Section 6 presents the first results and discussion of data assimilation method in the particular case of the Argentière glacier, where the ground beneath the snow consists of ice.

2 Snowpack model Crocus

Crocus is a one-dimensional numerical model simulating the thermodynamic balance of energy and mass of a snowpack. Its main objective is to describe in detail the evolution of internal snowpack properties based on the description of the evolution of morphological features of snow grains during their metamorphism. It takes as inputs meteorological variables such as air temperature, relative air humidity, wind speed, solar radiation, long-wave radiation, and amount and phase of precipitation. In this study within the French Alps, these meteorological conditions are taken from the SAFRAN reanalysis, which combines ground-based, radiosondes and remote sensing (cloudiness) observations with an a priori estimate of meteorological conditions from a numerical weather prediction (NWP) model (Durand et al., 1993; Durand, 2009). SAFRAN meteorological fields, assumed to be homogeneous for a given mountain range and elevation in the French Alps region, provide a description of the altitude dependency of meteorological variables. The output of Crocus includes scalar physical properties of the snowpack (snow depth, snow water equivalent (SWE), surface temperature, albedo, etc.) along with the internal physical properties for each layer (density, thickness, optical radius, etc.).

This study uses the latest version of the detailed snowpack model Crocus, recently incorporated into the land surface scheme ISBA within the SURFEX interface (Vionnet et al., 2012). Among other advantages over previous versions of Crocus, this allows seamless coupling of the snowpack to the state of the underlying ground.

3 Electromagnetic backscattering model (EBM)

3.1 Main components of the total backscattering coefficient

The Stokes vector, which contains the incoherent information related to the polarization of an electromagnetic wave (EMW), can be expressed as follows (Ulaby et al., 1981):

$$\mathbf{g} = \begin{bmatrix} \langle |E_\mathrm{h}|^2 \rangle + \langle |E_\mathrm{v}|^2 \rangle \\ \langle |E_\mathrm{h}|^2 \rangle - \langle |E_\mathrm{v}|^2 \rangle \\ 2\mathcal{R}e\langle E_\mathrm{h} E_\mathrm{v}^* \rangle \\ -2\mathcal{I}m\langle E_\mathrm{h} E_\mathrm{v}^* \rangle, \end{bmatrix} \quad (1)$$

where E_h and E_v represent the horizontal and vertical components of the Jones vector on the electric field, and $\langle . \rangle$ represents the expectation operator.

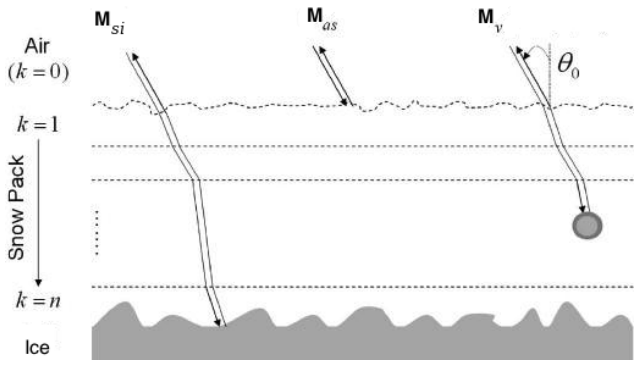

Figure 2. Main backscattering mechanisms occurring within a multilayer snowpack obtained from the radiative transfer equation at first order (Longepe et al., 2009): air–snow reflection ($\mathbf{M}_{as}$), volume scattering ($\mathbf{M}_{v}$) and reflection over the snow–ice interface ($\mathbf{M}_{si}$).

For given acquisition conditions, the Stokes vector of radiation scattered by a medium, $\mathbf{g}_s$, can be related to the incident one, $\mathbf{g}_i$, by a Stokes matrix $\mathbf{M}$ (Lee and Pottier, 2009) as $\mathbf{g}_s = \mathbf{M}\mathbf{g}_i$, with

$$\mathbf{M} = \begin{bmatrix} M_{11} & M_{12} & 0 & 0 \\ M_{21} & M_{22} & 0 & 0 \\ 0 & 0 & M_{33} & M_{34} \\ 0 & 0 & M_{43} & M_{44}, \end{bmatrix} \quad (2)$$

where $M_{11} = |\sigma^0_{\mathrm{vv}}|^2$ and $M_{22} = |\sigma^0_{\mathrm{hh}}|^2$ represent the co-polarized backscattering coefficients; $M_{12} = |\sigma^0_{\mathrm{vh}}|^2$ and $M_{21} = |\sigma^0_{\mathrm{hv}}|^2$ the cross-polarized backscattering terms; and $M_{33} = \mathcal{R}e(\sigma^0_{\mathrm{vv}}\sigma^0_{\mathrm{hh}} + |\sigma^0_{\mathrm{hv}}|^2)$, $M_{44} = \mathcal{R}e(\sigma^0_{\mathrm{vv}}\sigma^0_{\mathrm{hh}} - |\sigma^0_{\mathrm{hv}}|^2)$, $M_{34} = -\mathcal{I}m(\sigma^0_{\mathrm{vv}}\sigma^0_{\mathrm{hh}} - |\sigma^0_{\mathrm{hv}}|^2)$, and $M_{43} = \mathcal{I}m(\sigma^0_{\mathrm{vv}}\sigma^0_{\mathrm{hh}} + |\sigma^0_{\mathrm{hv}}|^2)$ are correlation terms. Due to the reflection symmetry, the other terms of $\mathbf{M}$ are equal to zero (Lee and Pottier, 2009).

The first-order solution of the radiative transfer (RT) equation provides the total backscattered information from a snowpack that consists of a combination of five scattering mechanisms: reflection at the surface air–snow interface, volume scattering, volume–ice and ice–volume interactions, and reflection from the snow–ice interface (Martini et al., 2003). Due to their small amplitude, the volume–ice and ice–volume contributions can be neglected (Floricioiu and Rott, 2001). The illustration of the three other mechanisms is shown in Fig. 2. The expression of the total polarimetric backscattered information can be written using the Mueller matrix corresponding to each mechanism:

$$\mathbf{M}_{\mathrm{snow}} = \mathbf{M}_{\mathrm{as}} + \mathbf{M}_{\mathrm{v}} + \mathbf{M}_{\mathrm{si}}. \quad (3)$$

The air–snow interface ($\mathbf{M}_{\mathrm{as}}$) and snow–ice interface backscattering ($\mathbf{M}_{\mathrm{si}}$) are modeled using the IEM introduced by Fung and Chen (2004), whereas the volume contribution ($\mathbf{M}_{\mathrm{v}}$) is calculated using the vector radiative transfer equation.

3.2 Air–snow interface backscattering

The matrix $\mathbf{M}_{as}$ represents the second-order polarimetric response backscattered by the air–snow interface. Its elements can be calculated from the air–snow interface roughness parameters, i.e., its correlation function $w(x)$ and its root-mean-square (rms) height σ_h, the incidence angle θ_0 and the emitted EM wave frequency f using the IEM (Fung and Chen, 2004). According to the IEM, the reflectivity may be expressed as

$$\sigma^0_{pq} = \frac{k_0^2}{4\pi}\exp\left(-2k_0^2\sigma_h^2\cos^2\theta_0\right) \sum_{n=1}^{\infty}|I^n_{pq}|^2\frac{W^n(2k_0\sin\theta_0,0)}{n!}, \quad (4)$$

where p and q are equal to h or v, indicating a horizontal or vertical polarization, and $k_0 = \frac{2\pi f}{c}$ represents the wave number. The detailed mathematical expressions of the surface spectrum $W(k)$ and the Fresnel reflection/transmission factor $|I^n_{pq}|$ can be found in Fung and Chen (2004).

3.3 Snow volume backscattering

The volume backscattering $\mathbf{M}_v$ depends on various scattering mechanisms occurring during the propagation through a multilayer snowpack, which can be categorized into four types: (1) transmission between two layers, (2) attenuation by the snow particles, (3) scattering and (4) coherent recombination. The amplitude of each mechanism depends largely on the dielectric properties of the snowpack medium. Therefore the permittivity of each layer, which characterizes its dielectric properties, needs to be calculated first.

3.3.1 Dry snow permittivity

Dry snow is considered to be a dense and heterogeneous medium with strongly variable physical properties. Therefore the variance of permittivity across a snow layer is relatively high. The SFT, introduced by Stogryn (1984), can model the permittivity of such a medium by using the effective permittivity (ϵ_{eff}) that takes into account the scattering effects among ice particles at high frequencies. The expression of ϵ_{eff} using the SFT is as follows (Huining et al., 1999):

$$\epsilon_{eff} = \epsilon_g + j\cdot\frac{4}{3}\delta_{\epsilon_g}\cdot k_0^3\cdot\sqrt{\epsilon_g}\cdot L^3, \quad (5)$$

where j is the imaginary unit; ϵ_g and δ_{ϵ_g} are the quasi-static permittivity and its variance; k_0 is the wave number; and $L = 0.85\,D/3$ is the correlation length, with D being the snow optical diameter.

3.3.2 Transmission between two layers

The snowpack consists of layers with different physical properties. Therefore the model needs to take into account the energy loss due to transmission between two layers. With the assumption of a smooth interface between two layers, the Fresnel transmission can be used. It is expressed through a matrix as follows (Ulaby et al., 1981):

$$\mathbf{T}_{k(k-1)} = \frac{\epsilon_{k-1}}{\epsilon k}\begin{bmatrix} \left|t^{vv}_{k(k-1)}\right|^2 & 0 & 0 & 0 \\ 0 & \left|t^{hh}_{k(k-1)}\right|^2 & 0 & 0 \\ 0 & 0 & g_{k(k-1)} & -h_{k(k-1)} \\ 0 & 0 & h_{k(k-1)} & g_{k(k-1)}, \end{bmatrix} \quad (6)$$

where k is the layer number and $k-1$ is the layer above it, $\left|t^{pp}_{k(k-1)}\right|^2$ represents the Fresnel transmission coefficients of the pp channel, and $g_{k(k-1)}$ and $h_{k(k-1)}$ are the terms of Mueller matrix related to the co-polarized correlation (Longepe et al., 2009):

$$g_{k(k-1)} = \frac{\cos\theta_{k-1}}{\cos\theta_k}\mathcal{R}e\left(t^{vv}_{k(k-1)}t^{hh*}_{k(k-1)}\right) \quad (7)$$

$$h_{k(k-1)} = \frac{\cos\theta_{k-1}}{\cos\theta_k}\mathcal{I}m\left(t^{vv}_{k(k-1)}t^{hh*}_{k(k-1)}\right).$$

3.3.3 Attenuation

The particles in a snowpack are generally considered to be spherical (Floricioiu and Rott, 2001; Koskinen et al., 2010). Due to the symmetry of the particle shape, the extinction of a wave propagating through the snowpack is independent of the polarization and may hence be represented by a scalar coefficient. The extinction is composed of an absorption and a scattering term:

$$\kappa_e = \kappa_a + \kappa_s. \quad (8)$$

It can also be computed through the effective permittivity ϵ_{eff} (Huining et al., 1999):

$$\kappa_e = 2k_0\,Im\left(\sqrt{\epsilon_{eff}}\right). \quad (9)$$

The attenuation matrix represents the gradual loss in EMW intensity while penetrating through a multilayer snowpack, composed of layers with different physical properties. It takes into account the energy loss by absorption and scattering mechanisms based on the extinction coefficient κ_e and thickness d of the layer, as well as the loss by transmission effect while an EM propagates through different layers:

$$\mathbf{Att}_{down}(k) = \prod_{i=1}^{k}\exp\left(-\frac{\kappa_e^i d^i}{\cos\theta_i}\right)\mathbf{T}_{i(i-1)}, \quad (10)$$

$$\mathbf{Att}_{up}(k) = \prod_{i=1}^{k}\mathbf{T}_{(i-1)i}\exp\left(-\frac{\kappa_e^i d^i}{\cos\theta_i}\right). \quad (11)$$

$\mathbf{Att}_{down}$ is the intensity loss (attenuation) when propagating from the surface to layer k, whereas $\mathbf{Att}_{up}$ represents the intensity loss from layer k to the surface. The exponential factor, which takes into account the gradual loss of energy throughout the layer, is deduced from the basic radiative transfer equation $dI = I\,\kappa_e\,dr$, where $r = d/\cos\theta$ and I is the EMW intensity.

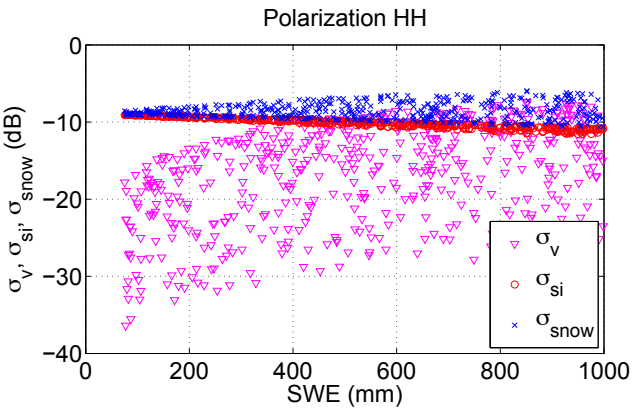

Figure 3. Test of EBM simulations on X-band, HH polarization for varying snow depth and optical diameter: snow density 250 kg m^{-3}, optical diameter 0.2–1 mm, and snow depth 30–400 cm. The glacier roughness is fixed at $\sigma_{si} = 0.9$ cm and $l_{si} = 8.6$ cm.

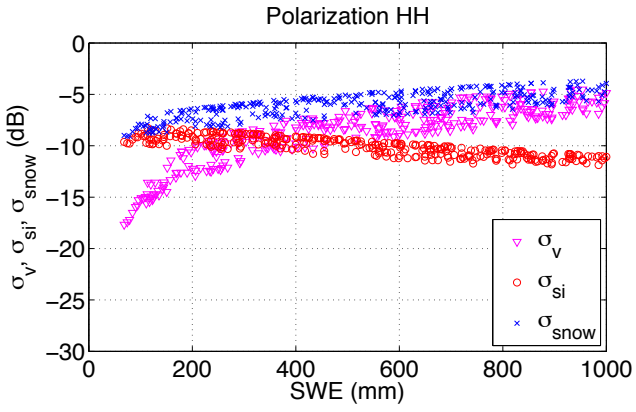

Figure 4. Test of EBM simulations on X-band, HH polarization for varying snow depth and density: snow density 200–600 kg m^{-3}, optical diameter 1 mm, and snow depth 30–400 cm. The glacier roughness is fixed at $\sigma_{si} = 0.9$ cm and $l_{si} = 8.6$ cm.

3.3.4 Scattering by the particles

The phase matrix $\mathbf{P}^k$, under the hypothesis of spherical particles, has the form shown in Eq. (2), where the cross-polarization terms P_{12} and P_{21}, which correspond to σ_{hv} and σ_{vh}, are equal to 0. In the backscattering case, with the assumption of spherical particles, the SFT phase matrix can be simplified to $\mathbf{P}^k = \frac{3\kappa_s}{8\pi}\mathbf{I}_4$, where $\mathbf{I}_4$ is the (4×4) identity matrix (Tsang et al., 2007). The assumption of spherical particles can simplify the modeling problem; however, it prevents the simulations of the backscattering coefficient over cross-polarization channels (HV and VH).

3.3.5 Calculation of the volume backscattering

Considering a snowpack made of n distinct layers, where θ_k is the incidence angle and d^k is the thickness of layer k (Fig. 2), the total contribution of the volume backscattering mechanism $\mathbf{M}_v$ can be written as follows:

$$\mathbf{M}_v = 4\pi \cos\theta_0 \sum_{k=1}^{n} \mathbf{Att}_{up}(k-1)\mathbf{T}_{(k-1)k} \cdot \frac{1 - \exp\left(-\frac{2\kappa_e^k d^k}{\cos\theta_k}\right)}{2\kappa_e^k} \mathbf{P}^k \mathbf{T}_{k(k-1)} \mathbf{Att}_{down}(k-1). \quad (12)$$

3.4 Snow–ice interface backscattering

The backscattering $\mathbf{M}_{si}$ of the snow–ice interface is computed as

$$\mathbf{M}_{si} = \cos\theta_0 \mathbf{Att}_{up}(n) \frac{\mathbf{R}(\theta_n)}{\cos\theta_n} \mathbf{Att}_{down}(n), \quad (13)$$

where $\mathbf{R}(\theta_n)$ represents the contribution of the snow–ice interface backscattering and can be determined using the IEM.

3.5 Sensitivity of the EBM to snowpack parameters

In order to assess the sensitivity of the EBM outputs with respect to the different properties of a snowpack, a set of simulations were run for various snowpack structures. A random data set was generated corresponding to a snow height varying from 30 to 400 cm (SWE from 75 to 1000 mm with snow density set at 250 kg m^{-3}). Measurements of the roughness parameters of air–snow interface and snow–ice interface are not available; therefore, empirical values for the correlation length l and the rms height σ from Oh et al. (1992) have been used. The values of $\sigma_{as} = 0.4$ cm and $l_{as} = 8.4$ cm, equivalent to a slightly rough surface, are used for the air–snow interface; however $\sigma_{si} = 0.9$ cm and $l_{si} = 8.6$ cm, corresponding to a rough surface, are chosen for the snow–ice interface due to the characteristics of ice beneath the snowpack over the study area.

The results of EBM simulations are plotted vs. SWE in Figs. 3 and 4. In Fig. 3, snow density is fixed at 250 kg m^{-3}, while the optical diameter is varied from 0.2 to 1 mm. The backscattering contribution at the air–snow interface, being inferior to −40 dB, is not represented here. As the SWE increases, the volume backscattering coefficient becomes more important until it reaches a value comparable to the snow–ice interface backscattering. The vertical dispersion of the volume backscattering represents the sensitivity of the EBM to optical diameter. Lowest values correspond to an optical diameter of 0.2 mm, whereas the highest ones correspond to an optical diameter of 1 mm.

In Fig. 4, where the optical diameter is fixed at 1 mm and snow density varies from 200 to 600 kg m^{-3}, the vertical dispersion of the volume backscattering represents the sensitivity of the EBM to snow density. By comparing Figs. 3 and 4, we can observe that the EBM is strongly sensitive to the optical diameter and moderately sensitive to the snow density.

Many studies have been carried out on the retrieval of different snowpack properties from SAR data, such as snow water equivalent (Shi and Dozier, 2000), liquid water content (Shi et al., 1993), and wet snow mapping (Nagler and Rott, 2000). In general, these studies concentrate on inverting the EBM, which enables the retrieval of such snowpack properties. For a multilayer snowpack, the number of observations, i.e., the number of SAR backscattering coefficients, is much smaller than the number of unknown variables, i.e., the snow properties of each layer. Classical estimation approaches based on the use of an inverse problem would not be viable. Instead, in our study, an adjoint operator of the direct EBM is developed to be used in a data assimilation scheme.

4 1D-Var data assimilation

4.1 Introduction to data assimilation

The aim of variational assimilation is to integrate observational data with guess variables through the use of an observation operator. The method concentrates on searching for a solution that minimizes simultaneously the distance between observations and simulation results and the distance between initial guess variables and the analyzed variables. A schematic of this process is presented in Fig. 1. The outputs of the EBM described in the previous section, such as backscattering coefficient at HH and VV polarizations, are used as elements of the observation operator $\mathbf{H}_{\mathrm{ebm}}(\boldsymbol{x})$:

$$\mathbf{H}_{\mathrm{ebm}}(\boldsymbol{x}) = \mathrm{vec}\left(\mathbf{M}_{\mathrm{snow}}\right), \tag{14}$$

where $\boldsymbol{x}$ represents the set of variables describing the snowpack properties (here, density and optical diameter for each snow layer).

The 1D-Var algorithm is based on the minimization of a cost function $J(\boldsymbol{x})$, defined as

$$J(\boldsymbol{x}) = \left(\boldsymbol{x} - \boldsymbol{x}_{\mathrm{g}}\right)^t \mathbf{B}^{-1} \left(\boldsymbol{x} - \boldsymbol{x}_{\mathrm{g}}\right) + \left(\boldsymbol{y}_{\mathrm{obs}} - \mathbf{H}_{\mathrm{ebm}}(\boldsymbol{x})\right)^t \mathbf{R}^{-1} \left(\boldsymbol{y}_{\mathrm{obs}} - \mathbf{H}_{\mathrm{ebm}}(\boldsymbol{x})\right), \tag{15}$$

where $\boldsymbol{x}$ is called the state vector, which can be modified after each iteration of the minimization, and $\boldsymbol{x}_{\mathrm{g}}$ is the initial guess of the state vector and remains constant during the whole process. Therefore, $\|\boldsymbol{x} - \boldsymbol{x}_{\mathrm{g}}\|^2$ serves as a distance between the modified profile and the starting point. The observed polarimetric response, $\boldsymbol{y}_{\mathrm{obs}}$, contains calibrated values of the backscattering coefficients σ^0 for different polarimetric channels. Therefore, $\|\boldsymbol{y} - \mathbf{H}_{\mathrm{ebm}}(\boldsymbol{x})\|^2$ represents the distance between simulated and observed radiometric quantities. The process also requires the estimation of the error covariance matrix of observations/simulations ($\mathbf{R}$) and of the guess error covariance matrix ($\mathbf{B}$).

4.2 Adjoint operator and minimization algorithm

In order to minimize the cost function J, one needs to calculate its gradient:

$$\nabla J(\boldsymbol{x}) = 2\mathbf{B}^{-1}\left(\boldsymbol{x} - \boldsymbol{x}_{\mathrm{g}}\right) - 2\nabla \mathbf{H}^t_{\mathrm{ebm}}(\boldsymbol{x}) \mathbf{R}^{-1} \left(\boldsymbol{y}_{\mathrm{obs}} - \mathbf{H}_{\mathrm{ebm}}(\boldsymbol{x})\right). \tag{16}$$

If the model is denoted $\mathbf{H}_{\mathrm{ebm}} : \mathcal{B} \rightarrow \mathcal{R}$, where $\mathcal{B}$ and $\mathcal{R}$ are the domain of definition of $\boldsymbol{x}$ and $\boldsymbol{y}$, then the function $\nabla \mathbf{H}^t_{\mathrm{ebm}}$ satisfying $\forall \boldsymbol{x}, \boldsymbol{y}, \langle \nabla \mathbf{H}^t_{\mathrm{ebm}} \boldsymbol{y}, \boldsymbol{x} \rangle_{\mathcal{B}} = \langle \boldsymbol{y}, \nabla \mathbf{H}_{\mathrm{ebm}} \boldsymbol{x} \rangle_{\mathcal{R}}$ is the adjoint operator of $\mathbf{H}_{\mathrm{ebm}}$. In our case, due to the complexity of the EBM, an analytical solution of the gradient is time consuming and unreliable. Therefore, numerical differentiation has been used to calculate the adjoint model.

Once the adjoint operator is developed, the minimization of J can be achieved using a gradient descent algorithm. Each iteration consists of modifying the vector $\boldsymbol{x}$ according to the Newton method until J is converged to its minimum:

$$\boldsymbol{x}_{n+1} = \boldsymbol{x}_n - \left(\nabla^2 J\left(\boldsymbol{x}_n\right)\right)^{-1} \nabla J\left(\boldsymbol{x}_n\right), \tag{17}$$

where $\nabla^2 J(\boldsymbol{x}_n)$ is the gradient of second order (Hessian) of J:

$$\nabla^2 J = 2\mathbf{B}^{-1} + 2\nabla \mathbf{H}^t_{\mathrm{ebm}} \mathbf{R}^{-1} \nabla \mathbf{H}_{\mathrm{ebm}}. \tag{18}$$

4.3 Estimation of error covariance matrices

With preset air–snow interface and snow–ice interface parameters, the original model input vector $\boldsymbol{x} = [\boldsymbol{x}_{\mathrm{Crocus}}\ \boldsymbol{x}_{\mathrm{air–snow}}\ \boldsymbol{x}_{\mathrm{snow–ice}}]^t$ may be reduced to the Crocus variables consisting in density and optical diameter for each snow layer:

$$\boldsymbol{x} = [\boldsymbol{x}_{\mathrm{Crocus}}] = [D_1, D_2, \ldots, D_n, \rho_1, \rho_2, \ldots, \rho_n]^t, \tag{19}$$

where D_i and ρ_i are respectively the optical diameter and the density of the ith layer of the snowpack. This means that the analysis process does not modify directly the thickness of each layer; however this parameter can be changed indirectly in the subsequent simulations by Crocus. At the first iteration of the algorithm, $\boldsymbol{x}$ is equal to $\boldsymbol{x}_{\mathrm{g}}$, given by the Crocus snow profile.

The covariance matrix $\mathbf{B}$, which represents the error of the guess profile, i.e., of the Crocus simulation, is a $(2n \times 2n)$ definite positive matrix. Each element of $\mathbf{B}$ is computed as

$$\mathbf{B}_{i,j} = \sigma_i \cdot \sigma_j \cdot \gamma_{ij}, \tag{20}$$

where σ_i and σ_j represent the standard deviation of the errors on x_i and x_j, which have been experimentally estimated to 0.3 mm and 65 kg m^{-3}, respectively, for optical diameter and snow density.

The coefficient γ_{ij} represents the correlation between errors on x_i and x_j and is modeled as

$$\gamma_{ij} = \beta e^{-\alpha \Delta h_{ij}}, \tag{21}$$

where Δh_{ij} is the distance in centimeters between layer i and layer j. The values of α and β depend on different types of correlations and can be split into three cases:

- correlation $D - D$: $\alpha = 0.11$ and $\beta = 1$;
- correlation $\rho - \rho$: $\alpha = 0.13$ and $\beta = 1$;
- correlation $D - \rho$: $\alpha = 0.15$ and $\beta = 0.66$.

These values are issued from an ensemble of slightly perturbed Crocus runs, obtained by varying their meteorological inputs over one winter season. The deviations between these runs, considered to be elementary perturbations, were then statistically studied and fitted with the model of Eq. (21) for each pair of variables.

In this case study, SAR data are only available for the HH channel; therefore the error covariance matrix $\mathbf{R}$ reduces to a scalar, deduced from the radiometric uncertainty of TerraSAR-X (0.5 dB) and the error of the EMB (inferred from the sensitivity of the EBM). The calculations at several altitudes over the Argentière glacier gives the average value of $\mathbf{R} = 0.03$.

4.4 General comments on the chosen analysis process

In general, modeling techniques are used to establish the relationship between the physical properties of a natural environment and observations measured by specific equipment (such as SAR or optical sensors). An inverse approach may then be developed to characterize the environment using the observations. However, such problems often require solving an underdetermined system, with a number of unknown quantities higher than the number of equations.

In our case, the length of the input state vector $\boldsymbol{x}$ can reach 100 (in the case of a snowpack with 50 layers, frequently generated by Crocus), whereas the output of the model only consists of backscattering coefficients corresponding to the polarimetric channels of SAR data. Therefore the realization of an inverse model is highly impractical.

Data analysis methods, on the other hand, require a vector of guess variables relatively close to the actual values. The snowpack variables calculated by Crocus are used as guess variables in our assimilation scheme. The fundamental goal is to modify the initial guess variables, while balancing the errors of the guess variables, modeling and measurements. It should be noted that, as the problem remains underdetermined, the analysis scheme only serves as a method to improve the initial guess variables using the new observations from SAR data. The quality of improvement is based on the estimation of the initial guess vector $\boldsymbol{x}_g$ and on the precision of the EBM.

Table 1. TerraSAR-X acquisition parameters.

Parameter	Value
TerraSAR-X products	Single-look complex image
Frequency (GHz)	9.65
Channels	HH
Incidence angle (°)	37.9892
Mode	Descending
Acquisition dates (2009)	6, 17, 28 Jan; 8, 19 Feb; 2, 13, 24 March,
Resolution (m)	1.477×2.44
Calibration gain (dB)	49.6802

5 Sensitivity and simulation of snowpack at X band

5.1 Study site: Argentière glacier

The area of interest covers the Argentière glacier (altitude: 2771 m; 45.94628° N, 7.00456° E). The size of the domain is approximately 5 km × 6 km. Over the glacier, altitude varies from 2400 to 3200 m, and the snowpack is essentially composed of dry snow.

5.2 Sensitivity of TerraSAR-X data

For this study, TerraSAR-X descending acquisitions over the region of Chamonix Mont-Blanc, France, from 6 January 2009 to 24 March 2009 are available for continuous assimilation, with a revisit time of 11 days. Table 1 provides the main features of TerraSAR-X data sets. Figure 5 shows the location and a TerraSAR-X image of Argentière glacier captured on 6 January 2009.

Meteorological forcing data provided by SAFRAN from 2400 to 3000 m altitude in steps of 100 m elevation on horizontal terrain were used to drive the detailed snowpack model Crocus throughout the entire season 2008–2009 (starting on 1 August 2008). In order to carry out the comparison between the backscattering coefficients σ_{sim} (obtained from the EBM using Crocus snowpack profile as an input) and σ_{TSX} (obtained from TerraSAR-X reflectivity), the images were multi-looked to (20 m × 20 m) wide pixels and a Frost filter (Frost, 1981) was applied using window size of 5×5 pixels.

In order to study the sensitivity of TerraSAR-X data to the changes in snow properties, Fig. 6 shows the comparison of TerraSAR-X backscattering coefficients (σ_{TSX}) on different dates at the altitudes of 2400, 2700 and 3000 m on Argentière glacier. For the period from 6 to 17 January (blue triangles) and from 8 to 19 February (red circles), it can be observed that the sets of comparison values are well below the equality line, which means the backscattering coefficients decreased between successive observations. The opposite effect

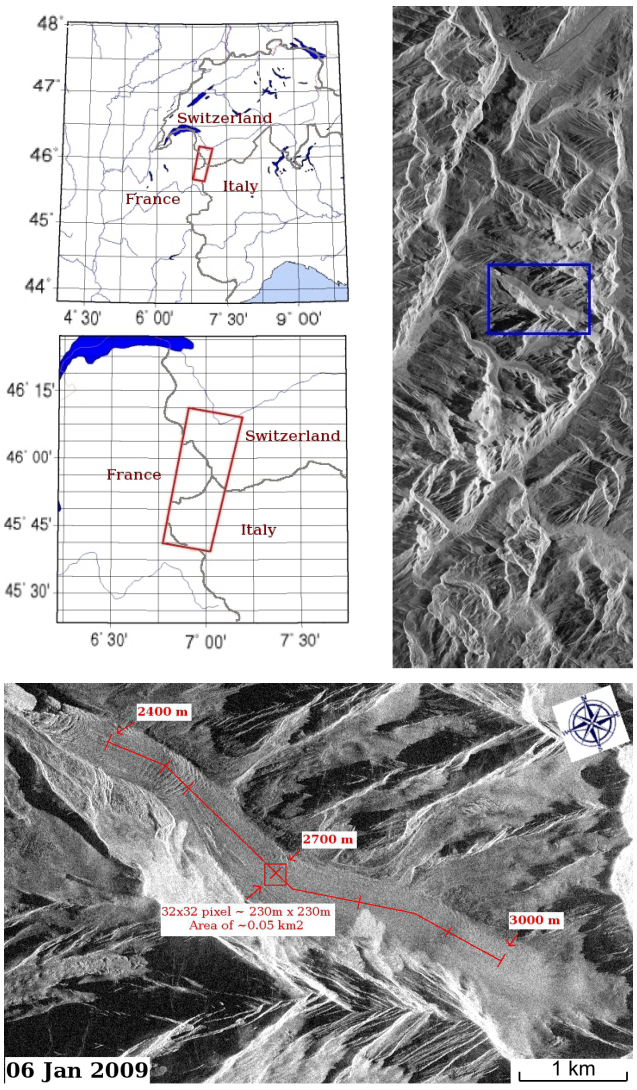

Figure 5. Top panels: location of the TerraSAR-X acquisition in the French Alps. Bottom panel: a cropped image on the Argentière glacier area. The approximate positions of different altitudes on the Argentière glacier: 2400, 2700 and 3000 m on the TerraSAR-X images are indicated. The red line represents the continuous trail on the glacier where the SAR data will be used in the case study; the marks on this line delineate each 100 m of altitude.

can be noted for the period from 17 January to 8 February (green crosses). The medium beneath the snowpack consists of glacier ice, and its roughness can be considered to be constant; therefore these increases and decreases in backscattering suggest that the σ_{TSX} can be related to the modification of the snow condition. As can be observed in the snow precipitation chart on the bottom right, the green period has significantly more snowfall than the other two periods.

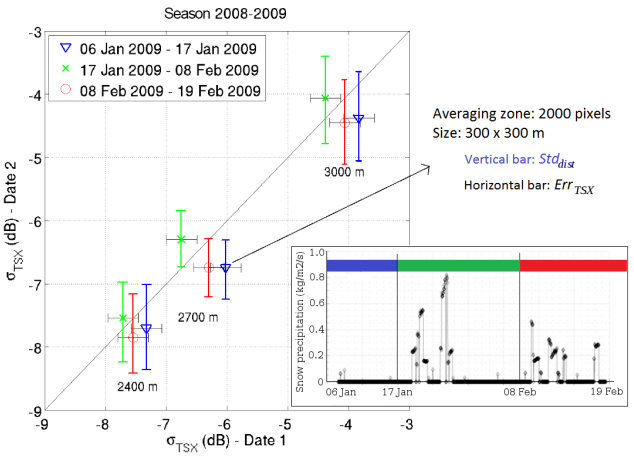

Figure 6. Comparison of TerraSAR-X reflectivities between two different dates of winter season 2008–2009 at the altitudes of 2400, 2700 and 3000 m on Argentière glacier. The small graph on the bottom right shows the snow precipitation level for each period of comparison.

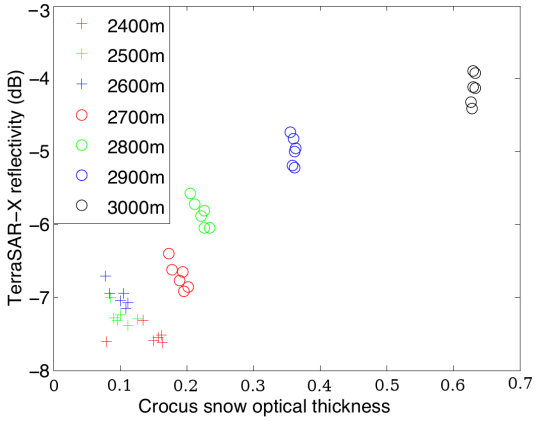

Figure 7. TerraSAR-X reflectivity plotted as function of optical thickness derived from Crocus output. Each point corresponds to a date of acquisition TerraSAR-X.

5.3 Simulation of Crocus snowpack data

The intrinsic parameters of a snowpack needed for EBM simulations are simulated by Crocus, which consist of a number of snow layers, their density, optical diameter, and thickness. These quantities are used as inputs for the simulation of the volume backscattering mechanism. The relation between open-loop (i.e., without assimilation) Crocus data and the TerraSAR-X reflectivity for different altitudes over the Argentière glacier is shown in Fig. 7. The optical thickness (τ) is the product of snow depth and the extinction coefficient (Tsang et al., 2007). In the case of multilayer snowpack, it is defined as

$$\tau = \sum_{k=1}^{n} \kappa_{\mathrm{e}}^{k} d^{k}, \tag{22}$$

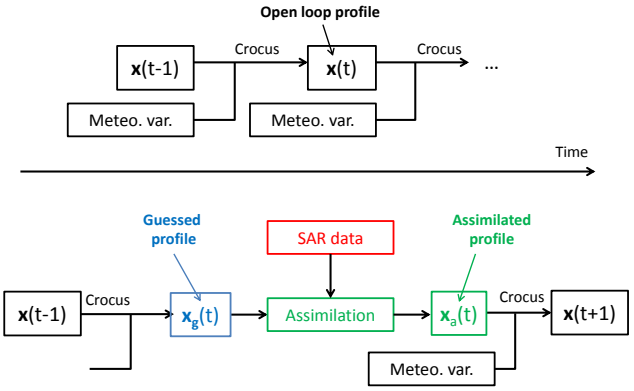

Figure 8. Implementation of SAR data assimilation in the Crocus temporal simulation of a snowpack.

where the extinction coefficient κ_e is calculated using Eq. (9) and d the thickness of the snow layer.

It can be observed that the snowpack stratigraphy provided by Crocus may be used to separate TerraSAR-X reflectivity at different altitudes. Figure 7 also indicates the sensitivity of the reflectivity to volume-related snow parameters.

6 Evaluation of the process and discussions

Crocus snow stratigraphic profiles were computed for seven different altitudes over the Argentière glacier, from 2400 to 3000 m. The level of liquid water content per volume (LWC_v) at the times and locations of analysis is 0 %; therefore the condition of dry snow is satisfied. Figure 5 shows the approximate locations of each study area on the glacier.

Figure 8 presents the implementation of the SAR data assimilation process into Crocus. The top part of the figure shows the Crocus simulation of snowpack without assimilation of SAR data. At instant t, Crocus simulates the snow stratigraphic profile from the previous state of snowpack (instant $t-1$) and the meteorological data hourly provided from SAFRAN. The time lag between instant t and instant $t-1$ is therefore one hour. We call this simulation "open loop". The bottom part of the figure shows the implementation of data assimilation into the execution of Crocus. Every 11 days, a TerraSAR-X acquisition is used to modify the snowpack stratigraphic profile of Crocus through an assimilation process. The snow profile before assimilation is called "guess", and the analyzed snow profile after assimilation is called "assimilated". Consequently, at the date of the first TerraSAR-X acquisition (6 January 2009), open-loop and guess profiles are identical. Once this first SAR acquisition is assimilated into Crocus, guess and assimilated profiles differ. This modification permits the constrainment of a physical snowpack simulation using external information acquired at different dates.

Table 2. Comparisons of RMSE (dB) between simulated ($\sigma_{snow} = H(\boldsymbol{x})$) and measured ($\sigma_{TSX}$) reflectivities for different types of profiles.

Date	$\boldsymbol{x}$ = open loop	$\boldsymbol{x}$ = guess	$\boldsymbol{x}$ = assimilated
6 Jan	3.6256	3.6256	3.2697
17 Jan	3.1677	3.3645	3.1302
28 Jan	3.4697	3.5326	3.3718
8 Feb	3.4649	3.3619	1.8071
19 Feb	3.3708	2.6463	1.2729
2 Mar	3.6877	1.7992	1.2276
13 Mar	3.7383	1.2482	1.0652
24 Mar	3.1840	0.6757	0.4370

Figure 9 shows the results of simulation and analysis using the TerraSAR-X time series from 6 January to 24 March 2009. The reflectivity on the glacier crevasse area (2600 m elevation) has a very high standard deviation due to the cracks and has therefore been masked. The red line corresponds to the TerraSAR-X reflectivities along the glacier, whereas the cyan diamond shape indicates the EBM simulations for the Crocus open-loop profiles. The blue triangles indicate the EBM simulation of the guess profiles. These guess profiles are in turn modified by the assimilation process to become the assimilated profiles. The EBM simulations of the assimilated profiles are shown in green circles. The assimilated profile is used to reinitialize Crocus for the next iteration, which then produces the guess profile for the next assimilation when a new SAR acquisition is available.

The agreement between TerraSAR-X reflectivity and the output of the EBM using Crocus simulated profiles can be observed in Fig. 9, where EBM simulations of assimilated profiles converge gradually over time toward the TerraSAR-X backscattering coefficient. The graph corresponding to 2 March 2009 shows that the convergence has been reached at all altitudes, as EBM simulations of guess and assimilated profiles are much closer to the TerraSAR-X measurements than the open-loop profiles.

Table 2 shows a comparison of root-mean-square error (RMSE) between simulated and measured reflectivities for different types of profile: open loop, guess and assimilated. It can be observed that the σ_{snow} values converge gradually toward the σ_{TSX} for the guess and assimilated profiles. At the last date of acquisition (24 March), the RMSEs for guess and assimilated profiles are below 1 dB, while the open-loop profile still gives an RMSE higher than 3 dB.

Figure 10 shows a detailed analysis of the modifications of the optical diameter and density of each layer due to data assimilation on 6 January, 8 February and 13 March 2009 at the altitude of 2400 m. It can be observed that the assimilation algorithm tends to modify the optical diameter and density in the deep layers which have a strong influence on the backscatter intensity and whose slight modification significantly reduce the discrepancy between TerraSAR-X

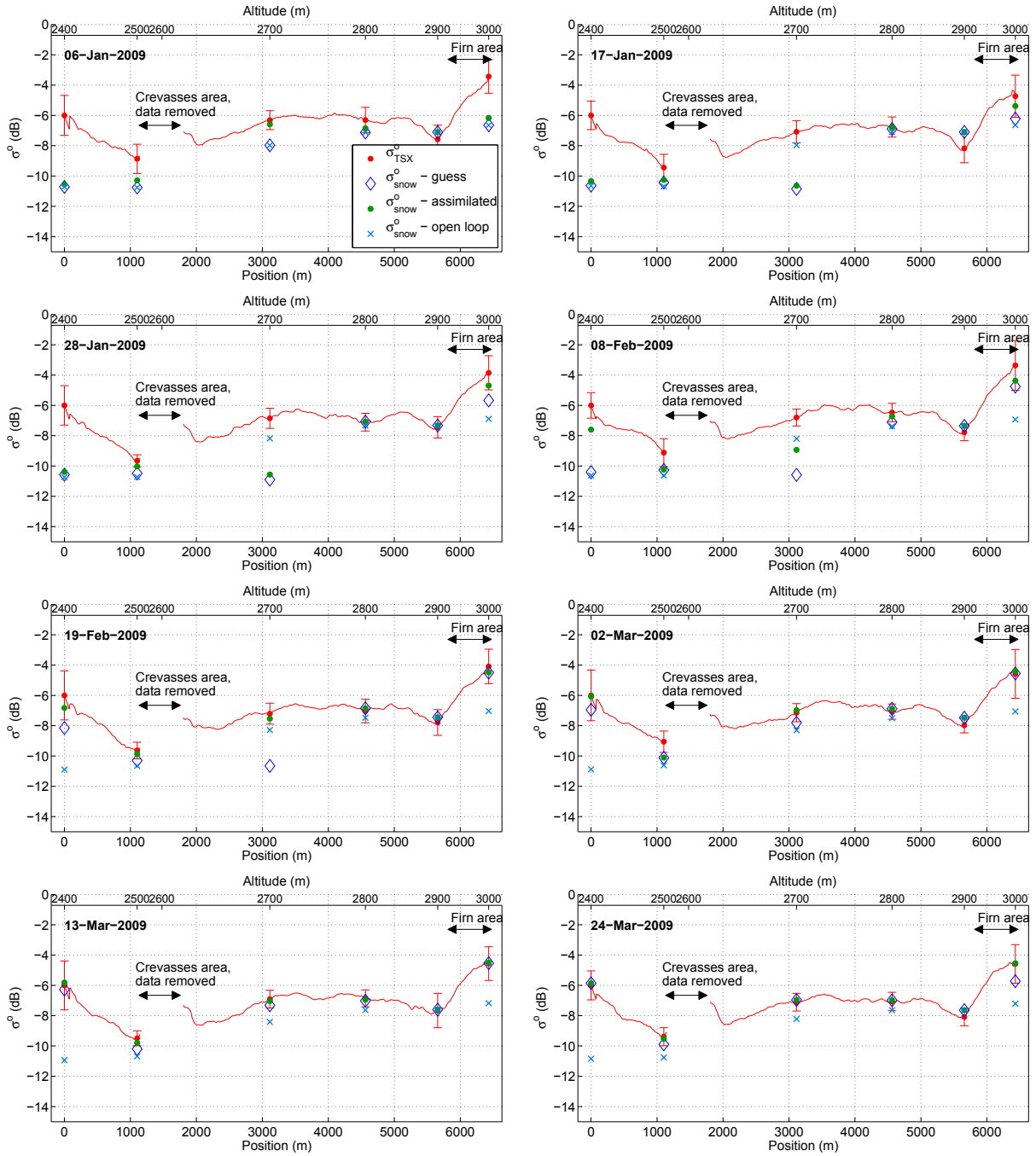

Figure 9. Results of simulation and analysis using eight TerraSAR-X acquisitions performed in winter 2009. σ_{TSX} (red) are mean values obtained from the SAR images over the Argentière glacier (corresponding to the red line of Fig. 5). σ_{sim} (blue) represents the output of simulations using Crocus snowpack variables as inputs. Simulations obtained after data analysis are shown in green. Error bars show the standard deviation of the measured reflectivities.

observations and Crocus simulations. The speed of the densification process is therefore faster in the Crocus simulations with assimilation. The snow profile on 8 February records a large change in the optical diameter (from 0.4 to 0.8–1.3 mm in the layers from 0 to 100 cm of snow height), which results in a variation in the simulated backscattering coefficient for the assimilated profile, which can be observed in Fig. 9 at 2400 m. Note that this large increase in the diameter results in a large discrepancy between open-loop and guess profiles on 13 March. It can also be noted that there is a difference of 20 cm in total snow depth between the open- and closed-loop simulations on 13 March, which shows that the modifications

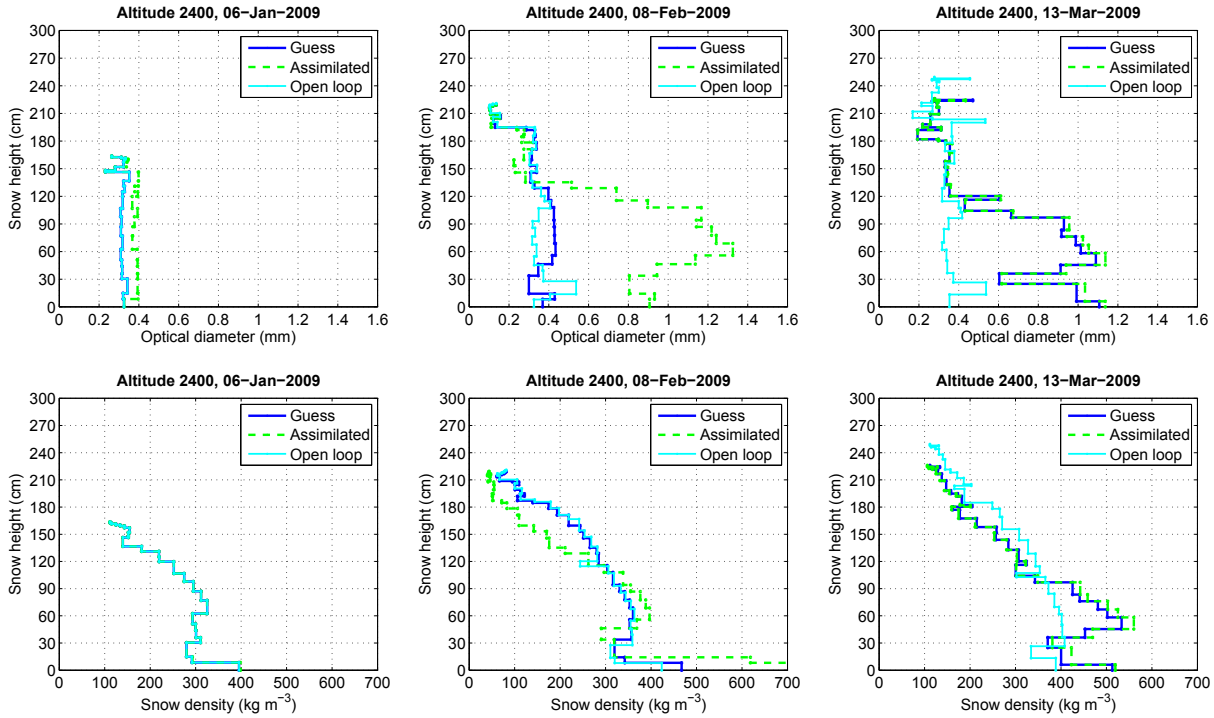

Figure 10. Results of 1D-Var data assimilation from some Crocus profiles, showing changes made by the data assimilation algorithm on optical diameter (top panels) and snow density (bottom panels) on 6 January (left panels), 8 February (middle panels) and 13 March (right panels). Note that the assimilation only affects directly the optical diameter and snow density. These direct modifications are injected into Crocus and propagate through the subsequent simulations, and may then lead to open-loop and assimilated profiles with different snow heights.

of optical diameter and snow density made by data assimilation also indirectly modify others physical properties of the Crocus-simulated snowpack.

These results show that we have combined three models (Crocus, EBM, adjoint model) and the TerraSAR-X data to constrain spatially and temporally the snowpack evolution. The use of data assimilation on SAR data to predict certain physical properties of snowpack has been developed in Nagler et al. (2008) and Takala et al. (2011). However, it is the first time that active X-band radar data have not been used directly to perform an assessment of snowpack properties but instead used to estimate physical parameters of each snow layer through a data assimilation algorithm. This algorithm needs to be further validated in the future using in situ measurements and advanced 3-D imaging techniques (Ferro-Famil et al., 2012).

7 Conclusions

This study presents a new system using data assimilation and a multilayer snowpack backscattering model based on the radiative transfer theory to constrain the evolution of a snowpack simulated by the snow model Crocus. The proposed new backscattering model adapted to X-band and higher frequencies enables a fairly accurate calculation of EMW losses in each layer of the snowpack. Through the use of 1D-Var data assimilation based on the linear tangent and adjoint operator of the EBM, we are able to modify, in a physically consistent way, the snowpack profiles calculated using the snowpack evolution model Crocus. This process has been applied to a time series of TerraSAR-X images and Crocus simulations during the winter of 2008–2009 over the Argentière glacier. Results show that SAR data can be taken into account to efficiently modify the evolution of snowpack simulated by Crocus. This process can be further developed and used in real applications such as large-scale snow cover monitoring or snowpack evolution over a long period of time.

This system, however, does have some limitations, like the inability to simulate and assimilate under wet snow conditions due to the hypothesis used in the EBM. Another important hypothesis made in this study concerns the spherical shape of snow grains. On the one hand, this assumption highly simplifies the modeling problem but, on the other hand, prevents the simulations over cross-polarization channels (HV and VH). The discussion on how to resolve these limitations should be addressed in another study on the modeling of electromagnetic waves interactions with a snowpack.

Future studies will concentrate on calibrating the assimilation process using in situ measurements. Direct field

measurements of the optical diameter using recently developed methods (Gallet et al., 2009; Arnaud et al., 2011) allow for a direct comparison to Crocus output (Morin et al., 2013). Future developments will also benefit from the recently finalized prognostic representation of optical diameter in Crocus (Carmagnola et al., 2014).

Acknowledgements. This work was funded through the European project GlaRiskAlp (2010–2013) on glacial hazards in the Western Alps, as well as Météo-France. TerraSAR-X data were provided by the German Aerospace Center (DLR). The authors would like to thank Matthieu Lafaysse from CNRM-GAME/CEN for their help with performing the Crocus runs. We thank CNES/TOSCA for funding through the CESTENG project. CNRM-GAME/CEN and GIPSA-Lab are part of LabEx OSUG@2020 (ANR10 LABX56).

Edited by: E. Larour

References

Arnaud, L., Picard, G., Champollion, N., Domine, F., Gallet, J., Lefebvre, E., Fily, M., and Barnola, J.: Measurement of vertical profiles of snow specific surface area with a 1 cm resolution using infrared reflectance: instrument description and validation, J. Glaciol., 57, 17–29, 2011.

Brun, E., David, P., Sudul, M., and Brunot, G.: A numerical model to simulate snowcover stratigraphy for operational avalanche forecasting, J. Glaciol., 128, 13–22, 1992.

Carmagnola, C. M., Morin, S., Lafaysse, M., Domine, F., Lesaffre, B., Lejeune, Y., Picard, G., and Arnaud, L.: Implementation and evaluation of prognostic representations of the optical diameter of snow in the SURFEX/ISBA-Crocus detailed snowpack model, The Cryosphere, 8, 417–437, doi:10.5194/tc-8-417-2014, 2014.

Courtier, P., Andersson, E., Heckley, W., Vasiljevic, D., Hamrud, M., Hollingsworth, A., Rabier, F., Fisher, M., and Pailleux, J.: The ECMWF implementation of three-dimensional variational assimilation (3D-Var), I: Formulation, Q. J. Roy. Meteorol. Soc., 124, 1783–1807, 1998.

De Lannoy, G. J. M., Reichle, R. H., Houser, P. R., Arsenault, K. R., Verhoest, N. E. C., and Pauwels, V. R. N.: Satellite-Scale Snow Water Equivalent Assimilation into a High-Resolution Land Surface Model, J. Hydrometeorol., 11, 352–369, doi:10.1175/2009JHM1192.1, 2010.

Dumont, M., Durand, Y., Arnaud, Y., and Six, D.: Variational assimilation of albedo in a snowpack model and reconstruction of the spatial mass-balance distribution of an alpine glacier, J. Glaciol., 58, 151–164, 2012.

Durand, Y.: Reanalysis of 47 years of climate in the French Alps (1958–2005): climatology and trends for snow cover, J. Appl. Meteorol. Clim., 48, 2487–2512, 2009.

Durand, Y., Brun, E., Mérindol, L., Guyomarc'h, G., Lesaffre, B., and Martin, E.: A meteorological estimation of relevant parameters for snow models, J. Glaciol., 18, 65–71, 1993.

Ferro-Famil, L., Leconte, C., Boutet, F., Phan, X., Gay, M., and Durand, Y.: PoSAR: A VHR tomographic GB-SAR system application to snow cover 3-D imaging at X and Ku bands, in: Radar Conference (EuRAD), 2012 9th European, Amsterdam, 130–133, 2012.

Floricioiu, D. and Rott, H.: Seasonal and short-term variability of multifrequency, polarimetric radar backscatter of Alpine terrain from SIR-C/X-SAR and AIRSAR data, IEEE T. Geosci. Remote, 39, 2634–2648, 2001.

Frost, V.: An adaptive filter for smoothing noisy radar images, Proc. IEEE, 69, 133–135, 1981.

Fung, A. and Chen, K.: An update on the IEM surface backscattering model, IEEE Geosci. Remote Sens. Lett., 1, 75–77, 2004.

Gallet, J.-C., Domine, F., Zender, C. S., and Picard, G.: Measurement of the specific surface area of snow using infrared reflectance in an integrating sphere at 1310 and 1550 nm, The Cryosphere, 3, 167–182, doi:10.5194/tc-3-167-2009, 2009.

Huining, W., Pulliainen, J., and Hallikainen, M.: Effective Permittivity of Dry Snow in the 18 to 90 GHz Range, Prog. Electromag. Res., 24, 119–138, 1999.

Koskinen, J., Pulliainen, J., Luojus, K., and Takala, M.: Monitoring of Snow-Cover Properties During the Spring Melting Period in Forested Areas, IEEE T. Geosci. Remote, 48, 50–58, 2010.

Lee, J. S. and Pottier, E.: Polarimetric Radar Imaging: From Basics to Applications, CRC Press, Boca Raton, FL, USA, 2009.

Longepe, N., Allain, S., Ferro-Famil, L., Pottier, E., and Durand, Y.: Snowpack Characterization in Mountainous Regions Using C-Band SAR Data and a Meteorological Model, IEEE T. Geosci. Remote, 47, 406–418, 2009.

Martini, A., Ferro-Famil, L., and Pottier, E.: Polarimetric study of scattering from dry snow cover in alpine areas, in: Geoscience and Remote Sensing Symposium, 2003, IGARSS '03, Toulouse, 854–856, 2003.

Morin, S., Domine, F., Dufour, A., Lejeune, Y., Lesaffre, B., Willemet, J.-M., Carmagnola, C., and Jacobi, H.-W.: Measurements and modeling of the vertical profile of specific surface area of an alpine snowpack, Adv. Water Resour., 55, 111–120, 2013.

Nagler, T. and Rott, H.: Retrieval of wet snow by means of multitemporal SAR data, IEEE T. Geosci. Remote, 38, 754–765, 2000.

Nagler, T., Rott, H., Malcher, P., and Müller, F.: Assimilation of meteorological and remote sensing data for snowmelt runoff forecasting, Remote Sens. Environ., 112, 1408–1420, 2008.

Oh, Y., Sarabandi, K., and Ulaby, F.: An empirical model and an inversion technique for radar scattering from bare soil surfaces, IEEE T. Geoscience Remote, 30, 370–381, 1992.

Shi, J. and Dozier, J.: Estimation of snow water equivalence using SIR-C/X-SAR, I. Inferring snow density and subsurface properties, IEEE T. Geosci. Remote, 38, 2465–2474, 2000.

Shi, J., Dozier, J., and Rott, H.: Deriving snow liquid water content using C-band polarimetric SAR, in: International Geoscience and Remote Sensing Symposium, 1993, IGARSS'93, Better Understanding of Earth Environment, vol. 3, 1038–1041, 1993..

Slater, A. G. and Clark, M. P.: Snow data assimilation via an ensemble Kalman filter, J. Hydrometeorol., 7, 478–493, doi:10.1175/JHM505.1, 2006.

Stogryn, A.: The bilocal approximation for the effective dielectric constant of an isotropic random medium, IEEE T. Antenn. Propagat., 32, 517–520, 1984.

Takala, M., Luojus, K., Pulliainen, J., Derksen, C., Lemmetyinen, J., Kärnä, J.-P., Koskinen, J., and Bojkov, B.: Estimating northern hemisphere snow water equivalent for climate research through assimilation of space-borne radiometer data and ground-based measurements, Remote Sens. Environ., 115, 3517–3529, 2011.

Toure, A., Goita, K., Royer, R., Kim, E., Durand, M., Margulis, S., and Lu, H.: A Case Study of Using a Multilayered Thermodynamical Snow Model for Radiance Assimilation, IEEE T. Geosci. Remote, 49, 2828–2837, 2011.

Tsang, L., Pan, J., Liang, D., Li, Z., Cline, D., and Tan, Y.: Modeling Active Microwave Remote Sensing of Snow Using Dense Media Radiative Transfer (DMRT) Theory With Multiple-Scattering Effects, IEEE T. Geosci. Remote, 45, 990–1004, 2007.

Ulaby, F. T., Moore, R. K., and Fung, A. K.: Microwave remote sensing: Active and passive, Volume III – From Theory to Applications, Addison-Wesley, Reading, Massachusetts, 1981.

Uppala, S. M., Kallberg, P. W., Simmons, A. J., Andrae, U., Bechtold, V. D. C., Fiorino, M., Gibson, J. K., Haseler, J., Hernandez, A., Kelly, G. A., Li, X., Onogi, K., Saarinen, S., Sokka, N., Allan, R. P., Andersson, E., Arpe, K., Balmaseda, M. A., Beljaars, A. C. M., Berg, L. V. D., Bidlot, J., Bormann, N., Caires, S., Chevallier, F., Dethof, A., Dragosavac, M., Fisher, M., Fuentes, M., Hagemann, S., Holm, E., Hoskins, B. J., Isaksen, L., Janssen, P. a. E. M., Jenne, R., Mcnally, A. P., Mahfouf, J.-F., Morcrette, J.-J., Rayner, N. A., Saunders, R. W., Simon, P., Sterl, A., Trenberth, K. E., Untch, A., Vasiljevic, D., Viterbo, P., and Woollen, J.: The ERA-40 re-analysis, Q. J. Roy. Meteorol. Soc., 131, 2961–3012, doi:10.1256/qj.04.176, 2005.

Vionnet, V., Brun, E., Morin, S., Boone, A., Faroux, S., Le Moigne, P., Martin, E., and Willemet, J.-M.: The detailed snowpack scheme Crocus and its implementation in SURFEX v7.2, Geosci. Model Dev., 5, 773–791, doi:10.5194/gmd-5-773-2012, 2012.

Wang, H., Pulliainen, J., and Hallikainen, M.: Extinction Behavior of Dry Snow at Microwave Range Up to 90 GHz by Using Strong Fluctuation Theory, Prog. Electromag. Res., 25, 39–51, 2000.

F. Ponton, E. Trouvé, M. Gay, A. Walpersdorf, R. Fallourd, J.M. Nicolas, F. Vernier, and J.L. Mugnier "Observation of the Argentière Glacier Flow Variability from 2009 to 2011 by TerraSAR-X and GPS Displacement Measurements", *IEEE Journal of Selected Topics in signal processing*, *Vol.* 7, *N°* 8, 2014.

Observation of the Argentière Glacier Flow Variability from 2009 to 2011 by TerraSAR-X and GPS Displacement Measurements

Fanny Ponton, Emmanuel Trouvé, *Senior Member, IEEE*, Michel Gay, Andrea Walpersdorf, Renaud Fallourd, Jean-Marie Nicolas, Flavien Vernier, and Jean-Louis Mugnier

***Abstract*—In this paper, 3 years of surface displacement measurements obtained by space-borne synthetic aperture radar (SAR) observations are presented over the Argentière glacier in the Mont-Blanc massif, France. This temperate glacier is instrumented by a network of four Global Positioning System (GPS) stations used as ground truth. Thirty-eight pairs of descending and ascending high-resolution TerraSAR-X (TSX) acquisitions covering the study region are used to derive displacement fields at 11-day intervals in spring and summer 2009 and summer 2011. The combination of ascending and descending pairs acquired over the same period allows 3-D displacement fields to be inverted. Our SAR analysis quantifies displacement rates from 10 cm/day at the altitude of 2600 m to 30 cm/day at the altitude of 1800 m. Time series of SAR displacement results are compared with *in situ* GPS measurements of a continuous station set up at the altitude of 2441 m. Both data sources present displacement of the same order of magnitude with an average value of 20 cm/day in 3-D and show intra-seasonal variabilities, with fast accelerations over short time intervals.**

***Index Terms*—Glacier displacement, Global Positioning System (GPS), synthetic aperture radar (SAR) images time series, TerraSAR-X.**

I. Introduction

MONITORING temperate mountain glaciers can be useful for different purposes. Glaciers are local indicators of the global climate state, so following their evolution provides useful information to assess the local effect of global warming [1] and to anticipate the economical impact, like the access to water resources. A better knowledge of parameters controlling physical processes allows dynamic models of glacier flow to be constrained [2]. However, only a few temperate glaciers are equipped with *in situ* measurement devices [3]. Climatic conditions and difficulties of access significantly limit the possibility to install stable instruments and to have continuous and numerous data sets. Remote sensing methods can be an effective alternative to monitor and study glaciers [4], [5]. In glaciology, optical imagery provides a large coverage and is used in many studies to identify glacier features such as frontal termini, summer snowline, accumulation, and ablation zones. It also provides glacier displacement fields, feature evolutions, snow cover thickness, and mass balances [6]–[8]. Nevertheless, the use of optical remote sensing methods over the Alpine glaciers is limited by cloudy weather and by the lack of sun illumination, which often occur in high mountain regions.

Synthetic aperture radar (SAR) images are acquired independently from the weather conditions. They allow surface displacement to be measured by using either the phase information (SAR interferometry) or the amplitude information by feature/texture tracking methods similar to those which are used with optical data. In past studies, SAR interferometry (InSAR) provided successfully results on glaciers having a stable surface state as rock glaciers [9] or with image couples acquired with a repeat pass delay from 1 to 3 days and during favourable meteorological conditions [10]–[12]. However, InSAR is limited by the loss of coherence, when precipitations, melt, and wind change the glacier surface state between two SAR images [12], [13]. This limitation often applies when the temporal baseline is long between image acquisitions. The German satellite TerraSAR-X (TSX) launched in 2007 provides high-resolution SAR imagery: 1 m in Spotlight mode and even higher (up to 0.25 m) with the Staring Spotlight mode [14]. During this time interval, surface state changes too much to keep a sufficient level of coherence on glaciers. An alternative method is to use the amplitude information by the so-called offset power tracking method [15], [16]. This technique provides a displacement in two dimensions (2-D): in slant range and azimuth directions. Moreover, using two pairs of images, acquired over the same period from descending and ascending orbits, allows the three dimensions (3-D: East North and Up directions) of the displacement fields to be derived [17]. In the SAR processing chains, elevation errors of digital elevation model (DEM), combined with orbital errors, result in topographic correction and georeferencing uncertainty. The comparison between GPS and SAR measures of glacier surface displacement shows errors as small

Manuscript received October 16, 2013; revised July 12, 2014; accepted July 28, 2014. Date of publication September 09, 2014; date of current version October 03, 2014. This work was supported by the EFIDIR project (ANR-07-MDCO-004, http://www.efidir.fr), granted by the French National Research Agency (ANR), and a CIBLE 2010 project granted by the "Région Rhône-Alpes."

F. Ponton, A. Walpersdorf, and J.-L. Mugnier are with the ISTerre, CNRS, Université Joseph Fourier, Maison des Géosciences, 38041 Saint-Martin-d'Hères, France (e-mail: pontonf@ujf-grenoble.fr; Andrea.Walpersdorf@ujf-grenoble.fr; jean-louis.mugnier@univ-savoie.fr).

E. Trouvé, F. Vernier, and R. Fallourd are with the LISTIC, Polytech Annecy-Chambéry, Université de Savoie, 74944 Annecy-le-Vieux, France (e-mail: emmanuel.trouve@univ-savoie.fr; flavien.vernier@univ-savoie.fr; renaud.fallourd@orange.fr).

M. Gay is with the GIPSA-lab, INPG, Université Joseph Fourier, 38402 Saint Martin d'Hères, France (e-mail: Michel.Gay@gipsa-lab.grenoble-inp.fr).

J.-M. Nicolas is with the LTCI, Télécom ParisTech, 75013 Paris, France (e-mail: jean-marie.nicolas@telecom-paristech.fr).

Color versions of one or more of the figures in this paper are available online at http://ieeexplore.ieee.org.

Digital Object Identifier 10.1109/JSTARS.2014.2349004

1939-1404 © 2014 IEEE Personal use is permitted, but republication/redistribution requires IEEE permission.
See http://www.ieee.org/publications_standards/publications/rights/index.html for more information.

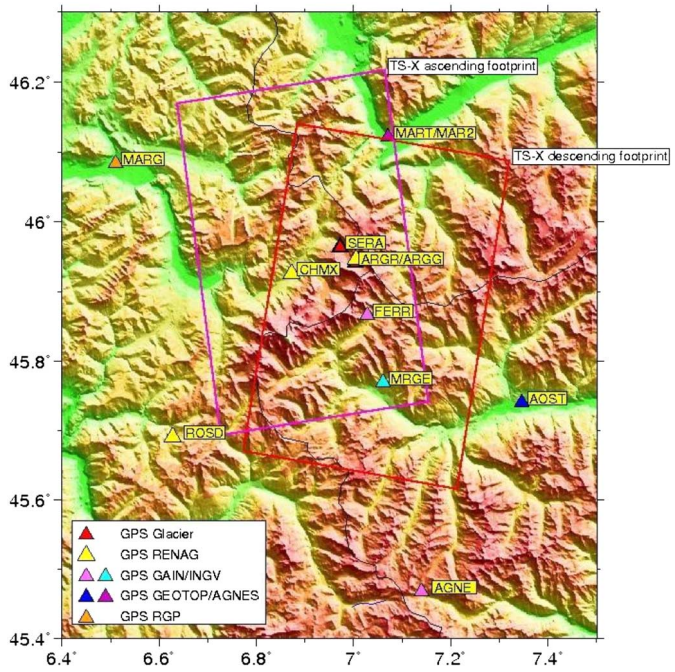

Fig. 1. Map of the Mont-Blanc massif, the red frame represents the area covered by descending TSX track and the purple the one covered by ascending track. Red triangle locates the GPS station SERA used to compare SAR results, others triangles show GPS stations completing the GPS processing.

as 2 cm/day, but they can reach values bigger than 1 m/day [17], [18]. Moreover, in summer, the vertical component of the displacement in SAR results contains both the displacement and ablation. The latter has to be quantified to compare displacement between both data sources [8].

In this paper, we present 3 years of the Argentière glacier surface displacement measured by TSX and GPS data. The Argentière glacier is situated in the Mont-Blanc massif (6° 57′E, 45° 55′N), between 1600 and 3400 m of altitude from the edge of its tongue to its top. It is about 10-km long and covers a surface of approximatively 12 km^2. For several decades, the Argentière glacier has been an experimental test site to acquire *in situ* and remotely sensed data for temperate glacier monitoring. It has been selected by the DLR (German Aerospace Center) to experiment airborne polarimetric SAR imagery over Alpine glaciers with two E-SAR campaigns in 2006 and 2007 [19]. It was representative of fast moving geophysical objects chosen by the EFIDIR project [Extraction and Fusion of Information for ground displacement measurements with Radar Imagery, ANR (French national research agency) 2008–2012], to develop methodologies to improve the precision of SAR-based displacement measurements. In this aim, high-resolution SAR images from satellites TerraSAR-X and Radarsat-2 have been acquired since the end of 2007 over our study area (Fig. 1). Moreover, the Argentière glacier is equipped with a GPS network. This local network is composed of two GPS stations implanted directly in the ice at 2770 m (ARGG) and 2440 m (SERA) of altitude and of two stations outside of the glacier: one on rock outcrops near the Argentière mountain hut at 2835 m (ARGR) and one in the town of Chamonix at 1121 m (CHMX). In this work, 2-D and 3-D surface displacement fields are derived using TSX images acquired in winter and summer 2009 and in summer 2011 and are compared with displacements obtained from the GPS analysis. GPS data providing *in situ* displacement measurements are considered as ground truth to validate remote sensing results [3] and to follow the displacement on continuous and extended time scales.

This paper is divided into three major sections. First, we present the data sets used to measure the displacement and the processing chains. Then, we present the 2-D displacements obtained from SAR imagery and GPS, and compare both data sources. The third section presents the 3-D displacement results and the corrections of ablation required to obtain the true vertical glacier displacement from TSX measurements.

II. Data Sets and Processing

A. TerraSAR-X Images

To measure glacier displacements from SAR imagery, 44 stripmap (SM) TerraSAR-X images have been acquired over the Chamonix Mont-Blanc test site. The SM acquisition mode allows a large spatial coverage [30 km in line of sight (LOS) in single polarization and 50 km in azimuth] with a high resolution (about 2 m on the ground). Except for the first eight images in 2009 acquired in a dual polarization (HH/HV), all images have been acquired in a single polarization mode (HH). In 2009, 13 images are available in ascending track and 15 in descending track. In 2011, 13 ascending track images and only 3 descending track images are available. From those images, we can form 11 and 12 pairs at 11-day intervals in 2009 and 11 and 2 pairs at 11-day intervals in 2011 (Table I). In 2009, five 11-day ascending pairs almost overlap 11-day descending pairs, which allow the computation of five 3-D displacement fields. To obtain a 3-D displacement field in 2011, only a 22-day pair for each track can be processed. The GPS and SAR data availability is summarized in Fig. 2. In this study, the displacements measured over different time intervals have been normalized, to quantify them on 1 day, using the centimeter per day as unit.

B. SAR Image Processing Chain

Displacement fields are derived from TSX images by the offset power tracking method using the Zero Mean Normalized Cross Correlation (ZNCC) function. We used the processing chain of the "EFIDIR Tools," an open source software developed in the ANR EFIDIR project context. Fig. 3 shows the different steps of the SAR processing.

1) An initial coregistration between the images is made by a simple translation. A single motion-free point, at a medium altitude, is used to determine the initial offsets between images. The geometric range deformation due to the topography is still present and will be compensated later in the processing. This strategy is preferable since there is no resampling (which may reduce the correlation performance) and the search area for the moving points is reduced after this initial translation.
2) A fast correlation technique developed in the EFIDIR Tools [20] is applied on the image pairs with a square reference window (range and azimuth resolution are almost

TABLE I
TSX IMAGES ACQUIRED OVER CHAMONIX MONT-BLANC TEST SITE; NUMBER OF PAIRS PROCESSED AND MAIN IMAGE CHARACTERISTICS

Periods	Images	Pairs	Track	Incidence (°)	Resolution (m)	
					Range	Azimuth
2009/01/06–2009/03/29	8	7	desc.	37	0.91	2.44
2009/05/29–2009/08/25	7	5	desc	37	1.36	2.05
2009/05/31–2009/10/21	13	11	asc.	44	1.36	1.95
2011/09/01–2011/09/23	3	3	desc.	37	1.36	2.05
2011/05/05–2011/09/25	13	12	asc.	44	1.36	1.95

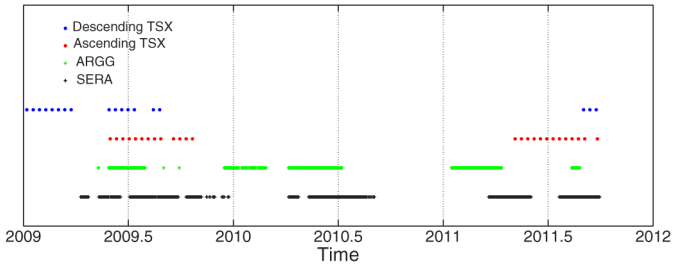

Fig. 2. Availability of SERA station GPS data (black crosses), of ARGG station GPS data (green crosses), of ascending track TSX images (red stars) and of descending track TSX images (blue stars).

equal) and a rather large size (typically 65×65 pixels) to obtain reliable results on textured area without any speckle filtering (to preserve the full resolution of single look images). The search window is set according to a maximum offset predictable from a DEM and the perpendicular baseline, and from the glacier maximum velocity. The position of the cross correlation peak is interpolated to obtain subpixel offset vectors. This method is applied in each pixel position and provides a dense offset field. On the glacier, these offsets are the sum of the displacement offsets and the geometrical offsets due to the baseline and the topography, which have not been compensated for at step 1.

3) Depending on the variations of the geometrical offsets along the glaciers, a postprocessing step can be necessary to obtain the offsets only due to the glacier motion. The geometrical offsets can be subtracted by using either the predictions from the DEM and the state vectors, which contain satellite orbital information, or the results of the subpixel correlation around the glaciers. At this stage, the offsets are converted from pixel to cm/day and provide the 2-D displacement v_{LOS} and v_{Az} in SAR geometry.
4) The displacement images and the similarity peak (correlation level) images are projected in ground geometry (latitude and longitude). This geocoding is performed by using the Synthetic Aperture Radar Look Up Table (SARLUT) tool [21]. The results obtained from both ascending and descending tracks are resampled on the DEM grid (4-m spacing).
5) A mask of pixels is built to select the areas where the displacement is measured with sufficient confidence. For the ZNCC function, empiric studies showed that displacement estimations are consistent when the value of the correlation peak is larger than 0.2 [16], [22]. Accordingly, areas of correlation level lower than 0.2 are removed.
6) Finally, when both ascending and descending pairs are available for almost the same period, four projections of almost the same displacement field are obtained: $V_{SAR} = [v_{LOS}^{des}, v_{Az}^{des}, v_{LOS}^{asc}, v_{Az}^{asc}]$. The weighted least square inversion technique [23] is applied to derive the East, North, and Up components of the 3-D displacement vector $V_{3D} = [v_E, v_N, v_U]$ over the moving areas visible by both tracks.

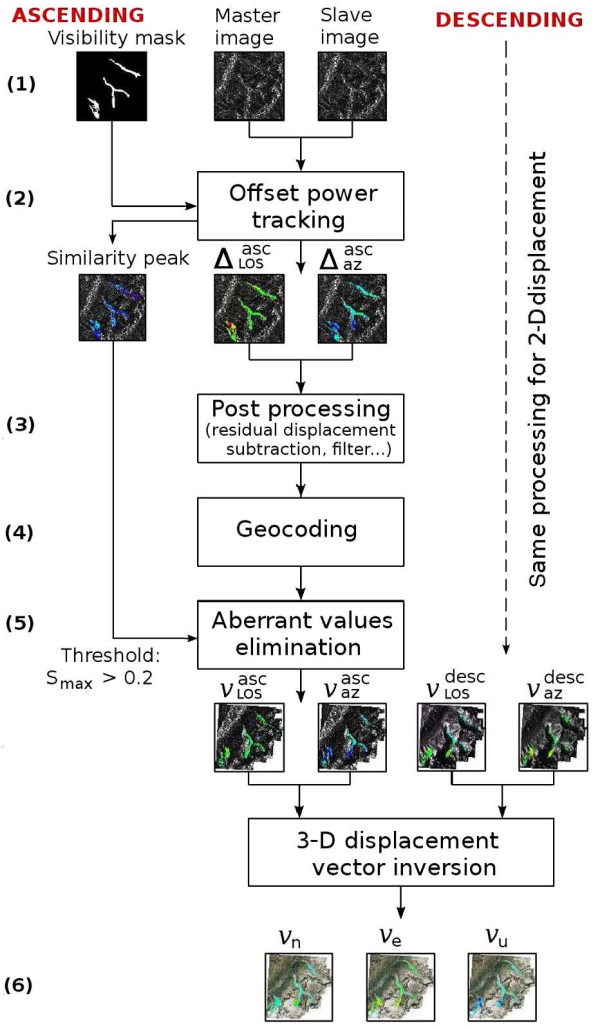

Fig. 3. Steps of SAR offset power tracking analysis, from SAR images to 3-D displacement results.

C. GPS Processing

Two GPS stations are installed on the glacier, but only the station SERA at 2440 m can be compared with the SAR results of this study. Due to the lack of texture for offset power tracking in the upper part of the glacier, no comparison is possible with the GPS station ARGG located at 2770 m, close to the accumulation area. The GPS equipment used for SERA is a Topcon GB1000 receiver with a PG-A 1 antenna. Data are collected since November 2008. Due to the larger amount of ice melt in the lower part of the glacier, the station setup collapsed several times and had to be manipulated, creating discontinuities in the data acquisition (Fig. 2). The GPS data analysis is done in a network of 30–45 stations, with the MITs GAMIT/GLOBK software version 10.4 [24]. The GPS analysis is done with a large network to be able to also measure tropospheric zenith total delay (ZTD) in this highly mountainous area.

For this study, the GPS processing provides an average position evaluated over 6-h sessions. Displacements are calculated over 11 days to be comparable with TSX results. An average position is estimated over four sessions of 1 day and an other average position 11 days later. The difference between both average values is normalized by 11 days to obtain a displacement in centimeter per day. To obtain a displacement every day, this processing is realized with a sliding window with a 1-day step. To determine the errors caused by the use of average values, average standard deviations are calculated for each displacement component. On the East, North, and Up components, we obtain $\sigma_{v_E} = 4.7$ cm, $\sigma_{v_N} = 3.0$ cm, and $\sigma_{v_U} = 1.6$ cm, respectively. This average dispersion of the GPS position contributes to an error in the magnitude of the 3-D displacement rate over 11 days of 1.1 cm/day. For the comparison with the SAR 2-D displacements obtained in the ascending and descending tracks, the GPS measurements are projected in the SAR image planes. The resulting uncertainty is equal to 0.89 cm/day in ascending geometry and 0.83 cm/day in descending geometry. These uncertainty values are retained for the SAR/GPS comparisons in the following sections.

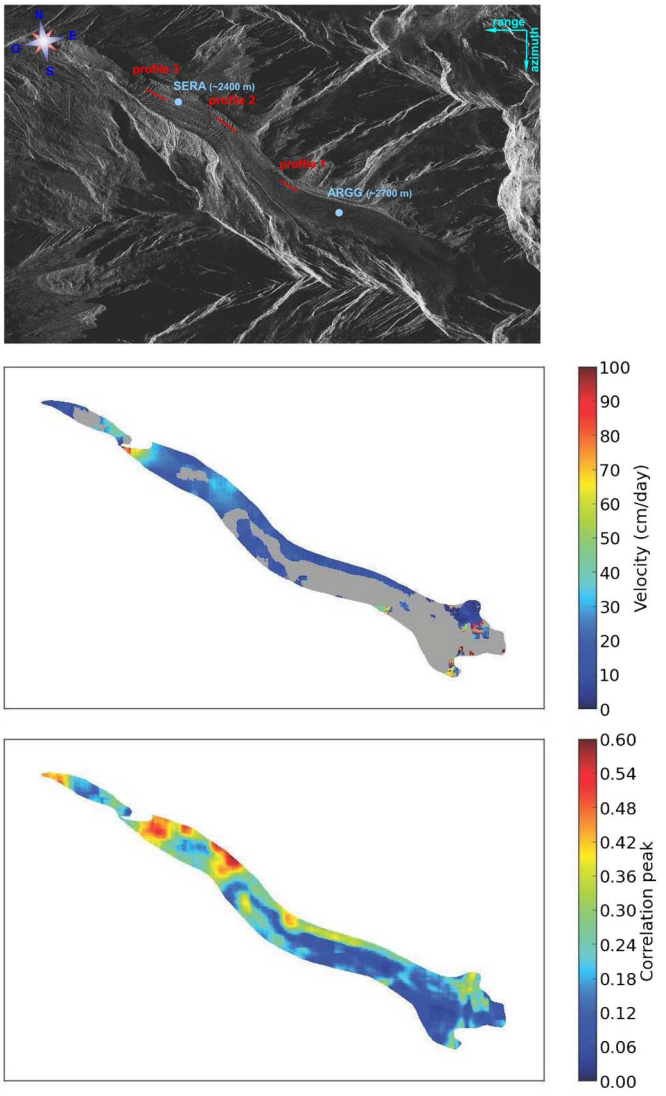

Fig. 4. TSX amplitude image of Argentière glacier in descending track (2009/08/14, 4900 × 3100 pixels); magnitude of the 2-D displacement field obtained by offset power tracking (2009/08/14–2009/08/25 pair) and associated correlation peak used to discard unreliable displacement measurements (threshold: 0.2).

III. 2-D Displacement Results

In this section, we present the results of glacier surface displacement estimated in TSX data along the two directions of the SAR images: range (LOS) and azimuth axis. They are compared with GPS measurements projected in the SAR LOS and azimuth directions.

A. Results Over Argentière Glacier

The amplitude images of the Argentière glacier are presented in both descending and ascending tracks in Figs. 4 and 5, respectively. The amplitude varies according to the surface state of the glacier, with differences between homogeneous areas made of snow, firn or ice which are free of texture, and areas containing rocks, crevasses, and seracs which create trackable features (cf. zooms in Fig. 5). The Argentière glacier surface is more visible in Fig. 4, because its main slope direction is almost in the LOS of the satellite in descending track. So, the surface of the glacier is not affected by layover areas, in spite of the surrounding high topography.

The magnitude of the 2-D displacement and the correlation peaks are illustrated in Fig. 4 for a descending pair and Fig. 5 for an ascending pair. The displacement fields obtained over the whole glacier contain magnitudes between 0 and 1.5 m/day, with large values in the upper part of the glacier which are aberrant. They are due to a poor matching during the offset power tracking process: the smooth surfaces, containing too few features as rocks or crevasses, prevent good cross correlation results. These measures can be discarded thanks to the low values of the correlation peak in this area: a threshold of 0.2 is applied to analyze only the results obtained with a sufficient level of confidence. A higher threshold value (0.4 or 0.5 as often used for optical data) would avoid some erroneous matching, but it would also discard most the correct results and make the SAR amplitude correlation useless over the glaciers

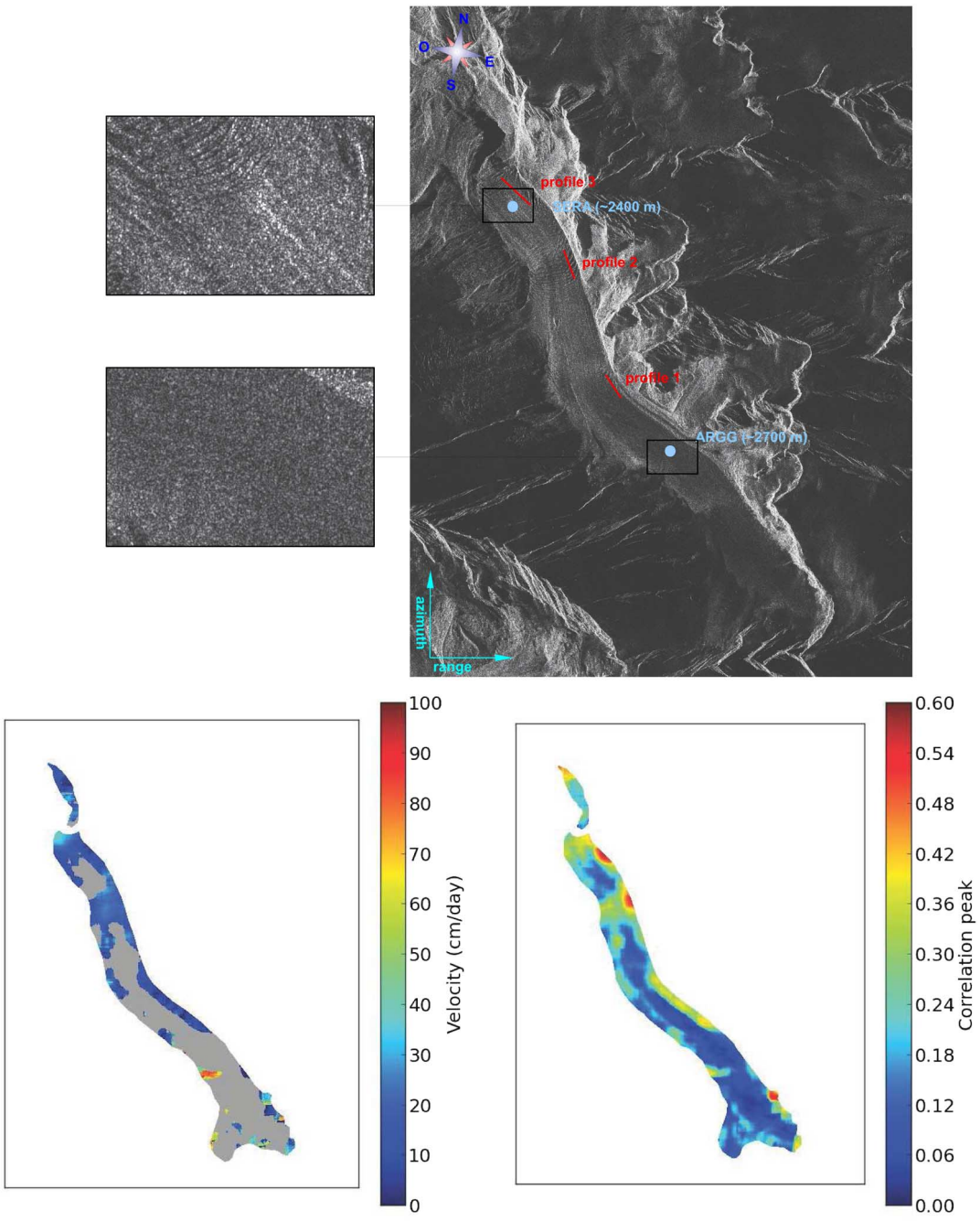

Fig. 5. TSX amplitude image of Argentière glacier in ascending track (2009/08/16, 3100 × 4100 pixels); zooms (300 × 200 pixels) around SERA and ARGG GPS stations illustrating textured and homogeneous amplitude areas corresponding to high correlation and low correlation, respectively; magnitude of the 2-D displacement field obtained by offset power tracking (2009/08/16–2009/08/27 pair) and associated correlation peak used to discard unreliable displacement measurements (threshold: 0.2).

of this area. On parts where offset power tracking gives reliable displacement values, three longitudinal profiles are extracted. The location of these profiles as well as the SERA GPS station are indicated on the amplitude images (Figs. 4 and 5) and the results are shown in Fig. 6. The glacier acceleration can be observed with slow displacements of 10 cm/day in the upper part and faster displacement of up to 30 cm/day in the lower part. The x-axis represents the distance from the upper part of the glacier, knowing that the Argentière glacier stretches over 10 km.

Fig. 7 shows the comparison between the magnitudes of the 2-D displacement obtained by offset power tracking in SAR ascending and descending geometries and the magnitudes of the GPS displacements projected in the same 2-D SAR geometry. We can observe the seasonal variability with smaller displacements in winter, when the weather is the coldest and when precipitations fall as solid snow, followed by accelerations during the spring when temperatures increase and ice melts. The GPS displacement results in Fig. 7(a) and (b) also show that intra-seasonal variabilities over 1 month is important with an

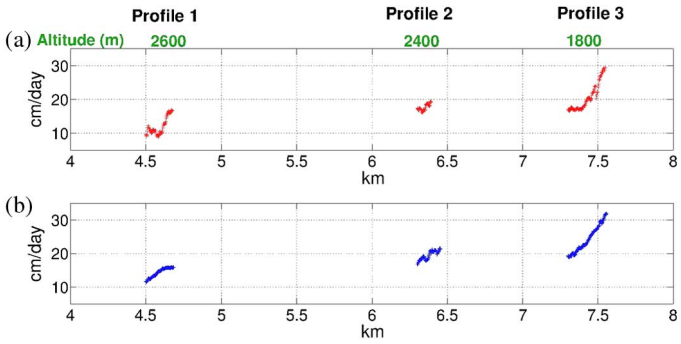

Fig. 6. Magnitude of the 2-D displacement fields computed in the SAR image planes of ascending track (2009/08/16–08/27 pair) and descending track (2009/08/14–08/25 pair) along three parts of longitudinal profiles illustrated in Figs. 4 and 5, respectively. The x-axis represents the distance from the upper part of the Argentière glacier. (a) Ascending geometry. (b) Descending geometry.

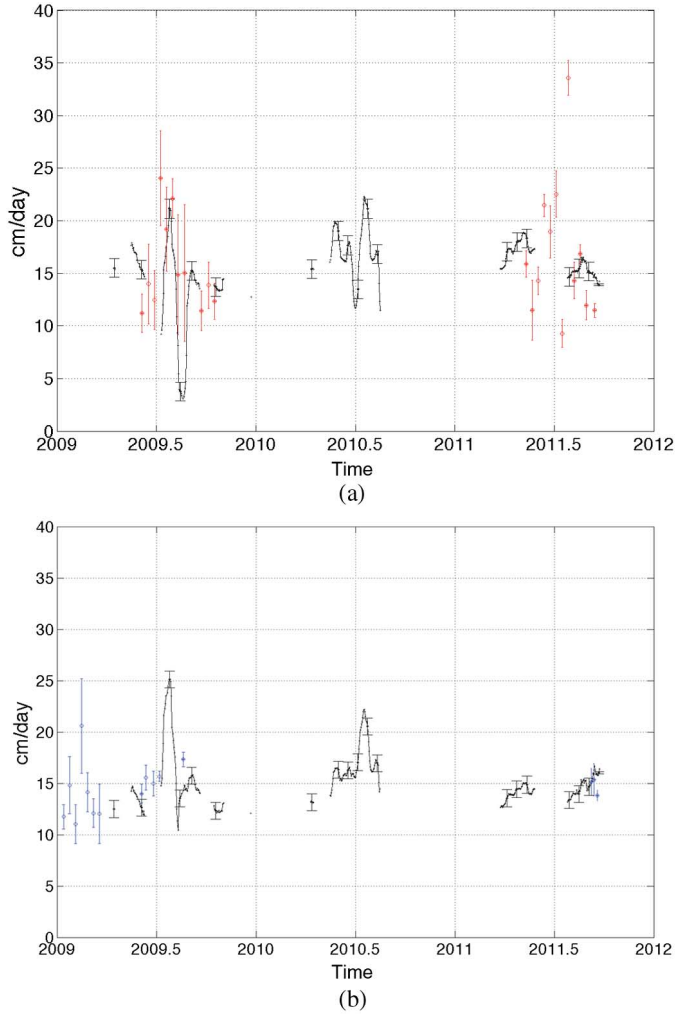

Fig. 7. Magnitude of the 2-D displacements obtained by offset power tracking over 11-day pairs in SAR ascending (in red) and descending (in blue) tracks. SAR measurements error bars are derived from the standard deviation in regions of interest near the SERA GPS station. The full circles indicate SAR results which can be compared with the available GPS measurements (in black). The GPS displacements (projected in the 2-D SAR image planes) are interpolated along the periodes of continuous acquisitions. GPS error bars are derived from the positioning dispersion and 11-day average.

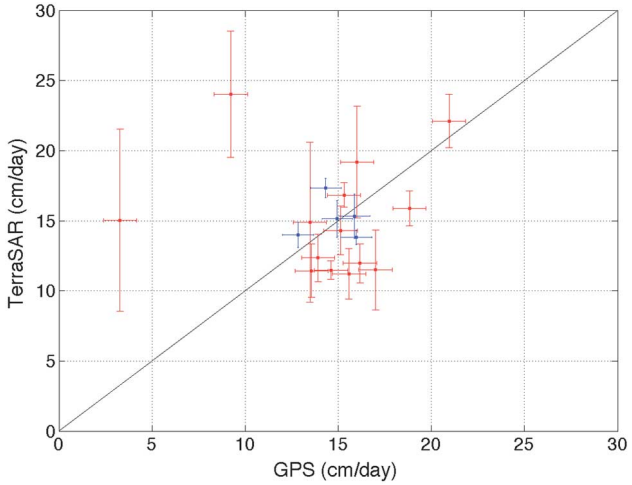

Fig. 8. Scatterplot of TerraSAR-X versus GPS measurments: magnitude of the 2-D displacement (cf. Fig. 7) for the 19 pairs (14 ascending in red, 5 descending in blue) where both data are available.

amplitude of 15 cm/day in 2009. Both sources show that the fastest displacements occur in August. During summer, the mean daily temperatures are positive on the glacier, and precipitations fall as rain. These two factors contribute to melt the glacier surface [25]. One hypothesis is that during surface melting, volumes of melt water are large enough to be drained to the ice bedrock interface. The lubricating effect of melt water leads to accelerations of the glacier [26], [27].

B. Error Analysis

To assess performances, the root mean square (rms) of the difference between the displacement magnitudes has been computed as

$$rms_{2D} = \sqrt{\frac{1}{N}\sum_{n=1}^{N}(X_{GPS}(n) - X_{SAR}(n))^2}$$

where $X_{SAR}(n)$ is the magnitude of the 2-D displacement measured in SAR image pair n, and $X_{GPS}(n)$ is the magnitude of the corresponding GPS measure projected in the LOS and azimuth plane. The rms is equal to 5.8 cm/day on the whole data set ($N = 19$ pairs), to 6.7 cm/day considering only ascending tracks ($N = 14$ pairs), and to 2.1 cm/day considering only descending tracks ($N = 5$ pairs). According to this comparison, SAR results are less precise than GPS results, but the precision, especially with descending track images, is sufficient to follow the main accelerations and decelerations of the glacier. Moreover, on textured areas, TerraSAR-X images can provide a spatial distribution of the glacier surface displacement every 11 days.

The difference between ascending and descending data may have a geometrical and a temporal explanation.

1) The main features creating the texture are the crevasses which are mostly oriented across the glacier. When they are perpendicular to the LOS, they create strong scatterers, whereas when they are perpendicular to the azimuth

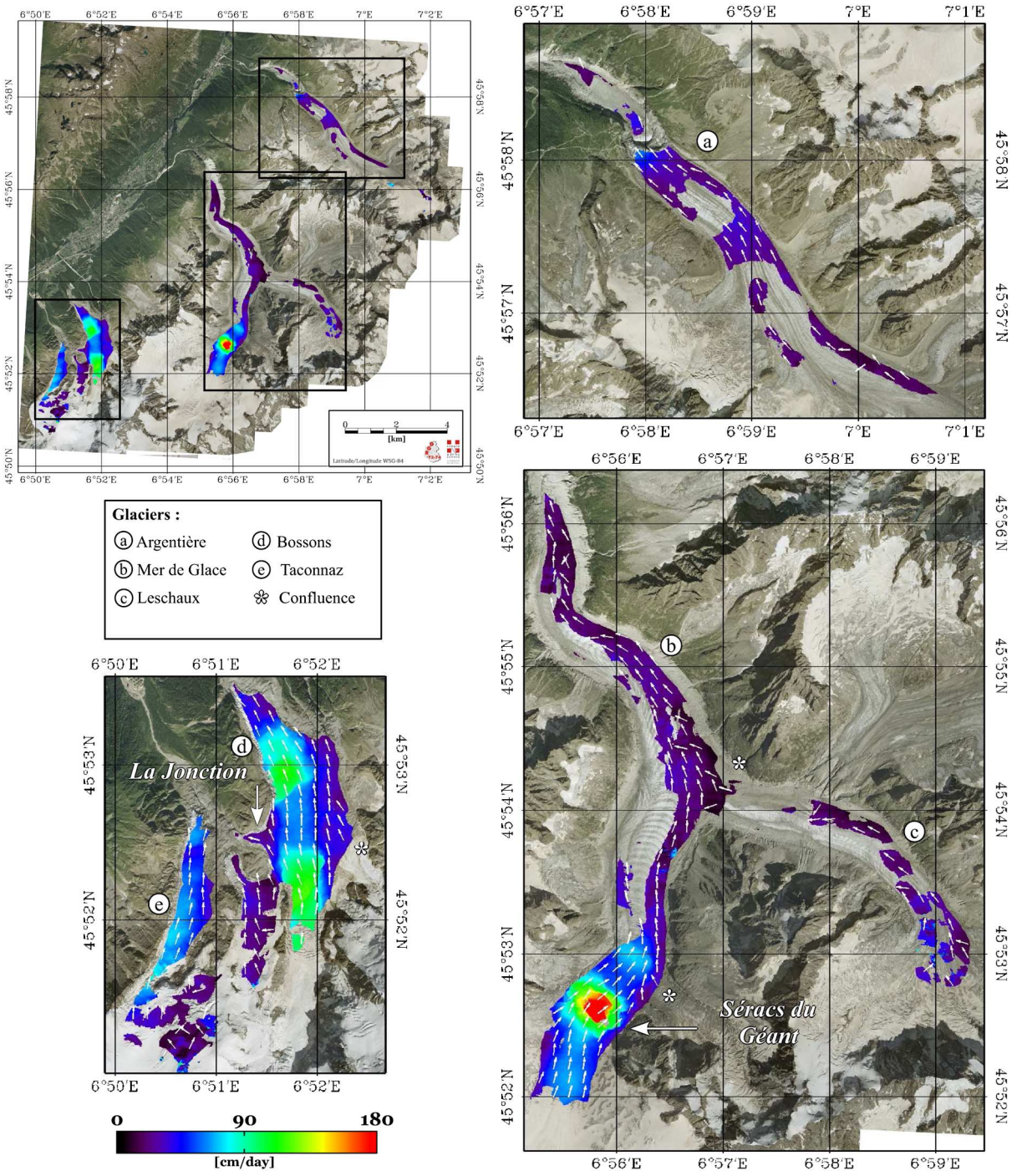

Fig. 9. 3-D displacement field on the Mont-Blanc massif, obtained by inversion of the offset power tracking results from the TSX 14/08/2009/08/14-25 pair (descending) and TSX 2009/08/16-27 pair (ascending). The colors provide the magnitude of the 3-D displacement and the arrows the orientation of the displacement in the horizontal plane.

direction (parallel to the range direction) they are less contrasted. Due to the NW-SE orientation of Argentière glacier, the crevasses are more perpendicular to the LOS in the descending tracks than in the ascending tracks (cf. Figs. 4 and 5).

2) The time of the acquisition is probably a second reason, which increases the performances in descending tracks: descending images are acquired early in the morning (5 AM GMT), whereas the ascending images are acquired at the end of the afternoon (5 PM GMT). From May to October, the glacier surface is usually free of snow below 2500 m. The surface melting and the presence of water are strongly dependent on the day illumination (sunny and cloudy) and probably creates more scattering variations between evening images than between morning images.

The results presented in Fig. 7(b) also show that the winter measurements (January–March 2009) have larger error bars than the two other data sets (summer 2009 and fall 2011). Those

winter images were acquired in dual polarization configuration for snow analysis, but the small difference in the resolution cannot explain this seasonal variation. The main difference in the results probably comes from the reduced texture due to the snow which fills up crevasses. Thanks to the wave penetration in dry snow, SAR amplitude correlation measurements are still feasible as illustrated by the results (whereas optical data cannot be used at this time of the year), but with an increased variability compared to the results obtained during the summer season on the same track.

Two other factors will affect the SAR results: the baseline between the orbits and time interval between the acquisitions. When the component of the baseline perpendicular to the LOS increases, the speckle becomes decorrelated and even the texture may be affected since the targets are seen from slightly different viewing angle. It decreases the correlation between images and may yield to less reliable results. For results presented in Figs. 4 (descending track) and 5 (ascending track), the perpendicular baselines are equal to 15 and 112 m, respectively. This may also explain that the 0.2 threshold applied on the correlation peak preserves a larger part of the glacier in the descending track. To increase the chance of using small baselines, it could be interesting to use longer intervals like 22-day pairs. When the area is changing rather fast (like on the Chamonix Mont-Blanc glaciers during the summer), the correlation after 22 or 33 days decreases and may become too low to perform reliable measurements. When the changes are limited, error could be reduced by computing displacement fields on longer intervals (the displacement signal increases compared to the pixel resolution) and by combining results obtained with different baselines and time intervals in a network strategy as in the SBAS (Small BAseline Subsets) approach [28] developed in multitemporal InSAR.

IV. 3-D Displacement Results

A. 3-D Displacement Fields in the Chamonix Mont-Blanc Valley

In this section, 3-D displacement results obtained by offset power tracking are presented. When image pairs in ascending and descending tracks are acquired over the same period, it is possible to combine 2-D results to inverse 3-D displacement fields (Fig. 3). However, image pairs are not acquired exactly at the same time. Descending track images are acquired 2 days before ascending track images. Image pairs overlap only on 9 common days. To justify our inversion, the uncertainty between the displacement on a 11-day interval, and the same displacement shifted by 2 days, is calculated, thanks to GPS data. The rms of the error is equal to 0.4 cm/day. As this value is negligible, the 3-D inversion has been applied on the five couples of ascending and descending pairs, which are available in 2009, and on the only couple available in 2011. Fig. 9 shows an example of 3-D displacement fields built from the pairs 2009/08/14–2009/08/25 in descending track and 2009/08/16–2009/08/27 in ascending track. Using the entire area covered by TSX images, we compute the displacement fields over four main glaciers of the Chamonix Mont-Blanc valley: Argentière, Mer-de-glace, Bossons, and Taconnaz. The magnitude values range between 0 and 180 cm/day. The fastest regions are located on the Mer-de-glace glacier and on the Bossons glacier; they correspond to steep icefalls leading to an acceleration of the displacement [8], [16]. The flow direction in the horizontal plane is represented by arrows on the zooms provided over the main glaciers.

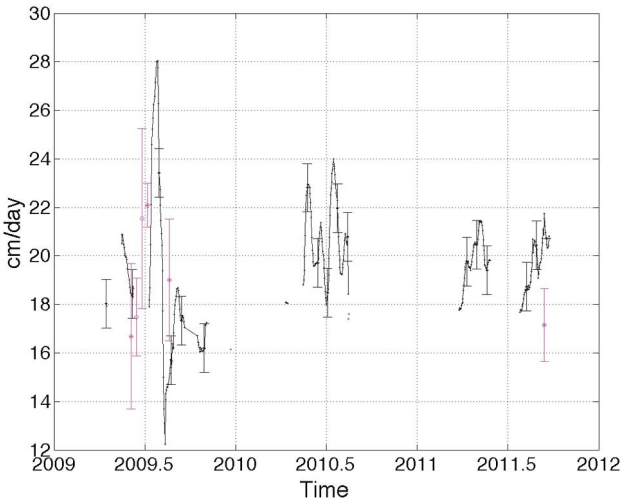

Fig. 10. Magnitude of the Argentière glacier 3-D displacement derived from TSX ascending and descending quasi-simultaneous 11-day pairs (in violet) and from the GPS station SERA (in black).

Fig. 9 also illustrates the spatial coverage obtained by the offset power tracking method. Areas of bad correlation are masked when the correlation peak is lower than 0.2 in one of the two pairs. There is no result in the upper parts of the glaciers, which are free of texture, whereas in the areas presenting crevasses or rock debris, 3-D displacement fields cover large areas like over the Mer-de-glace and the Bossons glaciers. For the Argentière glacier having a quite smooth surface, results are available only in the lower part, near crevasses, and seracs.

The comparison between the magnitudes of SAR 3-D displacements near the SERA station and GPS results is presented in Fig. 10. As for 2-D results, GPS displacement measurements highlight intra-seasonal variabilities on small time scales of 1 month. The fast acceleration followed by a very fast deceleration with an amplitude of 15 cm/day measured by the GPS in August 2009 is observed in the TSX results but with a reduced amplitude.

B. Correction of SAR Displacements for Ablation

For the comparison with the GPS results, we also computed the horizontal and vertical displacements from the 3-D displacement results. The results are presented in Table II with the magnitude, the slope and the azimuth w.r.t. North, of the glacier flow derived from the three components of the displacement vectors. The azimuth is around -50° and corresponds to the North West direction of the glacier flow. The slope is overestimated with respect to the flat surface topography of the glacier around the SERA station, probably because the Up component contains a systematic error due to ablation.

TABLE II
HORIZONTAL AND VERTICAL DISPLACEMENTS FROM TSX 3-D FIELDS MEASURED ON THE ARGENTIÈRE GLACIER NEAR THE SERA GPS STATION; MAGNITUDE, AZIMUTH W.R.T. NORTH AND SLOPE

Date	Horizontal (cm/day)	Vertical (cm/day)	Magnitude (cm/day)	Azimuth (°)	Slope (°)
2009/05/29–06/11	15.8	–5.2	16.6	–54.3	–18.2
2009/06/09–06/22	16.5	–5.7	17.5	–54.9	–19.0
2009/06/20–07/03	21.0	–4.8	21.5	–48.2	–12.8
2009/07/01–07/14	20.8	–7.6	22.1	–47.7	–20.1
2009/08/14–08/27	17.8	–6.7	19.0	–51.0	–20.6
2011/09/01–09/25	15.8	–6.7	17.2	–52.1	–22.9

TABLE III
TSX RESULTS CORRECTED FROM ABLATION VALUES AND GPS RESULTS

Date	Ablation (cm/day)	Corrected vertical (cm/day)	Corrected magnitude (cm/day)	Corrected slope (°)	GPS vertical (cm/day)	GPS magnitude (cm/day)	GPS slope (°)
2009/05/29–06/11	–2.1	–3.1	16.1	–11.1	–3.4	18.3	–10.4
2009/06/09–06/22	–3.5	–2.2	16.6	–7.5	–	–	–
2009/06/20–07/03	–3.6	–1.2	21.0	–3.2	–	–	–
2009/07/01–07/14	–4.1	–3.5	21.1	–9.5	–4.6	17.5	–15.1
2009/08/14–08/27	–6.3	–0.4	17.8	–1.3	–1.2	16.2	–4.2
2011/09/01–09/25	–4.1	–2.6	16.0	–9.3	–3.5	20.2	–9.8

The vertical component derived from SAR images contains the glacier displacement and the change of glacier elevation due to the ablation; especially in summer, ablation can create a systematic error in displacement [8]. The GPS measurements are not affected by ablation because the antenna is installed on a mast fixed over several meters in the ice.

To correct the vertical component of the SAR measurements, ablation values are estimated over TSX image intervals. The past studies already provide degree-day factor between ablation and positive degree days on Mont-Blanc massif glaciers [29]. At the altitude of the SERA station, the positive degree-day factor is equal to 0.55 cm w.e. $^{\circ}\mathrm{C}^{-1}$ on the Argentière glacier. As the water equivalent corresponds to the product of the density by the thickness of the layer, this factor is divided by the density of ice and the result is multiplied with positive degrees of the daily mean temperature to find the thickness of ice lost each day. The average thickness of lost ice layers provides the ablation in centimeter per day during intervals separating TSX image acquisitions. Ablation values and TSX results corrected from this ablation are presented in Table III. Since the comparison of SAR 3-D results with GPS results is only possible with four couples of ascending/descending pairs, it is difficult to assess the accuracy of this ablation correction. Before correction, the rms of the difference vector between SAR displacement and GPS displacement vectors is equal to 7 cm/day and the rms of the error between magnitudes is equal to 3.3 cm/day. After correction, the rms of the difference vector is equal to 6 cm/day and the rms of the error between magnitudes is equal to 3.2 cm/day. In Table III, we can observe that only the 2009/07/01–2009/07/14 and 2009/08/14–2009/08/27 couples are improved by the correction, with a significant error reduction and new slope and vertical component values closer to the GPS results.

V. CONCLUSION

In this paper, 2-D (range and azimuth) and 3-D (East, North, and Up) displacement fields obtained by offset power tracking with TerraSAR-X images are presented over Mont-Blanc massif glaciers, and more specifically over the Argentière glacier. 36 pairs of images at 11-day intervals and two pairs at 22-day intervals are processed to derive 2-D displacement fields, and six couples of ascending/descending pairs are combined to invert 3-D displacement fields on four main glaciers of the Chamonix valley. The results are compared and validated with *in situ* measurements resulting from 3 years of quasi-continuous GPS observations.

These results show the potential and limitations of SAR remote sensing to monitor the displacement of complex objects such as landslides or glaciers. In the textured areas due to crevasses and stone accumulation, usually the most changing and dangerous parts, high-resolution SAR data allow 2-D and even 3-D displacement fields to be derived, which can be useful to constrain ice flow models at the surface. However, the temporal sampling of SAR spaceborne data is still limited by the orbit cycles, 11 days for the TerraSAR-X data analyzed in this paper. GPS data, which can be collected only at a few points, allow continuous measurements useful to identify sudden accelerations and correlate them with meteorological events. We have shown that both measurements are feasible, despite heavy processing chains and GPS maintenance difficulties in such environment, and that the results are consistent.

In future works, such processing will be automatized to benefit from the regular acquisitions of the new SAR satellite missions. With regular observations, it becomes possible to build more image pairs (multiple of 4 days with the four Cosmo-SkyMed satellites, multiple of 6 days when the

two Sentinel-1 satellites will be operational) and to invert time series of displacement fields in order to benefit from the redundancy to reduce the uncertainty and fill-up missing measurements. The reconstruction of 3-D displacement fields by combining ascending and descending overlapping pairs can also be performed more often and a joint inversion of ascending and descending displacement time series should be possible to retrieve directly the 3-D displacement evolution.

ACKNOWLEDGMENT

The authors wish to thank the German Space Agency (DLR) for providing the TerraSAR-X data (Project MTH0232) and the Régie de Gestion des Pays de Savoie (RGD-73/74) for the access to the RIS 73-74 database. They would also like to thank the anonymous reviewers for providing precise comments and useful advice on this paper.

REFERENCES

[1] W. Haeberli, M. Hoelzle, F. Paul, and M. Zemp, "Integrated monitoring of mountain glaciers as key indicators of global climate change: The european alps," *Ann. Glaciol.*, vol. 46, no. 1, pp. 150–160, 2007.

[2] I. Bartholomew *et al.*, "Seasonal evolution of subglacial drainage and acceleration in a Greenland outlet glacier," *Nat. Geosci.*, vol. 3, no. 6, pp. 408–411, 2010.

[3] T. Redpath, P. Sirguey, S. Fitzsimons, and A. Kaab, "Accuracy assessment for mapping glacier flow velocity and detecting flow dynamics from ASTER satellite imagery: Tasman glacier, New Zealand," *Remote Sens. Environ.*, vol. 133, pp. 90–101, 2013.

[4] F. Paul, A. Kaab, M. Maisch, T. Kellenberger, and W. Haeberli, "The new remote-sensing-derived swiss glacier inventory: I. methods," *Ann. Glaciol.*, vol. 34, no. 1, pp. 355–361, 2002.

[5] J. Gao and Y. Liu, "Applications of remote sensing, GIS and GPS in glaciology: A review," *Prog. Phys. Geogr.*, vol. 25, no. 4, pp. 520–540, 2001.

[6] A. Kääb, "Monitoring high-mountain terrain deformation from repeated air-and spaceborne optical data: Examples using digital aerial imagery and ASTER data," *ISPRS J. Photogramm. Remote Sens.*, vol. 57, no. 1, pp. 39–52, 2002.

[7] A. Kääb, "Combination of SRTM and repeat ASTER data for deriving alpine glacier flow velocities in the Bhutan Himalaya," *Remote Sens. Environ.*, vol. 94, no. 4, pp. 463–474, 2005.

[8] E. Berthier *et al.*, "Surface motion of mountain glaciers derived from satellite optical imagery," *Remote Sens. Environ.*, vol. 95, no. 1, pp. 14–28, 2005.

[9] T. Strozzi, A. Kääb, and R. Frauenfelder, "Detecting and quantifying mountain permafrost creep from in situ inventory, space-borne radar interferometry and airborne digital photogrammetry," *Int. J. Remote Sens.*, vol. 25, no. 15, pp. 2919–2931, 2004.

[10] A. Luckman, T. Murray, and T. Strozzi, "Surface flow evolution throughout a glacier surge measured by satellite radar interferometry," *Geophys. Res. Lett.*, vol. 29, no. 23, pp. 10–1, 2002.

[11] J. Zhou *et al.*, "Movement estimate of the Dongkemadi glacier on the Qinghai–Tibetan plateau using L-band and C-band spaceborne SAR data," *Int. J. Remote Sens.*, vol. 32, no. 22, pp. 6911–6928, 2011.

[12] E. Trouvé *et al.*, "Combining airborne photographs and spaceborne SAR data to monitor temperate glaciers: Potentials and limits," *IEEE Trans. Geosci. Remote Sens.*, vol. 45, no. 4, pp. 905–924, Apr. 2007.

[13] T. Strozzi, A. Luckman, T. Murray, U. Wegmuller, and C. L. Werner, "Glacier motion estimation using SAR offset-tracking procedures," *IEEE Trans. Geosci. Remote Sens.*, vol. 40, no. 11, pp. 2384–2391, Nov. 2002.

[14] J. Mittermayer, S. Wollstadt, P. Prats-Iraola, and R. Scheiber, "The TerraSAR-X staring spotlight mode concept," *IEEE Trans. Geosci. Remote Sens.*, vol. 52, no. 6, pp. 3695–3706, Jun. 2014.

[15] H. Rott, F. Müller, T. Nagler, and D. Floricioiu, "The imbalance of glaciers after disintegration of Larsen-B ice shelf, Antarctic Peninsula," *Cryosphere*, vol. 5, no. 1, pp. 125–134, 2011.

[16] R. Fallourd *et al.*, "Monitoring temperate glacier displacement by multi-temporal TerraSAR-X images and continuous GPS measurements," *IEEE J. Sel. Topics Appl. Earth Observ. Remote Sens.*, vol. 4, no. 2, pp. 372–386, 2011.

[17] T. Nagler *et al.*, "Retrieval of 3D-glacier movement by high resolution X-band SAR data," in *Proc. IEEE Int. Geosci. Remote Sens. Symp. (IGARSS)*, 2012, pp. 3233–3236.

[18] D. J. Quincey *et al.*, "Ice velocity and climate variations for Baltoro glacier, Pakistan," *J. Glaciol.*, vol. 55, no. 194, pp. 1061–1071, 2009.

[19] T. Landes *et al.*, "Monitoring temperate glaciers by high resolution PolInSAR data: First analysis of Argentière E-SAR acquisitions and in-situ measurements," in *Proc. IEEE Int. Geosci. Remote Sens. Symp. (IGARSS)*, Barcelona, Spain, Jul. 2007, p. CDROM [Online]. Available: http://hal.archives-ouvertes.fr/hal-00164163

[20] F. Vernier *et al.*, "Fast correlation technique for glacier flow monitoring by digital camera and space-borne SAR images," *EURASIP J. Image Video Process.*, vol. 2011, no. 1, pp. 1–15, 2011.

[21] I. Pétillot *et al.*, "Radar-coding and geocoding lookup tables for the fusion of GIS and SAR data in mountain areas," *IEEE Geosci. Remote Sens. Lett.*, vol. 7, no. 2, pp. 309–313, Apr. 2010.

[22] K. Nakamura, K. Doi, and K. Shibuya, "Estimation of seasonal changes in the flow of Shirase glacier using JERS-1/SAR image correlation," *Polar Sci.*, vol. 1, no. 2, pp. 73–83, 2007.

[23] Y. Yan, "*Fusion de mesures de d éplacement issues d'imagerie sar: Application aux modélisations séismo-volcaniques*," Ph.D. dissertation, Université de Savoie, Chambéry, France, 2012.

[24] T. A. Herring, R. W. King, and S. C. McClusky, "Introduction to GAMIT/GLOBK, Release 10.4," Dept. Earth, Atmospheric, and Planetary Sciences, Massachusetts Inst. Technology, 2010.

[25] B. Anderson *et al.*, "Climate sensitivity of a high-precipitation glacier in New Zealand," *J. Glaciol.*, vol. 56, no. 195, pp. 114–128, 2010.

[26] P. Nienow *et al.*, "Hydrological controls on diurnal ice flow variability in valley glaciers," *J. Geophys. Res.: Earth Surface (2003–2012)*, vol. 110, no. F4, 2005.

[27] A. Shepherd *et al.*, "Greenland ice sheet motion coupled with daily melting in late summer," *Geophys. Res. Lett.*, vol. 36, no. 1, 2009.

[28] F. Casu, A. Manconi, A. Pepe, and R. Lanari, "Deformation time-series generation in areas characterized by large displacement dynamics: The SAR amplitude pixel-offset SBAS technique," *IEEE Trans. Geosci. Remote Sens.*, vol. 49, pp. 2752–2763, Jul. 2011.

[29] C. Vincent, "Influence of climate change over the 20th century on four french glacier mass balances," *J. Geophys. Res.: Atmos. (1984–2012)*, vol. 107, no. D19, pp. ACL–4, 2002.

Fanny Ponton was born in 1987, in Sainte-Marie-aux-Mines, France. She received the Master degree from the School and Observatory of Earth Sciences (EOST) Strasbourg, France, in 2010, and the Ph.D. degree in geophysics from the University of Grenoble, Grenoble, France, in 2013, for her works on the monitoring of glacier flow by space geodetic techniques. She has prepared these works at the Institut des Sciences de la Terre (ISTerre), Université Joseph Fourier, Grenoble, at Grenoble Image Parole Signal Automatique Laboratory (GIPSA-lab), and at the Laboratoire d'Informatique, Systèmes, Traitement de l'Information et de la Connaissance (LISTIC), Annecy.

Emmanuel Trouvé (M'00–SM'10) received the Engineering degree in electrical engineering from the Ecole Nationale Supérieure de Techniques Avancées, Paris, France, in 1990, the Ph.D. degree in signal and image processing from the Ecole Nationale Supérieure des Télécommunications, Paris, France, in 1996, and the "Habilitation à Diriger des Recherches" degree from the Université de Savoie, Chambéry, France, in 2006.

From 1996 to 1998, he worked with Thomson Marconi Sonar in Underwater Acoustic and Signal Processing. He has been working as an Associate Professor with the University of Savoie, Polytech Annecy-Chambéry, Laboratoire d'Informatique, Systèmes, Traitement de l'Information et de la Connaissance (1998–2008), then as a Professor of signal processing and computer vision. He has been coordinating several Research Projects, including two National Multilaboratory Projects supported by the French Research Agency: MEGATOR (Monitoring the Evolution of Alpine Glaciers by Optical and Radar Remote Sensing, 2004–2007) and EFIDIR (Extraction and Fusion of Information for Displacement measurement from SAR Imagery, 2008–2011). His research interests include synthetic aperture radar (SAR) image processing and data fusion in remote sensing.

Prof. Trouvé is the Treasurer of the French Chapter of IEEE GEOSCIENCE AND REMOTE SENSING SOCIETY.

Michel Gay received the Engineering degree in microelectronics from the Institute of Engineering Sciences of Montpellier, in 1987, and the Ph.D. degree in physics from the University Joseph Fourier, Grenoble, France, in 1999.

From 1979 to 1985, he was a Technician with the Institute of Botany and Teacher with the Academy of Montpellier. From 1988 to 2003, he was with Cemagref Grenoble, where he worked as an Electronics Engineer with the research unit of Torrential Erosion Snow and Avalanche. Since 2004, he has been employed as a Research Engineer with the CNRS Laboratory "Grenoble Image Parole Signal Automatique," Saint Martin D'Heres. He was the Co-Leader of four National Scientific projects and three European projects. His research interest includes image processing synthetic aperture radar (SAR), applied to the monitoring of snow and glaciers.

Andrea Walpersdorf received the Master degree in geophysics from the Institute for Geophysics and Meteorology of Cologne, Cologne, Germany, in 1993, and the Ph.D. degree in geophysics from Ecole Normale Supérieure and Institut de Physique du Globe, Paris, France, in 1997.

In 2000, she was employed as an Assistant Observatory Physicist with Grenoble Observatory for Universe Sciences (OSUG), carrying out her research work at the Institut des Sciences de la Terre (ISTerre), Grenoble, France. In 2008, she passed her "Habilitation aè Diriger des Recherches" (HDR). Since 2010, she has been Observatory Physicist with OSUG/ISTerre Grenoble. She is responsible for the French National Permanent GNSS (Global Navigation Satellite System) network for research purposes (RENAG) from 2010. Her research interests include GNSS geodesy for high precision positioning, applied to crustal deformation, meteorology, and glaciology.

Renaud Fallourd was born in 1983. He received the M.S. degree in physical methods in remote sensing from the University Paris Didero, Paris, France, in 2008, and the Ph.D. degree from the University of Grenoble in 2012, prepared at the University of Savoie, Polytech Annecy-Chambéry, Laboratoire d'Informatique, Systèymes, Traitement de l'Information et de la Connaissance (LISTIC) in collaboration with the Laboratoire Traitement et Communication de l'Information (LTCI), Telecom ParisTech, Paris, France.

His research interests include SAR image processing and photogrammetry, applied to glacier monitoring.

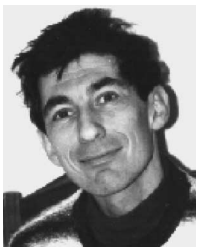

Jean-Marie Nicolas received the M.S. degree from the Ecole Normale Superieure de Saint Cloud, Paris, France, in 1979, and the Ph.D. degree in physics from the University of Paris XI, Paris, France, in 1982.

He was a Research Scientist with the Laboratoire d'Electronique Philips in medical imaging and was then with Thomson CSF, working in signal and image processing. Currently, he is a Professor with the Département TSI, Telecom ParisTech, Paris, France. His research interests include radar imaging.

Flavien Vernier was born in France, in 1977. He received the Master and Ph.D. degrees in computer science from the University of Franche-Compté, Besançon Cedex, France, in 2001 and 2004, respectively, prepared at the LIFC laboratory.

He was a Visiting Assistant Professor from 2005 to 2006 with the AlGorille Team of the LORIA Laboratory, Vanduvre-ls-Nancy, France. Since September 2006, he has been an Assistant Professor with the LISTIC Computer Science Laboratory, University of Savoie, Chambéry, France. His research interests include parallel and distributed computation, numerical algorithms and image processing.

Jean-Louis Mugnier was born in 1957. He received the Engineering degree in mining technics and the Ph.D. degree in tectonophysics from the University of Joseph Fourier, Grenoble, France, in 1980 and 1984, respectively.

Since 1985, he has been with the Centre National de la Recherche Scientifique (CNRS), where he has been a Research Director since 1994. Since 1990, he has been a Manager of the "measure and modelling of the recent deformation" team of the Laboratoire de Géodynamique des Chanes Alpines (LGCA), Grenoble Cedex, France. His research interests include active tectonics and fast erosion processes measurement.

Dr. Mugnier is a member of the Geological Society of America (GSA).

Bibliographie

[1] Fanglin Yang, Arun Kumar, Wanqiu Wang, Hann-Ming Henry Juang, and Masao Kanamitsu. Snow-albedo feedback and seasonal climate variability over North America. *Journal of Climate*, 14(22) :4245–4248, 2001.

[2] Teruo Aoki. Effects of snow physical parameters on shortwave broadband albedos. *Journal of Geophysical Research*, 108(D19), 2003.

[3] Roberta Pirazzini. Surface albedo measurements over Antarctic sites in summer. *Journal of Geophysical Research*, 109(D20), 2004.

[4] Mark G. Flanner and Charles S. Zender. Linking snowpack microphysics and albedo evolution. *Journal of Geophysical Research*, 111(D12), 2006.

[5] Michel Gay, Michel Fily, Christophe Genthon, Massimo Frezzotti, Hans Oerter, and Jan-Gunnar Winther. Snow grain-size measurements in Antarctica. *Journal of Glaciology*, 48(163) :527–535, 2002.

[6] Colbeck S.C. The layered character of snow covers. *Review of Geophysics*, 1991.

[7] Lesaffre et al. Objective determination of snow-grain characteristics from images. 1998.

[8] Thiel. *Les distances de chanfrein en analyse d images : fondements et applications.* PhD thesis, Université Joseph Fourier, September 1994.

[9] S. Surdyk and M. Fily. Comparison of the passive microwave spectral signature of the antarctic ice sheet with ground traverse data. *Annals of Glaciology*, 1993.

[10] Pirazzini et al. Snow grain size measurements in Dronning Maud Land, Antarctica, 2013.

[11] Leppanen L. Comparison of visual grain size and SSA of snow, 2013.

[12] R. Essery, E. Martin, H. Douville, A. Fernandez, and E. Brun. A comparison of four snow models using observations from an alpine site. *Climate Dynamics*, 15(8) :583–593, 1999.

[13] J.-C. Gallet, Florent Domine, C. S. Zender, and Ghislain Picard. Measurement of the specific surface area of snow using infrared reflectance in an integrating sphere at 1310 and 1550 nm. *The Cryosphere*, 3(2) :167–182, 2009.

[14] L. Arnaud, G. Picard, N. Champollion, Florent Domine, J. C. Gallet, E. Lefebvre, M. Fily, and J. M. Barnola. Measurement of vertical profiles of snow specific surface area with a 1 cm resolution using infrared reflectance : instrument description and validation. *Journal of Glaciology*, 57(201) :17–29, 2011.

[15] Florent Domine. Transformations of Snow at the Earth Surface and its Climatic and Environmental Consequences. In *Encyclopedia of Snow, Ice and Glaciers*, pages 1196–1203. Springer, 2014.

[16] Stammes K. at al. Numerically stable algorithm for discrete-ordinate-method radiative transfer in multiple scattering and emitting layered media. 1988.

[17] N. Calonne, C. Geindreau, F. Flin, S. Morin, B. Lesaffre, S. Rolland du Roscoat, and P. Charrier. 3-D image-based numerical computations of snow permeability : links to specific surface area, density, and microstructural anisotropy. *The Cryosphere*, 6(5) :939–951, September 2012.

[18] Laurent Arnaud, Michel Gay, Jean-Marc Barnola, and Paul Duval. Imaging of firn and bubbly ice in coaxial reflected light : a new technique for the characterization of these porous media. *Journal of Glaciology*, 44(147) :pp–326, 1998.

[19] AJ GOW. Restraints on thin section analysis of grain growth in unstrained polycrystalline ice. *Le Journal de Physique Colloques*, 48(C1) :C1–277, 1987.

[20] Arnaud Laurent. *Modélisation de la transformation de la neige en glace à la surface des calootes polaires : étude du transport des gaz dans ces milieux poreux.* PhD thesis, Université Joseph Fourier-Grenoble, 1997.

[21] Gay M. and J. Weiss. Automatic reconstruction of polycrystalline ice microstructure froIll image analysis : application to the EPICA ice core at Dome Concordia, Antarctica. *Journal of Glaciology*, 1999.

[22] Weiss, J. Vidot, M. Gay, L. Arnaud, P. Duval, and J.R. Petit. Dome Concordia ice microstructure : impurities effect on grain growth. *Annals of Glaciology*, 2002.

[23] L. Arnaud, J. Weiss, M. Gay, and P. Duval. Shallow-ice microstructure at Dome Concordia Antarctica. *Annals of Glaciology*, 2000.

[24] Duval and C. Lorius. Crystal size and climatic record down to the last ice age from Antarctic ice. *Earth and Planetary Science Letters*, 48 :59–64, 1980.

[25] H. V. Atkinson. An Overview of Grain Growth Theories for Pure Single Phase Systems. Technical report, DTIC Document, 1986.

[26] Ralph et al. The effects of particles and and solutes on grain boudary migration and grain growth. In *Materials Science Forum*, volume 94-96, pages 129–140, 1992.

[27] G. Durand, J. Weiss, V. Lipenkov, J. M. Barnola, G. Krinner, F. Parrenin, B. Delmonte, C. Ritz, P. Duval, R. Röthlisberger, and M. Bigler. Effect of impurities on grain growth in cold ice sheets. *Journal of Geophysical Research*, 111(F1), 2006.

[28] Rémy F., Testut L., and Legrésy B. Random fluctuations of snow accumulation over antarctica and their relation to sea level change. *Climate Dynamics*, 19(3-4) :267–276, July 2002.

[29] Hubert Gallée, Gilbert Guyomarc'h, and Eric Brun. Impact of snow drift on the Antarctic ice sheet surface mass balance : possible sensitivity to snow-surface properties. *Boundary-Layer Meteorology*, 99(1) :1–19, 2001.

[30] Massimo Frezzotti, Michel Pourchet, Onelio Flora, Stefano Gandolfi, Michel Gay, Stefano Urbini, Christian Vincent, Silvia Becagli, Roberto Gragnani, Marco Proposito, Mirko Severi, Rita Traversi, Roberto Udisti, and Michel Fily. New estimations of precipitation and surface sublimation in East Antarctica from snow accumulation measurements. *Climate Dynamics*, 23(7-8) :803–813, December 2004.

[31] J. P. F. Fortuin and J. Oerlemans. Parameterization of the annual surface temperature and mass balance of Antarctica. *Ann. Glaciol*, 14(7), 1990.

[32] Giovinetto M. B. Dependenceof Antarctic SurfaceMass Balanceon Temperature, Elevation, and Distance to Open Ocean. *Journal of Geophysical Research*, pages 3517–3531, 1990.

[33] Frezzotti et al. Snow dunes and glazed surfaces in Antarctica : new field and remote sensing data. *Annals of Glaciology*, 34, 2002.

[34] David G. Vaughan, Jonathan L. Bamber, Mario Giovinetto, Jonathan Russell, and A. Paul R. Cooper. Reassessment of net surface mass balance in Antarctica. *Journal of Climate*, 12(4) :933–946, 1999.

[35] Stuart. Glaciology, Victoria Land Traverse, l959-6o. Research, The ohio state University, 1961.

[36] *A Stratigraphic Method of Determining the Snow Accumulation Rate at Plateau Station, Antarctica, and Application to South Pole Queen Maud Land Traverse 2, 1965.* American Geophysical Union, 1971.

[37] D. Verfaillie, M. Fily, E. Le Meur, O. Magand, B. Jourdain, L. Arnaud, and V. Favier. Snow accumulation variability derived from radar and firn core data along a 600 km transect in Adelie Land, East Antarctic plateau. *The Cryosphere*, 6 :1345–1358, 2012.

[38] Massimo Frezzotti, Michel Pourchet, Onelio Flora, Stefano Gandolfi, Michel Gay, Stefano Urbini, Christian Vincent, Silvia Becagli, Roberto Gragnani, Marco Proposito, and others. Spatial and temporal variability of snow accumulation in East Antarctica from traverse data. *Journal of glaciology*, 51(172) :113–124, 2005.

[39] Emmanuel Trouve, Gabriel Vasile, Michel Gay, Lionel Bombrun, Pierre Grussenmeyer, Tania Landes, Jean-Marie Nicolas, Philippe Bolon, Ivan Petillot, Andreea Julea, Lionel Valet, Jocelyn Chanussot, and Mathieu Koehl. Combining Airborne Photographs and Spaceborne SAR Data to Monitor Temperate Glaciers : Potentials and Limits. *IEEE Transactions on Geoscience and Remote Sensing*, 45(4) :905–924, April 2007.

[40] Bombrun L. Thèse, Grenoble, October 2008.

[41] S. H. Zisk. A new, Earth-based radar technique for the measurement of lunar topography. *The moon*, 4(3-4) :296–306, 1972.

[42] Howard A Zebker and Richard M Goldstein. Topographic mapping from interferometric synthetic aperture radar observations. *Journal of Geophysical Research : Solid Earth (1978–2012)*, 91(B5) :4993–4999, 1986.

[43] Ian R. Joughin, Ronald Kwok, and Mark A. Fahnestock. Interferometric estimation of three-dimensional ice-flow using ascending and descending passes. *Geoscience and Remote Sensing, IEEE Transactions on*, 36(1) :25–37, 1998.

[44] Niels Reeh, Johan Jacob Mohr, Søren Nørvang Madsen, Hans Oerter, and Niels S. Gundestrup. Three-dimensional surface velocities of Storstrømmen glacier, Greenland, derived from radar interferometry and ice-sounding radar measurements. *Journal of Glaciology*, 49(165) :201–209, 2003.

[45] EJ Rignot. Fast recession of a West Antarctic glacier. *Science*, 281(5376) :549–551, 1998.

[46] A. L. Gray, K. E. Mattar, P. W. Vachon, R. Bindschadler, K. C. Jezek, R. Forster, and J. P. Crawford. InSAR results from the RADARSAT Antarctic Mapping Mission data : estimation of glacier motion using a simple registration procedure. In *Geoscience and Remote Sensing Symposium Proceedings, 1998. IGARSS'98. 1998 IEEE International*, volume 3, pages 1638–1640. IEEE, 1998.

[47] Johan J Mohr, Niels Reeh, and Soren N Madsen. Three-dimensional glacial flow and surface elevation measured with radar interferometry. *Nature*, 391(6664) :273–276, 1998.

[48] Massonet D. Radar Interferometry : Limits and Potential. *IEEE Geoscience and Remote Sensing*, 1993.

[49] Emmanuel Trouve, J.-M. Nicolas, and Henri Maitre. Improving phase unwrapping techniques by the use of local frequency estimates. *Geoscience and Remote Sensing, IEEE Transactions on*, 36(6) :1963–1972, 1998.

[50] L. Bombrun, M. Gay, E. Trouve, G. Vasile, and J. Mars. DEM Error Retrieval by Analyzing Time Series of Differential Interferograms. *IEEE Geoscience and Remote Sensing Letters*, 6(4) :830–834, October 2009.

[51] In *Synthetic Aperture Radar (EUSAR), 2008 7th European Conference on*, pages 1–4. VDE, 2008.

[52] R. Touzi, R.K. Raney, and F. Charbonneau. On the use of permanent symmetric scatterers for ship characterization. *IEEE Transactions on Geoscience and Remote Sensing*, 42(10) :2039–2045, October 2004.

[53] R. Touzi. Target Scattering Decomposition in Terms of Roll-Invariant Target Parameters. *IEEE Transactions on Geoscience and Remote Sensing*, 45(1) :73–84, January 2007.

[54] J.-P. Cocquerez et S. Philipp. *Analyse d'images : filtrage et segmentation.* Masson, 1995.

[55] J.-M. Beaulieu and R. Touzi. Segmentation of textured polarimetric SAR scenes by likelihood approximation. *IEEE Transactions on Geoscience and Remote Sensing*, 42(10) :2063–2072, October 2004.

[56] C. Tison, J.-M. Nicolas, F. Tupin, and H. Maître. A New Statistical Model for Markovian Classification of Urban Areas in High-Resolution SAR Images. *IEEE Transactions on Geoscience and Remote Sensing*, 42(10) :2046–2057, October 2004.

[57] J.-M. Beaulieu and R. Touzi. Segmentation of Textured Polarimetric SAR Scenes by Likelihood Approximation. *IEEE Transactions on Geoscience and Remote Sensing*, 42(10) :2063–2072, 0ctober 2004.

[58] L. M. Novak, M. C. Burl, R. D. Chaney, and G. J. Owirka. Optimal processing of polarimetric synthetic-aperture radar imagery. *The Lincoln Laboratory Journal,*, 3 :273–290, 1990.

[59] Yongjian Yu, Andrea Torre, and Shunji Huan. Partially correlated K-distribution for multilook polarimetric SAR imagery. In *Geoscience and Remote Sensing Symposium, 1996. IGARSS'96.'Remote Sensing for a Sustainable Future.', International*, volume 1, pages 60–62. IEEE, 1996.

[60] L. M. Novak. Target detection studies using fully polarimetric data collected by the Lincoln Laboratory MMW SAR'. In *IEE CONFERENCE PUBLICATION*, pages 167–167. INSTITUTION OF ELECTRICAL ENGINEERS, 1992.

[61] A. Lopès and F. Séry. Optimal Speckle Reduction for the Product Model in Multilook Polarimetric SAR Imagery and the Wishart Distribution. *IEEE Transactions on Geoscience and Remote Sensing*, 35(3) :632–647, 1997.

[62] L. Bombrun and J.-M. Beaulieu. Fisher Distribution for Texture Modeling of Polarimetric SAR Data. *IEEE Geoscience and Remote Sensing Letters*, 5(3), July 2008.

[63] L. Bombrun and J.-M. Beaulieu. Segmentation of Polarimetric SAR Data Based on the Fisher Distribution for Texture Modeling. In *Geoscience and Remote Sensing, IGARSS '08, Boston, USA*, 2008.

[64] J-M. Nicolas. Application de la Transformée de Mellin : Étude des Lois Statistiques de l'Imagerie Cohérente. In *Rapport de recherche, 2006D010*, 2006.

[65] Lionel Bombrun, Gabriel Vasile, Michel Gay, and Felix Totir. Hierarchical segmentation of polarimetric SAR images using heterogeneous clutter models. *Geoscience and Remote Sensing, IEEE Transactions on*, 49(2) :726–737, 2011.

[66] G. Vasile, J.-P. Ovarlez, F. Pascal, and C. Tison. Coherency Matrix Estimation of Heterogeneous Clutter in High Resolution Polarimetric SAR Images. *IEEE Transactions on Geoscience and Remote Sensing*, 48(4) :1809 – 1826, 2010.

[67] F. Pascal, J. P. Ovarlez, P. Forster, and P. Larzabal. Constant false alarm rate detection in spherically invariant random processes. In *European Signal Processing Conference, Vienna, Austria*, pages 2143–2146, 2004.

[68] E. Conte, A. DeMaio, and G. Ricci. Recursive estimation of the covariance matrix of a compound-Gaussian process and its application to adaptive CFAR detection. *IEEE Transactions on Image Processing*, 50(8) :1908–1915, 2002.

[69] F. Gini and M. V. Greco. Covariance matrix estimation for CFAR detection in correlated heavy tailed clutter. *Signal Processing*, 82(12) :1847–1859, 2002.

[70] K.T. Fang, S. Kotz, and K.W. Ng. *Symmetric Multivariate and Related Distributions*. Chapman & Hall, London, 1990.

[71] S. Zozor and C. Vignat. Some Results on the Denoising Problem in the Elliptically Distributed Context. *IEEE Transactions on Signal Processing*, 58(1) :134–150, 2010.

[72] F. Pascal, Y. Chitour, J. P. Ovarlez, P. Forster, and P. Larzabal. Covariance Structure Maximum-Likelihood Estimates in Compound Gaussian Noise : Existence and Algorithm Analysis. *IEEE Transactions on Signal Processing*, 56(1) :34–48, 2008.

[73] F. Pascal, P. Forster, J. P. Ovarlez, and P. Larzabal. Performance Analysis of Covariance Matrix Estimates in Impulsive Noise. *IEEE Transactions on Signal Processing*, 56(6) :2206–2216, 2008.

[74] J.S. Lee, D.L. Schuler, R.H. Lang, and K.J. Ranson. K-Distribution for Multi-Look Processed Polarimetric SAR Imagery. In *Geoscience and Remote Sensing, IGARSS '94, Pasadena, California, United States*, pages 2179–2181, 1994.

[75] C.C. Freitas, A.C. Frery, and A.H. Correia. The Polarimetric G Distribution for SAR Data Analysis. *Environmetrics*, 16 :13–31, 2005.

[76] L. Bombrun, G. Vasile, M. Gay, and F. Totir. Hierarchical Segmentation of Polarimetric SAR Images Using Heterogeneous Clutter Models. *IEEE Transactions on Geoscience and Remote Sensing*, 2010.

[77] O. Harant. *Méthodes statistiques en télédétection RSO polarimétrique haute résolution pour la modélisation et le suivi temporel des glaciers.* Université de Rennes, IETR, GIPSA-lab, 2012.

[78] E. Erten, A. Reigber, O. Hellwich, and P. Prats. Glacier Velocity Monitoring by Maximum Likelihood Texture Tracking. *IEEE Transactions on Geoscience and Remote Sensing*, 47(2) :394–405, 2009.

[79] O. Harant, L. Bombrun, G. Vasile, L. Ferro-Famil, and M. Gay. Displacement estimation by maximum-likelihood texture tracking. *Selected Topics in Signal Processing, IEEE Journal of*, 5(3) :398 –407, june 2011.

[80] A. Papoulis. *Probability, Random Variables, and Stochastic Processes.* 4th ed. Singapore : McGraw-Hill, 2002.

[81] O. Harant, L. Bombrun, G. Vasile, L. Ferro-Famil, R. Fallourd, M. Gay, E. Trouvé, J.M. Nicolas, and F. Tupin. Fisher pdf for maximum likelihood texture tracking with high resolution polsar data. In *8th European Conference on Synthetic Aperture Radar, EUSAR '10*, 2010.

[82] O. Harant, L. Bombrun, G. Vasile, M. Gay, and L. Ferro-Famil. Maximum likelihood texture tracking in highly heterogeneous polsar clutter. In *IGARSS*, 2010.

[83] N. Longepe, S. Allain, L. Ferro-Famil, E. Pottier, and Y. Durand. Snowpack characterization in mountainous regions using c-band sar data and a meteorological model. *Geoscience and Remote Sensing, IEEE Transactions on*, 47(2) :406 –418, feb. 2009.

[84] E. Brun, P. David, M. Sudul, and G. Brunot. A numerical model to simulate snowcover stratigraphy for operational avalanche forecasting. *Journal of Glaciology*, 128 :13–22, 1992.

[85] V. Vionnet, E. Brun, S. Morin, A. Boone, S. Faroux, P. Le Moigne, E. Martin, and J.-M. Willemet. The detailed snowpack scheme crocus and its implementation in surfex v7.2. *Geoscientific Model Development*, 5(3) :773–791, 2012.

[86] Xuan Vu Phan. *Assimilation de données radar satellitaires dans un modèle de métamorphisme de la neige.* PhD thesis, Université de Rennes IETR, GIPSA-lab, CEN, March 2014.

[87] A. Stogryn. The bilocal approximation for the effective dielectric constant of an isotropic random medium. *Antennas and Propagation, IEEE Transactions on*, 32(5) :517 – 520, may 1984.

[88] H. Wang, J. Pulliainen, and M. Hallikainen. Correlation functions and correlation lengths for dry snow. *Journal of Electromagnetic Waves and Applications*, 12(10) :1337–1347, 1998.

[89] George Hufford. A model for the complex permittivity of ice at frequencies below 1 THz. *International Journal of Infrared and Millimeter Waves*, 12(7) :677–682, 1991.

[90] A. Martini. *Télédétection d'un couvert neigeux en milieux alpins à partir de données SAR polarimétriques multi-fréquentielles et multi-temporelles.* PhD thesis, Université de Rennes 1, 2005.

[91] Ya-Qiu Jin. *Electromagnetic Scattering Modeling for Quantitative Remote Sensing.* World Scientific Pub Co Inc, 1994.

[92] W. Huining, J. Pulliainen, and M. Hallikainen. Effective permittivity of dry snow in the 18 to 90 ghz range. *Progress In Electromagnetics Research*, 24 :119 –138, 1999.

[93] L. Tsang, J. A. Kong, and R. T. Shin. *Theory of microwave remote sensing.* Wiley-Interscience, New York, 1985.

[94] F. T. Ulaby, R. K. Moore, and A. K. Fung. *Microwave remote sensing : Active and passive. Volume II - Radar Remote Sensing and Surface Scattering and Emission Theory.* Addison-Wesley, 1981.

[95] A.K. Fung, Z. Li, and K.S. Chen. Backscattering from a randomly rough dielectric surface. *Geoscience and Remote Sensing, IEEE Transactions on*, 30(2) :356 –369, mar 1992.

[96] Tzong-Dar Wu, K.S. Chen, Jiancheng Shi, and A.K. Fung. A transition model for the reflection coefficient in surface scattering. *Geoscience and Remote Sensing, IEEE Transactions on*, 39(9) :2040 –2050, sep 2001.

[97] A.K. Fung and K.S. Chen. An update on the iem surface backscattering model. *Geoscience and Remote Sensing Letters, IEEE*, 1(2) :75 – 77, april 2004.

[98] N. Longepe. *Apport de l'Imagerie SAR Satellitaire en Bandes L et C pour la Caractérisation du Couvert Neigeux.* PhD thesis, Université de Rennes 1, 2008.

[99] Xuan-Vu Phan, Laurent Ferro-Famil, Michel Gay, Yves Durand, and Marie Dumont. Comparison between DMRT simulations for multilayer snowpack and data from NoSREx report. In *Geoscience and Remote Sensing Symposium (IGARSS), 2014 IEEE International*, pages 5040–5043. IEEE, 2014.

[100] X. V. Phan, L. Ferro-Famil, M. Gay, Y. Durand, M. Dumont, S. Morin, S. Allain, G. D'Urso, and A. Girard. 1d-Var multilayer assimilation of X-band SAR data into a detailed snowpack model. *The Cryosphere*, 8(5) :1975–1987, October 2014.

[101] Ian Bartholomew, Peter Nienow, Douglas Mair, Alun Hubbard, Matt A King, and Andrew Sole. Seasonal evolution of subglacial drainage and acceleration in a Greenland outlet glacier. *Nature Geoscience*, 3(6) :408–411, 2010.

[102] Wilfried Haeberli, Martin Hoelzle, Frank Paul, and Michael Zemp. Integrated monitoring of mountain glaciers as key indicators of global climate change : the European Alps. *Annals of Glaciology*, 46(1) :150–160, 2007.

[103] Shilong Piao, Philippe Ciais, Yao Huang, Zehao Shen, Shushi Peng, Junsheng Li, Liping Zhou, Hongyan Liu, Yuecun Ma, Yihui Ding, and others. The impacts of climate change on water resources and agriculture in China. *Nature*, 467(7311) :43–51, 2010.

[104] TAN Redpath, P Sirguey, SJ Fitzsimons, and A Kaab. Accuracy assessment for mapping glacier flow velocity and detecting flow dynamics from ASTER satellite imagery : Tasman Glacier, New Zealand. *Remote Sensing of Environment*, 133 :90–101, 2013.

[105] Jay Gao and Yansui Liu. Applications of remote sensing, GIS and GPS in glaciology : a review. *Progress in Physical Geography*, 25(4) :520–540, 2001.

[106] Adina E Racoviteanu, Mark W Williams, and Roger G Barry. Optical remote sensing of glacier characteristics : a review with focus on the Himalaya. *Sensors*, 8(5) :3355–3383, 2008.

[107] Etienne Berthier, Yves Arnaud, David Baratoux, C Vincent, and F Rémy. Recent rapid thinning of the Mer de Glace glacier derived from satellite optical images. *Geophysical Research Letters*, 31(17), 2004.

[108] Surface motion of mountain glaciers derived from satellite optical imagery. *Remote Sensing of Environment*, 95(1) :14–28, March 2005.

[109] Andreas Kaab. Monitoring high-mountain terrain deformation from repeated air-and spaceborne optical data : examples using digital aerial imagery and ASTER data. *ISPRS Journal of Photogrammetry and remote sensing*, 57(1) :39–52, 2002.

[110] Ponton Fanny. *Mesure de la variabilité de dépla- cement 3D de glaciers alpins par GNSS et imagerie radar satellitaire.* PhD thesis, Université de Grenoble IsTerre, Gipsa-lab, Listic, November 2013.

[111] Renaud Fallourd. *Suivi des glaciers alpins par combinaison d'informations hétérogènes : images SAR Haute Résolution et mesures terrain.* PhD thesis, Université de Grenoble, 2012.

[112] Ivan Pétillot, Emmanuel Trouvé, Philippe Bolon, Andreea Julea, Yajing Yan, Michel Gay, and J-M Vanpé. Radar-coding and geocoding lookup tables for the fusion of GIS and SAR data in mountain areas. *Geoscience and Remote Sensing Letters, IEEE*, 7(2) :309–313, 2010.

[113] I Pétillot. *Combinaison d'informations hétérogènes : Intégration d'images RSO pour la surveillance des glaciers alpins.* PhD thesis, Université de Savoie, 2008.

[114] Yajing Yan. *Fusion de mesures de déplacement issues d'imagerie SAR : Application aux modélisations séismo-volcaniques.* PhD thesis, Université de Savoie, 2012.

[115] Kazuki Nakamura, Koichiro Doi, and Kazuo Shibuya. Estimation of seasonal changes in the flow of Shirase Glacier using JERS-1/SAR image correlation. *Polar Science*, 1(2) :73–83, 2007.

[116] Renaud Fallourd, Olivier Harant, Emmanuel Trouvé, J-M Nicolas, Michel Gay, Andrea Walpersdorf, J-L Mugnier, Jonathan Serafini, Diana Rosu, Lionel Bombrun, and others. Monitoring temperate glacier displacement by multi-temporal TerraSAR-X images and continuous GPS measurements. *Selected Topics in Applied Earth Observations and Remote Sensing, IEEE Journal of*, 4(2) :372–386, 2011.

[117] Brian Anderson, Andrew Mackintosh, Dorothea Stumm, Laurel George, Tim Kerr, Alexandra Winter-Billington, and Sean Fitzsimons. Climate sensitivity of a high-precipitation glacier in New Zealand. *Journal of Glaciology*, 56(195) :114–128, 2010.

[118] PW Nienow, AL Hubbard, BP Hubbard, DM Chandler, DWF Mair, MJ Sharp, and IC Willis. Hydrological controls on diurnal ice flow variability in valley glaciers. *Journal of Geophysical Research : Earth Surface*, 110(F4), 2005.

[119] Andrew Shepherd, Alun Hubbard, Peter Nienow, Matt King, Malcolm McMillan, and Ian Joughin. Greenland ice sheet motion coupled with daily melting in late summer. *Geophysical Research Letters*, 36(1), 2009.

[120] Fanny Ponton, Emmanuel Trouve, Michel Gay, Andrea Walpersdorf, Renaud Fallourd, Jean-Marie Nicolas, Flavien Vernier, and Jean-Louis Mugnier. Observation of the Argentière Glacier Flow Variability from 2009 to 2011 by TerraSAR-X and GPS Displacement Measurements. *IEEE Journal of Selected Topics in Applied Earth Observations and Remote Sensing*, 7(8) :3274–3284, August 2014.